

Dissertation zur Erlangung des Doktorgrades der Fakultät für  
Chemie und Pharmazie der Ludwig-Maximilians-Universität  
München

# **Atomic Layer Deposition for Energy Conversion and Storage Applications**

**Sebastian Häringer**

aus

Landau a. d. Isar, Deutschland

2023



## **Erklärung**

Diese Dissertation wurde im Sinne § 7 der Promotionsordnung vom 28. November 2011 von Herrn Prof. Dr. Thomas Bein betreut.

### **Eidesstattliche Versicherung**

Diese Dissertation wurde eigenständig und ohne unerlaubte Hilfe bearbeitet.

Dingolfing, den 17.10.2023

.....  
Sebastian Häringer

Dissertation eingereicht am: 17.10.2023

Erstgutachter: Prof. Dr. Thomas Bein

Zweitgutachter: Prof. Dr. Dina Fattakhova-Rohlfing

Mündliche Prüfung am: 22.02.2024

## Danksagung

Zu Beginn meiner Dissertation möchte ich mich bei all den wichtigen Menschen bedanken, ohne die das Erlangen meines Doktorgrades niemals zu Stande gekommen wäre.

Als Erstes möchte ich mich ganz herzlich bei meinem Doktorvater Professor Thomas Bein bedanken. Danke Thomas, für die Möglichkeit in deiner Arbeitsgruppe an so vielen verschiedenen Themen mit größter wissenschaftlicher Freiheit und unter Nutzung diverser Ressourcen und Methoden zu arbeiten. Dieser "Fuhrpark" sucht Seinesgleichen und ermöglichte mir nahezu alle wissenschaftlichen Problemstellungen selbstständig auf das Genaueste zu untersuchen. Meiner Meinung nach, eine optimale Vorbereitung für das weitere Berufsleben.

Desweiteren möchte ich Professor Dina Fattakhova-Rohlfing danken. Obwohl ich nicht direkt zu ihren Studenten gehörte und doch etwas geografische Distanz zwischen uns war, hatte sie immer ein offenes Ohr für meine wissenschaftlichen Probleme und diskutierte Lösungsvorschläge immer auf Augenhöhe. Vielen Dank für die gemeinsamen Projekte und die Übernahme des Zweitgutachtens.

Eingefädelt hat dieses große Projekt meines Lebens Dr. Alexander Hufnagel. Er nahm mich in 2016 als F-Praktikant auf, lehrte mich in den Künsten der Atomlagenabscheidung und zeigte mir die schönsten Seiten des AK Beins. Durch seine Begeisterung für die ALD und sein Engagement konnte ich dann meine Masterarbeit auf diesem Themengebiet anschließen und sein Erbe in Form meiner Doktorarbeit antreten. Vielen Dank für deine Geduld mir mir, deine Zeit und deine Freundschaft!

Noch niemand hat die Welt alleine gerettet, deshalb ist es umso wichtiger nach links und rechts zu schauen und sich gemeinsam um die großen Probleme zu kümmern. Vielen Dank an all meine Projektpartner, die mich auf ihren spannenden Reisen mitgenommen haben und meinen Blickwinkel ein um das andere Mal verändert haben.

Eine Gruppe von der Größe des AK Bein braucht immer einige Leute, die das Gefüge zusammen und den Kollegen den Rücken freihalten. Daher geht mein Dank an Tina Reuther für die exzellente Organisation der Ver- und Entsorgung, aller Bestellungen und der notwendigen Überwachung der sicherheitsrelevanten Regeln. Ebenfalls bedanken möchte ich mich bei Corinna Heidt, für ihr offenes Ohr, den Überblick über Anträge, Fristen und Verträge und ihr Engagement innerhalb der Gruppe. Nicht zu vergessen, einen herzlichen Dank an Steffen Schmidt, der sich hervorragend um die elektronenmikroskopische Geräte kümmert und als Anlaufstelle für Probleme zur Verfügung steht.

Große Ehre wurde mir zuteil, als ich in die beste Subgroup des AKs aufgenommen

wurde. Die Jünger Moses, dem ersten Wasserspalter, waren immer unglaublich kollegial, engagiert, hilfsbereit und in Notfällen kann man immer auf sie zählen. Vielen Dank an Chrissi, Daniel, Peter, Michi, Jonathan, FloZ, Melisande, Jenny und Markus für eure Hilfe und die tolle Zeit. In diesem Zuge möchte ich mich speziell bei Michi und Markus für die ausdauernden TEM-Messungen bedanken, ohne die diese Arbeit so nicht möglich gewesen wäre.

Während der Zeit als Doktorand erweitert man sein Wissen auf verschiedensten Gebieten ständig. Schade wäre es, wenn dieses Wissen nach Abschluss der Arbeit auch wieder verloren geht. Deshalb ist ein elementarer Teil der Doktorarbeit auch die Ausbildung der kommenden Generation von Chemikern. Vielen Dank an meine fleißigen und wissbegierigen Praktikanten, Bacheloranden und Masteranden, darunter Yao, Chris, Kathryn, Vivian, Andreas, Meli und Quirin. Ich hoffe ihr könnt das bei mir Gelernte auch in eurer Zukunft weiterhin gebrauchen und anwenden. Besonderer Dank geht an Quirin. Vermittelt von Peter, führte er bei mir seine Bachelorarbeit, sein F-Praktikum und nun auch seine Masterarbeit durch. Durch seinen Fleiß, seine Selbstständigkeit und sein schnelles Auffassungsvermögen hat er einen großen Beitrag zu verschiedenen Projekten geleistet.

In jeder größeren Gruppe gibt es Menschen, mit denen man sich versteht, mal mehr und mal weniger. Dann gibt es aber auch diejenigen, wo sich aus Sympathie, gemeinsamen Interessen und ähnlichen Wertvorstellungen auch eine Freundschaft über die Arbeit hinaus entwickeln kann. Zeit mit diesen Kollegen und Freunden zu verbringen, sei es im wissenschaftlichen Austausch, beim Spinnen neuer Hirngespinnste, Erkundungstouren am Campus oder aber auch einfach ohne triftigen Grund, habe ich als sehr wertvoll empfunden und möchte mich deshalb bei FloZ, Michi, Andreas, Ed, Meli, Roman, Niklas, Sabrina, Daniel, Stephan, Marcella, Peter, Derya, Berni, FloG, Andi J. und Z., Anderson und Lisa sehr herzlich bedanken. Ihr habt mir die Zeit im AK Bein versüßt.

Natürlich möchte ich mich auch bei allen, nicht persönlich Genannten vom AK Bein für die meist nette und produktive Atmosphäre bedanken. Die letzten eineinhalb Jahre waren nicht leicht, da natürlich auch die sozialen Aspekte der Universität sehr unter der Pandemie gelitten haben. Umso wichtiger ist es, sich für den Zusammenhalt innerhalb der Gruppe einzusetzen und sich an allen Aufgaben zu beteiligen.

Der größte Dank gilt meiner Frau und meiner Familie. Diese gaben mir immer die notwendige Sicherheit und volle Unterstützung um Neues auszuprobieren und nach Rückschlägen wieder motiviert weiter zu machen. Gerade in den letzten Monaten bin ich aufopferungsvoll von meiner Frau kulinarisch und seelisch versorgt worden, ich weiß nicht, wie ich es ohne dich geschafft hätte. Ohne euch wäre ich nicht da, wo ich jetzt bin. Danke!

## Abstract

Limitation of global warming and a responsible utilization of available resources is of paramount importance more than ever. Thus motivated, this thesis deals with the development of new materials and innovative concepts for energy conversion applications, with the goal to store the surplus of regenerative energy either in form of chemical bonds in hydrogen or directly in optimized electrochemical energy storage devices.

Common concepts of water electrolysis, photoelectrochemical water-splitting and electrochemical energy storage with differently produced nanostructures will be introduced in Chapter 1. Additionally, as degradation mechanisms often take place on the interface between different materials, atomic layer deposition (ALD) has been proven to be an optimal method to functionalize or stabilize the surface of advanced materials. Large part of presented projects in this thesis will be supported by ALD, due to its unique property to deposit conformal films on porous and high surface area substrates with a precise control over the film thickness. The basic principles of ALD and a short overview of different material classes for energy conversion applications will also be presented in Chapter 1.

Chapter 2 describes the basic principles of characterization methods used in this thesis. Instrumental means of obtaining crystallographic, optical, compositional, morphological and electrochemical information are discussed.

In the first part of this thesis (Chapter 3, 4, 5 and 6), we will deal with different techniques for hydrogen production based on water splitting. In Chapter 3 we develop a novel way for the preparation of a water oxidation catalysts for proton exchange membrane (PEM) electrolysis. In multiple deposition steps we create a highly nanostructured, conductive and oxidation-stable electrode with a low noble metal loading. Using carbon soot as immobilized, nanostructured template, a niobium-doped titania coating is consecutively applied via ALD. After a heating step, the conductive and corrosion-stable support is loaded with an approximately 1 nm thick coating of crystalline  $\text{IrO}_2$ , again by ALD. The resulting electrodes show a high activity towards the oxygen evolution reaction in acidic media despite their ultra low noble metal loading. At the end, different ways for the implementation in a PEM electrolyzer are suggested.

Chapter 4 presents a literature overview of current developments in the field of carbon based oxygen evolution catalysts. These are of great interest due to their huge structural and compositional variety and unrestricted abundance. The first section introduces the concept and mechanism of oxygen evolution catalysis for carbon based materials, highlighting the necessity for modifications of "pure" carbon allotropes. Different concepts for enhancement of stability and activity are elucidated in the following sections, ranging from unintentionally doped carbon over heteroatom-doped carbon compounds and carbon/transition metal compounds to metal oxide composites with carbon being mainly the conductive support. A special focus of this review is on ordered carbon framework structures (metal organic or covalent organic frameworks) which are an emerging class of porous and crystalline materials. Here, certain physical

properties can be envisioned via exchange of structural building blocks.

Chapter 5 and 6 are dedicated to photoelectrochemical water-splitting, either for the oxygen or the hydrogen evolution reaction under light. Therefore, molybdenum-doped bismuth vanadate is used as a photoanode (Chapter 5) and lithium-doped copper oxide (Chapter 6) as photocathode. Both electrode materials suffer from corrosion under working conditions, making a protection of the semiconductor necessary. In these projects different metal oxide coatings have been applied via atomic layer deposition; whereby in both cases an only 2.5 nm thick amorphous layer of niobium-doped titanium oxide led to pin-hole free protection while allowing charge carrier transfer. By means of an additionally applied catalyst, the desired gaseous products could be generated. Detailed studies on the electrochemical performance and corrosion mechanisms are included.

The second part of the thesis deals with different components for electrochemical energy storage using lithium-ions. Chapter 7 describes the promising way of increasing the energy density of batteries by decreasing the overall amount of electrochemically inactive material with freestanding electrodes. Two different strategies are presented to fabricate antimony doped tin oxide (ATO)-based hybrid materials and their usage as anode without additional current collector. Freeze-cast ATO composites with reduced graphene oxide (rGO) demonstrate an impressive rate and cycling performance at loading currents. Finally, a freestanding full cell is obtained by the combination with a freestanding  $\text{LiFe}_{0.2}\text{Mn}_{0.8}\text{PO}_4$ /rGO cathode.

Chapter 8 explores the stabilization effect of a lithium niobate (LNO) protection layer on a lithium cobalt oxide cathode (LCO) in order to extend the cycle life time at higher cut-off potentials. Unprotected LCO undergoes several phase transitions above a certain potential leading to surface degeneration and structure pulverization of the electrode. Atomic layer deposited LNO with an optimized thickness prevents these negative effects, leading to optimized stability.

Last, but not least, in Chapter 9 we enlarge the family of imidazolate-containing covalent organic frameworks (COFs) for the use as lithium-ion solid state electrolyte. We design two new COFs with increased pore size and density of lithium conduction moieties in order to get more insight in conduction behavior and underlying mechanism. Unfortunately, we were not able to confirm literature reports and propose possible reasons for this. Therefore, this work highlights the importance of exact analysis of new material classes before moving to applications.

In conclusion, this thesis shows the great potential of functional enhancements by modification of interfaces either by protection or by functionalization. For this purpose, atomic layer deposition is the method of choice for recent and upcoming challenges in a variety of energy conversion applications.



# Contents

Erklärung . . . . .	iii
Danksagung . . . . .	iv
Abstract . . . . .	vi
<b>1 Introduction</b>	<b>5</b>
1.1 Responsible Handling of Resources . . . . .	5
1.2 Scope of this Thesis . . . . .	7
1.3 Basics of Atomic Layer Deposition: an Overview . . . . .	8
1.3.1 General Principle of ALD . . . . .	8
1.3.2 ALD Growth Characteristics – Linearity, Saturation, and ALD Window . . . . .	9
1.3.3 Types of ALD . . . . .	11
1.3.4 ALD Reactants . . . . .	12
1.3.5 <i>In-Situ</i> Characterization Techniques . . . . .	15
1.4 Atomic Layer Deposition in Energy Conversion Applications . . . . .	16
1.4.1 Water Electrolysis . . . . .	17
1.4.2 Photoelectrochemical Water-Splitting . . . . .	21
1.4.3 Electrochemical Energy Storage . . . . .	28
1.5 References . . . . .	41
<b>2 Methods</b>	<b>57</b>
2.1 X-Ray Diffraction . . . . .	57
2.2 Spectroscopic Ellipsometry . . . . .	57
2.3 Electron Microscopy . . . . .	59
2.3.1 Scanning Electron Microscopy . . . . .	59
2.3.2 Transmission Electron Microscopy . . . . .	61
2.4 UV-Vis Spectroscopy . . . . .	62
2.5 X-Ray Photoelectron Spectroscopy . . . . .	63
2.6 Sorption . . . . .	64
2.7 Hall Effect Measurement with Van der Pauw Method . . . . .	66
2.8 Electrochemical Characterization . . . . .	68
2.8.1 Cyclic Voltammetry (CV) . . . . .	68
2.8.2 Electrochemical Impedance Spectroscopy . . . . .	70
2.8.3 Chronoamperometry and Chronopotentiometry . . . . .	71

<b>3</b>	<b>Carbon-templated Conductive Oxide Supports for Oxygen Evolution Catalysis</b>	<b>75</b>
3.1	Introduction . . . . .	76
3.2	Results and Discussion . . . . .	78
3.2.1	Preparation and Characterization of Carbon Soot Templates . . . . .	78
3.2.2	ALD of NTO Coatings . . . . .	78
3.2.3	ALD of IrO <sub>2</sub> . . . . .	80
3.2.4	Electrode Preparation and Characterization . . . . .	81
3.2.5	Electrochemical Characterization . . . . .	83
3.2.6	Post-mortem Analysis of a Ti/C/NTO/IrO <sub>2</sub> electrode . . . . .	85
3.3	Conclusions and Outlook . . . . .	86
3.4	Experimental Details . . . . .	86
3.4.1	Deposition of Carbon Soot Nanostructures . . . . .	87
3.4.2	ALD of NTO layers . . . . .	87
3.4.3	ALD of IrO <sub>2</sub> layers . . . . .	87
3.4.4	Electrode Characterization . . . . .	88
3.4.5	Electrochemical Characterization . . . . .	88
3.5	References . . . . .	89
3.6	Appendix . . . . .	92
<b>4</b>	<b>Carbonaceous Oxygen Evolution Reaction Catalysts: From Defect and Doping-Induced Activity over Hybrid Compounds to Ordered Framework Structures</b>	<b>99</b>
4.1	Introduction: Catalytic Activity of Pure Carbon Allotropes and Necessity of Heteroatom Doping or Surface Modification . . . . .	100
4.1.1	OER Activity of Undoped Carbon Structures and Necessity of Heteroatom Doping . . . . .	102
4.1.2	OER Activity in Carbon/Transition Metal (Metal Oxide) Composites: Conductive Carbon Matrices and Synergistic Effects . . . . .	107
4.1.3	Stability of Carbon-Based Electrocatalysts under OER Conditions . . . . .	108
4.2	Undoped and Unintentionally Doped Carbon Structures: From Synthesis to Surface Modifications . . . . .	109
4.2.1	Synthesis and Catalytic Activity of Low Doping Level Carbon Materials . . . . .	109
4.2.2	Surface Functionalization . . . . .	114
4.3	Metal-Free, Heteroatom-Doped Carbon Composites . . . . .	116
4.3.1	Single-Atom Doping . . . . .	117
4.3.2	Multiheteroatom Doping . . . . .	121
4.4	Metal (Metal Oxide)/Carbon Hybrids . . . . .	124
4.4.1	TMO/Carbon Composites for OER . . . . .	124
4.4.2	Transition Metal Single-Atom Catalysts (SACs) . . . . .	128
4.4.3	Mixed Metal Oxide/Carbon Composites for OER . . . . .	130
4.4.4	Metal/Metal Oxide/Carbon Composites for OER . . . . .	138

---

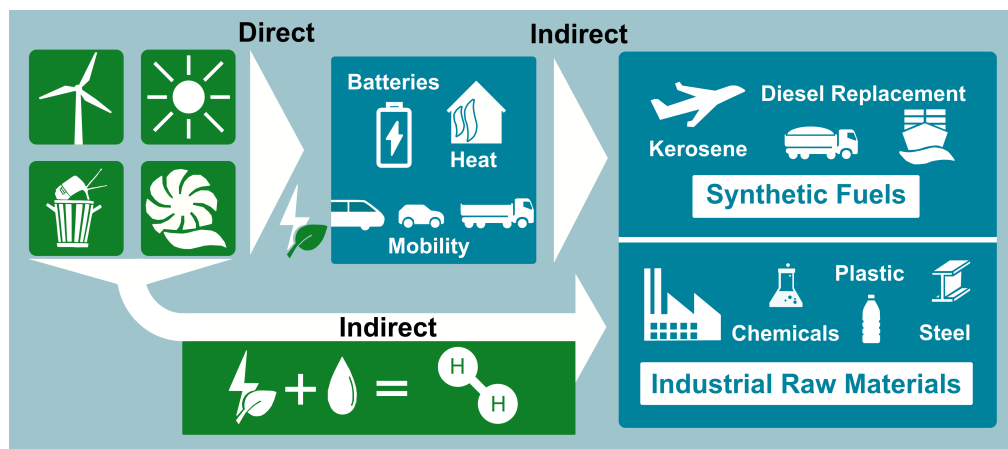
4.5	Carbon-Based Ordered Framework Structures . . . . .	140
4.5.1	MOFs . . . . .	141
4.5.2	COF Structures . . . . .	145
4.6	Conclusion and Perspective . . . . .	150
4.7	Acknowledgements . . . . .	152
<b>5</b>	<b>Ultra-thin Protective Coatings for Sustained Photoelectrochemical Water Oxidation with Mo:BiVO<sub>4</sub></b>	<b>165</b>
5.1	Introduction . . . . .	166
5.2	Results and Discussion . . . . .	169
5.2.1	Electrode Preparation . . . . .	169
5.2.2	Optical Characterization . . . . .	171
5.2.3	Structural Characterization . . . . .	171
5.2.4	Electrochemical Characterization . . . . .	172
5.3	Conclusion . . . . .	175
5.4	Experimental Section . . . . .	175
5.5	References . . . . .	177
5.6	Appendix . . . . .	180
<b>6</b>	<b>How Photocorrosion Can Trick You: a Detailed Study on Low-bandgap Li doped CuO Photocathodes for Solar Hydrogen Production</b>	<b>187</b>
6.1	Introduction . . . . .	188
6.2	Results and Discussion . . . . .	190
6.3	Conclusion . . . . .	198
6.4	References . . . . .	199
6.5	Appendix . . . . .	204
6.5.1	Experimental Details . . . . .	204
6.5.2	Additional Figures . . . . .	208
<b>7</b>	<b>Overcoming the Challenges of Freestanding Tin Oxide-based Composite Anodes to Achieve High Capacity and Increased Cycling Stability</b>	<b>223</b>
7.1	Introduction . . . . .	224
7.2	Results and Discussion . . . . .	226
7.3	Conclusion . . . . .	239
7.4	Experimental Section . . . . .	240
7.5	References . . . . .	242
7.6	Appendix . . . . .	246
<b>8</b>	<b>Protection of Lithium Cobalt Oxide by Atomic Layer Deposition of Lithium Niobate for High-Voltage Cycling</b>	<b>261</b>
8.1	Introduction . . . . .	262
8.2	Results and Discussion . . . . .	264
8.2.1	ALD of Lithium Niobate Coatings . . . . .	264

8.2.2	Characterization of LNO-coated LCO . . . . .	265
8.2.3	Electrochemical Characterization . . . . .	266
8.2.4	Post-mortem analysis . . . . .	272
8.3	Conclusions and Outlook . . . . .	273
8.4	Experimental Details . . . . .	273
8.5	References . . . . .	275
8.6	Appendix . . . . .	278
<b>9</b>	<b>Enlarging the Imidazolate-based COF family for Lithium-Ion Conduction</b>	<b>287</b>
9.1	Introduction . . . . .	288
9.2	Results and Discussion . . . . .	290
9.3	Conclusions and Outlook . . . . .	294
9.4	Experimental Details . . . . .	294
9.5	References . . . . .	295
9.6	Supporting Information . . . . .	297
<b>10</b>	<b>Conclusions and Outlook</b>	<b>315</b>
	<b>Publications and Conference Contributions</b>	<b>317</b>

# 1 Introduction

## 1.1 Responsible Handling of Resources

On 12 December 2015, 196 parties signed the Paris Agreement as a legally binding international treaty on climate change in order to limit global warming to 1.5 °C in year the 2050 compared to pre-industrial levels.<sup>[1]</sup> The hope is to avoid irreversible tipping points in this way, such as the melting of the permafrost or the weakening of the Gulf Stream. With the adoption of the Kyoto Protocol in the year 1997,<sup>[2]</sup> efforts have been made to reduce greenhouse gas emissions, but with the new budgets based on the limitation of the global temperature rise below 2 °C, if possible to 1.5 °C, a significant tightening of the target is represented and a strong recalibration and acceleration of the associated reductions and the planned measures is required.



**Scheme 1.1:** Schematic presentation of direct and indirect electrification possibilities. Here, electricity from renewable energy technologies such as solar energy, wind power, hydroelectric power or biomass is either consumed directly or takes an indirect conversion step to hydrogen. In a second step, this green hydrogen can then be used to produce synthetic fuels or industrial raw materials.

In the context of Germany, the current decision of the Bundesverfassungsgericht (BVG) on the climate protection act is expected to have a significant influence on politics.<sup>[3]</sup> According to court ruling, it is essentially forbidden to shift responsibility for combating climate change to the next generation, which, due to the lack of effec-

tiveness of current measures has increasingly less room for maneuver and would have to fear a significant threat to constitutionally guaranteed freedoms.

This judgement represents a turning point for the previous approach. It justifies the need to implement measures with significant greenhouse gas reduction potential more quickly and more comprehensively than previously planned, for the benefit of future generations. The judgement is ultimately based on the fact that emission saved today is more valuable than one saved tomorrow; this will expand the future room for maneuver. In order to achieve Germany's climate protection goals, it needs technologies and products that replace fossil fuels previously used in the areas of industry, transport, electricity and heating.

Especially in the end-use sectors of buildings, transport and industry, a systematic changeover in energy sources by direct and indirect electrification must take place by 2030 in order to adapt the course to climate neutrality in 2045.<sup>[4]</sup> Notably, the decarbonization of electricity supply can be achieved much faster than that of the non-electrical energy supply.<sup>[4]</sup> The way to renewable energies via direct electrification is characterized by a particularly high conversion efficiency and in addition, many electrifying technologies are already available and are steadily gaining market share (e.g., battery electric vehicles and heat pumps). However, improvements of technologies in the battery sector are desired in order to compete with long-term existing fossil-fuel vehicles. Besides minimizing costs, the focus lies on abundant, stable and safe materials for the use in the transport sector.

In addition to direct electrification, indirect electrification of energy supply via renewable hydrogen and e-fuels plays an important role. The use of renewables via hydrogen and e-fuels is particularly relevant for the production of primary steel, materials used in chemical industry and end uses that are difficult to electrify, such as high-temperature processes or air traffic. In addition, the flexible generation of hydrogen can make a significant contribution to the integration of fluctuating renewable electricity surplus. However, in comparison to the direct electrification, indirect electrification with hydrogen and e-fuels is still in its infancy. A core challenge is the lack of competitiveness. This is partly due to high efficiency losses and high costs that arise along the comparatively long conversion chains and are associated with a significantly increased demand for electricity. A striking example of this is the traffic sector, where the electricity requirement per driven kilometer is around five times higher for e-fuels than for battery-electric vehicles.<sup>[5]</sup> The main advantage of hydrogen and e-fuels is that in some applications they can go beyond the limits of electrification, for example for ammonia production, primary steel production, basic chemicals as well as air and shipping traffic. According to the FORECAST sector model, the industrial sector in

Germany will need around 40 TWh of hydrogen in 2030.<sup>[4]</sup>

In order to be able to meet Germany's demand for green hydrogen, in 2020 the government adopted and published the national hydrogen strategy where the cost-efficient production, infrastructure implementation and upscaling of hydrogen plants for the future are funded.<sup>[6]</sup> Research and development of materials for the direct and especially for the indirect electrification is of key importance and will be described in the following chapters.

## 1.2 Scope of this Thesis

In the field of energy conversion applications ranging from (photo)electrocatalysis to batteries, the interface between different phases plays a crucial role for the efficiency and stability. The change of surface area by nanostructuring or the modification of the surface by ultrathin films offers the possibility to overcome problems and limitations of energy conversion and energy storage devices. This thesis details progress made in the fields of oxygen evolution catalysis, photoelectrochemical water-splitting and lithium-ion batteries enabled by the utilization of thin and ultrathin conformal oxide films prepared by atomic layer deposition (ALD), nanostructuring of metal oxides and their combination. It further describes the theoretical background, working principles, challenges, practical aspects and state-of-the-art of ALD with special emphasis on its applications towards oxygen evolution catalysis (OER), photoelectrochemical (PEC) water-splitting and lithium-ion batteries (LIBs). In a later chapter, the progress in the field of carbon-based catalysts for the oxygen evolution reaction will be summarized. Additionally, special focus lies on the development of new materials for lithium-ion batteries and the challenges for their successful design and characterization.

## 1.3 Basics of Atomic Layer Deposition: an Overview

### 1.3.1 General Principle of ALD

Atomic layer deposition is a self-limiting growth technique for production of thin films based on the alternating exposure of two gaseous precursors and their exclusive self-saturating reactions with the surface of the pristine substrate and the growing film, resulting in the sequential deposition of (sub)monolayers.<sup>[7,8]</sup> In the 1960s, first fundamental works on ALD, back then called "Molecular Layering", were carried out in Russia by Aleskovskii and co-workers.<sup>[9,10]</sup> Related developments were pursued in the 1970s by Suntola and his Finnish co-workers for the growth of luminescent ZnS and Al<sub>2</sub>O<sub>3</sub> insulator films for electroluminescent flat-panel displays.<sup>[11,12]</sup> They introduced the name "atomic layer epitaxy" (ALE) for this kind of controlled growth. With the decreasing device dimensions in microelectronics, the deposition of high-k oxides became more and more attractive in the 1990s, leading to the investigation of the controlled growth of several other material by ALD. It was around the year 2000, when the term ALE was changed to ALD, as most of the ALD-grown materials were found to be amorphous, without showing any epitaxial structure related to the underlying substrates.<sup>[13]</sup> Since then, a wide range of different ALD processes for oxides, nitrides, chalcogenides and metals have been developed.<sup>[8,14]</sup>

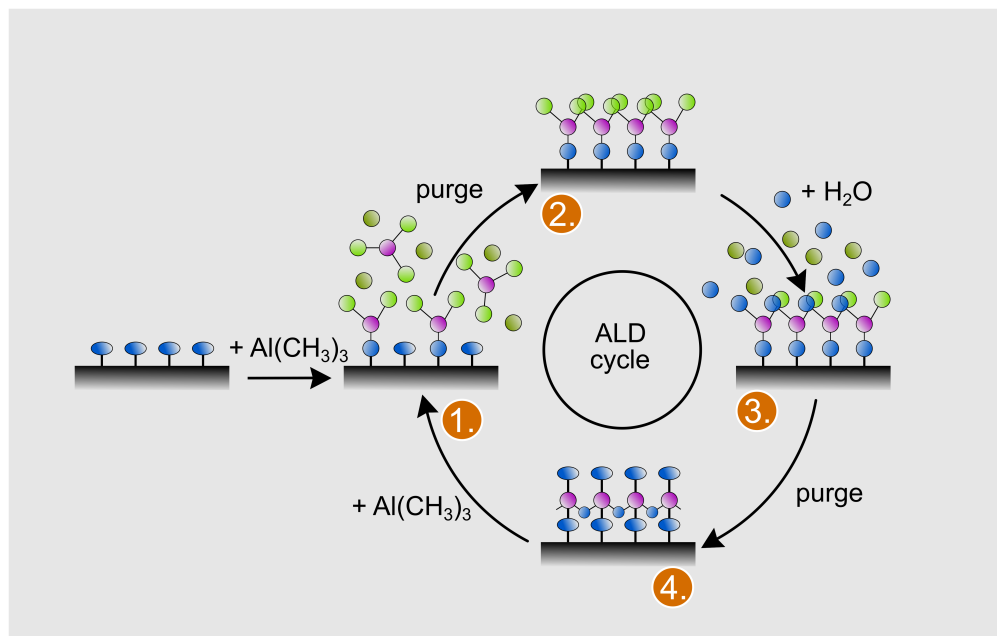


**Figure 1.1:** Basic principle of ALD, illustrated by the process for deposition of Al<sub>2</sub>O<sub>3</sub> using TMA and H<sub>2</sub>O.

In contrast to other chemical vapour deposition methods (like CVD or PVD), ALD relies on at least two self-limiting gas-solid reactions, i.e., chemisorption reactions, enabling the uniform coating of high aspect ratio structures.<sup>[7,8]</sup> These reaction steps are separated by the removal of unreacted precursors and side-products from the reaction chamber. By this, one ALD cycle typically consists of four steps as illustrated in Figure 1.1. For didactic reasons, the probably most studied ALD process, the deposition of aluminium oxide from trimethylaluminium (TMA,  $\text{Al}(\text{CH}_3)_3$ ) and water, is used to exemplify the basic principle of ALD.<sup>[15]</sup> First, TMA is introduced into the reactor and a reaction between TMA and the reactive sites, e.g., terminating hydroxyl groups on the surface of oxides, starts taking place (step 1). Once all accessible OH groups have been consumed, the remaining unreacted precursor and the gaseous by-products are removed from the reaction chamber (step 2). After this, the second reactant, typically a non-metal reactant (here  $\text{H}_2\text{O}$ ), is pulsed into the reactor (step 3) hydrolyzing the previously formed  $-\text{O}-\text{Al}(\text{CH}_3)_2$  surface-bound moieties. After the removal of excess water and by-products once again (step 4), a (sub)monolayer of  $\text{Al}_2\text{O}_3$  is grown in the optimal case. By repetition of this cycle, thicker films can be grown.<sup>[7,15]</sup>

Most of the time, a full and dense monolayer can't be achieved in one cycle due to the steric hindrance of bulky precursor molecules shielding other possible reactive sites from additional precursor. As a consequence, a thickness control down to sub-monolayer coverage is achieved, which can be of key importance for the synthesis of supported catalysts.<sup>[8]</sup> Additionally, as the growth is limited by available surface sites and not by mass transport, all surfaces can be coated conformally and with (nearly) equal thickness, making ALD a strong and unique tool for changing the surface properties of advanced materials.

### 1.3.2 ALD Growth Characteristics – Linearity, Saturation, and ALD Window

In an ideal ALD process, the amount or thickness of deposited material increases linearly with the number of ALD cycles. This "growth per cycle" or GPC reflects the amount of material deposited per ALD cycle and is not so much dependent on the chemical reaction kinetics during the deposition process but determined by the number of reactive surface sites and the steric hindrance of the ligands.<sup>[8,15]</sup> The first ALD cycles occur on the surface of the starting substrate and the ALD-grown material and tend to delay the linearity of GPC, but after a sufficient number of ALD reaction cycles the GPC is expected to settle to a constant value. The starting of ALD growth is strongly dependent on the surface and can be divided in four different types, namely *linear growth*, *substrate-enhanced growth* and *substrate-inhibited growth* (type 1 and type

2).<sup>[15]</sup>

For achieving a linear ALD growth in a self-terminating gas-solid reaction, the saturation of all accessible sites is necessary. With the change of exposure time of both precursor doses, a constant GPC should be reached (Figure 1.2).<sup>[15]</sup> If no saturation can be observed, the ALD process has partial CVD character or the gas-solid reaction relies not only on irreversible adsorption. For the second case, an elongation of precursor residence time in the reactor allowing a termination of the adsorption reaction may help to achieve completion.<sup>[15]</sup>

In contrast to CVD, ALD shows only a weak temperature dependence and within a certain temperature window, the so-called "ALD window", a temperature independent growth per cycle can be observed. The ALD window is limited by excessively low temperatures, where the lack of thermal energy restricts the irreversible gas-solid surface reaction.<sup>[7,8,15]</sup> In rare cases, a distinctly faster growth is observed, related to multilayer physisorption of the precursor on the surface.

At high temperatures, thermal decomposition of the precursor on the hot surface leads to an increasing GPC. Additionally, thermal desorption of chemisorbed species can lead to a decreased GPC. In some cases, although self-saturating chemisorption is reached within the ALD window, a decrease in GPC can be observed because of the lower amount of reactive sites on the growth surface for increasing temperatures.<sup>[7,8,15]</sup>

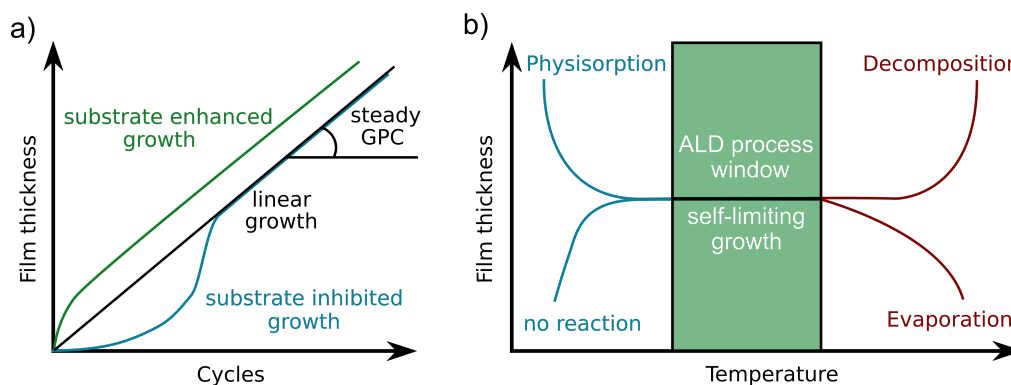


**Figure 1.2:** Function of the linear increase of film thickness as a number of ALD cycles (a) and temperature window (b).

In general, several different ways regarding how the deposited material is arranged on the surface during ALD growth are possible. These are described as growth modes. By the definition of ALD, where multilayer adsorption is excluded, a *two-dimensional growth* is expected for the growth of a full monolayer per cycle.<sup>[16,17]</sup> Here, a layer-by-layer growth can be observed, where the deposited material always settles in the lowest unfilled material layer and a complete coverage of the substrate is achieved.

However, in most ALD processes this growth mode is not quite valid.<sup>[15]</sup> Especially in the first cycles of ALD, an *island growth* can be observed, where the new material units are preferentially deposited on the ALD-grown material. This type of growth can be nicely utilized in the field of catalysis, where a very thin distribution of sometimes expensive catalyst on a supporting material can be realized.<sup>[16–18]</sup> It is clear that island growth may change to another growth mode, when the islands have coalesced into a continuous layer. In addition to the aforementioned commonly occurring modes, a *random deposition* as third growth mode is also possible. Here, the material units are deposited with an equal probability on all surface sites.<sup>[19,20]</sup> Figure 1.3 shows the three different deposition modes schematically.

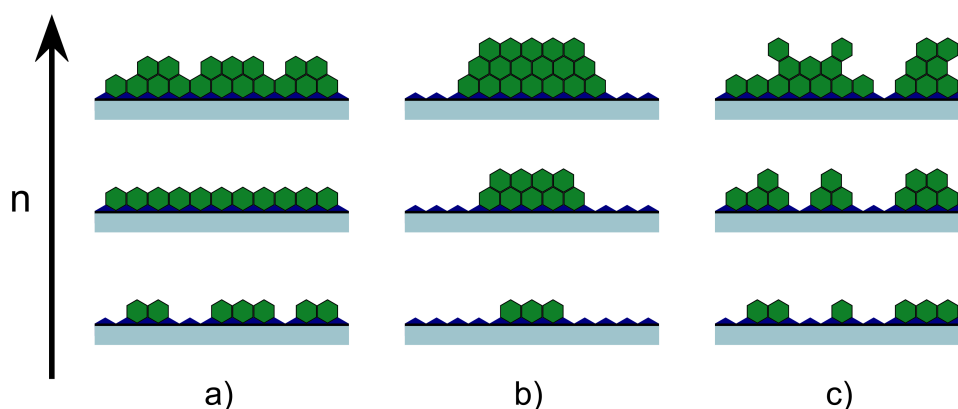


**Figure 1.3:** Schematic illustration with increasing cycle number  $n$  of *two-dimensional growth* (a), *island growth* (b) and *random deposition* (c).

### 1.3.3 Types of ALD

In general, a distinction between three different types of ALD processes is possible: thermal ALD, catalytic ALD and plasma-enhanced ALD (PE-ALD).<sup>[7,8,15,21]</sup> These differ mainly in the driving force for the self-limiting gas-solid reaction. In the case of thermal ALD, the two precursor reactions are driven by the formation of thermodynamically favored surface species and volatile byproducts. The desired gas-solid reactions should be highly exothermic processes to ensure the irreversibility of the process. Many different compounds are accessible via thermal ALD, including noble metals, metal oxides, nitrides and chalcogenides. Advantages include the easy implementation of the ALD process compared to the other types. However, for thermal ALD there are also some drawbacks, as not all materials are accessible and a certain amount of impurities can't be excluded through small CVD contributions to the material deposition.<sup>[7]</sup>

The second type of process, catalytic ALD, is much less known and is rarely used due to its complexity. Here, between the two commonly used precursor pulses, a gaseous catalyst reagent is added to facilitate surface reactions at low temperatures. This kind of ALD process is very interesting for the deposition on thermally fragile substrates (e.g., electronic components, polymers or biological samples) and is mainly used for the growth of SiO<sub>2</sub> utilizing pyridine or ammonia as Lewis base catalyst.<sup>[7,21]</sup>

Plasma-enhanced ALD (PE-ALD) also bypasses the need of thermal energy as driving force for the gas-solid surface reaction by utilization of a preactivated reactant obtained by means of a plasma source. Typical plasmas are generated by the introduction of the co-reactant (e.g., O<sub>2</sub>, H<sub>2</sub>, N<sub>2</sub>, and NH<sub>3</sub> or combinations of these) into an inductively or capacitively coupled or microwave-induced Ar plasma zone. Any excited electrons in the plasma gas are able to transfer their energy to the co-reactant molecules, causing ionization, excitation or dissociation thus yielding electrons, ions, radicals and photons. The generated radicals or other energetic species in the plasma induce the reactions with the adsorbed precursor species that are not possible using thermal energy.<sup>[7,21]</sup>

The main advantages of PE-ALD compared to conventional thermal ALD include a higher film density with lower impurity content, a better stoichiometry of target compounds and resulting improved electronic properties. Additionally, the auxiliary energy of the radicals enables the deposition at lower substrate temperatures and increases the choice of precursors for the deposition of a specific coating, due to the different gas-solid reaction mechanisms.<sup>[7,21]</sup>

Obviously, there are also specific disadvantages using PE-ALD. The highly active radicals easily recombine on contact with solid surfaces, limiting their penetration depth into high aspect ratio structures. Secondly, other plasma components such as ions and UV photons may generate specific defects on sensitive substrates and films. Additionally, as earlier mentioned for catalytic ALD, the use of a plasma increases the complexity of the deposition and requires more complicated and therefore expensive reactor designs.<sup>[7,21]</sup>

### 1.3.4 ALD Reactants

Since the invention of ALD in the 1970s, there has been a lot of research on processes for different target compounds and a huge variety suitable for atomic layer deposition of metals, metal nitrides, fluorides and chalcogenides was found (see Figure 1.4). In general, the deposition of different elements is only possible if the used precursor fulfills several necessary requirements.<sup>[8,15]</sup> First, they need to be gaseous or vaporizable

at elevated temperatures, which need to be lower than the ALD reaction temperature to enable material transportation through the gas phase.

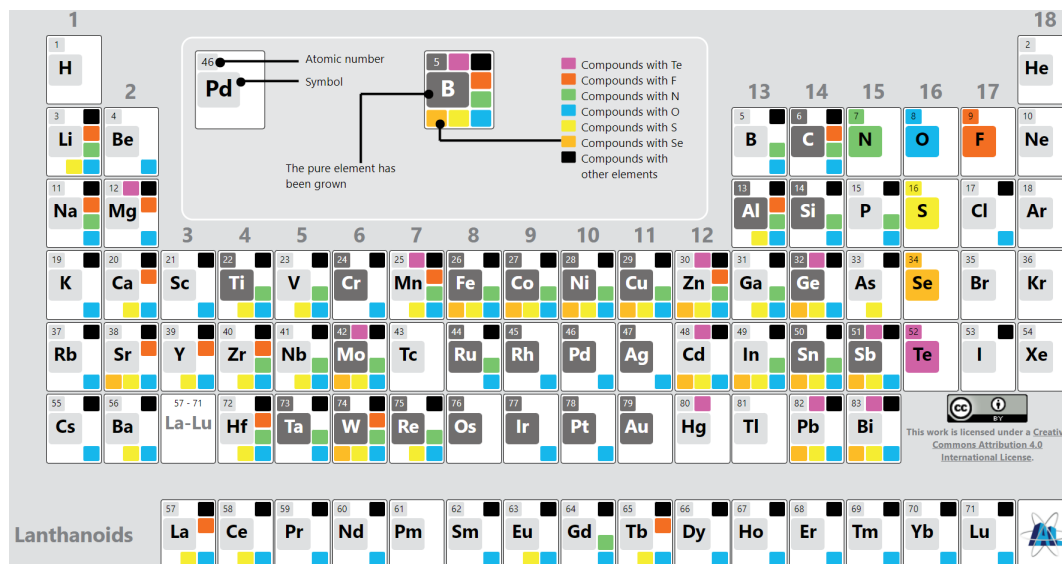


Figure 1.4: Overview of reported possible material combinations by ALD.<sup>[22]</sup>

After arrival in the reactor chamber, the precursor needs to react with the surface sites of the growth substrates in a saturating, irreversible manner and additionally with the subsequent co-reactants. Here, a rapid reaction favoring the side of products is more advantageous. The formed by-products should be inert and not interfere with precursors or ALD growth. The reactants also shouldn't dissolve in the film and must not decompose thermally, neither during the storage, at the sublimation temperature nor at the ALD process temperature in order to prevent impurities in the formed film and to keep good control over the process. For industrial application it is very important that the precursor is safe and easy to handle, preferably non-toxic and non corrosive towards the substrate and the reactor components.<sup>[8,14,15]</sup>

Typically, the combination of a metal and a non-metal containing precursor is used to obtain ALD growth. Metal precursors can be divided into alkyls, alkoxides, cyclopentadienyls,  $\beta$ -diketonates, amides and imides, amidinates, phosphines, silyls, halides and pure elements (see Figure 1.5).<sup>[8,15]</sup> Amongst these, each type offers advantages and disadvantages regarding reactivity, stability, gaseous by-products, handling and impurities left in the film. Depending on the desired application, one should evaluate benefits and drawbacks in order to find the best solution.

For non-metal ALD reactants, there is a much smaller selection compared to metal reactants. For thermal ALD processes, the hydrides of non-metal elements, like water

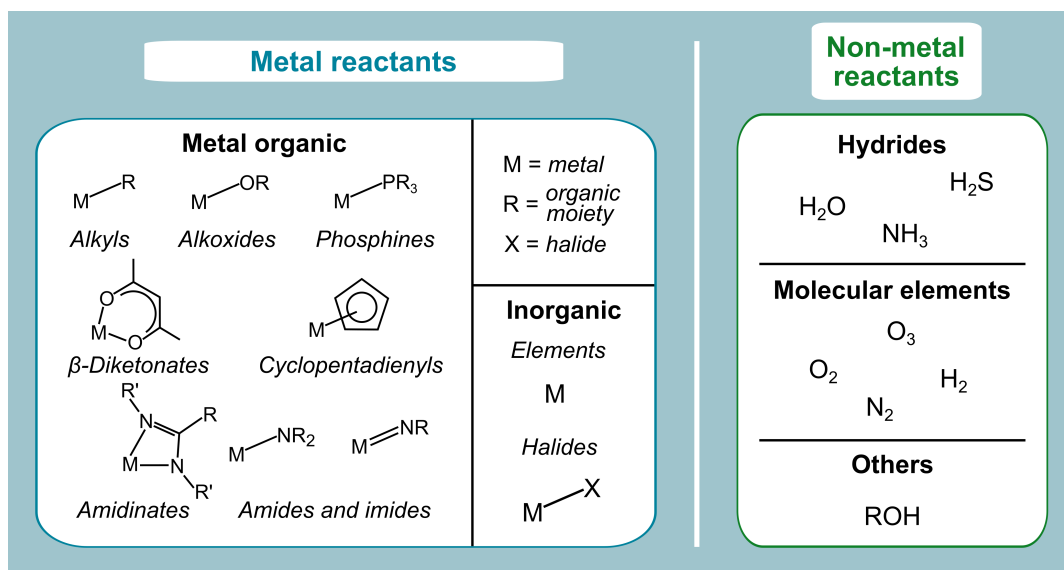


Figure 1.5: Overview of classes of metal and non-metal reactants used in ALD.<sup>[8]</sup>

( $H_2O$ ), ammonia ( $NH_3$ ) or hydrogen sulfide ( $H_2S$ ) are commonly used in order to grow oxides, nitrides and sulfides, respectively.<sup>[7,8,15]</sup> These offer generally a high stability and good reactivity over a broad temperature range and are relatively easy to handle. Additionally to these, ozone ( $O_3$ ) can be used for the deposition of oxides. Especially for the reaction with metal-containing precursors having bulky ligands, which are less reactive with water, ozone has shown favorable results. For example, the reaction of ozone with  $Ir(acac)_3$  results in ALD growth of  $IrO_2$  at a temperature of 200 °C, whereas no reaction with water can be observed.<sup>[23]</sup> Of course, there are also some drawbacks for the use of ozone as reactant, as it can also oxidize the surface of the underlying substrate or even destroy a carbon-based template. As mentioned earlier, PE-ALD uses preactivated reactants for atomic layer deposition offering specific benefits and disadvantages. Most common are the plasmas of oxygen ( $O_2$ ), hydrogen ( $H_2$ ), nitrogen ( $N_2$ ), ammonia ( $NH_3$ ) or a combination of those.<sup>[7,8,15]</sup> An overview of typically used metal and non-metal reactants is given in Figure 1.5.

By innovative combination of these different precursors it is possible to deposit a variety of conformal and functional films ranging from pure metals (e.g., Al, Ti, Pt, Ru and Ir)<sup>[24–32]</sup> to binary or ternary metal oxides (e.g.,  $Al_2O_3$ ,  $TiO_2$ , ZnO,  $Nb_2O_5$ ,  $RuO_2$ ,  $IrO_2$ )<sup>[12,33–44]</sup> to nitrides (e.g., AlN, GaN, TiN, TaN)<sup>[44–53]</sup> and to different chalcogenides (e.g., ZnS,  $TiS_2$ , CdSe).<sup>[54–61]</sup> These materials can be doped during deposition, either by alternation of pulse sequence and consecutive heating or by mixing of applied precursors prior to deposition. Additionally, by the combination of different ALD processes,

nanolaminates with element gradients can be created.<sup>[62]</sup>

### 1.3.5 *In-Situ* Characterization Techniques

Due to the closed vacuum system of the ALD reactors, the investigation of the process parameters sometimes seems like a "black box", where only a subsequent analysis after several cycles is possible.<sup>[7]</sup> In order to understand the growth mechanism and support the ALD process development by monitoring the substrate surface or generated species in real time, several different *in-situ* techniques have been implemented into the ALD work-flow.

In order to monitor film growth as a function of the number of ALD cycles by measuring the mass gain per cycle, a quartz crystal microbalance (QCM) can be used. Here, a quartz crystal coated with metal electrodes is placed within the reactor during deposition. By probing the resonance frequency of the oscillating piezoelectric crystal, the added mass can be determined with a resolution below  $1 \text{ ng cm}^{-1}$ . Key challenges include the prevention of backside deposition and dealing with temperature effects of the quartz crystal. Special care needs to be taken for data analysis as apparent mass transients and apparent mass drifting can lead to misinterpretation.<sup>[63–65]</sup>

A quadrupole mass spectrometer (QMS) can be used to measure the composition of gaseous species present in the reactor or the exhaust line. Hereby, a fraction of the reactor gas is ionized by electron impact from a hot filament and subsequently separated on the basis of its mass-charge ratio. Commercially available QMS are relatively easy to implement on ALD reactors by means of sample withdrawal at the exhaust line through a small pinhole. This allows for a time-resolved monitoring of reaction products generated both from the sample and the reactor wall surface.<sup>[66–69]</sup>

Spectroscopic ellipsometry (SE, see also section 2.2) is another powerful tool for *in-situ* characterization and very helpful for fast process development. It is based on the change in polarization of an incident light beam upon reflection from the sample. By applying a specific theoretical model for the change of polarization, the change in film thickness and important optical and electrical material properties, like refractive index or bandgap, can be calculated. When everything is set up well, a thickness resolution of 0.1 nm can be achieved for SE, nearly making monolayer growth visible.<sup>[70]</sup>

Gas-phase and surface infrared spectroscopy can also be used to evaluate growth mechanisms during deposition. Here, the absorption of infrared light by vibrational transitions of molecular species either in the gas-phase or on the surface is measured. Typically, a differential spectrum is used to monitor the change of surface and gas-phase composition due to a high signal-to-noise ratio during deposition.<sup>[71–76]</sup>

In general, both spectroscopic and ellipsometric *in-situ* characterization techniques struggle by the coating of the excitation and detection windows implemented in the ALD reactor. This can be prevented by "blocking" the precursor by a stream of inert gas or a switchable shutter during precursor pulses. Because of this issue, other more complex photon, electron- and ion-based spectroscopic techniques (e.g., X-ray photoelectron spectroscopy, low-energy ion spectroscopy or scanning tunneling microscopy) have been developed as supporting analysis methods for use *in-vacuo*, but here a movement of the sample to an attached additional chamber is commonly necessary in order to avoid coating of instrument parts and is therefore not suitable for the analysis during deposition.<sup>[7]</sup>

### 1.4 Atomic Layer Deposition in Energy Conversion Applications

The coating of geometrically complex surfaces with pinhole-free films with utmost control of coating thickness gives ALD a unique advantage. Especially when converting energy into another form, for example light into electricity or *vice versa* (in solar cells and light-emitting diodes), light into chemical energy and *vice versa* (photosynthesis and chemiluminescence) or electricity into chemical energy and *vice versa* (electrolyzers, fuel cells and batteries) the charge carriers are always transported to and away from an interface after the transfer of electrons has taken place at the phase boundary.<sup>[77]</sup> This electron transfer is the most crucial step in many energy conversion processes and occurs at the interface of two (or more) materials, which are strongly dependent on the type of device. In batteries and electrolyzers there is typically a solid-liquid interface, where the charge carriers are transferred into molecules or ions in the electrolyte.<sup>[77]</sup> Making this conversion step as efficient as possible can help to save enormous amounts of energy. The control of this interface by means of a thin functional layer can have a major impact on the energy conversion application. In this context, the unique properties of atomic layer deposition make it ideally suited for the preparation of energy conversion devices by conformal coating of structured substrates and especially of nanoporous frameworks.<sup>[77,78]</sup> These offer an increased geometric area of their interfaces and - depending on the process - a potentially higher throughput of charge carriers.

The use of ALD in energy conversion devices can be generally divided into three different categories. Firstly, ALD thin films for a direct device function, like light absorbers in solar cells, conductive supports or electrocatalysts in electrolyzers, or lithium

uptake in batteries. Secondly, ALD can be used to separate interfaces and protect the active material against erosion or corrosion in electrochemical devices.<sup>[77]</sup> Finally, ALD can be used for interface engineering, such as defect passivation in solar cells or prevention of charge recombination by tunnel barriers, and for a change of the electronic structure of an underlying semiconductor. The following section of this work will focus on the basics of water electrolysis and energy storage in lithium-ion batteries and the application of ALD thin films in these energy conversion applications.

### 1.4.1 Water Electrolysis

#### Basics of Water Electrolysis

In standard water electrolysis, upon applying an electrochemical driving force, water is split into hydrogen and oxygen at the interface of the respective electrodes, i.e., hydrogen at the cathode and oxygen at the anode.<sup>[79,80]</sup>



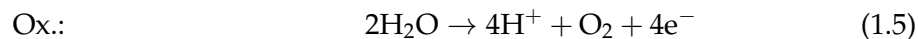
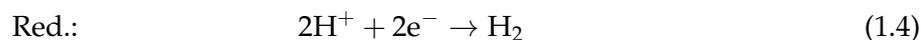
The required voltage for the reversible water splitting reaction can be calculated from Gibbs free ( $\Delta G$ ) energy according to equation 1.2 under standard conditions, where  $n$  is the number of involved electrons,  $F$  the Faraday's constant ( $96500 \text{ C mol}^{-1}$ ) and  $\Delta G$  the change of Gibbs free energy ( $237.22 \text{ kJ mol}^{-1}$ ).<sup>[79,80]</sup>

$$E_{rev} = \frac{\Delta G}{nF} = 1.23 \text{ V} \quad (1.2)$$

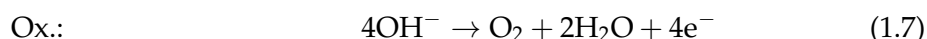
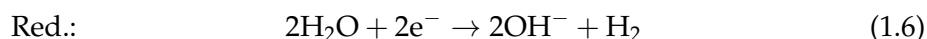
Due to the generation of entropy during water splitting, it is also instructive to consider the change in enthalpy  $\Delta H$  for potential calculations. Taking a change of enthalpy of  $\Delta H = 285.84 \text{ kJ mol}^{-1}$  under standard conditions ( $p^0 = 1 \text{ bar}$ ,  $T^0 = 298 \text{ K}$ ) into account, a theoretical minimum required voltage for thermo-neutral ( $E_{TN}$ ) water electrolysis is obtained.<sup>[79,80]</sup>

$$E_{TN} = \frac{\Delta H}{nF} = \frac{\Delta G}{nF} + \frac{T\Delta S}{nF} = 1.48 \text{ V} \quad (1.3)$$

As outlined before, the water-splitting reaction takes place on two spatially separated electrodes and can therefore - from a mechanistic point of view - be separated into the hydrogen evolution reaction (HER) and the oxygen evolution reaction (OER).<sup>[79,80]</sup> Depending on the pH value of the electrolyte (acidic or alkaline) the formulation of the two half-cell reactions is possible. Under acidic conditions, protons are the main redox active species:

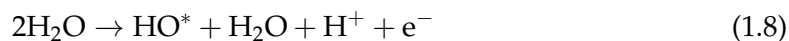


In alkaline media, hydroxide anions are mainly involved in the redox reactions:



### Oxygen Evolution Reaction

Independent of the acidic or alkaline media, the water oxidation step always involves a four-electron transfer process, leading to a typically much higher overpotential to drive at significant rates than the hydrogen evolution reaction. Many different reaction mechanisms have been proposed, often depending on the catalyst materials, which consist of at least two different adsorption intermediates ( $\text{HO}^*$  and  $\text{O}^*$ ) with a suggested third  $\text{HOO}^*$  intermediate. For DFT calculations, the classic DFT peroxide pathway suggested by Rossmeisl et al. is used to calculate the reaction energetics.<sup>[81,82]</sup>



Due to the rather complex OER mechanism, the search of novel, highly active catalysts in order to decrease the overpotential and increase the overall efficiency of water electrolysis is of strong research interest. Many different transition metal electrodes with defined porosity and nanomorphology have been investigated for OER under acidic, alkaline or neutral pH-regime. No matter which metal is used, due to cost minimization the dispersion on a cheap, high surface-area support is a key challenge for OER catalysts.<sup>[79,80]</sup>

Chapter 4 gives an overview of different carbon-based oxygen evolution reaction catalysts ranging from "pure" or unintentionally doped carbon allotropes over heteroatom-doped carbonaceous materials and carbon/ transition metal compounds to metal oxide

composites where the role of carbon is mainly assigned to be a conductive support. Special focus of this work is on the recent developments in the field of ordered carbon framework structures, where a rational design allows to deepen the understanding of the OER mechanism.

Currently used technologies for hydrogen production from water can be divided into three different categories: alkaline, polymer electrolyte membrane (PEM) and solid oxide electrolyzers (SOE). Solid oxide electrolyzers typically operate at temperatures above 500 °C with water in the form of steam. However, the most efficient and promising methods for water splitting are alkaline water electrolyzers and PEM electrolyzers.<sup>[79]</sup> Their operating principles are shown in Figure 1.6.

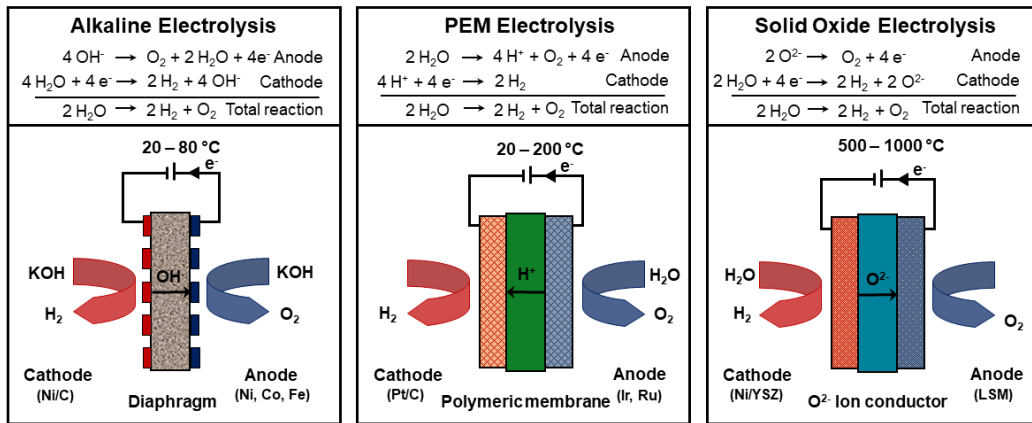


**Figure 1.6:** Schematic illustration of the three different main types of electrolyzers. Adapted from<sup>[79]</sup>

In alkaline electrolyzers, the anode and cathode electrodes are immersed in a liquid alkaline electrolyte, most commonly potassium hydroxide. The two electrodes are separated by a diaphragm permeable for OH<sup>-</sup> which has the function of separating the product gases. In solid oxide and PEM electrolyzers the solid electrolytes, either ceramic or polymer, fulfill the role of gas separator.<sup>[79,80,83]</sup> The main advantages of alkaline electrolysis are low cost due to the use of non-noble metal electrodes as well as a good long-term stability. However, concerning the method of alkaline water splitting three major weak points have to be mentioned: low partial load range, limited current density and low operating pressure. These disadvantages can mainly be attributed to the diaphragm and the electrolyte, as the gas separator is not completely tight and causes problems due to gas permeation. This leads to safety issues as well as a loss of efficiency.<sup>[79,84]</sup> During the last years, a new trend in alkaline electrolysis emerged based on polymeric membranes with anionic (OH<sup>-</sup>) conductivity, also known as anion

exchange membranes (AEM). This new technology, named solid alkaline electrolysis, is promising since it can combine the strengths of both alkaline and PEM electrolysis.<sup>[85]</sup>

In a PEM electrolyzer a proton-conducting membrane (e.g., Nafion<sup>®</sup>) is coated with two thin porous layers of electrocatalysts on each side.<sup>[79,80,86]</sup> Typically the catalysts are carbon-supported Pt on the cathode and TiO<sub>2</sub>-supported IrO<sub>2</sub> on the anode side. The gaseous products (hydrogen and oxygen) accumulate at the backsides of the PEM cell and are collected with titanium separator plates. PEM electrolysis has a number of advantages over the alkaline electrolysis, including higher power density, faster response to load changes and the possibility of pressurized operation.<sup>[79,80,86]</sup> One of the key challenges of PEM electrolysis is the corrosive acidic regime, provided by the proton exchange membrane, which requires the use of special materials. The employed materials must withstand the harsh corrosive low pH conditions and the high applied overpotential, especially at high current densities. The required corrosion resistance not only applies to the used catalysts, but also for current collectors and separator plates. Only a few materials can be selected that can perform in this harsh environment. This demands the use of scarce, expensive materials and components such as noble metal catalysts (platinum group metals-PGM e.g., Pt, Ir and Ru) as well as titanium based current collectors and separator plates.<sup>[79,80,86]</sup>

Concerning the noble elements and their oxides, it was found that RuO<sub>2</sub> shows the lowest overpotentials for the oxygen evolution reaction (OER), but suffers from corrosion in acidic and oxidizing environment.<sup>[87]</sup> By mixing RuO<sub>2</sub> with the promising IrO<sub>2</sub> a significant improvement in stability during the OER can be achieved. By adding relatively small amounts of IrO<sub>2</sub>, the corrosion rate of the oxide could be reduced to about 4 % of the original value.<sup>[88]</sup> In addition to ruthenium, iridium based catalysts show the best catalytic properties for the OER in acid electrolytes. At the same time, less severe corrosion can be observed compared to Ru. Therefore, the great majority of studies on PEM water electrolysis for the OER have focused on these catalysts.<sup>[89]</sup>

Suitable OER rates and reasonable stability have also been obtained with other mixed oxides, such as Ru<sub>x</sub>Ir<sub>y</sub>Ta<sub>z</sub>O<sub>2</sub>,<sup>[90]</sup> Ru<sub>x</sub>Ir<sub>y</sub>Co<sub>z</sub>O<sub>2</sub>,<sup>[91,92]</sup> Ru<sub>x</sub>Ir<sub>y</sub>Sn<sub>z</sub>O<sub>2</sub>,<sup>[93]</sup> Sn<sub>x</sub>Ru<sub>1-x</sub>O<sub>2</sub>,<sup>[94]</sup> Ir<sub>x</sub>Sn<sub>1-x</sub>O<sub>2</sub><sup>[95]</sup> and Ir<sub>x</sub>Ti<sub>y</sub>Pt<sub>z</sub>O<sub>2</sub>.<sup>[96]</sup> These materials, due to their content of inexpensive metal oxides, are more economically priced than pure Ir and Ru-based catalysts. However, the resulting reduced conductivity compared to pure IrO<sub>2</sub> can be a concern, and recent research focuses on the lowering of the Ir-content by increasing the mass-based catalytic activity. The decreased iridium amount is thereby essential for making PEM electrolysis an economically competitive technology for future green hydrogen production. The ability of thin film deposition on nanostructured templates is shown in Chapter 3, where an OER catalyst consisting of a conductive oxide coated by an ultra-thin

film of IrO<sub>2</sub> is created by ALD.

### 1.4.2 Photoelectrochemical Water-Splitting

Photoelectrochemical (PEC) water-splitting is another electrolysis related process to generate green hydrogen from water and solar energy. Since the pioneering work of Fujishima and Honda in 1972, who used an illuminated TiO<sub>2</sub> photoanode to split water into H<sub>2</sub> and O<sub>2</sub>,<sup>[97]</sup> PEC water-splitting on semiconducting materials has been studied extensively.<sup>[98–103]</sup> A typical PEC cell is composed of two conductively connected electrodes (at least one photoelectrode) immersed in an aqueous electrolyte. Upon illumination with light the semiconductor absorbs photons with an energy higher than its bandgap ( $E_g$ ), resulting in separation of electron-hole pairs, which are then able to drive reduction and oxidation reactions if charge injections into the reactants are thermodynamically favourable.<sup>[98]</sup> The electrons can be inserted at the cathode, where typically a p-type semiconductor is used. The oxidation reaction at the anodic side is driven by an n-type semiconductor. By spatial separation of the electrodes and the corresponding half-cells it is possible to collect the generated hydrogen to serve as a means of energy storage or to feed it into subsequent processing like e-fuel production. For potential commercialization, a solar-to-hydrogen (STH) conversion rate of at least 10 % is desired.<sup>[98–102]</sup> However, there are still some major drawbacks for PEC water-splitting devices, including low stability and limited efficiency to meet the necessary requirements.<sup>[98–102]</sup>

It is worth noting that the PEC water splitting takes place at the interface of electrodes and electrolyte. Therefore, it is necessary to understand the conditions of the interface so as to have more insights into the entire reaction processes.<sup>[103]</sup> The following section will give a short introduction into the theory of PEC water-splitting, how it is working, which requirements need to be fulfilled and the key challenges to be met for a commercial application.

#### Semiconductor-Electrolyte Interface

When a semiconductor is immersed into a redox-active electrolyte, an equalization of the Fermi level with the electrochemical potential takes place by a flow of charges between the two phases leading to the formation of a Helmholtz double layer.<sup>[103–105]</sup> This junction between solid and electrolyte can be compared to a Schottky barrier at a semiconductor-metal interface. In addition to the short-range potential drop at the Helmholtz double layer (inner (IHP) and outer (OHP) Helmholtz layer (II), about 3–5 Å in thickness), a further long range potential ( $\phi$ ) drop within the electrolyte at low

ion concentration in the so called Gouy diffuse layer (III) can be observed (Figure 1.7a).

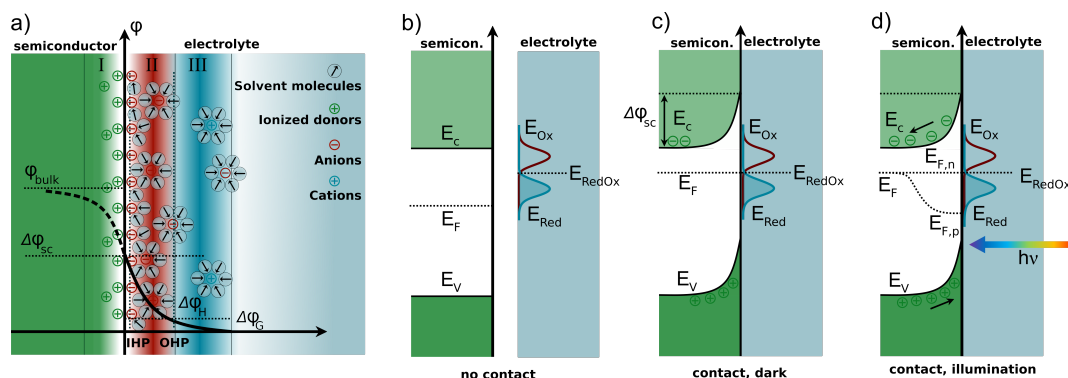


**Figure 1.7:** Model of the double-layer structure of an n-type semiconductor electrode in contact with the electrolyte under equilibrium conditions (a). Electron energy profile for an isolated n-type semiconductor (b), a semiconductor liquid junction at equilibrium in the dark (b) and a semiconductor-liquid junction under illumination (c).<sup>[105]</sup>

For a solid semiconductor, a space charge layer (I) with thickness of  $\approx 0.1-1 \mu\text{m}$  is formed because of the nonequilibrium of Fermi level ( $E_F$ ) between semiconductor and the redox potential of the electrolyte ( $E_{\text{RedOx}}$ ) which dictates the electrode potential. Depending on the type of semiconductor, the potential of the space charge layer ( $\phi_{\text{SC}}$ ) is shifted downwards for p-type and upwards for n-type semiconductors (so called *band bending*).<sup>[103,104]</sup> For example at a p-type semiconductor, with excess holes in the bulk (more positive Fermi level), in order to equilibrate, holes flow from the surface of the semiconductor into the electrolyte, leaving a negative charge behind. Resulting from Fermi-Dirac-statistics, the Fermi level lies in the middle between valence and conduction band for an intrinsic semiconductor as there are equal numbers of holes and electrons. By doping of the semiconductor the Fermi level shifts to more positive potential for cations and more negative potentials for anions. For low or moderately doped semiconductors, the shift in the Fermi level mainly appears across the space charge region as there are only few energy states available compared to the electrolyte.<sup>[103-105]</sup>

### Charge Carrier Generation

Photons with an energy equal or higher than the bandgap of a semiconductor can be absorbed by electrons in the valence band (VB). These photoexcited electrons can then be transferred from the top of the valence band to the bottom of the empty conduction band (CB), leaving positively charged holes ( $h^+$ ) in the VB. The photogenerated electron-hole pairs (excitons) can travel to the surface of the semiconductor and act as redox species for water-splitting, organic decomposition or the reduction of  $\text{CO}_2$ . Due

to recombination of the electron-hole pairs within the semiconductor, an external bias is commonly applied in a PEC system in order to promote the migration of the excited charges and suppress the opportunity of recombination.<sup>[104,106]</sup> For the reduction of water to hydrogen, electrons in the CB need to have a reduction potential more negative than the redox potential of  $H^+/H_2$ , which is defined as 0 V vs. Normal Hydrogen Electrode (NHE). Water oxidation can take place for a hole potential more positive than the redox potential of  $H_2O/O_2$  which is according to equation 1.2  $E_{RedOx} = -1.23$  V.<sup>[103,104]</sup> Therefore, the used semiconductor requires at least a theoretical bandgap of 1.23 eV. Supposing that only photons with energy larger than the bandgap of the semiconductor can be completely absorbed and that all of the absorbed photons can be converted into one elementary charge of current, the theoretical photocurrent density,  $j_{ph,max}$ , can be calculated using equation 1.12, where  $E_g$  is the bandgap of the semiconductor and  $I(\lambda)$  represents the photon flux at wavelength of  $\lambda$ .

$$j_{ph,max} = e \int_{\lambda_{min}}^{\lambda_{E_g}} I(\lambda) d\lambda \quad (1.12)$$

As outlined in equation 1.3, a much higher energy is necessary to drive the photocatalytic reaction due to energy losses, hence, a distinct overpotential is required to drive the two redox reactions and to build up the driving force for charge carrier transportation.<sup>[103,104]</sup> Minimum required bandgaps for a single device photoelectrochemical water-splitting system range from 2.0 eV up to 3.0 eV according to literature.<sup>[107]</sup> The potential at which the HER/OER starts under light irradiation is defined as the photocurrent onset potential ( $E_{onset}$ ) and is influenced by the open circuit photovoltage ( $V_{ph}$ ) and the kinetic overpotential ( $\eta_k$ ).<sup>[108,109]</sup> According to equation 1.13 an increase of ( $V_{ph}$ ) or a decrease of ( $\eta_k$ ) leads to an decrease in ( $E_{onset}$ ).

$$E_{RedOx} - E_{onset} = V_{ph} - \eta_k \quad (1.13)$$

Besides the width of the bandgap, the levels of VB and CB are also very important. Here, the position of the VB must be more positive than the potential of  $O_2$  in order to allow the oxygen production from water.<sup>[110,111]</sup> Moreover, the CB of the semiconductor must be more negative than the required redox potential for the hydrogen evolution. Several different semiconducting materials like silicon, silicon carbide, metal oxides and chalcogenides have been explored as possible electrode materials (small overview of commonly used materials in Fig. 1.8). The general trend for metal oxides shows a very deep (positive vs. NHE) valence band position, facilitating stable oxidation reactions, simultaneously showing a large bandgap and therefore a limited light absorption. However, non-metal semiconductors with smaller bandgaps and higher light

absorption show more negative band positions with the risk of photocorrosion during the oxygen evolution reaction.

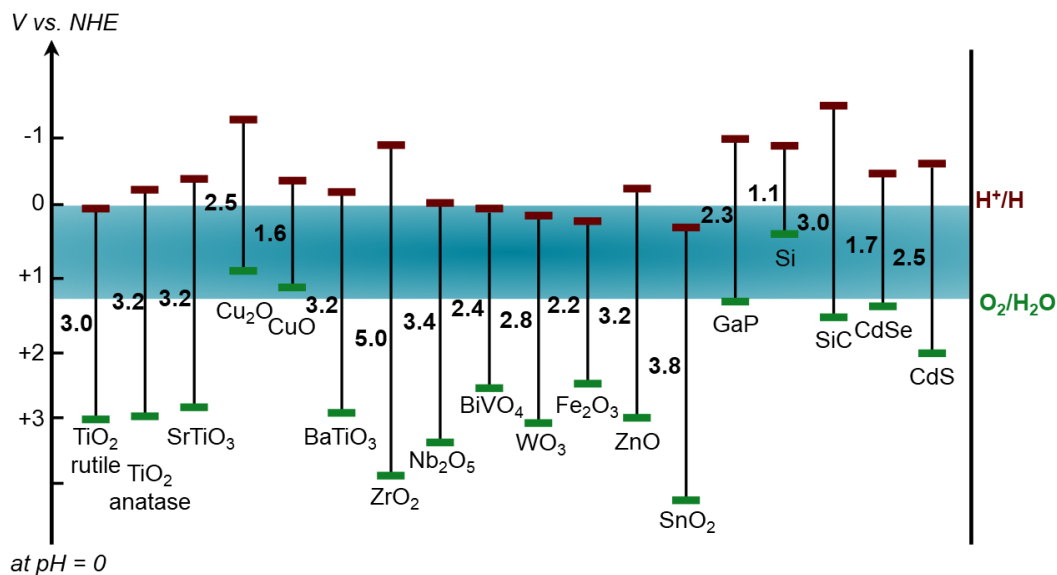


**Figure 1.8:** Overview of band positions and magnitudes of commonly used semiconductors, inspired by Jing et al.<sup>[112]</sup>

### Challenges in PEC Water-Splitting Materials over the years

As already mentioned above, a main requirement for bringing PEC water-splitting systems into commercial application is an STH conversion rate of at least 10 %. This conversion rate is highly dependent on the bandgap and the resulting photocurrent and onset-potential of the material. In addition to the bandgap requirements, electrode materials should consist of abundant and low-cost elements, easily processable devices and most importantly be robust enough to withstand continuous and long-term PEC operation in the presence of electrolyte and oxygen.<sup>[103]</sup> For many decades,  $\text{TiO}_2$  ( $E_g = 3.0\text{-}3.2$  eV) and  $\text{WO}_3$  ( $E_g = 2.7$  eV) have garnered an enormous amount of attention due to their easy processability and remarkable stability under PEC working conditions. A big drawback of these classical transition-metal oxides is the rather large bandgap, only absorbing a small fraction of the available solar spectrum. In general, the solar spectrum (Fig. 1.9) of light ranges from ultraviolet (UV) rays ( $\lambda < 400$  nm) over visible light (400 nm to 800 nm) up to infrared (IR) rays ( $\lambda > 800$  nm). Under AM1.5G conditions, 4 % of the total solar energy are in the UV region, 53 % in the visible and the remaining 43 % in the IR range. Using equation 1.12, a semiconductor with a bandgap of 2.0 eV can absorb light up to a wavelength of 600 nm leading to

a theoretical maximum efficiency of approximately 16 % for a quantum efficiency of 100 %.<sup>[104]</sup>

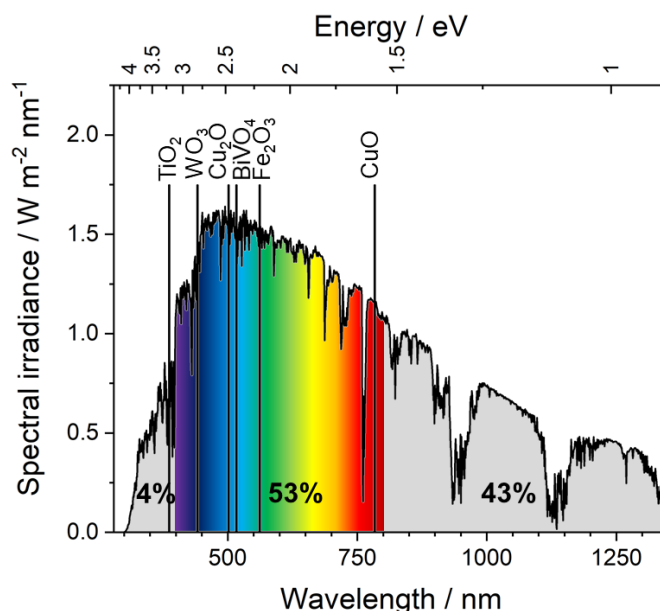


**Figure 1.9:** Solar spectrum under AM1.5G conditions with the bandgaps of photoelectrode material candidates.<sup>[104]</sup>

In reality, there is no quantum efficiency of 100 %. Reasons can be found in the rather short life time of the photogenerated charge carriers due to a bad separation and a high concentration of charge recombination centers. The excited electrons tend to recombine with holes, this being a major factor of energy losses in photoelectrodes as only a small portion of excited charge carriers can be utilized for the respective water-splitting reaction.<sup>[98–103]</sup> For instance, n-type semiconductor hematite ( $\text{Fe}_2\text{O}_3$ ) has a bandgap of 2.2 eV and a suitable valence band position for the oxygen evolution reaction.<sup>[113,114]</sup> However, hematite generally suffers from rather poor PEC activity showing a strong anodic shift in on-set potential and a low to moderate photon conversion efficiency. Many different strategies have been applied in order to overcome these issues ranging from nanostructuring in order to provide a shorter transport path for the photogenerated holes<sup>[113,115–123]</sup> over improving the charge transport properties of hematite via doping with various elements<sup>[117,124–129]</sup> to enhancing hole injection behavior by applying a co-catalyst on the surface.<sup>[116,130–136]</sup> Solar water oxidation photocurrents of up to approximately  $4 \text{ mA cm}^{-2}$  are still considerably lower than the theoretical maximum photocurrent of  $12 \text{ mA cm}^{-2}$  at standard conditions under AM1.5G. The proper extraction of photogenerated charges remains an unsolved problem and motivates ongoing research.<sup>[113,114,137]</sup>

Another promising candidate for PEC water-splitting is bismuth vanadate ( $\text{BiVO}_4$ ) with a bandgap of 2.4 eV and beneficial band positions.<sup>[101,138–140]</sup> The mixing of the  $s^2$  cation  $\text{Bi}^{3+}$  with the  $d^0$  cation  $\text{V}^{5+}$  creates a coupling between the  $s$  and O  $2p$  orbitals forcing an upward dispersion of the valence band, whereas the coupling between the  $d$  bands from the  $d^0$  cation and the  $p$  band from the  $s^2$  cation leads to a low conduction-band minimum.<sup>[138]</sup> Depending on the crystal structure,  $\text{BiVO}_4$  can either behave like a p-type semiconductor with tetragonal zircon structure or as n-type semiconductor with monoclinic scheelite structure (see Figure 1.10).<sup>[141]</sup> However,  $\text{BiVO}_4$  suffers from poor electron transport due to limited overlap between vanadium and bismuth orbitals in the conduction band, reducing the theoretical maximum photocurrent. Doping of  $\text{BiVO}_4$  with  $\text{Mo}^{6+}$  or  $\text{W}^{6+}$  can lead to an increased electronic conductivity and thus higher carrier collection efficiencies.<sup>[142–145]</sup> Like hematite,  $\text{BiVO}_4$  has rather slow oxidation reaction kinetics which makes the use of co-catalysts such as cobalt phosphate or Fe and Ni oxyhydroxides essential.<sup>[145–149]</sup>

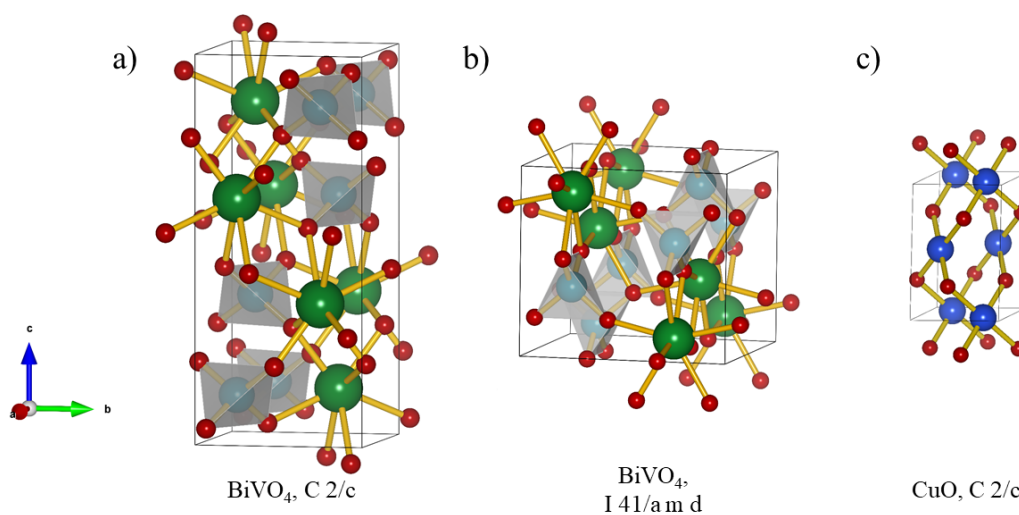


**Figure 1.10:** Crystal structures of n-type scheelite  $\text{BiVO}_4$  (a), p-type tetragonal  $\text{BiVO}_4$  (b) and tenorite  $\text{CuO}$ ; oxygen (red), copper (blue), bismuth (green), tetragonally coordinated vanadium (turquoise).

The latter act as water oxidation catalysts, or reduce surface recombination by prevention of back-electron transfer or by chemical passivation of surface traps.<sup>[150]</sup> The underlying mechanism is still not clear and constitutes a topic of present research activities. With optimized charge carrier collection efficiency applying a type II heterojunction combined with nanostructuring not exceeding the carrier diffusion length (70 - 200 nm), a record value of 6.72  $\text{mA cm}^{-2}$  measured at 1.23 V vs. RHE under AM1.5G was achieved.<sup>[151]</sup> This corresponds to  $\approx 90\%$  of the theoretical current den-

sity for  $\text{BiVO}_4$ . However, in comparison to earlier discussed metal oxides, the stability under working conditions is rather poor. Corrosion or more specifically, the dissolution of vanadium ions and the degradation of the pristine material to photocatalytic inactive species limits the performance. In this context, Chapter 5 of this thesis shows an innovative way to protect the surface of  $\text{Mo:BiVO}_4$  by utilization of atomic layer deposition of an ultra-thin protection layer of corrosion stable niobium doped titanium oxide and consecutive deposition of a transition metal oxide based catalyst on top. To reach the goal of STH efficiencies of 10 % and higher, however, materials with a smaller band gap than  $\text{BiVO}_4$  are needed.<sup>[101]</sup>

In this context, the combination with a photocathode with a lower band gap in a tandem cell can increase the amount of accessible sunlight. One approach is to use analogues of binary copper oxide ( $\text{Cu}_2\text{O}$ ,  $E_g = 2.47$  eV;  $\text{CuO}$ ,  $E_g = 1.58$  eV) which possess a suitable bandgap and band energy levels for the hydrogen evolution reaction.<sup>[152–156]</sup> However, these are not stable under aqueous conditions.<sup>[157]</sup> Various protection techniques with different metal oxides have been applied resulting in high current densities of up to  $8 \text{ mA cm}^{-2}$  vs. RHE at 0 V for  $\text{Cu}_2\text{O}$ . With its low bandgap,  $\text{CuO}$  is a perfect candidate for a tandem cell bottom electrode, but its intrinsic instability has not been viewed as detrimental as in the case of  $\text{Cu}_2\text{O}$ .<sup>[158]</sup> Suffering from a strong charge carrier localization makes the doping with various dopants like Li, Mg, Fe, Co, Ni, Zn necessary.<sup>[152,157,159–163]</sup> The photoelectrochemical behavior of  $\text{Li:CuO}$  will be discussed in detail in Chapter 6. While  $\text{Li:CuO}$  also suffers from corrosion under working conditions, a corrosion stable, but charge permeable amorphous niobium doped titanium oxide layer will be applied via ALD and subsequently equipped with a Pt catalyst to promote efficient hydrogen evolution.

As outlined above, today there is no single semiconducting material which can satisfy the required performance and either photocurrent or conversion efficiency to meet efficiency and stability goals due to their intrinsic limitations on performance such as large bandgap, short charge-carrier lifetime, low conductivity and severe photocorrosion under illumination.<sup>[103]</sup> Some of these challenges can be met by surface modification of the semiconductor either by protection or enhancement of charge extraction.

Atomic layer deposition is the technique of choice to coat nanostructured semiconductors due to its unique properties. M. F. Lichterman et al. proposed the requirements for protective films under the acronym "SABOR", meaning "Stable in the thermodynamic, kinetic, and mechanical senses when incorporated onto the semiconductor, immersed in the electrolyte, and operated at the potentials of interest; Active catalytically for the OER/HER, either possessing intrinsic catalytic activity or integrating the activity of a cocatalyst; capable of providing Built-in electronic asymmetry to allow for the

separation of electrons and holes, or to allow for a separate buried junction to perform efficiently; Optically transparent to provide optical properties that are optimized for the transmission of light; and, capable of providing low Resistance, to allow for charge-carrier conduction with minimal performance loss due to  $iR$  drops".<sup>[164]</sup> Although the device complexity increases with protective thin films, a greater variety of possible semiconducting materials can be thought of as the direct parasitic semiconductor-electrolyte junction can be avoided. Typically, metal oxides or a combination of those are utilized for protective layers by ALD, e.g.,  $\text{SiO}_2$ ,<sup>[165,166]</sup>  $\text{TiO}_2$ ,<sup>[167-176]</sup>  $\text{NiO}_x$ ,<sup>[177-179]</sup> and  $\text{CoO}_x$ .<sup>[180]</sup> Among these,  $\text{TiO}_2$  is probably most promising due to the rather large bandgap and the high stability under working conditions. Most of the time, comparatively thick layers (up to 100 nm) need to be applied in order to get a pin-hole free protection film on top of the semiconductor.<sup>[181]</sup> Reasons include the crystalline deposition of  $\text{TiO}_2$  by atomic layer deposition and the resulting voids between formed crystallites. However, by incorporation of niobium oxide within the titanium oxide layers, suppression of the crystallization is possible and one can obtain pin-hole free and corrosion-stable films for an ultra-thin thickness of few nanometers. As outlined before, this unique property of ALD is used in Chapters 3, 5 and 6.

### 1.4.3 Electrochemical Energy Storage

Rechargeable batteries, or secondary batteries, are the most attractive method for direct storage of electrochemical energy. For the transformation from a fossil fuel based society to an renewable one, batteries are believed to be one major key factor.<sup>[182-184]</sup> Already today, the global market for electric vehicles explodes due to the announcement of several governments around the world to ban fossil fuel driven cars in the future. Therefore, the need for next-generation secondary batteries with higher performance in terms of energy density, specific power, charge/discharge efficiency, operating voltage, cycle durability, safety and reduced cost is tremendously high. Until now, lithium-ion batteries (LIBs) are most widely used due to their high energy density, small memory effect and low self-discharge rate. Several different attempts for the performance enhancement and development of new materials for LIBs are made in this thesis. The following section will provide an overview of lithium-ion batteries, underlying principles and some important materials.

#### General Principle of Battery Technology

In general, a battery is a source of electric power containing one or more electrochemical cells. Depending on the device and application, these may be connected in series

or parallel to provide the desired voltage and power. Each electrochemical cell itself consists of two half-cells connected via an ion-conductive, but electronically insulating electrolyte. These half-cells exhibit a certain potential (relative to the standard hydrogen electrode) that can be calculated using Nernst's equation (equation 1.14).<sup>[182]</sup>

$$E_{half-cell} = E^0 - \frac{RT}{z_e F} \ln Q \quad (1.14)$$

Here,  $E^0$  is the standard electrode potential derived from equation 1.2,  $z_e$  the number of electrons transferred,  $F$  the Faraday's constant,  $T$  the temperature,  $R$  the gas constant and  $Q$  the reaction quotient. If an external electrical conductor connects both half cells, the electromotive forces try to equalize resulting in an open circuit voltage ( $V_{OC}$ ), which is defined as:

$$E_{cell} = E_{cathode} - E_{anode} \quad (1.15)$$

The anode is defined as negative electrode, where the oxidation reaction takes place and electrons are released into the external circuit, whereas the reduction and uptake of electrons occurs at the cathode. During the discharge cycle of a battery, the reaction and electron transfer take place spontaneously, while for charging of the battery a certain voltage has to be applied. This implies that the sign of electrodes inverts and the negative electrode becomes the positive one. For simplification of further discussion, the electrodes will be denoted as their discharging name.<sup>[182]</sup>

A schematic overview of the most commonly used lithium-ion battery is shown in Figure 1.11. It is typically composed of a graphite anode and a transition-metal oxide based cathode, which are separated electronically by a thin film separator and an electrolyte. Each electrode is composed of a metal current collector, the active material, additives that increase the electrical conductivity (usually various types of carbon) and additives enhancing adhesion, mechanical strength and the ease of processing (typical polymeric binders, such as polyvinylidene fluoride).<sup>[185]</sup> During discharge, lithium ions diffuse from a lithiated anode into the delithiated cathode leading to oxidation and reduction of the two electrodes, respectively. The process is inverted for charging by a power source.

Depending on the used anode and cathode materials, the cell voltage and the theoretical capacity of the LIB can vary due to its dependence on the number of lithium-ions ( $n_{Li}$ ) involved in lithiation and delithiation. The maximum theoretical capacity  $Q_{theoretical}$  of a certain material is normalized per unit weight ( $Ah\ g^{-1}$ ) and can be calculated by equation 1.16:

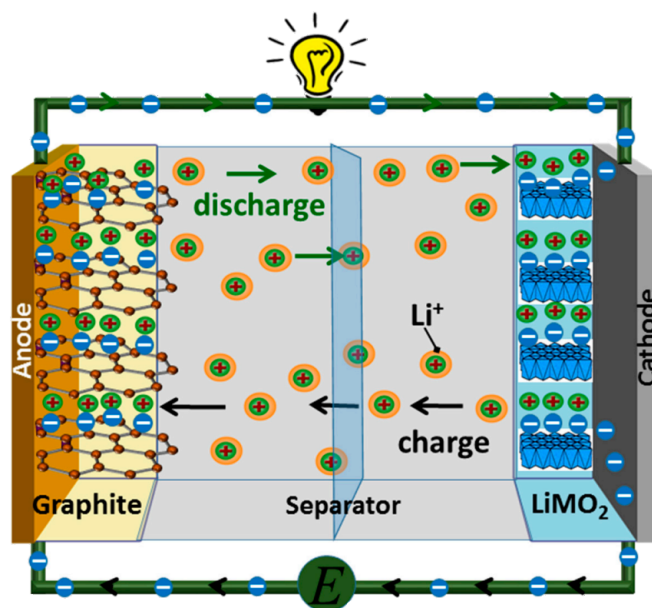


Figure 1.11: Schematic of the operation principles for rechargeable lithium-ion batteries.<sup>[186]</sup>

$$Q_{theoretical} = \frac{n_{Li}F}{3600M_W} \quad (1.16)$$

However, in practice the obtained capacity is most of the time of distinctly lower value.<sup>[182,183]</sup> The so-called specific capacity of a material is calculated by multiplying the measured current with time needed for a complete discharge or charge of the battery cell. This specific capacity is dependent on the rate of charging current, due to the different lithium insertion and extraction reactions of different materials. It is therefore necessary to state the charging current rate in addition to the specific capacity in order to compare potential electrode materials.

Especially for mobile application of LIBs the energy per weight and volume play an important role.<sup>[187]</sup> The specific energy is referred to as gravimetric and volumetric energy density and can be calculated by multiplying the theoretical capacity by the cell voltage and the inverse weight or volume.

Chapter 7 of this thesis deals in a more specific manner with the improvement of gravimetric energy density by development of a freestanding tin oxide based anode, where the metal current collector can be left out. In Chapter 8, the specific capacity of a lithium cobalt oxide cathode is increased by stabilization of the active material applying an ultrathin lithium niobate layer via ALD. Doing this, the cycling to a higher potential is possible and more lithium can contribute to the storage reaction. Additionally in Chapter 9, new imidazolate-based covalent organic frameworks will be investigated

as potential lithium solid-state electrolyte. For a better classification of the obtained results, the following sections will give a short overview of current developments in the fields of cathodes, anodes and electrolytes.

### High-capacity Anode Materials

For realizing next-generation lithium-ion batteries with higher energy densities, longer cycle life and better safety, the development of improved anode materials is necessary, as their choice greatly influences battery capacity and operating voltage. Figure 1.12 shows the potential vs.  $\text{Li}/\text{Li}^+$  plotted as function of the specific capacity of commonly used and potential negative anode materials.<sup>[184]</sup> The capacity increases from graphite and porous carbons to fine particle systems, nitrides, different alloys to metallic lithium with a capacity of approximately  $4000 \text{ Ah kg}^{-1}$ .

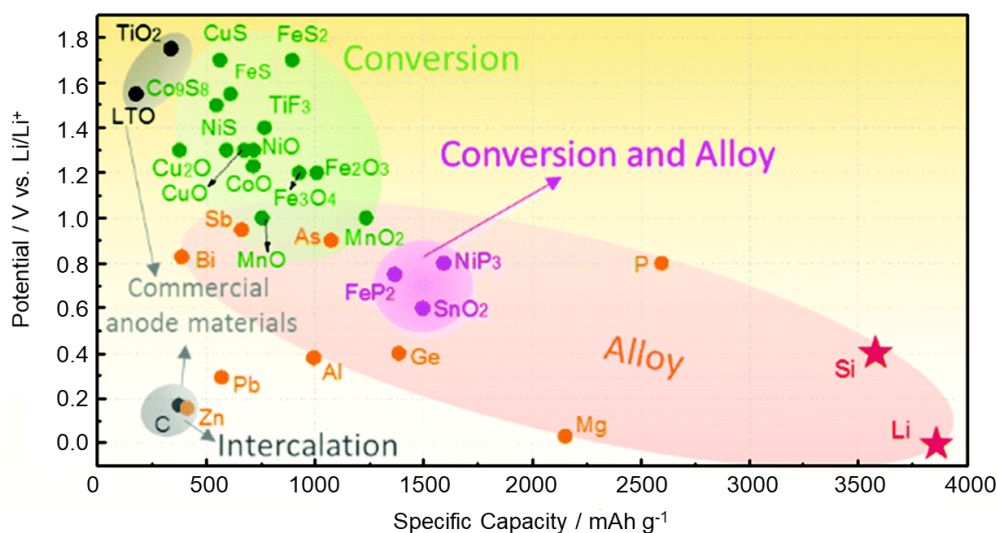
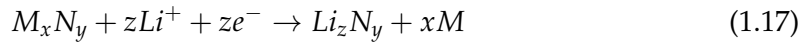


**Figure 1.12:** Schematic illustration of active anode materials for next-generation LIBs.<sup>[184]</sup>

These anode materials can be divided into three different groups depending on their lithium insertion reaction mechanism: intercalation, conversion and alloying materials. Typical intercalation materials are  $\text{TiO}_2$ ,  $\text{Li}_4\text{Ti}_5\text{O}_{12}$  (LTO) and carbon based materials like graphite, porous carbon, carbon nanotubes and graphene.<sup>[184]</sup> Graphite and LTO are used in commercial lithium-ion batteries, whereas graphite is still the material of choice due to its low cost, high abundance, low delithiation potential, high Li diffusivity, relatively low volume change, high electrical conductivity and good cycle life time. Graphite offers a gravimetric capacity of  $372 \text{ mAh g}^{-1}$  due to the intercalation of 1 Li atom per 6 C atoms between the graphene planes.

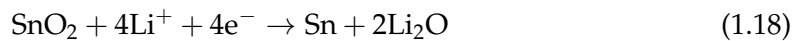
Another group of anode materials are so-called conversion materials with a general formula of  $M_xN_y$ , where M represents a transition metal like Mn, Ni, Co, Fe, Ti etc. and N is typically a non-metal like O, S, F, P, N. Conversion materials are based on the full conversion of the transition metal from oxidized to metallic state.<sup>[184,188,189]</sup>



These conversion reactions often consume more than one Li atom per transition metal atom, resulting in very high capacities and energy densities. However, these anodes typically demonstrate a higher working potential (1.0-1.8 V vs. Li/Li<sup>+</sup>), large voltage hysteresis and high initial irreversible capacity due to the demanding chemical reorganization resulting in a short cycle life time.<sup>[184,188,189]</sup>

The third class of alloy forming anode materials comprises mainly group IV (Si, Ge, Sn, Pb) or group V (P, As, Sb, Bi) or light metals (Li, Mg, Al).<sup>[184,188,189]</sup> These form highly reactive alloys upon insertion of lithium, resulting in significant structural and volume changes. Thereby, they are capable of reaching super high specific capacities at low working potentials, but struggle with the strong volume changes upon lithium alloying.

Among these classes, SnO<sub>2</sub> has recently attracted much attention as a promising anode material combining conversion as well as alloying features, which results in a high theoretical capacity of 1494 mAh g<sup>-1</sup>.<sup>[188,190-192]</sup> The lithiation and delithiation of SnO<sub>2</sub> can be subdivided into two main steps. First, SnO<sub>2</sub> undergoes a conversion reaction resulting in the formation of metallic Sn embedded into a Li<sub>2</sub>O matrix (equation 1.18) followed by the alloying reaction between lithium and previously formed metallic Sn (equation 1.19) yielding Li<sub>x</sub>Sn (0 ≤ x ≤ 4.4).



However, the conversion reaction of macroscopic SnO<sub>2</sub> is not reversible, thus limiting the theoretical capacity to 782 mAh g<sup>-1</sup> for the alloying step.<sup>[188,191,193-195]</sup> Another serious issue of SnO<sub>2</sub> as anode material is the huge volume change during conversion and alloying reactions of up to 358 % causing internal stress, electrical connectivity failures and a potential pulverization of the electrode.<sup>[196,197]</sup> One way to overcome these challenges is the use of nanostructured tin oxide particles embedded in a carbonaceous support matrix (e.g., reduced graphene oxide (rGO), carbon nanotubes (CNTs) or car-

bon nanofibers) which can buffer the huge volume changes and provide enough electrical conductivity.<sup>[192,198–205]</sup> Further improvement of the material can be achieved for the intrinsic conductivity enhancement via doping with antimony, enabling faster lithium insertion/extraction.<sup>[192,206–209]</sup> Additionally, SnO<sub>2</sub> nanoparticles below 10 nm in size have shown the ability for a reversible conversion reaction upon lithiation, reaching capacities above 800 mAh g<sup>-1</sup>, whereas for bigger particles only the alloying behavior can be observed. Reduction of particle size and the associated higher surface to volume ratio increases the contact area with electrolyte and promotes fast lithium-ion diffusion within the electrode, leading to a better capacity retention at higher loading currents.

The above optimization strategies have been implemented in 2018 in our group, when antimony-doped tin oxide (ATO) nanoparticles were embedded in a graphene matrix synthesised by a microwave assisted *in-situ* synthesis in *tert*-butanol. The hybrid nanocomposite showed a high gravimetric capacity of 1226 mAh g<sup>-1</sup> at a charging rate of 1C and excellent stability with a good capacity retention of 77 % after 1000 cycles.<sup>[210]</sup>

Beside the increase in specific capacity of the active material, there is also the possibility of decreasing the overall electrode weight by replacing or omitting the commonly used copper foil current collector. The resulting, so-called freestanding electrodes are an innovative concept but require specific features and a more complex electrode production compared to conventional electrode manufacturing. In Chapter 7 two ways for the creation of freestanding ATO-based carbon composites are compared, resulting in the first freestanding full cell of the working group.

A relatively new class of anode materials are so-called covalent organic frameworks (COFs). These are based on a modular system, where pre-designed organic building blocks are forming a crystalline porous network with a two- or three-dimensional topology via covalent bonds and  $\pi$ - $\pi$  stacking interactions. By adjustment of the building blocks, the pore size, shape, interface and environment can be predetermined via either polycondensation or post-synthetic functionalization. An important feature for the synthesis of highly crystalline frameworks is the reversibility of bond formation in order to avoid the formation of an amorphous product, by promoting the thermodynamically most stable crystalline framework. Correspondingly, several reversible organic reactions such as boroxine, boronate ester, Schiff base, triazine, Knoevenagel, imide, amide and other bond formations were successfully employed for the synthesis of crystalline COFs.<sup>[211]</sup> Several different comprehensive overviews are given in the literature about the emerging field of functional COFs.<sup>[211–213]</sup>

Anchored redox active units within the COF skeleton, as well as open channels with accelerated ion transport are expected to be favourable in comparison to commonly used carbon materials in anodes. Active sites for lithium storage have been reported

either as functional groups or in the linkage motif of the COF. Nearly all types of linkages for 2D-COFs have been examined for LIBs, such as boronate-ester,  $\beta$ -keto-enamine, imine, imide, CTFs,  $sp^2$  (C=C) and hex-aza.<sup>[214–220]</sup> Special attention is on so-called exfoliated 2D nanosheets as they have shown to increase their specific capacity upon cycling up to a highest value of  $1536 \text{ mAh g}^{-1}$  for an imine-based COF on CNTs, competing easily with inorganic or pure carbon-based analogues (see Figure 1.13).<sup>[221]</sup> Here, the high lithium storage ability is attributed to a  $14\text{-Li}^+$  storage per COF monomer with 1 lithium per C=N group and 6 per benzene ring of the COF backbone. Until now, this massive enhancement in capacity could only be observed for exfoliated COFs, which leads to the conclusion that some problems exist for bulk COFs, including accessibility of the active sites and conductivity perpendicular to the planes.

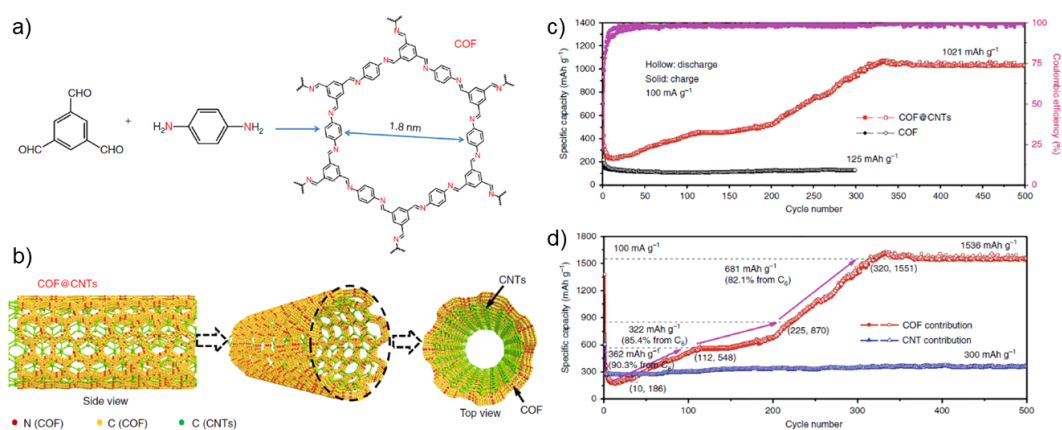


**Figure 1.13:** Schematic depiction of the synthesis of COF (a) and the structure of COF@CNTs with few COF layers covering the exterior surface of CNTs (b). Cycling performances of COF and COF@CNTs at  $100 \text{ mA g}^{-1}$  (c) and (d) with the capacity contribution of COF (based on the mass of COF) in COF@CNTs at  $100 \text{ mA g}^{-1}$ .<sup>[221]</sup>

However, conductivity and stability are the main challenges for COFs as potential anode material for next-generation LIB. Additional focus should be on the charge storage mechanism for COFs in order to understand, interpret and develop the electrochemical properties of the covalent organic frameworks.

### Solid-State Electrolytes

Today, almost all commercial lithium-ion batteries are based on a liquid, non aqueous electrolyte comprised of a 1.2 M solution of lithium hexafluorophosphate ( $\text{LiPF}_6$ ) in a mixture of ethylene carbonate and ethyl methyl carbonate. In order to improve the formation of a stable and ionically conductive solid-electrolyte interface (SEI), some

additives like vinylene carbonate are used. This electrolyte exhibits a high conductivity of  $\approx 10 \text{ mS cm}^{-1}$  at room temperature and is electrochemically stable up to 4.8 V vs. Li/Li<sup>+</sup>. However, the electrolyte undergoes decomposition above 70 °C, is very sensitive towards hydrolysis and is highly flammable. Additionally, the growth of Li dendrites at the anode side is possible, which can lead to short-circuits and a failure of the battery. Based on these negative attributes, the use of non-flammable solid-state electrolytes as replacement is a focus of current research.<sup>[222-224]</sup>

In general, a potential electrolyte for lithium-ion batteries should fulfill a series of requirements. A sufficient chemical and electrochemical stability over a wide potential window is highly desired, as well as a high ionic conductivity at the level of at least  $1 \text{ mS cm}^{-1}$ . Of course, there should be no detectable electronic conductivity in order to avoid short-circuit conditions. In order to enable efficient charge transport, a lithium-ion transference number above 0.3 is required. In addition, fulfilling the demands of economy and exhibiting an acceptable operational and environmental safety is crucial for the commercialization of an electrolyte.<sup>[222,223]</sup>

High ionic conductivity is one of the key factors that determine the possibility of applying a solid-state electrolyte in LIBs. In solid electrolytes, the lithium diffusion takes place inside certain channels, where the binding energy of the lithium ion is favorably low. This can either be inside three-dimensional framework structures for inorganic crystalline electrolytes or along molecular dipoles, providing sites for coordination bonds with lithium-ions, which is the case for polymer + salt electrolytes.<sup>[222,225]</sup>

Different quantitative models exist for the description of the temperature dependence of ionic conductivity. The Arrhenius model is suited for systems with immobile matrices where charge transport occurs as ion hopping between energy barrier-separated sites.<sup>[222,226]</sup> It is usually applicable for crystalline solids with long-range structural order. The frequency of successful jumps  $\Gamma$  through the energy barrier decreases exponentially with the barrier height  $U_B$  in dependence of the temperature  $T$  and the Boltzmann constant  $k_B$  ( $\nu_0$ ) represents the pre-exponential factor):

$$\Gamma = \nu_0 \exp\left(-\frac{U_B}{k_B T}\right) \quad (1.20)$$

Upon applying an external field, the energy barrier height in direction of the field decreases and the frequency of successful jumps in this direction becomes greater than in the opposite way. Under these conditions, the drift velocity ( $v_d$ ) of the charge carriers can be expressed as

$$v_d = \frac{Eq a^2}{2k_B T} c_v v_0 \exp\left(-\frac{U_B}{k_B T}\right) \quad (1.21)$$

Here,  $Eq a^2/2$  describes the additional energy potential which charges experience in the external field and  $c_v$  is the probability of finding a free site in the forced direction of movement. The conductivity can then be described in dependence of the charge carrier mobility  $\mu$  for the recalculated drift velocity:

$$\sigma = nq\mu = \frac{q^2 a^2}{2k_B T} n c_v v_0 \exp\left(-\frac{U_B}{k_B T}\right) \quad (1.22)$$

The pre-exponential factor is dependent on the concentration of charge carriers and available conduction sites and inversely proportional to the temperature (often denoted as  $A/T$ ). The second part is an exponential type dependence on the height of the barrier  $U_B$ , the so-called activation energy. In a typical Arrhenius plot, the logarithm of  $\sigma T$  is plotted against  $1000/T$ . The activation energy can then be calculated from the slope of a fitted linear function.

Another important value for lithium-ion electrolytes is the transference number  $t^+$ , which is expressed as the ratio of charge carried by lithium-ions ( $I_C$ ) to the total electric charge ( $I_C + I_A$ ) transferred through the cell:<sup>[226]</sup>

$$t^+ = \frac{I_C}{I_C + I_A} \quad (1.23)$$

Applying the Bruce-Vincent-Evans technique, the lithium-ion transference number ( $t_{Li^+}$ ) can be calculated upon application of a constant DC polarization ( $\Delta V$ ) and the observation of the initial ( $I_0$ ) and steady-state ( $I_{ss}$ ) current values in dependence of their respective resistance values ( $R_0$  and  $R_{ss}$ ).<sup>[227-230]</sup>

$$t_{Li^+} = \frac{I_{ss}(\Delta V - I_0 R_0)}{I_0(\Delta V - I_{ss} R_{ss})} \quad (1.24)$$

Different classes of solid-state lithium-ion electrolytes are topics of current research. These can be roughly divided into the two main groups of solid polymer electrolytes and inorganic solid electrolytes.<sup>[224]</sup> Polymer electrolytes are based on lithium salts dissolved in solid polymer materials, where one of the most promising polymers is poly-ethylene oxide (PEO) offering a high donor number for lithium-ions. A main drawback is the low conductivity, which is typically in the range of  $10^{-6}$  to  $10^{-8}$  S  $cm^{-1}$  depending on the molecular weight of PEO and the used lithium salt.<sup>[231]</sup> Several different approaches towards enhancing the conductivity have been explored, including

the implementation of passive ceramic fillers such as  $\text{Al}_2\text{O}_3$ ,  $\text{TiO}_2$  and  $\text{SiO}_2$ .<sup>[232–236]</sup> These additives can act, on the one hand, as suppressor of PEO crystallization, and on the other hand promote the ion pair dissociation, weakening the bonds between the lithium ions and the salt anions.

The other main class of solid-state lithium-ion electrolytes are inorganic solid electrolytes, which include crystalline, partially crystalline and amorphous glasses with the ability for lithium conduction.<sup>[224]</sup> These exhibit a high thermal stability and ionic conductivity among solid electrolytes. Due to the conduction of ions through vacancies or interstitial sites, the lithium-ion transference number is close to 1. Inorganic solid electrolytes are mostly comprised of oxides and sulfides and show a wide electrochemical stability window of 0-5 V, but are not truly thermodynamically stable. Oxide-based solid electrolytes contain different types of structural motifs (e.g., argyrodite, garnet, perovskite), where pathways through the crystal structure enable good lithium transport.<sup>[224,237]</sup> An overview of characterized inorganic solid electrolytes is given in Figure 1.14, showing the conductivity of different conductors at room temperature. So far, the material with the highest conductivity at room temperature is  $\text{Li}_{10}\text{GeP}_2\text{S}_{12}$  (LGPS) with a conductivity above  $10^{-2} \text{ S cm}^{-1}$ . This super high conductivity is attributed to the lower electronegativity of S compared to O, which results in weaker binding of lithium ions along the conduction pathways.<sup>[238]</sup>

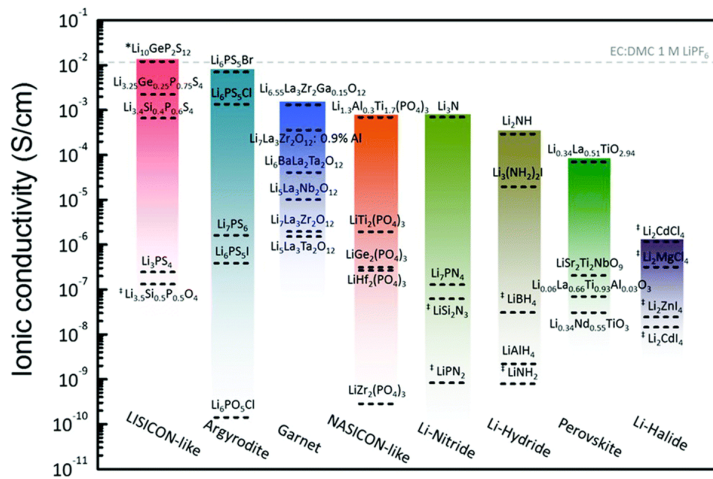


Figure 1.14: Reported total ionic conductivity of solid-state lithium-ion conductors at room temperature.<sup>[237]</sup>

Organic framework based solid-state electrolytes have recently attracted attention, due to their open framework structure and the use of abundant materials.<sup>[224,239]</sup> Beside metal-organic frameworks, covalent organic frameworks are of high interest for

solid-state electrolytes in lithium-ion batteries. They can be divided into all solid-state electrolytes and solid-like electrolytes, where most of the liquid is trapped in the pores of the COF material. The safety issue regarding flammability is reduced but not completely solved for these kinds of electrolytes. Different strategies have been applied for the use of COFs as electrolyte. Initial studies immersed COFs into a solution of lithium salt in organic solvents, resulting in a lithium-ion conductivity in the range of  $10^{-4}$  S cm<sup>-1</sup> and transference number of 0.7-0.8.<sup>[240-242]</sup>

Other groups have anchored immobilized ionic centres within the linkage motif of the COFs. Du et al. proposed a novel type of ionic covalent organic framework constructed with a spiroborate linkage, where sp<sup>3</sup>-hybridized anionic boron centres allowed the tunable use of counter cations. Upon incorporation of Li<sup>+</sup> and consecutive solvation with propylene carbonate (PC), a conductivity of  $3.05 \times 10^{-5}$  S cm<sup>-1</sup> could be achieved.<sup>[243]</sup>

A similar approach was demonstrated by Hu et al. who designed a series of crystalline imidazolate-based ionic COFs.<sup>[244]</sup> They obtained conductivity values in the range of  $10^{-3}$  S cm<sup>-1</sup> for their most conductive COF, concluding that the lithium-ions can freely move through the intrinsic channels in the presence of PC as organic solvent. In Chapter 9 of this thesis, we expand the family of imidazolate-based ionic COFs by doubling the active sites and increasing the pore size. Unfortunately, we were not able to reproduce the interesting results presented by Hu et al..<sup>[244]</sup>

The absence of any solvent is realized in COF-based all solid state electrolytes. Here, the anions are covalently tethered to the inside of the pores of a sulfonated covalent organic framework exhibiting exceptional ion conductivity of  $2.7 \times 10^{-5}$  S cm<sup>-1</sup> and a high lithium-ion transference number of 0.9 at room temperature, showing the great potential of COFs for solid-state lithium-ion electrolytes.<sup>[245]</sup>

However, in order to get more attention in the field of lithium-ion batteries, the ionic conductivity of COFs must be increased. Additionally, the lithium conduction mechanism in COFs should be clarified in order to show the additional benefit of using COFs, which will be a significant challenge for the upcoming years.

### High-voltage Cathode Materials

Beside anode and electrolyte, the cathode or positive electrode during discharge completes a full battery cell. Since the energy density is mainly determined by operating voltage and specific capacity, the focus of current cathode research is on the development of new materials and the improvement of the working potential of existing active materials. Upon charging of a battery, lithium ions are extracted from the cathode side

leaving empty voids in the crystalline structure.<sup>[184]</sup> When a consumer is connected to the battery, the potential built within the cathode structure pulls lithium back from the anode side. Keeping this concept in mind, one can understand why active materials for the cathode side need to offer a rigid cage-structure in order to store a decent amount of lithium in the charged state, as well as maintaining the structure for continuous cycling. Therefore, oxide based transition metal materials are the dominating class of commercialized cathode materials due to their relatively high stability, capacity and working potential.<sup>[183,187]</sup> These materials can be classified into layered, spinel and olivine structures (Figure 1.15) and show different insertion mechanisms depending on their crystal structure.<sup>[246]</sup> Representative, important examples are  $\text{LiCoO}_2$  (LCO),<sup>[247,248]</sup>  $\text{LiMn}_2\text{O}_4$  (LMO),<sup>[249–251]</sup>  $\text{LiFePO}_4$  (LFP),<sup>[252,253]</sup>  $\text{LiNi}_{0.33}\text{Co}_{0.33}\text{Mn}_{0.33}\text{O}_2$  (NCM333 or NCM)<sup>[254–256]</sup> and  $\text{LiNi}_{0.8}\text{Co}_{0.15}\text{Al}_{0.05}\text{O}_2$  (NCA).<sup>[254,257]</sup>

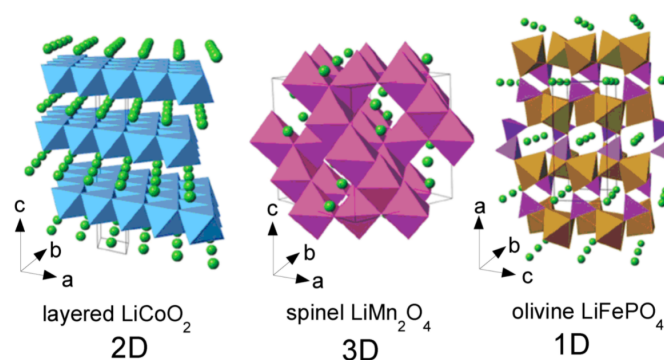


**Figure 1.15:** Crystal structures of three lithium-insertion compounds.<sup>[246]</sup>

Among these, lithium cobalt oxide exhibits the highest theoretically calculated maximum volumetric energy density ( $272 \text{ mAh g}^{-1}$ ,  $1142 \text{ mAh cm}^{-3}$ ) which is highly important for the use in portable electronics, where space is critical.<sup>[258,259]</sup> Compared to the other cathode materials currently used in commercial LIBs, LCO still holds an absolute advantage due to its easy synthesis, high volumetric energy density, excellent cycle stability, high initial Coulombic efficiency, high-voltage plateau and stable charge/discharge voltage (see Figure 1.16).

In 1980, Goodenough et al. discovered lithium cobalt oxide as a viable layered structure cathode material and in 1991 it was successfully commercialized in LIBs by the Sony Corporation. It crystallizes in the  $\alpha\text{-NaFeO}_2$  structure, where oxygen is arranged in a cubic close-packing (ccp) and  $\text{Li}^+$  and  $\text{Co}^{3+}$  are ordered in alternating (111) planes. Upon slight distortion of the lattice to a hexagonal symmetry, LCO crystallizes in the space group  $R\bar{3}m$  with  $a = 2.82 \text{ \AA}$  and  $c = 14.08 \text{ \AA}$ . During discharge, the oxygen layers rearrange to a distorted ccp oxygen lattice, resulting in an irreversible hexagonal close

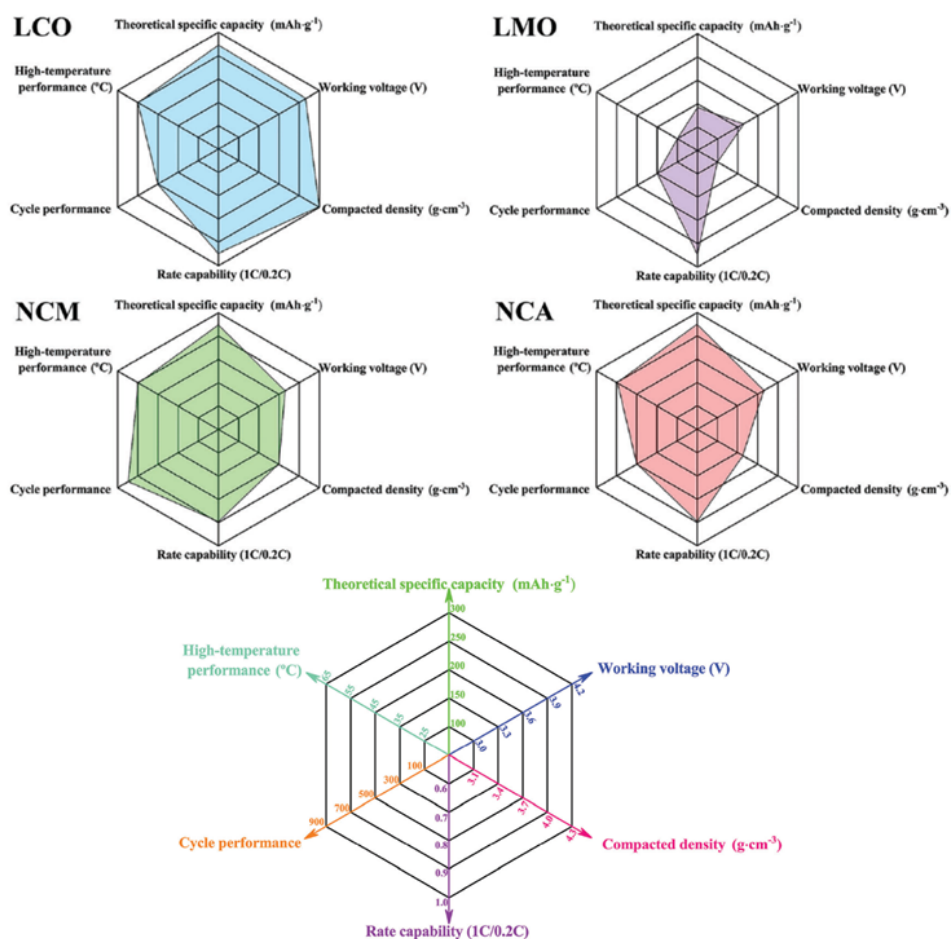


**Figure 1.16:** Performance comparison of cathode materials in portable electronic products showing  $\text{LiCoO}_2$  (LCO),  $\text{LiMn}_2\text{O}_4$  (LMO),  $\text{LiNi}_{0.33}\text{Co}_{0.33}\text{Mn}_{0.33}\text{O}_2$  (NCM333 or NCM) and  $\text{LiNi}_{0.8}\text{Co}_{0.15}\text{Al}_{0.05}\text{O}_2$  (NCA).<sup>[187]</sup>

packing in  $\text{CoO}_2$  after all lithium-ions have been removed.<sup>[248,260,261]</sup> LCO-based batteries have typically an upper voltage limit of 4.2 V vs.  $\text{Li}/\text{Li}^+$  equaling a specific capacity of  $137 \text{ mAh g}^{-1}$  and extraction of 0.5 Li per LCO. However, cycling to voltages greater than 4.2 V causes a significant structural instability and severe capacity fading.<sup>[262–267]</sup> Reasons behind this include dissolution of Co and a loss of O from the lattice when the upper cut-off potential exceeds 4.2 V.

In order to overcome these critical problems, many different strategies have been reported trying to promote long-term stability at high cut-off voltages, e.g., single<sup>[268–270]</sup> and mixed element doping,<sup>[271–273]</sup> morphology control,<sup>[274]</sup> post-thermal treatment<sup>[275–277]</sup> and modifications of electrolyte, separator and binder.<sup>[278–283]</sup>

Promising results have also been shown by protecting the electrode surface using

different solid lithium ion conductive coatings, which can impede a direct contact of electrode and electrolyte and subsequently suppress side reactions, promote surface charge transfer, inhibit the dissolution of transition metal ions and prevent the structure from transformation and pulverization.<sup>[284–286]</sup> Among these surface coating methods, a great deal of attention has been paid to the atomic layer deposition (ALD) of various metal oxide coatings, including Al<sub>2</sub>O<sub>3</sub>, TiO<sub>2</sub> and ZrO<sub>2</sub>.<sup>[287–290]</sup> These coatings significantly enhanced the cyclic performance and rate capability of various cathode materials, but lack in ionic conductivity.<sup>[287–290]</sup>

In Chapter 8 of this thesis we develop a process for the atomic layer deposition of a lithium niobate protective coating for an LCO based cathode which shows promising results regarding capacity and cycling stability.

## 1.5 References

- [1] Council Decision (EU) 2016/1841 of 5 October 2016 on the conclusion, on behalf of the European Union, of the Paris Agreement adopted under the United Nations Framework Convention on Climate Change.
- [2] UNFCCC (1997) Kyoto Protocol to the United Nations Framework Convention on Climate Change adopted at COP3 in Kyoto, Japan, on 11 December 1997.
- [3] Beschluss des Ersten Senats vom 24. März 2021 - 1 BvR 2656/18 -, Rn. 1-270.
- [4] G. Luderer, C. Kost, D. Sörgel, Ariadnereport: Deutschland auf dem Weg zur Klimaneutralität 2045: Szenarien und Pfade im Modellvergleich, Ariadnereport, Kopernikus-Projekte: Aridane, Bundesministerium für Bildung und Forschung, 2021.
- [5] F. Ueckerdt, C. Bauer, A. Dirnaichner, J. Everall, R. Sacchi, L. G., *Nat. Clim. Chang.* **2021**, *11*, 384–393.
- [6] Referat Öffentlichkeitsarbeit, *Die Nationale Wasserstoffstrategie*, Bundesministerium für Wirtschaft und Energie (BMWi), Deutschland, 2020.
- [7] J. Dendooven, C. Detavernier in *Atomic Layer Deposition in Energy Conversion Applications*, John Wiley & Sons, Ltd, 2017, Chapter 1, pp. 1–40.
- [8] V. Miikkulainen, M. Leskelä, M. Ritala, R. L. Puurunen, *J. Appl. Phys.* **2013**, *113*, 021301.
- [9] S. I. Koltsov, V. B. Aleskovskii, *Zh. Prikl. Khim* **1967**, *40*, 872.

- [10] A. M. Shevjakov, G. N. Kuznetsova, V. B. Aleskovskii in Proceedings of the second USSR conference on high-temperature chemistry of oxides, Leningrad, USSR, pp. 26–29.
- [11] T. Suntola, J. Antson, *International patent FIN 52359 US 4 058 430 1974*, publication Nov 15, 1977.
- [12] T. Aaltonen, M. Alnes, O. Nilsen, L. Costelle, H. Fjellvag, *J. Mater. Chem.* **2010**, *20*, 2877.
- [13] R. L. Puurunen, *Chem. Vap. Depos.* **2014**, *20*, 332–344.
- [14] A. L. Johnson, J. D. Parish in *Organometallic Chemistry: Volume 42, Vol. 42*, The Royal Society of Chemistry, **2019**, pp. 1–53.
- [15] R. L. Puurunen, *J. Appl. Phys.* **2005**, *97*, 121301.
- [16] R. L. Puurunen, W. Vandervorst, *J. Appl. Phys.* **2004**, *96*, 4878.
- [17] R. K. Grubbs, N. J. Steinmetz, S. M. George, *J. Vac. Sci. Technol. B* **2004**, *22*, 1811.
- [18] R. L. Puurunen, W. Vandervorst, *J. Appl. Phys.* **2004**, *96*, 7686.
- [19] K. Kukli, M. Ritala, R. Matero, M. Leskelä, *J. Cryst. Growth* **2002**, *212*, 459.
- [20] R. L. Puurunen, *J. Appl. Phys.* **2004**, *95*, 4777.
- [21] J. Lu, J. W. Elam, P. C. Stair, *Surf. Sci. Rep.* **2016**, *71*, 410–472.
- [22] adapted from <https://www.atomiclimits.com/alddatabase/>, (accessed 1 Dez 2021).
- [23] S. Bystrova, A. A. I. Aarnink, J. Holleman, R. A. M. Wolters, *J. Electrochem. Soc.* **2005**, *152*, G522.
- [24] Y. J. Lee, S.-W. Kang, *J. Vac. Sci. Technol. A* **2002**, *A 20*, 1983.
- [25] Y. J. Lee, S.-W. Kang, *Electrochem. Solid-State Lett.* **2002**, *5*, C91.
- [26] E. Färm, M. Kemell, M. Ritala, M. Leskelä, *J. Phys. Chem. C* **2008**, *C 112*, 15791.
- [27] E. Färm, M. Kemell, E. Santala, M. Ritala, M. Leskelä, *J. Electrochem. Soc.* **2010**, *157*, K10.
- [28] M. Kemell, M. Ritala, M. Leskelä, R. Groenen, S. Lindfors, *Chem. Vap. Deposition* **2008**, *14*, 347.
- [29] C. Henkel, S. Abermann, O. Bethge, E. Bertagnolli, *Semicond. Sci. Technol.* **2009**, *24*, 125013.
- [30] D. Gu, H. Baumgart, T. M. Abdel-Fattah, G. Namkoong, *ACS Nano* **2010**, *4*, 753.

- 
- [31] S. M. Rossnagel, A. Sherman, F. Turner, *J. Vac. Sci. Technol. B* **2000**, B 18, 2016.
- [32] H. Kim, S. M. Rossnagel, *J. Vac. Sci. Technol. A* **2002**, A 20, 802.
- [33] R. L. Puurunen, *Appl. Surf. Sci.* **2005**, 245, 6.
- [34] K. Kukli, M. Ritala, M. Leskelä, *J. Electrochem. Soc.* **2001**, 148, F35.
- [35] M. Putkonen, M. Nieminen, L. Niinistö, *Thin Solid Films* **2004**, 466, 103.
- [36] M. Lulla, J. Asari, J. Aarik, K. Kukli, R. Rammula, U. Tapper, E. Kauppinen, V. Sammelselg, *Microchim. Acta* **2006**, 155, 195.
- [37] J. I. Skarp, P. J. Soininen, P. T. Soininen, *Appl. Surf. Sci.* **1997**, 112, 251.
- [38] M. Ritala, M. Juppo, K. Kukli, A. Rahtu, M. Leskelä, *J. Phys. IV France* **1999**, 9, Pr8/1021.
- [39] R. Matero, A. Rahtu, M. Ritala, M. Leskelä, T. Sajavaara, *Thin Solid Films* **2000**, 368, 1.
- [40] D. H. Levy, D. Freeman, S. F. Nelson, P. J. Cowdery-Corvan, L. M. Irving, *Appl. Phys. Lett.* **2008**, 92, 92101.
- [41] O.-K. Kwon, J.-H. Kim, H.-S. Park, S.-W. Kang, *J. Electrochem. Soc.* **2004**, 151, G109.
- [42] S. H. Kwon, O. K. Kwon, J. H. Kim, S. J. Jeong, S. W. Kim, S. W. Kang, *J. Electrochem. Soc.* **2007**, 154, H773.
- [43] S. Choi, Y. K. Cha, B. S. Seo, S. Park, J. H. Park, S. Shin, K. S. Seol, J. B. Park, Y. S. Jung, Y. Park, Y. Park, I. K. Yoo, S. H. Choi, *J. Phys. D: Appl. Phys.* **2007**, 40, 1426.
- [44] J. Hämäläinen, M. Kemell, F. Munnik, U. Kreissig, M. Ritala, M. Leskelä, *Chem. Mater.* **2008**, 20, 2903.
- [45] R. L. Puurunen, A. Root, S. Haukka, E. I. Iiskola, M. Lindblad, A. O. I. Krause, *J. Phys. Chem. B* **2000**, B104, 6599.
- [46] R. L. Puurunen, M. Lindblad, A. Root, A. O. I. Krause, *Phys. Chem. Chem. Phys.* **2001**, 3, 1093.
- [47] K.-E. Elers, M. Ritala, M. Leskelä, L.-S. Johansson, *J. Phys. IV France* **1995**, 5, C5/1021.
- [48] F. G. McIntosh, E. L. Piner, J. C. Roberts, M. K. Behbehani, M. E. Aumer, N. A. El-Masry, S. M. Bedair, *Appl. Surf. Sci.* **1997**, 112, 98.
- [49] M. A. Khan, J. N. Kuznia, D. T. Olson, *Appl. Phys. Lett.* **1993**, 63, 3470.

- [50] V. Pore, M. Heikkilä, M. Ritala, M. Leskelä, S. Areva, *J. Photochem. Photobiol.* **2006**, A177, 68.
- [51] L. Hiltunen, M. Leskelä, M. Mäkelä, L. Niinistö, E. Nykänen, P. Soininen, *Thin Solid Films* **1988**, 166, 149.
- [52] H. C. M. Knoops, L. Baggetto, E. Langereis, M. C. M. van de Sanden, J. H. Klootwijk, F. Roozeboom, R. A. H. Niessen, P. H. L. Notten, W. M. M. Kessels, *J. Electrochem. Soc.* **2008**, 155, G287.
- [53] J. Musschoot, Q. Xie, D. Deduytsche, S. V. den Berghe, R. L. V. Meirhaeghe, C. Detavernier, *Microelectron. Eng.* **2009**, 86, 72.
- [54] V. Pore, M. Ritala, M. Leskelä, *Chem. Vap. Deposition* **2007**, 13, 163.
- [55] B. W. Sanders, A. Kitai, *Chem. Mater.* **1992**, 4, 105.
- [56] S. Jeon, S. Bang, S. Lee, S. Kwon, W. Jeong, H. Jeon, H. J. Chang, H.-H. Park, *J. Korean Phys. Soc.* **2008**, 53, 3287.
- [57] Y. S. Kim, S. J. Yun, *Appl. Surf. Sci.* **2004**, 229, 105.
- [58] J. R. Bakke, J. S. King, H. J. Jung, R. Sinclair, S. F. Bent, *Thin Solid Films* **2010**, 518, 5400.
- [59] Y. Z. Feng, S. P. Guo, *J. Mater. Sci. Lett.* **1996**, 15, 1824.
- [60] E. Kurtz, H. D. Jung, T. Hanada, Z. Zhu, T. Sekiguchi, T. Yao, *J. Cryst. Growth* **1998**, 184/185, 242.
- [61] E. M. Larramendi, Z. B. K. Gutierrez, O. de Melo, U. Woggon, D. Schikora, K. Lischka, *J. Cryst. Growth* **2010**, 312, 1807.
- [62] S. Zhang, H. Hajiyani, A. G. Hufnagel, J. Kampmann, B. Breitbach, T. Bein, D. Fattakhova-Rohlfing, R. Pentcheva, C. Scheu, *Z. Phys. Chem* **2020**, 234, 683–698.
- [63] J. W. Elam, M. D. Groner, S. M. George, *Rev. Sci. Instrum.* **2002**, 73, 2981–2987.
- [64] M. N. Rocklein, S. M. George, *Anal. Chem.* **2003**, 75, 4975–4982.
- [65] G. Sauerbrey, *Z. Phys.* **1959**, 155, 206–222.
- [66] J. H. Block, *Ber. Bunsenges. phys. Chem.* **1977**, 81, 777.
- [67] M. Juppo, A. Rahtu, M. Ritala, M. Leskelä, *Langmuir* **2000**, 16, 4034–4039.
- [68] W. Paul, H. Steinwedel, *Z. Naturforsch. A* **1953**, 8, 448–450.
- [69] M. Ritala, M. Juppo, K. Kukli, A. Rahtu, M. Leskelä, *J. Phys. IV France* **1999**, 9, 1021–1028.

- 
- [70] E. Langereis, S. B. S. Heil, H. C. M. Knoop, W. Keuning, M. C. M. van de Sanden, W. M. M. Kessels, *J. Phys. D: Appl. Phys.* **2009**, *42*, 073001.
- [71] Y. J. Chabal, *Surf. Sci. Rep.* **1988**, *8*, 211–357.
- [72] A. C. Dillon, A. W. Ott, J. D. Way, S. M. George, *Surf. Sci.* **1995**, *322*, 230–242.
- [73] D. N. Goldstein, J. A. McCormick, S. M. George, *J. Phys. Chem. C* **2008**, *112*, 19530–19539.
- [74] J. Kwon, M. Dai, M. D. Halls, E. Langereis, Y. J. Chabal, R. G. Gordon, *J. Phys. Chem. C* **2009**, *113*, 654–660.
- [75] B. A. Sperling, W. A. Kimes, J. E. Maslar, *Appl. Surf. Sci.* **2010**, *256*, 5035–5041.
- [76] W. Xu, P. C. Lemaire, K. Sharma, R. J. Gasvoda, D. M. Hausmann, S. Agarwal, *J. Vac. Sci. Technol. A* **2021**, *39*, 032402.
- [77] J. Bachmann, *Beilstein J. Nanotechnol* **2014**, *5*, 245–248.
- [78] V. Cremers, R. L. Puurunen, J. Dendooven, *Appl. Phys. Rev.* **2019**, *6*, 021302.
- [79] B. Pitschak, J. Mergel, *Electrolytic Processes. In: Töpler J., Lehmann J. (eds) Hydrogen and Fuel Cell*, Springer, Berlin, Heidelberg, **2016**.
- [80] S. Shiva Kumar, V. Himabindu, *Mater. Sci. Energy Technol.* **2019**, *2*, 442–454.
- [81] J. Rossmeisl, Z. -. Qu, H. Zhu, G. -. Kroes, J. K. Nørskov, *J. Electroanal. Chem.* **2007**, *607*, 83–89.
- [82] S. Laha, Y. Lee, F. Podjaski, D. Weber, V. Duppel, L. M. Schoop, F. Pielhofer, C. Scheurer, K. Müller, U. Starke, K. Reuter, B. V. Lotsch, *Adv. Energy Mater.* **2019**, 1803795.
- [83] V. I. Sharma, B. Yildiz, *J. Electrochem. Soc.* **2010**, *157*, B441–B448.
- [84] V. Schröder, B. Emonts, H. Janßen, H. P. Schulze, *Chem. Eng. Technol.* **2004**, *27*, 847–851.
- [85] J. R. Varcoe, P. Atanassov, D. R. Dekel, A. M. Herring, M. a. Hickner, P. a. Kohl, A. R. Kucernak, W. E. Mustain, K. Nijmeijer, K. Scott, T. Xu, L. Zhuang, *Energy Environ. Sci.* **2014**, *7*, 3135–3191.
- [86] M. M. Carmo, D. L. Fritz, J. Mergel, D. Stolten, *Int. J. Hydrogen Energy* **2013**, *38*, 4901–4934.
- [87] C. Iwakura, K. Hirao, H. Tamura, *Electrochim. Acta* **1977**, *22*, 329–334.
- [88] R. Kötz, S. Stucki, *Electrochim. Acta* **1986**, *31*, 1311–1316.

- [89] F. M. Sapountzi, J. M. Gracia, C. (-J. Weststrate, H. O. Fredriksson, J. ( Niemantsverdriet, *Prog. Energy Combust. Sci.* **2017**, *58*, 1–35.
- [90] A. T. Marshall, S. Sunde, M. Tsytkin, R. Tunold, *Int. J. Hydrog. Energy* **2007**, *32*, 2320–2324.
- [91] S. Siracusano, N. Van Dijk, E. Payne-Johnson, V. Baglio, A. S. Aricò, *Appl. Catal. B* **2015**, *164*, 488–495.
- [92] J. L. Corona-Guinto, L. Cardéno-García, D. C. Martínez-Casillas, J. M. Sandoval-Pineda, P. Tamayo-Meza, R. Silva-Casarin, R. G. González-Huerta, *Int. J. Hydrog. Energy* **2013**, *38*, 12667–12673.
- [93] A. T. Marshall, R. G. Haverkamp, *Electrochim. Acta* **2010**, *55*, 1978–1984.
- [94] K. Kadakia, M. K. Datta, O. I. Velikokhatnyi, P. Jampani, S. K. Park, S. J. Chung, P. N. Kumta, *J. Power Sources* **2014**, *245*, 362–370.
- [95] A. Marshall, B. Børresen, G. Hagen, M. Tsytkin, R. Tunold, *Mater. Chem. Phys.* **2005**, *94*, 226–232.
- [96] L. Da Silva, V. Alves, S. Trasatti, J. Boodts, *J. Electroanal. Chem.* **1997**, *427*, 97–104.
- [97] A. Fujishima, K. Honda, *Nature* **1972**, *238*, 37–38.
- [98] T. Hisatomi, J. Kubota, K. Domen, *Chem. Soc. Rev.* **2014**, *43*, 7520–7535.
- [99] C. Ros, T. Andreu, J. R. Morante, *J. Mater. Chem. A* **2020**, *8*, 10625–10669.
- [100] J. Joy, J. Mathew, S. C. George, *Int. J. Hydrog. Energy* **2018**, *43*, 4804–4817.
- [101] K. Sivula, R. van de Krol, *Nat. Rev. Mater.* **2016**, *1*, 15010.
- [102] W. Yan, R. R. Prabhakar, J. Tan, S. D. Tilley, J. Moon, *Chem. Soc. Rev.* **2019**, *48*, 4979–5015.
- [103] X. -. Xu, L. Pan, X. Zhang, L. Wang, J. -. Zhou, *Adv. Sci.* **2019**, *6*, 1801505.
- [104] D. J. Martin, *Investigation into High Efficiency Visible Light Photocatalysts for Water Reduction and Oxidation*, Springer, Berlin, Heidelberg, **2015**.
- [105] C. Ding, J. Shi, Z. Wang, C. Li, *ACS Catal.* **2017**, *7*, 675.
- [106] G. Wang, Y. Ling, H. Wang, L. Xihong, Y. Li, *J. Photochem. Photobiol. C* **2014**, *19*, 35.
- [107] J. Gan, X. Lu, Y. Tong, *Nanoscale* **2014**, *6*, 7142.
- [108] C. Ding, J. Shi, Z. Wang, C. Li, *ACS Catal.* **2017**, *7*, 675.
- [109] X. Yang, C. Du, R. Liu, J. Xie, D. Wang, *J. Cataly.* **2013**, *304*, 86.

- 
- [110] J. Li, N. Wu, *Catal. Sci.* **2015**, *5*, 1360.
- [111] Z. Huang, L. Pan, J. Zou, X. Zhang, L. Wang, *Nanoscale* **2014**, *6*, 1444.
- [112] D. Dengwei Jing, L. Guo, L. Zhao, X. Zhang, H. Liu, M. Li, S. Shen, G. Liu, X. Hu, X. Zhang, K. Zhang, L. Ma, P. Guo, *Int. J. Hydrog. Energy* **2010**, *35*, 7087–7097.
- [113] A. Kay, I. Cesar, M. Grätzel, *J. Am. Chem. Soc.* **2006**, *128*, 15714–15721.
- [114] J. Y. Kim, G. Magesh, D. H. Youn, J. -. Jang, J. Kubota, K. Domen, S. L. Lee, *Sci. Rep.* **2013**, *3*, 2681.
- [115] B. M. Klahr, T. W. Hamann, *J. Phys. Chem. C* **2011**, *15*, 8393–8399.
- [116] S. C. Riha, B. M. Klahr, E. C. Tyo, S. Seifert, S. Vajda, M. J. Pellin, T. W. Hamann, A. B. F. Martinson, *ACS Nano* **2013**, *7*, 2396–2405.
- [117] H. K. Dunn, J. M. Feckl, A. Müller, D. Fattakhova-Rohlfing, J. Morehead, S. G. and Roos, L. M. Peter, C. Scheu, T. Bein, *Phys. Chem. Chem. Phys.* **2014**, *16*, 24610–24620.
- [118] S. U. M. Khan, J. Akikusa, *J. Phys. Chem. B* **1999**, *49*, 7184–7189.
- [119] A. A. Tahir, K. G. U. Wijayantha, S. Saremi-Yarahmadi, M. Mazhar, V. McKee, *Chem. Mater.* **2009**, *21*, 3763–3772.
- [120] K. Sivula, R. Zboril, F. Le Formal, R. Robert, A. Weidenkaff, J. Tucek, J. Frydrych, M. Grätzel, *J. Am. Chem. Soc.* **2010**, *132*, 7436–7444.
- [121] O. Zandi, A. R. Schon, H. Hajibabaei, T. W. Hamann, *Chem. Mater.* **2016**, *28*, 765–771.
- [122] M. Stefik, M. Cornuz, N. Mathews, T. Hisatomi, S. Mhaisalkar, M. Grätzel, *Nano Lett.* **2012**, *12*, 5431–5435.
- [123] P. Chakthranont, B. A. Pinaud, L. C. Seitz, A. J. Forman, T. F. Jaramillo, *Adv. Mater. Interfaces* **2016**, *3*, 1500626.
- [124] A. J. Abel, I. Garcia-Torregrosa, A. M. Patel, B. Opananont, J. B. Baxter, *J. Phys. Chem. C* **2015**, *119*, 4454–4465.
- [125] N. T. Hahn, C. B. Mullins, *Chem. Mater.* **2010**, *22*, 6474–6482.
- [126] D. -. Qin, Y. -. Li, T. Wang, Y. Li, X. -. Lu, J. Gu, Y. -. Zhao, Y. -. Song, C. -. Tao, *J. Mater. Chem. A* **2015**, *3*, 6751–6755.
- [127] O. Zandi, B. M. Klahr, T. W. Hamann, *Energy Environ. Sci.* **2013**, *6*, 634–642.
- [128] T. W. Kim, K. -. Choi, *Science* **2014**, *343*, 990–994.

- [129] C. D. Bohn, A. K. Agrawal, E. C. Walter, M. D. Vaudin, A. A. Herzing, P. M. Haney, A. A. Talin, V. A. Szalai, *J. Phys. Chem. C* **2012**, *116*, 15290–15296.
- [130] C. G. Morales-Guio, M. T. Mayer, A. Yella, S. D. Tilley, M. Grätzel, X. Hu, *J. Am. Chem. Soc.* **2015**, *137*, 9927–9936.
- [131] L. M. Peter, K. G. U. Wijayantha, A. A. Tahir, *Faraday Discuss.* **2012**, *155*, 309–322.
- [132] B. Klahr, S. Gimenez, F. Fabregat-Santiago, J. Bisquert, T. W. Hamann, *J. Am. Chem. Soc.* **2012**, *134*, 16693–16700.
- [133] D. K. Zhong, J. Sun, H. Inumaru, D. R. Gamelin, *J. Am. Chem. Soc.* **2009**, *131*, 6086–6087.
- [134] C. Du, X. Yang, M. T. Mayer, H. Hoyt, J. Xie, G. McMahon, G. Bischooping, D. Wang, *Angew. Chem. Int. Ed.* **2013**, *52*, 12692–12695.
- [135] M. M. Tallarida, C. Das, D. Cibrev, K. Kukli, A. Tamm, M. Ritala, T. Lana-Villarreal, R. Gomez, M. Leskelä, D. Schmeisser, *J. Phys. Chem. Lett.* **2014**, *5*, 3582–3587.
- [136] O. Zandi, T. W. Hamann, *J. Phys. Chem. Lett.* **2014**, *5*, 1522–1526.
- [137] P. S. Bassi, Gurudayal, L. H. Wong, J. Barber, *Phys. Chem. Chem. Phys.* **2014**, *16*, 11834–11842.
- [138] J. K. Cooper, S. Gul, F. M. Toma, L. Chen, P.-A. Glans, J. Guo, J. W. Ager, J. Yano, I. D. Sharp, *Chem. Mater.* **2014**, *26*, 5365–5373.
- [139] Z. Zhao, Z. Li, Z. Zou, *Phys. Chem. Chem. Phys.* **2011**, *13*, 4746–4753.
- [140] J. K. Cooper, S. Gul, F. M. Toma, L. Chen, Y.-S. Liu, J. Guo, J. W. Ager, J. Yano, I. D. Sharp, *J. Phys. Chem. C* **2015**, *119*, 2969–2974.
- [141] T. D. Nguyen, V. -. Nguyen, S. Nanda, D. -. N. Vo, V. H. Nguyen, T. V. Tran, L. X. Nong, T. T. Nguyen, L. -. Bach, B. Abdullah, S. -. Hong, T. V. Nguyen, *Environ. Chem. Lett.* **2020**, *18*, 1779–1801.
- [142] Y. Liang, T. Tsubota, L. P. A. Mooij, R. van de Krol, *J. Phys. Chem. C* **2011**, *115*, 17594–17598.
- [143] M. Li, L. Zhao, L. Guo, *Int. J. Hydrog. Energy* **2010**, *35*, 7127–7133.
- [144] H. Ye, J. Lee, J. S. Jang, A. J. Bard, *J. Phys. Chem. C* **2010**, *114*, 13322–13328.
- [145] D. K. Zhong, S. Choi, D. R. Gamelin, *J. Am. Chem. Soc.* **2011**, *133*, 18370–18377.
- [146] H. Ye, H. S. Park, A. J. Bard, *J. Phys. Chem. C* **2011**, *115*, 12464–12470.
- [147] F. F. Abdi, R. van de Krol, *J. Phys. Chem. C* **2012**, *116*, 9398–9404.

- 
- [148] T. W. Kim, K.-S. Choi, *Science* **2014**, *343*, 990–994.
- [149] X. Shi, K. Zhang, K. Shin, M. Ma, J. Kwon, I. T. Choi, J. K. Kim, H. K. Kim, D. H. Wang, J. H. Park, *Nano Energy* **2015**, *13*, 182–191.
- [150] T. W. Hamann, *Dalton Trans.* **2012**, *41*, 7830–7834.
- [151] Y. Pihosh, I. Turkevych, K. Mawatari, J. Uemura, Y. Kazoe, S. Kosar, K. Makita, T. Sugaya, T. Matsui, D. Fujita, M. Tosa, M. Kondo, T. Kitamori, *Sci. Rep.* **2015**, *5*, 11141.
- [152] F. P. Koffyberg, F. A. Benko, *J. Appl. Phys.* **1982**, *53*, 1173–1177.
- [153] B. K. Meyer, A. Polity, D. Reppin, M. Becker, P. Hering, P. J. Klar, T. Sander, C. Reindl, J. Benz, M. Eickhoff, C. Heiliger, M. Heinemann, J. Bläsing, A. Krost, S. Shokovets, C. Müller, C. Ronning, *Phys. Status Solidi B* **2012**, *249*, 1487–1501.
- [154] M. Heinemann, B. Eifert, C. Heiliger, *Phys. Rev. B Condens. Matter* **2013**, *87*, 115111.
- [155] D. Chauhan, V. Satsangi, S. Dass, R. Shrivastav, *Bull. Mater. Sci.* **2006**, *29*, 709.
- [156] L. C. Olsen, R. C. Bohara, M. W. Urie, *Appl. Phys. Lett.* **1979**, *34*, 47–49.
- [157] S. Kakuta, T. Abe, *ECS Solid State Lett.* **2009**, *12*, P1–P3.
- [158] Y. K. Jeong, G. M. Choi, *J. Phys. Chem. Solids* **1996**, *57*, 81–84.
- [159] T. Iijima, Y. Toyoguchi, J. Nishimura, H. Ogawa, *J. Power Sources* **1980**, *5*, 99–109.
- [160] S. P. Kuksenko, *Russ. J. Appl. Chem.* **2004**, *77*, 1019–1021.
- [161] C.-Y. Chiang, Y. Shin, S. Ehrman, *Chem. Soc. Rev.* **2011**, *159*, B227–B231.
- [162] P. Chand, A. Gaur, A. Kumar, U. Kumar Gaur, *Appl. Surf. Sci.* **2014**, *307*, 280–286.
- [163] C.-Y. Chiang, Y. Shin, S. Ehrman, *Energy Procedia* **2014**, *61*, 1799–1802.
- [164] M. F. M. F. Lichterman, K. Sun, S. Hu, X. Zhou, M. T. McDowell, M. R. Shaner, M. R. Richter, E. J. Crumlin, A. I. Carim, F. H. Saadi, B. S. Brunshwig, N. S. Lewis, *Catal. Today* **2016**, *262*, 11.
- [165] A. Q. Contractor, J. O. M. Bockris, *Electrochim. Acta* **1984**, *29*, 1427–1434.
- [166] D. V. Esposito, I. Levin, T. P. Moffat, A. A. Talin, *Nat. Mater.* **2013**, *12*, 562–568.
- [167] B. Seger, T. Pedersen, A. B. Laursen, P. C. K. Vesborg, O. Hansen, I. Chorkendorff, *J. Am. Chem. Soc.* **2013**, *135*, 1057–1064.
- [168] B. Seger, D. S. Tilley, T. Pedersen, P. C. K. Vesborg, O. Hansen, M. Grätzel, I. Chorkendorff, *RSC Adv.* **2013**, *3*, 25902–25907.

- [169] C. Ros, T. Andreu, M. D. Hernandez-Alonso, G. P. Perez, J. Arbiol, J. R. Morante, *ACS Appl. Mater. Interfaces* **2017**, *9*, 17932–17941.
- [170] C. Ros, N. M. Carretero, J. David, J. Arbiol, T. Andreu, J. R. Morante, *ACS Appl. Mater. Interfaces* **2019**, *11*, 29725–29735.
- [171] Y. W. Chen, J. D. Prange, S. Dühnen, Y. Park, M. Gunji, C. E. D. Chidsey, P. C. McIntyre, *Nat. Mater.* **2011**, *10*, 539–544.
- [172] A. G. Scheuermann, D. Q. Lu, T. Ito, C. E. D. Chidsey, P. C. McIntyre, *ECS Trans.* **2014**, *64*, 265–276.
- [173] T. Moehl, J. Suh, L. Sévery, R. Wick-Joliat, S. D. Tilley, *ACS Appl. Mater. Interfaces* **2017**, *9*, 43614.
- [174] A. Paracchino, V. Laporte, K. Sivula, M. Grätzel, E. Thimsen, *Nat. Mater.* **2011**, *10*, 456–461.
- [175] Y.-F. Lim, C. S. Chua, C. J. J. Lee, D. Chi, *Phys. Chem. Chem. Phys.* **2014**, *16*, 25928–25934.
- [176] J. Azevedo, S. D. Tilley, M. Schreier, M. Stefik, C. Sousa, J. P. Araújo, A. Mendes, M. Grätzel, M. T. Mayer, *Nano Energy* **2016**, *24*, 10–16.
- [177] W. L. Jang, Y. M. Lu, W. S. Hwang, T. L. Hsiung, H. P. Wang, *Appl. Phys. Lett.* **2009**, *94*, 92–95.
- [178] C. Y. Lin, Y. H. Lai, D. Mersch, E. Reisner, *Chem. Sci.* **2012**, *3*, 3482–3487.
- [179] C. Ros, T. Andreu, J. David, J. Arbiol, J. R. Morante, *J. Mater. Chem. A* **2019**, *7*, 21892–21902.
- [180] J. Yang, K. Walczak, E. Anzenberg, F. M. Toma, G. Yuan, J. Beeman, A. Schwartzberg, Y. Lin, M. Hettick, A. Javey, J. W. Ager, J. Yano, H. Frei, I. D. Sharp, *J. Am. Chem. Soc.* **2014**, *136*, 6191–6194.
- [181] K. Sivula, *ChemCatChem* **2014**, 2796–2797.
- [182] Y. Kato, Z. Ogumi, J. M. P. Martin, *Lithium-Ion Batteries: Overview, Simulation, and Diagnostics*, Pan Stanford Publishing, **2019**.
- [183] X. Lin, M. Salari, L. M. R. Arava, P. M. Ajayanc, M. W. Grinstaff, *Chem. Soc. Rev.* **2016**, *45*, 5848–5887.
- [184] F. Wu, J. Maier, Y. Yu, *Chem. Soc. Rev.* **2020**, *49*, 1569–1614.
- [185] P. Roy, S. K. Srivastava, *J. Mater. Chem. A* **2015**, *13*, 2454.
- [186] M. Madian, A. Eychmüller, L. Giebeler, *Batteries* **2018**, *4*, 7.

- 
- [187] L. Wang, B. Chen, J. Ma, G. Cui, L. Chen, *Chem. Soc. Rev.* **2018**, *47*, 6505–6602.
- [188] S. Goriparti, E. Miele, F. De Angelis, E. Di Fabrizio, R. Proietti Zaccaria, C. Capiglia, *J. Power Sources* **2014**, *257*, 421–443.
- [189] M. R. Palacin, *Chem. Soc. Rev.* **2009**, *38*, 2565–2575.
- [190] X. Zhao, J. Zhang, J. Zhang, C. Gong, X. Gu, Z. Ma, J. Zhou, L. Yu, Z. Zhang, *J. Power Sources* **2015**, *294*, 223–231.
- [191] Y. Deng, C. Fang, G. Chen, *J. Power Sources* **2016**, *304*, 81–101.
- [192] V. Raju, X. Wang, W. Luo, X. Ji, *Chem. Eur. J.* **2014**, *20*, 7686–7691.
- [193] L. Yin, S. Chai, F. Wang, J. Huang, J. Li, C. Liu, X. Kong, *Ceram. Int.* **2016**, *42*, 9433–9437.
- [194] Q. Guo, S. Chen, X. Qin, *Mater. Lett.* **2014**, *119*, 4–7.
- [195] E. Grigorova, T. S. Mandzhukova, M. Khristov, M. Yoncheva, R. Stoyanova, E. Zhecheva, *J. Mater. Sci.* **2011**, *46*, 7106–7113.
- [196] H. Kim, J. Cho, *J. Mater. Chem.* **2008**, *18*, 771–775.
- [197] N. Li, C. R. Martin, B. Scrosati, *Electrochim. Solid State Lett.* **2000**, *3*, 316.
- [198] O. Cevher, M. O. Guler, U. Tocoglu, H. Akbulut, *Int. J. Energy Res.* **2014**, *38*, 499–508.
- [199] J. Liang, X. Y. Yu, H. Zhou, H. B. Wu, S. Ding, X. W. Lou, *Angew. Chem. Int. Ed.* **2014**, *53*, 12803–12807.
- [200] test, *Designing Electrolytes for Lithium-Ion and Post-Lithium Batteries*, Jenny Stanford Publishing, **2021**.
- [201] M. J. Reddy, S. H. Ryu, A. M. Shanmugharaj, *Nanoscale* **2016**, *8*, 471–482.
- [202] G. Wu, M. Wu, D. Wang, L. Yin, J. Ye, S. Deng, Z. Zhu, W. Ye, Z. Li, *Appl. Surf. Sci.* **2014**, *315*, 400–406.
- [203] K. Zhao, L. Zhang, R. Xia, Y. Dong, W. Xu, C. Niu, L. He, M. Yan, L. Qu, L. Mai, *Small* **2016**, *12*, 588–594.
- [204] M. Zhang, Z. Sun, T. Zhang, D. Sui, Y. Ma, Y. Chen, *Carbon* **2016**, *102*, 32–38.
- [205] D. Zhou, L. Song, X. Li, Z. Fan, *Electrochim. Acta* **2016**, *207*, 9–15.
- [206] V. Müller, M. Rasp, G. Štefanić, J. Ba, S. Günther, J. Rathousky, M. Niederberger, D. Fattakhova-Rohlfing, *Chem. Mater.* **2009**, *21*, 5229–5236.
- [207] K. Peters, P. Zeller, G. Stefanic, V. Skoromets, H. Němec, P. Kužel, D. Fattakhova-Rohlfing, *Chem. Mater.* **2015**, *27*, 1090–1099.

- [208] Y. S. Kim, W. B. Kim, Y. L. Joo, *J. Mater. Chem. A* **2014**, *2*, 8323–8327.
- [209] J. Santos Pena, T. Brousse, L. Sanchez, J. Morales, D. M. Scheich, *J. Power Sources* **2001**, *97-98*, 232–234.
- [210] F. Zoller, K. Peters, P. M. Zehetmaier, P. Zeller, M. Döblinger, T. Bein, Z. Sofer, D. Fattakhova-Rohlfing, *Adv. Funct. Mater.* **2018**, *28*, 1706529.
- [211] S. Kandambeth, V. S. Kale, O. Shekhah, H. N. Alshareef, M. Eddaoudi, *Advanced Energy Materials* **2021**, 2100177.
- [212] M. S. Lohse, T. Bein, *Adv. Funct. Mater.* **2018**, *28*, 1705553.
- [213] N. Keller, T. Bein, *Chem. Soc. Rev.* **2021**, *50*, 1813–1845.
- [214] D. -. Yang, Z.-Q. Yao, D. Wu, Y.-H. Zhang, Z. Zhou, X.-H. Bu, *J. Mater. Chem. A* **2016**, *4*, 18621–18627.
- [215] J. J. Yoo, S. J. Cho, G. Y. Jung, S. H. Kim, K. H. Choi, J. H. Kim, C. K. Lee, S. K. Kwak, S. Y. Lee, *Nano Lett.* **2016**, *16*, 3292–3300.
- [216] W. Wang, V. S. Kale, Z. Cao, S. Kandambeth, W. Zhang, J. Ming, P. T. Parvatkar, E. Abou-Hamad, O. Shekhah, L. Cavallo, M. Eddaoudi, H. N. Alshareef, *ACS Energy Lett.* **2020**, *5*, 2256–2264.
- [217] G. Wang, N. Chandrasekhar, B. P. Biswal, D. Becker, S. Paasch, E. Brunner, M. Addicoat, M. Yu, R. Berger, X. Feng, *Adv. Mater.* **2010**, *31*, 1901478.
- [218] L. Bai, Q. Gao, Y. Zhao, *J. Mater. Chem. A* **2016**, *4*, 14106–14110.
- [219] H. Liao, H. Ding, B. Li, X. Ai, C. Wang, *J. Mater. Chem. A* **2014**, *2*, 8854–8858.
- [220] S. Xu, G. Wang, B. P. Biswal, M. Addicoat, S. Paasch, W. Sheng, X. Zhuang, E. Brunner, T. Heine, R. Berger, X. Feng, *Angew. Chem. Int. Ed.* **2019**, *58*, 859–863.
- [221] Z. Lei, Q. Yang, Y. Xu, S. Guo, W. Sun, H. Liu, L.-P. Lv, Y. Zhang, Y. Wang, *Nat. Commu.* **2018**, *9*, 576.
- [222] W. Wieczorek, J. Plochanski, *Designing Electrolytes for Lithium-Ion and Post-Lithium Batteries*, Jenny Stanford Publishing, **2021**.
- [223] G. -. Nazri, G. Pistoia, *Lithium Batteries: Science and Technology*, Kluwer Academic, MA, USA, **2004**.
- [224] Y. Yun Zheng, Y. Yao, J. Ou, M. Li, D. Luo, H. Dou, Z. Li, K. Amine, A. Yu, Z. Chen, *Chem. Soc. Rev.* **2020**, *49*, 8790–8839.
- [225] M. Myounggu Park, X. Zhang, M. Chung, G. B. Less, A. M. Sastry, *J. Power Sources* **2010**, *195*, 7904–7929.

- 
- [226] D. A. Porter, K. E. Easterling, *Phase Transformations in Metals and Alloys*, 2nd edition, Chapman & Hall, **1992**.
- [227] P. G. Bruce, *Solid State Ion.* **1988**, *30*, 918–922.
- [228] J. R. Akridge, M. Balkanski, *Solid State Microbatteries*, Kluwer Academic, MA, USA, **1990**.
- [229] P. M. Blonsky, D. F. Shriver, P. Austin, H. R. Allcock, *Solid State Ion.* **1986**, *18*, 258–264.
- [230] A. Nishimoto, M. Watanabe, Y. Ikeda, S. Kohjiya, *Electrochim. Acta* **2014**, *1998*, 1177–1184.
- [231] D. Golodnitsky, E. Strauss, E. Peled, S. Greenbaum, *J. Electrochem. Soc.* **2015**, *162*, A2551–A2566.
- [232] P. K. Singh, B. Bhattacharya, R. K. Nagarale, *J. Appl. Polym. Sci.* **2010**, *118*, 2976–2980.
- [233] G. M. Hou, M. Q. Zhang, Y. F. Huang, W. H. Ruan, *RSC Adv.* **2016**, *6*, 83406–83411.
- [234] A. Sarnowska, I. Polska, L. Niedzicki, M. Marcinek, A. Zalewska, *Electrochim. Acta* **2011**, *57*, 180–186.
- [235] N. Lago, O. Garcia-Calvo, J. M. Lopezdelamo, T. Rojo, M. Armand, *ChemSusChem* **2015**, *8*, 3039–3043.
- [236] H. Kasemägi, M. Klintonberg, A. Aabloo, J. O. Thomas, *Electrochim. Acta* **2003**, *48*, 2273–2278.
- [237] J. C. J. C. Bachman, S. Muy, A. Grimaud, H. H. Chang, N. Pour, S. F. Lux, O. Paschos, F. Maglia, S. Lupart, P. Lamp, L. Giordano, Y. Shao-Horn, *Chem. Rev.* **2016**, *116*, 140–162.
- [238] N. Kamaya, K. Homma, Y. Yamakawa, M. Hirayama, R. Kanno, M. Yonemura, T. Kamiyama, Y. Kato, S. Hama, K. Kawamoto, A. Mitsui, *Nature Mater* **2011**, *10*, 682–686.
- [239] S. -. Zeng, X. -. Huang, Y. -. Ma, L. -. Zhi, *New Carbon Mater.* **2021**, *36*, 1–18.
- [240] J. H. Park, K. Suh, M. R. Rohman, W. Hwang, M. Yoon, K. Kim, *Chem. Commun.* **2015**, *51*, 9313–9316.
- [241] D. A. Vazquez-Molina, G. S. Mohammad-Pour, C. Lee, M. W. Logan, X. Duan, J. K. Harper, F. J. Uribe-Romo, *J. Am. Chem. Soc.* **2016**, *138*, 9767–9770.

- [242] K. Zhang, B. Zhang, M. Weng, J. Zheng, S. Li, F. Pan, *Phys. Chem. Chem. Phys.* **2019**, *21*, 9883–9888.
- [243] Y. Du, H. Yang, J. M. Whiteley, S. Wan, Y. Jin, S. H. Lee, W. Zhang, *Angew. Chem. Int. Ed.* **2016**, *55*, 1737–1741.
- [244] Y. Hu, N. Dunlap, S. Wan, S. Lu, S. Huang, I. Sellinger, M. Ortiz, Y. Jin, S.-h. Lee, W. Zhang, *J. Am. Chem. Soc.* **2019**, *141*, 7518–7525.
- [245] K. K. Jeong, S. Park, G. Y. Jung, S. H. Kim, Y. H. Lee, S. K. Kwak, S. Y. Lee, *J. Am. Chem. Soc.* **2019**, *141*, 5880–5885.
- [246] C. M. Julien, A. Mauger, K. Zaghbi, H. Groult, *Inorganics* **2014**, *2*, 132–154.
- [247] K. Mizushima, P. C. Jones, P. J. Wiseman, J. B. Goodenough, *Mater. Res. Bull.* **1980**, *15*, 783–789.
- [248] S. Kalluri, M. Yoon, M. Jo, S. Park, S. Myeong, J. Kim, S. X. Dou, Z. P. Guo, J. Cho, *Adv. Energy Mater.* **2017**, *7*, 1601507.
- [249] M. M. Thackeray, W. I. F. David, P. G. Bruce, J. B. Goodenough, *Mater. Res. Bull.* **1983**, *18*, 461–472.
- [250] A. R. Armstrong, P. G. Bruce, *Nature* **1996**, *381*, 499–500.
- [251] G. J. Xu, Z. H. Liu, C. J. Zhang, G. L. Cui, L. Q. Chen, *J. Mater. Chem. A* **2015**, *3*, 4092–4123.
- [252] A. K. Padhi, K. S. Nanjundaswamy, J. B. Goodenough, *J. Electrochem. Soc.* **1997**, *144*, 1188–1194.
- [253] J. J. Wang, X. L. Sun, *Energy Environ. Sci.* **2015**, *8*, 1110–1138.
- [254] M. D. Radin, S. Hy, M. Sina, C. Fang, H. Liu, J. Vinckeviciute, M. Zhang, M. S. Whittingham, Y. S. Y. S. Meng, A. Van der Ven, *Adv. Energy Mater.* **2017**, *7*, 1602888.
- [255] S. -. Jung, H. Gwon, J. Hong, K. -. Park, D. -. Seo, H. Kim, J. Hyun, W. Yang, K. Kang, *Adv. Energy Mater.* **2014**, *4*, 1300787.
- [256] P. Yan, J. Zheng, M. Gu, J. Xiao, J. G. Zhang, C. M. Wang, *Nat. Commun.* **2017**, *8*, 14101.
- [257] J. Kim, H. Cho, H. Y. Jeong, H. Ma, J. Lee, J. Hwang, M. Park, J. Cho, *Adv. Energy Mater.* **2017**, *7*, 1602559.
- [258] A. Kraytsberg, Y. Ein-Eli, *Adv. Energy Mater.* **2012**, *2*, 922–939.
- [259] B. Qiu, M. H. Zhang, Y. G. Xia, Z. P. Liu, Y. S. Meng, *Chem. Mater.* **2017**, *29*, 908–915.

- 
- [260] G. G. Amatucci, J. M. Tarascon, L. C. Klein, *J. Electrochem. Soc.* **1996**, *143*, 1114–1123.
- [261] D. Ensling, G. Cherkashinin, S. Schmid, S. Bhuvaneswari, A. Thissen, W. Jaegermann, *Chem. Mater.* **2014**, *26*, 3948–3956.
- [262] A. Kraysberg, Y. Ein-Eli, *Adv. Energy Mater.* **2012**, *2*, 922–939.
- [263] S. Kalluri, M. Yoon, M. Jo, S. Park, S. Myeong, J. Kim, S. X. Dou, Z. Guo, J. Cho, *Adv. Energy Mater.* **2017**, *7*, 1601507.
- [264] L. Wang, B. Chen, J. Ma, G. Cui, L. Chen, *Chem. Soc. Rev.* **2018**, *47*, 6505–6602.
- [265] D. D. MacNeil, J. R. Dahn, *J. Electrochem. Soc.* **2002**, *149*, A912.
- [266] J. W. Fergus, *J. Power Sources* **2010**, *195*, 939–954.
- [267] C. Li, H. P. Zhang, L. J. Fu, H. Liu, Y. P. Wu, E. Rahm, R. Holze, H. Q. Wu, *Electrochim. Acta* **2006**, *51*, 3872–3883.
- [268] R.-Z. Yin, Y.-S. Kim, S.-J. Shin, I. Jung, J.-S. Kim, S.-K. Jeong, *J. Electrochem. Soc.* **2012**, *159*, A253–A258.
- [269] R. Sathiyamoorthi, P. Shakkthivel, T. Vasudevan, *Mater. Lett.* **2007**, *61*, 3746–3750.
- [270] J.-M. Kim, S. Tsuruta, N. Kumagai, *Electrochem. Commun.* **2007**, *9*, 103–108.
- [271] Q. Liu, X. Su, D. Lei, Y. Qin, J. Wen, F. Guo, Y. A. Wu, Y. Rong, R. Kou, X. Xiao, F. Agyesse, J. Bareño, Y. Ren, W. Lu, Y. Li, *Nat. Energy* **2018**, *3*, 936–943.
- [272] C. Nithya, R. Thirunakaran, A. Sivashanmugam, S. Gopukumar, *ACS Appl. Mater. Interfaces* **2012**, *4*, 4040–4046.
- [273] L. M. Zhang, X. B. Wang, S. Tao, G. X. Wu, X. Z. Su, S. Q. Wei, H. F. Zhao, W. S. Chu, *Mater. Lett.* **2016**, *179*, 34–37.
- [274] P. M. Zehetmaier, A. Cornélis, F. Zoller, B. Böller, A. Wisnet, M. Döblinger, D. Böhm, T. Bein, D. Fattakhova-Rohlfing, *Chem. Mater.* **2019**, *31*, 8685–8694.
- [275] Z. Chen, J. R. Dahn, *Electrochem. Solid-State Lett.* **2004**, *7*, A11.
- [276] J. Zhang, Y. J. Xiang, Y. Yu, S. Xie, G. S. Jiang, C. H. Chen, *J. Power Sources* **2004**, *132*, 187–194.
- [277] J.-H. Shim, K.-S. Lee, A. Missyul, J. Lee, B. Linn, E. C. Lee, S. Lee, *Chem. Mater.* **2015**, *27*, 3273–3279.
- [278] J. Y. Lee, Y. M. Lee, B. Bhattacharya, Y.-C. Nho, J.-K. Park, *Electrochim. Acta* **2009**, *54*, 4312–4315.

- [279] Y. S. Jung, A. S. Cavanagh, L. Gedvilas, N. E. Widjonarko, I. D. Scott, S.-H. Lee, G.-H. Kim, S. M. George, A. C. Dillon, *Adv. Energy Mater.* **2012**, *2*, 1022–1027.
- [280] N. Yabuuchi, Y. Kinoshita, K. Misaki, T. Matsuyama, S. Komaba, *J. Electrochem. Soc.* **2015**, *162*, A538–A544.
- [281] G.-g. Park, Y.-k. Park, J.-k. Park, J.-w. Lee, *RSC Adv.* **2017**, *7*, 16244–16252.
- [282] W. J. Li, M. Hirayama, K. Suzuki, R. Kanno, *Solid State Ion.* **2016**, *285*, 136–142.
- [283] Y. Sun, K. Suzuki, K. Hara, S. Hori, T.-a. Yano, M. Hara, M. Hirayama, R. Kanno, *J. Power Sources* **2016**, *324*, 798–803.
- [284] M. Kato, T. Hayashi, G. Hasegawa, X. Lu, T. Miyazaki, Y. Matsuda, N. Kuwata, K. Kurihara, J. Kawamura, *Solid State Ion.* **2017**, *308*, 54–60.
- [285] J. Xie, J. Zhao, Y. Liu, H. Wang, C. Liu, T. Wu, P.-C. Hsu, D. Lin, Y. Jin, Y. Cui, *Nano Res.* **2017**, *10*, 3754–3764.
- [286] O. Lidor-Shalev, N. Leifer, M. Ejgenberg, H. Aviv, I. Perelshtein, G. Goobes, M. Noked, *Batter. Supercaps* **2021**, *4*, 1739.
- [287] Y. S. Jung, A. S. Cavanagh, A. C. Dillon, M. D. Groner, S. M. George, S.-H. Lee, *J. Electrochem. Soc.* **2010**, *157*, A75.
- [288] J.-T. Lee, F.-M. Wang, C.-S. Cheng, C.-C. Li, C.-H. Lin, *Electrochim. Acta* **2010**, *55*, 4002–4006.
- [289] X. Li, J. Liu, X. Meng, Y. Tang, M. N. Banis, J. Yang, Y. Hu, R. Li, M. Cai, X. Sun, *J. Power Sources* **2014**, *247*, 57–69.
- [290] D. Zuo, G. Tian, D. Chen, H. Shen, C. Lv, K. Shu, Y. Zhou, *Electrochim. Acta* **2015**, *178*, 447–457.

## 2 Methods

For the investigation of material properties many different methods can be used. However, only the combination of these techniques leads to a complete information concerning the structure, shape, morphology and electrochemical properties of a certain material. Within this chapter the applied experimental and characterization methods and their theoretical background will be briefly introduced.

### 2.1 X-Ray Diffraction

X-ray diffraction (XRD) is one of the most important techniques in materials science and is used for non-destructive structure determination of crystalline materials. Besides phase composition, unit cell and lattice parameters, the size of crystalline domains can be determined. The method is based on the principle of constructive interference of monochromatic X-rays scattered by the periodic lattice planes in crystalline materials.

Bragg's law describes the requirement for constructive interference (see Equation 2.1). It is fulfilled when a multitude  $n$  of the radiation wavelength  $\lambda$  is equal to the path difference. This difference consists of the lattice spacing  $d$  and the diffraction angle  $\theta$  (see Figure 2.1).<sup>[1,2]</sup>

$$n \cdot \lambda = 2d \cdot \sin(\theta) \quad (2.1)$$

Based on the broadening of the measured reflections, the average crystallite size  $D$  can be calculated by using the Scherrer equation (see Equation 2.2).

$$D = \frac{K \cdot \lambda}{\beta \cdot \cos(\theta)} \quad (2.2)$$

$K$  describes a geometrical factor called Scherrer coefficient (0.9 for spherical particle),  $\beta$  is the full width at half maximum (FWHM) of the respective reflection,  $\lambda$  is the wavelength of the X-rays ( $\lambda(\text{Cu-K}\alpha) = 1.5406 \text{ \AA}$ ) and  $\theta$  is the Bragg diffraction angle of the respective diffraction peak.<sup>[1,2]</sup>

### 2.2 Spectroscopic Ellipsometry

Spectroscopic ellipsometry is a common optical technique for the determination of the thickness and the optical constants of thin films. It relies on the polarization changes of light caused by reflection or transmission from a material structure. The polarization

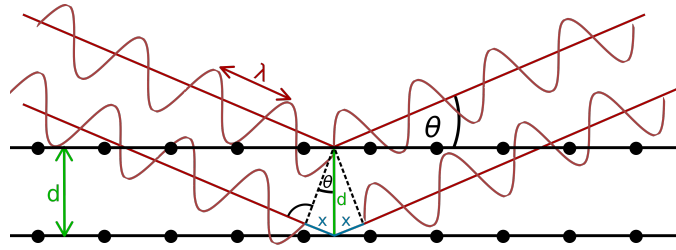


**Figure 2.1:** Schematic drawing of the diffraction of X-rays on a periodic lattice illustrating Bragg's law.

change is represented as an amplitude ratio  $\Psi$  and the phase difference  $\Delta$ . The measured response depends on the optical properties and thickness of individual materials. Ellipsometry is mostly used to determine the thickness of films, but it can also be applied to characterize composition, crystallinity, roughness, doping concentration and other material properties associated with a change in optical response. A schematic setup is depicted in Figure 2.2.

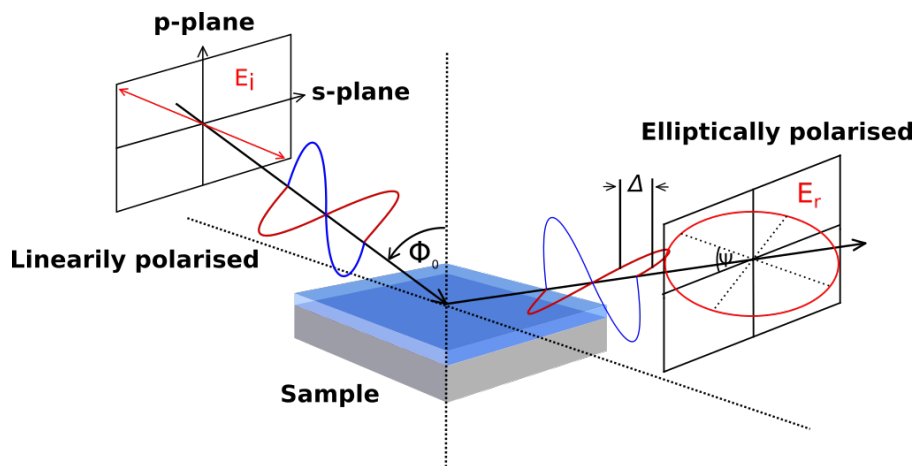


**Figure 2.2:** Schematic setup of an ellipsometric measurement.

Electromagnetic radiation is emitted by a light source and linearly polarized before it is reflected off a sample. Thereby the light gets elliptically polarized due to different reflectivity for the components of the incident beam which are perpendicular (s-plane) and parallel (p-plane) to the plane of incidence. The amplitudes of the s and p components are denoted by  $r_s$  and  $r_p$  after reflection and normalization to their initial values (Figure 2.3).<sup>[3]</sup>

The change of polarization can be described by the complex ratio  $\rho$  of the reflection coefficients  $r_s$  and  $r_p$ , which leads to the basis for the fundamental equation of ellipsometry with the amplitude ratio  $\Psi$  and the phase difference  $\Delta$ :

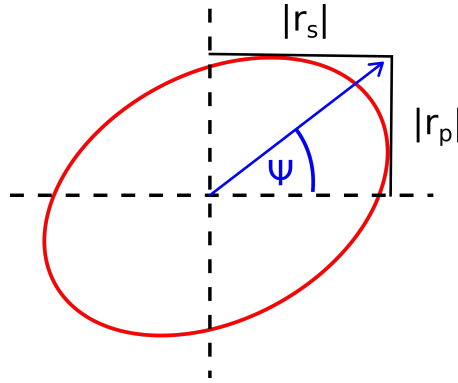


**Figure 2.3:** Field vector of elliptically polarized light and the amplitude of the different components  $r_s$  and  $r_p$ .

$$\rho = \frac{r_p}{r_s} = \tan(\Psi)e^{i\Delta} \quad (2.3)$$

Ellipsometry is an indirect method as the optical constants cannot be calculated directly from the measured  $\Psi$  and  $\Delta$ . Therefore ellipsometry data analysis requires an optical model defined by the optical constants and layer thickness of a sample. Using an iterative procedure (least-squares optimization), the unknown optical constants and thickness parameters are varied and  $\Psi$  and  $\Delta$  values are calculated using the Fresnel equations. The best matching values for  $\Psi$  and  $\Delta$  to the experimental data are then used to calculate the optical constants and thickness parameters of the sample.<sup>[3]</sup>

## 2.3 Electron Microscopy

Electron microscopy is an important tool to study the morphology and phase composition of nano-materials. This analytical method is based on the interaction of an electron beam with the sample. The generated signals provide information about the external surface morphology, the internal microstructure or the chemical composition using scanning electron microscopy (SEM) and transmission electron microscopy (TEM) together with energy dispersive X-ray spectroscopy (EDX).

### 2.3.1 Scanning Electron Microscopy

The working principle of SEM is based on scanning the sample surface with an electron beam, typically generated by a field emission gun with an acceleration voltage between 1 kV and 30 kV. Magnetic condensers and objective lens systems are used to reduce and focus the spot size of the electron beam to a diameter of 2 nm to 10 nm, which is important for a high resolution (Figure 2.4). The interaction of the incident electrons with the sample results in an emission of electrons and photons. The detected signals are collected and the information is used to produce an image of the surface. There

are two signals which can be used for creating an image, secondary and backscattered electrons. Secondary electrons (SE) are generated by inelastic scattering of the primary electrons. They are used for high-resolution images of the surface morphology. Because of the low energy of these electrons ( $<50$  eV), only those electrons that are generated near to the sample surface can escape into the vacuum and be detected.<sup>[4]</sup>

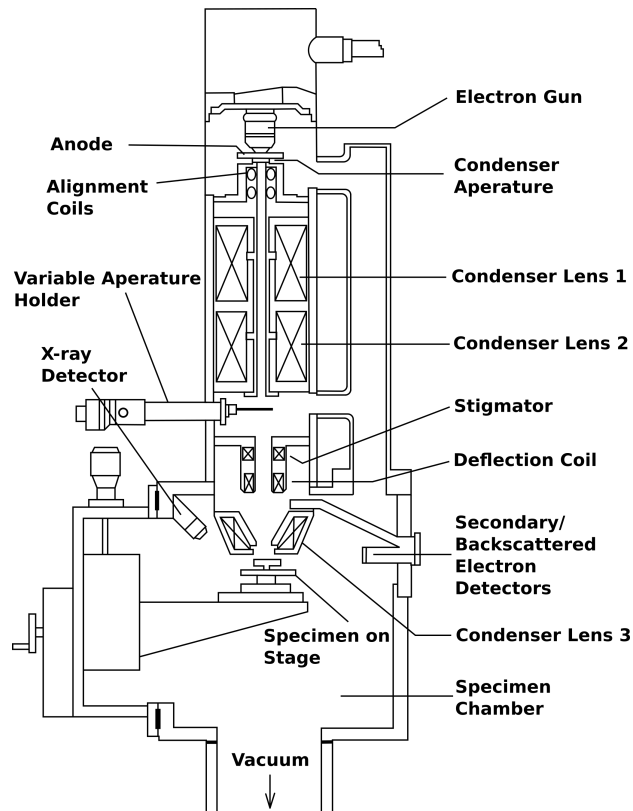


Figure 2.4: Illustration of a scanning electron microscope.<sup>[5]</sup>

Additionally, backscattered electrons (BSE) are generated by elastic scattering of the primary beam and therefore have a higher energy than SE. Due to the strong dependence of back scattered electrons on the atomic number, the BSE can be used to obtain information about the elemental distribution in a specimen. Moreover, the quantitative composition of the material of interest can be further investigated by analysis of characteristic X-rays generated in the interaction volume of the primary beam. These characteristic X-rays are created when an electron from an inner shell is ejected by the primary electrons and outer shell electrons fill the inner shell vacancies. During this transition the atom emits radiation of a very short wavelength. These X-rays are characteristic for an element and can be utilized for chemical composition analyses.<sup>[4]</sup>

### 2.3.2 Transmission Electron Microscopy

TEM analysis can be used to determine the sample morphology and the phase composition at a very high resolution of up to 0.1 nm (HR-TEM). In contrast to SEM, a wide area of the sample is illuminated with the primary electron beam passing through the sample. Usually acceleration voltages in the range of 80 – 400 kV are applied to send electrons through a very thin sample (below 100 nm). After focussing the transmitted electrons with several lens systems, the electrons are detected with a contrast caused by thickness variation in the specimen, the elemental composition and the density of the sample (Figure 2.5).

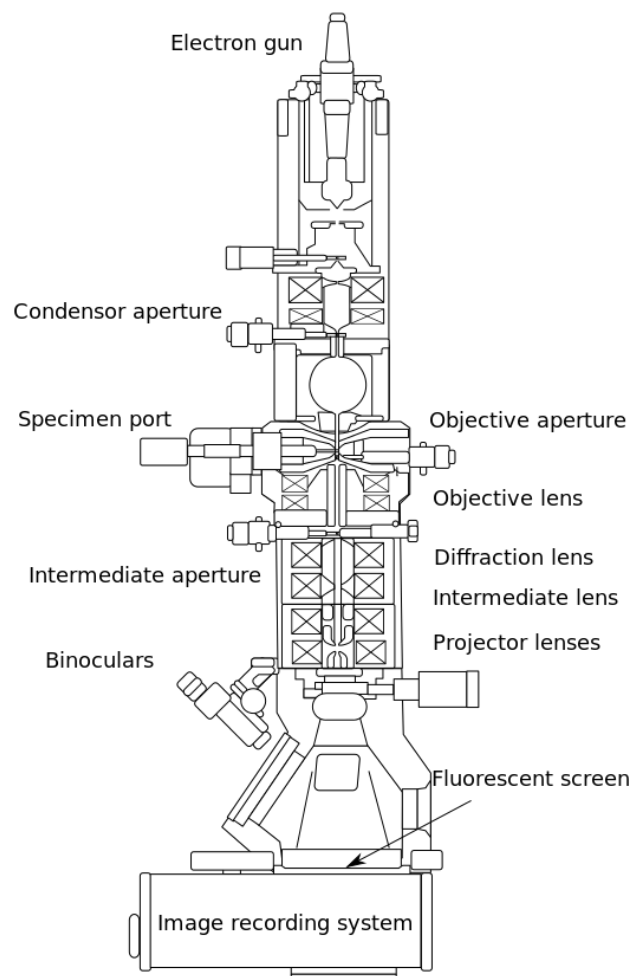


Figure 2.5: Illustration of a transmission electron microscope.<sup>[6]</sup>

In TEM diffraction mode electron diffraction (ED) patterns can be generated that reveal the crystal structure of the analyzed material. Scanning transmission electron microscopy (STEM) enables imaging by scanning the sample like SEM but with a much higher resolution because of a highly focussed primary beam. High angle scattered

electrons are then recorded by a ring detector located around the optical axis resulting in imaging with a high mass contrast in the so-called high-angle annular dark-field mode (HAADF).<sup>[7]</sup>

## 2.4 UV-Vis Spectroscopy

Ultraviolet-Visible (UV-Vis) spectroscopy can provide valuable insights in the electronic structure of materials by probing optical transitions from the ground state to various excited states. This method is often applied for the quantitative and qualitative determination of the absorption properties of solutions or solid materials. The relation between absorbance and concentration of the absorbing species is generally given by the Beer-Lambert law:

$$A(\lambda) = -\log \frac{I}{I_0} = \epsilon(\lambda) \cdot c \cdot L \quad (2.4)$$

Where the absorbance  $A(\lambda)$  at a certain wavelength is equal to the negative logarithm of the measured intensity  $I$  divided by the intensity of the incident beam  $I_0$  (measured without inserted sample). By calculation of the absorbance one can determine the concentration of the absorbing species  $c$  with the material-specific extinction coefficient  $\epsilon$  and the pathlength  $L$  through the sample.<sup>[4,8]</sup> For this measurement it is assumed that all light is either absorbed, reflected or transmitted resulting in the following equation:

$$\%A + \%R + \%T = 1 \quad (2.5)$$

The calculation of the correct absorbance value requires that the substrate's reflectance is being taken into account. For this purpose, the samples are measured in both transmission and reflectance mode. Additionally the transmittance and reflectance of the uncoated substrate are measured as a reference. The absorbance of the material  $A_M$  at a given wavelength  $\lambda$  is then calculated from the experimental reflectance and transmittance data, using the expression:

$$A_M = -\log_{10} \frac{T_{S+M}(\lambda)/T_S(\lambda)}{1 - \frac{R_{S+M}(\lambda) - R_S(\lambda)}{T_S(\lambda)^2}} \quad (2.6)$$

Here  $T_{S+M}(\lambda)/T_S(\lambda)$  and  $R_{S+M}(\lambda)/R_S(\lambda)$  correspond to the wavelength-dependent transmittance and reflectance of the substrate and the coated substrate, respectively.

By absorbing light of a defined wavelength, electrons from the valence band (VB) will be excited into the conduction band (CB). By applying the Tauc relation (Equation 2.7) the band gap of semiconducting materials can be evaluated by means of the measured UV-Vis spectra.<sup>[9]</sup>

$$\alpha \cdot h\nu = C \cdot (h\nu - E_g)^n \quad (2.7)$$

Here the absorption coefficient  $\alpha$  multiplied with the photon energy  $h\nu$  is related to the band gap energy  $E_g$ .  $C$  is a constant and the value of  $n$  specifies the type of transition. For direct transitions  $n$  takes the value of  $1/2$ , for indirect transitions  $n$  is equal to 2. By plotting  $(\alpha \cdot h\nu)^2$  against  $h\nu$  in the so called Tauc plot, the direct band gap can be estimated. The intersection with the abscissa obtained from extrapolating the linear regime of the resulting plot yields the  $E_g$  value of the examined material.

## 2.5 X-Ray Photoelectron Spectroscopy

X-ray photoelectron spectroscopy (XPS) is a commonly used surface sensitive and quantitative spectroscopic technique for the determination of the elemental composition, the empirical formula, and the chemical and electronic state of the elements existing within a material. XPS is also known as Electron Spectroscopy for Chemical Analysis (ESCA) because of the chemical information that this technique provides. This analytical technique is based on the photoelectric effect depicted schematically in Figure 2.6. In order to collect the electrons emitted from the sample, ultra-high vacuum (UHV) is required (below  $10^{-7}$  hPa). XPS can only determine the composition on the surface of the substrate to a depth of about 2 nm.

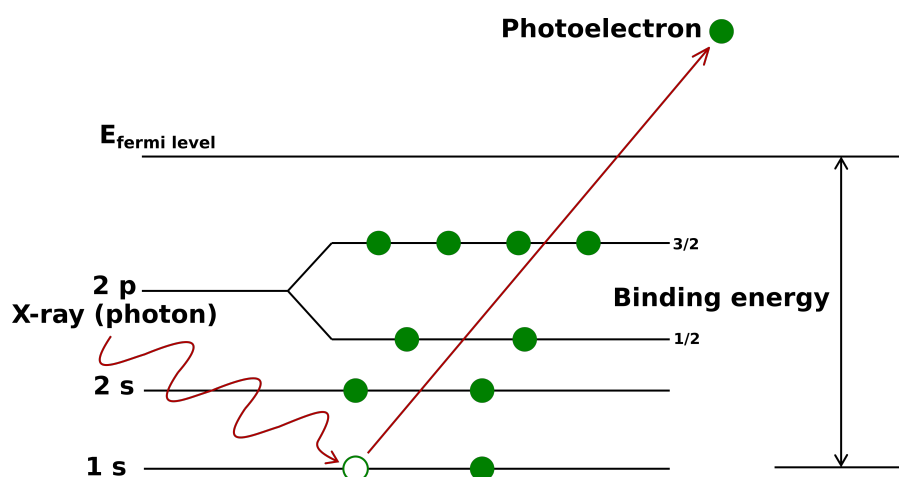


**Figure 2.6:** Schematic drawing of the formation of photoelectrons through X-ray radiation.

For an XPS measurement the sample is irradiated with characteristic X-rays (such as Mg  $K_\alpha$  or Al  $K_\alpha$ ) with a certain energy  $h\nu$  leading to the displacement of a core level electron with the Energy  $E_b$ . The emitted photoelectron has then the kinetic energy  $E_k$ . For the relationship between incident X-ray photon energy  $h\nu$ ,  $E_b$  and  $E_k$  the following equation is valid:

$$E_b = E_k - h \cdot \nu - \phi \quad (2.8)$$

The kinetic energy  $E_k$  is measured by the instrument and  $\phi$  is the work function of

the spectrometer. This is an adjustable instrumental correction factor which depends on the spectrometer and the material. As  $h\nu$  is known from the applied characteristic X-ray source, the binding energy  $E_b$  of the emitted electrons can be calculated from the measured  $E_k$ . As the binding energy  $E_b$  is characteristic for each element, the composition of the material can be determined by plotting  $E_b$  against the amount of electrons measured. The area under the peak is proportional to the amount of element in the material. Based on small shifts in the peak positions of an element, often the oxidation state can also be identified.<sup>[4,10]</sup>

## 2.6 Sorption

Sorption is a powerful tool to study porous materials, in particular the surface area, porosity, pore size and pore size distribution.<sup>[11]</sup> The principle of sorption measurements is based on physisorption, mainly consisting of van der Waals interactions between the adsorbed gas molecules (adsorbate) and the surface of the porous sample (adsorbent). Sorption measurements are usually carried out using argon, krypton or nitrogen as adsorbates. The measurements are performed by recording the amount of adsorbate adsorbed by an adsorbent as a function of varying relative pressure at a constant temperature (usually at 77 K, the boiling point of nitrogen). In 1985 the IUPAC recommended six basic types for the classification of physisorption isotherms.<sup>[11]</sup> Due to the identification of new characteristic types of isotherms with close relationship to particular pore structures, an updated version with a refined classification of physisorption isotherms and associated hysteresis loops (see Figure 2.7) was proposed.<sup>[12]</sup>

The characteristic shapes and hystereses of those isotherms are dependent on the structure and the size of the porous system and the interaction strength between adsorbate and adsorbents.

Type I isotherms are given by typical microporous materials (pores  $< 2$  nm) showing a reversible behavior. Due to the small pore diameter of these materials, a steep increase of adsorbed volume at small relative pressures can be observed. The micropores are consequently filled, reaching a maximum value defined by the accessible micropore volume. Type I isotherms can further be divided into Type Ia for materials with narrow micropores ( $< 1$  nm) and Type Ib for materials with a range of wider micropores and narrow mesopores ( $< 2.5$  nm).

Reversible Type II and Type III isotherms are characterized by unrestricted multilayer adsorption on nonporous and macroporous (pores  $< 50$  nm) materials with strong and weak adsorbate-adsorbent interactions, respectively.

In the case of Type IV isotherms, the adsorption behaviour is mainly determined by the adsorbent-adsorptive interactions in mesopores (pores between 2 nm - 50 nm) and also by the interactions between the molecules in the condensed state. The initial monolayer-multilayer adsorption takes the same path as the corresponding part of a Type II isotherm and is followed by pore condensation. Here, the gas condenses to a liquid-like phase in a pore at a pressure  $p$  smaller than the saturation pressure  $p_0$

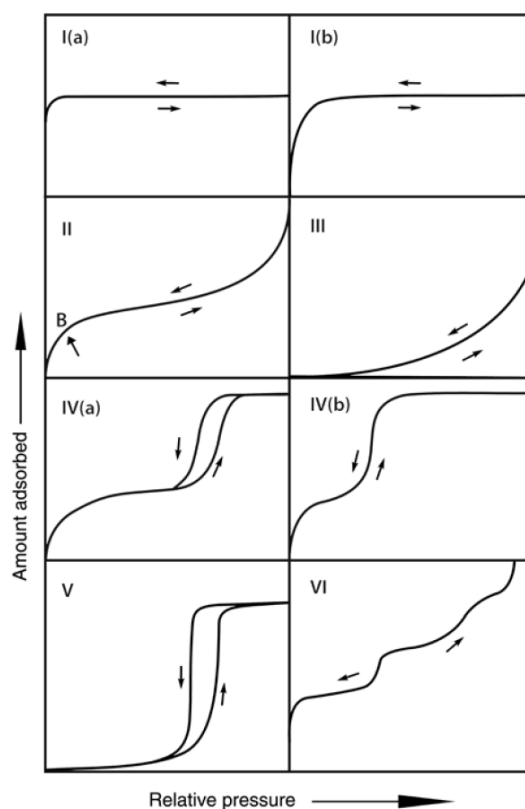


**Figure 2.7:** Classification of physisorption isotherms.<sup>[12]</sup>

of the bulk liquid. Type IVa isotherms are accompanied by hysteresis of the capillary condensation. This occurs for pore widths exceeding  $\approx 4$  nm. Completely reversible Type IVb isotherms are observed for mesopores of smaller width exhibiting conical or cylindrical pore shape, which is typical for covalent organic frameworks.<sup>[12]</sup>

The shape of Type V isotherms is very similar to that of Type III due to the weak adsorbate-adsorbent interactions. The hysteresis loop can be attributed to capillary condensation within the mesopores.

Type VI shows a stepwise multilayer adsorption on a highly uniform and non-porous surface. Each step in the uptake represents the capacity for an adsorbed monolayer on the surface.

Several models and theories have been developed to interpret the results of sorption measurements on microporous and non-microporous materials, for example the Langmuir theory, Freundlich method or the Brunauer-Emmett-Teller (BET) theory. The BET theory is based on three main assumptions, which state that a) there is no interaction between adsorptive species within each layer; b) the energy of adsorption in all layers is the same except in the first layer due to the adsorbent-adsorbate interactions; c) the number of adsorbed layers becomes infinite at  $p/p_0 = 1$ .<sup>[11]</sup> For low pressures ( $p/p_0 < 0.3$ ) the BET equation can be expressed in simple and linear form:

$$\frac{1}{n\left[\frac{p_0}{p} - 1\right]} = \frac{1}{n_m C} + \frac{C-1}{n_m C} \frac{p_0}{p} \quad (2.9)$$

where  $n$  is the adsorbed gas quantity,  $n_m$  the adsorbed monolayer gas quantity,  $p_0$  the saturation pressure,  $p$  the equilibrium pressure and  $C$  the BET constant. With the BET plot of  $1/n[p_0/p-1]$  against  $p/p_0$  a linear plot is derived, where the adsorbed monolayer gas quantity  $n_m$  can be determined from the intercept  $1/n_m C$  and the slope  $(C-1)/n_m C$ . From this, the specific surface area  $A_S(\text{BET})$  of the material can be calculated according to the equation:

$$A_S(\text{BET}) = \frac{n_m \cdot L \cdot a_m}{m_s} \quad (2.10)$$

With the Avogadro constant  $L$ , the molecular cross section area  $a_m$  and the sample mass  $m_s$ . For nitrogen adsorption measurements, it is supposed that nitrogen forms a closed-packed BET monolayer resulting in  $a_m(\text{N}_2) = 0.162 \text{ nm}^2$  at 77 K.

## 2.7 Hall Effect Measurement with Van der Pauw Method

Hall effect measurements with the van der Pauw Method can be used to determine the electrical properties of different samples. This method is based in principle on the Lorentz force. Basically, this describes the force (here voltage) acting perpendicular to the moving direction of a point charge in an applied perpendicular magnetic field. With the "right hand rule" the direction of the force on a charge carrier based on its direction of motion and the direction of the applied magnetic field can be determined.

A Hall effect measurement system can be used to determine several material parameters, such as the carrier mobility ( $\mu$ ), the carrier concentration ( $n$ ), the Hall coefficient ( $R_H$ ), the resistivity or the conductivity type (n or p). The resistivity of a certain material can be determined using a four-point probe or the van der Pauw measurement technique. Here the bulk resistance is calculated from the sheet resistance of the sample, whereas the sheet resistance  $R_S$  can be calculated from a series of resistance measurements shown in Figure 2.8.

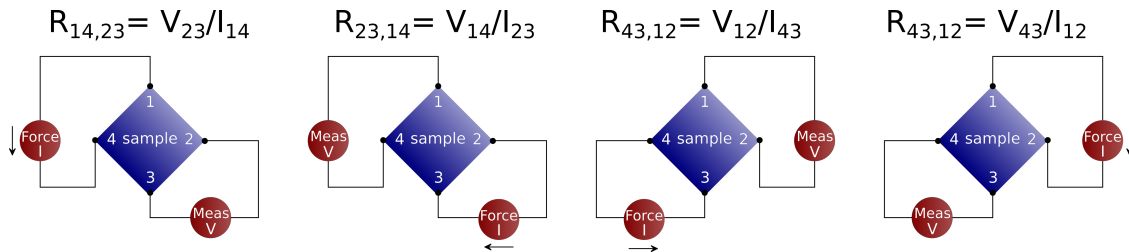


**Figure 2.8:** Resistance measurements based on the van der Pauw technique.

For van der Pauw resistivity measurements, the current is forced on adjacent nodes.

Then the voltage is measured on adjacent nodes on the opposite side so everything that is being forced and measured is on nearest pins.

$$R_A = \frac{R_{21,34} + R_{12,43} + R_{43,12} + R_{34,21}}{4} \quad (2.11)$$

$$R_B = \frac{R_{32,41} + R_{23,14} + R_{14,23} + R_{41,32}}{4}$$

The sheet resistance  $R_S$  can be calculated from  $R_A$  and  $R_B$  with the van der Pauw equation:

$$e^{\left(-\frac{\pi R_A}{R_S}\right)} + e^{\left(-\frac{\pi R_B}{R_S}\right)} = 1 \quad (2.12)$$

The product of the sheet resistance  $R_S$  and sample thickness ( $d$ ) leads to the resistivity  $\rho$  and therefore to the conductivity  $\sigma$  of the material.

$$\rho = \frac{1}{\sigma} = R_S \cdot d \quad (2.13)$$

Additionally, the charge carrier concentration ( $n_c$ ) and the mobility ( $\mu$ ) can be obtained from the Hall voltage ( $V_H$ ). The Hall voltage is measured by applying both a magnetic field perpendicular to the sample and a current through the sample. The magnitude of the Hall voltage is equal to  $\frac{IB}{qnd}$ , where  $I$  is the current flow,  $B$  is the magnetic field,  $d$  is the sample thickness and  $q$  ( $1.602 \cdot 10^{-19}$  C) is the elementary charge. In some cases, it is convenient to use layer or sheet density ( $n_s = nd$ ) instead of bulk density. One then obtains the sheet density of charge carriers by measuring the Hall voltage:

$$n_s = \frac{IB}{qV_H} \quad (2.14)$$

The Hall mobility ( $\mu$ ) can be determined by Equation 2.15 from the sheet density and mobility.

$$\mu = \frac{V_H}{R_S IB} = \frac{1}{qn_s R_S} \quad (2.15)$$

## 2.8 Electrochemical Characterization

### 2.8.1 Cyclic Voltammetry (CV)

Cyclic voltammetry (CV) is the most important potential technique for the characterization of electrochemical properties of different materials.<sup>[13]</sup> CVs are typically measured in a three-electrode setup containing a working electrode, at which the reaction of interest is investigated, a reference electrode with a constant defined potential and a counter electrode. A schematic representation of an electrochemical cell for CV experiments in acidic electrolyte is shown in Figure 2.9.

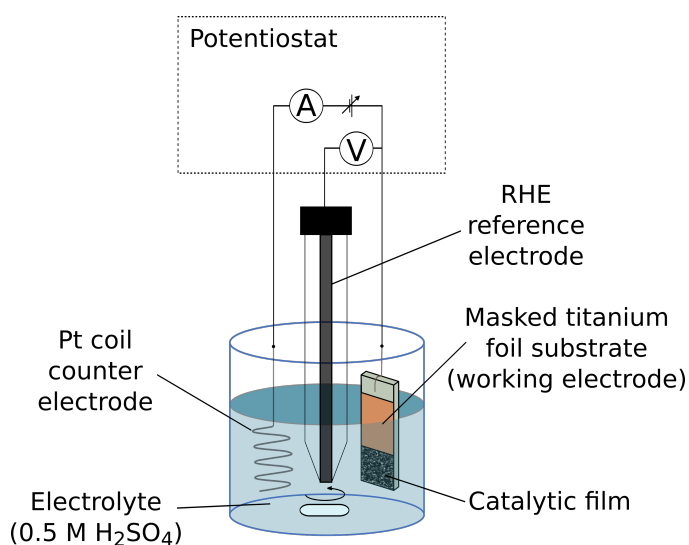


**Figure 2.9:** Three-electrode setup for electrochemical measurements (example).

The potential of the working electrode is swept with a certain scan rate  $\nu$  over a potential range  $\Delta E$ , while the current  $i$  is recorded (Figure 2.10a). A typical current response from a random redox couple is shown in Figure 2.10b (one Gauss-type peak for a single electrode reaction), from which the peak voltage ( $E_p$ ) and peak current ( $i_p$ ) can be identified. The ratio of peak currents and the difference of peak voltage ( $\Delta E_p$ ) in cathodic and anodic segments can be used to determine if the electrochemical system is reversible. The capacity of the reaction can be calculated by integration of the current curve with respect to potential and scan rate. Applying the voltage versus capacity profiles (Figure 2.10c), the discharge and the charge plateaus will correspond to the cathodic and anodic peak voltages. For a known electrode weight, the y-axis can be specified as specific current (in units of  $\text{A g}^{-1}$ ) and the integral value will provide the specific capacity (in units of  $\text{mAh g}^{-1}$ ). For catalytic reactions in liquids, the exposed area which is exposed to the electrolyte is more important than the mass of the electrode. Therefore, it is more convenient to use the current density (in units of  $\text{A cm}^{-2}$ ) than the specific current.

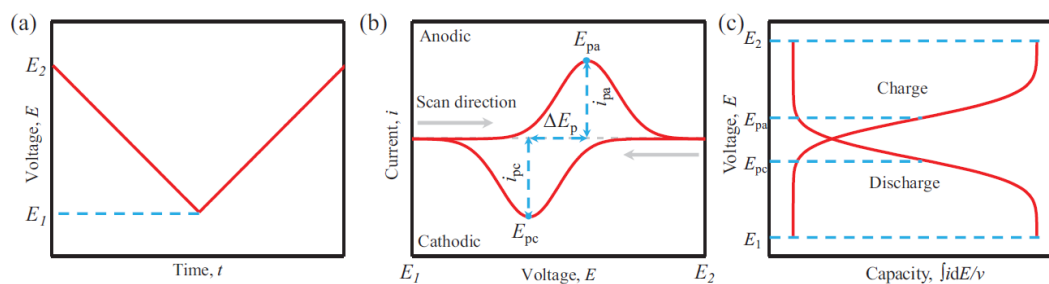


**Figure 2.10:** (a) Cyclic potential sweep and (b) the resulting cyclic voltammogram. (c) voltage versus integral current curves.<sup>[14]</sup>

The scan rate of the measurement controls how fast the applied potential is changed. When increasing the scan rate, higher currents are observed due to a decrease in the size of diffusion layer.<sup>[15,16]</sup> By this, the real electrochemically active surface (ECAS) for an electrode immersed in electrolyte can be determined by CV. At a potential where only capacitive currents flow and no electrochemical reaction takes place, the measured current  $i_{cap}$  is proportional to the scan rate  $dE/dt$  and the electrode capacitance  $C$  (Equation 2.16).

$$i_{cap} = C \frac{dE}{dt} \quad (2.16)$$

By plotting  $i_{cap}$  vs.  $dE/dt$ , a line with slope  $C$  is obtained, allowing determination of the electrode capacitance, which is proportional to the electrochemically active surface area.

For a given potential, where the measured current is assigned to a charge transfer between redox active species, the Randles-Sevcik equation (see Equation 2.17) describes the dependence of the peak current  $i_p$  on the scan rate. For electrochemically reversible electron transfer processes involving freely diffusing redox species, plots of  $i_p$  versus  $\nu^{1/2}$  should be linear. For known scan rate and peak currents, the diffusion coefficient of the diffusing species ( $D_0$ ,  $\text{cm}^2 \text{s}^{-1}$ ) can be obtained by taking electrode surface area  $A$  ( $\text{cm}^2$ ) and the bulk concentration of the analyte  $C^0$  ( $\text{mol cm}^{-3}$ ) into account. Additionally, Faraday constant  $F$ , number of charges  $n$ , temperature  $T$  and molar gas constant  $R$  complete Equation 2.17.

$$i_p = 0.446nFAC^0 \left( \frac{nF\nu D_0}{RT} \right)^{1/2} \quad (2.17)$$

### 2.8.2 Electrochemical Impedance Spectroscopy

Electrochemical impedance spectroscopy (EIS) is a powerful and widely used non-invasive technique for the characterization of electrode processes and complex interfaces. An electrochemical system can be described as the combination of physical components such as capacitors and resistors, where a linear, frequency-dependent response between applied potential and current is given. The most common technique is to measure the impedance under an applied sinusoidal potential with a low amplitude ( $\approx 10$  mV) over a wide frequency range (0.1 - 1 MHz). When representing an electrochemical cell as an electrical equivalent circuit (EEC, known as Randles circuit), it is important to account for every subsequent process, e.g. electrolyte/electrode double layer, charge carrier transfer kinetics and diffusion of active species. For the proper characterization of the working electrode, it is important to minimize side processes and reactions between the other components of the electrochemical set-up.<sup>[14]</sup>

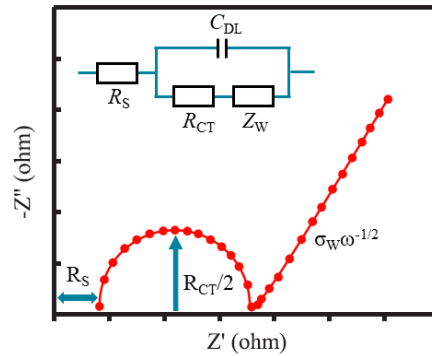


**Figure 2.11:** Randles circuit model and the corresponding Nyquist plot composed of the series resistance  $R_S$ , the charge transfer resistance  $R_{CT}$  connected, the Warburg impedance  $Z_W$  and the parallel connected double layer capacity  $C_{DL}$ .<sup>[14]</sup>

EIS data are usually presented either as Nyquist plot (the real part vs. the negative imaginary part of the impedance) or as Bode plot (the log of the impedance  $Z$  and phase shift vs. log of frequency). An exemplary Nyquist plot and the corresponding EEC is given in Figure 2.11. Here,  $R_S$  represents the series resistance, which combines the resistances of wiring, electrode materials and electrolyte. At the interface between electrode and electrolyte, double layers are formed (see section 1.4.2), which are presented by  $C_{DL}$ . This double layer capacity is set parallel to the charge transfer resistance  $R_{CT}$  and the Warburg impedance  $Z_W$ , which is based on a semi-infinite linear diffusion and is inversely proportional to the square root of frequency.<sup>[17]</sup> For a given potential, where diffusion of active species and therefore the Warburg impedance is negligible, the real and imaginary parts of impedance can be expressed as Equation 2.18 and Equation 2.19 with  $\omega$  as angular frequency.

$$Z_{Re} = R_S + \frac{R_{CT}}{1 + \omega^2 C_{DL}^2 R_{CT}^2} \quad (2.18)$$

$$Z_{Im} = -\frac{\omega C_{DL} R_{CT}^2}{1 + \omega^2 C_{DL}^2 R_{CT}^2} \quad (2.19)$$

For low applied frequency regions, the double layer capacitor can be treated as blocked and be removed from the equivalent circuit. The impedance is simplified to Equation 2.20, where  $\sigma_W$  is the Warburg coefficient. By fitting the linear relationship between  $Z_{Re}$  and  $\omega^{1/2}$  the Warburg coefficient can be obtained and the diffusion coefficient  $D_0$  can be calculated according to Equation 2.21.

$$Z = R_S + R_{CT} + \sigma_W \omega^{-1/2} \quad (2.20)$$

$$D_0 = \frac{R^2 T^2}{2 A^2 n^4 F^4 C^2 \sigma_W^2} \quad (2.21)$$

Here,  $R$  is the gas constant ( $8.314 \text{ J mol}^{-1} \text{ K}^{-1}$ ),  $T$  is the temperature (298 K),  $A$  is the surface area of the electrode,  $n$  is the number of electrons participating per formula unit,  $F$  is the Faraday constant ( $96485 \text{ C mol}^{-1}$ ) and  $C$  is the concentration of active species in the electrode.

### 2.8.3 Chronoamperometry and Chronopotentiometry

The long-term stability of electrodes is very important. In chronoamperometry (CA) a fixed potential is applied to the electrode and the current changes are recorded. In (PEC) water electrolysis, where the concentration of the electrolyte is stable, the decrease in current density can then be attributed to a reduced activity and stability of the electrode. In chronopotentiometry (CP) a fixed current is applied to the electrode and the potential changes to a value at which the flux of the electroactive species is sufficient to supply the applied current.<sup>[15,16]</sup> In electrocatalysis it is common practice to use CP to observe the overpotential of a reaction catalyzed by the electrode at a fixed current density. For commercial applications, the overpotential should be minimized and the stability should be as high as possible.

Galvanostatic measurements are a special form of chronopotentiometric techniques and are typically used to determine the specific capacity, reversibility, stability and rate capability of a battery material. In a typical measurement, a defined constant current is applied to the working electrode causing oxidation/reduction of the observed material (see Figure 2.12). The resulting potential change is recorded and the current is inverted at a distinct potential point (cut-off potential). Depending on the type of investigated electrode, the start and end point has to be chosen carefully. As the measurement is conducted against a Li/Li<sup>+</sup> reference, the starting point is typically at 3.0 V vs. Li/Li<sup>+</sup>. A cathode will then be charged by increasing the current to reach a distinct potential, whereas for an anode the potential will be decreased to a maximum lowest point of 0.01 V vs. Li/Li<sup>+</sup>. Reversible insertion and extraction reactions should exhibit the same integral of oxidation/reduction current and therefore the same capacity. Depending on

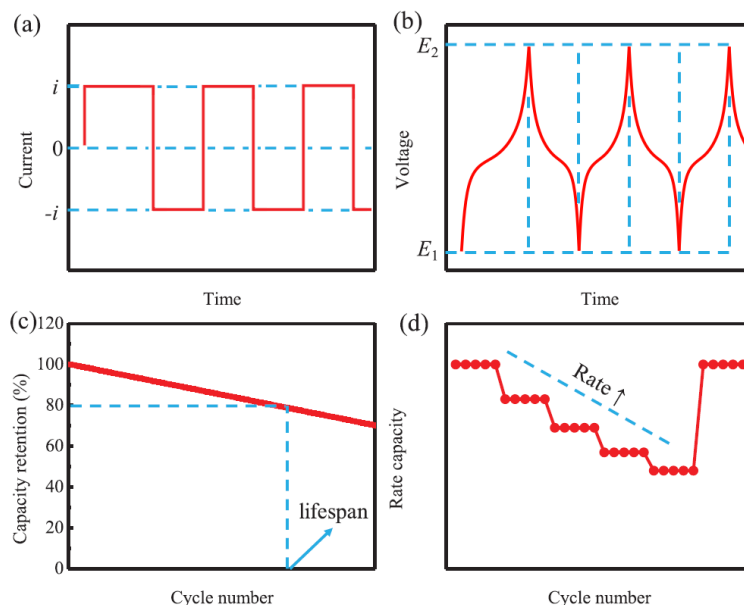


**Figure 2.12:** (a) Applied current profile and (b) the resulting galvanostatic charge/discharge curve of a generic battery electrode. (c) Typical cycle stability and (d) rate capability performance. According to Yang et al.<sup>[14]</sup>

the current applied compared to the active electrode mass, charging and discharging rates can be specified. The cycling stability and rate performance can be determined by repeated cycling experiments at different charging rates.<sup>[14]</sup>

Li-insertion and conductivity measurements were carried out using an ECC-PAT-Core electrochemical test cell from EL-Cell GmbH, an AUTOLAB potentiostat/galvanostat PGSTAT302N with FRA32M module operating with a Nova 1.11 software. The set-up of the ECC-PAT-Core testing cell is schematically depicted in Figure 2.13.

The main parts of the assembly are the stainless steel upper (4) and lower plunger (9), which serve as current collector and are contacted via the lid (3) and the cell base (11), respectively. In-between are the working (8) and counter electrode (5), which are separated by an insulation sleeve (7) and an electrolyte-soaked glass fiber separator (6). For half-cell experiments, Li foil is used as counter electrode, while the working electrode is either freestanding, coated on aluminum foil as anode or coated on copper foil as cathode. The insulation sleeve (7) has an integrated Li reference ring, which is in contact with the electrolyte and a reed contact on the outside in order to relate the applied voltage to Li/Li<sup>+</sup> reference potential. For Li-ion conductivity measurements the solid state electrolytes are contacted via the stainless steel current collectors. The cell is airtight, closed by a PE seal (10) which is pressed via lid and cell base in the bracket (2) by turning the wing nut (1).

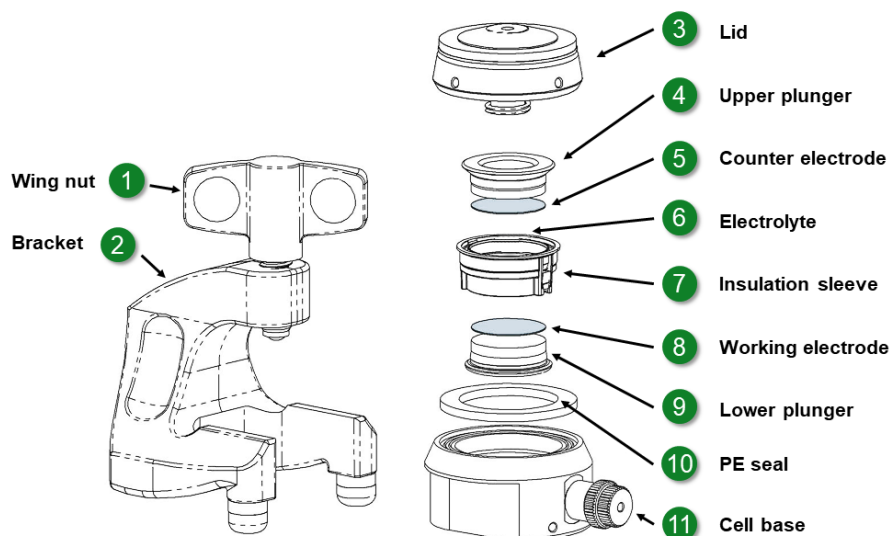


Figure 2.13: Construction of the ECC-PAT-Core electrochemical testing cell.<sup>[18]</sup>

## References

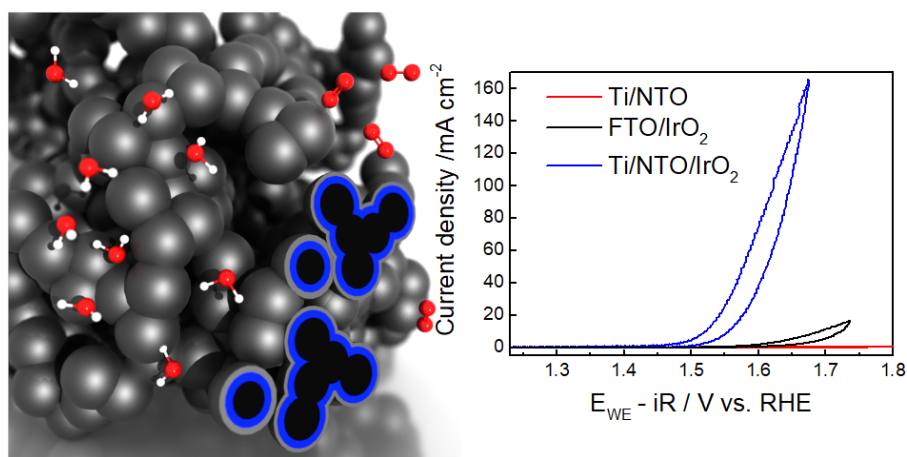
- [1] L. Spiess, G. Teichert, R. Schwarzer, H. Behnken, C. Genzel, *Moderne Röntgenbeugung - Röntgendiffraktometrie für Materialwissenschaftler, Physiker und Chemiker*, Vieweg+Teubner Verlag, **2009**.
- [2] A. Le Bail, I. Madsen, L. M. D. Cranswick, J. K. Cockcroft, P. Norby, A. D. Zuev, A. Fitch, J. Rodriguez-Carvajal, C. Giacobozzo, R. B. Von Dreele, P. Scardi, N. C. Popa, R. Allmann, L. A. Solovyov, B. Hinrichsen, U. Schwarz, A. Altomare, A. Moliterni, R. Caliendo, R. Rizzi, N. V. Y. Scarlett, M. Jansen, R. E. Dinnebier, S. J. L. Billinge, *Powder Diffraction*, The Royal Society of Chemistry, **2008**, p001–p582.
- [3] <https://www.jawoollam.com/resources/ellipsometry-tutorial>, (accessed 18 Feb 2017).
- [4] D. A. Skoog, F. J. Holler, S. R. Crouch, *Principles of Instrumental Analysis*, Thomson, **2007**.
- [5] adapted from <https://cmrf.research.uiowa.edu/scanning-electron-microscopy>, (accessed 18 Feb 2017).
- [6] <https://en.wikipedia.org/wiki/Transmission-electron-microscopy>, (accessed 30 Nov 2021).
- [7] D. B. Williams, C. B. Carter, *Transmission Electron Microscopy - A Textbook for Materials Science*, Springer US, **2009**.
- [8] G. Wedler, H.-J. Freund, *Lehrbuch der Physikalischen Chemie*, 6. Edition, Wiley-VCH, **2012**.

- 
- [9] R. Tauc, J. Grigorovici, A. Vancu, *Phys. Status Solidi B* **1966**, *15*, 627–637.
- [10] C. C. Chusuei, D. Goodman, *Encyclopedia of Physical Science and Technology* **2002**, *17*, (Ed.: R. A. Meyers), 921–938.
- [11] K. S. W. Sing, D. H. Everett, R. a. W. Haul, L. Moscou, R. a. Pierotti, J. Rouquérol, T. Siemieniewska, *Pure Appl. Chem.* **1985**, *54*, 603–619.
- [12] M. Thommes, K. Kaneko, A. V. Neimark, J. P. Olivier, F. Rodriguez-Reinoso, J. Rouquerol, K. S. Sing, *Pure Appl. Chem.* **2015**, *87*, 1051–1069.
- [13] N. Elgrishi, K. J. Rountree, B. D. McCarthy, E. S. Rountree, T. T. Eisenhart, J. L. Dempsey, *Journal of Chemical Education* **2018**, *95*, 197–206.
- [14] X. Yang, A. L. Rogach, *Adv. Energy Mater.* **2019**, *9*, 1900747.
- [15] A. J. Bard, L. R. Faulkner, *Electrochemical Methods: Fundamental and Applications*, 2nd ed. John Wiley & Sons: Hoboken, NJ, **2001**.
- [16] J.-M. Savéant, *Elements of Molecular and Biomolecular Electrochemistry*, John Wiley & Sons: Hoboken, NJ, **2006**.
- [17] C. Brett, A. M. O. Brett, *Electrochemistry: Principles, Methods, and Applications*, Oxford University Press, Oxford, **1993**.
- [18] <https://el-cell.com/download/1669/>, (accessed 02 Dez 2021).

### 3 Carbon-templated Conductive Oxide Supports for Oxygen Evolution Catalysis

This chapter is based on the following publication:

Alexander G. Hufnagel<sup>‡</sup>, Sebastian Häring<sup>‡</sup>, Michael Beetz, Bernhard Böller, Dina Fattakhova-Rohlfing and Thomas Bein\*, *Nanoscale*, 2019, 11,14285.



---

<sup>‡</sup>These authors contributed equally.

Sebastian Häring developed the deposition process for the carbon-templated conductive oxide support, performed conductivity measurements, morphological investigations, electrochemical measurements and wrote the corresponding parts of the manuscript.

## Abstract

We present a novel route for the preparation of supported IrO<sub>2</sub> catalysts for the oxygen evolution reaction in proton exchange membrane electrolyzers. It uses carbon soot as a nanostructure template, which is sequentially coated with a conductive niobium-doped titanium oxide (NTO) layer and an ultrathin, highly pure IrO<sub>2</sub> catalyst layer by atomic layer deposition (ALD). The NTO acts as an oxidation-stable conductor between the metal current distributor and the catalyst. The highly controlled film growth by ALD enables the fabrication of electrodes with a very low noble metal loading. Nonetheless, these electrodes exhibit very high catalytic activity and good stability under cyclic and constant load conditions. At an IrO<sub>2</sub> content of less than 10 percent by mass of the oxide material and an area-based Ir content of 153 μg cm<sup>-2</sup>, the nanostructured NTO/IrO<sub>2</sub> electrode achieves an oxygen evolution current density of 1 mA cm<sup>-2</sup> at an overpotential of ≈250 mV, which is significantly lower than the reported values for particulate NTO/IrO<sub>2</sub> catalysts.

## 3.1 Introduction

If an energy economy independent from fossil fuels is to be established, large-scale hydrogen production from renewable energy sources should replace the current practice of steam reforming natural gas. As renewable energy is mostly harvested in the form of electricity (photovoltaics, wind turbines etc.), hydrogen evolution by electrolysis of water is an obvious, attractive choice. The more recent proton exchange membrane (PEM) electrolysis technology has experienced an upsurge in research interest in recent years due to its advantages over the well-established alkaline water electrolysis, including faster response to load changes (important when the power supply is fluctuating, as is the case with most renewables) as well as higher current densities and consequently more compact system design.<sup>[1,2]</sup> However, the acidic environment, coupled with the high anodic potential at the oxygen-evolving electrode, necessitates a stable oxygen evolution catalyst, which is also efficient and connected via a low-resistance pathway to the current collector. Because of its excellent catalytic activity and long-term stability, state-of-the-art oxygen evolution catalysts for the acidic environment of the PEM anode are based on IrO<sub>2</sub>, which at 0.001 ppm abundance (by mass) in the earth's crust is one of the rarest elements.<sup>[2]</sup> Due to this scarcity, many attempts have been made to reduce the loading of the anode with IrO<sub>2</sub>. An established method is the dispersion of the IrO<sub>2</sub> on a high-surface-area support material, which is also stable against corrosion and oxidation. The state-of-the-art support material is TiO<sub>2</sub>.<sup>[3-7]</sup> However, due to the low intrinsic conductivity of TiO<sub>2</sub>, a high IrO<sub>2</sub> loading is typically needed to establish a continuous conductive pathway to the current collector.<sup>[2]</sup>

Transparent conductive oxide materials (TCOs) provide a solution to this quandary. A porous TCO support can be coated with an IrO<sub>2</sub>-based catalyst and provide the conductive pathway to the current collector.<sup>[8-14]</sup> In such a configuration, the expensive

$\text{IrO}_2$  is only used in the function where it is difficult to replace (i.e. as an OER catalyst), whereas the current conduction can be handled by the much cheaper TCO. To ensure maximum utilization of the  $\text{IrO}_2$  and thus enable catalysts with a very low  $\text{IrO}_2$  loading, the electrochemically active surface area (ECSA) must be maximized. This can be achieved by either applying the  $\text{IrO}_2$  in the shape of extremely small nanoparticles or as an ultrathin ( $\leq 1$  nm) film. A high  $\text{IrO}_2$  loading to achieve conductivity is thus not necessary. Niobium-doped titanium oxide (NTO,  $\text{Nb}:\text{TiO}_2$ ) can be assembled into a variety of porous structures and has shown promise as such an oxidation-stable yet conductive catalyst support material for the oxygen electrode in both electrolyzers and fuel cells.<sup>[9,10,15,16]</sup> While existing studies have used NTO powders loaded with  $\text{IrO}_2$ , we propose that nanostructured films with easily accessible meso- and macropores can be of great advantage as they are based on a continuous conductive matrix, ensuring good current conduction, while the large pores facilitate electrolyte access and gas evacuation. In PEM fuel cells, such films are formed by commercially available carbon black agglomerate particles.<sup>[17,18]</sup> However, the considerably higher anode potential in PEM electrolyzers precludes the use of carbon, which undergoes anodic oxidation at  $\geq 1$  V vs. RHE.<sup>[19]</sup> Lately, nanomaterials have been developed that replicate the morphology of carbon in stable oxide materials for a number of applications, including photodetectors and Li-ion battery electrodes.<sup>[20-26]</sup> The conversion of the carbon black nanostructure into a porous TCO material is expected to result in a conductive and oxidation-stable OER catalyst support that is well suited for PEM electrolyzer applications. This replication can be achieved by atomic layer deposition (ALD), which excels at controlled thin film growth. ALD combines unrivaled conformality in porous structures with subnanometer thickness control and the ability to prepare doped and mixed materials by alternating deposition of multiple components. It is thus ideally suited to prepare ternary oxide films with a complex morphology, using a hard template, such as carbon black, to direct the resulting film morphology.

Here, we demonstrate the preparation and performance characterization of a new type of OER catalyst structure for PEM electrolysis. We used atomic layer deposition to grow macroporous support structures of NTO on carbon-based hard templates derived from flame soot. We then apply a conformal, ultrathin film ( $\approx 1$  nm) of pure, crystalline  $\text{IrO}_2$  to the surface of the NTO support and examine its performance as an OER electrode in an acidic electrolyte. This entirely new approach to the production of a nanostructure-supported OER catalyst results in electrodes with impressive performance and stability in spite of their very low  $\text{IrO}_2$  loading. The combination of the nanostructure provided by the easily scalable soot template with the precisely controlled NTO deposition and tunable ultra-low  $\text{IrO}_2$  loading by ALD make this a very attractive electrode concept for overcoming the challenges involved in PEM electrolyzer anode design.

## 3.2 Results and Discussion

### 3.2.1 Preparation and Characterization of Carbon Soot Templates

The multi-step preparation of the nanostructured OER electrodes requires a solid template to direct the final morphology. For this purpose, we prepared carbon soot substrates with accurate control over thickness and morphology by manually drawing smooth, heat-resistant substrates such as soda-lime glass (SLG), fused silica and Ti foil through the flame of a wick burner fueled with 2-propanol (Figure 3.1a). We found this to be the preferred fuel as it ensures a good rate of soot deposition and leaves no low-volatility residue in the deposited film. The burner was constructed so as to produce a wide sheet of flame that covers the entire substrate, which allows for homogeneous growth on large areas. The thickness can be easily tuned in the micrometer range by repeatedly drawing the substrate through the flame. Figure 3.1b, c shows cross-section

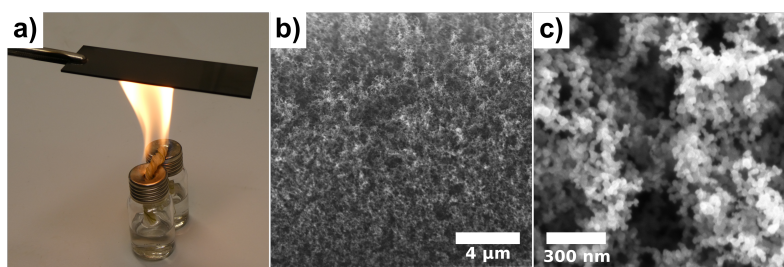


**Figure 3.1:** Photo image of carbon film preparation (a). Cross-sectional SEM micrographs of a 2-propanol soot layer on SLG (b, c).

SEM micrographs of a soot layer deposited on SLG. The structure is highly porous yet continuous. It consists of primary carbon particles that are spherical and  $\approx 30$  to 50 nm in diameter. These form extended interwoven chains similar to the aggregate secondary particles found in commercial carbon blacks.<sup>[27]</sup> The pore system is highly interconnected with a wide distribution of pore sizes, ranging from tens to hundreds of nanometers. We expect this structure to be well suited for an OER catalyst support as it allows easy electrolyte access and gas egress, and the interconnected web ensures electrical contact and mechanical stability.

### 3.2.2 ALD of NTO Coatings

The next step of the electrode preparation procedure is the application of the NTO layer, which serves as a corrosion-stable current conductor. We used alternating ALD of  $\text{TiO}_2$  and  $\text{NbO}_x$  from titanium(IV) isopropoxide (TTIP), niobium(V) ethoxide (NEO) and water to prepare these layers on carbon-soot templates grown on Ti foil as well as on flat fused silica and Si(100) substrates. The mixing ratio of  $\text{Nb}/(\text{Ti}+\text{Nb})$  in the resulting layers was varied from 3 to 29 % by varying the cycle ratio of the two ALD processes (Table S1). The elemental ratio, determined by EDX from as-deposited films grown on

carbon soot on fused silica, very accurately tracks the cycle ratio of the two ALD processes, allowing for accurate adjustment of the Nb content in the films. To crystallize the oxide layers and activate the niobium dopant, the films were then heat-treated in 5 % H<sub>2</sub>/N<sub>2</sub>. Sample XRD patterns of NTO-coated carbon soot films (soot layer ≈10 μm, oxide layer ≈80 nm) after treatment at different temperatures are shown in Figure 3.6. A striking difference is observed between the as-deposited samples containing 3 and 20 % Nb, respectively. While a low Nb content results in a highly crystalline anatase phase already during deposition, the high Nb content effectively prevents crystallization of the film material under the conditions of the deposition.<sup>[28]</sup> After heating to 600 °C, the NTO film with 20 % Nb has crystallized in the anatase lattice as well. After treatment at 700 °C, the film with a low Nb content has undergone quantitative phase transformation into the rutile modification, while a high Nb content prevents this transition and the film is still composed exclusively of the anatase phase.<sup>[29]</sup> Despite the relatively high niobium content, no segregation of a separate NbO<sub>x</sub> phase is visible in the XRD data. Rather, a shift of the reflections of the TiO<sub>2</sub> phases to lower angles is observed, most obviously in the anatase (101) reflection at 25.3 ° 2θ. This shift indicates that the Nb is incorporated into the anatase lattice, expanding it without changing the crystal structure.<sup>[30]</sup> The approximate crystallite size was calculated from the broadening of the anatase (101) and rutile (110) reflections using the Scherrer equation (equation 3.1, Table S2, K = 0.9). Figure 3.7 shows SEM images of a flat 20 % Nb NTO layer on fused silica after deposition and after annealing at 700 °C. The as-deposited amorphous layer shows no obvious visible features. By contrast, the annealed layer consists of a mosaic of large crystals on the order of 10 μm. This is evidence of explosive crystallization, which has been previously observed in ALD NTO.<sup>[28,31]</sup> Niemelä, Hirose, Hasegawa, and Karppinen showed that the conductivity-limiting mechanism in ALD NTO films changes from grain-boundary scattering at low Nb contents to intra-grain phonon scattering in the larger grains found at high Nb levels.<sup>[32]</sup> They concluded that for applications where high conductivity is required, the high-Nb regime is advantageous. We assume that a similar explosive crystallization process also takes place on the carbon supports, resulting in the fairly large crystallite sizes on the order of the carbon soot primary particles (cf. Table S2) and ensuring good grain-boundary contact of the nanostructured NTO, which is a key requirement for good conductivity throughout the nanostructured layer. The conductivity of NTO thin films with different Nb contents and heat treatments was measured using the van der Pauw method on fused silica substrates. As-deposited, the conductivity was below the detection limit in all cases. Figure 3.2 shows the conductivities obtained by annealing at 600 or 700 °C. At both temperatures a similar trend is observed with a clear conductivity maximum at 20 % Nb. Between 10 and 30 % Nb, conductivity of films annealed at 700 °C is markedly higher than that achievable by annealing at 600 °C. The conditions as which the highest conductivity (440 S cm<sup>-1</sup>) was observed were chosen for the electrocatalyst supports for use in OER electrode preparation. These supports consist of a ≈20 μm soot layer deposited on titanium foil, coated with a 20 % Nb NTO layer of 40 or 80 nm by ALD

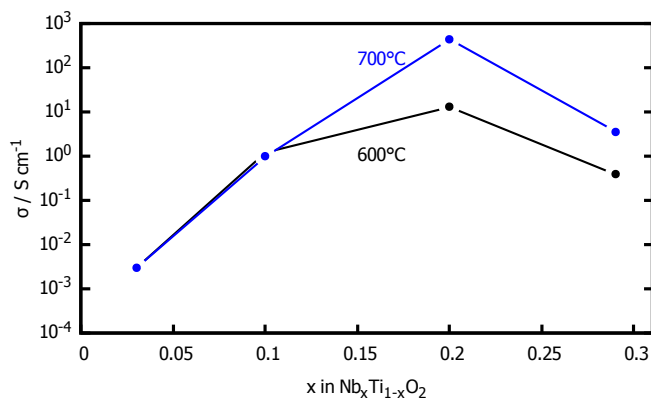


**Figure 3.2:** Conductivity of annealed NTO films on fused silica.

and annealed at 700 °C in 5 %H<sub>2</sub>/N<sub>2</sub>.

### 3.2.3 ALD of IrO<sub>2</sub>

To finalize the OER electrodes, the iridium oxide catalyst phase has to be applied with a low mass loading and high dispersion onto the carbon/NTO structure. One way to achieve this is a conformal ultrathin film, prepared by ALD. The atomic layer deposition of iridium metal and iridium oxide has been extensively studied.<sup>[33–39]</sup> It was reported by Hämäläinen, Kemell, Munnik, et al. that both iridium metal and iridium(IV) oxide can be grown using Ir(acac)<sub>3</sub> and ozone as precursors.<sup>[35,37]</sup> At temperatures up to 195 °C, crystallographically pure IrO<sub>2</sub> is obtained. At higher temperatures, the resulting films exhibited increasing amounts of metallic Ir according to XRD. Because of this, a deposition temperature of 188 °C was chosen for this study. This resulted in the growth of rutile IrO<sub>2</sub> with no crystalline impurities or Ir metal detectable by XRD (Figure 3.8). The thickness of the IrO<sub>2</sub> films was determined by spectroscopic ellipsometry on oxide-terminated Si(100) substrates. Good fits were obtained by modeling the IrO<sub>2</sub> layer using a dual Lorentz oscillator model as proposed by Kohli, Niles, Rithner, and Dorhout.<sup>[40]</sup> The nucleation and growth behavior of the Ir(acac)<sub>3</sub>/O<sub>3</sub> ALD process has recently been studied by Mattinen, Hämäläinen, Gao, et al., who report a very long nucleation delay of 120 cycles and a growth rate of 0.033 nm cycle<sup>-1</sup>. As the present study investigates extremely low IrO<sub>2</sub> loading for oxygen evolution catalysis, the films studied here were deposited within this nucleation regime, where complete substrate coverage and uniformity cannot be presupposed. The use of an Al<sub>2</sub>O<sub>3</sub> underlayer to aid nucleation, as demonstrated by Hämäläinen, Hatanpää, Puukilainen, et al., was avoided as it might inhibit electrical contact between the conductive support and the IrO<sub>2</sub> film.<sup>[37]</sup> The composition of ALD IrO<sub>2</sub> films on single crystal Si substrates was investigated by XPS (Figures 3.9 and 3.10). The detail XP spectrum of the Ir 4f region (Figure 3.10) shows the Ir 4f<sub>7/2</sub> and Ir 4f<sub>5/2</sub> signals are centered on binding energies of 61.9 and 64.9 eV, respectively, which is in good agreement with reported values for

anhydrous  $\text{IrO}_2$ .<sup>[41]</sup> No evidence of metallic iridium was found, leading us to conclude that the ALD process yields films in which the iridium is exclusively present as iridium(IV) oxide.

### 3.2.4 Electrode Preparation and Characterization

To prepare OER catalyst electrodes, the catalyst support structure described above was subjected to 50 ALD cycles of the  $\text{IrO}_2$  process, which resulted in a layer thickness of between 0.64 and 0.87 nm on Si witness substrates, determined by ellipsometry. Fluoride-doped tin oxide (FTO) substrates were processed in the same  $\text{IrO}_2$  ALD process to obtain a flat catalyst electrode. Due to the small amount of  $\text{IrO}_2$  present in

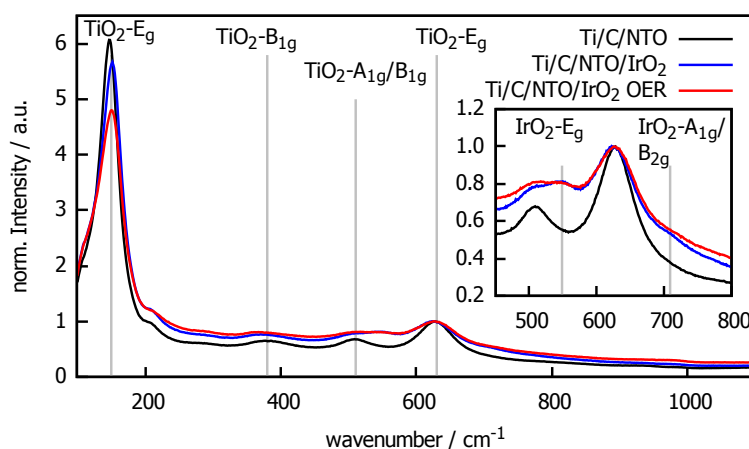


**Figure 3.3:** Raman spectra of a carbon/NTO support (black), support with  $\text{IrO}_2$  layer (blue) and electrode after electrochemical testing (red). The inset shows a magnification of the  $\text{IrO}_2$  signals. Assignment of signals according to refs [42, 43].

the nanostructured electrodes as well as the small particle size, crystalline  $\text{IrO}_2$  could not be detected by XRD. Figure 3.3 shows Raman spectra of a Ti/C/NTO film and a Ti/C/NTO/ $\text{IrO}_2$  film. The anatase crystal is strongly scattering and its signals dominate the spectra. The  $E_g$ ,  $B_{1g}$  and  $A_{1g}$  modes can be clearly assigned, according to Stagi, Carbonaro, Corpino, et al., who also observed the small shoulder at  $200\text{ cm}^{-1}$ .<sup>[43]</sup>  $\text{IrO}_2$  has distinct Raman signals at  $560\text{ cm}^{-1}$  ( $E_g$ ) and  $720\text{ cm}^{-1}$  ( $A_{1g}$ ,  $B_{2g}$ ).<sup>[42]</sup> Despite the small amount of  $\text{IrO}_2$  deposited onto the electrode support, these signals can be clearly observed in the magnification of their Raman spectra (inset in Figure 3.3). The  $E_g$  signal appears as a peak between the neighboring anatase signals and the  $A_{1g}/B_{2g}$  signal is visible as a shoulder on the  $\text{TiO}_2$  peak centered on  $628\text{ cm}^{-1}$ . Scanning (SEM) and transmission (TEM) electron microscopy was used to investigate the structure and composition of the electrodes (Ti/C/NTO/ $\text{IrO}_2$ ). Figure 3.4a shows an SEM image of the fractured cross-section of a Ti/C/NTO/ $\text{IrO}_2$  electrode. The porous nanostructure of the carbon soot has been preserved through the NTO deposition, annealing and  $\text{IrO}_2$

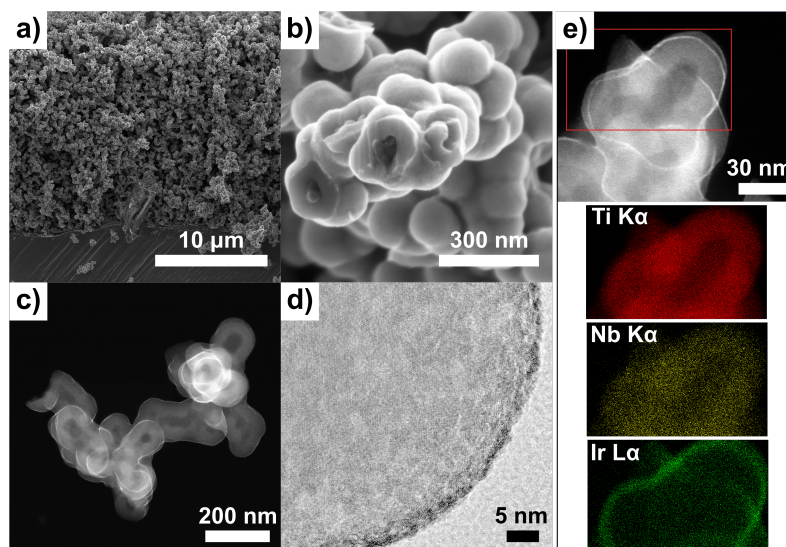


**Figure 3.4:** Cross-sectional SEM secondary electron image of a complete electrode (Ti/C/NTO/IrO<sub>2</sub>) (a). SEM back-scattered electron image of a fracture site in the oxide nanostructure (b). HAADF-STEM image of one isolated particle of the electrode structure (c). Bright-field TEM image of part of an electrode particle (d). EDX element distribution maps of the area highlighted by the red frame in the STEM image (e).

deposition. There is no evidence of pore clogging at the surface of the carbon layer and the deeper pores are still accessible. Figure 3.11 shows EDX element distribution maps for Ti, Nb and Ir of a similar cross-section. All three are evenly distributed throughout the entire thickness of the nanostructured film. We therefore expect a similar composition in terms of the Nb content of the NTO, and thus uniform conductivity, as well as the IrO<sub>2</sub> catalyst loading of the entire electrode. The atomic ratio Ir/(Ti+Nb+Ir), determined by area-averaged EDX excluding the substrate, was found to be 3-4 % at different spots of the cross-section, which corresponds to an IrO<sub>2</sub> mass fraction of 7-9.5 % of the oxide material. Figure 3.4b shows a detail back-scattered electron image of the fracture face of a carbon/oxide particle. Due to the atomic number contrast inherent to this type of image, the components of the structure can be clearly distinguished. The carbon support (darkest) is still present, encased by the NTO layer. Everything is covered by the IrO<sub>2</sub> layer, which appears brightest due to its high atomic weight. No major holes in the iridium oxide layers are visible. An HAADF-STEM image of a particle from the electrode structure is shown in Figure 3.4c. This imaging mode also shows the thin IrO<sub>2</sub> layer, bright due to its high scattering cross-section, evenly coating the outside of the particle. The continuous inner pore structure containing the carbon template is also visible. A detail TEM image of a single particle is shown in Figure 3.4d. It reveals that the IrO<sub>2</sub> layer consists of closely packed crystalline particles. This implies that the electrode presents a large surface area of IrO<sub>2</sub> to the electrolyte, which is in good electrical contact with the underlying NTO. Figure 3.4e shows a HAADF-STEM image of

an electrode particle together with EDX element distribution maps of the marked area. Ti and Nb are co-located in the center of the particle with the exception of the template hollow. Iridium is found at the surface, as demonstrated by the strong signal observed at the particle circumference, where the electron beam passes tangentially through the particle surface rather than axially, thus exciting a larger volume of  $\text{IrO}_2$ .

### 3.2.5 Electrochemical Characterization

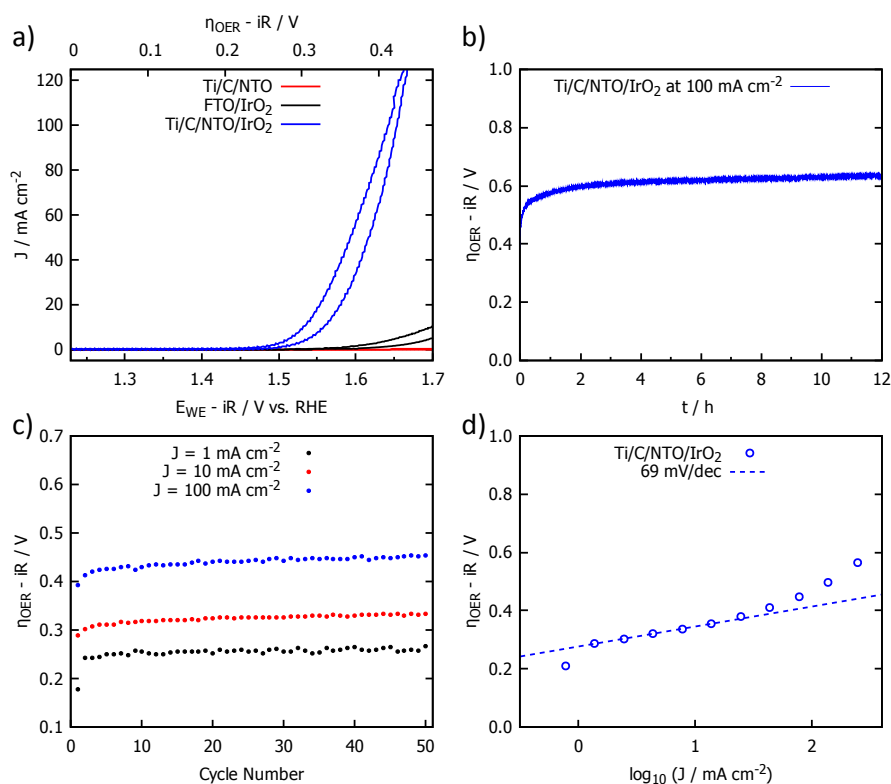


**Figure 3.5:** Cyclovoltammograms (2<sup>nd</sup> cycles) of Ti/C/NTO/IrO<sub>2</sub>, Ti/C/NTO and FTO/IrO<sub>2</sub> electrodes recorded in 0.5 M H<sub>2</sub>SO<sub>4</sub> at 20 mV s<sup>-1</sup> (a). Chronopotentiometric stability data of a Ti/C/NTO/IrO<sub>2</sub> electrode at 100 mA cm<sup>-2</sup> (b). OER overpotentials at 1, 10 and 100 mA cm<sup>-2</sup> extracted from the anodic scans of prolonged cycling of a Ti/C/NTO/IrO<sub>2</sub> electrode (c). Tafel plot of a Ti/C/NTO/IrO<sub>2</sub> electrode (d).

With the successful application of the iridium oxide, this Ti/C/NTO/IrO<sub>2</sub> structure represents the completed OER electrode. Its oxygen evolution activity was investigated in a three-electrode electrochemical cell using gently stirred 0.5 M H<sub>2</sub>SO<sub>4</sub> as the electrolyte. All electrochemical measurements were performed at room temperature. First, in order to investigate whether the IrO<sub>2</sub> layer in the electrode nanostructure is indeed fully contacted and accessible to the electrolyte, we performed cyclic voltammetry at varying scan speeds in the range between 0.55 and 0.85 V vs. RHE, where no faradaic

process is observed (Figure 3.12a). As expected for a capacitive region, the currents are fairly constant in the scanned potential range. The currents at 0.70 V were extracted from the cathodic and anodic scans and plotted against the scan rate in Figure 3.12b. As a reference, the same experiment was performed with an FTO electrode coated with the same IrO<sub>2</sub> layer. The capacitive currents follow a linear trend in both cases, though some deviation is observed for the nanostructured electrode at the highest currents. The slopes give the capacitance of the flat and nanostructured electrodes as 28 μF cm<sup>-2</sup> and 3570 μF cm<sup>-2</sup>, respectively. The direct calculation of the electrochemically active surface area would require an accurate value for the reference capacitance, which is difficult to obtain, as it depends on the material preparation as well as pseudocapacitance effects of IrO<sub>2</sub>.<sup>[44,45]</sup> We therefore restrict our analysis to comparing the two electrodes investigated here. Assuming that the capacitive behavior of the IrO<sub>2</sub> film is the same on both the FTO and Ti/C/NTO substrates, the relative specific ECSA is given by the ratio of the two capacitances. For FTO a roughness factor of ≈1.2 was determined by atomic force microscopy. The ECSA of the Ti/C/NTO/IrO<sub>2</sub> electrode is therefore 1.2 times the capacitance ratio, i.e. 153 cm<sup>2</sup><sub>ECSA</sub>/cm<sup>2</sup><sub>geo</sub>. Figure 3.5a shows cyclic voltammograms of a Ti/C/NTO/IrO<sub>2</sub> electrode, a reference sample with no IrO<sub>2</sub> layer and another reference with the same ALD IrO<sub>2</sub> applied to an FTO substrate. The nanostructured electrode with no IrO<sub>2</sub> coating shows no significant water oxidation current below 1.7 V vs. RHE. By comparison, the Ti/C/NTO/IrO<sub>2</sub> electrode exhibits significant water oxidation activity with an onset at about 1.45 V vs. RHE at 0.5 mA cm<sup>-2</sup> and reaches a current density of 100 mA cm<sup>-2</sup> at 1.64 V vs. RHE. The FTO/IrO<sub>2</sub> sample also catalyzes the OER. Its current is much lower as a result of the smaller surface area. The Ti/C/NTO/IrO<sub>2</sub> electrode was subjected to 50 consecutive CV cycles and the overpotentials at 1, 10 and 100 mA cm<sup>-2</sup> (anodic scans) are plotted in Figure 3.5c (see Figure 3.13 for full CV cycles). The three data sets show the same trend with a rise of about 35 mV over the first three cycles, followed by a much slower rise by about 20 mV over the course of the remaining cycles. Small jumps in the overpotential are a result of bubble formation and detachment. The overpotential at 1 mA cm<sup>-2</sup> is between 240 and 260 mV for all but the first cycle. This is a much smaller overpotential than that reported for oxide-supported catalysts with comparable IrO<sub>2</sub> content. For comparison, Hu et al. reported an overpotential of 300 mV for an NTO catalyst with 17 wt% IrO<sub>2</sub>, while Tong et al. measured 397 mV with 13 wt% IrO<sub>2</sub> on ATO at the same current density.<sup>[9,14]</sup>

The long-term stability of the Ti/C/NTO/IrO<sub>2</sub> under constant load was investigated by chronopotentiometry over 12 h at a constant current density of 100 mA cm<sup>-2</sup>. After an initial increase, the overpotential steadies out at ≈0.6 V with a slight positive drift over the duration of the measurement (Figure 3.5). No sudden potential jumps, which might indicate a failure of the catalyst structure or conductivity, can be observed. The ramifications for the stability of the Ti/C/NTO/IrO<sub>2</sub> electrode structure are discussed below. A Tafel plot, constructed from data recorded after 50 CV cycles of a Ti/C/NTO/IrO<sub>2</sub> electrode, is shown in Figure 3.5d. The overpotential follows a linear

trend between  $\approx 1$  and  $30 \text{ mA cm}^{-2}$  with a slope of  $69 \text{ mV}$  per decade. This is comparable, though slightly higher, than values reported for Sb:SnO<sub>2</sub>-supported (ATO) IrO<sub>2</sub> catalysts.<sup>[11,14]</sup> Tong et al. reported  $62 \text{ mV dec}^{-1}$  at  $13 \text{ wt\% IrO}_2$  loading.<sup>[14]</sup> Assuming a  $1 \text{ nm}$  thick crystalline compact layer of IrO<sub>2</sub> evenly coating the support with the surface area calculated above, this corresponds to an iridium loading of  $153 \text{ } \mu\text{g cm}^{-2}$  ( $178 \text{ } \mu\text{g cm}^{-2}$  of IrO<sub>2</sub>). This value should be viewed as an upper limit, as the IrO<sub>2</sub> layer thickness determined by ellipsometry was consistently smaller than  $1 \text{ nm}$ . At this loading, a current density of  $100 \text{ mA cm}_{\text{geom}}^{-2}$  corresponds to a mass-based current of  $654 \text{ A g}_{\text{Ir}}^{-1}$  ( $561 \text{ A g}_{\text{IrO}_2}^{-1}$ ). During potential cycling, this is attained at  $\eta_{\text{OER}} \leq 460 \text{ mV}$  in all 50 cycles (Figure 3.5c). During chronopotentiometric testing, the required overpotential rises to  $620 \text{ mV}$  over the course of  $12 \text{ h}$  (Figure 3.5b). For comparison, Hu et al. report an initial mass activity of  $\approx 400 \text{ A g}_{\text{IrO}_2}^{-1}$  at  $\eta_{\text{OER}} = 470 \text{ mV}$  for NTO loaded with  $17 \text{ wt\% IrO}_2$  and  $1500 \text{ A g}_{\text{IrO}_2}^{-1}$  for a  $26 \text{ wt\%}$  loading.<sup>[9]</sup> Oh et al. observed initially  $100 \text{ A g}_{\text{Ir}}^{-1}$  at  $\eta_{\text{OER}} = 310 \text{ mV}$  for an ATO-supported  $20 \text{ wt\% IrO}_x$  catalyst, which reduced to  $\approx 60 \text{ A g}_{\text{Ir}}^{-1}$  after a  $15 \text{ h}$  chronopotentiometric experiment at  $1 \text{ mA cm}_{\text{geom}}^{-2}$ .

### 3.2.6 Post-mortem Analysis of a Ti/C/NTO/IrO<sub>2</sub> electrode

As our electrodes exhibited some change in their performance characteristics during cycling and constant load operation, we investigated the aging of the Ti/C/NTO/IrO<sub>2</sub> nanostructure under OER conditions by *ex-situ* analysis of the electrode used in the chronopotentiometric stability test (Figure 3.5b). As shown in Figure 3.14, the Ti substrate is visible in several places on the electrode, where the catalyst nanostructure delaminated as a result of prolonged intense bubble formation. We note, however, that in an actual PEM electrolyzer the catalyst structure is firmly sandwiched between the current collector and the PEM and that the removal of larger parts of the catalyst structure is thereby prohibited. The cell impedance was  $\approx 3 \text{ } \Omega$  before and after the stability test. Together with the high catalytic activity observed throughout the experiment, this leads us to conclude that the conductivity of the NTO phase did not suffer at the high applied potential and that electronic contact with the IrO<sub>2</sub> layer was retained. The Raman spectrum after electrochemical testing, repeated rinsing with ultrapure water and drying at  $60 \text{ } ^\circ\text{C}$  is shown as the red curve in Figure 3.3. The signals from both the anatase NTO and the IrO<sub>2</sub> phase are still observed after  $> 12 \text{ h}$  exposure to the acidic electrolyte and highly anodic potential. Both phases, therefore, show remarkable stability. However, the electrode after OER stability testing shows slightly diminished IrO<sub>2</sub> signal intensities compared to the pristine electrode, which indicates that some of the catalyst material was lost during the measurement. The HAADF-STEM image in Figure 3.15a reveals that the structure is still conformally coated with the strongly scattering IrO<sub>2</sub> overlayer, though it no longer appears as well-formed and continuous as before the OER experiments (cf. Figure 3.4c). From these results as well as the slight rise in overpotential during the stability measurement we conclude that the IrO<sub>2</sub> layer was partially removed during the experiment. Dissolution of the IrO<sub>2</sub> is unlikely to be the cause of this as the reported rate of dissolution of crystalline IrO<sub>2</sub> during OER

in acidic media is on the order of  $0.1 \text{ ng cm}^{-2} \text{ min}^{-1}$ , juxtaposed to the  $\text{IrO}_2$  loading of  $178 \text{ } \mu\text{g cm}^{-2}$ , calculated for the  $\text{Ti/C/NTO/IrO}_2$  electrode.<sup>[46]</sup> More likely is a loss of adhesion at the  $\text{NTO/IrO}_2$  interface, which would cause the  $\text{IrO}_2$  film to flake off. We expect that close scrutiny of this interface will pinpoint ways to improve its durability by optimizing the deposition and annealing steps.

### 3.3 Conclusions and Outlook

We have demonstrated a new type of oxide-based anode structure for PEM water electrolysis. It uses NTO as an oxidation-stable conductive link between the metal current distributor and the catalyst, which takes the shape of an ultrathin  $\text{IrO}_2$  film with optimum utilization of the noble metal for OER catalysis. The material shows competitive activity and promising stability at a low Ir loading  $\leq 153 \text{ } \mu\text{g cm}^{-2}$ . The activity of Ir-based ternary oxides such as  $\text{Ru}_x\text{Ir}_y\text{O}_2$  has been demonstrated to be superior to that of  $\text{IrO}_2$ .<sup>[2]</sup> As the ALD method lends itself well to the controlled preparation of mixed oxides, we expect that  $\text{IrO}_2$  in our system could be easily replaced with an even more active catalyst. We envision that the anode system reported here can be applied in practical PEM electrolyzers in a number of ways. Using existing ALD particle coating technology and commercial carbon black as the substrate, supported catalyst powders could be made and used for ink-based MEA preparation. Alternatively, our method could be used to deposit a soot layer onto typical current distributor materials (e.g. Ti foam) and add the ALD NTO and  $\text{IrO}_2$  layers. The result would be an integrated current collector/porous catalyst with optimal conductive contact at the interfaces and excellent Ir utilization at low loading. This could be used directly as the anode in MEA assembly. ALD has a reputation as an expensive technique that is difficult to scale to large areas. However, the high power density of PEM electrolyzers implies that the geometric electrode areas to be coated are quite moderate even for larger systems. State-of-the-art PEM stacks have a cell area of several hundred square centimeters.<sup>[2]</sup> Existing ALD tools for industrial production can process substrate surface areas of several square meters per batch and larger reactors are in development.<sup>[47]</sup> If efficient reclamation of the excess Ir used in the ALD process is taken into account, it is conceivable that the cost savings due to the reduced  $\text{IrO}_2$ -loading and elimination of ink-based electrode deposition can easily balance the cost of ALD for this application.

### 3.4 Experimental Details

The substrates, SLG microscope slides, Ti foil (Alfa Aesar, 99.5 %, 0.25 mm) and polished Si (100) single crystal wafers were used as received. Fused silica (GVB GmbH, FN08) and FTO-coated (Pilkington,  $7 \text{ } \Omega \text{ square}^{-1}$ ) glass slides were cleaned prior to use by sequential sonication in Extran<sup>®</sup> solution, ultrapure water and 2-propanol for 15 min each and dried using nitrogen.

### 3.4.1 Deposition of Carbon Soot Nanostructures

Carbon soot nanostructured films were grown by repeatedly drawing the substrates through the top third of the flame of a custom-built wick burner fueled by technical grade 2-propanol. The flame sheet was approximately 4 cm wide at the base and 8 cm high. Typically, a microscope slide (25 × 75 mm) was drawn back and forth all the way through the flame within 1 s and this was repeated 10 times, resulting in a homogeneous soot film of  $\approx 20$   $\mu\text{m}$ . Fused silica and Ti foil samples were prepared in the same way.

### 3.4.2 ALD of NTO layers

TiO<sub>2</sub> and NbO<sub>x</sub> layers were grown using a Picosun R-200 Advanced ALD reactor at a temperature of 200 °C and a base pressure of 2 hPa. Nitrogen (Air Liquide, 99.999 %) was used as the purge and carrier gas. The carrier gas line flow during pulses was 40 sccm. Titanium tetraisopropoxide (TTIP, Aldrich, 99.999 %) was evaporated from a stainless steel vessel at 85 °C, niobium ethoxide (NEO, Strem, 99.9+ %) was supplied from a glass vessel at 160 °C. Ultrapure water (MilliQ, 18.2 M $\Omega$  cm) was held in a stainless steel cylinder at 19 °C. Each TiO<sub>2</sub> ALD cycle comprised two TTIP pulses (1.6 s pulse, 4.5 s static exposure, 6 s purge) and one water pulse (2 s pulse, 4.5 s static exposure, 7.5 s purge). The resulting GPC was 0.038 nm cycle<sup>-1</sup> with a non-uniformity of 4 % across a 20 cm wafer.

NbO<sub>x</sub> was deposited using cycles of four NEO pulses (1.6 s pulse, 6.5 s static exposure, 6 s purge) and one water pulse as in the TiO<sub>2</sub> process. The GPC was 0.068 nm cycle<sup>-1</sup> and the non-uniformity was 4 %. Mixed oxide layers were grown by interspersing one NbO<sub>x</sub> cycle in the TiO<sub>2</sub> process at regular intervals as shown in Table S1. Before being used as electrodes, the films were annealed in forming gas (5 % vol. H<sub>2</sub>, 95 % vol. N<sub>2</sub>, Air Liquide ARCAL F5) at 700 °C with a heating rate of 6 °C min<sup>-1</sup> and a dwell time of 120 min.

### 3.4.3 ALD of IrO<sub>2</sub> layers

Ir(acac)<sub>3</sub> (technical grade) was kindly donated by Heraeus Holding GmbH (Germany) and used as received. IrO<sub>2</sub> ALD was carried out in the same reactor at 188 °C. The carrier gas line flow during pulses was 40 sccm. Ir(acac)<sub>3</sub> was sublimated from a borosilicate glass container at 185 °C. Ozone was supplied by an ozone generator (INUSA AC2025) from a feed of 500 sccm 1 % N<sub>2</sub>/O<sub>2</sub> (Air Liquide, 99.9995 %). Each cycle consisted of three Ir(acac)<sub>3</sub> pulses and one ozone pulse, separated by purge intervals. An Ir(acac)<sub>3</sub> pulse comprised a 1.6 s pulse, 5 s static exposure and 10 s purge time. For the ozone pulse the times were 4 s, 2 s and 10 s, respectively. 50 cycles were used for the OER catalyst coatings, which resulted in a layer thickness of 0.64 to 0.87 nm, determined by spectroscopic ellipsometry on Si(100) substrates.

### 3.4.4 Electrode Characterization

ALD film thicknesses were determined by spectroscopic ellipsometry (J. A. Woollam M-2000D) on Si(100) substrates. TiO<sub>2</sub>, NbO<sub>x</sub> and NTO layers were modeled using a Cauchy function. IrO<sub>2</sub> layers were modeled using a dual Lorentz oscillator model as reported by Kohli et al.<sup>[40]</sup> X-ray diffraction patterns were recorded on a Bruker D8 Discover diffractometer using Ni-filtered Cu K $\alpha$  radiation ( $\lambda = 0.154178$  nm). The source was operated at 30 mA and 40 kV. Reference XRD reflection data were obtained from the ICSD database. The crystallite size  $p$  was calculated using the Scherrer equation (equation 3.1), where  $K$  is the Scherrer constant, FWHM is the line broadening at half-maximum and  $\theta$  is the Bragg angle.

$$p = \frac{K\lambda}{\text{FWHM} \cos\theta} \quad (3.1)$$

The conductivity of NTO films on fused silica was measured using the van der Pauw method (ECOPIA, Model HMS 3000, 0.55 T). The samples were contacted using spring-loaded gold-plated pins. SEM images were acquired on an FEI Helios NanoLab G3 UC FEG-SEM equipped with an Oxford Instruments EDX detector at acceleration voltages between 2 and 20 kV. Cross-section samples were prepared by fracturing the film samples on Ti foil using a pair of pliers. TEM and HAADF-STEM images were acquired on a FEI Titan Themis 80-300 kV with an acceleration voltage of 300 kV. For TEM imaging, particles were scraped off the electrode films, suspended in absolute ethanol and deposited on a holey carbon-coated copper grid. Raman spectra were recorded using an Olympus BX41 optical microscope (10x, N.A. 0.25 objective lens) coupled to a Horiba monochromator and Symphony CCD detector. A 20 mW HeNe laser, attenuated by an OD 0.3 filter was used for excitation. The resulting spectra were normalized by the height of the anatase  $E_g$  line at 628 cm<sup>-1</sup>. For X-ray photoelectron spectroscopy (XPS) a VSW TA10 X-ray source and a VSW HA100 hemispherical analyzer were used. All spectra were measured with non-monochromatic Mg K $\alpha$  radiation. Fits of the photoelectron peaks are based on a convolution of a Doniach-Šunjić-function and a Gaussian function and the subtraction of a linear background.

### 3.4.5 Electrochemical Characterization

FTO/IrO<sub>2</sub> working electrodes were prepared by contacting the FTO with Ag-based conductive lacquer, the active area was limited by masking with PTFE adhesive tape with a 0.238 cm<sup>2</sup> circular hole. Ti/C/NTO/IrO<sub>2</sub> and Ti/C/NTO electrodes were contacted via the Ti foil and masked with epoxy to obtain a comparable active area. Experiments were performed in a three-electrode electrochemical cell, using a coiled Pt wire as the counter electrode and a hydrogen electrode (Gaskatel HydroFlex<sup>®</sup>) as the reference electrode. The latter was checked against a Hg/HgO reference electrode before and after the experiments and showed no drift in relative potential. The electrolyte was aqueous 0.5 M H<sub>2</sub>SO<sub>4</sub>, which was gently stirred during the measurements (in air). All

experiments were performed at room temperature. A Metrohm Autolab PGSTAT302N potentiostat/galvanostat was used for cyclic voltammetry, chronopotentiometry and impedance spectroscopy. The CV and CP measurements were corrected for 95 % of the  $iR$ -drop. The cell resistance was determined as the high frequency real axis intercept of impedance spectra recorded at 1 V vs. RHE. It was typically 3  $\Omega$  for the electrodes on Ti and 12  $\Omega$  for electrodes on FTO. Tafel plots were constructed by galvanostatically holding an exponentially increasing range of current densities and reading out the stabilized overpotential after 30 s.

### 3.5 References

- [1] J. H. Russell, L. J. Nuttall, A. P. Fickett, *Am. Chem. Soc. Div. Fuel Chem. Prepr. Pap.* **1973**, *18*, 24–40.
- [2] M. Carmo, D. L. Fritz, J. Mergel, D. Stolten, *Int. J. Hydrogen Energy* **2013**, *38*, 4901–4934.
- [3] M. Lopez, A. Schleunung, P. Biberbach, *US Patent*, US7976989 (B2), **2011**.
- [4] M. Lopez, A. Schleunung, P. Biberbach, *US Patent*, US8263290 (B2), **2012**.
- [5] B. Klose-Schubert, D. Herein, H.-G. Reitz, *US Patent*, US2014322631 (A1), **2014**.
- [6] M. Bernt, H. A. Gasteiger, *J. Electrochem. Soc.* **2016**, *163*, F3179–F3189.
- [7] E. Oakton, D. Lebedev, M. Povia, D. F. Abbott, E. Fabbri, A. Fedorov, M. Nachtegaal, C. Copéret, T. J. Schmidt, *ACS Catal.* **2017**, *7*, 2346–2352.
- [8] A. T. Marshall, R. G. Haverkamp, *Electrochim. Acta* **2010**, *55*, 1978–1984.
- [9] W. Hu, S. Chen, Q. Xia, *Int. J. Hydrogen Energy* **2014**, *39*, 6967–6976.
- [10] C. Hao, H. Lv, C. Mi, Y. Song, J. Ma, *ACS Sustainable Chem. Eng.* **2016**, *4*, 746–756.
- [11] H.-S. Oh, H. N. Nong, T. Reier, A. Bergmann, M. Gliech, J. Ferreira de Araújo, E. Willinger, R. Schlögl, D. Teschner, P. Strasser, *J. Am. Chem. Soc.* **2016**, *138*, 12552–12563.
- [12] C. Hao, H. Lv, Q. Zhao, B. Li, C. Zhang, C. Mi, Y. Song, J. Ma, *Int. J. Hydrogen Energy* **2017**, *42*, 9384–9395.
- [13] C. Massué, V. Pfeifer, X. Huang, J. Noack, A. Tarasov, S. Cap, R. Schlögl, *ChemSusChem* **2017**, *10*, 1943–1957.
- [14] J. Tong, Y. Liu, Q. Peng, W. Hu, Q. Wu, *J. Mater. Sci.* **2017**, *52*, 13427–13443.
- [15] Y. Liu, J. M. Szeifert, J. M. Feckl, B. Mandlmeier, J. Rathousky, O. Hayden, D. Fattakhova-Rohlfing, T. Bein, *ACS Nano* **2010**, *4*, 5373–5381.
- [16] K.-W. Park, K.-S. Seol, *Electrochem. Commun.* **2007**, *9*, 2256–2260.
- [17] Y. Shao, J. Liu, Y. Wang, Y. Lin, *J. Mater. Chem.* **2009**, *19*, 46–59.

- [18] I. Khalakhan, R. Fiala, J. Lavková, P. Kúš, A. Ostroverkh, M. Václavů, M. Vorokhta, I. Matolínová, V. Matolín, *Fuel Cells* **2016**, *16*, 652–655.
- [19] S. Maass, F. Finsterwalder, G. Frank, R. Hartmann, C. Merten, *J. Power Sources* **2008**, *176*, 444–451.
- [20] X. Deng, L. Mammen, H.-J. Butt, D. Vollmer, *Science* **2012**, *335*, 67–70.
- [21] S. Liu, M. Sakai, B. Liu, C. Terashima, K. Nakata, A. Fujishima, *RSC Adv.* **2013**, *3*, 22825–22829.
- [22] K. Senevirathne, V. Neburchilov, V. Alzate, R. Baker, R. Neagu, J. Zhang, S. Campbell, S. Ye, *J. Power Sources* **2012**, *220*, 1–9.
- [23] Y. Cao, S. Deng, Q. Hu, Q. Zhong, Q.-P. Luo, L. Yuan, J. Zhou, *RSC Adv.* **2015**, *5*, 85969–85973.
- [24] A. E. Kandjani, Y. M. Sabri, M. R. Field, V. E. Coyle, R. Smith, S. K. Bhargava, *Chem. Mater.* **2016**, *28*, 7919–7927.
- [25] S. Lu, H. Wang, J. Zhou, X. Wu, W. Qin, *Nanoscale* **2017**, *9*, 1184–1192.
- [26] M. Putkonen, P. Heikkilä, A. T. Pasanen, H. Rautkoski, L. Svärd, P. Simell, M. Vähä-Nissi, T. Sajavaara, *J. Vac. Sci. Tech. A* **2017**, *36*, 01A102.
- [27] K. Kinoshita, *Carbon - Electrochemical and Physicochemical Properties*, 1st ed., John Wiley and Sons, Inc., **1988**.
- [28] V. Pore, M. Ritala, M. Leskelä, T. Saukkonen, M. Järn, *Cryst. Growth Des.* **2009**, *9*, 2974–2978.
- [29] J. Arbiol, J. Cerdà, G. Dezanneau, A. Cirera, F. Peiró, A. Cornet, J. R. Morante, *J. Appl. Phys.* **2002**, *92*, 853–861.
- [30] Y. Furubayashi, T. Hitosugi, Y. Yamamoto, K. Inaba, G. Kinoda, Y. Hirose, T. Shimada, T. Hasegawa, *Appl. Phys. Lett.* **2005**, *86*, 252101.
- [31] J.-P. Niemelä, H. Yamauchi, M. Karppinen, *Thin Solid Films* **2014**, *551*, 19–22.
- [32] J.-P. Niemelä, Y. Hirose, T. Hasegawa, M. Karppinen, *Appl. Phys. Lett.* **2015**, *106*, 042101.
- [33] S. Choi, Y.-K. Cha, B.-S. Seo, S. Park, J.-H. Park, S. Shin, K. S. Seol, J.-B. Park, Y.-S. Jung, Y. Park, Y. Park, I.-K. Yoo, S.-H. Choi, *J. Phys. D: Appl. Phys.* **2007**, *40*, 1426.
- [34] S.-W. Kim, S.-H. Kwon, D.-K. Kwak, S.-W. Kang, *J. Appl. Phys.* **2008**, *103*, 023517.
- [35] J. Hämäläinen, M. Kemell, F. Munnik, U. Kreissig, M. Ritala, M. Leskelä, *Chem. Mater.* **2008**, *20*, 2903–2907.
- [36] K. Knapas, M. Ritala, *Chem. Mater.* **2011**, *23*, 2766–2771.
- [37] J. Hämäläinen, T. Hatanpää, E. Puukilainen, T. Sajavaara, M. Ritala, M. Leskelä, *J. Mater. Chem.* **2011**, *21*, 16488–16493.
- [38] J. Hämäläinen, M. Ritala, M. Leskelä, *Chem. Mater.* **2014**, *26*, 786–801.

- [39] M. Mattinen, J. Hämäläinen, F. Gao, P. Jalkanen, K. Mizohata, J. Räisänen, R. L. Puurunen, M. Ritala, M. Leskelä, *Langmuir* **2016**, *32*, 10559–10569.
- [40] S. Kohli, D. Niles, C. D. Rithner, P. K. Dorhout, *Adv. X-Ray Anal.* **2002**, *45*, 352–358.
- [41] S. J. Freakley, J. Ruiz-Esquiús, D. J. Morgan, *Surf. Interface Anal.* **2017**, *49*, 794–799.
- [42] A. V. Korotcov, Y.-S. Huang, K.-K. Tiong, D.-S. Tsai, *J. Raman Spectrosc.* **2007**, *38*, 737–749.
- [43] L. Stagi, C. M. Carbonaro, R. Corpino, D. Chiriu, P. C. Ricci, *Phys. Status Solidi B* **2015**, *252*, 124–129.
- [44] C. C. L. McCrory, S. Jung, J. C. Peters, T. F. Jaramillo, *J. Am. Chem. Soc.* **2013**, *135*, 16977–16987.
- [45] S. Zhao, H. Yu, R. Maric, N. Danilovic, C. B. Capuano, K. E. Ayers, W. E. Mustain, *J. Electrochem. Soc.* **2015**, *162*, F1292–F1298.
- [46] S. Cherevko, S. Geiger, O. Kasian, N. Kulyk, J.-P. Grote, A. Savan, B. R. Shrestha, S. Merzlikin, B. Breitbach, A. Ludwig, K. J. J. Mayrhofer, *Catal. Today* **2016**, *262*, 170–180.
- [47] J. Maula, *Chin. Opt. Lett* **2010**, *8*, 53–58.

## 3.6 Appendix

### Carbon Soot Template



**Figure 3.6:** Photograph of as-deposited carbon soot on soda-lime glass (SLG).

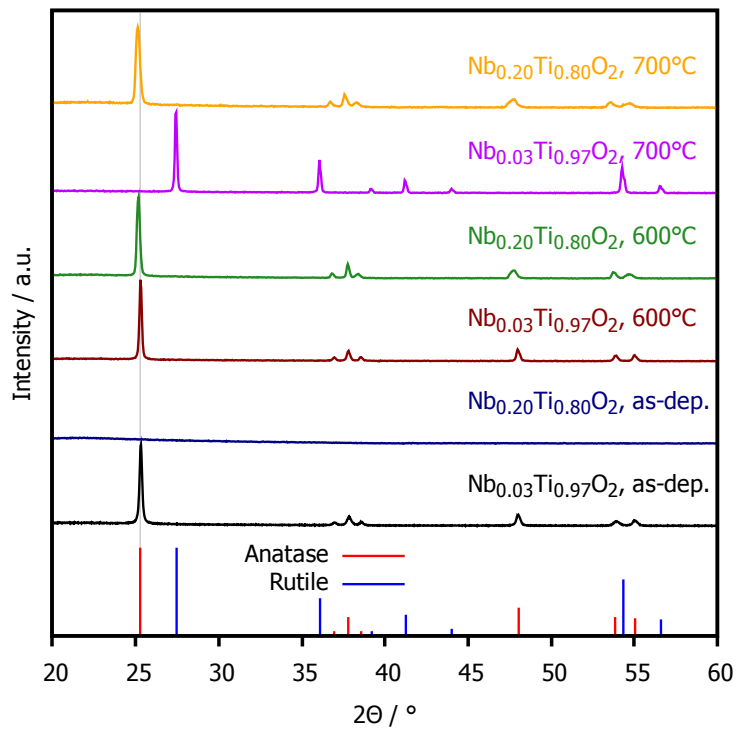
### Carbon NTO Scaffolds

**Table 3.1:** Compositions of NTO prepared for this study. In the cycle sequence column, Ti represents one  $\text{TiO}_2$  ALD cycle and Nb one  $\text{NbO}_x$  ALD cycle.

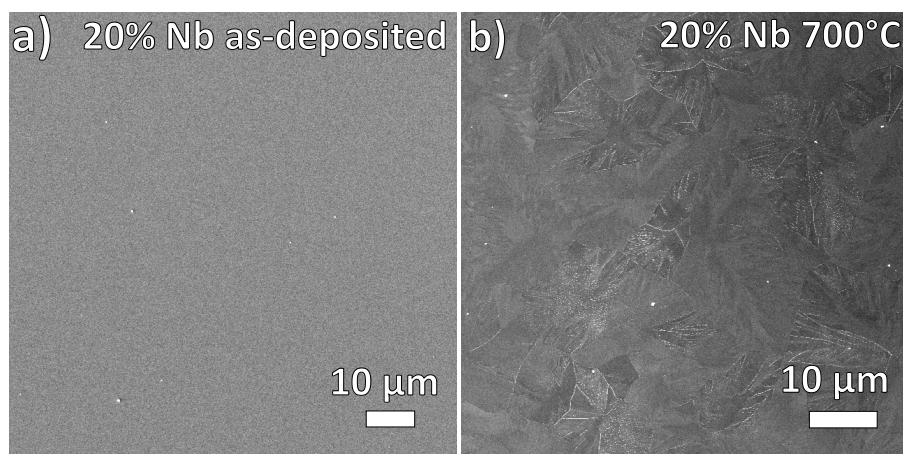
Theor. composition	ALD cycle sequence	composition (EDX)
Ti:0.97; Nb:0.03	(20 x Ti + 1 x Nb) x n	Ti:0.97; Nb:0.03
Ti:0.91; Nb:0.09	(14 x Ti + 1 x Nb) x n	Ti:0.90; Nb:0.10
Ti:0.82; Nb:0.18	(6 x Ti + 1 x Nb) x n	Ti:0.80; Nb:0.20
Ti:0.75; Nb:0.25	(4 x Ti + 1 x Nb) x n	Ti:0.71; Nb:0.29

**Table 3.2:** Crystallite sizes of carbon-templated NTO films calculated using the Scherrer equation.

composition (EDX)	cr. size (as-dep.) [nm]	cr. size (600 °C) [nm]	cr. size (700 °C) [nm]
$\text{Ti}_{0.97}\text{Nb}_{0.03}\text{O}_2$	46	50	56 (rutile)
$\text{Ti}_{0.80}\text{Nb}_{0.20}\text{O}_2$	amorphous	38	29

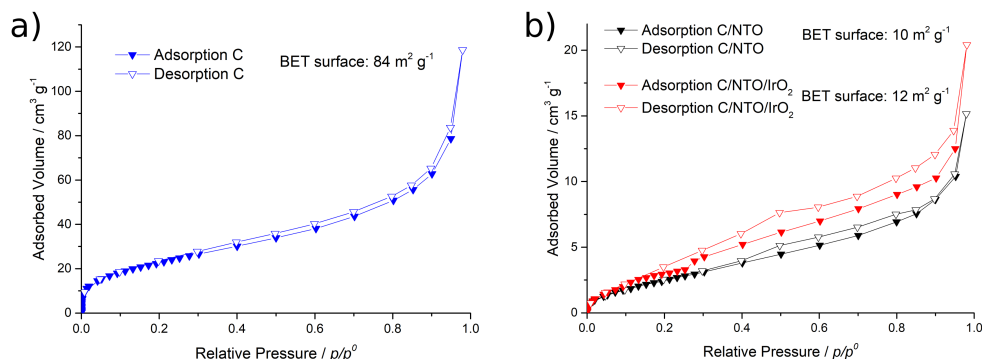


**Figure 3.7:** X-ray diffractograms of NTO-coated carbon soot samples on fused silica. The data have been normalized and offset for visual clarity.



**Figure 3.8:** Top-view SEM images of a compact as-deposited NTO layer (≈80 nm, 20 % Nb) on fused silica (a). The same layer after annealing at 700 °C (b).

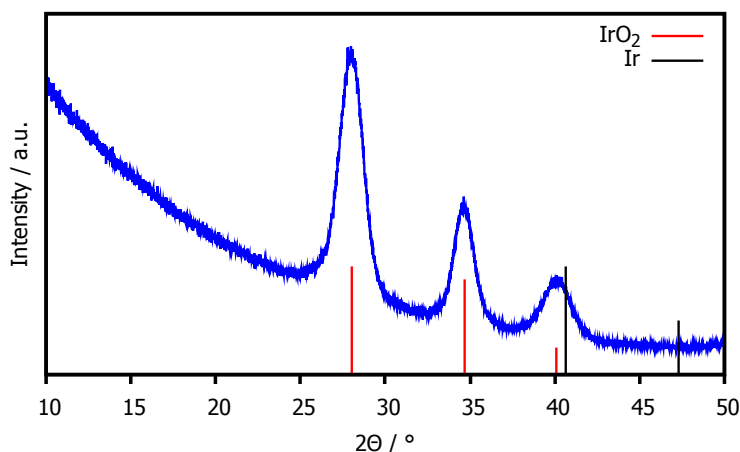
## Nitrogen sorption



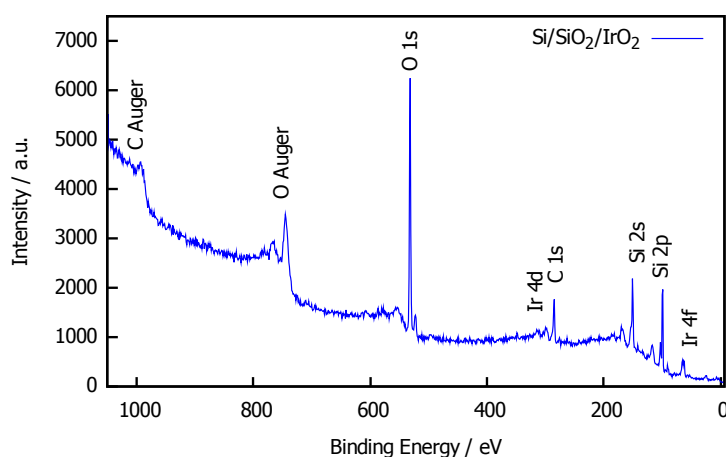
**Figure 3.9:** Nitrogen sorption isotherms of carbon soot (a), C/NTO and C/NTO/IrO<sub>2</sub> (b) powder samples measured at 77 K.

Figure 3.9 shows the nitrogen sorption isotherms recorded for pure carbon soot, NTO on carbon soot and iridium oxide on the C/NTO scaffold. The decrease of surface area per weight can be attributed to the enhanced mass of niobium-doped titanium oxide in comparison to pure carbon soot. The type II isotherm indicates a nonporous material with some textural porosity for the three different materials. Sorption data were collected on a Quantachrome Autosorb 1 at 77 K in a pressure range from  $p/p_0 = 0.001$  to 0.98. The sample was heated prior to the measurement for 24 h at 120 °C under vacuum. The BET model was applied between 0.05 and 0.2  $p/p_0$ .

### Further Characterization of ALD IrO<sub>2</sub>



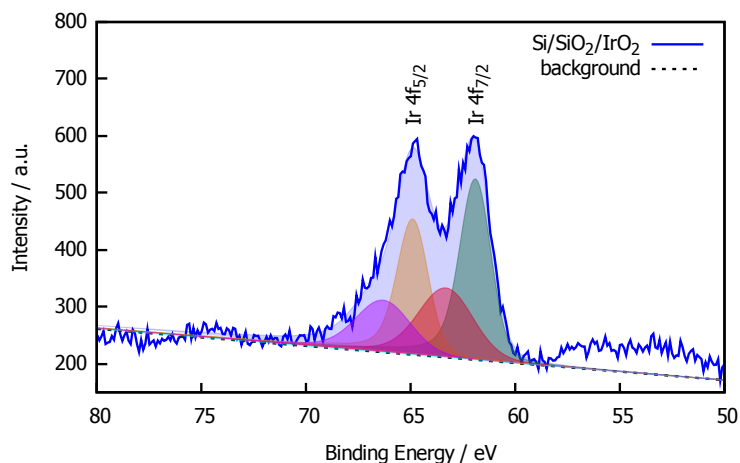
**Figure 3.10:** Grazing incidence XRD pattern of an  $\approx 10$  nm ALD IrO<sub>2</sub> film on oxide-terminated Si (100).



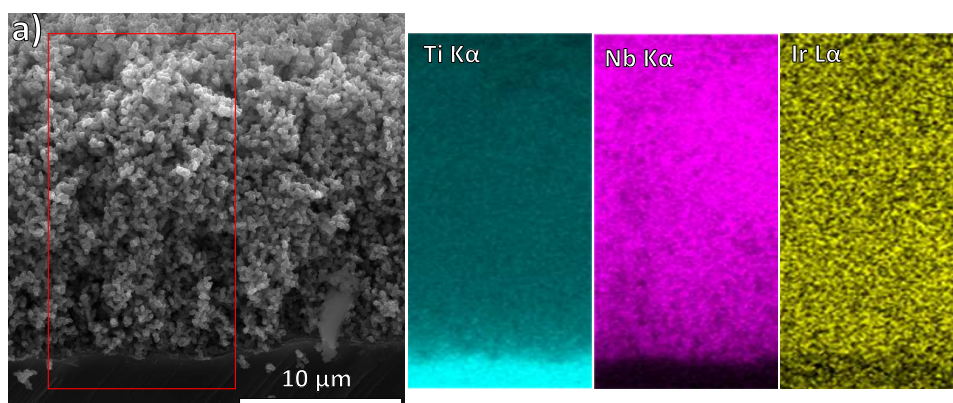
**Figure 3.11:** Survey XPS spectrum, recorded from an  $\approx 1$  nm ALD IrO<sub>2</sub> layer on oxide-terminated Si.

Figure 3.11 shows a survey X-ray photoelectron spectrum of a  $\leq 1$  nm thick ALD IrO<sub>2</sub> layer on oxide-terminated silicon. The strong signals are the O 1s, C 1s, Si 2s, Si 2p and Ir 4f lines. The presence of adventitious carbon is a result of the sample transfer in air from the ALD to the XPS chamber. The strong Si signals signify that either the IrO<sub>2</sub> film is thin enough for photoelectrons from the underlying Si and SiO<sub>2</sub> to pass through it or that it is discontinuous. A detail XP spectrum of the Ir 4f region is shown in Figure 3.12. The Ir 4f<sub>7/2</sub> and Ir 4f<sub>5/2</sub> signals are centered on binding energies of 61.9 and 64.9 eV, respectively, which is in good agreement with reported values for anhydrous IrO<sub>2</sub>.<sup>[1]</sup>

No peak or shoulder is visible at 60.8 eV, which is the reported Ir 4f<sub>7/2</sub> binding energy of metallic Ir. The Ir 4f signal was fitted using four components as reported for IrO<sub>2</sub> and good fits were obtained without an added metallic component.<sup>[1]</sup> From these results we conclude that the ALD process yields films in which the iridium is exclusively present as iridium(IV) oxide.



**Figure 3.12:** Detail XPS spectrum of the Ir 4f signal region, recorded from an approximately 1 nm thick ALD IrO<sub>2</sub> layer on oxide-terminated Si. Fitting parameters according to ref [1].



**Figure 3.13:** Cross-sectional SEM image of a Ti/C/NTO/IrO<sub>2</sub> electrode with EDX element distribution maps of Ti, Nb and Ir.

## Electrochemical Characterization

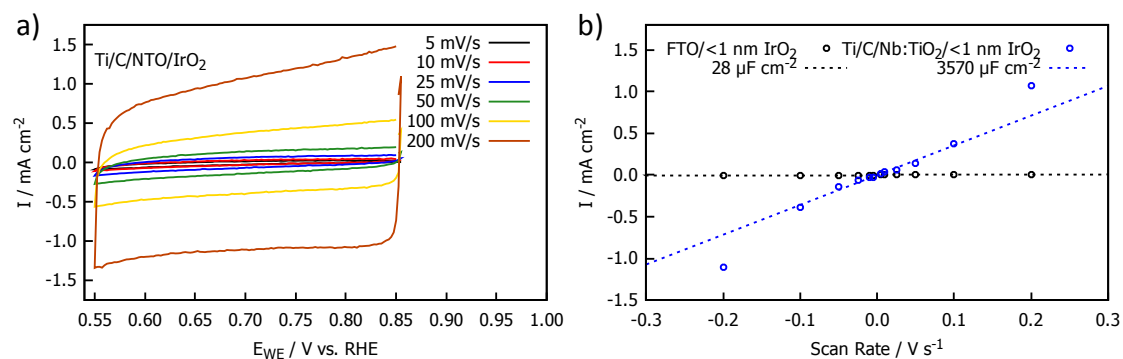


**Figure 3.14:** Cyclic voltammograms of a Ti/C/NTO/IrO<sub>2</sub> electrode at various scan speeds (a). Capacitive currents extracted from the CV scans in (a), compared to an FTO/IrO<sub>2</sub> electrode (b).

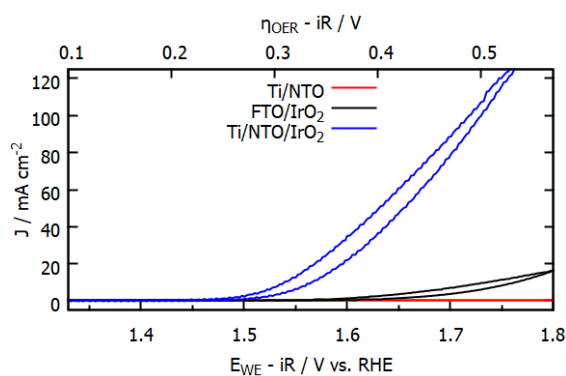


**Figure 3.15:** Uncorrected cyclic voltammograms (2<sup>nd</sup> cycle each) of Ti/C/NTO/IrO<sub>2</sub>, Ti/C/NTO and FTO/IrO<sub>2</sub> electrodes recorded in 0.5 M H<sub>2</sub>SO<sub>4</sub> at 20 mV s<sup>-1</sup>.

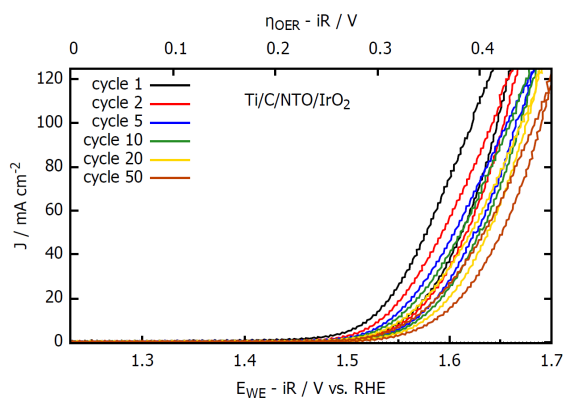


**Figure 3.16:** Cyclic voltammograms of a Ti/C/NTO/IrO<sub>2</sub> electrode at 20 mV s<sup>-1</sup>.

---

## Post-mortem Analysis

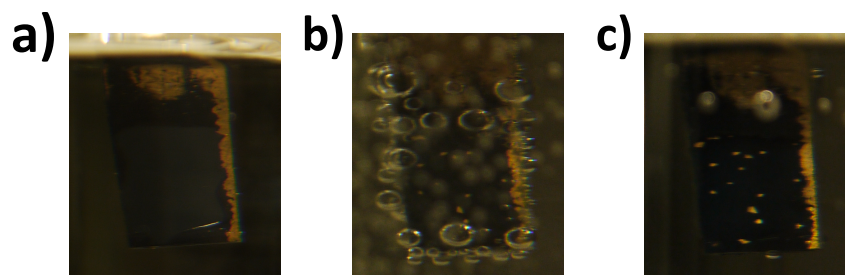


**Figure 3.17:** Photographs of a Ti/C/NTO/IrO<sub>2</sub> electrode in the electrolyte before (a), during (b) and after (c) water oxidation for 12 h at 100 mA cm<sup>-2</sup>.

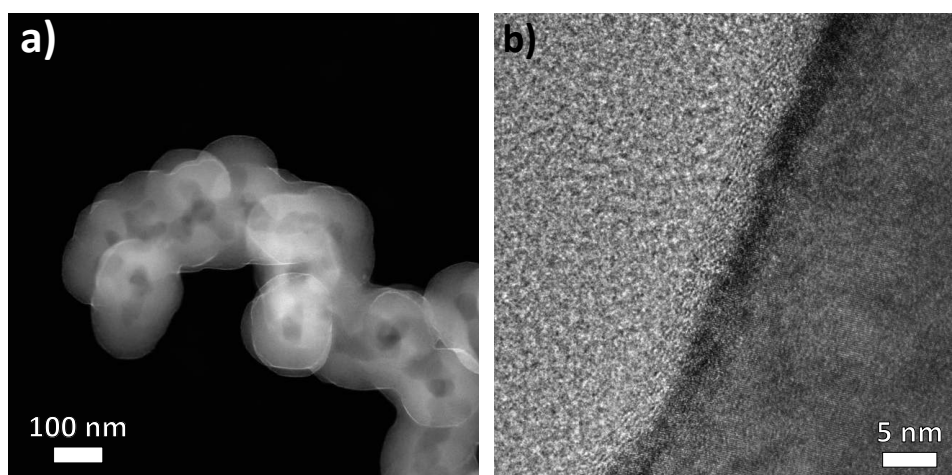


**Figure 3.18:** HAADF-STEM image of the Ti/C/NTO/IrO<sub>2</sub> electrode structure after the 12 h stability test (a). BF-TEM detail image of the structure from (a).

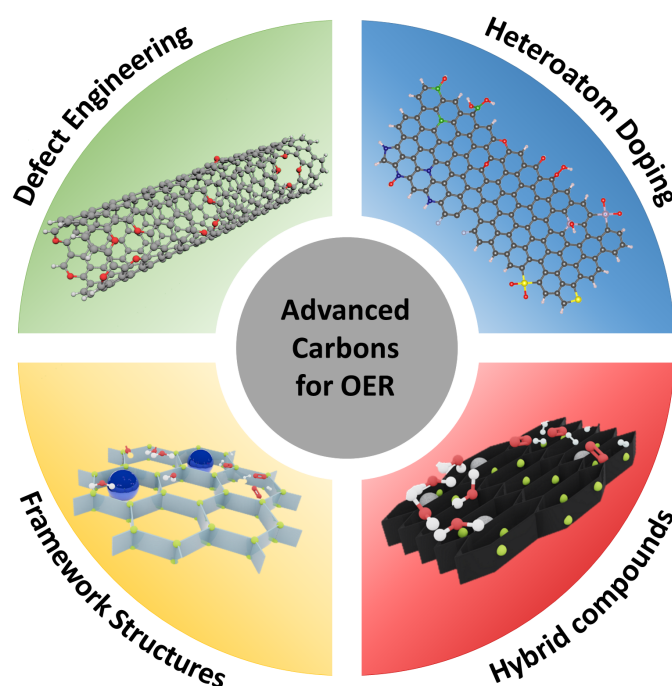
## References

- [1] S. J. Freakley, J. Ruiz-Esquius, D. J. Morgan, *Surf. Interface Anal.* **2017**, *49*, 794–799.

# 4 Carbonaceous Oxygen Evolution Reaction Catalysts: From Defect and Doping-Induced Activity over Hybrid Compounds to Ordered Framework Structures

This chapter is based on the following publication:

Florian Zoller, Sebastian Häring, Daniel Böhm, Jan Luxa, Zdeněk Sofer,\* and Dina Fattakhova-Rohlfing\*, *Small*, 2021, 2007484.



Sebastian Häring was responsible for summary and discussion on metal-free and heteroatom-doped carbon composite materials and contributed to parts of the section on metal (metal oxide)/ carbon hybrids.

## Abstract

Oxygen evolution reaction (OER) is expected to be of great importance for the future energy conversion and storage in form of hydrogen by water electrolysis. Besides the traditional noble-metal or transition metal oxidebased catalysts, carbonaceous electrocatalysts are of great interest due to their huge structural and compositional variety and unrestricted abundance. This review provides a summary of recent advances in the field of carbonbased OER catalysts ranging from "pure" or unintentionally doped carbon allotropes over heteroatom-doped carbonaceous materials and carbon/ transition metal compounds to metal oxide composites where the role of carbon is mainly assigned to be a conductive support. Furthermore, the review discusses the recent developments in the field of ordered carbon framework structures (metal organic framework and covalent organic framework structures) that potentially allow a rational design of heteroatomdoped 3D porous structures with defined composition and spatial arrangement of doping atoms to deepen the understanding on the OER mechanism on carbonaceous structures in the future. Besides introducing the structural and compositional origin of electrochemical activity, the review discusses the mechanism of the catalytic activity of carbonaceous materials, their stability under OER conditions, and potential synergistic effects in combination with metal (or metal oxide) co-catalysts.

## 4.1 Introduction: Catalytic Activity of Pure Carbon Allotropes and Necessity of Heteroatom Doping or Surface Modification

Driven by the awareness of the global warming potential of a large-scale green-house gas emission from the combustion of fossil fuels as well as economic considerations, enormous investments in renewable energy sources were made in the last decades.<sup>[1,2]</sup> Generation of "green" hydrogen by water electrolysis is thereby regarded to gain importance in the upcoming years to convert and store intermittent renewable electrical energy in form of chemical energy.<sup>[3]</sup> Hydrogen as a versatile energy carrier can thereby directly be used as fuel or employed in industrial processes replacing petrochemically generated hydrogen or even hydrocarbons (if combined with CO<sub>2</sub> electrolysis) allowing for a decarbonization in chemical industry (also known as "Power-to-X" concept).<sup>[3,4]</sup> Prerequisite for an efficient conversion of electrical energy by water splitting is the catalysis of both half-reactions, namely, the hydrogen evolution reaction (HER:  $\text{H}^+ + \text{e}^- \rightarrow \frac{1}{2} \text{H}_2$  (acidic),  $2 \text{H}_2\text{O} + 2 \text{e}^- \rightarrow \text{H}_2 + 2 \text{OH}^-$  (alkaline)) and the oxygen evolution reaction (OER:  $2 \text{H}_2\text{O} \rightarrow \text{O}_2 + 4 \text{H}^+ + 4 \text{e}^-$  (acidic),  $4 \text{OH}^- \rightarrow \text{O}_2 + 2 \text{H}_2\text{O} + 4 \text{e}^-$  (alkaline)). There is a considerable research interest in the development of novel, highly active catalysts for the OER at the anode to increase the overall efficiency of electrolysis. This is explained by the fact that the OER requires a relatively high overpotential due to a rather complex four electron and proton-coupled pH-dependent reaction mechanism.<sup>[5]</sup> The relatively recent but already advanced acidic proton exchange membrane (PEM)

electrolysis technology, which enjoys an upswing in the industrial and research interest, relies on scarce noble metal OER catalyst iridium and its oxide and is therefore limited regarding a large-scale application.<sup>[6]</sup> Well-established electrolysis under alkaline conditions offers the advantage of a possible use of earth-abundant, nonnoble transition metal oxides (TMOs) with a special focus on the highly OER active Fe-doped Ni(OH)<sub>2</sub> as well as cobalt-based electrocatalysts.<sup>[7,8]</sup> One drawback of alkaline OER employing conventional TMO electrodes is however the partially low intrinsic conductivity of OER active "nonnoble metal" TMOs (e.g., NiO, Co<sub>3</sub>O<sub>4</sub>) that are mainly semiconductors or insulators, and therefore allowing only a limited possible current density due to high voltage losses in the electrolysis cell.<sup>[9,10]</sup>

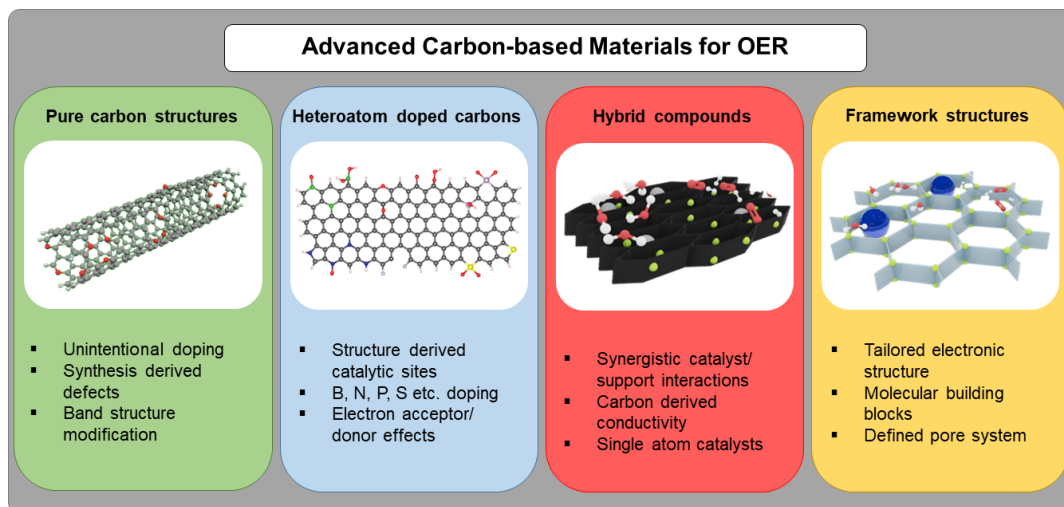
Carbon-based OER catalysts offer distinct advantages over pure metal and metal oxide-based OER catalysts: they offer an unprecedented structural variety and, in combination with heteroatoms, also an unrestricted compositional diversity and a good to excellent electrical conductivity.<sup>[11]</sup> From the perspective of electrode design, carbon offers a light weight combined with a high mechanical flexibility. This combination increases the electrode stability under oxygen gas evolution (bubble formation), which can otherwise deteriorate rigid, nonflexible oxide structures under high current densities.<sup>[12]</sup> From an ecological and economical perspective, virtually unrestricted availability of carbon and inexpensive synthesis are beneficial for a potential large-scale application of electrolysis technology.

In the following work, we want to introduce the structural and compositional origin of the electrocatalytic activity of various types of pure, heteroatom-doped, and hybrid carbon-based OER catalysts to give an overview of the recent developments in this field of research.

At this point, we want to refer to series of excellent review articles published in the recent years introducing various aspects of carbon-based electrocatalysis as well as OER catalysis in particular.

The first highly recommended overview articles to be mentioned were presented by Wu et al. in 2016 on carbon nanocomposite catalyst for oxygen reduction reaction (ORR) and OER followed by a work from Zhang et al. in 2017 on carbon-based electrocatalysts for the hydrogen and OER.<sup>[13,14]</sup> More recent general review articles covering the topic of carbon-based electrocatalysts and to some extent OER catalysis include papers by Lai et al. and Deng et al. on 3D porous carbon electrodes for electrocatalytic applications and electrochemical energy storage, as well as a work from Younis et al. discussing noble metal-free 2D carbon-based electrocatalysts for water splitting.<sup>[15-17]</sup>

A more specific but also highly recommended review article from Zhu et al. from 2017 discusses perovskite/carbon composite catalysts concerning their application in oxygen electrocatalysis and thereby presents an overview over the different types of interactions of carbon and metal oxides affecting the OER/ ORR activity.<sup>[18]</sup> Finally, a review by Chen et al. from 2018 should be mentioned covering the topic of nanocarbon/oxide composites as bifunctional catalysts in alkaline fuel cell applications.<sup>[19]</sup>



**Scheme 4.1:** Schematic presentation of the different classes of advanced carbonaceous materials and composites within this review

Our review sets its focus first on a critical discussion of the origin of OER activity in pure and heteroatom-doped carbon structures as well as highly active transition metal (metal oxide)/ carbon composite electrodes with a relation to the applied synthesis route and resulting nanomorphologies (Scheme 4.1). In this context, most recent and promising examples of the individual classes of carbon-based OER catalysts are discussed in more detail. Additionally, the influence of heteroatoms and dopants on the structure and OER activity is critically assessed. Besides updating the literature on the most prominent carbon-based electrocatalysts, our work adds an overview of the recently introduced class of ordered carbon framework structures for electrocatalysis that have not been discussed in the earlier reviews mentioned above. Special focus is drawn to the relatively recent developments in the field of ordered 3D carbon (covalent organic framework (COF)) and carbon/ metal (metal organic framework (MOF)) framework structures for OER catalysis. By offering various advantages over classical nonordered carbons, 2D and 3D heteroatom-doped carbon structures with a precisely controllable porosity, composition and local geometry of heteroatoms, and/or metal active sites are envisioned to allow the synthesis of carbon-based OER catalysts with even further increased electrocatalytic activity. Finally, an often neglected discussion about the corrosion stability of carbonaceous OER catalysts completes this literature overview.

#### 4.1.1 OER Activity of Undoped Carbon Structures and Necessity of Heteroatom Doping

The overall efficiency of an OER catalyst is determined by three independent material properties, namely, the number of catalytically active sites, the intrinsic activity of the sites, and the electrical conductivity of the electrode (Figure 4.1).<sup>[20]</sup>

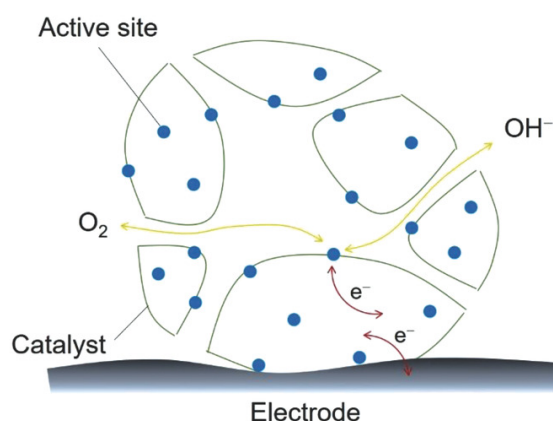


**Figure 4.1:** Schematic illustration of the required features for OER catalysts. Reproduced with permission.<sup>[21]</sup> Copyright 2018, Wiley-VCH.

The electrical conductivity of carbonaceous structures is generally moderate to high and thus is typically not regarded as the limiting factor. The conductivity of graphene-based compounds greatly depends on their composition including the type of doping and the doping level as well as the type and the amount of defects, which are very much affected by the synthesis method.

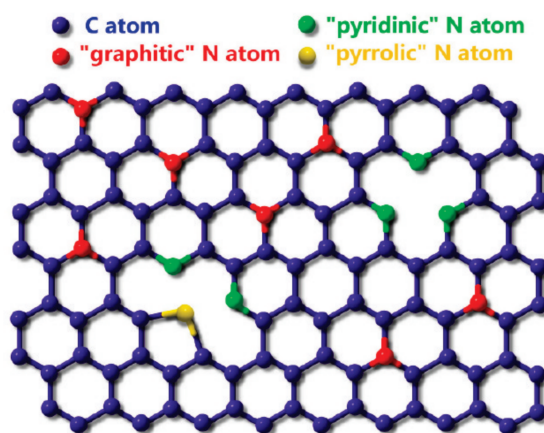


**Figure 4.2:** Schematic illustration of varying local environment of doped nitrogen in graphene. Reproduced with permission.<sup>[22]</sup> Copyright 2009, American Chemical Society.

Doping with nitrogen or other foreign atoms can follow via a substitution of carbon in the graphitic structure with the formation of so-called "graphitic" N in case of nitrogen, Figure 4.2, or cause topological defects which act as scattering centers in the graphene lattice (so-called "pyridinic" N and "pyrrolic" N in case of nitrogen, Figure 4.2). As a consequence of the distorted lattice structure, a reduction of density of states (DOS) near the Fermi energy is expected. This opens a gap in the band structure of the zero-gap semiconductor of pristine graphene, which theoretically lowers the con-

ductivity in the doped homolog.<sup>[22]</sup> A work on chemical vapor deposition (CVD) synthesized graphene by Wei et al. showed a reduction of the mobility from 300–1200 to 200–450 cm<sup>2</sup> V<sup>-1</sup> s<sup>-1</sup> for the N-doped graphene over the undoped homolog.<sup>[22]</sup> Other carbon allotropes investigated as OER catalysts include carbon nanotubes (CNTs) which theoretically exhibit intrinsic mobilities exceeding 106 cm<sup>2</sup> V<sup>-1</sup> s<sup>-1</sup> and measured mobilities of 2–8 × 10<sup>4</sup> cm<sup>2</sup> V<sup>-1</sup> s<sup>-1</sup> for undoped nanotubes but also strongly depend on the amount of defects caused by the synthesis method and dopants.<sup>[23,24]</sup> Fragments (exfoliated graphene nanoribbons) or graphene oxide thereby show lower mobilities of only up to ≈200 cm<sup>2</sup> V<sup>-1</sup> s<sup>-1</sup>.<sup>[22]</sup>

There is however a conflict between the conductivity and the electrocatalytic activity of carbon structures. It is widely accepted that pristine, undoped sp<sup>2</sup> hybridized carbon exhibits only poor intrinsic OER activity, which is ascribed to the symmetric distribution of valence and conduction band.<sup>[25,26]</sup> These are rather the defects introduced by synthetic methods or heteroatom doping that create the OER active sites. This explains the intensive research activity on heteroatom (N, S, P, B, etc.) doped carbon structures for OER catalysis in the recent years, which is further discussed with selected examples in Section 3. The origin of catalytic activity is thereby assigned to lattice defects introduced by heteroatoms as schematically depicted in Figure 4.9. The lattice defects can i) act as active sites on their own, ii) tune the electronic structure of the surrounding carbon phase, and/or iii) modulate the hydrogen binding energy.<sup>[16,20,22]</sup> For N-doped graphene, a modulation of the electronic structure of graphene in the vicinity of dopants resulting in catalytically active carbon sites is explained by a conjugation between the nitrogen lone-pair electrons and the graphene π-system.<sup>[27]</sup> More specifically, the more electronegative nitrogen withdraws electron density from the neighboring carbon atoms to transform them into OER active sites, but does not show a favorable OER activity as active site itself.<sup>[27]</sup>

The simplest case of nitrogen doping is given by a carbonto-nitrogen substitution resulting in an isostructural graphitic nitrogen-doped single-walled carbon nanotube (SWCNT) or graphene structure. Further possibilities include pyridinic N with a present vacancy, and a pyrrolic N. The latter is either accompanied by a vacancy or obtained by a Stone–Wales rotational defect, and can be combined with protonation or oxidation.<sup>[28]</sup>

The multistep OER mechanism on doped carbon species is not fully described on an atomistic level in detail yet. However, significant progress has been made in elucidating potential active sites, the potential-determining step (PDS), and the spatial relation to doping atoms and defects in N-doped graphene or CNTs by theoretical methods based on the assumption of a four-step single-site water nucleophilic attack mechanism.<sup>[27,28]</sup>

In a recent work by Murdachaew and Laasonen, the active sites in undoped and N-doped SWCNTs and graphene with doping concentrations of around 1 at% were theoretically examined by density functional theory (DFT) methods. The authors compared the active sites originating from different lattice defects (atomic substitutions, vacancies, and Stone–Wales rotations) and different nitrogen functionalities (graphitic, oxidized, pyridinic, and Stone–Wales pyrrolic nitrogen systems) regarding their differ-

ence in binding energy of adsorption intermediates ( $\Delta G^*O - \Delta G^*OH$ ) of the PDS of the OER mechanism to calculate respective overpotentials as depicted in Figure 4.3 with their corresponding structures.<sup>[28]</sup>

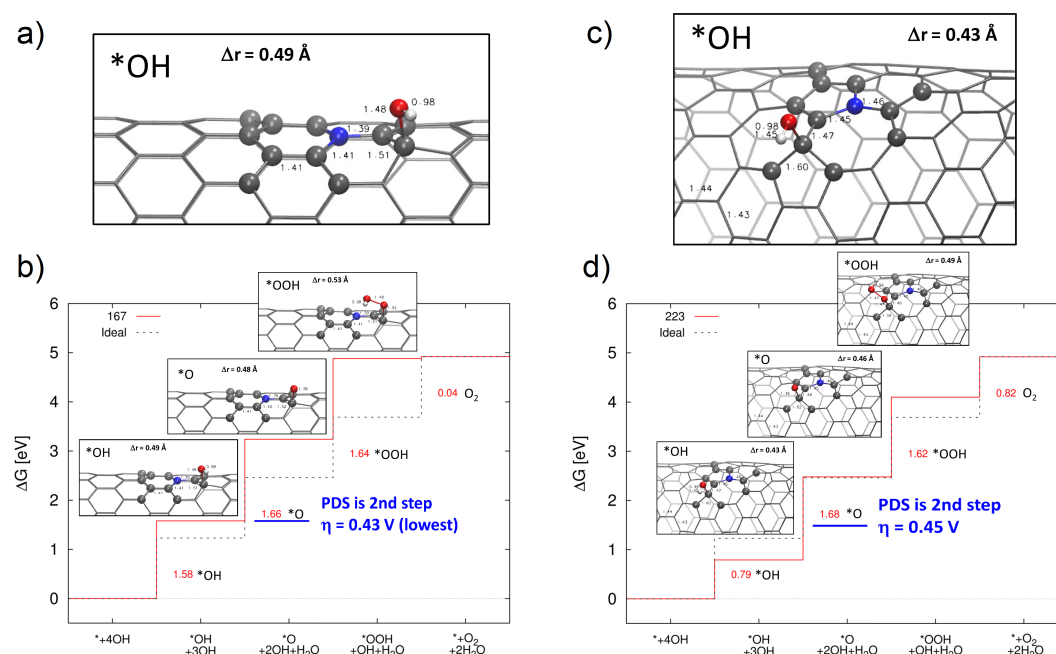


**Figure 4.3:** Calculated OER free energy step diagram (red line) for the b) graphitic N1-SWNT and d) Stone-Wales pyrrolic N1b-SWNT system. The dotted black line shows for comparison the step diagram for the ideal case (step height 1.23 eV). Panels (a) and (c) as well as the insets show the structures and some interatomic distances of the \*OH (panels (a) and (c)), \*O, and \*OOH intermediates, and the  $\Delta r$  values are the radial displacements of the underlying C atoms upon adsorption of the intermediate. The PDS and the corresponding overpotential  $\eta_{\text{OER}}$  are also indicated. Reproduced (adapted) with permission.<sup>[28]</sup> Copyright 2018, American Chemical Society. Original article direct link: <https://pubs.acs.org/doi/10.1021/acs.jpcc.8b08519>. Permissions related to the material excerpted should be directed to the ACS.

Initial step in the assumed OER mechanism, which is also widely accepted for transition metal (metal oxide) active sites, is the binding of an \*OH adsorption intermediate at the partially negative charged carbon atom. In a second step, an \*O intermediate is formed by a proton-coupled electron transfer reaction, followed by the formation of a peroxide (\*OOH) intermediate as third step. The second and the third steps are both regarded as possible PDS or rate-determining step of the overall reaction (indicated in Figure 4.3b, d with corresponding overpotential). Finally, the reaction cycle is completed by the fourth step corresponding to the release of one oxygen molecule and the regeneration of the carbon active site.

It could be further shown by DFT methods that the carbon active sites also follow the so-called scaling relation. This relation, which was introduced initially for isolated

or noncooperative active sites on transition metals and metal oxides, describes a linear dependency between the absorption energies of intermediates (\*OH, \*O, and \*OOH) that does not allow for an independent optimization of the individual reaction steps by modification of the active site.<sup>[28,29]</sup>

Besides nitrogen-doped carbon, a variety of single and multiheteroatom doping experiments were conducted to enhance the overall OER activity. The overview of heteroatom doping with some selected examples is discussed in Section 3.

Beyond nitrogen, also other nonmetal heteroatoms such as O, B, P, or S can be introduced in sp<sup>2</sup> hybridized carbon structures to alter the electronic structure of surrounding carbon and thereby tune the electrocatalytic properties. Selected examples that show an improved OER performance include S-doped CNT-graphene nanolobes or N and O co-doped carbon hydrogel films.<sup>[30,31]</sup> Codoping carbon with a second or third heteroatom can thereby further enhance the OER activity due to synergistic effects between the dopants and due to doping-induced defects.<sup>[25]</sup>

The synergistic effect of N and P co-doping was investigated by Zhu et al. on a porous 3D carbon nanofiber hybrid material. By DFT calculations on pristine, N-doped as well as N and P-codoped carbon, the authors could verify the formation of electroactive sites with optimized charge distribution, which coactivated the neighboring carbon atoms (Figure 4.4a) via charge transfer between the carbon and the heteroatoms.<sup>[32]</sup> Results on the calculated overpotentials versus differences in the adsorption energies of OER intermediates, which typically form a "volcano" plot (Figure 4.4b), further confirm a slightly lower required overpotential for the dual doped carbon as compared to the single nitrogen-doped carbon structure. The former is significantly lower than the pristine carbon or even an IrO<sub>2</sub> reference structure. Indication of a synergistic effect of the N, P dualdoped carbon could be further attributed to an increased DOS at the Fermi level as compared to single N-doped or the pristine carbon structure (Figure 4.4c).<sup>[32]</sup>

However, clear reaction mechanisms describing the effects of multiheteroatom-doped carbon OER catalysts are still yet to develop. It is expected that it is not the intrinsic activity alone that is the cause of an enhancement by the co-doping, but mere a combination of several factors including defect density, nanomorphology, and conductivity that leads to an even higher electrocatalytic activity as compared to single doped counterparts.

Vapor-based or wet-chemical synthesis methods that are typically employed for fabrication of doped carbon structures provide limited possibilities for rational design and arrangement of heteroatoms around active site carbon atoms. Furthermore, analysis of the sites is often limited to spectroscopic measurements of ensembles, which further complicates the investigation of the OER active sites on the atomic level required for a detailed understanding of the mechanism. A chance to overcome this issue by the use of carbon-based framework structures with precisely defined atomic arrangements inherited by molecular building blocks is introduced in Section 5.

### 4.1.2 OER Activity in Carbon/Transition Metal (Metal Oxide) Composites: Conductive Carbon Matrices and Synergistic Effects

Besides the metal-free carbon-based OER catalysts, metal and metal oxide electrodes as well as single atom catalyst bound carbon structures were intensively investigated in the recent years with results presented in Section 4 in detail. At this point, the motivation and benefits of these composite catalysts should be highlighted.

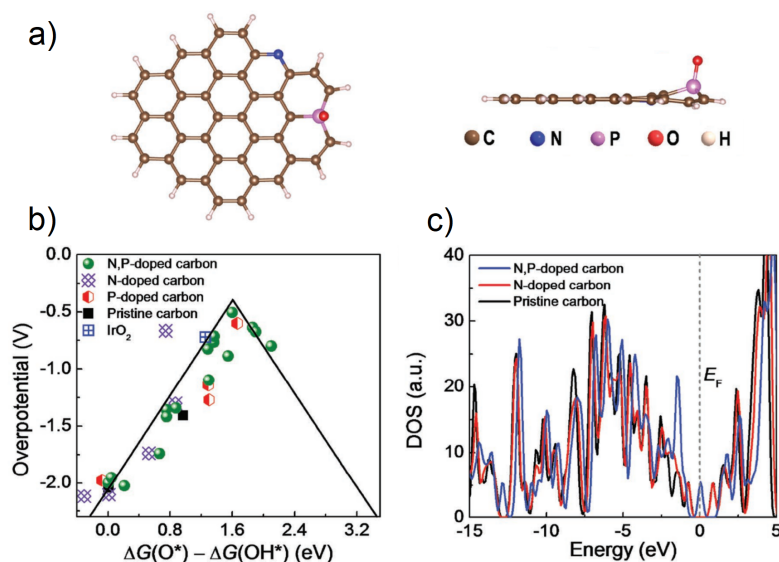


**Figure 4.4:** a) Initial structure of N and P co-doped carbons and the corresponding structures. b) Volcano plots of OER overpotential versus the difference between the adsorption energy of O\* and OH\*, i.e.,  $\Delta G(O^*) - \Delta G(OH^*)$ , for the simulated carbon structures. c) The DOS for the chemically doped carbon structures. Reproduced (adapted) with permission.<sup>[32]</sup> Copyright 2017, Wiley-VCH.

Main advantages of a carbon-based composite electrodes are the high conductivity, structural variety, and robustness as well as flexibility with a possible high surface area and porous morphology enabled by complex continuous 3D structures.<sup>[15,16]</sup>

As discussed in the previous section, heteroatom (N, O, B, S, P, etc.) doping can further modulate the electronic structure leading to a further increased conductivity and formation of carbon active sites, but also modify the interface for an efficient binding of an inorganic phase.<sup>[16]</sup> The combination of nonmetal (focus on nitrogen) and transition metal doping led to the development of Me-N-carbon composites with outstanding OER activity.<sup>[14]</sup> For an introduced Co, N co-doped porous graphene like carbon nanosheet composite, the nonmetal doping with nitrogen is expected to present potential nucleation and anchor sites for Co and Co<sub>3</sub>O<sub>4</sub> nanocrystals.<sup>[33]</sup> According to Zhang et al., it is however not always clear whether the transition metal actually participates in the OER, as a similarly low overpotential has been observed also for only heteroatom-doped carbons.<sup>[14]</sup>

Another broad class of composite compounds is TMOs, nitrides, phosphides, etc.,

supported on various types of (heteroatom-doped) carbon substrates. The catalytic activity of these composites is mainly determined by the intrinsic activity of the typically nanosized inorganic phase. Thus, the catalytic activity of N-doped carbon composites reported by Zhang et al. follows the trend  $\text{FeNi} > \text{CoNi} > \text{FeCo} < \text{Ni} < \text{Fe}$ , which is the same as the activity trend of unsupported first-row transition metal (oxy)hydroxides in alkaline media determined in the group of Boettcher group earlier.<sup>[7,8]</sup> The trend thereby follows the Sabatier principle with an optimum in the adsorption strength of OER reaction intermediates on transition metal and oxide crystal facets, which can be used for the construction of a "volcano" curve of electrocatalytic activity of composite compounds.<sup>[34]</sup>

A synergistic effect of carbon/transition metal (metal oxide) composite catalyst is also reported for the composite class of core-shell structures. The OER transition metal (or metal oxide) active core is covered by a thin carbon shell, which increases the stability against dissolution under operation conditions and prevents agglomeration of small metal or oxide particles, which is a well-known cause for catalyst inactivation. The core structure of transition metal particles as well as their oxides, carbides, nitrides, phosphides, sulfides, or selenides is thereby regarded to affect the electronic structure of the thin carbon shell to increase its OER activity.<sup>[14,35]</sup>

To extend our knowledge about synergistic effects on the OER mechanism of metal-heteroatom-carbon composites, a rational material design and synthesis is required, which gives a precise control over the composition, porosity, and surface functionalization acting as anchor sites for the metal active sites.<sup>[36]</sup> All these requirements can be potentially met by carbon-based framework structures known as COFs and MOF that consist of molecular building blocks and eventually metal ions as coordination sites and linking nodes, respectively. These material classes will be introduced in more detail in Section 5.

#### 4.1.3 Stability of Carbon-Based Electrocatalysts under OER Conditions

The stability of carbon-based OER catalyst is often referred to as insufficient for long-term industrial application in PEM electrolyzer anodes when compared to TMOs catalysts such as  $\text{IrO}_2$ .<sup>[37]</sup> It has to be however kept in mind that also  $\text{IrO}_2$ , the "gold standard" of OER catalysts for PEM electrolysis, undergoes corrosion, albeit at a low rate.<sup>[38]</sup> There are recent studies on carbon corrosion related to the OER catalysis concerning carbon electrodes,<sup>[39,40]</sup> support material,<sup>[41,42]</sup> and hybrid OER catalyst.<sup>[43,44]</sup> Furthermore, the stability of carbonaceous materials was thoroughly investigated regarding the application as ORR catalysts supports in fuel cells.<sup>[45,46]</sup> The major concern using carbonaceous OER catalysts and support materials is thereby an oxidation-driven corrosion process that can lead either to a degradation or inactivation of the catalyst, or a loss of contact to attached metal (or metal oxide) nanoparticles.<sup>[37]</sup>

It is the low thermodynamic stability represented by low standard electrochemical potentials of 0.207 V versus standard hydrogen electrode (SHE) for  $\text{CO}_2$  and 0.518 V versus SHE for CO formation by oxidation, respectively, that presents the challenge

for the application of carbonaceous materials under OER conditions at potentials exceeding 1.23 V versus SHE.<sup>[47]</sup> However, it is the reaction kinetics (corrosion rate) that decides on the durability of the carbonaceous material under certain operation conditions. Thus, for the use of carbonaceous materials as supports in fuel cell electrodes, it should be kept in mind that a typical operation cathode potential of  $\approx 0.9$  V versus SHE significantly exceeds the onset potential of the carbon oxidation reaction. However, even in these thermodynamically unfavorable conditions, the corrosion reaction kinetic is still slow and negligible even for longterm operation. It is mainly the prolonged extended open-circuit potential step, or startup and shutdown cycles with possible reverse current conditions and resulting high potentials, that are reported to lead to a significant carbon corrosion.<sup>[45]</sup>

At even higher potentials required for OER, the carbon oxidation is further accelerated but can still be suppressed. The total anode current is given by the sum of the OER current and the carbon oxidation reaction current. Under constant current conditions with independent and competitive reactions, the overpotential, or more precisely, the decrease in overpotential is mainly determined by the most facile reaction, so that this reaction is responsible for a dominant portion of the overall current. A highly active OER catalyst on a carbon support or a metal-free carbonaceous OER catalyst with low overpotential thereby dominate the overall reaction kinetics, resulting in a low corrosion rate and high faradaic efficiency toward oxygen evolution.<sup>[47,48]</sup>

Experimentally, carbon corrosion was investigated by means of *in-situ* surface-enhanced infrared spectroscopy, which proposes an initial CO<sub>2</sub> formation followed by an ongoing CO release under OER conditions.<sup>[47]</sup> Furthermore, differential electrochemical mass spectroscopy was successfully applied to investigate the reasons for the decreased faradaic efficiency of the OER (93 % at a potential of 1.45 V vs reversible hydrogen electrode (RHE)) for a carbon-supported IrO<sub>x</sub> catalyst, which was attributed to an ongoing carbon oxidation.<sup>[37]</sup> At the same time, there are different examples demonstrating that carbonaceous electrocatalysts can be operated with sufficient stability even at high current densities. Thus, Lee et al. reported a stable operation of a highly OER active IrCoO<sub>x</sub>/C electrocatalyst over 216 h at a current density of 5 mA cm<sup>-2</sup> at a potential between 1.5 and 1.6 V versus RHE.<sup>[42]</sup> After all, this indicates the possibility of a stable intermediate term operation of carbon-based OER catalysts, but also emphasizes the requirement for the development of electrocatalyst with high intrinsic activity.

## 4.2 Undoped and Unintentionally Doped Carbon Structures: From Synthesis to Surface Modifications

### 4.2.1 Synthesis and Catalytic Activity of Low Doping Level Carbon Materials

“Pure,” defect-free carbon materials have almost no appreciable activity toward OER catalysis as shown by various literature reports.<sup>[49–57]</sup> However, their performance can

be drastically improved by introducing (non-) metal dopants like boron,<sup>[52]</sup> nitrogen, oxygen,<sup>[52,53,56,58]</sup> and phosphorous,<sup>[54]</sup> by inducing defects<sup>[53]</sup> or by the formation of hybrid materials.<sup>[49–51,55,59]</sup> The concepts of doping and formation of heterostructures, which are intensively discussed in literature, will be reviewed in Sections 3 and 5.

The publications on nondoped defect-rich carbon materials for OER catalysis are scarce. Thus, Jia et al. reported the OER activity of defective graphene (DG),<sup>[53]</sup> which was prepared from nitrogen-doped graphene by a high temperature pyrolysis strategy. The heat treatment decreased the N content from around 3.7 to 0.7 at% as evidenced by X-ray photoelectron spectroscopy (XPS). The resulting DG possessed a lot of structural defects, like pentagons, heptagons, and octagons that were assembled in different manner inside the graphene network. Linear sweep voltammetry (LSV) clearly demonstrated the beneficial effect of introducing defects or dopants into carbon materials on their electrocatalytic activity, as “pure” graphene has no obvious catalytic activity toward OER. The comparison of doped and defect-rich graphene reveals that the latter has a superior performance with a current density of 10 mA cm<sup>-2</sup> reached at a potential of 1.57 V versus RHE, and a decreased Tafel slope (97 mV dec<sup>-1</sup>) indicating a favorable kinetics. The OER activity is even in the same range as a commercial Ir/C catalyst. Moreover, the DG features also a promising long-term OER stability shown by a 60 h chronopotentiometry measurement at a current density of 5 mA cm<sup>-2</sup> with no obvious change in the catalytic activity. The high OER activity of DG was ascribed by Jia et al. to the large amount of highly catalytic defect atomic sites supported by mechanistic OER pathway calculations.<sup>[53]</sup>

The OER catalytic activity and stability of graphene is also dependent on its structural integrity. The latter is linked to the number of stacked layers as reported by Garcia-Miranda Ferrari et al. who prepared mono-, multi-, and few-layer graphene by CVD.<sup>[60]</sup> The authors have shown that the OER current density of the monolayer and the few-layer graphene suffers drastically decreases upon repeated LSV scans. The reduction in the electrocatalytic activity is accompanied by the destruction of the graphene sheets, which was clearly visible in corresponding Raman maps. The authors have explained the observed degradation by an insufficient structural integrity of graphene on the macroscale, which is not high enough to accommodate the changes in oxidation state during the OER. As another reason, they have suggested the mechanical destruction of the surface of the graphene sheets by frictional forces induced by the collapse of the formed oxygen bubbles (Figure 4.5).

Multilayer graphene shows higher cycling stability. The destruction of the top layer in this material occurs as well, but the many underlying layers still maintain its overall stability. Interestingly, the repeated LSV measurements show an increase in the OER activity assigned to the formation of defects. Consequently, the authors concluded that only multilayer graphene grown by CVD is applicable as OER catalyst in contrast to few- or mono-layer graphene.<sup>[60]</sup>

The importance of defects for the catalytic OER activity of carbon materials was also reported by Zhao et al. who investigated a carbon quantum dot/graphene (CQD/

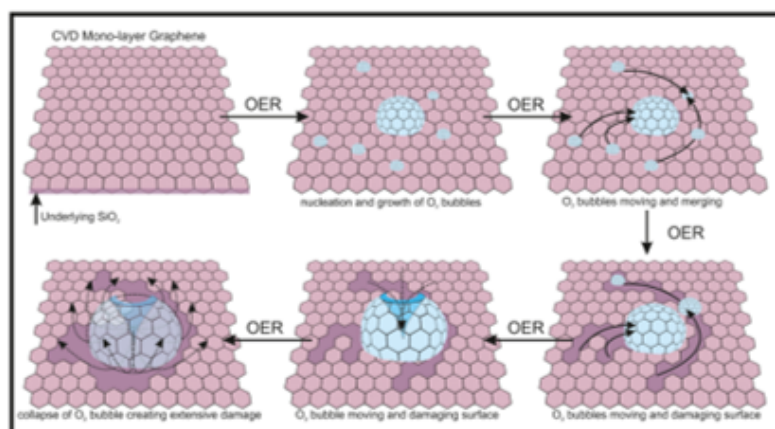


**Figure 4.5:** Schematic pathway of oxygen bubble-induced damage of mono-layer graphene during OER. Reproduced with permission.<sup>[60]</sup> Copyright 2019, Wiley-VCH.

graphene) hybrid material.<sup>[59]</sup> The hybrid material was prepared by electrochemical exfoliation of graphite in propylene carbonate followed by a solvothermal step and a final annealing step. XPS analysis of the samples revealed a small oxygen content; further impurities have not been detected or are below the detection limit of XPS. The CQD/graphene composite reached a current density of  $10 \text{ mA cm}^{-2}$  at a potential of 1.58 V versus RHE in 1 M KOH being only slightly higher as compared to a commercial  $\text{RuO}_2$  catalyst (1.56 V vs RHE). Besides the favorable kinetics, the hybrid material showed an excellent stability with almost no changes in LSV after 2000 cycles. The authors attributed the good catalytic OER performance to the intimate contact between CQDs and graphene sheets enabling a rapid charge transfer, and to the numerous edge sites/defects on CQDs and graphene sheets providing a high content of catalytic active sites.<sup>[59]</sup>

CNTs attracted also lots of interest as quasi “pure-carbon” based catalysts for OER. CNTs are typically produced by CVD, which entails, however, the use of metal catalysts like nickel, cobalt, or iron that cannot be removed completely. Consequently, commercially available pure and high-quality CNTs are contaminated by 0.5–2.0 wt% of metallic impurities.<sup>[61]</sup> These impurities drastically influence the electrochemical performance as demonstrated, e.g., by Suryanto et al.<sup>[61]</sup> The authors introduced a new two-step method (Figure 4.6) enabling the reduction of metallic impurities at the surface and the interior of multi-walled carbon nanotubes (MWCNTs) down below 0.01 wt%.<sup>[61]</sup> In the first step, the as-received MWCNTs are treated with acid to remove surface bonded metallic impurities resulting in raw MWCNTs (r-MWCNT). The r-MWCNT is subsequently mixed with melamine and heated to 1000 °C under an inert gas atmosphere yielding MeIMWCNT, followed by an additional acid treatment. These steps are repeated for multiple times. After the fourth purification cycle, the metal content is decreased to 100 ppm, equaling to a reduction of 98.8 % (Figure 4.6b).

The authors demonstrated that the OER performance of unpurified r-MWCNT (solid

black line) and acid-washed r-MWCNT (black dashed line) is very similar. The unpurified melamine-treated MelMWCNTs (solid red line) reveal an improved performance as compared to the r-MWCNT samples, together with the appearance of the characteristic  $\text{Ni}^{2+}/^{3+}$  redox feature. The authors reported that Ni, Fe, and Co ions entrapped in the interior of the MWCNTs are moved to the outside, which causes an opening of the nanotubes and thus an increase in the surface area after the melamine treatment. These structural issues were accounted for the enhanced OER performance. However, the acid-treated, purified MelMWCNTs (equaling to a removal also of those metal ions that have been moved from the interior by the melamine treatment) revealed a higher overpotential and a lower current density (Figure 4.6), which leads to a conclusion that the OER performance of MWCNTs is highly influenced by the amount of metallic impurities.<sup>[61]</sup>

Cheng et al. also analyzed CNTs that had metallic impurities like cobalt, iron, molybdenum, or nickel of around 3.45 wt%, and hydrochloric acid-treated CNTs whose trace metal content was decreased to 1.38 wt%.<sup>[62]</sup> However, the authors observed only little differences in the electrocatalytic activity of both types of CNTs. Moreover, Cheng et al. could show that the number of walls drastically influence the OER performance of CNTs. The highest activity was observed for three-walled CNTs (CNTs-3) with an onset potential of 1.64 V versus RHE and a current density of  $56 \text{ mA cm}^{-2}$  at 1.8 V versus RHE. The catalytic activity of CNTs with an increased or decreased number of walls is declined following a volcano-type dependency. The authors ascribe this behavior to the dual functionality of CNTs. The outer walls offer absorption and dissociation sites for different oxygen-containing species, and the inner walls enable fast electron transfer. With increasing number of walls, there is a reduced driving force for electrons to tunnel from outer to inner walls, thus reducing the OER activity. Moreover, the authors also compared the performance of the CNTs-3 to other carbon materials like graphite or activated carbon. Among three materials, the CNTs-3 has demonstrated the highest OER activity per surface area. Additionally, its performance was even superior to conventional 20 wt% Ru-C and 50 wt% Pt-C electrocatalysts.<sup>[62]</sup> Ali et al. also observed a correlation between the number of walls of MWCNTs and their resistance and electrocatalytic performance. The authors found that the resistance of CNTs gradually decreases with increasing number of walls (from three to five), but the electrocatalytic performance does not follow this trend. For the MWCNT-3, the onset potential of 1.63 V versus RHE and a current density of  $0.45 \text{ mA cm}^{-2}$  were measured, which change to 1.60 V versus RHE and  $0.89 \text{ mA cm}^{-2}$  in case of the MWCNT-4. The performance of the MWCNT-5 is however very similar to that of MWCNT-4, thus an additional increase in the number of walls does not result in a further enhancement of the OER performance.<sup>[63]</sup>

To assess the true electrocatalytic activity of CNTs only not by metal impurities, Gao et al. prepared SWCNTs in a metal-catalyst-free procedure using a  $\text{SiO}_2$ -coated Si wafer as substrate.<sup>[51]</sup> The resulting SWCNTs have an onset potential of 1.54 V and a current density of  $10 \text{ mA cm}^{-2}$  at an overpotential of 670 mV under basic conditions

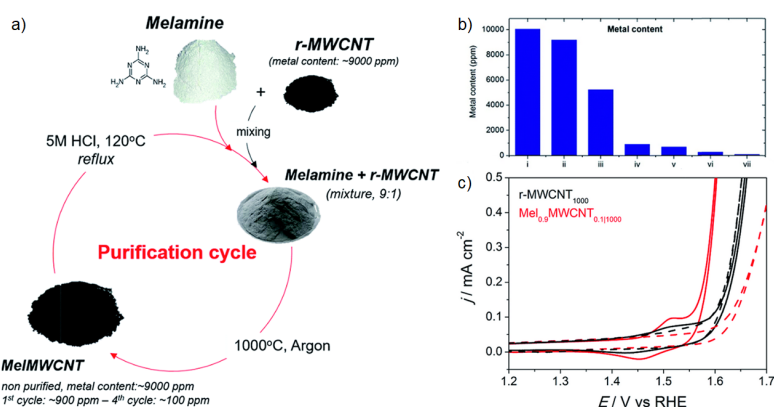


**Figure 4.6:** a) Schematic synthesis process of MWCNTs with ultra-low amount of metal impurities, b) metal content depending on the number of purification cycle and c) LSV curves of different unpurified (solid lines) and purified (dashed lines) MWCNT products: MWCNTs pyrolyzed at 1000 °C (rMWCNT<sub>1000</sub>) (black lines) and melamine-treated MWCNTs (Mel<sub>0.9</sub>MWCNT<sub>0.1/1000</sub>). Reproduced with permission.<sup>[61]</sup> Copyright 2018, The Royal Society of Chemistry.

(0.1 M KOH). The authors demonstrated that the electrocatalytic activity can be drastically increased by loading the SWCNTs with buckminsterfullerene (C<sub>60</sub>). The best performing C<sub>60</sub>/SWCNT composite revealed an onset potential of 1.46 V and a current density of 10 mA cm<sup>-2</sup> at an overpotential of 460 mV, which equals to a 5.3 and 50 times higher current density as compared to pure SWCNTs and C<sub>60</sub> under the same conditions, respectively. The C<sub>60</sub>/SWCNT composite has even a 1.2 times higher activity in comparison to a conventional RuO<sub>2</sub> catalyst. The authors explained the improved catalytic activity of C<sub>60</sub>/SWCNT by the more favorable kinetics toward OER as compared to SWCNTs, C<sub>60</sub> or RuO<sub>2</sub> reference samples.<sup>[51]</sup>

Due to their good electrical conductivity, CNTs are also often combined with non-carbonaceous materials, like metal oxides, phosphides, and sulfides, improving their catalytic activity as discussed later.

A compact overview of promising undoped or unintentionally doped carbon materials is given in Table 4.1.

**Table 4.1:** Comparison of different undoped and unintentionally doped carbons regarding their OER activity.

Material	Impurity/doping elements	Impurity/doping level	Electrolytes	Potential [mV] versus RHE at 10 mA cm <sup>-2</sup>	Tafel slope [mV dec <sup>-1</sup> ]	Ref.
Graphene	N/A	N/A	1 M KOH	No activity	N/A	[53]
Defective graphene	N	0.7 at%	1570	97	N/A	
Few-layer graphene	N/A	N/A	0.1 M KOH	1610@ 0.85 μA cm <sup>-2</sup>	N/A	[60]
Multilayer graphene	N/A	N/A		1400@ 3.23 mA cm <sup>-2</sup>	N/A	
Carbon QD/graphene	O	N/A	1 M KOH	1579	44	[59]
Raw CVD-MWCNT	Fe, Co, Ni, O	Ni: 9907 ppm Fe: 102 ppm Co: 71 ppm	1 M KOH	N/A	N/A	[61]

## 4 Carbonaceous Oxygen Evolution Reaction Catalysts

HCl-treated MWCNTs		Ni: 5204 ppm Fe: 19 ppm Co: 44 ppm		1690	153	
HCl/melamine-treated MWCNTs		Ni: 107 ppm Fe: 13 ppm Co: <1 ppm		1630	64	
HCl-treated three-walled CNTs	Fe, Co, Ni, Mo	1.38 wt% trace metal content	1 M KOH	1680	60/120	[62]
C <sub>60</sub>	N/A	N/A	0.1 M KOH	2250	50.5	[51]
SWCNT	O, Si	N/A		1900	79.7	
C <sub>60</sub> /SWCNT	O, Si	N/A		1690	46.7	
Surface-oxidized MWCNT	Fe, Co, Ni, O	Ni: ≈25 ppm Fe: ≈30 ppm Co: <1 ppm O: 1.0 at %	0.1 M KOH	1700@ 3.4 mA cm <sup>-2</sup>	73	[64]
Surface-oxidized MWCNT	Fe, Co, Ni, O	Ni: 3300 ppm Fe: 3 ppm Co: 32 ppm O: 2.2 at%	1 M KOH	1590	41	[57]
Surface-oxidized carbon black	O	Ni, Fe, Co: N.D. O: 8.87 at%	0.1 M KOH	1850	69.1	[65]
Oxidized laser-induced graphene	O	Ni, Fe, Co: N.D. O: 11.6 at%	1 M KOH	1594	49	[66]
Plasma-etched carbon cloth	O	13.09 at%	1 M KOH	1680	N/A	[67]
Activated carbon cloth	O	11.3 at%	0.1 M KOH	1380	124	[68]
Acidically oxidized carbon cloth	O	≈4.7 at%	0.1 M KOH	1707	82	[69]
Plasma-functionalized carbon cloth	O	5.9 at%	1 M KOH	1593	66.7	[70]
Tyramine-functionalized GO	N, O	N: 34.3 at% O: 9.8 at%	0.5 M KOH	1760@ 2 mA cm <sup>-2</sup>	69	[71]
Lysine-functionalized rGO	N, O	N: 6.1 at% O: 14 at%	0.5 M KOH	1560	80	[72]
NH <sub>2</sub> -functionalized carbon dots	N	11.8 at%	0.1 M KOH	1600@ 16.5 mA cm <sup>-2</sup>	N/A	[73]

### 4.2.2 Surface Functionalization

Surface oxidation of CNTs is another interesting strategy to improve the performance of this material class. Surface-oxidized CNTs can be prepared by acid, O<sub>2</sub> plasma, hydrothermal, and electrochemical treatment or a combination of two or more of these techniques.<sup>[57,64,74]</sup> The resulting surface-oxidized CNTs have commonly a superior OER activity as compared to the raw CNTs. The improved performance is generally attributed to the typically high surface hydrophilicity and the large amount of ketonic C=O groups influencing the electronic structure of the neighboring carbon atoms, which increases the adsorption of water molecules and oxygenated intermediates. A subsequent hydrothermal treatment can further modulate the oxygen functional groups toward a higher amount of C=O (Figure 4.7).<sup>[57,64,74]</sup> Defects are also often discussed in context of surface-oxidized CNTs and their influence on the OER activity. However, in contrast to many other carbonaceous OER catalysts, a low amount of defects is reported to be more favorable as an increased electrical conductivity can be achieved, which is also important for a high OER activity.<sup>[64]</sup>

Lu et al. prepared surface-oxidized MWCNTs by combing the three mentioned techniques of acid, hydrothermal, and electrochemical treatment. The best activity was demonstrated by mildly oxidized MWCNTs whose performance was drastically increased as compared to strongly or weakly oxidized MWCNTs. The authors showed that the activity toward OER can be further enhanced by a hydrothermal treatment followed by electrochemical activation. The resulting surface-oxidized MWCNTs reached a current density of 10 mA cm<sup>-2</sup> at a potential of around 1.6 V versus RHE measured

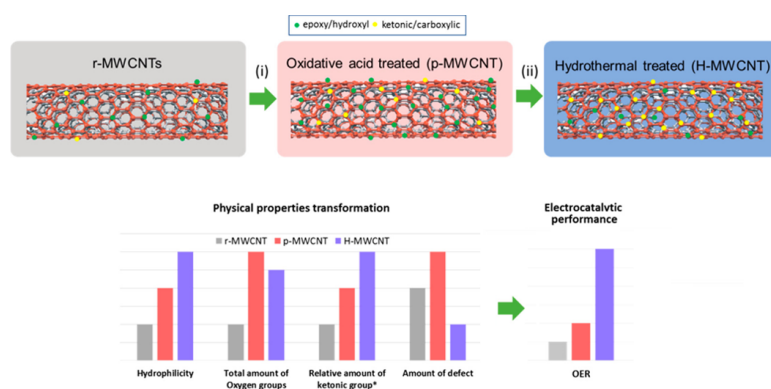


**Figure 4.7:** Schematic sequence of raw (r-MWCNT), piranha acid-treated (p-MWCNT), and hydrothermal-treated MWCNTs (H-MWCNT), their physical properties and the resulting relative OER activity. Reproduced with permission.<sup>[64]</sup> Copyright 2016, American Chemical Society.

in 1 M KOH, equaling to an overpotential of 360 mV. Although nickel impurities were still detected inside the nanotubes after the acid treatment, the authors demonstrated that they did not contribute significantly to the overall performance.<sup>[57]</sup>

Surface oxidation as a means to enhance the OER activity is applicable not only to CNTs. There are also reports on surface oxidized carbon black,<sup>[65]</sup> graphene,<sup>[66,67]</sup> and carbon cloth (CC).<sup>[68–70]</sup> The increased OER activity of those materials, as compared to the untreated equivalents, is mainly associated with the increasing amount of ketonic groups.<sup>[65–68]</sup> Cheng et al. reported, e.g., surface-oxidized CC prepared via a piranha acid treatment.<sup>[69]</sup> Untreated CC has only a poor catalytic performance toward OER, with an onset overpotential of 474 mV and an overpotential of 649 mV to reach  $5 \text{ mA cm}^{-2}$ . After acidic oxidation of the CC, a drastically improved performance can be observed. Excessive oxidation should be however avoided due to a decreased electrical conductivity of the resulting material. The best performing oxidized CC has an onset potential of 328 mV versus RHE and reaches a current density of  $10 \text{ mA cm}^{-2}$  at an overpotential of 477 mV. The oxidized CC delivers also excellent long-term durability with a loss in current density of only 9.7 % over 1000 cycles.<sup>[69]</sup>

Another surface functionalization strategy of carbonaceous materials is presented by Sapner et al. who prepared tyramine-functionalized GO (T-GO) and lysine-functionalized rGO (Ly-rGO) materials as catalysts for OER.<sup>[71,72]</sup> GO as a reference material demonstrates rather moderate catalytic activity (current density of  $10 \text{ mA cm}^{-2}$  achieved at a potential of 1.88 V vs RHE) in 0.5 M KOH.<sup>[72]</sup> After functionalization with tyramine, the potential to reach  $10 \text{ mA cm}^{-2}$  is reduced to around 1.7 V versus RHE. Chronoamperometric measurements demonstrate a high stability of T-GO during OER (Figure 4.8c). The improved performance is ascribed to the functional groups of tyramine, which enhance the electron transfer at the interface via a postulate four step process depicted in Figure 4.8.<sup>[71]</sup>

Functionalization of GO with lysine, which is accompanied by the reduction of GO

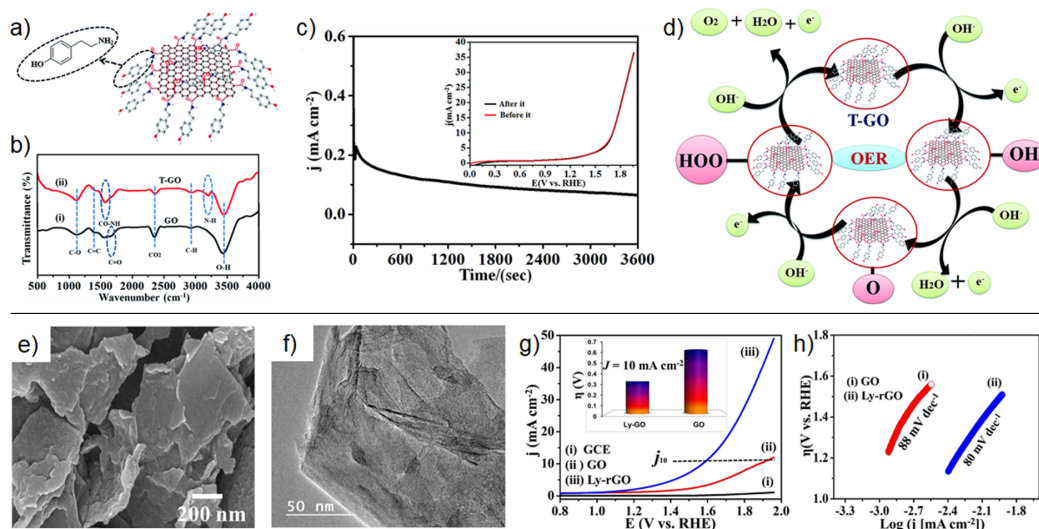


**Figure 4.8:** a) Schematic structure of tyramine surface-functionalized GO (T-GO), b) Fourier-transform infrared spectra of GO and T-GO, c) chronoamperometric current stability at 1.39 V versus RHE of T-GO and the corresponding LSV curves before and after this measurement in the inset. d) Probable OER reaction mechanism of T-GO. e) SEM and f) TEM image of lysine surface-functionalized rGO (Ly-rGO) and the resulting LSV curve, g) overpotential at  $10 \text{ mA cm}^{-2}$ , and h) Tafel slope. a-d) Reproduced (adapted) with permission.<sup>[71]</sup> Copyright 2019, The Authors. Published by The Royal Chemical Society. e-h) Reproduced (adapted) with permission.<sup>[72]</sup> Copyright 2020, American Chemical Society.

to rGO, results in a further enhancement of the OER activity represented by a potential of 1.56 V versus RHE to reach  $10 \text{ mA cm}^{-2}$  and a Tafel slope of  $80 \text{ mV dec}^{-1}$  (Figure 4.8g, h). The authors suggest that the increased performance can be attributed to the various functional groups of lysine enabling an advanced multistep OER.<sup>[72]</sup>

Surface functionalization was applied also for carbon nanodots (CDs) to increase their OER activity.<sup>[73]</sup> Liu et al. have synthesized CDs with a particle size distribution of 4–8 nm in an electrochemical method and functionalized them with amidogen and phosphorous surface groups. Such functionalization is mandatory as the "pure" CDs have no obvious catalytic activity toward OER. The best performing  $\text{NH}_2$ -CDs reached a current density of  $16.5 \text{ mA cm}^{-2}$  at a potential of 1.6 V versus RHE, even outperforming an  $\text{IrO}_2/\text{C}$  reference catalyst ( $13.2 \text{ mA cm}^{-2}$ , 1.6 V vs RHE).<sup>[73]</sup>

### 4.3 Metal-Free, Heteroatom-Doped Carbon Composites

Beside the introduction of defects and the functionalization of the surface, the OER activity of carbon materials can be further enhanced by heteroatom doping. Various heteroatoms including B, N, O, F, P, and S have been used to tailor the structural, electrical, and chemical properties of carbon nanomaterials. The break of electroneutrality

results in a doping-induced charge transfer which leads to the formation of catalytically active carbon centers while keeping the beneficial electrical conductivity.<sup>[27,28]</sup> Depending on the doped element, several different configurations are possible for the implementation in the carbon network (Figure 4.9). In general, there exist two main synthetic approaches for the heteroatom-doping of nanocarbons resulting in single-doped, co-doped, and multi-doped OER catalysts. The first approach includes an in situ doping during carbon synthesis, and the second a postsynthetic treatment of pre-formed carbon materials. Several different materials with tunable molecular structure and morphology have been developed so far and will be reviewed in this chapter regarding the doping level and the doping element.

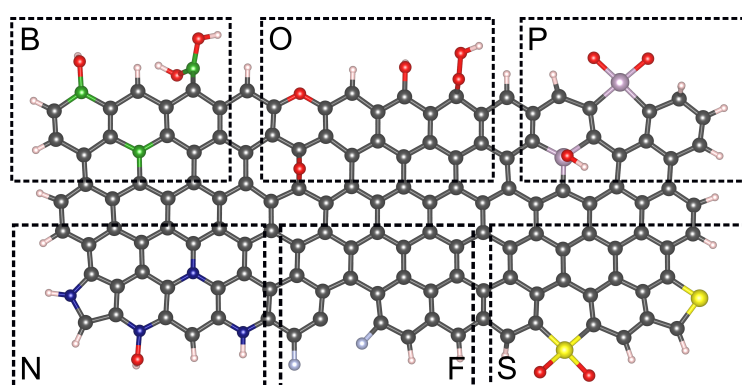


**Figure 4.9:** Schematic summary of the heteroatom doping configurations. Gray, green, navy, red, blue, orchid, and yellow represent C, B, N, O, F, P, and S atoms, respectively.

### 4.3.1 Single-Atom Doping

Modulating the electronic structure of carbon-based materials often leads to a change in catalytic activity while keeping the beneficial properties like a high conductivity and a good stability, which are crucial for a potential long-term application. A compact overview of promising single-heteroatom-doped carbon materials is shown in Table 4.2. Nitrogen doping of different carbon materials has a long history especially for the ORR,<sup>[75–79]</sup> however the application of this process to graphene (nitrogen-doped graphene, NG) to enhance its OER activity was demonstrated only in 2013 by Lin et al.<sup>[80]</sup> NG with a doping ratio of 2.4 at% N was prepared via a simple pyrolysis of graphene oxide and polyaniline (PANI). The OER catalytic activity of this material with an overpotential of 416 mV at a current density of 1 mA cm<sup>-2</sup> in 0.1 M KOH outperformed the undoped graphene and a commercial Pt/C catalyst. Due to the fact that the atomic size of nitrogen is similar to that of carbon, it can be easily incorporated in the graphene framework substituting carbon in several different forms, including pyridinic N, pyrrolic N, and quaternary N. Therefore, in the same year, Zhao et al. synthesized a nitrogen-doped carbon material by pyrolyzing the hybrid of a melamine/formaldehyde

polymer and nickel nitrate at 700 °C and consecutive etching of the metal oxide showing a current density of 10 mA cm<sup>-2</sup> at an overpotential of 380 mV measured in 0.1 M KOH.<sup>[81]</sup> Based on the XPS measurements of N-doped carbons with different N/C ratios, the authors proposed that the high oxygen evolution activity originates from pyridinic-N or/and quaternary-N-related active sites.

**Table 4.2:** Comparison of different single-heteroatom-doped metal-free nanocarbons regarding the OER activity.

Doping elements	Material	Precursors	Doping level	Electrolytes	Potential [mV] versus RHE at 10 mA cm <sup>-2</sup>	Tafel slope [mV dec <sup>-1</sup> ]	Ref.
B	Multi-walled CNTs	Boric acid	B 1.51–2.37 at%	0.1 M KOH	1881	N/A	[82]
N	Few-layer graphene	PANI	N 2.4 at%	0.1 M KOH	1646@	N/A	[80]
N	CNTs on rGO	Ethylene diamine	N 3.9 at%	0.1 M KOH	1768	N/A	[83]
N	Graphite nano-material	Melamine formaldehyde	N 3.54 at%	0.1 M KOH	1610	N/A	[81]
N	Surface N-doped CNTs	Pyridine	N 2.38 at%	0.1 M KOH	1780	N/A	[84]
N	Graphene nanotube hybrids	Ethylene, ammonia	N 0.53 at%	0.1 M KOH	1630	83	[85]
N	Graphitic C <sub>3</sub> N <sub>4</sub> nanosheets/graphene composite	Melamine	N ≈57 at%	0.1 M KOH	1759	68.5	[86]
N	Graphene	Ammonia	N 3.97 at%	0.1 M KOH	1786@	N/A	[87]
N	CNTs	Acetonitrile	N 2.4 at%	0.1 M KOH	1680	N/A	[88]
N	Graphite nano-material	Carbon cloth	N 1.92 at%	1.0 M KOH	1850	98	[89]
N	Graphene nanoribbons	Melamine L-cysteine	N 5.9 at%	1.0 M KOH	1590	47	[90]
N	Graphitic carbon microtubes	Facial cotton	N 2.0 at%	0.1 M KOH	1520	N/A	[91]
N	CNTs-supported C <sub>3</sub> N <sub>4</sub>	Melamine CNT-CF	N/A	1.0 M KOH	1600	N/A	[92]
N	Multi-walled CNTs	PANI emeraldine salt	N 0.5 at%	1.0 M NaOH	1550	68	[56]
N	Defect-rich porous graphitic carbon	Nitrogen-enriched polydopamine analog	N 9.36 at%	1.0 M KOH	1590	57	[14]
N	Carbon nanocages	Ammonia	N 3.05 at%	0.1 M NaOH	1690	N/A	[93]
N	N-doped graphite on carbon black	1-butyl-3-methylimidazolium bromide	N 1.23 at%	0.5 M H <sub>2</sub> SO <sub>4</sub>	1700	226	[94]
N	N-doped carbon nanosheets	Citric acid Ammonium chloride	N 2.46 at%	0.1 M KOH	1640	142	[95]
N	Graphene-supported N-doped carbon	Glucaminium-based ionic liquids	N 26 at%	1.0 M KOH	1560	52	[96]
N	Graphitic mesoporous C <sub>3</sub> N <sub>4</sub>	Guanidine hydrochloride	N 48 at%	1.0 M KOH	1606	52.4	[97]
F	Fluorinated graphdiyne Carbon cloth	Carbon Cloth, 1,3,4-triethynyl-2,4,6-trifluorobenzene	N/A	1.0 M KOH 0.5 M H <sub>2</sub> SO <sub>4</sub>	1690 1800	128 192	[98]
P	P-doped graphene	Red phosphorus graphite	P 0.83 at%	1.0 M KOH	1560	62	[54]
P	P-doped graphitic carbon	Sugar sulfuric acid red phosphorus	P 6.7 at%	1.0 M KOH	1690	179	[99]
S	CNT-graphene nanolobes	Thiourea Benzylsulfide	S 1.19 at%	1.0 M KOH	1580	95	[31]

Three years later, Yang et al. also confirmed that pyridinic N with p-type doping character is responsible for the OER activity of N-doped carbons proven by X-

ray absorption near-edge structure (XANES) spectroscopic measurements on N-doped graphene.<sup>[90]</sup> In a novel strategy developed by the authors, N-doped graphene nanoribbons with an interconnected 3D network architecture were synthesized via the pyrolysis of a mixture of melamine and L-cysteine under argon atmosphere. The material showed a low overpotential of 360 mV at 10 mA cm<sup>-2</sup> measured in 1.0 M KOH with a small Tafel slope of 47 mV dec<sup>-1</sup>, which is even lower than for Ir/C (54 mV dec<sup>-1</sup>). In the XANES spectra, the broadening of the pyridinic-N peak at  $\approx 398.0$  eV from 0.8 to 1.15 eV was observed, while the other peaks, including graphitic and pyrrolic N, remained unchanged. The authors ascribed the energy increase to adsorbed OOH\* and O\* intermediates on carbon atoms next to the pyridinic-N during OER. Hence, a high amount of pyridinic-N seems important for a good OER performance.

Several different single N-doped graphene-based materials<sup>[80,85–87,90,92,95,96]</sup> are known until now. These compounds are typically synthesized by either pyrolysis of nitrogen-containing carbon precursors like PANI or melamine, or by treatment of preformed graphene with ammonia-based chemicals. However, the synthesis of graphene often involves TMOs like iron oxide. In this case, it is very important to remove the metal catalysts completely, as even the smallest impurities may alter the catalytic activity in a strong way.<sup>[100]</sup>

Another method to the synthesis of the defect-rich and ultrathin N-doped carbon nanosheets (NCNs) was developed by Jiang et al. who prepared the OER catalyst by simply pyrolyzing a mixture of citric acid and NH<sub>4</sub>Cl at a temperature of 1000 °C under Ar atmosphere (Figure 4.10).<sup>[95]</sup> NH<sub>4</sub>Cl acts in this case not only as nitrogen source for the NCNs but also as a foaming agent to construct a cross-linked 3D porous network structure with a high surface area of more than 1700 m<sup>2</sup> g<sup>-1</sup>. The material has an overpotential of 410 mV at 10 mA cm<sup>-2</sup> measured in 0.1 M KOH with a comparably high Tafel slope of 142 mV dec<sup>-1</sup>, and a stable performance over 12 000 s at 1.5 V versus RHE at a current density of 2 mA cm<sup>-2</sup>. DFT calculations suggest that carbon atoms located at the armchair edge and adjacent to the graphitic N dopants act as the intrinsic active sites for OER.

Nitrogen-doped CNTs can also be used as single-heteroatomdoped carbon catalyst. This material can be produced by CVD of nitrogen-containing precursor like ethylene diamine or acetonitrile on different substrates always with the need of iron as a catalyst.<sup>[56,83,84,88]</sup> Another possibility is a posttreatment of preformed CNTs with nitrogen-containing species and a consecutive pyrolysis step. Davodi et al. have obtained nitrogen-doped MWCNTs (NMWNTs) by mixing preformed MWCNTs with PANI emeraldine salt followed by sonication and subsequent pyrolysis at a temperature of 800 °C for 1 h under argon atmosphere (Figure 4.11).<sup>[56]</sup> The obtained NMWNTs show a superior OER catalytic activity with a small overpotential of 320 mV at 10 mA cm<sup>-2</sup> measured in 1.0 M NaOH and a Tafel slope of 68 mV dec<sup>-1</sup>, and excellent stability in chronoamperometric measurements at a constant voltage of 1.56 V versus RHE for more than 25 h. XPS measurements reveal the important role of pyridinic N as the main active sites for OER. In addition, the metal-free catalyst shows also excellent stability

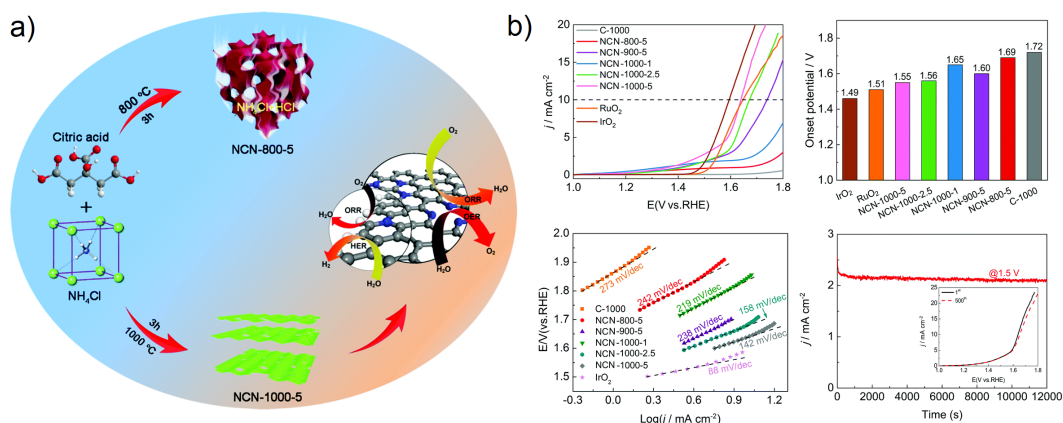


**Figure 4.10:** a) Schematic illustration of procedure for synthesizing N-doped carbon nanosheets (NCNs) and b) electrochemical characterization of NCNs including LSV curves, onset potentials, Tafel plots, and  $i-t$  plot at the applied potential of 1.5 V versus RHE. Reproduced (adapted) with permission.<sup>[95]</sup> Copyright 2019, The Royal Society of Chemistry.

in chronoamperometric measurements at a constant voltage of 1.56 V versus RHE for more than 25 h.

Graphitic nitrogen-doped carbons<sup>[89,91,93,94,97,101]</sup> also demonstrate a good activity toward the OER. Wahab et al. , e.g., used a mesoporous SBA-15 silica nanotemplate to structure polymerized guanidine hydrochloride as a single-carbon/nitrogen source (gMesoCN).<sup>[97]</sup> After pyrolysis, they obtained a metal-free graphitic mesoporous carbon nitride with a nitrogen content of 48 at% and a surface area of  $406 \text{ m}^2 \text{ g}^{-1}$ . Structural characterization showed the successful formation of a graphitic carbon nitride framework with uniformly sized pore channels of 4.56 nm. The mesoporous material showed an overpotential of 376 mV at  $10 \text{ mA cm}^{-2}$  measured in 1.0 M KOH with a Tafel slope of  $52.4 \text{ mV dec}^{-1}$ . In long-term stability test, they observed a 98.4 % retention of current density after 24 h at a voltage of 1.6 V versus RHE.

Additionally to nitrogen doping, several other single heteroatoms such as B,<sup>[82]</sup> F,<sup>[98]</sup> P,<sup>[54,99]</sup> and S<sup>[31]</sup> have been used to tune the electrochemical properties for effective OER. For example, Xiao et al. realized edge-selective P doping of graphene by simply ball-milling of graphite and red phosphorus followed by several washing steps with water and annealing in argon atmosphere at  $650 \text{ }^\circ\text{C}$ .<sup>[54]</sup> In this way, the authors were able to introduce up to 0.83 at% P in the carbon network. The P-doped few-layer graphene showed a small overpotential of 330 mV at  $10 \text{ mA cm}^{-2}$  measured in 1.0 M KOH with a Tafel slope of  $62 \text{ mV dec}^{-1}$ . Besides the phosphorous doping, the authors have observed a large fraction of oxygen in the structure leading to defects with comparable effects as described in Section 2. Although traces of iron were present in their material, the authors have demonstrated that the high electrocatalytic activity mainly originates from the P dopant.

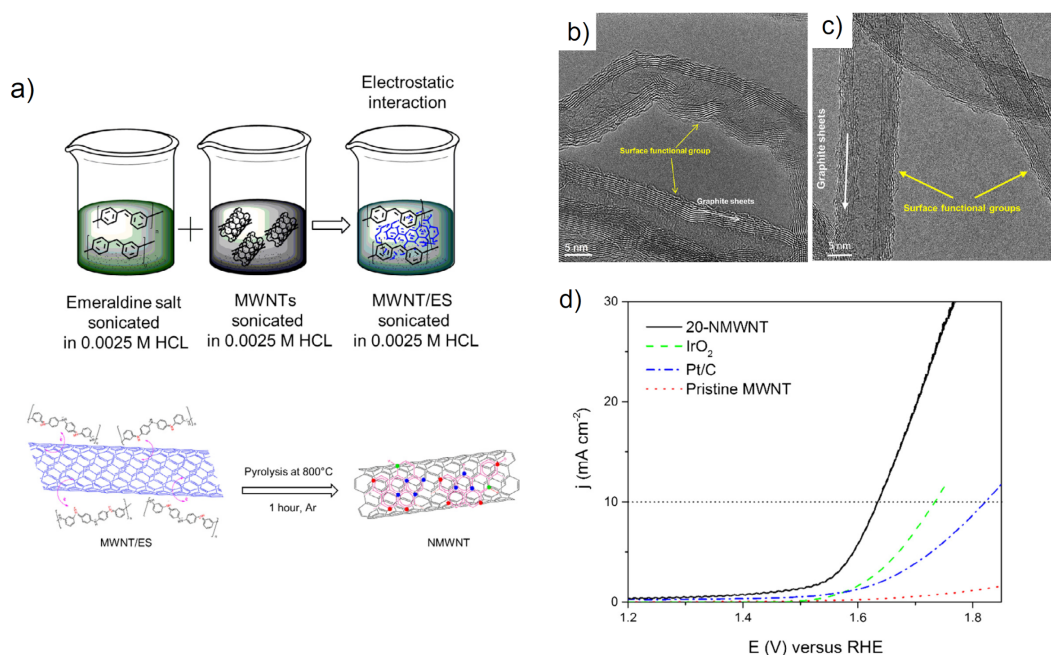


**Figure 4.11:** a) Schematic illustration of the synthesis procedure of N-doped MWCNTs (NMWNTs), high-resolution TEM (HRTEM) images of 20-NMWNT b) before and c) after pyrolysis and d) electrochemical characterization of the 20-NMWNT. Reproduced (adapted) with permission.<sup>[56]</sup> Copyright 2017, The Authors. Published by Elsevier Inc.

### 4.3.2 Multiheteroatom Doping

Numerous examples described in the previous section demonstrate that electrocatalysts with a high OER activity can be obtained via doping of different carbon materials with nitrogen atoms as elaborated in Section 3.1. A further improvement in conductivity, stability, and activity is assumed for the doping with two or more heteroatoms due to positive synergistic effects between the dopants. Difficulties lie in the control of the doping amount and the characterization of active sites and catalytic effects. Several different combinations of heteroatoms have been developed such as N,B,<sup>[102,103]</sup> N,O,<sup>[30,104]</sup> N,F,<sup>[105,106]</sup> N,P,<sup>[49,107,108]</sup> N,S<sup>[109–113]</sup> and even trivalent doped materials like N,O,F,<sup>[114]</sup> N,F,P,<sup>[115]</sup> N,P,S<sup>[116]</sup> were synthesized.

An overview of these materials and their OER performance is given in Table 4.3.

**Table 4.3:** Comparison of different multiheteroatom-doped metal-free nanocarbons regarding the OER activity.

Doping elements	Material	Precursors	Doping level	Electrolytes	Potential [mV] versus RHE at 10 mA cm <sup>-2</sup>	Tafel slope [mV dec <sup>-1</sup> ]	Ref.
B, N	Unzipped MWCNTs	Boron oxide Ammonia Thermal annealing	B 11.3 at% N 11.1 at%	0.1 M NaOH	1872	N/A	[102]
B, N	Graphitic carbon spheres	Boric acid Methyl violet	B 1.51 at% N 7.94 at%	0.1 M KOH	1992	N/A	[103]

#### 4 Carbonaceous Oxygen Evolution Reaction Catalysts

N, O	CNT- graphene composite	Graphene oxide CNTs Ammonium hydroxide	N 7.59 at% O 15.72 at%	0.1 M KOH	1690	141	[30]
N, O	Graphene nanosheets/ carbon cloth composite	Methane Carbon cloth	N 2.05 at% O 8.86 at%	1.0 M KOH	1580	38	[104]
N, F	Graphene nanosheets	Resin KF	N 0.89 at% F 0.49 at%	1.0 M KOH	1570	78	[105]
N, F	N,F-co-doped carbon black	Melamine Poly-tetrafluoroethylene	N 4.78 at% F 0.7 at%	0.1 M KOH	1609	69	[106]
N, P	P-C <sub>3</sub> N <sub>4</sub> -Nanosheets	Melamine Ethylene diphosphonic acid	N 13.2 wt% P 0.9 wt%	0.1 M KOH	1630	61.6	[49]
N, P	Graphitic carbon	Aniline Phytic acid Ammonium persulfate	N 3.2 at% P 1.1 at%	0.1 M KOH	1950	330	[107]
N, P	Hollow carbon nanofiber	Triphenylphosphine Polyacrylonitrile Dicyanamide Electrospinning	N/A	0.1 M KOH	1550	248	[108]
N, S	Graphene/CNT composite	Urea thiourea	N 0.71 at% S 1.26 at%	0.1 M KOH	1908	103	[109]
N, S	N,S-doped graphitic sheets	Melamine Nickel sulfate	N 2.1 at% S 0.8 at% O 3.8 at%	0.1 M KOH	1600	71	[110]
N, S	N,S-doped CNTs	Polydopamine 2-mercaptoethanol	N 3.8 at% S 5.6 at%	1.0 M KOH	1560	56	[111]
N, S	N,S-doped graphene nanosheets	Melamine Dibenzyl sulfide	N 11.55 at% S 3.66 at%	1.0 M KOH	1529	62	[112]
N, S	N,S-doped graphene	Dopamine 2-mercaptoethanol	N 4.29 at% S 1.35 at%	1.0 M KOH	1511	109	[117]
N, O, F	Porous graphite	Aniline phytic acid OCC	N 0.46 at% O 16.4 at% P 0.32 at%	1.0 M KOH 0.5 M H <sub>2</sub> SO <sub>4</sub>	1660 1700	84 200	[114]
N, F, P	N,F,P-doped graphene	PANI Hexafluorophosphate	N 7.11 at% F 0.33 at% P 0.37 at%	0.1 M KOH	1810	136	[115]
N, P, S	Sponge like C <sub>3</sub> N <sub>4</sub>	Aminoguanidine hydrochloride Phosphoric acid Methanesulfonic acid	N 41.36 at% P 1.68 at% S 1.59 at%	0.1 M KOH	1560	64	[116]

Gao et al. have developed an elegant approach to obtain a trifunctional N,P co-doped hollow carbon nanofiber membrane using the coaxial electrospinning of a triphenylphosphine containing polyvinylpyrrolidone (PVP) core solution together with a dicyandiamide containing polyacrylonitrile (PAN) shell solution.<sup>[108]</sup> Pyrolysis of the nanofibers at 1000 °C under argon resulted in N,P-co-doped hollow nanofibers with a tunable doping content depending on the concentration of used PAN. Due to the plentiful active sites, continuous pathways, and benign mass transfer channels in this material, a current density of 10 mA cm<sup>-2</sup> was reached at a very low overpotential of 330 mV in 0.1 M KOH. Additionally, the N,P-doped hollow fibers showed a better stability than IrO<sub>2</sub> under continuous operation for 20 000 s. However, the material exhibited a high Tafel slope of 248 mV dec<sup>-1</sup> as compared to 97 mV dec<sup>-1</sup> for IrO<sub>2</sub>, which indicates nonfavorable OER kinetics.<sup>[108]</sup>

An example of controlled doping for effective synergistic effects between different heteroatoms was shown by Zhao et al.<sup>[112]</sup> Based on their previous work on site-defined doping of acetylinic groups of graphdiyne, the authors were able to synthesize a stereodefined heteroelement co-doped catalyst by introducing both S and sp-N

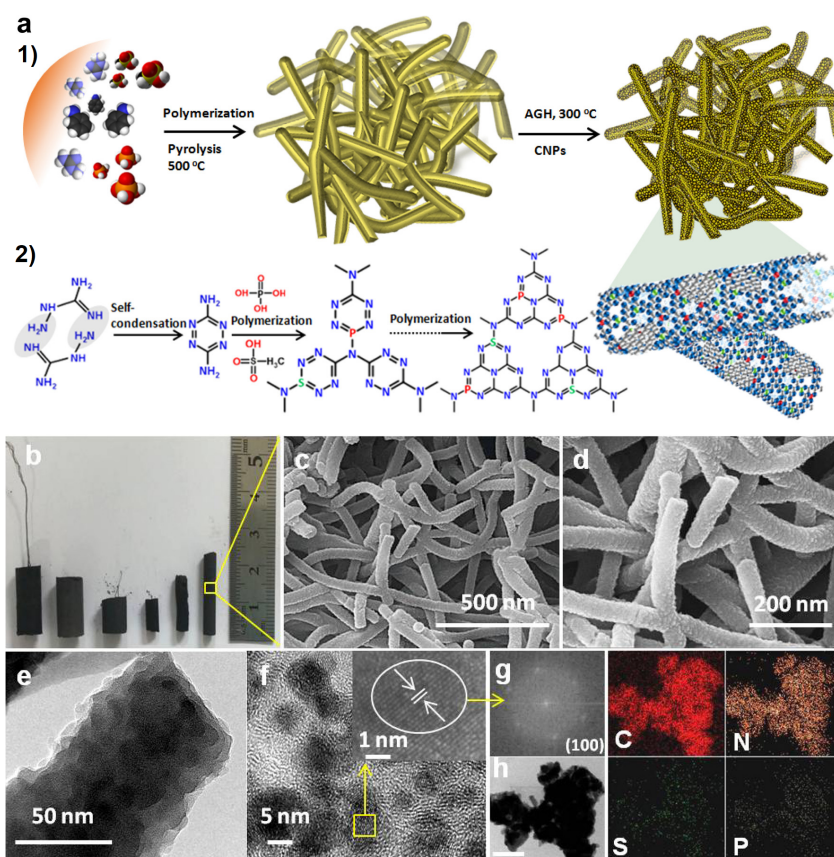


**Figure 4.12:** a) Schematics showing the synthesis of P,S-CNS catalysts, and the reaction mechanism for the formation of the C-N polymeric complex. b) Photographs of as-synthesized cylindrical sponge-like P,S-CNS structure. c,d) SEM, e) TEM, and f) HRTEM images of P,S-CNS catalyst (inset show enlarged view). Corresponding g) fast Fourier transform (FFT) pattern of the crystallite in the inset of (f). h) TEM and the elemental maps of C, N, P, and S of P,S-CNS (scale, 300 nm). Reproduced (adapted) with permission.<sup>[116]</sup> Copyright 2017, American Chemical Society.

atoms. This was achieved by heating melamine and dibenzyl sulfide together with few-layer graphdiyne at different calcination temperatures for 150 min. The highest electrocatalytic activity was measured for the material pyrolyzed at 900 °C with a nitrogen and sulfur content of 11.55 and 3.66 at%, respectively. This catalyst has shown an outstanding OER performance with an overpotential of 299 mV at 10 mA cm<sup>-2</sup> measured in O<sub>2</sub>-saturated 1.0 M KOH, and even a smaller Tafel slope (62 mV dec<sup>-1</sup>) than the RuO<sub>2</sub> (69 mV dec<sup>-1</sup>), pointing to even faster OER kinetics of the carbonaceous material than the noble metal catalyst. By tuning the doping concentration, the authors found that the introduction of sp<sup>2</sup>-N in addition to a higher concentration of S decreases the overpotential significantly.<sup>[112]</sup>

Shinde and co-workers extended the number of dopants even further.<sup>[116]</sup> P,S-doped carbon nitride sponges (P,S-CNS) were obtained by polymerization of aminoguanidine

in the presence of phosphoric and sulfonic acid followed by a pyrolysis step and a consecutive crystallization of aminoguanidine CNPs with ethylene (Figure 4.12). The resulting P,S-CNS with a high surface area of  $1474 \text{ m}^2 \text{ g}^{-1}$  exhibited a low overpotential of 330 mV at  $10 \text{ mA cm}^{-2}$  in LSV measurements on rotating disk electrode (RDE) in 0.1 M KOH. This value was even lower than that of  $\text{RuO}_2$  with 340 mV. The Tafel slope of  $64 \text{ mV dec}^{-1}$  also outperformed that of  $\text{RuO}_2$  with  $88 \text{ mV dec}^{-1}$ . XPS measurements indicated significant changes in N-bonding configurations with P and S dopants as compared to that of pure  $\text{C}_3\text{N}_4$  leading to the superior performance of the system.

## 4.4 Metal (Metal Oxide)/Carbon Hybrids

TMOs are highly popular and efficient catalysts for the OER with a variety of respective reports in the literature.<sup>[118,119]</sup> As of now, catalysts based on precious metals such as Ir or Ru are considered state of the art.<sup>[118]</sup> However, the price and scarcity of these metals make them unsustainable for large-scale applications, which motivates the search for possible earthabundant and cheaper alternatives.<sup>[120]</sup> The nonnoble TMOs are intensively investigated as OER catalysts, however they generally suffer from a low electronic conductivity limiting the currents that can be achieved in electrode assemblies.<sup>[121]</sup> One of the most popular approaches to increase the conductivity of TMO-based electrodes is their hybridization with highly conductive carbonaceous supports to form composite OER electrocatalysts. In this section, we provide an overview of the recent nonnoble metal oxide/carbon composite, mixed metal oxides/carbon composites, and core-shell metal oxide/carbon composite materials showing promising OER performance.

### 4.4.1 TMO/Carbon Composites for OER

#### Cobalt Oxide-Containing Composites

Cobalt oxides generally show sufficiently high OER activity,<sup>[122,123]</sup> with  $\text{Co}_3\text{O}_4$  being one of the most popular compounds especially in combination with carbon-based materials. Thus, Zhang et al. synthesized an electrocatalyst composed of  $\text{Co}_3\text{O}_4$  nanoparticles anchored on a nitrogen-doped reduced graphene oxide using hydrothermal reaction.<sup>[124]</sup> The beneficial combination of the nanosized character of the anchored particles with the high conductivity of graphene resulted in a very active catalyst with performance values similar to that of commercially available  $\text{RuO}_2$ . The impact of the carbonaceous substrate on the catalytic activity of the  $\text{Co}_3\text{O}_4$ -based composites was investigated by Asiri et al. who deposited  $\text{Co}_3\text{O}_4$  nanoparticles on graphene oxide (GO), graphene (G) and CNTs.<sup>[125]</sup> Among tested compounds, the graphene-based hybrid material exhibited the highest activity with an overpotential of 535 mV at  $10 \text{ mA cm}^{-2}$  and a Tafel slope of  $127 \text{ mV dec}^{-1}$  in 1.0 M KOH.

Besides the origin and the morphology of the carbonaceous substrate, the activity of composites also depends on the morphology of the cobalt oxide catalyst as shown

for a hybrid material based on  $\text{Co}_3\text{O}_4$  nanorods combined with CNTs.<sup>[126]</sup> By utilization of a diethylenetriamine-assisted synthesis, the authors obtained well-defined  $\text{Co}_3\text{O}_4$  nanorods anchored onto MWCNTs (Figure 4.13a–f) resulting in a well-connected network with high surface area. Main features of this catalyst are a low overpotential of 309 mV at  $10 \text{ mA cm}^{-2}$  in  $1.0 \text{ M KOH}$ , a very low Tafel slope of  $51 \text{ mV dec}^{-1}$ , and a high stability (Figure 4.13g–j).

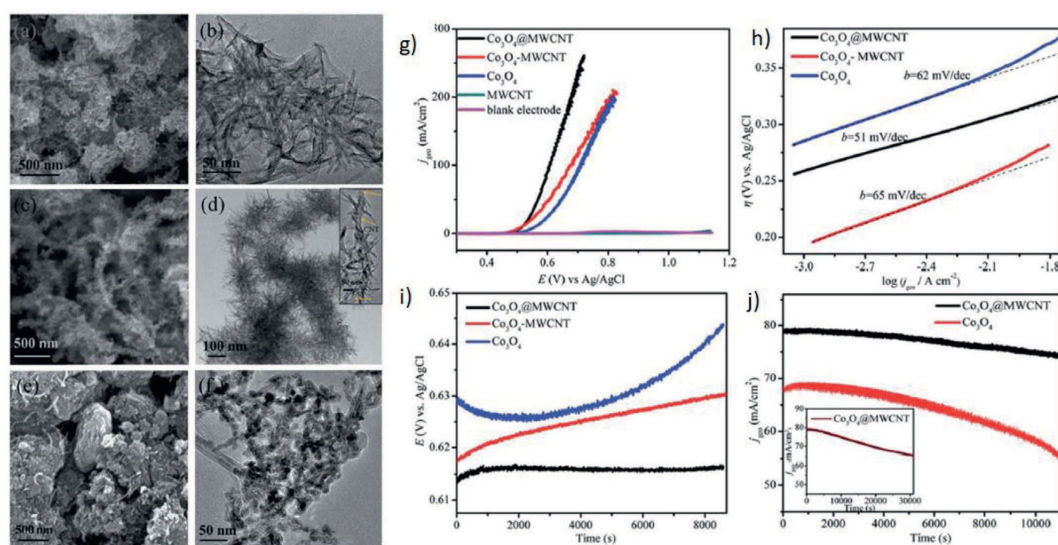


**Figure 4.13:** a) SEM image of  $\text{Co}_3\text{O}_4$ . b) TEM image of  $\text{Co}_3\text{O}_4$ . c) SEM image of  $\text{Co}_3\text{O}_4$ @MWCNT. d) TEM image of  $\text{Co}_3\text{O}_4$ @MWCNT. e) SEM image of  $\text{Co}_3\text{O}_4$ -MWCNT. f) TEM image of  $\text{Co}_3\text{O}_4$ -MWCNT. g) LSV curves, h) Tafel slope curves, i) galvanostatic profile at  $20 \text{ mA cm}^{-2}$ , and j) stability tests of  $\text{Co}_3\text{O}_4$ @MWCNT composite materials. Reproduced with permission.<sup>[126]</sup> Copyright 2014, The Royal Society of Chemistry.

There are several additional reports on similar hybrid materials to be found in the literature with a varying morphology of metal oxide but quite a performance similar to those of some of the commercially available catalysts.<sup>[127–129]</sup> However, one of the challenges in understanding the mechanistic aspects of composite compounds is the identification of synergistic effects between the active particles and the substrate. To address this issue, Leng et al. performed the first-principle simulations and found that the Co–O–C bonds play a crucial role toward the OER activity by introducing an extra step in deprotonation of  $\text{HO}^*$ .<sup>[130]</sup> Using the first-principle simulation results, the authors proposed a method for the synthesis of  $\text{Co}_3\text{O}_4$ /graphene composites, resulting in a material with OER overpotential of 316 mV at  $10 \text{ mA cm}^{-2}$  and a Tafel slope of  $46 \text{ mV dec}^{-1}$ .

### Iron Oxide-Containing Composites

Besides cobalt oxides, iron oxides attract a lot of attention as potential OER catalysts. Being very cheap, abundant, and benign, iron oxide is however poorly conducting. Therefore, for this class of materials, the hybridization with conductive carbon-based supports generally improves the electrocatalytic performance. Thus, Bandal et al. synthesized a hybrid catalyst composed of Fe<sub>2</sub>O<sub>3</sub> nanorods on CNTs using simple coprecipitation method.<sup>[131]</sup> The hybridization has dramatically increased the electrical conductivity of the material and improved its OER performance for OER, characterized by an overpotential of 383 mV and a Tafel slope of 61 mV dec<sup>-1</sup>. The authors have demonstrated that the ratio between the iron oxide and the CNTs affects the electrochemical performance, with the highest activity obtained for the composite with the equal ratios of iron oxide and the CNTs.

Even better electrocatalytic performance has been achieved for the composite compound containing Fe<sub>2</sub>O<sub>3</sub>, NiS<sub>x</sub>, and reduced graphene oxide,<sup>[132]</sup> which reaches a current density of 10 mA cm<sup>-2</sup> at an overpotential of 330 mV in 1 M KOH solution. The authors concluded that a beneficial charge transfer from Ni sites to Fe sites takes place, whereas the reduced graphene oxide provides a good electrical conductivity. Importantly, this catalyst exhibited a significantly higher stability than the commercially available RuO<sub>2</sub>. Wang et al. constructed an FeP, Fe<sub>2</sub>O<sub>3</sub>, and N-doped graphene composite by electrospinning of iron acetylacetonate and PAN followed by several chemical and heat treatment steps. The obtained material showed activity toward multiple electrocatalytic reactions including OER.<sup>[133]</sup> In this composite, FeP was the active material for the hydrogen evolution, while Fe<sub>3</sub>O<sub>4</sub> and N-doped carbon contributed to the catalytic activity of the catalyst toward OER.

In a very recent paper, Hof et al. have shown that the average size of iron oxide nanoparticles can be tuned depending on the choice of carbon starting material (Figure 4.14).<sup>[134]</sup> Flake graphite, micrographite, and graphitic nanocarbon solutions with a differing carbon lattice size were treated with iron(II)-tetrafluoroborate salts in tetrahydrofuran leading in a decoration of the graphene sheets with iron oxide nanoparticles. For the smaller carbon lattice size, the authors also observed a smaller nanoparticle size. The higher dispersion, surface area, and electrical contact resulted in a better OER performance with an overpotential of 430 mV at 1 mA cm<sup>-2</sup> in 0.1 M KOH.

### Nickel Oxide-Containing Composites

Doped nickel oxides have the highest intrinsic OER activity among transition nonnoble metal oxide catalysts, but again a low electric conductivity limits the performance of these compounds especially in thick electrode layers. Hybridization with carbonaceous substrates is therefore actively pursued also for this class of compounds, with synthesis approaches similar to those described in the sections above. One of the best recently published catalysts based on NiO/C delivered a low overpotential of 220 mV with a Tafel slope of 55 mV dec<sup>-1</sup> in 1.0 M KOH solution.<sup>[135]</sup> Dehydrated sucrose sugar was

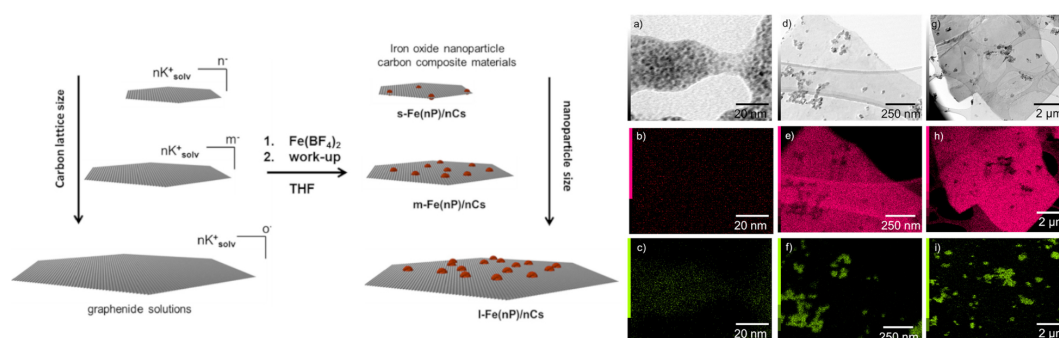


**Figure 4.14:** Left: Reaction scheme for the synthesis of different iron oxide nanoparticle carbon composite materials, right, a-i) HR-STEM images of the different composite material together with the corresponding iron edge and carbon edge energy-dispersive X-ray spectroscopy maps. Reproduced (adapted) with permission.<sup>[134]</sup> Copyright 2019, American Chemical Society.

used as carbon template for NiO nanostructures deposited in a facile wet chemical method.

Xu et al. used an elegant way to obtain nickel nanoparticles encapsulated in few-layer nitrogen-doped graphene,<sup>[35]</sup> which was realized via the pyrolysis of a Ni-based MOF obtained from 1,4-benzenedicarboxylic acid, triethylenediamine, and nickel nitrate. The thickness of the graphene layer and the level of nitrogen doping are dependent on the annealing temperature and could be tuned to achieve the maximum performance of the resulting catalyst. The highest OER activity was observed for the sample heated at 800 °C, which showed an overpotential of 280 mV at a current density of 10 mA cm<sup>-2</sup> in 1.0 M KOH and a relatively low Tafel slope of 45 mV dec<sup>-1</sup>, outperforming commercial IrO<sub>2</sub>. The authors concluded that the content and structure of the N-doped graphene layers as well as the electrochemically active surface area of the catalyst are crucial for the high OER activity.

In a probably unintended way, Silva et al. prepared a NiO hollow fiber/carbon composite showing a good electrochemical activity toward the OER with an overpotential of 340 mV at a current density of 10 mA cm<sup>-2</sup> with a Tafel slope of 84 mV dec<sup>-1</sup>.<sup>[136]</sup> The hollow fibers were prepared via solution blow spinning of nickel nitrate solution together with PVP followed by heating steps. Carbon from polyenic branch of PVP resisted the fring treatment and acted as an agglomerating agent, enabling a good conductivity between the formed NiO nanoparticles. Other reports include, e.g., NiO/CNT or NiO composite with N-doped graphene.<sup>[137–139]</sup>

An overview on recent metal (metal oxide)/carbon hybrid materials is provided in Table 4.4.

**Table 4.4:** Comparison of different TMO/carbon hybrids regarding the OER activity.

Transitionmetal elements	Carbon materi-als	Synthesis methods	Contents	Electrolytes	Potential [mV] versus RHE at 10 mA cm <sup>-2</sup>	Tafel slope [mV dec <sup>-1</sup> ]	Ref.
Co	N-doped carbon	MOF derived	Co ≈33 wt%	0.1 M KOH	1530	83	[122]
Co	Co <sub>3</sub> O <sub>4</sub> -embedded carbon/ rGO	MOF derived	N/A	0.1 M KOH	1612	62	[124]
Co	N-doped rGO	Hydrothermal synthesis	N/A	0.1 M KOH	1910	204	[101]
Co	CNT, GO, graphene	Precipitation method	N/A	1.0 M KOH	1765	157	[125]
Co	MWCNTs	Diethyltriamine directed anchoring	Co ≈49 wt%	1.0 M KOH	1539	51	[126]
Co	Amorphous, graphitic carbon	Solvothermal synthesis	Co ≈26.3 wt%	0.1 M KOH	1645	53	[127]
Co	B,N-decorated graphene	Precipitation method, NH <sub>3</sub> posttreatment	N/A	0.1 M KOH	1525	57	[128]
Co	Graphene	Electrochemical synthesis	Co ≈51.8 wt%	0.1 M KOH	1530	101	[129]
Co	rGO	Electrostatic interaction and growth	Co ≈7.4 wt%	1.0 M KOH	1576	47	[130]
Fe	Oxidized MWCNTs	Precipitation method	N/A	1.0 M KOH	1640	62	[131]
Fe	NiSx/rGO	Solvothermal synthesis	N/A	1.0 M KOH	1560	36	[132]
Fe	N,P-doped carbon nanofibers	Electrospinning	N/A	1.0 M KOH	1560	90	[133]
Fe	Graphenide	Precipitation method	Fe ≈15-20 wt%	0.1 M KOH	1690	40	[134]
Ni	Amorphous carbon	Facile wet chemical method	Ni ≈60-80 wt%	1.0 M KOH	1450	55	[135]
Ni	N-doped graphene	MOF derived	Ni ≈74.6 wt%	1.0 M KOH	1510	45	[35]
Ni	Carbon hollow fibers	Solution blow spinning	Ni ≈10 wt%	1.0 M KOH	1570	84	[136]
Ni	N-doped carbon	Precipitation method	Ni ≈18 wt%	0.1 M KOH	1576	70	[137]
Ni	CNTs	Precipitation method	N/A	1.0 M KOH	1531	82	[138]
Ni	Disordered and graphitic carbon	MOF derived	N/A	1.0 M KOH	1620	100	[140]

#### 4.4.2 Transition Metal Single-Atom Catalysts (SACs)

In recent years, SACs for OER have drawn great attention as the downsizing of nanoparticles is taken a step further in order to enhance the specific mass activity. However, reducing the metal particles size to nanoclusters or even to single atoms increases the surface free energy and makes their aggregation or Ostwald ripening easy. Anchoring and strong binding of SACs on a suitable support is therefore mandatory. Carbon-based materials have shown to facilitate the requirements for SACs as they offer a large surface area and promote a strong metal-support interaction by the implementation of heteroatoms leading to a coordinated single metallic atom center. Supported by computational calculations and advanced characterization techniques such as high-angle annular dark-field scanning-transmission electron microscopy (HAADF-STEM) and X-ray absorption spectroscopy, the structure and special catalytic activity of SACs can

be revealed.<sup>[141]</sup> More detailed reviews regarding the complete field of electrocatalytic applications of SACs have been published recently by Zhu et al.,<sup>[142]</sup> Zhang et al.<sup>[143]</sup> as well as by Lee et al. .<sup>[42]</sup>

Several synthetic strategies are commonly used to obtain atomically dispersed catalysts including pyrolysis of various precursors at high temperatures,<sup>[141]</sup> impregnation of the support material with metal precursor,<sup>[144–146]</sup> co-precipitation of different metal cations from solution, physical, and chemical deposition methods (e.g., atomic layer deposition or CVD)<sup>[142,143]</sup> and by chemical or photochemical reduction of the active species.<sup>[143]</sup>

A slightly different route was used by Wu et al. who grew a Co-based MOF on KCl particles and obtained nitrogen-doped carbon nanosheets with a high site fraction of single Co atoms of  $\approx 15.3$  wt% after pyrolysis at a temperature of 750 °C.<sup>[141]</sup> The presence of isolated Co atoms with a dot size of 0.10–0.40 nm on carbon sheets was confirmed by HAADF-STEM. More structural information about Co atoms was obtained from X-ray absorption fine structure (XAFS). A dominating Co–N coordination peak was attributed to a four coordination structure whereas no hint for Co–Co cluster existed. The highly dispersed Co on the nitrogen-doped carbon sheets led to a high electrocatalytic activity toward OER with an overpotential of 310 mV at 10 mA cm<sup>-2</sup> in 0.1 M KOH and a low Tafel slope of 74 mV dec<sup>-1</sup> outperforming conventional IrO<sub>2</sub> and Pt/C catalysts. Several other groups also investigated Co-based SACs on carbon-based materials and assigned the high catalytic activity to C–N<sub>4</sub> centers supported by DFT calculations and XAFS measurements.<sup>[144,146,147]</sup>

The atomically fine dispersion of iron atoms was analyzed by some researching groups as well.<sup>[148–150]</sup> Beside nitrogen-doping, additional sulfur doping of the carbon material showed a further enhancement of the catalytic activity. Pan et al. designed a polymerization–pyrolysis–evaporation strategy to synthesize atomically dispersed Fe–N<sub>4</sub> sites anchored on N-doped porous carbon.<sup>[151]</sup> After polymerization of urea and pyromellitic dianhydride in the presence of ZnCl<sub>2</sub> and FeCl<sub>3</sub>, the obtained product was heated at 920 °C for 3 h under Ar atmosphere followed by a leaching step in sulfuric acid. Structural characterization with HAADF-STEM and EXAFS measurements revealed homogeneously dispersed Fe on the carbon material with an Fe–N coordination. The resulting material delivered a potential of 1660 mV versus RHE at 10 mA cm<sup>-2</sup> in 1.0 M KOH and a low Tafel slope of 96 mV dec<sup>-1</sup>.

Single-atom nickel-based catalysts have shown the most promising results regarding the OER performance.<sup>[152–156]</sup> The herein reported materials only need overpotentials of  $\approx 230$ –330 mV in order to reach a current density of 10 mA cm<sup>-2</sup>. In a detailed study, Hou et al. showed that a quadruple coordination of Ni by nitrogen and/or sulfur inside a carbon nanosheet matrix resulted in a high electrochemical activity.<sup>[153]</sup> The material showed an outstanding performance with a small overpotential of 280 mV at 10 mA cm<sup>-2</sup> in 1.0 M KOH and a low Tafel slope of 45 mV dec<sup>-1</sup>, and a stable performance for over 2000 cycles.

Aforementioned transition metal elements were investigated in any arrangement

possible in order to get insights in coordination effects and to increase the already high catalytic activity further.<sup>[157–160]</sup>

Beside the typically used transition metals for OER, Guan et al. used a nature-inspired mononuclear manganese embedded in nitrogen-doped graphene.<sup>[161]</sup> The authors observed a remarkable catalytic activity comprising an overpotential of 337 mV at 10 mA cm<sup>-2</sup> in 1.0 M KOH and a low Tafel slope of 55 mV dec<sup>-1</sup>. The authors attributed the electrochemical activity to the mononuclear manganese ion coordinated with four nitrogen atoms in the graphene matrix, which was confirmed by structural characterization and DFT calculations.

An overview on recent SAC/carbon compounds is provided in Table 4.5. However, it should be noted that the research on SACs is still in the infant stage concerning synthesis, characterization, and mechanism studies at the same time. Therefore, promising future developments can be expected.

**Table 4.5:** Comparison of different metal single-atom/carbon hybrids regarding the OER activity.

Transitionmetal elements	Carbon materials	Synthesis methods	Electrolytes	Potential versus RHE at 10 mA cm <sup>-2</sup> [mV]	Tafel slope [mV dec <sup>-1</sup> ]	Ref.
Co	N-doped graphene	Impregnation method	1.0 M KOH	1616	73	[144]
Co	N-doped carbon	MOF derived	1.0 M KOH	1610	70	[147]
Co	CNTs	MOF derived	1.0 M KOH	1640	85	[146]
Co	N-doped graphene	MOF derived	0.1 M KOH	1540	74	[141]
Fe	N,S-doped graphitic carbon	Impregnation method	0.1 M KOH	1600	82	[148]
Fe	N-doped graphitic carbon	MOF derived	0.1 M KOH	1620	80	[149]
Fe	N,S-doped graphitic carbon	Impregnation method	0.1 M KOH	1640	59	[150]
Fe	N-doped porous carbon	Polymerization + pyrolysis	1.0 M KOH	1660	95	[151]
Ni	N-doped graphene	Hydrothermal synthesis	1.0 M KOH	1561	63	[152]
Ni	Porous carbon nanosheets	Hydrothermal synthesis	1.0 M KOH	1510	45	[153]
Ni	N-doped graphene	CVD + etching	1.0 M KOH	1500	59	[154]
Ni	Defective graphene	Impregnation method	1.0 M KOH	1500	47	[155]
Ni	Defective carbon	Impregnation method	1.0 M KOH	1454	42	[117]
Co,Fe	N-doped graphitic carbon	Impregnation method	1.0 M KOH	1539	37	[157]
Ni,Fe	Polymeric carbon nitride	Polymerization + pyrolysis	1.0 M KOH	1540	38	[158]
Fe,Ni	N-doped CNTs	Impregnation method	0.1 M KOH	1650	60	[159]
Co, Ni	N-doped porous, graphitic carbon	MOF derived	0.1 M KOH	1590	72	[160]
Mn	N-doped graphene	Impregnation method	1.0 M KOH	1567	55	[161]

#### 4.4.3 Mixed Metal Oxide/Carbon Composites for OER

##### Mixed TMO/Carbon Composites

Another group of popular composite materials for OER includes mixed metal oxides containing at least two different transition metals. Among investigated materials, the combination of cobalt and iron seems to be particularly promising. For example, Bian et

al. synthesized a nanosized composite based on  $\text{CoFe}_2\text{O}_4$  and graphene using simple hydrothermal method combining graphene oxide with respective metal nitrates.<sup>[162]</sup> The resulting composite delivered respectable performance for both ORR as well as OER and, importantly, a significant higher stability in OER than a reference Pt/C catalyst. The use of CNTs instead of graphene in another study resulted in an OER catalyst with a very low Tafel slope of  $30 \text{ mV dec}^{-1}$  and an overpotential of  $314 \text{ mV}$ .<sup>[163]</sup> The high catalytic activity was ascribed to the presence of PANI-modified CNTs offering more active sites for uniform  $\text{CoFe}_2\text{O}_4$  nanoparticles attachment leading to a good electrical contact and enhanced stability. Another way to tune the performance of  $\text{CoFe}_2\text{O}_4$ /graphene composite is to introduce doping as was shown in a recent paper by Madakannu et al.<sup>[164]</sup> The authors introduced nickel as a doping substitute for cobalt. The OER performance of the doped catalyst was dependent on the degree of doping, with  $\text{Co}_{0.75}\text{Ni}_{0.25}\text{Fe}_2\text{O}_4/\text{rGO}$  showing the highest performance. The same trend was also observed in another study where a similar approach was used.<sup>[165]</sup> In this case, the optimal ratio between Co and Fe was tested and an optimal value of  $\text{Co:Fe} = 2:1$  has delivered a low overpotential of  $337 \text{ mV}$  at  $10 \text{ mA cm}^{-2}$ . One of the best mixed metal oxide composite catalysts combines  $\text{Co}_3\text{Fe}_7\text{O}_x$  with nitrogen-doped graphene derived from Schiff bases.<sup>[166]</sup> Importantly, such a catalyst delivered current density of  $10 \text{ mA cm}^{-2}$  at an overpotential of  $328 \text{ mV}$  for at least 15 h with a low Tafel slope of  $31 \text{ mV dec}^{-1}$ .

Other metal ion combinations have been also reported, although the amount of respective publications is much lower than that of the compositions described above. For example, Xia et al. have synthesized  $\text{NiCo}_2\text{O}_4$  composite with hierarchical porous graphene-like material.<sup>[167]</sup> To further enhance its performance, the authors have introduced an additional doping with gold in an attempt to stabilize the active  $\text{Co}_{4+}$  and  $\text{Ni}_{3+}$  sites. Despite the porous structure of graphene support and the gold doping, the material did not outperform the already reported compounds and have demonstrated even larger overpotentials and lower current densities than the comparable materials reported by other groups.

**Table 4.6:** Comparison of different mixed metal oxide/carbon hybrids regarding their OER activity.

Metal oxide	Carbon materials	Synthesis methods	Electrolytes	Potential versus RHE at $10 \text{ mA cm}^{-2}$ [mV]	Tafel slope [mV $\text{dec}^{-1}$ ]	Ref.
$\text{CoFe}_2\text{O}_4$	rGO	Solvothermal synthesis	0.1 M KOH	1690	N/A	[162]
$\text{CoFe}_2\text{O}_4$	PANI-MWCNTs	Precipitation method	1.0 M KOH	1544	31	[163]
$\text{Co}_{0.75}\text{Ni}_{0.25}\text{Fe}_2\text{O}_4$	rGO	Microwave-assisted synthesis	0.1 M KOH	1670	85	[164]
$\text{Co}, \text{CoFe}_2\text{O}_4$	rGO	Hydrothermal synthesis	1.0 M KOH	1570	31	[165]
$\text{Co}_3\text{Fe}_7\text{O}_x$	N-doped carbon	Solvothermal synthesis, precipitation method	1.0 M KOH	1558	31	[166]
$\text{MnVO}_x$	N-doped rGO	Hydrothermal synthesis	0.1 M KOH	1650	271	[168]
$\text{Ni}_x\text{Fe}_y\text{O}_z$	Carbon nanofibers	Electrospinning	1.0 M KOH	1540	42	[169]

#### 4 Carbonaceous Oxygen Evolution Reaction Catalysts

$\text{NiO}_x @ \text{MnO}_x$	Graphene nanosheets	Layer-by-layer self-assembly method	1.0 M KOH	1602	40	[170]
$\text{NiCo}_2\text{O}_4$	Graphene nanosheets	Precipitation/hydrothermal method	0.1 M KOH	1680	164	[171]
$\text{MoO}_2 - \text{Co}_2\text{Mo}_3\text{O}_8$ (Fe, V, Co, Ni)-doped $\text{MnO}_2$	Carbon	MOF derived	1.0 M KOH	1550	88	[172]
	Carbon fiber paper	Co-electrodeposition	1.0 M KOH	1620	104	[173]
$\text{SrTi}_{0.1}\text{Fe}_{0.85}\text{Ni}_{0.05}\text{O}_{3-\delta}$	CNTs	Sol-gel synthesis + CVD	0.1 M KOH	1710	98	[174]
$\text{Sm}_{0.5}\text{Sr}_{0.5}\text{CoO}_{3-\delta}$	N-doped graphene	Electrospinning	0.1 M KOH	1630	115	[175]
$(\text{PrBa}_{0.5}\text{Sr}_{0.5})_{0.95}\text{Co}_{1.5}\text{Fe}_{0.5}\text{O}_{5+\delta}$	N-doped graphene	Electrospinning	0.1 M KOH	1550	74	[176]
$(\text{Nd}_{0.6}\text{Sr}_{0.4})_3((\text{CoFe})_{0.85}\text{Nb}_{0.15})_2\text{O}_7$	S-doped carbon tubes	Sol-gel synthesis + CVD	1.0 M KOH	1650	89	[177]
$\text{LaNiO}_3$	N-doped CNTs	Sol-gel synthesis + CVD	0.1 M KOH	1620	78	[178]

In terms of graphene support, nitrogen-doped graphene seems to be particularly popular due to its inherently high conductivity, which promotes the overall OER activity. Such a support was used for the  $\text{CuCo}_2\text{O}_4$  and  $\text{MnVO}_4$ -based composite catalysts.<sup>[168]</sup> In both cases, the hybrid catalysts performed much better than the unsupported counterparts, which confirms the synergistic effect of graphene matrix. Importantly, both composite materials exhibited relatively low overpotentials with that of  $\text{CuCo}_2\text{O}_4$  being superior with the value of 360 mV.<sup>[168]</sup>

While anchoring the metal oxide nanoparticles on the surface of carbonaceous materials is probably the most popular way to obtain composite catalysts, the other hybrid morphologies such as nanowires with embedded nanoparticles can also be prepared. Thus, Chen et al. have prepared a composite catalyst using Ni- and Fe-embedded PVP polymer nanofibers as precursors.<sup>[169]</sup> In the next step, the precursor was heated in air at 250 °C to form the nickel-iron oxide/carbon composite material. The catalyst prepared in this way is competitive with ruthenium and iridium oxides for OER. Its activity most likely originates from the interconnected fibrous structure that makes the active sites easily accessible. Importantly, the overpotential to reach the current density of 10 mA cm<sup>-2</sup> can be as low as 310 mV for optimized catalyst composition and loading.

Apart from the inherent catalytic activity of composite materials, there is also a question of long-term stability as was shown in a paper by Wang et al.<sup>[170]</sup> In their work, the authors combined nanocrystalline nickel oxide with amorphous manganese oxide suspended on graphene nanosheets. Despite the promising initial catalytic activity, the catalytic activity of this material has deteriorated within few hours of continuous use. Other mixed metal oxide composite materials include, e.g., doped  $\text{MnO}_2$  supported on carbon fibers,  $\text{MoO}_2 - \text{Co}_2\text{Mo}_3\text{O}_8 @ \text{C}$ , or  $\text{NiCo}_2\text{O}_4$  nanoplatelets on graphene support. Although none of these catalysts has exhibited outstanding OER performance yet (see also Table 4.6), the published papers open a way to the nearly endless possible combinations of transition metals and carbonaceous support, which could enable the discovery of an active and stable composite OER catalyst in the future.<sup>[171-173]</sup>

### Perovskite/Carbon Composites

A special class of inorganic materials for carbon composite formation is represented by perovskites with a general formula  $ABO_3$ . The perovskite structure is thereby highly versatile, with tunable properties allowing classical applications as electro-ceramic dielectrics, metallic conductors, superconductors, or light absorbing or emitting semiconductors.<sup>[179–181]</sup> The possibility of partial substitution of A and/or B site cations leading to a formal  $A_{1-x}A'_x B_{1-y}B'_y O_3$  composition allows to precisely tune the materials properties and the electronic structure, which was exploited for the fabrication of highly active perovskite OER catalyst in the recent years.<sup>[175,182,183]</sup> However, a main issue concerning the application of most perovskites is their rather limited electronic conductivity, with few exceptions (e.g.,  $LaNiO_{3-\delta}$ ) that are not necessarily OER active and vice versa (Figure 4.15).<sup>[184]</sup>

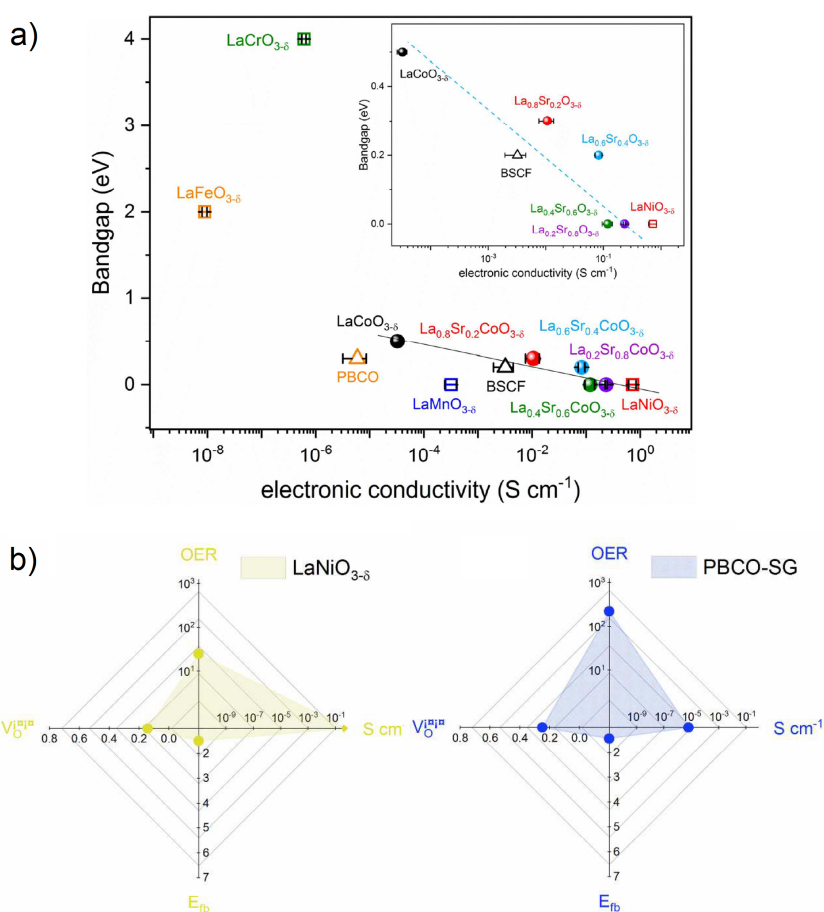


**Figure 4.15:** a) Conductivity of various perovskite composition versus DFT-calculated band gaps. b) Profile of  $LaNiO_{3-\delta}$  and  $PBCO-SG$  ( $PrBaCo_2O_{6-\delta}$ ) powders combining OER activity with conductivity, amount of oxygen vacancies and the flatband potential. Reproduced (adapted) with permission.<sup>[184]</sup> Copyright 2018, American Chemical Society.

In addition, high calcination temperatures required for the perovskite synthesis often lead to the formation of relatively large crystalline domains, which further reduce the number of OER available active sites. This fact renders carbon composite formation a valid solution to increase the overall conductivity, which was intensively explored in the recent years. However, the carbon/perovskite composites also show various synergistic effects that further enhance the overall OER activity. A detailed summary is given in a recommended recent work by Zhu et al.<sup>[18]</sup>

The factors influencing the OER activity of the perovskite-containing composites include the filling of the perovskite  $E_g$  band (which is influenced by the B-site cation), the number of oxygen vacancies of the perovskite, the nanomorphology of the inorganic phase, and the formed perovskite/carbon interface, as well as the amount and chemical nature (graphene, CNTs, etc., including heteroatom doping) of the carbon structure.<sup>[18,184,185]</sup>

Synergistic effects of carbon and perovskite regarding OER catalysis depicted in Figure 4.16 are the ligand effect based on an electronic interaction of two neighboring metals or oxides (in this case carbon and perovskite). This charge delocalization is commonly believed to enhance the intrinsic conductivity and leads to more favorable adsorption energies of OER intermediates, increasing the overall OER activity of the composite.<sup>[18,175]</sup>

A second major synergistic effect discussed in the literature is the formation of interfacial heterostructures originating from the formation of covalent bonds between two neighboring phases, or the formation of a new phase with enhanced catalytic activity.<sup>[18,174]</sup>

Finally, a spillover effect may enhance the OER performance by transferring the product species oxygen to the neighboring carbon surface to liberate active sites and therefore increase the catalytic turnover.<sup>[18]</sup>

Recent examples of perovskite/carbon composites catalyst for water oxidation include the sol-gel synthesis of micrometer-sized  $\text{SrTi}_{0.1}\text{Fe}_{0.85}\text{Ni}_{0.05}\text{O}_{3-\delta}$  (STFN) perovskite particles, which are coated by CNTs via a CVD method with a reported temperature optimum of 700 °C. The resulting STFN/CNT-700 fabricated by Wu et al. shows an onset potential of 1.59 V versus RHE and a reported overpotential of 480 mV to reach 10 mA  $\text{cm}^{-2}$  with a stable operation over 30 h. In this work, the synergistic effect of the perovskite/carbon composite was validated by a reference experiment, in which perovskite and commercially available CNTs intermixed only physically without formation of chemical bonds. The reference compound exhibited a higher conductivity but showed a lower electrochemical performance as compared to the CVD grown CNTs directly on the perovskite structure.<sup>[174]</sup>

The synergistic effects in perovskite/carbon composites were demonstrated also by Bu et al. who performed DFT calculations that were validated experimentally. In this work, the authors presented the rational synthesis of porous, perovskite-type  $\text{Sm}_{0.5}\text{Sr}_{0.5}\text{CoO}_{3-\delta}$  hollow nanofibers (SSC-HF) that were hybridized with cross-linked, 3D, N-doped graphene (3DNG) resulting in a hybrid catalyst denoted as SSC-HF-3DNG

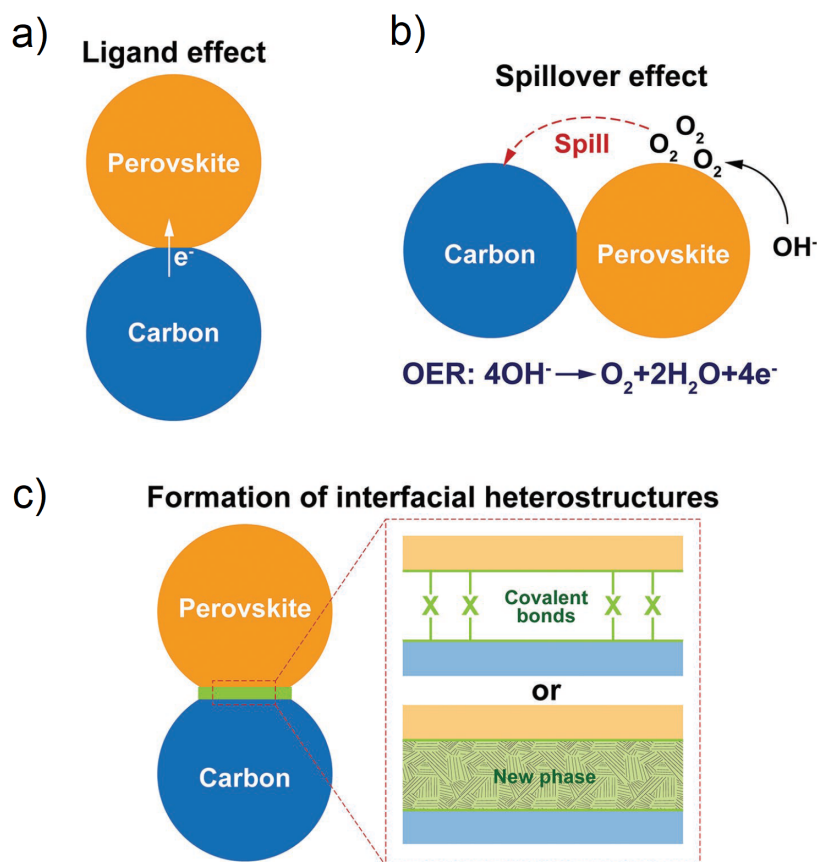


**Figure 4.16:** Schematic illustration of possible origins of the synergistic effect toward OER catalysis between the perovskite and carbon structure: a) ligand effect; b) spillover effect, and c) formation of interfacial heterostructures. Reproduced (adapted) with permission.<sup>[18]</sup> Copyright 2017, Wiley-VCH.

(SSC-HG).<sup>[175]</sup> The materials were obtained via electrospinning of metal salt precursor, pore forming Pluronic F127 polymer, additional oil for the introduction of micropores, and PAN polymer as further carbon source. After calcination, a hybrid structure of hollow porous fibers with a diameter of around 150 nm and high surface area of over  $21 \text{ m}^2 \text{ g}^{-1}$  for the perovskite alone is obtained. The 3D, N-doped graphene structure has provided a high conductivity and further enhanced the OER activity of the perovskite by synergistic effects investigated by theoretical methods. DFT calculations (Figure 4.17a, b) suggest an electron transfer from the N-doped carbon to cobalt atoms of the perovskite structure, which thereby increases the d-band center of these atom and leads to a higher degree of Co-oxygen hybridization by a higher overlap of the Co 3d and O 2p band (Figure 4.17b). These interactions are beneficial for the OER as they promote the activation and participation of lattice oxygen.<sup>[175]</sup> The SSC-HG exhibits a high OER activity with a low onset potential of 1.53 V versus RHE and an overpotential of 400 mV to reach a current density of  $10 \text{ mA cm}^{-2}$ , which outperforms the  $\text{IrO}_2$

reference under same conditions.<sup>[175]</sup>

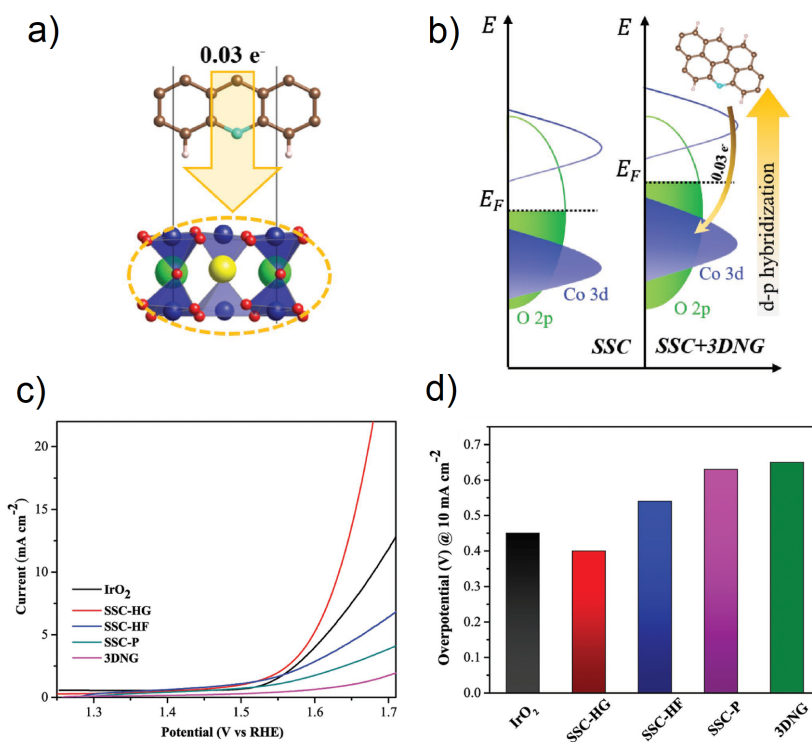


**Figure 4.17:** DFT calculation configuration of perovskite (SSC) and 3D-N-doped (3DNG) carbon (SSC-HG) and the corresponding electron transfer. b) Schematic band diagrams of SSC and SSC+3DNG. The electron transfer from 3DNG enhances the orbital hybridization between Co 3d and O 2p and enhances the OER activity. c) Polarization curves and d) overpotentials at a current density of  $10 \text{ mA cm}^{-2}$  in 0.1 M KOH solution of SSC-HG, SSC-HF (perovskite without 3DNG), SSC-P (bulk perovskite), 3DNG, and IrO<sub>2</sub>. Reproduced (adapted) with permission.<sup>[175]</sup> Copyright 2018, Wiley-VCH.

In a second work by the same authors, a 3DNG obtained via electrospinning and calcination was employed for the formation of a composite hollow and porous fiber structure with the cationordered perovskite ( $\text{PrBa}_{0.5}\text{Sr}_{0.5})_{0.95}\text{Co}_{1.5}\text{Fe}_{0.5}\text{O}_{5+\delta}$  (PBSCF).<sup>[176]</sup> The composite electrode showed a remarkably low onset potential of 1.52 V versus RHE compared to 1.51 V versus RHE for IrO<sub>2</sub> tested under the same conditions and a overpotential of only 320 mV to reach a current density of  $10 \text{ mA cm}^{-2}$ , which outperformed the IrO<sub>2</sub> reference ( $\eta_{\text{OER}} = 440 \text{ mV}$ ) significantly. The high OER activity of the composite was again explained by an increased covalency between transition metals and lattice oxygen in PBSCF triggered by the electron transfer of 3DNG, as has been shown above for a similar morphology but with different perovskite active material. The OER active sites are thereby supposed to be located not on the carbon but rather on the PBSCF, which is regarded to be positively affected by the interaction with the

N-doped carbon framework.<sup>[176]</sup>

A last example introduced by Bu et al. introduces the formation of a composite catalyst consisting of Ruddlesden–Popper-type S-adsorbed  $(\text{Nd}_{0.6}\text{Sr}_{0.4})_3((\text{Co}_{\text{Fe}})_{0.85}\text{Nb}_{0.15})_2\text{O}_7$ , metal sulfides, and hollow S-doped carbon fibers as depicted in Figure 4.18.<sup>[177]</sup> The synthesis approach includes the formation of an  $\text{Nd}_{0.4}\text{Sr}_{0.6}\text{Co}_{0.6}\text{Fe}_{0.3}\text{Nb}_{0.1}\text{O}_{3-\delta}$  matrix (S-NSCFNb), which is transformed to a Co-Fe nanoparticle-coated perovskite structure termed R-NSCFNb upon reduction in  $\text{H}_2$  atmosphere. The final composite catalyst (C-NSCFNb), which contains hollow S-doped carbon tubes at the surface, is formed in a combined carbonization and sulfurization step in  $\text{C}_3\text{H}_8/\text{H}_2\text{S}$  at  $600\text{ }^\circ\text{C}$ . The composite catalyst exhibits a remarkably high OER performance in alkaline media with an onset potential of 1.48 V versus RHE, significantly outperforming the Co-Fe nanoparticle decorated perovskite (R-NSCFNb) with 1.51 V versus RHE or an  $\text{IrO}_2$  reference electrode under same measurement conditions. The low overpotential required to reach  $10\text{ mA cm}^{-2}$  of 420 mV and an outstanding stability of 370 h under continuous operation exceeds other literature reports on the stability of perovskite OER catalysts.<sup>[177]</sup>

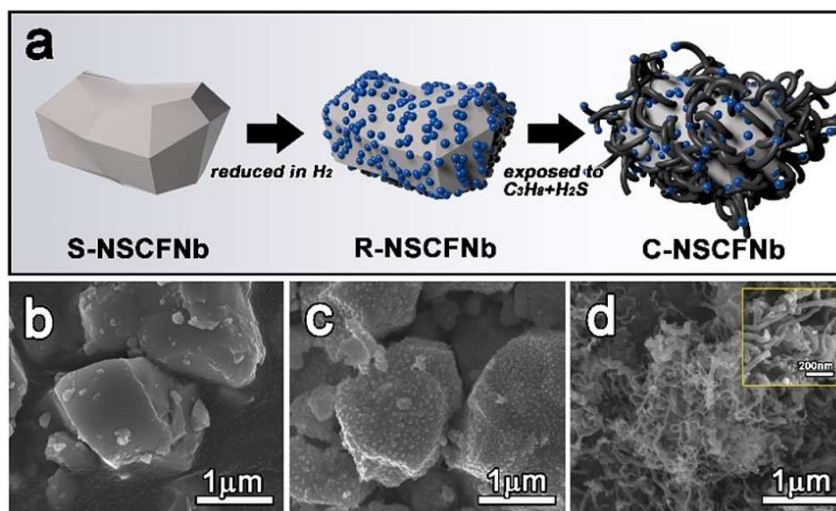


**Figure 4.18:** a) Schematic illustration of the synthesis procedure of C-NSCFNb; b-d) SEM images of  $(\text{Nd}_{0.6}\text{Sr}_{0.4})_3((\text{Co}_{\text{Fe}})_{0.85}\text{Nb}_{0.15})_2\text{O}_7$  (S-NSCFNb), Co-Fe nanoparticle-coated perovskite (R-NSCFNb), and final composite catalyst with hollow S-doped carbon tubes (C-NSCFNb). Reproduced (adapted) with permission.<sup>[177]</sup> Copyright 2019, Wiley-VCH.

Other perovskite/carbon composite systems investigated recently include a  $\text{LaNiO}_3$  nanoparticle/N-doped CNT composite catalyst prepared by Chen et al. , which exhibits a remarkable OER activity with a reported overpotential of 390 mV to reach a current density of  $10\text{ mA cm}^{-2}$  outperforming a  $\text{RuO}_2$  reference under same measurement conditions. The high OER activity was attributed to the employed polyol synthesis method yielding small perovskite nanoparticles with more exposed active site and a strong binding of the N-doped CNTs to the  $\text{LaNiO}_3$  phase, which facilitates charge transfer and increases the OER activity by synergistic effects.<sup>[183]</sup>

The introduced examples of perovskite/carbon composite OER catalysts show only a recent and small cutout of the overwhelming variety that can be achieved for this class of material by changes in composition, nanomorphology and synthesis procedures (e.g., carbonization or posttreatments). By combining synthetic approaches with theoretical methods, further knowledge about the electronic structure of respective composites could be gained that guides a rational synthesis toward further improved OER catalysts.

#### 4.4.4 Metal/Metal Oxide/Carbon Composites for OER

Another interesting group of materials suitable as composite catalysts for OER are metal/metal oxides combined with conductive carbonaceous support. The advantage of these materials stems from their intrinsic high catalytic activity. Another advantage is the presence of metal oxide on the surface of deposited metal particles, which ensures that the catalysts are generally much less prone to further oxidation, making them stable for OER. Nickel and cobalt are particularly popular for this purpose as will be discussed further on. Using nickel nitrate and nitrogen-doped graphene, Faisal et al. have prepared conductive composite material with Ni/NiO nanoparticles dispersed over the graphene support.<sup>[186]</sup> The morphology of this composite material is shown in Figure 4.19a–f and its OER performance in Figure 4.19g–j. This catalyst exhibited good electrochemical performance in ORR, HER as well as OER where it delivered performance similar to commercial Ru/C catalyst (see Figure 4.19g).

Similar method using a hydrothermal treatment instead of simple heat treatment resulted in a graphene aerogel decorated with Ni/NiO nanoparticles in a different paper.<sup>[187]</sup> It was shown that the OER overpotential is strongly dependent on the nickel content, where the overpotential values decreased gradually with nickel content reaching a low overpotential value of 320 mV at 10 mA cm<sup>-2</sup>. Although high electrocatalytic activity is one of the key properties for catalysts, their mechanical properties also play a critical role as they should be as robust and/or flexible as possible. One of the feasible ways to improve mechanical properties is to deposit OER active materials on top of carbon fibers as was shown recently for Ni/NiO.<sup>[188]</sup> Such a catalyst was prepared by electrodeposition of Ni followed by calcination to introduce surface oxidation of nickel coating. Due to the fibrous structure, the material can be transformed into various shapes. Even under mechanical stress such a catalyst can deliver the current density of 10 mA cm<sup>-2</sup> at an overpotential of 300 mV. The authors ascribed this to the formation of Ni (III) species on the interface between carbon fibers and deposited layer. Finally, similar catalyst can be prepared using CNTs.

Another popular metal employed in metal/metal oxides composites is cobalt with several reports in the literature. The OER performance of these materials is similar to those described in the previous paragraphs with overpotentials around 350 mV at 10 mA cm<sup>-2</sup>. The synthetic methods were also quite similar to previous reports.<sup>[189,190]</sup>

Recent examples of metal/metal oxide/carbon-based hybrid materials are also summarized in Table 4.7.

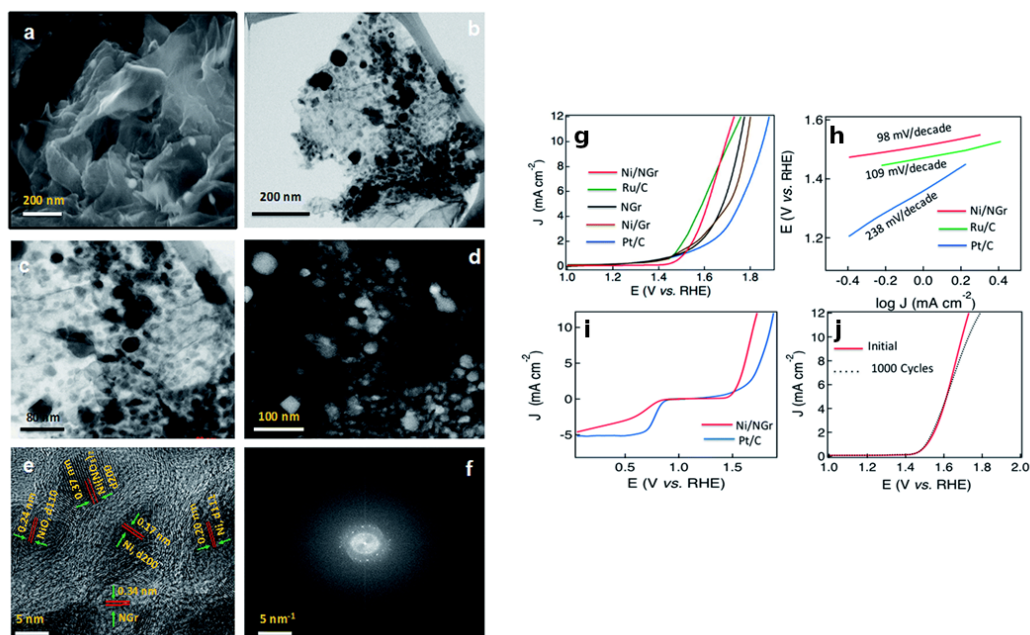


**Figure 4.19:** a) SEM, b) TEM, c) bright-field STEM, d) HAADF-STEM and e) HRTEM images of nickel/nickel oxide with N-doped graphene. e) The lattices of nickel and nickel oxide nanoparticles embedded into the graphene lattice are marked in the HRTEM image; f) the corresponding FFT image of Ni/NGr showing adjacent nickel atoms with the hexagonal graphene pattern. g) LSV curves of Ni/NGr, Ru/C, NGr, Ni/Gr, and Pt/C at a scan rate of  $10 \text{ mV s}^{-1}$  in  $0.1 \text{ M KOH(aq)}$ . h) The Tafel plots of Ni/NGr, Ru/C, and Pt/C. i) LSV curves of Ni/NGr and Pt/C on an RDE (1600 rpm) in  $\text{O}_2$ -saturated  $0.1 \text{ M KOH(aq)}$  at a scan rate of  $10 \text{ mV s}^{-1}$  showing the electrocatalytic activities toward both ORR and OER. j) Comparison of LSV curves of Ni/NGr initially and after 1000 cycles for the OER. Reproduced (adapted) with permission.<sup>[186]</sup> Copyright 2018, The Royal Chemical Society.

**Table 4.7:** Comparison of different perovskite/carbon composites and metal/metal oxide composites with carbon regarding their OER activity.

Metal oxide	Carbon materials	Synthesis methods	Electrolytes	Potential [mV] versus RHE at $10 \text{ mA cm}^{-2}$	Tafel slope [ $\text{mV dec}^{-1}$ ]	Ref.
Ni, NiO	N-doped graphene	Impregnation + annealing	$0.1 \text{ M KOH}$	1620	98	[186]
Ni, NiO	Graphene aerogel	Solvothermal method + annealing	$0.1 \text{ M KOH}$	1550	61	[187]
Ni, NiO	Carbon fibers	Electrodeposition	$1.0 \text{ M KOH}$	1530	60	[124]
Ni, NiO	Carbon fibers	Solution blow spinning	$1.0 \text{ M KOH}$	1508	88	[191]
Ni, NiO	3D porous carbon	Carbonization + calcination	$1.0 \text{ M KOH}$	1583	97	[192]
Ni, $\text{Co}_3\text{O}_4$	N-doped carbon	Impregnation + annealing	$1.0 \text{ M KOH}$	1580	52	[193]
Co, $\text{Co}_3\text{O}_4$	N-doped carbon nanosheets	MOF derived	$0.1 \text{ M KOH}$	1580	94	[189]
Co, $\text{Co}_3\text{O}_4$	N-doped graphene	Freeze drying + thermal treatment	$0.1 \text{ M NaOH}$	1684	92	[190]

## 4.5 Carbon-Based Ordered Framework Structures

MOFs and COFs are classes of porous materials that consist of metal (or organic nodes) and organic linkers, offering a huge structure variability. Due to the high amount of carbon atoms, MOF and COF materials can be classified to a certain degree as carbon-based compounds. Therefore, they are discussed in this review as well. The molecular structure and resulting properties of MOFs and COFs can be precisely modulated by the selection of different building blocks with various functionalities, thus influencing structural characteristics like porosity or crystallinity and electronic properties like band gap or conductivity. Hence, MOFs and COFs can be designed for application as OER catalyst as well.<sup>[194–197]</sup> OER catalytic active MOFs and COFs structures are comprised of functional organic motives that contain heteroatoms like O, N, S, P, B. Moreover, in case of MOFs, catalytic active elements like Fe, Co, Ni, Mn can be chosen as metal nodes, which could additionally enhance the OER activity.<sup>[197,198]</sup> Another important feature of MOFs and COFs is their large surface area and high porosity enabling a good accessibility of the active sites accompanied by a rapid mass transport.<sup>[197]</sup> Moreover, the high porosity of MOF and COF structures can also be used to incorporate highly catalytic active guest species such as metal-containing particles. The periodicity of the pore structure with controllable size, morphology and location of the pores enables the rational location of the catalytic guest species, which can induce synergistic effects between the host structure and the guest species resulting typically in an improved overall catalytic activity (Figure 4.20).<sup>[197,199]</sup>

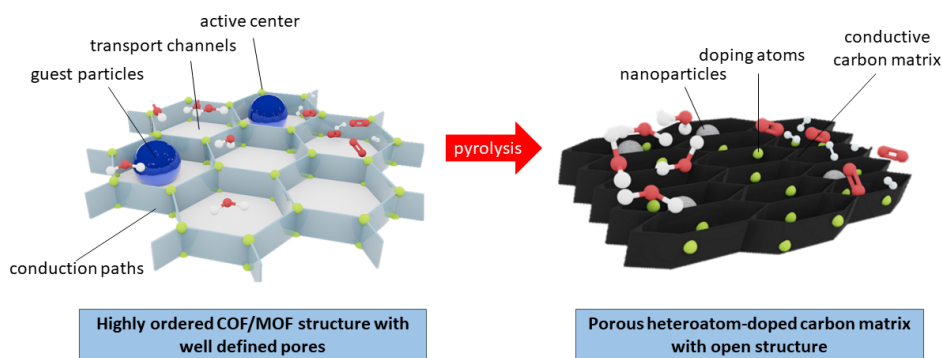


**Figure 4.20:** Schematic presentation of an organic framework with the well-defined pores offering various possibilities of metal- and heteroatom doping and guest particle storage.

A major drawback of MOFs and COFs is however their typically low electrical con-

ductivity, which can nevertheless be alleviated by the addition of conductive supports such as CNTs, carbon fibers or reduced graphene oxide.<sup>[196,200–202]</sup> Another issue of many MOF and COF materials is their often limited chemical stability under acidic or basic conditions, which hamper their application as OER catalysts.<sup>[200,203]</sup>

Besides being used directly as OER electrocatalyst, MOFs and COFs can serve as precursors or templates for the synthesis of even more active nanostructures such as heteroatom-doped carbons, transition metal-functionalized carbons, or metal oxides/sulfides/nitrides/carbides,<sup>[197,198,204–207]</sup> depending on the applied postsynthetic conditions.

The different strategies of designing MOF and COF-based catalysts for OER will be discussed in the following two sections. The interested reader is also referred to the recently published reviews by Liang et al.,<sup>[205]</sup> Quin et al.,<sup>[206]</sup> Xue et al.,<sup>[198]</sup> and Zheng et al.<sup>[199]</sup> dealing mainly with MOF and MOF-derived OER catalysts.

#### 4.5.1 MOFs

There are only few publications reporting the OER catalysts of pristine MOF materials, which is mainly due to their low electrical conductivity as mentioned above. 2D MOFs seems to be however an interesting option as they have typically a sheets thickness of only a few nanometers, which enables a fast mass and charge carrier transport accompanied by a large amount of easily accessible catalytic centers.<sup>[208,209]</sup> Xing et al., e.g., reported a 2D hexaaminotriphenylene Co-MOF ( $\text{Co}_3(\text{HITP})_2$ ), which demonstrates a relative high conductivity of up to  $11.5 \text{ S cm}^{-1}$ .<sup>[200]</sup> The conductivity is induced by an in-plane  $\pi$ -d conjugated network formed by hybrids of transition metal node d-orbitals and frontier orbits of the conjugated ligands. Beside the good conductivity, the porous structure and the high amount of catalytic active Co-N<sub>4</sub> centers are additionally assigned as the main reasons for the excellent OER activity of  $\text{Co}_3(\text{HITP})_2$  resulting in a low overpotential of 254 and 300 mV to reach 10 and 50  $\text{mA cm}^{-2}$ , respectively, and a low Tafel slope of  $86.5 \text{ mV dec}^{-1}$  outperforming  $\text{IrO}_2$  and  $\text{RuO}_2$  reference catalysts drastically. Moreover,  $\text{Co}_3(\text{HITP})_2$  is also very stable under electrocatalytic conditions showing only 1 % decay at a current density of  $16 \text{ mA cm}^{-2}$  within 12 h. Additionally, the morphology and microstructure of  $\text{Co}_3(\text{HITP})_2$  remain stable during the long-term measurement. Only the Co(II) nodes are oxidized to Co(III) which is however quite common, as Co(II) is the active phase toward OER.<sup>[200]</sup>

A further strategy for increasing the electrical conductivity and using pristine MOFs for OER was reported by Xue et al. who introduced missing linkers into a cobalt terephthalate MOF structure by partially replacing the terephthalate linkers by carboxyferrocene (Fc) (Figure 4.21).<sup>[210]</sup> Introducing Fc into the MOF structure induced a change of the electronic structure and generated catalytically highly active unsaturated  $\text{Co}^{2+}$  sites resulting in a drastically improved electrocatalytic performance. The defective MOF arrays that were directly grown on a nickel foam substrate (CoBDC-Fc-NF) revealed a very low overpotentials of 178 mV to reach  $10 \text{ mA cm}^{-2}$  and 267 mV to obtain  $500 \text{ mA cm}^{-2}$ , outperforming the nonfunctionalized CoBDC-NF material (365 mV,

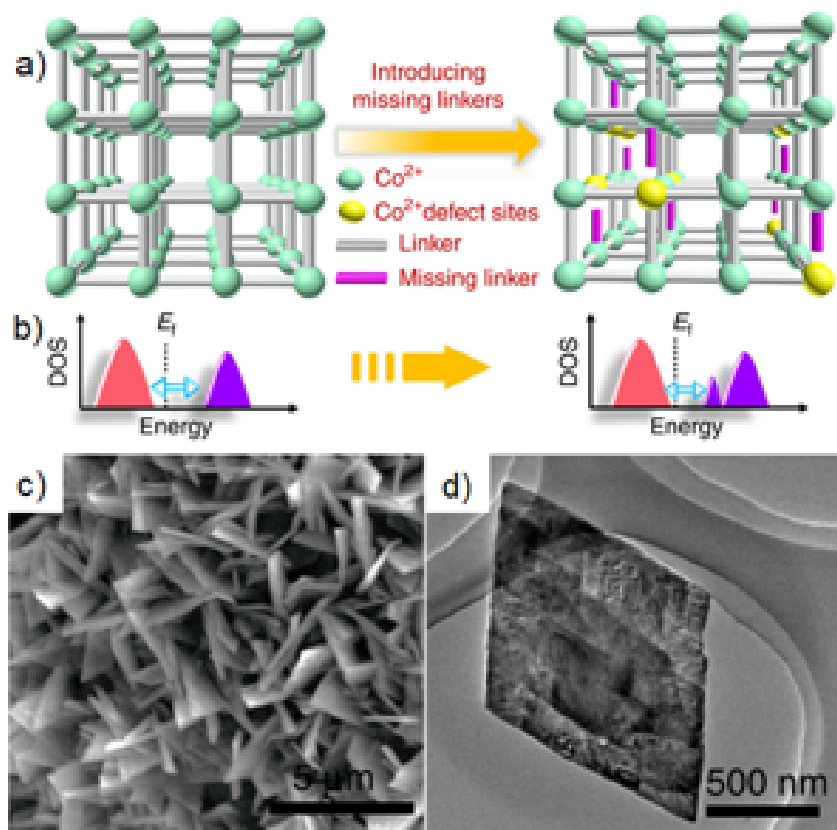


**Figure 4.21:** a) Schematic structures of Co-MOF and missing linker Co-MOF, b) influencing their electronic structures; c) SEM and d) TEM images of the missing linker Co-MOF (CoBDC-Fc-NF). Reproduced (adapted) with permission.[125] Copyright 2019, The Authors. Published by Nature Research.

500  $\text{mA cm}^{-2}$ ) and a  $\text{RuO}_2$ -NF reference catalyst (557 mV, 500  $\text{mA cm}^{-2}$ ). The high electrocatalytic activity was accompanied by a high stability with almost no change in the catalytic activity during 80 h chronopotentiometric measurements at 100  $\text{mA cm}^{-2}$ .<sup>[210]</sup>

The use of bimetallic or multimetallic MOFs is another strategy to increase the conductivity and the catalytic activity of MOFs through synergistic effects.<sup>[198,208,209,211–215]</sup> Yang et al. , e.g., prepared different Co,Ni and Co,Fe 2D MOFs and analyzed their catalytic performance. The CoFe-MOF demonstrated the highest activity yielding an overpotential of 355 mV to obtain 10  $\text{mA cm}^{-2}$ , thus outperforming the monometallic Co-MOF (397 mV at 10  $\text{mA cm}^{-2}$ ). Interestingly, the bimetallic CoNi-MOF has an inferior catalytic activity featuring a higher overpotential (501 mV at 10  $\text{mA cm}^{-2}$ ) as compared to Co-MOF.<sup>[208]</sup> Another Co,Fe 2D MOF reported by Xu et al. has an even lower overpotential of 277 mV to reach 10  $\text{mA cm}^{-2}$ . The superior performance can be assigned to the unique interpenetrating mesopore and micropore networks of the MOF, which is very favorable to achieve a high accessibility of the catalytic active sites and enable a rapid mass transport.<sup>[216]</sup>

For a more detailed overview on multimetallic MOF OER catalysts, the interested reader is recommended to the minireview of Xue et al.<sup>[198]</sup>

The formation of MOF/carbon composites can be another strategy to improve the electrical conductivity and thus the OER activity. Different MOF/carbon heterostructures have been reported using, e.g., rGO,<sup>[202,214,217,218]</sup> CNTs,<sup>[201,219]</sup> or carbon black<sup>[220,221]</sup> as carbonaceous support materials. Zheng et al. combined the strategies of using a bimetallic MOF and a carbonaceous support. The bimetallic porphyrin-based CoNi-MOF has superior electrocatalytic properties (381 mV at 10 mA cm<sup>-2</sup>) as compared to the monometallic Co- and Ni-MOFs (432 and 435 mV at 10 mA cm<sup>-2</sup>, respectively). The performance of the bimetallic CoNi-MOF can be further improved by formation of a composite with rGO. The resulting CoNi-MOF/rGO composite has an overpotential of 318 mV at 10 mA cm<sup>-2</sup>. The good performance can be ascribed to the synergistic effects between the CoNi-MOF and rGO. Thereby, rGO improves the overall conductivity and prevents the CoNi-MOF nanosheets from agglomeration, thus increasing the amount of accessible catalytic sites.<sup>[222]</sup> Recently, Thangavel et al. reported a trimesic acid-based NiFe-MOF/graphene nanoplatelet (GNP) composite, which has a superior OER performance with a very small overpotential of 220 mV to obtain 10 mA cm<sup>-2</sup> outperforming the monometallic Ni-MOF (317 mV) and the bimetallic NiFe-MOF (240 mV).<sup>[218]</sup> The performance can be further increased by replacing the carbon fiber paper substrate by 3D nickel foam resulting in an overpotential of 180 mV to obtain 20 mA cm<sup>-2</sup>. Moreover, the NiFe-MOF/GNP composite has also a high durability with no obvious change in activity during a 96 h measurement at an applied potential of 10 mA cm<sup>-2</sup>. The authors attributed the excellent performance to the increased electrical conductivity achieved by using GNPs as conducting support and a partial replacement of the Ni nodes by Fe. A further advantage of the NiFe-MOF/GNP composite is its fast charge transfer kinetics. The authors evaluated the performance of the NiFe-MOF/GNP composite also as an anode for the OER in alkaline anion exchange membrane water electrolysis (AAEMWE) using MoNi<sub>4</sub>/MoO<sub>2</sub> as cathode and ultra-pure water as electrolyte. The AAEMWE reached a high current density of 540 mA cm<sup>-2</sup> at an applied cell voltage of 1.85 V accompanied by a superior stability of >1000 h in continuous electrolysis, which renders MOF-based materials suitable for practical application.<sup>[218]</sup>

In the mentioned examples, the carbonaceous materials are used as conducting supports improving the electrical conductivity at the macroscopic scale. On the local level, however, the limited conductivity of MOFs is still an issue caused by size exclusion effects that are defined by the pore aperture, hence hindering the full exploitation of the inherent OER potential of MOFs.<sup>[199,223]</sup> Using graphene oxide as an integral building unit in the construction of MOFs could be a possible strategy to utilize the full OER potential of MOF materials.<sup>[223]</sup>

The porous structure of MOF materials renders them also an ideal host for OER active metal and metal-based nanoparticles. The MOF framework typically confines the size and the shape of the incorporated catalysts and prevents them from leaching and agglomeration during the electrocatalytic relations, thus resulting in a highly

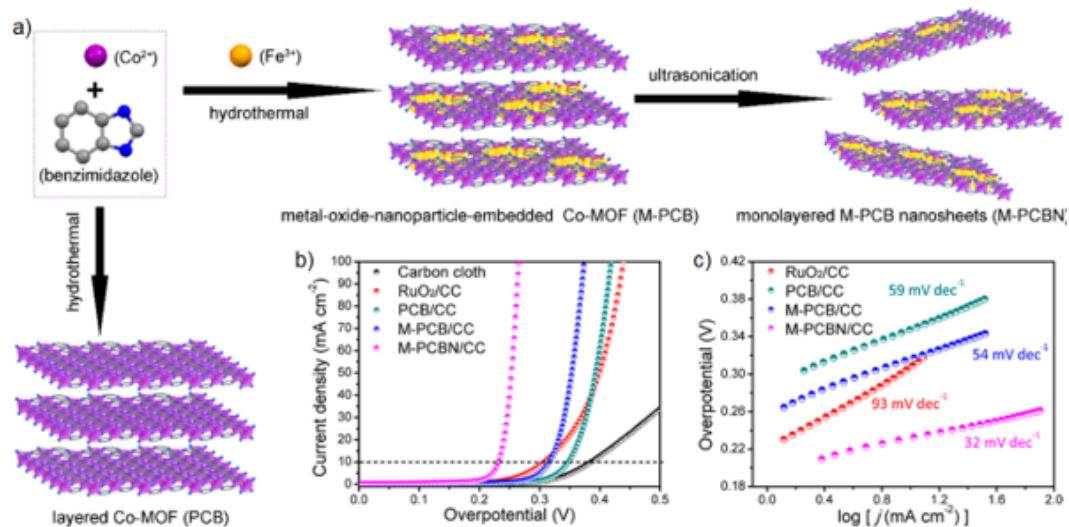


**Figure 4.22:** a) Synthesis scheme of pristine (PCB), CoFeO<sub>x</sub> nanoparticle-embedded bulk (M-PCB), and monolayered CoFeO<sub>x</sub>-embedded Co-MOF. b) Polarization curves and c) Tafel plots of these Co-MOF materials coated onto carbon cloth substrate. Reproduced (adapted) with permission.[131] Copyright 2020, American Chemical Society.

active and stable OER performance.<sup>[197,199]</sup> A nanoparticle-functionalized MOF was recently reported by Zhang et al. who prepared CoFeO<sub>x</sub> nanoparticles embedded into a monolayered benzimidazole-based Co-MOF (M-PCBN) (Figure 4.22a).<sup>[224]</sup> The M-PCBN demonstrated a drastically improved electrocatalytic performance as compared to the bulk equivalent and the pristine MOF which resulted in overpotentials of 232, 316, and 348 mV at 10 mA cm<sup>-2</sup>, respectively (Figure 4.22b), demonstrating the benefits of introducing highly catalytic active nanoparticles. Beside a very small Tafel slope of 32 mV dec<sup>-1</sup> (Figure 4.22c), M-PCBN also exhibited good electrocatalytic stability evidenced by a 60 h chronoamperometric measurement at 1.48 V versus RHE. The authors also demonstrated that the OER performance is highly dependent on the utilized substrate. Coating M-PCBN onto copper foam instead of CC resulted in an even lower overpotential of 185 mV at 10 mA cm<sup>-2</sup>. As the main active catalytic sites, high-valent Co atoms located at the interface of the CoFeO<sub>x</sub> nanoparticles and the M-PCBN framework were suggested, which was also supported by spin-polarized DFT calculations. The Fe atoms were shown to be inactive toward OER due to their saturated octahedral configuration.<sup>[224]</sup>

Formation of nanoparticles inside the MOF framework can be also achieved by a controlled partial pyrolysis strategy, which preserves the skeleton structure of the MOF while generating catalytic highly active nanoparticles.<sup>[225]</sup> MOFs and their modified/functionalized analogs can be also pyrolyzed or calcined completely serving as periodically arranged precursors for preparation of doped carbons, metal incorporated (doped) carbons, and diverse metal-containing compounds with a controlled

morphology.<sup>[206]</sup> In this context, the interested reader on MOF-derived carbon-based materials and composites is also advised to the recently published reviews by Wang et al.<sup>[226]</sup> and Du et al..<sup>[207]</sup>

As has been mentioned in Section 2, metal-free doped carbons are of great interest as OER catalysts. However, the homogenous distribution of the dopants inside the carbon structure is very challenging. In contrast, MOFs exhibit a homogenous distribution of the heteroatoms which can be even maintained after pyrolysis. MOFs containing low boiling point metal nodes can even be used for the formation of metal-free doped carbons, as these metals are carbothermally reduced and evaporated during the pyrolysis procedure.<sup>[227,228]</sup>

The standard approaches for catalyst synthesis usually produce materials that suffer from aggregation and low electrical conductivity. For this reason, MOFs have been shown to be promising templates for advanced catalyst design. One of reported examples uses MOFs based on  $MFe_2O_4$  (where  $M = Mn, Fe, Co, Ni$ ) and 2,5-dioxido-1,4-benzenedicarboxylic acid.<sup>[229]</sup> Via a simple pyrolysis of PANI-decorated nickel foams, one can obtain a porous composite material (Figure 4.23a) whose performance and stability are shown in Figure 4.23b-e. The resulting material has a highly porous structure, which enables facile electron transfer and results in an overall high OER catalytic performance with overpotential values as low as 240 mV. The use of nickel foam as a porous support has also been reported previously.<sup>[230]</sup> Similarly, structured composite material based on Co oxides can be prepared by a two-step thermal conversion strategy. Unlike the previously mentioned material, this composite exhibits much higher overpotential and a lower Tafel slope possibly due to lower porosity of the mentioned composite material. An interesting concept of design was reported by Sun et al.<sup>[231]</sup> The authors used core-shell structure of particles with the composition of  $Co_xNi_{1-x}@Co_yNi_{1-y}O$ . Due to used MOFs precursor, a highly porous nanostructured material was obtained whose performance was highly dependent on the composition of the core as well as shell particles. Optimal performance was achieved using the molar Co:Ni ratio of 1:1. The reported synthetic route paves the way for future composites with even higher OER performance.

Apart from the composition of MOFs, their morphology also plays a crucial role in the OER activity of the catalysts. In a recent paper, the authors compared 1D, 2D, and 3D MOFs as supports for Co, Ni, and Cu oxides.<sup>[232]</sup> Their findings show that the as-prepared composites were highly oriented and, importantly, delivered the overpotential of 208 mV at  $10 \text{ mA cm}^{-2}$  for  $Co_3O_4/C$  composite. This value is one of the best for MOFs-derived composites in the literature.

#### 4.5.2 COF Structures

Besides MOFs, COF-based materials attracted recently considerable attention for application as OER catalysts. COFs consist of organic building blocks that are linked reversibly by covalent bonds resulting in crystalline porous organic polymers with a controllable and predictable porous structure. COFs are very interesting as their

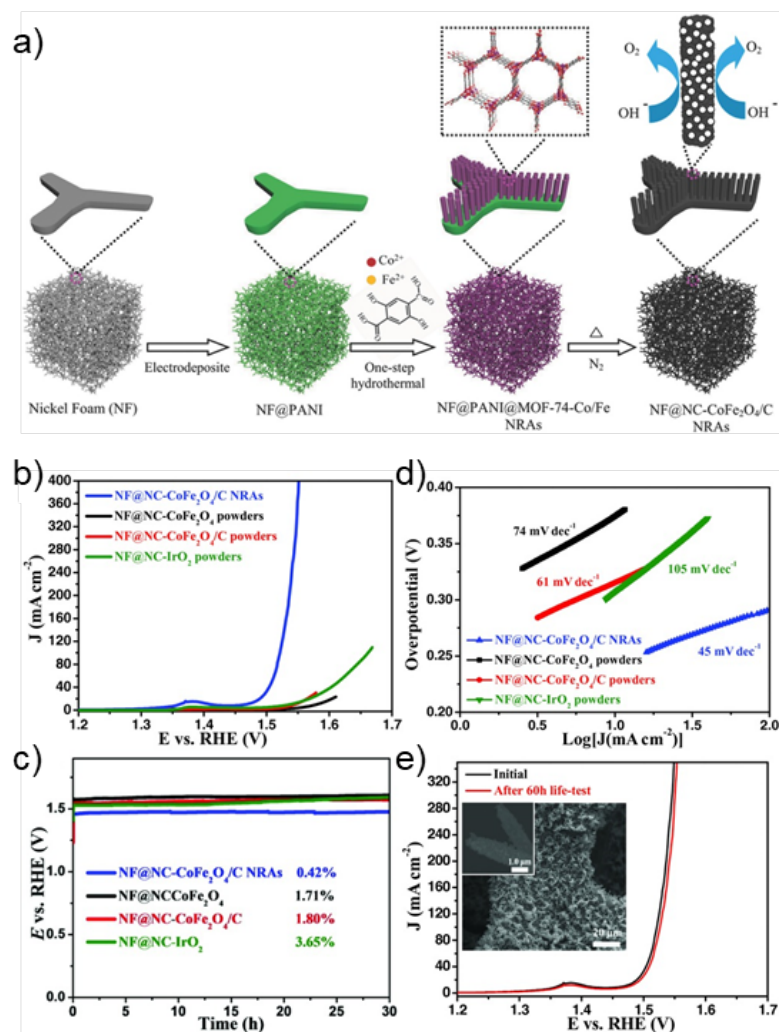


**Figure 4.23:** a) Schematic illustration of PANI-assisted synthesis of a bimetal-organic framework NRAs and its derived porous CoFe<sub>2</sub>O<sub>4</sub>/C NRAs. b) LSV curves, c) Tafel plots and d) chronopotentiometry curves of NF@NC-CoFe<sub>2</sub>O<sub>4</sub>/C NRAs composite samples in 1 M KOH solution. e) Durability test of the composite materials. Reproduced (adapted) with permission.[135] Copyright 2016, Wiley-VCH.

porosity, pore size and their electronic and catalytic properties can be controlled by the design of the building blocks and their linkage motives.<sup>[194,233–235]</sup> In order to design OER active COF structures, the results on heteroatomdoped graphene are often used as a scaffold. On this basis, DFT calculations reported by Yang et al. proposed a high OER activity for a phenazine-linked 2D-COF (COF-C<sub>4</sub>N) featuring a graphene like structure, an N-enriched character, hexagonal pores, and a good chemical stability, which was confirmed experimentally (Figure 4.24). COF-C<sub>4</sub>N demonstrates an excellent OER activity and stability equaling to an overpotential of 349 mV at 10 mA cm<sup>-2</sup> outperforming other N-doped carbonaceous materials. Partial DOS and molecular or-

bital wave function calculations revealed that the C4 sites as the mainly active catalytic centers inside the COF-C<sub>4</sub>N structure, resulting in a preferential downhill trend in the corresponding reaction pathway calculation.<sup>[236]</sup>

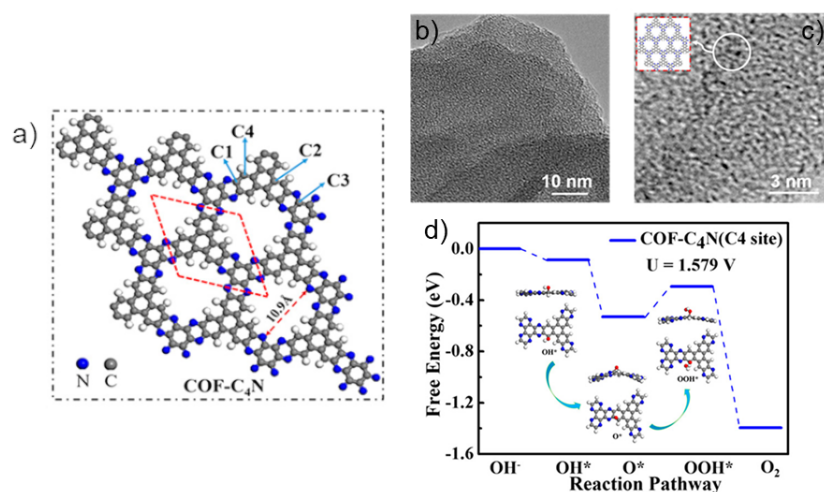


**Figure 4.24:** a) Schematic sequence of a theoretically optimized COF-C<sub>4</sub>N monolayer. b) TEM images of COF-C<sub>4</sub>N demonstrating the stacking of the individual monolayers and c) the hexagonal pores. d) Free energy diagram for the OER pathway of COF-C<sub>4</sub>N and the schematic reaction processes at the mainly active C4-site. Reproduced (adapted) with permission.<sup>[140]</sup> Copyright 2019, American Chemical Society.

The thiadiazole-based COF reported by Mondal et al. exhibits an even lower overpotential of 320 mV to reach a current density of 10 mA cm<sup>-2</sup> outperforming the benchmark catalyst IrO<sub>2</sub>/C.<sup>[234]</sup> Moreover, the authors also demonstrated that the crystallinity of the analyzed COFs plays a substantial role for OER activity. The thiadiazole-based COF is additionally very stable as shown by time-dependent chronopotentiometry measurements current densities of up to 50 mA cm<sup>-2</sup>. Post analytical characterization after the stability test revealed no change in the crystalline structure. The active site inside the COF structure was calculated to be the C2-site confirming the practical results.<sup>[234]</sup>

The electrocatalytic performance can be further enhanced by introducing co-catalysts like Co,<sup>[194,235,237,238]</sup> Ni,<sup>[239,240]</sup> Fe,<sup>[239,240]</sup> V,<sup>[237]</sup> Ni<sub>3</sub>N,<sup>[241]</sup> Ni(OH)<sub>2</sub>,<sup>[242]</sup> or Co(OH)<sub>2</sub><sup>[242]</sup> into the COF framework. Gao et al. reported, e.g., a COF-SO<sub>3</sub>H obtained by a condensation reaction of 2,5-diaminobenzenesulfonic and 2,4,6-triformyl-phloroglucinol, which was further functionalized by ammoniation to obtain NH<sub>4</sub>@COF-SO<sub>3</sub>. The NH<sub>4</sub>@COF-SO<sub>3</sub> material was then used to synthesize metalincorporated Ni<sub>x</sub>Fe<sub>1-x</sub>@COF-SO<sub>3</sub> and Co<sub>x</sub>V<sub>1-x</sub>@COF-SO<sub>3</sub> via cation exchange reactions.<sup>[237,239]</sup> The metal-free NH<sub>4</sub>@COF-SO<sub>3</sub> system demonstrated a rather poor OER activity equaling to an overpotential of 543 mV to reach 10 mA cm<sup>-2</sup>.<sup>[239]</sup> However, the incorporation of the metallic species drastically improved the electrocatalytic performance. The highest activity was reported for Co<sub>0.5</sub>V<sub>0.5</sub>@COF-SO<sub>3</sub> with an overpotential of 318 mV to reach



The materials having both micro- and macropores are beneficial for the fast mass transport and especially for enhancing the diffusion-limited OER. The microporosity yields a high surface area providing more active sites, which ameliorate the formation of O<sub>2</sub> via the OER reaction. The macropores enable a high fast transport of the formed O<sub>2</sub> bubbles away from the surface.<sup>[235]</sup> Synthesis of COFs with large pores is however quite challenging. Zhao et al. developed a new strategy to assemble COFs with their inherent microporous nature into a superstructure having interconnected macropores by using monodisperse polystyrene (PS) spheres as hard template (Figure 4.25a). Moreover, the bipyridine units of the resulting macroporous COF (macro-TpBpy) can be used to coordinate Co(OAc)<sub>2</sub> (macro-TpBpy-Co) (Figure 4.25b) while still maintaining the macroporosity as evidenced by SEM image (Figure 4.25c).<sup>[235]</sup> Functionalization of macro-TpBpy with Co-containing species drastically improves the OER activity resulting in overpotentials of 380 and 430 mV to reach 10 and 50 mA cm<sup>-2</sup>, respectively, as compared to the pure macro-TpBpy COF that is practically inactive. Moreover, due to the macroporous structure of macro-TpBpy-Co, the mass transfer and the accessibility of the active sites are increased, which is especially beneficial at high applied potentials equaling to high oxygen pressures.<sup>[235]</sup>

COFs typically contain a large number of uniformly distributed heteroatoms like B, N, O and S,<sup>[216,243,244]</sup> which make COFs attractive precursors for heteroatom-doped carbons. The advantage of using doped carbons have been intensively discussed in Sections 1 and 3. Additionally, carbonization of the highly porous COF materials results typically in porous carbons. A high porosity can be beneficial for the infiltration with electrolyte increasing the accessibility of the catalytic active sites and a rapid charge transfer.<sup>[244,245]</sup> In order to ensure the porosity after the pyrolysis step, the use of templates can be helpful as was demonstrated by Xu et al. In their work, a 2D triazine-based COF was functionalized with phytic acid as a template, resulting after pyrolysis in hierarchical porous N,P-co-doped 2D carbons. The COF-derived carbons exhibited an excellent OER performance reaching a current density of 10 mA cm<sup>-2</sup> at a potential of 1.99 V versus RHE drastically outperforming the Pt/C reference catalyst (1.01 mA cm<sup>-2</sup> at 1.99 V vs RHE).<sup>[243]</sup>

The combination of high porosity and a large amount of functional groups renders COFs also suitable hosts for uniformly incorporated and anchored metal-containing species as mentioned above. The resulting modified COFs can be additionally converted into porous carbons loaded with metal or metal oxide nanoparticles. The pores of the COFs thereby limit the growth of the metal (metal oxide) particles, prevent them from aggregation and migration, and assure their homogenous distribution in the resulting carbon material.<sup>[216,246]</sup> Using this strategy, Co<sub>3</sub>O<sub>4</sub>,<sup>[247]</sup> FeS,<sup>[248]</sup> RuO<sub>2</sub>,<sup>[246]</sup> Fe/Co,<sup>[244]</sup> and Ni/Fe<sup>[216]</sup> carbon composites have been successfully prepared and evaluated as OER catalysts. Among the mentioned examples, the RuO<sub>2</sub>/carbon composite exhibited the highest OER activity. Micro-mesoporous N-rich carbons with homogeneously distributed RuO<sub>2</sub> nanoparticles were derived by heating a triazinebased COF (IISERP-COF1) loaded with Ru(acac)<sub>3</sub> at 370 °C in air. The composite revealed a cur-

rent density  $10 \text{ mA cm}^{-2}$  at a potential of 1.44 V versus RHE.<sup>[246]</sup>

A compact overview of COF and COF-based materials is given in Table 4.8.

**Table 4.8:** Comparison of different MOF/COF-based materials regarding their OER activity.

Material	Electrolytes	Potential [mV] versus RHE at $10 \text{ mA cm}^{-2}$	Tafel slope [mV dec <sup>-1</sup> ]	Ref.
2D Co-MOF	1.0 M KOH	1484	86.5	[200]
Defective Co-MOF	1 M KOH	1408	51	[210]
2D Co,Fe-MOF	0.1 M KOH	1585	49.1	[208]
2D Co,Ni-MOF		1731	107.9	
Mesoporous 2D Co,Fe-MOF	1 M KOH	1507	31	[209]
Fe,Co,Mn,Ni-MOF-74@Ni-foam	1 M KOH	1480@ $50 \text{ mA cm}^{-2}$	41.3	[215]
Co,Ni-MOF	1.0 M KOH	1611	75	[150]
Co,Ni-MOF/rGO		1548	48	
Ni,Fe-MOF	1 M KOH	1470	55	[218]
Ni,Fe-MOF/graphene nanoplatelets		1450	51	
CoFeO <sub>x</sub> nanoparticle/Co-MOF/carbon cloth	1.0 M KOH	1462	32	[224]
CoFeO <sub>x</sub> nanoparticle/Co-MOF@Cu-foam		1415	N/A	
NiCo/Fe <sub>3</sub> O <sub>4</sub> /MOF-74	1.0 M KOH	1468	29	[225]
MOF-derived CoFe <sub>2</sub> O <sub>4</sub> /C nanorods@NC-coated Ni-foam	1.0 M KOH	1370	45	[229]
MOF-derived core-shell Co <sub>x</sub> Ni <sub>1-x</sub> @Co <sub>y</sub> Ni <sub>1-y</sub> @C	0.1 M KOH	≈1810	126	[231]
MOF-derived 2D Co <sub>3</sub> O <sub>4</sub> /C	1 M KOH	1490	50.1	[232]
MOF-derived 2D Cu <sub>2</sub> O/S-doped C		1543	65.6	
Thiadiazol-based COF	1 M KOH	1550	39	[234]
Highly conjugated 2D COF	1.0 M KOH	1579	64	[236]
Co/macro-microporous COF	0.1 M KOH	1610	54	[235]
Co/COF	Phosphate buffer pH = 7	1630	59	[194]
Co/COF@Cu-foam	1 M KOH	1500	99	[238]
Co <sub>0.5</sub> V <sub>0.5</sub> /COF	1.0 M KOH	1548	62	[237]
Ni <sub>0.5</sub> Fe <sub>0.5</sub> /COF	1 M KOH	1538	83	[239]
Cyclen/Ni <sub>0.5</sub> Fe <sub>0.5</sub> /COF	1.0 M KOH	1506	43	[240]
Ni(OH) <sub>2</sub> /COF	0.1 M KOH	1488	38.9	[242]
COF-derived 2D nanocarbon	0.1 M KOH	1875	N/A	[243]
Ni/Fe-clusters/COF-derived C/CNT	0.1 M KOH	1550	61	[216]
Fe,Co/COF-derived C	1 M KOH	1600	91	[244]
RuO <sub>2</sub> /COF-derived C	1 M KOH	1440	65	[246]
ZIF-67/COF-derived Co <sub>3</sub> O <sub>4</sub> /N-doped C	1 M KOH	1560	79	[247]
FeS/Fe <sub>3</sub> C/COF-derived N,S co-doped C	1 M KOH	1800	81	[248]

## 4.6 Conclusion and Perspective

Carbonaceous OER catalysts gained considerable attention in the recent years due to their high structural and compositional variety and ultimately by their promising electrocatalytic activity competing with or surpassing that of conventional metal oxide or metal hydroxide electrodes and even noble metal reference electrodes, mostly under alkaline conditions. The outstanding OER activity with low overpotentials is achieved due to the combination of high intrinsic OER activity provided by defect and heteroatom-doped structures, high possible surface areas, and also due to the high electrical conductivity. Based on the analysis of the most recent developments, the intention of this review was to highlight the material parameters with applied synthesis approaches that influence the OER activity of carbon atoms as active sites in such catalysts and hybrid structures. Strategies such as defect engineering and heteroatom doping were discussed. Although these strategies are undoubtedly required to induce the OER activity of carbon atoms in carbonaceous materials, they often decrease the electrical conductivity that is however required for an overall high OER electrode activity and becomes decisive at high current densities.

3D (porous) N-doped as well as multiheteroatom-doped graphene type carbon structures are considered the best nanomorphology for “pure” or hybrid carbonaceous OER catalysts known today. Hybrid catalysts employing these structures together with nano-sized transition metal or metal oxide particles reach a current density of  $10 \text{ mA cm}^{-2}$  at overpotentials as low as  $\approx 300 \text{ mV}$  for S, N co-doped carbon and  $\approx 315 \text{ mV}$  for hybrid structures such as NiO/C. This can be explained by a combination of a high surface area and conductive network heteroatom-doped carbon structure, the highly OER active inorganic nanoparticles with high available surface area, and additional synergistic effects further enhancing the OER activity of neighboring carbon atoms due to a modulation of the electronic structure. However, the wet-chemical or vapor-based synthesis methods that are typically employed for fabrication of these structures provide limited possibilities for a rational design and arrangement of heteroatoms around active site carbon atoms.

A relatively new group of promising OER active materials is SACs. The main advantages of SACs are their high surface area and the strong metal-support interaction resulting in a promising OER activity. Research is however still in the infant stage, as synthesis of single metal atoms or at least nanoclusters without aggregation is quite challenging.

A main focus of this work was also dedicated to the relatively recent advances in the field of ordered 3D carbon (COF) and carbon/metal (MOF) framework structures for OER catalysis, which are envisioned to possess the potential for highly active carbon-based OER catalyst in the future. The 3D framework structures offer various advantages over classical 3D porous carbon. Through the choice of molecular linkers and metallic (MOF) or carbonaceous (COF) nodes, their geometry and composition can be precisely tuned, providing a defined porosity and a defined spatial location and content of the heteroatoms. By the choice of specific building blocks (e.g., electron donor or acceptor moieties), the electronic structure of the crystalline framework structures can further be manipulated, possibly enabling a faster electron/hole transfer from the catalytically active sites on the surface and throughout the structure also by an enhanced electrical conductivity.

The framework structures can also be pyrolyzed to further increase their electrical conductivity. This approach of ordered framework structures for OER catalysis already led to the formation of composite catalysts with outstanding performance surpassing that of nonordered structures. For a defective cobalt MOF on a nickel foam substrate, the overpotential as low as  $178 \text{ mV}$  at a current density of  $10 \text{ mA cm}^{-2}$  was reported, combined with a high stability upon potential cycling and continuous operation. Metal-free COF structures also showed promising OER performances, with the lowest overpotential of  $320 \text{ mV}$  at  $10 \text{ mA cm}^{-2}$  reported for a thiadiazole-based COF, outperforming an IrO<sub>2</sub>/C benchmark catalyst.

The structural and compositional control in periodic framework materials can also be used to attach small OER active transition metal (metal oxide) nanoparticles or SACs via functional groups or coordination sites incorporated by the molecular building blocks.

---

This strategy enables a rational design and precise control over spatial distribution of catalytically active sites not accessible in conventional 3D carbon structures, which may further be used to deepen our understanding of the OER mechanism on carbonaceous materials and synergistic effects of metal/carbon structures.

## 4.7 Acknowledgements

The authors gratefully acknowledge funding from the German Federal Ministry of Education and Research (BMBF) within the Kopernikus Project P2X: Flexible use of renewable resources – research, validation and implementation of "Power-to-X" concepts (Project number DBD01751). The work was supported by the Deutsche Forschungsgemeinschaft (DFG, German Research Foundation) under Germany's Excellence Strategy – EXC 2089/1 – 390776260 (e-conversion Cluster of Excellence). J.L. and Z.S. were supported by Czech Science Foundation (GACR no. 20–16124J). Open access funding enabled and organized by Projekt DEAL.

## References

- [1] S. Oberthür, C. Roche Kelly, *Int. Spect.* **2008**, *43*, 35–50.
- [2] U. D. o. E. -. DOE, Dollars from Sense - The Economic Benefits of Renewable Energy, Report, National Renewable Energy Laboratory (U.S. Department of Energy - DOE), **1997**.
- [3] S. Inage, *Wiley Interdiscip. Rev.: Energy Environ.* **2015**, *4*, 115–132.
- [4] N. Armaroli, V. Balzani, *ChemSusChem* **2010**, *4*, 21–36.
- [5] M. E. Lyons, S. Floquet, *Phys. Chem. Chem. Phys.* **2011**, *13*, 5314–35.
- [6] M. Bernt, A. Hartig-Weiß, M. F. Tovini, H. A. El-Sayed, C. Schramm, J. Schröter, C. Gebauer, H. A. Gasteiger, *Chem. Ing. Tech.* **2020**, *92*, 31–39.
- [7] M. S. Burke, S. Zou, L. J. Enman, J. E. Kellon, C. A. Gabor, E. Pledger, S. W. Boettcher, *J. Phys. Chem. Lett.* **2015**, *6*, 3737–42.
- [8] M. S. Burke, L. J. Enman, A. S. Batchellor, S. Zou, S. W. Boettcher, *Chem. Mater.* **2015**, *27*, 7549–7558.
- [9] D. Adler, *Radiat. Eff.* **1970**, *4*, 123–131.
- [10] Y. Matsumoto, E. Sato, *Mater. Chem. Phys.* **1986**, *14*, 397–426.
- [11] B. Marinho, M. Ghislandi, E. Tkalya, C. E. Koning, G. de With, *Powder Technol.* **2012**, *221*, 351–358.
- [12] R. Zhang, A. Palumbo, J. C. Kim, J. Ding, E.-H. Yang, *Ann. Phys.* **2019**, *531*, 1800507.

- [13] G. Wu, A. Santandreu, W. Kellogg, S. Gupta, O. Ogoke, H. Zhang, H.-L. Wang, L. Dai, *Nano Energy* **2016**, *29*, 83–110.
- [14] L. Zhang, J. Xiao, H. Wang, M. Shao, *ACS Catal.* **2017**, *7*, 7855–7865.
- [15] J. Lai, A. Nsabimana, R. Luque, G. Xu, *Joule* **2018**, *2*, 76–93.
- [16] X. Deng, J. Li, L. Ma, J. Sha, N. Zhao, *Mater. Chem. Front.* **2019**, *3*, 2221–2245.
- [17] M. A. Younis, S. Lyu, Q. Zhao, C. Lei, P. Zhang, B. Yang, Z. Li, L. Lei, Y. Hou, X. Feng, *BMC Mater.* **2019**, *1*, 6.
- [18] Y. Zhu, W. Zhou, Z. Shao, *Small* **2017**, *13*, 1603793.
- [19] M. Chen, L. Wang, H. Yang, S. Zhao, H. Xu, G. Wu, *J. Power Sources* **2018**, *375*, 277–290.
- [20] M. Wu, J. Liao, L. Yu, R. Lv, P. Li, W. Sun, R. Tan, X. Duan, L. Zhang, F. Li, J. Kim, K. H. Shin, H. Seok Park, W. Zhang, Z. Guo, H. Wang, Y. Tang, G. Gorgolis, C. Galiotis, J. Ma, *Chem. – Asian J.* **2020**, *15*, 995–1013.
- [21] H.-F. Wang, C. Tang, Q. Zhang, *Adv. Funct. Mater.* **2018**, *28*, 1803329.
- [22] D. Wei, Y. Liu, Y. Wang, H. Zhang, L. Huang, G. Yu, *Nano Letters* **2009**, *9*, 1752–1758.
- [23] T. Dürkop, B. M. Kim, M. S. Fuhrer, *J. Phys.: Condens. Matter* **2004**, *16*, R553–R580.
- [24] G. Pennington, A. Akturk, N. Goldsman in International Semiconductor Device Research Symposium, 2003, pp. 412–413.
- [25] X. Wu, C. Tang, Y. Cheng, X. Min, S. P. Jiang, S. Wang, *Chem. - Eur. J.* **2020**, *26*, 3906–3929.
- [26] V. Mazánek, J. Luxa, S. Matějková, J. Kučera, D. Sedmidubský, M. Pumera, Z. Sofer, *ACS Nano* **2019**, *13*, 1574–1582.
- [27] M. Li, L. Zhang, Q. Xu, J. Niu, Z. Xia, *J. Catal.* **2014**, *314*, 66–72.
- [28] G. Murdachaew, K. Laasonen, *J. Phys. Chem. C* **2018**, *122*, 25882–25892.
- [29] A. J. Medford, A. Vojvodic, J. S. Hummelshøj, J. Voss, F. Abild-Pedersen, F. Studt, T. Bligaard, A. Nilsson, J. K. Nørskov, *J. Catal.* **2015**, *328*, 36–42.
- [30] S. Chen, J. Duan, M. Jaroniec, S.-Z. Qiao, *Adv. Mater.* **2014**, *26*, 2925–2930.
- [31] A. M. El-Sawy, I. M. Mosa, D. Su, C. J. Guild, S. Khalid, R. Joesten, J. F. Rusling, S. L. Suib, *Adv. Energy Mater.* **2016**, *6*, 1–12.
- [32] Y. P. Zhu, Y. Jing, A. Vasileff, T. Heine, S.-Z. Qiao, *Adv. Energy Mater.* **2017**, *7*, 1602928.
- [33] X. Liu, I. S. Amiinu, S. Liu, K. Cheng, S. Mu, *Nanoscale* **2016**, *8*, 13311–13320.
- [34] I. C. Man, H.-Y. Su, F. Calle-Vallejo, H. A. Hansen, J. I. Martínez, N. G. Inoglu, J. Kitchin, T. F. Jaramillo, J. K. Nørskov, J. Rossmeisl, *ChemCatChem* **2011**, *3*, 1159–1165.

- 
- [35] Y. Xu, W. Tu, B. Zhang, S. Yin, Y. Huang, M. Kraft, R. Xu, *Adv. Mater.* **2017**, *29*, 1605957.
- [36] Y. P. Zhu, C. Guo, Y. Zheng, S.-Z. Qiao, *Acc. Chem. Res.* **2017**, *50*, 915–923.
- [37] H.-S. Oh, H. N. Nong, T. Reier, A. Bergmann, M. Gliech, J. Ferreira de Araújo, E. Willinger, R. Schlögl, D. Teschner, P. Strasser, *J. Am. Chem. Soc.* **2016**, *138*, 12552–12563.
- [38] S. Cherevko, T. Reier, A. R. Zeradjanin, Z. Pawolek, P. Strasser, K. J. J. Mayrhofer, *Electrochem. Commun.* **2014**, *48*, 81–85.
- [39] Y. Yi, G. Weinberg, M. Prenzel, M. Greiner, S. Heumann, S. Becker, R. Schlögl, *Catal. Today* **2017**, *295*, 32–40.
- [40] S. Geiger, O. Kasian, A. M. Mingers, S. S. Nicley, K. Haenen, K. J. J. Mayrhofer, S. Cherevko, *ChemSusChem* **2017**, *10*, 4140–4143.
- [41] I. S. Filimonenkov, C. Bouillet, G. Kéranguéven, P. A. Simonov, G. A. Tsirlina, E. R. Savinova, *Electrochim. Acta* **2019**, *321*, 134657.
- [42] W. H. Lee, H. N. Nong, C. H. Choi, K. H. Chae, Y. J. Hwang, B. K. Min, P. Strasser, H.-S. Oh, *Appl. Catal. B* **2020**, *269*, 118820.
- [43] S. Möller, S. Barwe, S. Dieckhöfer, J. Masa, C. Andronesco, W. Schuhmann, *ChemElectroChem* **2020**, *7*, 2680–2686.
- [44] S. Möller, S. Barwe, J. Masa, D. Wintrich, S. Seisel, H. Baltruschat, W. Schuhmann, *Angew. Chem. Int. Ed.* **2020**, *59*, 1585–1589.
- [45] P. Kanninen, B. Eriksson, F. Davodi, M. E. M. Buan, O. Sorsa, T. Kallio, R. W. Lindström, *Electrochim. Acta* **2020**, *332*, 135384.
- [46] H.-S. Oh, K. H. Lim, B. Roh, I. Hwang, H. Kim, *Electrochim. Acta* **2009**, *54*, 6515–6521.
- [47] H. Jang, S. Chung, J. Lee, *Electrochim. Acta* **2021**, *365*, 137276.
- [48] J. Yang, S. Park, K. y. Choi, H.-S. Park, Y.-G. Cho, H. Ko, H.-K. Song, *ACS Sustainable Chem. Eng* **2018**, *6*, 9566–9571.
- [49] T. Y. Ma, J. Ran, S. Dai, M. Jaroniec, S. Z. Qiao, *Angew. Chem. Int. Ed.* **2015**, *54*, 4646–4650.
- [50] Y. Lin, Q. Lu, F. Song, L. Yu, A. K. Mechler, R. Schlögl, S. Heumann, *Angew. Chem. Int. Ed.* **2019**, *58*, 8917–8921.
- [51] R. Gao, Q. Dai, F. Du, D. Yan, L. Dai, *J. Am. Chem. Soc.* **2019**, *141*, 11658–11666.
- [52] T. Sun, J. Wang, C. Qiu, X. Ling, B. Tian, W. Chen, C. Su, *Adv. Sci.* **2018**, *5*, 1800036.
- [53] Y. Jia, L. Zhang, A. Du, G. Gao, J. Chen, X. Yan, C. L. Brown, X. Yao, *Adv. Mater.* **2016**, *28*, 9532–9538.

- 
- [54] Z. Xiao, X. Huang, L. Xu, D. Yan, J. Huo, S. Wang, *Chem. Comm.* **2016**, 52, 13008–13011.
- [55] N. Alzate-Carvajal, L. M. Bolivar-Pineda, V. Meza-Laguna, V. A. Basiuk, E. V. Basiuk, E. A. Baranova, *ChemElectroChem* **2020**, 7, 428–436.
- [56] F. Davodi, M. Tavakkoli, J. Lahtinen, T. Kallio, *J. Catal.* **2017**, 353, 19–27.
- [57] X. Lu, W.-L. Yim, B. H. R. Suryanto, C. Zhao, *J. Am. Chem. Soc.* **2015**, 137, 2901–2907.
- [58] C. Tang, H.-F. Wang, X. Chen, B.-Q. Li, T.-Z. Hou, B. Zhang, Q. Zhang, M.-M. Titirici, F. Wei, *Adv. Mater.* **2016**, 28, 6845–6851.
- [59] M. Zhao, J. Zhang, H. Xiao, T. Hu, J. Jia, H. Wu, *Chem. Comm.* **2019**, 55, 1635–1638.
- [60] A. García-Miranda Ferrari, D. A. C. Brownson, C. E. Banks, *ChemElectroChem* **2019**, 6, 5446–5453.
- [61] B. H. R. Suryanto, T. Fang, S. Cheong, R. D. Tilley, C. Zhao, *J. Mater. Chem. A* **2018**, 6, 4686–4694.
- [62] Y. Cheng, C. Xu, L. Jia, J. D. Gale, L. Zhang, C. Liu, P. K. Shen, S. P. Jiang, *Appl. Catal. B* **2015**, 163, 96–104.
- [63] A. Ali, D. Akyüz, M. A. Asghar, A. Koca, B. Keskin, *Int. J. Hydrogen Energy* **2018**, 43, 1123–1128.
- [64] B. H. R. Suryanto, S. Chen, J. Duan, C. Zhao, *ACS Appl. Mater. Interfaces* **2016**, 8, 35513–35522.
- [65] B. H. R. Suryanto, C. Zhao, *Chem. Comm.* **2016**, 52, 6439–6442.
- [66] J. Zhang, M. Ren, L. Wang, Y. Li, B. I. Yakobson, J. M. Tour, *Adv. Mater.* **2018**, 30, 1707319.
- [67] Z. Liu, Z. Zhao, Y. Wang, S. Dou, D. Yan, D. Liu, Z. Xia, S. Wang, *Adv. Mater.* **2017**, 29, 1606207.
- [68] K. Huang, A. Hu, C. Huang, Y. Li, H. Zhou, Y. Xu, Q. Tang, S. Zhou, C. Chen, X. Chen, *ChemNanoMat* **2020**, 6, 542–549.
- [69] N. Cheng, Q. Liu, J. Tian, Y. Xue, A. M. Asiri, H. Jiang, Y. He, X. Sun, *Chem. Comm.* **2015**, 51, 1616–1619.
- [70] Q. Che, Q. Ma, J. Wang, G. Wang, Y. Zhu, R. Shi, P. Yang, *Mater. Lett.* **2020**, 265, 127411.
- [71] V. S. Sapner, B. B. Mulik, R. V. Digraskar, S. S. Narwade, B. R. Sathe, *RSC Adv.* **2019**, 9, 6444–6451.
- [72] V. S. Sapner, P. P. Chavan, B. R. Sathe, *ACS Sustainable Chem. Eng* **2020**, 8, 5524–5533.

- 
- [73] J. Liu, S. Zhao, C. Li, M. Yang, Y. Yang, Y. Liu, Y. Lifshitz, S.-T. Lee, Z. Kang, *Adv. Energy Mater.* **2016**, *6*, 1502039.
- [74] L. Li, H. Yang, J. Miao, L. Zhang, H.-Y. Wang, Z. Zeng, W. Huang, X. Dong, B. Liu, *ACS Energy Lett.* **2017**, *2*, 294–300.
- [75] I. L. Alonso-Lemus, F. J. Rodriguez-Varela, M. Z. Figueroa-Torres, M. E. Sanchez-Castro, A. Hernandez-Ramírez, D. Lardizabal-Gutierrez, P. Quintana-Owen, *Int. J. Hydrogen Energy* **2016**, *41*, 23409–23416.
- [76] S. Maldonado, K. J. Stevenson, *J. Phys. Chem. B* **2005**, *109*, 4707–4716.
- [77] N. Muthuswamy, M. E. M. Buan, J. C. Walmsley, M. Rønning, *Catal. Today* **2018**, *301*, 11–16.
- [78] A. C. Ramírez-Pérez, J. Quílez-Bermejo, J. M. Sieben, E. Morallón, D. Cazorla-Amorós, *Electrocatalysis* **2018**, *9*, 697–705.
- [79] M. Sun, Z. Xie, X. Wu, X. Deng, C. Liu, Q. Huang, B. Huang, *J. Solid State Electrochem.* **2017**, *21*, 2909–2920.
- [80] Z. Lin, G. H. Waller, Y. Liu, M. Liu, C. P. Wong, *Carbon* **2013**, *53*, 130–136.
- [81] Y. Zhao, R. Nakamura, K. Kamiya, S. Nakanishi, K. Hashimoto, *Nat. Commun.* **2013**, *4*, 2–8.
- [82] Y. Cheng, Y. Tian, X. Fan, J. Liu, C. Yan, *Electrochim. Acta* **2014**, *143*, 291–296.
- [83] H. W. Park, D. U. Lee, Y. Liu, J. Wu, L. F. Nazar, Z. Chen, *J. Elektrochem. Soc.* **2013**, *160*, A2244–A2250.
- [84] G.-L. Tian, Q. Zhang, B. Zhang, Y.-G. Jin, J.-Q. Huang, D. S. Su, F. Wei, *Adv. Funct. Mater.* **2014**, *24*, 5956–5961.
- [85] G. L. Tian, M. Q. Zhao, D. Yu, X. Y. Kong, J. Q. Huang, Q. Zhang, F. Wei, *Small* **2014**, *10*, 2251–2259.
- [86] J. Tian, Q. Liu, A. M. Asiri, K. A. Alamry, X. Sun, *ChemSusChem* **2014**, *7*, 2125–2130.
- [87] L. Wang, F. Yin, C. Yao, *Int. J. Hydrogen Energy* **2014**, *39*, 15913–15919.
- [88] R. M. Yadav, J. Wu, R. Kochandra, L. Ma, C. S. Tiwary, L. Ge, G. Ye, R. Vajtai, J. Lou, P. M. Ajayan, *ACS Appl. Mater. Interfaces* **2015**, *7*, 11991–12000.
- [89] M. S. Balogun, W. Qiu, H. Yang, W. Fan, Y. Huang, P. Fang, G. Li, H. Ji, Y. Tong, *Energy Environ. Sci.* **2016**, *9*, 3411–3416.
- [90] H. B. Yang, J. Miao, S. F. Hung, J. Chen, H. B. Tao, X. Wang, L. Zhang, R. Chen, J. Gao, H. M. Chen, L. Dai, B. Liu, *Sci. Adv.* **2016**, *2*, 1–12.
- [91] J. C. Li, P. X. Hou, S. Y. Zhao, C. Liu, D. M. Tang, M. Cheng, F. Zhang, H. M. Cheng, *Energy Environ. Sci.* **2016**, *9*, 3079–3084.
- [92] Z. Peng, S. Yang, D. Jia, P. Da, P. He, A. M. Al-Enizi, G. Ding, X. Xie, G. Zheng, *J. Mater. Chem. A* **2016**, *4*, 12878–12883.

- 
- [93] N. Jia, Q. Weng, Y. Shi, X. Shi, X. Chen, P. Chen, Z. An, Y. Chen, *Nano Research* **2018**, *11*, 1905–1916.
- [94] Y. Zhu, T. Zhang, J. Y. Lee, *ChemElectroChem* **2018**, *5*, 583–588.
- [95] H. Jiang, J. Gu, X. Zheng, M. Liu, X. Qiu, L. Wang, W. Li, Z. Chen, X. Ji, J. Li, *Energy Environ. Sci.* **2019**, *12*, 322–333.
- [96] M. Zhao, T. Li, L. Jia, H. Li, W. Yuan, C. M. Li, *ChemSusChem* **2019**, *12*, 5041–5050.
- [97] M. A. Wahab, J. Joseph, L. Atanda, U. K. Sultana, J. N. Beltramini, K. Ostrikov, G. Will, A. P. O'Mullane, A. Abdala, *ACS Appl. Energy Mater.* **2020**, *3*, 1439–1447.
- [98] C. Xing, Y. Xue, B. Huang, H. Yu, L. Hui, Y. Fang, Y. Liu, Y. Zhao, Z. Li, Y. Li, *Angew. Chem. Int. Ed.* **2019**, *58*, 13897–13903.
- [99] M. Khalid, A. M. Honorato, A. A. Pasa, H. Varela, *Mater. Sci. Energy Technol.* **2020**, *3*, 508–514.
- [100] S. Klaus, Y. Cai, M. W. Louie, L. Trotochaud, A. T. Bell, *J. Phys. Chem. C* **2015**, *119*, 7243–7254.
- [101] Z. Zhang, Z. Yi, J. Wang, X. Tian, P. Xu, G. Shi, S. Wang, *J. Mater. Chem. A* **2017**, *5*, 17064–17072.
- [102] A. Zehtab Yazdi, H. Fei, R. Ye, G. Wang, J. Tour, U. Sundararaj, *ACS Appl. Mater. Interfaces* **2015**, *7*, 7786–7794.
- [103] X. Huang, Q. Wang, D. Jiang, Y. Huang, *Catal. Commun.* **2017**, *100*, 89–92.
- [104] D. Li, B. Ren, Q. Jin, H. Cui, C. Wang, *J. Mater. Chem. A* **2018**, *6*, 2176–2183.
- [105] X. Yue, S. Huang, J. Cai, Y. Jin, P. K. Shen, *J. Mater. Chem. A* **2017**, *5*, 7784–7790.
- [106] P. Zhu, J. Gao, X. Chen, S. Liu, *Int. J. Hydrogen Energy* **2020**, *45*, 9512–9521.
- [107] J. Zhang, Z. Zhao, Z. Xia, L. Dai, *Nat. Nanotechnol.* **2015**, *10*, 444–452.
- [108] Y. Gao, Z. Xiao, D. Kong, R. Iqbal, Q. H. Yang, L. Zhi, *Nano Energy* **2019**, *64*, 103879.
- [109] X. Zhao, X. Zou, X. Yan, C. L. Brown, Z. Chen, G. Zhu, X. Yao, *Inorg. Chem. Front.* **2016**, *3*, 417–421.
- [110] C. Hu, L. Dai, *Adv. Mater.* **2017**, *29*, 1–9.
- [111] K. Qu, Y. Zheng, Y. Jiao, X. Zhang, S. Dai, S.-Z. Qiao, *Adv. Energy Mater.* **2017**, *7*, 1602068.
- [112] Y. Zhao, N. Yang, H. Yao, D. Liu, L. Song, J. Zhu, S. Li, L. Gu, K. Lin, D. Wang, *J. Am. Chem. Soc.* **2019**, *141*, 7240–7244.
- [113] X. Li, Y. Xu, Y. Li, X. Fan, G. Zhang, F. Zhang, W. Peng, *J. Colloid Interface Sci.* **2020**, *577*, 101–108.
- [114] J. Lai, S. Li, F. Wu, M. Saqib, R. Luque, G. Xu, *Energy Environ. Sci.* **2016**, *9*, 1210–1214.
-

- 
- [115] J. Zhang, L. Dai, *Angew. Chem. Int. Ed.* **2016**, *55*, 13296–13300.
- [116] S. S. Shinde, C. H. Lee, A. Sami, D. H. Kim, S. U. Lee, J. H. Lee, *ACS Nano* **2017**, *11*, 347–357.
- [117] J. Li, S. Gadipelli, *Chem. - Eur. J.* **2020**, *n/a*, DOI 10.1002/chem.202002702.
- [118] N.-T. Suen, S.-F. Hung, Q. Quan, N. Zhang, Y.-J. Xu, H. M. Chen, *Chem. Soc. Rev.* **2017**, *46*, 337–365.
- [119] M. Tahir, L. Pan, F. Idrees, X. Zhang, L. Wang, J.-J. Zou, Z. L. Wang, *Nano Energy* **2017**, *37*, 136–157.
- [120] M.-I. Jamesh, X. Sun, *J. Power Sources* **2018**, *400*, 31–68.
- [121] F. Hu, S. Zhu, S. Chen, Y. Li, L. Ma, T. Wu, Y. Zhang, C. Wang, C. Liu, X. Yang, L. Song, X. Yang, Y. Xiong, *Adv. Mater.* **2017**, *29*, 1606570.
- [122] X. Yang, J. Chen, Y. Chen, P. Feng, H. Lai, J. Li, X. Luo, *Nano-Micro Lett.* **2017**, *10*, 15.
- [123] J. Zhang, F. Li, W. Chen, C. Wang, D. Cai, *Electrochim. Acta* **2019**, *300*, 123–130.
- [124] T. Zhang, C. He, F. Sun, Y. Ding, M. Wang, L. Peng, J. Wang, Y. Lin, *Sci. Rep.* **2017**, *7*, 43638.
- [125] A. M. Asiri, K. Akhtar, S. B. Khan, *Ceram. Int.* **2019**, *45*, 13340–13346.
- [126] Y.-X. Zhang, X. Guo, X. Zhai, Y.-M. Yan, K.-N. Sun, *J. Mater. Chem. A* **2015**, *3*, 1761–1768.
- [127] A. R. Jadhav, H. A. Bandal, A. H. Tamboli, H. Kim, *J. Energy Chem.* **2017**, *26*, 695–702.
- [128] Y. Tong, P. Chen, T. Zhou, K. Xu, W. Chu, C. Wu, Y. Xie, *Angew. Chem. Int. Ed.* **2017**, *56*, 7121–7125.
- [129] A. Li, C. Wang, H. Zhang, Z. Zhao, J. Wang, M. Cheng, H. Zhao, J. Wang, M. Wu, J. Wang, *Electrochim. Acta* **2018**, *276*, 153–161.
- [130] M. Leng, X. Huang, W. Xiao, J. Ding, B. Liu, Y. Du, J. Xue, *Nano Energy* **2017**, *33*, 445–452.
- [131] H. A. Bandal, A. R. Jadhav, A. A. Chaugule, W. J. Chung, H. Kim, *Electrochim. Acta* **2016**, *222*, 1316–1325.
- [132] G. Zhu, X. Xie, Y. Liu, X. Li, K. Xu, X. Shen, Y. Yao, S. A. Shah, *Appl. Surf. Sci.* **2018**, *442*, 256–263.
- [133] M. Wang, C. Zhang, T. Meng, Z. Pu, H. Jin, D. He, J. Zhang, S. Mu, *J. Power Sources* **2019**, *413*, 367–375.
- [134] F. Hof, M. Liu, G. Valenti, E. Picheau, F. Paolucci, A. Pénicaud, *J. Phys. Chem. C* **2019**, *123*, 20774–20780.
- [135] A. Q. Mugheri, A. Tahira, U. Aftab, M. I. Abro, S. R. Chaudhry, L. Amaral, Z. H. Ibupoto, *RSC Adv.* **2019**, *9*, 5701–5710.

- [136] V. D. Silva, T. A. Simões, F. J. A. Loureiro, D. P. Fagg, F. M. L. Figueiredo, E. S. Medeiros, D. A. Macedo, *Int. J. Hydrogen Energy* **2019**, *44*, 14877–14888.
- [137] V. C. Hoang, K. N. Dinh, V. G. Gomes, *Carbon* **2020**, *157*, 515–524.
- [138] A. Roy, A. Ray, S. Saha, M. Ghosh, T. Das, B. Satpati, M. Nandi, S. Das, *Electrochim. Acta* **2018**, *283*, 327–337.
- [139] A. Xie, J. Zhang, X. Tao, J. Zhang, B. Wei, W. Peng, Y. Tao, S. Luo, *Electrochim. Acta* **2019**, *324*, 134814.
- [140] Z. Xie, H. Tang, Y. Wang, *ChemElectroChem* **2019**, *6*, 1206–1212.
- [141] J. Wu, H. Zhou, Q. Li, M. Chen, J. Wan, N. Zhang, L. Xiong, S. Li, B. Y. Xia, G. Feng, M. Liu, L. Huang, *Adv. Energy Mater.* **2019**, *9*, 1900149.
- [142] C. Zhu, Q. Shi, S. Feng, D. Du, Y. Lin, *ACS Energy Lett.* **2018**, *3*, 1713–1721.
- [143] Q. Zhang, J. Guan, *Adv. Funct. Mater.* **2020**, *30*, 2000768.
- [144] Q. Zhang, Z. Duan, M. Li, J. Guan, *Chem. Commun.* **2020**, *56*, 794–797.
- [145] X. Sun, S. Sun, S. Gu, Z. Liang, J. Zhang, Y. Yang, Z. Deng, P. Wei, J. Peng, Y. Xu, C. Fang, Q. Li, J. Han, Z. Jiang, Y. Huang, *Nano Energy* **2019**, *61*, 245–250.
- [146] S. Dilpazir, H. He, Z. Li, M. Wang, P. Lu, R. Liu, Z. Xie, D. Gao, G. Zhang, *ACS Appl. Energy Mater.* **2018**, *1*, 3283–3291.
- [147] F. Sun, Q. Li, H. Xue, H. Pang, *ChemElectroChem* **2019**, *6*, 1273–1299.
- [148] P. Chen, T. Zhou, L. Xing, K. Xu, Y. Tong, H. Xie, L. Zhang, W. Yan, W. Chu, C. Wu, Y. Xie, *Angew. Chem. Int. Ed.* **2017**, *56*, 610–614.
- [149] L. Ma, S. Chen, Z. Pei, Y. Huang, G. Liang, F. Mo, Q. Yang, J. Su, Y. Gao, J. A. Zapien, C. Zhi, *ACS Nano* **2018**, *12*, PMID: 29432686, 1949–1958.
- [150] J. Zhang, M. Zhang, Y. Zeng, J. Chen, L. Qiu, H. Zhou, C. Sun, Y. Yu, C. Zhu, Z. Zhu, *Small* **2019**, *15*, 1900307.
- [151] Y. Pan, S. Liu, K. Sun, X. Chen, B. Wang, K. Wu, X. Cao, W.-C. Cheong, R. Shen, A. Han, Z. Chen, L. Zheng, J. Luo, Y. Lin, Y. Liu, D. Wang, Q. Peng, Q. Zhang, C. Chen, Y. Li, *Angew. Chem. Int. Ed.* **2018**, *57*, 8614–8618.
- [152] H. Fei, J. Dong, Y. Feng, C. S. Allen, C. Wan, B. Voloskiy, M. Li, Z. Zhao, Y. Wang, H. Sun, P. An, W. Chen, Z. Guo, C. Lee, D. Chen, I. Shakir, M. Liu, T. Hu, Y. Li, A. I. Kirkland, X. Duan, Y. Huang, *Nat. Catal.* **2018**, *1*, 63–72.
- [153] Y. Hou, M. Qiu, M. G. Kim, P. Liu, G. Nam, T. Zhang, X. Zhuang, B. Yang, J. Cho, M. Chen, C. Yuan, L. Lei, X. Feng, *Nat. Comm.* **2019**, *10*, 1392.
- [154] H.-J. Qiu, P. Du, K. Hu, J. Gao, H. Li, P. Liu, T. Ina, K. Ohara, Y. Ito, M. Chen, *Adv. Mater.* **2019**, *31*, 1900843.
- [155] L. Zhang, Y. Jia, G. Gao, X. Yan, N. Chen, J. Chen, M. T. Soo, B. Wood, D. Yang, A. Du, X. Yao, *Chem* **2018**, *4*, 285–297.

- 
- [156] Y. Li, Z.-S. Wu, P. Lu, X. Wang, W. Liu, Z. Liu, J. Ma, W. Ren, Z. Jiang, X. Bao, *Adv. Sci.* **2020**, *7*, DOI 10.1002/advs.201903089.
- [157] L. Bai, C.-S. Hsu, D. T. L. Alexander, H. M. Chen, X. Hu, *Journal of the American Chemical Society* **2019**, *141*, 14190–14199.
- [158] C. Wu, X. Zhang, Z. Xia, M. Shu, H. Li, X. Xu, R. Si, A. I. Rykov, J. Wang, S. Yu, S. Wang, G. Sun, *J. Mater. Chem. A* **2019**, *7*, 14001–14010.
- [159] Y. Cheng, S. He, J.-P. Veder, R. De Marco, S.-z. Yang, S. Ping Jiang, *ChemElectroChem* **2019**, *6*, 3478–3487.
- [160] Z. Li, H. He, H. Cao, S. Sun, W. Diao, D. Gao, P. Lu, S. Zhang, Z. Guo, M. Li, R. Liu, D. Ren, C. Liu, Y. Zhang, Z. Yang, J. Jiang, G. Zhang, *Appl. Catal. B* **2019**, *240*, 112–121.
- [161] J. Guan, Z. Duan, F. Zhang, S. D. Kelly, R. Si, M. Dupuis, Q. Huang, J. Q. Chen, C. Tang, C. Li, *Nat. Catal.* **2018**, *1*, 870–877.
- [162] W. Bian, Z. Yang, P. Strasser, R. Yang, *J. Power Sources* **2014**, *250*, 196–203.
- [163] Y. Liu, J. Li, F. Li, W. Li, H. Yang, X. Zhang, Y. Liu, J. Ma, *J. Mater. Chem. A* **2016**, *4*, 4472–4478.
- [164] I. Madakannu, I. Patil, B. A. Kakade, K. R. D. Kasibhatta, *Mater. Chem. Phys.* **2020**, *252*, 123238.
- [165] J. Geng, L. Kuai, E. Kan, Q. Wang, B. Geng, *ChemSusChem* **2015**, *8*, 659–664.
- [166] X. Lin, X. Li, F. Li, Y. Fang, M. Tian, X. An, Y. Fu, J. Jin, J. Ma, *J. Mater. Chem. A* **2016**, *4*, 6505–6512.
- [167] W.-Y. Xia, N. Li, Q.-Y. Li, K.-H. Ye, C.-W. Xu, *Sci. Rep.* **2016**, *6*, 23398.
- [168] X. Xing, R. Liu, K. Cao, U. Kaiser, G. Zhang, C. Streb, *ACS Appl. Mater. Interfaces* **2018**, *10*, 44511–44517.
- [169] H. Chen, X. Huang, L.-J. Zhou, G.-D. Li, M. Fan, X. Zou, *ChemCatChem* **2016**, *8*, 992–1000.
- [170] C. C. Wang, Z. Yu, X. T. Wang, B. Lin, *Int. J. Hydrogen Energy* **2018**, *43*, 18992–19001.
- [171] D. U. Lee, B. J. Kim, Z. Chen, *J. Mater. Chem. A* **2013**, *1*, 4754–4762.
- [172] Y. Li, H. Xu, H. Huang, C. Wang, L. Gao, T. Ma, *Chem. Comm.* **2018**, *54*, 2739–2742.
- [173] Z. Ye, T. Li, G. Ma, Y. Dong, X. Zhou, *Adv. Funct. Mater.* **2017**, *27*, 1704083.
- [174] X. Wu, J. Yu, G. Yang, H. Liu, W. Zhou, Z. Shao, *Electrochim. Acta* **2018**, *286*, 47–54.
- [175] Y. Bu, G. Nam, S. Kim, K. Choi, Q. Zhong, J. Lee, Y. Qin, J. Cho, G. Kim, *Small* **2018**, *14*, 1802767.

- [176] Y. Bu, H. Jang, O. Gwon, S. H. Kim, S. H. Joo, G. Nam, S. Kim, Y. Qin, Q. Zhong, S. K. Kwak, J. Cho, G. Kim, *J. Mater. Chem. A* **2019**, *7*, 2048–2054.
- [177] Y. Bu, S. Kim, O. Kwon, Q. Zhong, G. Kim, *ChemElectroChem* **2019**, *6*, 1520–1524.
- [178] J. Chen, X. Shen, Y. Pan, C. Liu, S. Y. Hwang, Q. Xu, Z. Peng, *J. Mater. Chem. A* **2018**, *6*, 3996–4002.
- [179] A. S. Bhalla, R. Guo, R. Roy, *Mater. Res. Innovations* **2000**, *4*, 3–26.
- [180] Q. Van Le, H. W. Jang, S. Y. Kim, *Small Methods* **2018**, *2*, 1700419.
- [181] P. Roy, N. Kumar Sinha, S. Tiwari, A. Khare, *Solar Energy* **2020**, *198*, 665–688.
- [182] R. K. Hona, F. Ramezanipour, *Angew. Chem. Int. Ed.* **2019**, *58*, 2060–2063.
- [183] J. Chen, J. Wu, Y. Liu, X. Hu, D. Geng, *Phys. Status Solidi A* **2018**, *215*, 1800380.
- [184] X. Cheng, E. Fabbri, Y. Yamashita, I. E. Castelli, B. Kim, M. Uchida, R. Haumont, I. Puente-Orench, T. J. Schmidt, *ACS Catal.* **2018**, *8*, 9567–9578.
- [185] C. T. Alexander, A. M. Abakumov, R. P. Forslund, K. P. Johnston, K. J. Stevenson, *ACS Appl. Energy Mater.* **2018**, *1*, 1549–1558.
- [186] S. N. Faisal, E. Haque, N. Noorbehesht, H. Liu, M. M. Islam, L. Shabnam, A. K. Roy, E. Pourazadi, M. S. Islam, A. T. Harris, A. I. Minett, *Sustainable Energy Fuels* **2018**, *2*, 2081–2089.
- [187] F. E. Sarac Oztuna, T. Beyazay, U. Unal, *J. Phys. Chem. C* **2019**, *123*, 28131–28141.
- [188] Z. Zhang, S. Liu, F. Xiao, S. Wang, *ACS Sustainable Chem. Eng* **2017**, *5*, 529–536.
- [189] X. He, J. Tan, F. Yin, B. Chen, X. Liang, G. Li, H. Yin, *Int. J. Hydrogen Energy* **2019**, *44*, 24184–24196.
- [190] B. He, X. Chen, J. Lu, S. Yao, J. Wei, Q. Zhao, D. Jing, X. Huang, T. Wang, *Electroanalysis* **2016**, *28*, 2435–2443.
- [191] V. D. Silva, R. A. Raimundo, T. A. Simões, F. J. Loureiro, D. P. Fagg, M. A. Morales, D. A. Macedo, E. S. Medeiros, *Int. J. Hydrogen Energy* **2021**, *46*, 3798–3810.
- [192] Y. Li, J. Huang, G. Rao, C. Wu, X. Du, Y. Sun, X. Wang, C. Yang, *Appl. Surf. Sci.* **2020**, *530*, DOI 10.1016/j.apsusc.2020.147192.
- [193] B. Dong, J.-Y. Xie, Z. Tong, J.-Q. Chi, Y.-N. Zhou, X. Ma, Z.-Y. Lin, L. Wang, Y.-M. Chai, *Chin. J. Catal.* **2020**, *41*, 1782–1789.
- [194] H. B. Aiyappa, J. Thote, D. B. Shinde, R. Banerjee, S. Kurungot, *Chem. Mater.* **2016**, *28*, 4375–4379.
- [195] Q. Shi, S. Fu, C. Zhu, J. Song, D. Du, Y. Lin, *Mater. Horiz.* **2019**, *6*, 684–702.
- [196] D. Senthil Raja, C.-L. Huang, Y.-A. Chen, Y. Choi, S.-Y. Lu, *Appl. Catal. B* **2020**, *279*, 119375.
- [197] Y. Yan, T. He, B. Zhao, K. Qi, H. Liu, B. Y. Xia, *J. Mater. Chem. A* **2018**, *6*, 15905–15926.

- 
- [198] J.-Y. Xue, C. Li, F.-L. Li, H.-W. Gu, P. Braunstein, J.-P. Lang, *Nanoscale* **2020**, *12*, 4816–4825.
- [199] F. Zheng, Z. Zhang, C. Zhang, W. Chen, *ACS Omega* **2020**, *5*, 2495–2502.
- [200] D. Xing, Y. Wang, P. Zhou, Y. Liu, Z. Wang, P. Wang, Z. Zheng, H. Cheng, Y. Dai, B. Huang, *Appl. Catal. B* **2020**, *278*, 119295.
- [201] L. Yaqoob, T. Noor, N. Iqbal, H. Nasir, N. Zaman, K. Talha, *J. Alloys Compd.* **2021**, *850*, 156583.
- [202] L. Yaqoob, T. Noor, N. Iqbal, H. Nasir, M. Sohail, N. Zaman, M. Usman, *Renewable Energy* **2020**, *156*, 1040–1054.
- [203] M. Gu, S.-C. Wang, C. Chen, D. Xiong, F.-Y. Yi, *Inorg. Chem.* **2020**, *59*, 6078–6086.
- [204] Y.-W. Li, W.-J. Zhang, J. Li, H.-Y. Ma, H.-M. Du, D.-C. Li, S.-N. Wang, J.-S. Zhao, J.-M. Dou, L. Xu, *ACS Appl. Mater. Interfaces* **2020**, *12*, 44710–44719.
- [205] Q. Liang, J. Chen, F. Wang, Y. Li, *Coord. Chem. Rev.* **2020**, *424*, 213488.
- [206] X. Qin, D. Kim, Y. Piao, *Carbon Energy* **2021**, *3*, 66–100.
- [207] L. Du, L. Xing, G. Zhang, S. Sun, *Carbon* **2020**, *156*, 77–92.
- [208] C. Yang, W.-J. Cai, B.-B. Yu, H. Qiu, M.-L. Li, L.-W. Zhu, Z. Yan, L. Hou, Y.-Y. Wang, *Catal. Sci. Technol.* **2020**, *10*, 3897–3903.
- [209] J. Xu, X. Zhu, X. Jia, *ACS Sustainable Chem. Eng* **2019**, *7*, 16629–16639.
- [210] Z. Xue, K. Liu, Q. Liu, Y. Li, M. Li, C.-Y. Su, N. Ogiwara, H. Kobayashi, H. Kitagawa, M. Liu, G. Li, *Nat. Commun.* **2019**, *10*, 5048.
- [211] J. Duan, S. Chen, C. Zhao, *Nat. Commun.* **2017**, *8*, 15341.
- [212] X.-L. Wang, L.-Z. Dong, M. Qiao, Y.-J. Tang, J. Liu, Y. Li, S.-L. Li, J.-X. Su, Y.-Q. Lan, *Angew. Chem. Int. Ed.* **2018**, *57*, 9660–9664.
- [213] F. Zheng, D. Xiang, P. Li, Z. Zhang, C. Du, Z. Zhuang, X. Li, W. Chen, *ACS Sustainable Chem. Eng* **2019**, *7*, 9743–9749.
- [214] F. Zheng, Z. Zhang, D. Xiang, P. Li, C. Du, Z. Zhuang, X. Li, W. Chen, *J. Colloid Interface Sci.* **2019**, *555*, 541–547.
- [215] M. Zhang, W. Xu, T. Li, H. Zhu, Y. Zheng, *Inorg. Chem.* **2020**, *59*, 15467–15477.
- [216] Q. Xu, J. Qian, D. Luo, G. Liu, Y. Guo, G. Zeng, *Adv. Sustainable Syst.* **2020**, *4*, 2000115.
- [217] A. Xie, J. Du, F. Tao, Y. Tao, Z. Xiong, S. Luo, X. Li, C. Yao, *Electrochim. Acta* **2019**, *305*, 338–348.
- [218] P. Thangavel, M. Ha, S. Kumaraguru, A. Meena, A. N. Singh, A. M. Harzandi, K. S. Kim, *Energy Environ. Sci.* **2020**, *13*, 3447–3458.
- [219] Y. Fang, X. Li, F. Li, X. Lin, M. Tian, X. Long, X. An, Y. Fu, J. Jin, J. Ma, *J. Power Sources* **2016**, *326*, 50–59.

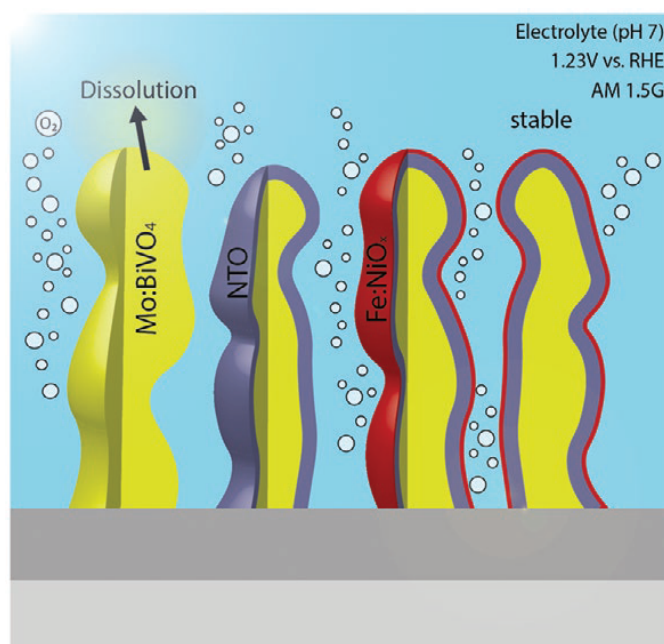
- [220] T. Fan, F. Yin, H. Wang, X. He, G. Li, *Int. J. Hydrogen Energy* **2017**, *42*, 17376–17385.
- [221] W.-Z. Cheng, J.-L. Liang, H.-B. Yin, Y.-J. Wang, W.-F. Yan, J.-N. Zhang, *Rare Met.* **2020**, *39*, 815–823.
- [222] X. Zheng, Y. Cao, D. Liu, M. Cai, J. Ding, X. Liu, J. Wang, W. Hu, C. Zhong, *ACS Appl. Mater. Interfaces* **2019**, *11*, 15662–15669.
- [223] M. Jahan, Z. Liu, K. P. Loh, *Adv. Funct. Mater.* **2013**, *23*, 5363–5372.
- [224] W. Zhang, Y. Wang, H. Zheng, R. Li, Y. Tang, B. Li, C. Zhu, L. You, M.-R. Gao, Z. Liu, S.-H. Yu, K. Zhou, *ACS Nano* **2020**, *14*, 1971–1981.
- [225] X. Wang, H. Xiao, A. Li, Z. Li, S. Liu, Q. Zhang, Y. Gong, L. Zheng, Y. Zhu, C. Chen, D. Wang, Q. Peng, L. Gu, X. Han, J. Li, Y. Li, *J. Am. Chem. Soc.* **2018**, *140*, 15336–15341.
- [226] H.-F. Wang, L. Chen, H. Pang, S. Kaskel, Q. Xu, *Chem. Soc. Rev.* **2020**, *49*, 1414–1448.
- [227] Y. Qian, Z. Hu, X. Ge, S. Yang, Y. Peng, Z. Kang, Z. Liu, J. Y. Lee, D. Zhao, *Carbon* **2017**, *111*, 641–650.
- [228] L. Ge, Y. Yang, L. Wang, W. Zhou, R. De Marco, Z. Chen, J. Zou, Z. Zhu, *Carbon* **2015**, *82*, 417–424.
- [229] X.-F. Lu, L.-F. Gu, J.-W. Wang, J.-X. Wu, P.-Q. Liao, G.-R. Li, *Adv. Mater.* **2017**, *29*, 1604437.
- [230] X. Kuang, Y. Luo, R. Kuang, Z. Wang, X. Sun, Y. Zhang, Q. Wei, *Carbon* **2018**, *137*, 433–441.
- [231] D. Sun, L. Ye, F. Sun, H. García, Z. Li, *Inorg. Chem.* **2017**, *56*, 5203–5209.
- [232] J. Zhou, Y. Dou, A. Zhou, L. Shu, Y. Chen, J.-R. Li, *ACS Energy Lett.* **2018**, *3*, 1655–1661.
- [233] Y. Wan, L. Wang, H. Xu, X. Wu, J. Yang, *J. Am. Chem. Soc.* **2020**, *142*, 4508–4516.
- [234] S. Mondal, B. Mohanty, M. Nurhuda, S. Dalapati, R. Jana, M. Addicoat, A. Datta, B. K. Jena, A. Bhaumik, *ACS Catal.* **2020**, *10*, 5623–5630.
- [235] X. Zhao, P. Pachfule, S. Li, T. Langenhahn, M. Ye, C. Schlesiger, S. Praetz, J. Schmidt, A. Thomas, *J. Am. Chem. Soc.* **2019**, *141*, 6623–6630.
- [236] C. Yang, Z.-D. Yang, H. Dong, N. Sun, Y. Lu, F.-M. Zhang, G. Zhang, *ACS Energy Lett.* **2019**, *4*, 2251–2258.
- [237] Z. Gao, Z. Yu, Y. Huang, X. He, X. Su, L. Xiao, Y. Yu, X. Huang, F. Luo, *J. Mater. Chem. A* **2020**, *8*, 5907–5912.
- [238] H. Huang, F. Li, Y. Zhang, Y. Chen, *J. Mater. Chem. A* **2019**, *7*, 5575–5582.
- [239] Z. Gao, L. L. Gong, X. Q. He, X. M. Su, L. H. Xiao, F. Luo, *Inorg. Chem.* **2020**, *59*, 4995–5003.

- 
- [240] X. Feng, Z. Gao, L. Xiao, Z. Lai, F. Luo, *Inorg. Chem. Front.* **2020**, *7*, 3925–3931.
- [241] S. Nandi, S. K. Singh, D. Mullangi, R. Illathvalappil, L. George, C. P. Vinod, S. Kurungot, R. Vaidhyanathan, *Adv. Energy Mater.* **2016**, *6*, 1601189.
- [242] D. Mullangi, V. Dhavale, S. Shalini, S. Nandi, S. Collins, T. Woo, S. Kurungot, R. Vaidhyanathan, *Adv. Energy Mater.* **2016**, *6*, 1600110.
- [243] Q. Xu, Y. Tang, X. Zhang, Y. Oshima, Q. Chen, D. Jiang, *Adv. Mater.* **2018**, *30*, 1706330.
- [244] D. Wu, Q. Xu, J. Qian, X. Li, Y. Sun, *Chem. - Eur. J.* **2019**, *25*, 3105–3111.
- [245] X. Peng, L. Zhang, Z. Chen, L. Zhong, D. Zhao, X. Chi, X. Zhao, L. Li, X. Lu, K. Leng, C. Liu, W. Liu, W. Tang, K. P. Loh, *Adv. Mater.* **2019**, *31*, 1900341.
- [246] D. Chakraborty, S. Nandi, R. Illathvalappil, D. Mullangi, R. Maity, S. K. Singh, S. Haldar, C. P. Vinod, S. Kurungot, R. Vaidhyanathan, *ACS Omega* **2019**, *4*, 13465–13473.
- [247] G.-L. Zhuang, Y.-F. Gao, X. Zhou, X.-Y. Tao, J.-M. Luo, Y.-J. Gao, Y.-L. Yan, P.-Y. Gao, X. Zhong, J.-G. Wang, *Chem. Eng. J.* **2017**, *330*, 1255–1264.
- [248] F. Kong, X. Fan, A. Kong, Z. Zhou, X. Zhang, Y. Shan, *Adv. Funct. Mater.* **2018**, *28*, 1803973.

## 5 Ultra-thin Protective Coatings for Sustained Photoelectrochemical Water Oxidation with Mo:BiVO<sub>4</sub>

This chapter is based on the following publication:

M. Beetz, S. Häring, P. Elsässer, J. Kampmann, L. Sauerland, F. Wolf, M. Günther, A. Fischer\* and T. Bein\* *Advanced Functional Materials*, **2021**, 2011210.



Sebastian Häring developed and optimized the deposition process for the ultra-thin protective coatings, contributed to the electrochemical analysis of the photoelectrodes and wrote the corresponding parts of the manuscript.

## Abstract

As global warming caused by the greenhouse effect is becoming one of the major issues of the 21st century, hydrogen as an alternative to fossil-based fuels and other energy carriers has gained importance in current research. One promising approach to produce hydrogen is photoelectrochemical water splitting, which uses solar energy combined with suitable semiconducting photoabsorber electrodes to generate hydrogen and oxygen from water. However, most water splitting applications reported to date suffer from degradation of the photoabsorber, resulting in a loss of activity after just a few seconds or minutes. Here, a new approach using conformal ultra-thin and oxidation-stable protective layers is presented on Mo:BiVO<sub>4</sub> thin films combined with a thin Fe<sub>0.1</sub>Ni<sub>0.9</sub>O water oxidation co-catalyst, applied by electrochemical deposition, to achieve unprecedented photocurrent densities of up to 5.6 mA cm<sup>-2</sup> under simulated AM1.5G illumination and a neutral pH while providing more stable electrodes for water oxidation.

## 5.1 Introduction

With increasing demands for renewable energy sources and substitution of fossil fuels in the next few years, the development of new energy storage solutions is of great importance. Hydrogen generated with energy from intermittent sustainable sources such as solar or wind is an attractive way to store energy.<sup>[1-5]</sup> Photoelectrochemical water splitting uses sunlight to dissociate water into hydrogen and oxygen by means of semiconductor absorber electrodes. Especially bismuth vanadate (BiVO<sub>4</sub>) exhibits potential as a suitable ternary oxide for photoelectrochemical water oxidation due to its great light absorption abilities of a substantial part of the visible spectrum, which allows for theoretical photocurrents of up to 7.5 mA cm<sup>-2</sup> under AM1.5G illumination (100 mW cm<sup>-2</sup>).<sup>[6]</sup> However, recent studies featured a maximum photocurrent of 0.7 mA cm<sup>-2</sup> or 1.9 mA cm<sup>-2</sup> at 1.23 V versus RHE under simulated AM1.5G illumination (400 - 700 nm LED at 100 mW cm<sup>-2</sup>) using 1 at% tungsten-doped bismuth vanadate (W:BiVO<sub>4</sub>)<sup>[7]</sup> or 10 at% molybdenum-doped bismuth vanadate (Mo:BiVO<sub>4</sub>)<sup>[8]</sup> without any additional water-oxidation co-catalysts, respectively, featuring some of the highest photocurrents ever achieved using this material. The comparability of bare photocurrents is quite difficult, if other factors like long-term stability, experimental conditions (pH of the electrolyte, illumination spectra, applied voltage, usage of sacrificial agents) or the effect of doping are not taken into account. Doping of BiVO<sub>4</sub> enhances charge separation and increases the charge carrier densities while lowering the surface charge transfer resistance. Theoretical calculations also indicate the importance of doping sites for adsorption of OH, O, and OOH species on the interface of the semiconductor.<sup>[9]</sup> The far from theoretical photoelectrochemical activity primarily suffers from the materials' slow water-oxidation kinetics at the semiconductor/electrolyte interface since charge recombination and charge transfer resistance are rather unfavorable for bare

$\text{BiVO}_4$ .<sup>[10]</sup> The water-oxidation kinetics can be significantly enhanced using a suitable water-oxidation catalyst like cobalt phosphate (CoPi) or iron-doped nickel oxides on the interface to the electrolyte.<sup>[8,11–13]</sup> Using this approach, the  $\text{Mo:BiVO}_4/\text{CoPi}$  electrode can offer one of the highest photocurrent densities of all known materials in this field.<sup>[10,14]</sup> Rohloff et al.<sup>[8]</sup> achieved  $4.6 \text{ mA cm}^{-2}$  at 1.23 V versus RHE under simulated AM1.5G illumination (400 - 700 nm LED at  $100 \text{ mW cm}^{-2}$ ) using the most active 10 at%  $\text{Mo:BiVO}_4$  combined with CoPi as water-oxidation co-catalyst to overcome the slow water-oxidation kinetics. However, its long-term stability is rather poor compared to other long-known materials like hematite.<sup>[15–17]</sup> In this context, corrosion, especially dissolution or degradation of the pristine material to inactive species, was shown to be a limiting factor for the stability of various kinds of electrodes used in photoelectrochemical devices.<sup>[18–21]</sup> In the past, there have been several attempts to increase the stability of  $\text{BiVO}_4$  using protective layers.<sup>[19]</sup> However, most approaches, like atomic layer deposition (ALD), usually require rather thick layers, such as 40 nm of  $\text{TiO}_2$ , to achieve a homogenous and pin-hole free protective layer. Additionally, this leads to a strong reduction of the achieved photocurrent density compared to unprotected materials.<sup>[5,22–24]</sup> Further,  $\text{TiO}_2$  is prone to crystallization as rutile and anatase under operating conditions of an electrode, thus forming a discontinuous layer of  $\text{TiO}_2$  nanoparticles on top of the electrode rather than a conformal protective layer, causing short lifetimes of minutes to hours of previously reported protective coatings.

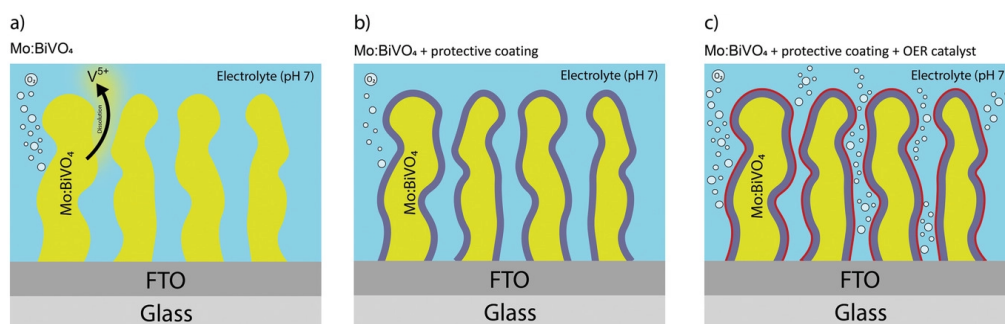


**Figure 5.1:** Schemes of  $\text{Mo:BiVO}_4$ -based photoanodes under operating conditions showing the protection strategy for enhanced durability and performance. a) Pure  $\text{Mo:BiVO}_4$  suffers from corrosion during oxygen evolution by leaching vanadium(V) ions into the electrolyte. b) A thin protective coating prevents the dissolution of vanadium(V) ions in the electrolyte at reduced photoelectrochemical activity. c) An additional OER catalyst on-top of the protection layer enables effective water oxidation at reduced corrosion.

Here, we present a protection strategy based on ALD using ultra-thin (2.5 nm), conformal and oxidation-stable protection layers of niobium-doped titanium oxide (NTO,  $\text{Nb:TiO}_2$ ), while maintaining photocurrents comparable to those of the unprotected  $\text{Mo:BiVO}_4$  thin films for long time periods (Figure 5.1). NTO has been shown to be suitable as an oxidation-stable amorphous protection layer which showed impressive long-term stability in various water oxidation applications.<sup>[5,25–27]</sup> The electrochemical

performance of the system could further be increased using an iron-doped nickel oxide co-catalyst, applied via electrochemical deposition (ECD) on top of the protection layer, featuring record activities of up to  $5.6 \text{ mA cm}^{-2}$ . After 16 h under operating conditions, those photocurrents stabilized at a constant photocurrent of  $4.7 \text{ mA cm}^{-2}$ . In contrast, the unprotected Mo:BiVO<sub>4</sub> reaches its highest photoelectrochemical activity with  $1.9 \text{ mA cm}^{-2}$  after 2 h, subsequently suffering from a constant loss in photoelectrochemical performance down to  $1.2 \text{ mA cm}^{-2}$  after more than 16 h due to constant degradation of the photoabsorber. To enable comparable photocurrents, all measurements were performed under simulated AM1.5G backside illumination with a 455 nm LED, calibrated to  $100 \text{ mW cm}^{-2}$  under consideration of the spectral mismatch of the LED to the sun's spectrum. To this end, the spectral mismatch from the LED to the AM1.5G spectrum was determined using the spectrum of the LED and the spectral photocurrent response of a Hamamatsu Si-diode to calibrate the LED's intensity accordingly. To ensure comparability and reliability of this calibration a linear sweep voltammogram using a Xe lamp AM 1.5 solar simulator (Solar Light Co. Model 16S, class ABA), calibrated using a Si-photodiode, and our calibrated 455 nm LED was recorded (see Figure 5.13, Supporting Information). The photocurrent response using this calibration is comparable in a range from 0.5 - 1.5 V versus RHE for both illumination types and exhibits similar photocurrents under our operating conditions of 1.23 V.

## 5.2 Results and Discussion

### 5.2.1 Electrode Preparation

The Mo:BiVO<sub>4</sub> thin films (with molybdenum content of 10 at%) were prepared using a dip-coating procedure under controlled atmospheric conditions, similar to the procedure previously described by Rohloff et al.<sup>[8]</sup> The molybdenum content of 10 at% was chosen due to its superior photoelectrochemical activity compared to higher or lower doping levels, featuring an optimum domain size and film thickness for efficient water-oxidation. The as-prepared thin films were annealed and calcined at 450 °C under air for 2 h resulting in bright-yellow and opaque films as shown in Figure 5.2a.

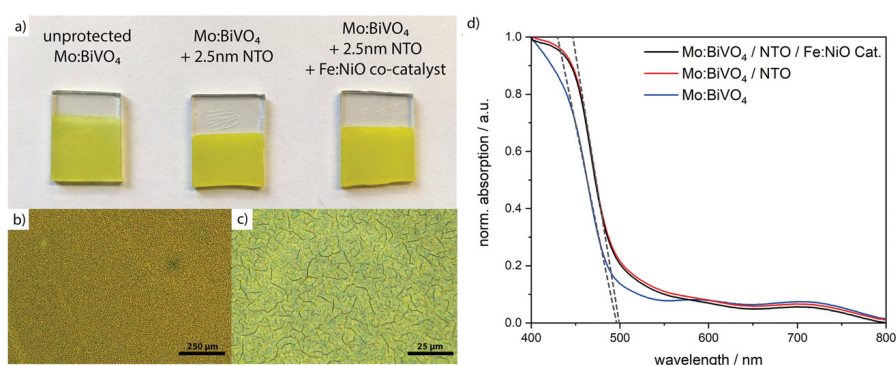


**Figure 5.2:** a) left-to-right: Photographs of an as-prepared Mo:BiVO<sub>4</sub> thin-film (left) with an additional 2.5 nm NTO protection layer (middle), and additional Fe:NiO-co-catalyst layer grown by electrochemical deposition (right). b,c) Light microscope images at different magnifications showing the homogeneity of the MBV+NTO+Cat films. d) UV/Vis spectra of the different Mo:BiVO<sub>4</sub> films on FTO coated glass substrates.

Thin protection layers (1, 2.5, 5, and 10 nm) of NTO, AlO<sub>x</sub> and SnO<sub>x</sub>, respectively, were grown on top of the as-prepared Mo:BiVO<sub>4</sub> thin films using ALD, which already showed improved stability of photoanodes in previously reported publications.<sup>[5,27–31]</sup> The thickness of the applied ALD protective layers was monitored using ellipsometry on Si wafers and verified by SEM and FIB/TEM characterization (see Figure 5.3b–d).

Photoelectrochemical activities resulting from applying the various protection layers and thicknesses revealed that protection layers thicker than 5 nm led to a significant reduction of the photoelectrochemical performance of the material. Further, the SnO<sub>x</sub> and AlO<sub>x</sub> protected electrodes suffered from severe degradation after a few minutes under operating conditions (AM1.5G and 1.23 V vs RHE at pH 7). Chronoamperometric measurements of protected Mo:BiVO<sub>4</sub> electrodes using various thicknesses of SnO<sub>x</sub>, AlO<sub>x</sub> and NTO are shown in Figures 5.9–5.11 (Supporting Information). While SnO<sub>x</sub> protected Mo:BiVO<sub>4</sub> films exhibited photocurrent densities of up to 1.23 mA cm<sup>-2</sup> in the case of the 2 nm protective layer, comparable to the 2.5 nm NTO protected electrodes, the activity halved after 5 min and further decreased to even lower photocurrents of 0.20 mA cm<sup>-2</sup> after 180 min. AlO<sub>x</sub> protected Mo:BiVO<sub>4</sub> films achieved photocurrents of

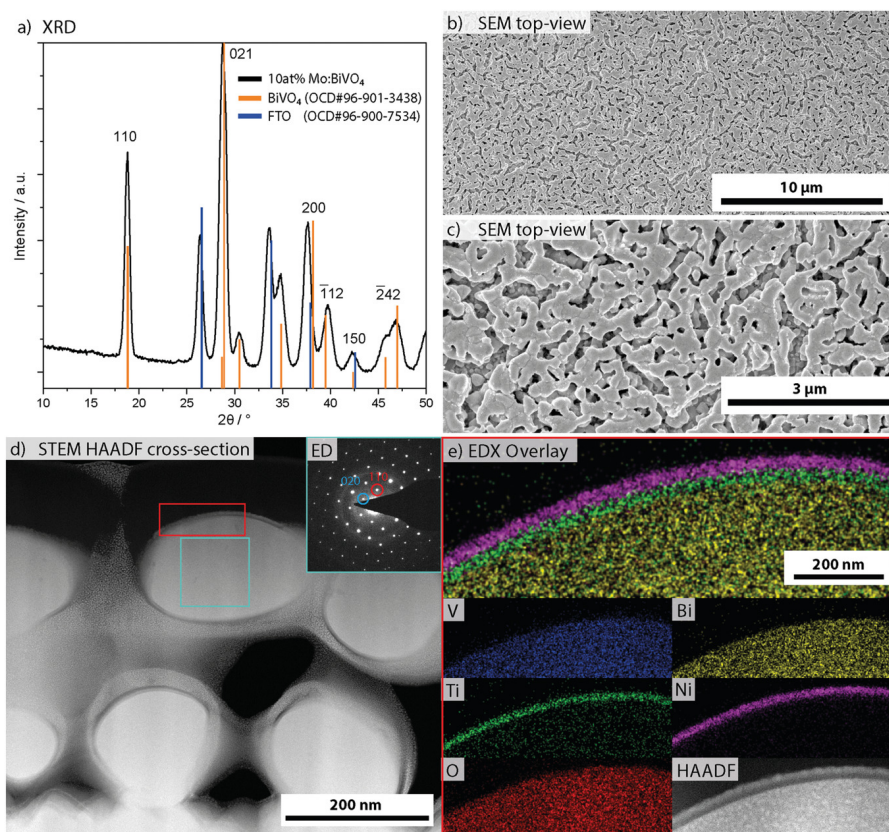


**Figure 5.3:** a) XRD diffraction pattern of the MBV+NTO+Cat shows distinct reflections which can be assigned to  $\text{BiVO}_4$  (Crystallography Open Database (COD# 96-901-3438) and the subjacent FTO layer (COD# 96-900-7534). b,c) SEM images of the  $\text{Mo:BiVO}_4$  thin films with NTO protection layer and  $\text{FeNiO}_x$  co-catalyst at different magnifications. d) STEM-HAADF image from a FIB-prepared cross-section. The blue rectangle marks the area where the corresponding electron diffraction (ED) pattern was obtained. The red rectangle marks the area of the acquired EDX maps, seen in e). e) STEM-HAADF EDX maps of a prepared FIB lamella showing Bi and V co-localized in the  $\text{Mo:BiVO}_4$  phase, with the Ti containing NTO protection-layer and the Ni containing co-catalyst layer (image selection in red box). The overlay EDX map shows the position of Bi, Ti and Ni in their respective color. The single crystal electron diffraction pattern of a single  $\text{Mo:BiVO}_4$  crystal (blue square in TEM image) is shown in the inset.

up to  $1.7 \text{ mA cm}^{-2}$ , also suffering from heavy degradation with photocurrents down to  $0.17 \text{ mA cm}^{-2}$  after 180 min, in the case of the thinnest 1.5 nm protective layer, while thicker protective layers were completely photoelectrochemically inactive. This behavior can be attributed to the lack of conductivity of the  $\text{AlO}_x$  and  $\text{SnO}_x$  coatings, which becomes dominant at increasing thicknesses.

Since NTO-protected  $\text{Mo:BiVO}_4$  with a thickness of 2.5 nm of the protective layer emerged as the only photoelectrochemically stable electrode in this study while maintaining adequate photocurrents under the above conditions, the following studies were

only performed using the 2.5 nm NTO Mo:BiVO<sub>4</sub> electrodes. Chronoamperometric electrochemical measurements of all protection layers and thicknesses can be found in the Supporting Information, Figures 5.8-5.10.

To further enhance efficiency, we applied an Fe<sub>0.1</sub>Ni<sub>0.9</sub>O oxygen evolution co-catalyst on top of the protected Mo:BiVO<sub>4</sub> thin films, using electrochemical deposition under galvanostatic conditions following a synthesis route described by Abdi et al.<sup>[7]</sup>

Pure Mo:BiVO<sub>4</sub> thin films, those with 2.5 nm NTO protective layer and those with additional Fe<sub>0.1</sub>Ni<sub>0.9</sub>O co-catalyst are referred to as "MBV", "MBV+ NTO" and "MBV+ NTO+ Cat", respectively, in the following.

### 5.2.2 Optical Characterization

Photographs of the freshly prepared MBV, MBV+NTO and MBV+NTO+Cat thin-film electrodes are shown in Figure 5.2a. All films are opaque and reveal the typical bright green-yellowish color of BiVO<sub>4</sub>. The protected films appear visually brighter, which can be attributed to the enhanced scattering of the NTO protection layer on top of the Mo:BiVO<sub>4</sub> and its high refractive index caused by TiO<sub>2</sub>. Light microscopy images demonstrate the homogeneity of the deposited thin films (Figure 5.2b, c). Larger magnifications already reveal the porous and worm-like structure, which is typical for Mo:BiVO<sub>4</sub> synthesized by this route.<sup>[8,32-35]</sup> UV-VIS optical absorption spectroscopy shows the typical absorption of BiVO<sub>4</sub> on FTO-coated glass. Evaluation of the optical absorption using the Tauc-method reveals an indirect optical bandgap of  $\approx 2.4$  eV for the unprotected as well as for the protected Mo:BiVO<sub>4</sub> films, which agrees with previously reported bandgaps.<sup>[31,36]</sup> However, these measurements show a slight shift to longer wavelengths in the absorption spectra for NTO coated films while the bandgap remains unchanged (see Figure 5.2d). We attribute this behavior to the additional contribution of the NTO protection layer.

### 5.2.3 Structural Characterization

The XRD pattern of an as-deposited Mo:BiVO<sub>4</sub> thin-film on FTO (Figure 5.3a) shows distinct reflections of the phase-pure scheelite BiVO<sub>4</sub> phase and the subjacent FTO layer. The monoclinic scheelite has proven to be the most photoelectrochemically active phase of BiVO<sub>4</sub>, exhibiting also the highest stability under ambient conditions.<sup>[37]</sup> A shift to lower scattering angles in the diffraction pattern indicates a slightly larger unit cell corresponding to an enlargement of the d-spacing and hence the successful incorporation of molybdenum inside the crystal lattice (Figure 5.3a). The amorphous NTO protection layer and the co-catalyst layers are not visible in the XRD due to their very small layer thicknesses of equal or less than 2.5 nm. Scanning electron microscopy (SEM) reveals the previously described formation of the worm-like porous structure with an average diameter of  $\approx 300$  nm and pores of  $\approx 50$  nm in-between (Figure 5.3b,c).

Single crystal electron diffraction on a prepared FIB lamella further proves the presence of the desired scheelite-type structure of Mo:BiVO<sub>4</sub> (see Figure 5.3d-inset). The

atomic ratios determined from the EDX elemental maps of Bi, V, Mo, and Ti were found to be 45.5 %, 46.3 %, 4.57 %, and 3.65 %, respectively, which corresponds to the expected ratios of the stoichiometric composition of 10 at% Mo:BiVO<sub>4</sub> and the titanium containing NTO protective layer.

### 5.2.4 Electrochemical Characterization

The photoelectrochemical performance regarding water-oxidation was investigated using cyclic-voltammetry, linear sweep voltammetry and chronoamperometry under atmospheric conditions (under air, room temperature and 967 hPa air pressure) using a H<sub>3</sub>PO<sub>4</sub>/NaOH buffer at pH 7 as electrolyte with a platinum-coil as counter electrode and a reversible hydrogen electrode (RHE) as reference. Linear sweep voltammetry (see Figure 5.4) of the unmodified Mo:BiVO<sub>4</sub> thin films exhibits a photocurrent response of 1.4 mA cm<sup>-2</sup> at 1.23 V versus RHE, which is comparable to previously reported experiments.<sup>[8,38,39]</sup>

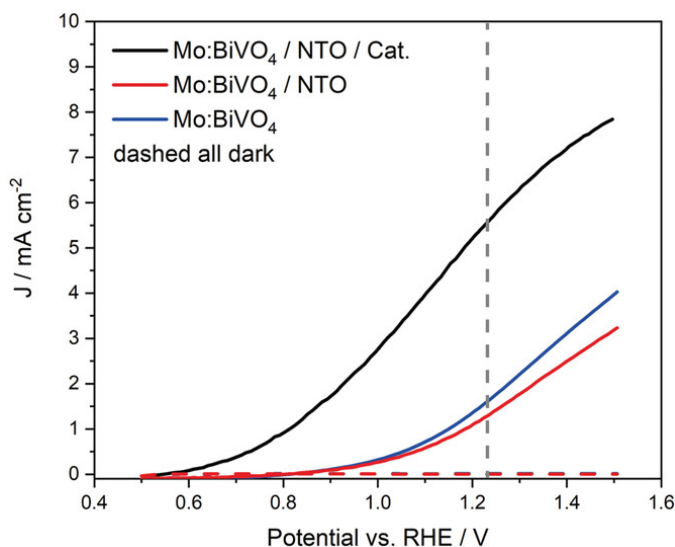


**Figure 5.4:** Linear sweep voltammetry of untreated Mo:BiVO<sub>4</sub> thin films (blue), with protective NTO coating (red) and protective NTO coating as well as deposited FeNiO<sub>x</sub> oxygen evolution catalyst (black). While the unprotected Mo:BiVO<sub>4</sub> reaches 1.5 mA cm<sup>-2</sup>, the protected one with additional catalyst reaches up to 5.6 mA cm<sup>-2</sup>. Without illumination the measured currents of all samples are shown as dashed line. The measurements were performed in pH 7 H<sub>3</sub>PO<sub>4</sub>/NaOH buffer solution, under simulated AM1.5G (455 nm LED calibrated to AM1.5G illumination) back side illumination and at a scan rate of 20 mV s<sup>-1</sup>.

Modification of the Mo:BiVO<sub>4</sub> with a 2.5 nm NTO protective layer results in a slight decrease in electrochemical activity to 1.3 mA cm<sup>-2</sup> at 1.23 V versus RHE, which can be explained by the non-conductive properties of the amorphous NTO, entailing an increased resistance for charge carriers traveling to the electrolyte interface. The depo-

sition of an  $\text{Fe}_{0.1}\text{Ni}_{0.9}\text{O}$  co-catalyst on top of the NTO layer results in a strong increase of electrochemical performance with photocurrents of  $5.6 \text{ mA cm}^{-2}$  at 1.23 V versus RHE. This demonstrates an increase in activity by a factor of four to the pristine MBV electrode and thus, to the best of our knowledge, establishes previously unattained activities for this type of material in terms of morphology, utilized pH value and illumination. However, at 1.5 V versus RHE the photocurrent density exceeds the theoretical maximum of  $7.5 \text{ mA cm}^{-2}$ . We attribute these corrosion currents to the dissolution of our catalyst, the protective layer or the FTO, which is used as a substrate under these harsh conditions.

The long-term stability was further investigated using chronoamperometric measurements for 16 h at 1.23 V versus RHE under chopped illumination using on-off cycles of 10 min duration (see Figure 5.5). The unprotected  $\text{Mo:BiVO}_4$  electrode (blue) achieved  $2.5 \text{ mA cm}^{-2}$  spontaneous current density at  $t = 0 \text{ s}$ , which stabilized at a steady-state current density of  $1.5 \text{ mA cm}^{-2}$  after 2 min. The photocurrent response increased to a maximum of about  $1.9 \text{ mA cm}^{-2}$  (at 1.23 V versus RHE) steady-state current over the following 2 h.

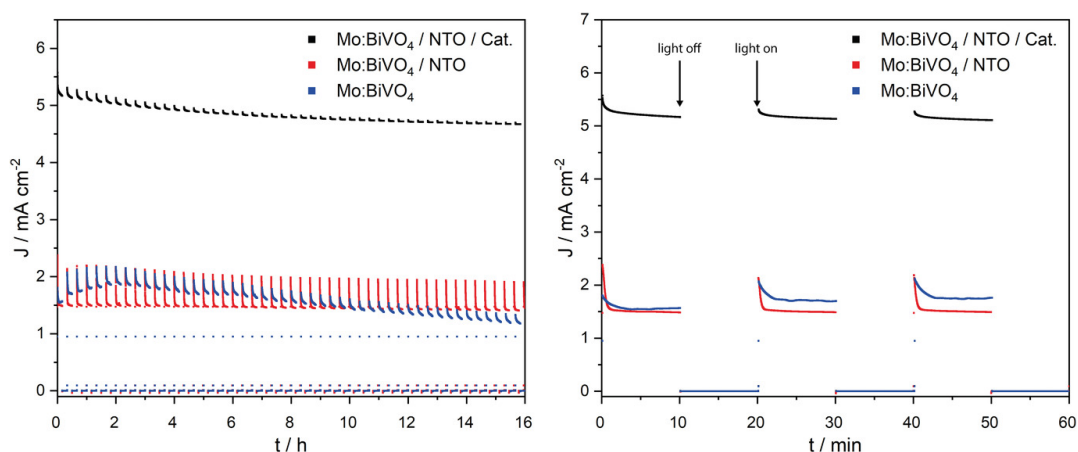


**Figure 5.5:** Chronoamperometric measurements for 16 h under chopped illumination (left) and a zoom-in of the first 60 min (right). Unmodified  $\text{Mo:BiVO}_4$  (blue) shows a constant degradation of the photocurrent after 2 h. NTO-protected  $\text{Mo:BiVO}_4$  shows a constant current without any signs of degradation for more than 16 h. An applied water oxidation catalyst ( $\text{Fe}_x\text{Ni}_{1-x}\text{O}$ ) increases the photoelectrochemical performance by a factor of 4.

The increase of photocurrent density can most likely be attributed to progressing corrosion of the electrode, probably of the photoabsorber itself. The dissolution of  $\text{Mo:BiVO}_4$  into the electrolyte leads to a loss of active material and therefore to reduced activity in the following hours of the long-time stability test. According to previous studies,  $\text{BiVO}_4$  undergoes leaching of  $\text{V}^{5+}$ -ions into the electrolyte during photo-induced corrosion, forming  $\text{Bi}_2\text{O}_3$  or Bi metal.<sup>[18,40,41]</sup> We confirmed the leaching of vanadium ions with ICP-OES measurements of the electrolyte after photoelectrochemistry for 2 h (Figure 5.8, Supporting Information). Thereby, the vanadium(V) concen-

trations, which are detected in the electrolyte after 2 h of the stability test, are strongly dependent on the type and the thickness of the protective layer. Not surprisingly, bare MBV shows the strongest dissolution effect, whereas thicker protective layers of more than 5 nm NTO inhibit the dissolution almost completely, but also strongly reduce the photoelectrochemical activity. Hereby, a 2.5 nm NTO layer exhibits the best compromise between good photoelectrochemical performance and corrosion stability of the material.

These findings are in agreement with previously reported studies of this material. Our NTO-protected electrodes exhibit slightly lower photocurrents of  $\approx 2.0 \text{ mA cm}^{-2}$  in the beginning, but remain at a stable photocurrent density over the entire 16 h measurement, outperforming the unprotected electrodes after 10 h. Application of an  $\text{Fe}_{0.1}\text{Ni}_{0.9}\text{O}$  co-catalyst on-top of the NTO-protected  $\text{Mo:BiVO}_4$  increases the photoelectrochemical activity by a factor of 4 compared to MBV, to about  $5.6 \text{ mA cm}^{-2}$  at the start of the measurement, stabilizing at  $4.9 \text{ mA cm}^{-2}$  after more than 16 h while maintaining its photoactive capabilities. Remarkably, the shape of the transient current responses (Figure 5.5) changes between the NTO-protected  $\text{Mo:BiVO}_4$  electrodes without co-catalyst and the NTO-protected  $\text{Mo:BiVO}_4$  electrodes with additional co-catalyst. These transients derive from the filling/emptying of surface states at the electrolyte/semiconductor interfaces, where photo-generated holes oxidize the water molecules.<sup>[42]</sup> However, these holes can also undergo recombination with electrons, reducing the number of available holes for the watersplitting process. This process can be described by the charge transfer efficiency  $\eta_{\text{transfer}}$ , which is defined as the ratio between the current used for water oxidation and the total current of holes generated. Compared to the pure  $\text{Mo:BiVO}_4$ , NTO-protected electrodes exhibit a much higher ratio of instantaneous current  $j_{\text{ini}}$  to steady-state current  $j_{\text{ss}}$  during the whole measurement. The ratio of  $j_{\text{ss}}$  to  $j_{\text{ini}}$  can be described as the hole transfer efficiency  $\eta_{\text{transfer}}$  and is commonly discussed in literature to compare minority carrier transfer efficiencies.<sup>[43–45]</sup>  $\eta_{\text{transfer}}$  for unprotected  $\text{Mo:BiVO}_4$  was calculated to be 84 %, which is comparable to the previously reported transfer efficiency.<sup>[8]</sup> However, the NTO-protected electrodes only show a hole transfer efficiency of 60 %, which indicates a lowered PEC (photoelectrochemical) performance due to the accumulation of charges that cannot be transported to the catalytically active sites and therefore undergo recombination, reducing the charge transfer efficiency. Remarkably, the hole transfer efficiency with the additional  $\text{Fe}_{0.1}\text{Ni}_{0.9}\text{O}$  co-catalyst layer increases to 93 %, which explains the outstanding performance of our MBV+NTO+Cat electrodes.

This behavior can be attributed to the fact that the conductivity and charge transport in Nb-doped titania is generally quite poor compared to other metal oxides or to  $\text{BiVO}_4$  itself, which leads to hole accumulation on its interface to the electrolyte.<sup>[46]</sup> However, the application of an  $\text{Fe}_{0.1}\text{Ni}_{0.9}\text{O}$  co-catalyst leads to faster transient current responses, indicating the fast and effective hole transfer capabilities of the catalyst.

## 5.3 Conclusion

In conclusion, we were able to demonstrate a strategy for producing highly active and long-term stable photoanodes for water splitting oxidation applications. 10 at%-Mo:BiVO<sub>4</sub> was used as photo-absorbing semiconductor, protected against dissolution with a conformal, amorphous and oxidation-stable niobium-doped titanium oxide ALD coating and combined with Fe<sub>0.1</sub>Ni<sub>0.9</sub>O as highly active water oxidation co-catalyst. The doping of niobium in titania suppresses the undesired crystallization of titanium dioxide and enables the formation of ultra-thin, contiguous layers on the corrugated photoabsorber surfaces. This strategy enables photoelectrochemical current densities of up to 5.6 mA cm<sup>-2</sup> at pH 7 under AM1.5G illumination at 1.23 V versus RHE with unprecedented stability for more than 16 h. Thereby, these modified photoanodes outperform unmodified Mo:BiVO<sub>4</sub> by a factor of 4 and undoped BiVO<sub>4</sub> by a factor of 5. Such layers protect the actual photoactive semiconducting material while being thin enough for rapid charge transfer at the electrode-electrolyte interface. The added Fe<sub>0.1</sub>Ni<sub>0.9</sub>O co-catalyst exhibits excellent catalytic abilities for water oxidation, which increases the hole transfer efficiencies toward the electrolyte and allows for the significant photocurrent increase compared to bare 10 at%-Mo:BiVO<sub>4</sub> electrodes. This study shows the importance of designing an oxidation-stable and ultra-thin protective layer like NTO combined with a highly active water oxidation co-catalyst such as Fe<sub>0.1</sub>Ni<sub>0.9</sub>O to achieve both high performance and long-term stability with Mo:BiVO<sub>4</sub> photoanodes.

## 5.4 Experimental Section

*Chemicals Origin:* Chemicals stated in the experimental part were exclusively supplied by the following suppliers: Vanadium(V) oxytriethoxide: Aldrich, Bi(2-ethylhexanoate): Alfa Aesar, MoO<sub>2</sub>(acac)<sub>2</sub>: Aldrich, Chloroform: VWR, Iron(II) chloride: Aldrich, Nickel(II) chloride: Aldrich.

*Synthesis of Mo:BiVO<sub>4</sub> Thin Films:* The synthesis of the Mo:BiVO<sub>4</sub> thin films was performed similar to a procedure of Rohloff et al.<sup>[8]</sup> with a molybdenum content of 10 at%. 0.7 mmol (123  $\mu$ L) of VO(OEt)<sub>3</sub> were dissolved in 1.5 mL chloroform. After stirring for 10 min, 0.7 mmol (445 mg) Bi(2-ethylhexanoate) and 0.072 mmol (22.6 mg) MoO<sub>2</sub>(acac)<sub>2</sub> were added to the solution. After stirring overnight, the precursor was dip-coated on FTO-coated substrates at 300 mm min<sup>-1</sup> withdrawal speed. The as-prepared films were dried at 60 °C for 15 min. After an aging step at 100 °C for 12 h, the films were calcined at 450 °C for 2 h (heating ramp of 0.5 °C min<sup>-1</sup>) under atmospheric conditions.

*Deposition of the Protection Layers by ALD:* The NTO protection layer was grown using a sandwich methodology with alternating TiO<sub>2</sub> and NbO<sub>x</sub> layers, according to Hufnagel et al.,<sup>[27]</sup> employing a Picosun R-200 Advanced ALD reactor at a temperature of 200 °C and a base pressure of 2 hPa. Nitrogen gas (Air Liquide, 99.999 %) was used as purging and carrier gas. Titanium tetraisopropoxide (TTIP, Aldrich, 99.999 %) was evaporated from a stainless steel vessel at 85 °C, niobium ethoxide (NEO, Strem, 99.9+ %) was

supplied from a glass vessel at 160 °C. Ultrapure water (MilliQ, 18.2 M $\Omega$  cm) was held in a stainless steel cylinder at 19 °C. Each TiO<sub>2</sub> ALD cycle comprised two TTIP pulses (1.6 s pulse, 4.5 s static exposure, 6 s purge) and one water pulse (2 s pulse, 4.5 s static exposure, 7.5 s purge). The resulting growth per cycle (GPC) was 0.038 nm cycle<sup>-1</sup>. NbO<sub>x</sub> was deposited using cycles of four NEO pulses (1.6 s pulse, 6.5 s static exposure, 6 s purge) and one water pulse as in the TiO<sub>2</sub> process. The growth per cycle was 0.068 nm cycle<sup>-1</sup>. Mixed oxide layers were grown by interspersing one NbO<sub>x</sub> cycle in the TiO<sub>2</sub> process every 10 intervals. Amorphous tin oxide and aluminum oxide layers were deposited in the same ALD machine at 200 °C. Trimethylaluminum (TMA, Strem, min. 98 %) was kept at 19 °C as well as the ultrapure water. One AlO<sub>x</sub> ALD cycle comprised one TMA pulse (0.1 s pulse, 4 s static exposure, 6 s purge) and one water pulse (0.1 s pulse, 4 s static exposure, 6 s purge). The resulting growth per cycle (GPC) was 0.1 nm cycle<sup>-1</sup>. Tetrakis(dimethylamino)tin(IV) (TDMASn, Strem, 99 %) was evaporated from a stainless steel cylinder at 75 °C. Ozone was produced by an ozone generator (INUSA AC2025). SnO<sub>x</sub> was deposited using cycles of two TDMASn pulses (1.6 s pulse, 7.5 s static exposure, 7.5 s purge) and one ozone pulse (2 s pulse, 6 s static exposure, 4 s purge). The growth per cycle was 0.14 nm cycle<sup>-1</sup>. The thickness of the ALD deposited ultra-thin protective layers was determined using ellipsometry (J. A. Woollam M-2000D) with films grown under identical conditions on Si(110) substrates. NTO, SnO<sub>x</sub> and AlO<sub>x</sub> layers were modelled using a Cauchy function.

*Electrode Characterization:* X-ray diffraction (XRD) patterns were recorded on a Bruker D8 Discover diffractometer using Cu-K $\alpha$  radiation with  $\lambda = 1.54178$  Å. The Open Crystallography Database (OCD) was used as XRD reference dataset. Crystallite sizes were estimated using the Scherrer equation. SEM images and FIB lamella preparation was done using an FEI Helios Nanolab G3 UC, equipped with a Schottky-type Field-Emitter and Ga<sup>+</sup>-focused ion beam, operated between 1 and 30 kV. (S)TEM images and EDX maps were acquired on an FEI Titan Themis 80–300 microscope operated at 300 kV acceleration voltage, equipped with an X-FEG electron source, a monochromator, a Cs-corrector and a HAADF detector.

*Electrochemical Deposition of Fe<sub>0.1</sub>Ni<sub>0.9</sub>O Co-Catalyst:* The iron-doped nickel oxide co-catalyst was deposited on the previously prepared and ALD-protected Mo:BiVO<sub>4</sub> thin films using consecutive cathodic electrodeposition, similar to reported procedures.<sup>[47–50]</sup> A 0.1 × 10<sup>-3</sup> M precursor solution containing Fe(II)Cl<sub>2</sub> and Ni(II)Cl<sub>2</sub> was used to deposit the co-catalyst by applying -0.1 mA at galvanostatic conditions for 20 s. The voltage for the deposition varied between -0.5 and -0.8 V versus RHE. The as-deposited films were rinsed with water and dried at 60 °C for 2 h.

*Photoelectrochemical Characterization:* All samples were prepared for photoelectrochemical characterization by contacting the FTO substrate using Ag-based conductive lacquer. The sample area was determined by applying PTFE adhesive tape with a reflective coating as mask. The mask contained a circular hole with a diameter of 0.5 cm which corresponds to an exposed area of 0.1963 cm<sup>2</sup>. The photoelectrochemical experiments were performed using a three-electrode setup with coiled Pt wire as counter

electrode and a reversible hydrogen electrode (Gaskatel HydroFlex) as reference electrode. A  $\text{H}_3\text{PO}_4/\text{NaOH}$  buffer solution at pH 7 was used as electrolyte. The electrolyte was stirred during all measurements using a rod stirrer to prevent local concentration gradients. The samples were illuminated by a 455 nm LED, calibrated to AM1.5G conditions using a calibrated Si diode under consideration of the spectral mismatch. All experiments were performed at room temperature and under air. Cyclic voltammetry, linear sweep voltammetry, galvanostatic experiments as well as electrochemical deposition of the  $\text{Fe}_{0.1}\text{Ni}_{0.9}\text{O}$  co-catalyst were performed using a Metrohm Autolab PGSTAT302N potentiostat/galvanostat.

## 5.5 References

- [1] L. L. Mastropasqua, I. Pecenati, A. Giostri, S. Campanari, *Appl. Energy* **2020**, *261*, 114392.
- [2] R. P. Micena, O. R. Llerena-Pizarro, T. M. de Souza, J. L. Silveira, *Int. J. Hydrogen Energy* **2020**, *45*, 2308.
- [3] D. P. Pham, S. Lee, A. H. T. Le, E.-C. Cho, Y. H. Cho, J. Yi, *Chem. Commun.* **2020**, *116*, 107926.
- [4] L. Pan, Y. Liu, L. Yao, R. Dan, K. Sivula, M. Grätzel, A. Hagfeldt, *Nat. Commun.* **2020**, *11*, 318.
- [5] J. Kampmann, S. Betzler, H. Hajiyani, S. Häringer, M. Beetz, T. Harzer, J. Kraus, B. V. Lotsch, C. Scheu, R. Pentcheva, D. Fattakhova-Rohlfing, T. Bein, *Nanoscale* **2020**, *12*, 7766.
- [6] B. S. Kalanoor, H. Seo, S. S. Kalanur, *Mater. Sci. Technol.* **2018**, *1*, 49.
- [7] F. F. Abdi, N. Firet, R. van de Krol, *ChemCatChem* **2013**, *5*, 490.
- [8] M. Rohloff, B. Anke, S. Zhang, U. Gernert, C. Scheu, M. Lerch, A. Fischer, *Sustainable Energy Fuels* **2017**, *1*, 1830.
- [9] X. Zhao, J. Hu, S. Chen, Z. Chen, *Phys. Chem. Chem. Phys.* **2018**, *20*, 13637.
- [10] M. Barzgar Vishlaghi, A. Kahraman, S. Kaya, *J. Phys. Chem. C* **2020**, *124*, 1337.
- [11] D. K. Zhong, D. R. Gamelin, *J. Am. Chem. Soc.* **2010**, *132*, 4202.
- [12] Y. Kai-Hang, L. Haibo, H. Duan, X. Shuang, Q. Weitao, L. Mingyang, H. Yuwen, M. Wenjie, J. Hongbing, Y. Shihe, *Nat. Commun.*, *10*, 3687.
- [13] Y. Y. Pihosh, I. Turkevych, K. Mawatari, J. Uemura, Y. Kazoe, S. Kosar, K. Makita, T. Sugaya, T. Matsui, D. Fujita, M. Tosa, M. Kondo, T. Kitamori, *Sci. Rep.* **2015**, *5*, 11141.
- [14] S. Kosar, Y. Pihosh, R. Bekarevich, K. Mitsuishi, K. Mawatari, Y. Kazoe, T. Kitamori, M. Tosa, A. B. Tarasov, E. A. Goodilin, Y. M. Struk, M. Kondo, I. Turkevych, *Appl. Nanosci.* **2019**, *9*, 1017.

- [15] P. Dias, A. Vilanova, T. Lopes, L. Andrade, A. Mendes, *Nano Energy* **2016**, *23*, 70.
- [16] O. Zandi, T. W. Hamann, *Phys. Chem. Chem. Phys.* **2015**, *17*, 22485.
- [17] Z. Z. Zhang, I. Karimata, H. Nagashima, S. Muto, K. Ohara, K. Sugimoto, T. Tachikawa, *Nat. Commun.* **2019**, *10*, 4832.
- [18] S. Zhang, M. Rohloff, O. Kasian, A. M. Mingers, K. J. J. Mayrhofer, A. Fischer, C. Scheu, S. Cherevko, *J. Mater. Chem. C* **2019**, *123*, 23410.
- [19] D. Lee, A. Kvit, K.-S. Choi, *Chem. Mater* **2018**, *30*, 4704.
- [20] S. S. Zhang, I. Ahmet, S.-H. Kim, O. Kasian, A. M. Mingers, P. Schnell, M. Kölbach, J. Lim, A. Fischer, K. J. J. Mayrhofer, S. Cherevko, B. Gault, R. van de Krol, C. Scheu, *ACS Appl. Energy Mater.* **2020**, *3*, 9523.
- [21] A. Qayum, M. Guo, J. Wei, S. Dong, X. Jiao, D. Chen, T. Wang, *J. Mater. Chem. A* **2020**, *8*, 10989.
- [22] T. Moehl, J. Suh, L. Sévery, R. Wick-Joliat, S. D. Tilley, *ACS Appl. Mater. Interfaces* **2017**, *9*, 43614.
- [23] M. F. M. F. Lichterman, K. Sun, S. Hu, X. Zhou, M. T. McDowell, M. R. Shaner, M. R. Richter, E. J. Crumlin, A. I. Carim, F. H. Saadi, B. S. Brunshwig, N. S. Lewis, *Catal. Today* **2016**, *262*, 11.
- [24] C. Ros, T. Andreu, J. R. Morante, *J. Mater. Chem. A* **2020**, *8*, 10625.
- [25] C. Das, P. Roy, M. Yang, H. Jha, P. Schmuki, *Nanoscale* **2011**, *3*, 3094.
- [26] M. Hannula, H. Ali-Löyty, K. Lahtonen, E. Sarlin, J. Saari, M. Valden, *Chem. Mater.* **2018**, *30*, 1199.
- [27] A. G. Hufnagel, S. Häring, M. Beetz, B. Böller, D. Fattakhova-Rohlfing, T. Bein, *Nanoscale* **2019**, *11*, 14285.
- [28] B. J. O'Neill, D. H. K. Jackson, J. Lee, C. Canlas, P. C. Stair, C. L. Marshall, J. W. Elam, T. F. Kuech, J. A. Dumesic, G. W. Huber, *ACS Catal.* **2015**, *5*, 1804.
- [29] Q. Peng, J. S. Lewis, P. G. Hoertz, J. T. Glass, G. N. Parsons, *J. Vac. Sci. Technol.* **2012**, *30*, 010803.
- [30] S. Seo, S. Jeong, H. Park, H. Shin, N.-G. Park, *Chem. Commun.* **2019**, *55*, 2403.
- [31] J. Y. Kim, *Key Eng. Mater.* **2017**, *753*, 156.
- [32] D. T. T. Trinh, W. Khanitchaidecha, D. Channei, A. Nakaruk, *Res. Chem. Intermed.* **2019**, *45*, 5217.
- [33] Y. Liu, Y. Jiang, F. Li, F. Yu, W. Jiang, L. Xia, *J. Mater. Chem. A* **2018**, *6*, 10761.
- [34] L. Meng, W. Tian, F. Wu, F. Cao, L. Li, *J. Mater. Sci. Technol.* **2019**, *35*, 1740.
- [35] M. Huang, J. Bian, W. Xiong, C. Huang, R. Zhang, *J. Mater. Chem. A* **2018**, *6*, 3602.
- [36] F. Opoku, K. K. Govender, C. G. C. E. van Sittert, P. P. Govender, *New J. Chem.* **2017**, *41*, 11701.

- 
- [37] S. Tokunaga, H. Kato, A. Kudo, *Chem. Mater* **2001**, *13*, 4624.
- [38] S. K. Pilli, T. E. Furtak, L. D. Brown, T. G. Deutsch, J. A. Turner, A. M. Herring, *Energy Environ. Sci.* **2011**, *4*, 4025.
- [39] J. A. Seabold, K. Zhu, N. R. Neale, *Phys. Chem. Chem. Phys.* **2014**, *16*, 1121.
- [40] X. X. Yao, X. Zhao, J. Hu, H. Xie, D. Wang, X. Cao, Z. Zhang, Y. Huang, Z. Chen, T. Sritharan, *Science* **2019**, *19*, 976.
- [41] F. M. Toma, J. K. Cooper, V. Kunzelmann, M. T. McDowell, J. Yu, D. M. Larson, N. J. Borys, C. Abelyan, J. W. Beeman, K. M. Yu, J. Yang, L. Chen, M. R. Shaner, J. Spurgeon, F. A. Houle, K. A. Persson, I. D. Sharp, *Nat. Commun.* **2016**, *7*, 12012.
- [42] F. A. L. Laskowski, J. Qiu, M. R. Nellist, S. Z. Oener, A. M. Gordon, S. W. Boettcher, *Sustainable Energy Fuels* **2018**, *2*, 1995.
- [43] L. M. Peter, *J. Solid State Electrochem.* **2013**, *17*, 315.
- [44] L. M. Peter, *Chem. Rev.* **1990**, *90*, 753.
- [45] L. M. Abrantes, L. M. Peter, *J. Electroanal. Chem.* **1983**, *150*, 593.
- [46] D. Tafalla, P. Salvador, *J. Electroanal. Chem.* **1989**, *270*, 285.
- [47] Q. J. Wang, Y.-W. Chung, *Encyclopedia of Tribology*, p. s.l, Springer US, Boston, MA, **2013**.
- [48] S. Mandati, B. V. Sarada, S. R. Dey, S. V. Joshi, *Semiconductors – Growth and Characterization*, InTech, London, **2018**.
- [49] S. Jiao, L. Xu, K. Hu, J. Li, S. Gao, D. Xu, *J. Mater. Chem. C* **2010**, *114*, 269.
- [50] S. P. Mahesh, S. Seung Wook, G. V. Uma, K. Jihun, J. Hye Won, K. Soon Hyung, J. H. Kim, *J. Mater. Chem. A* **2018**, *6*, 20678.

## 5.6 Appendix

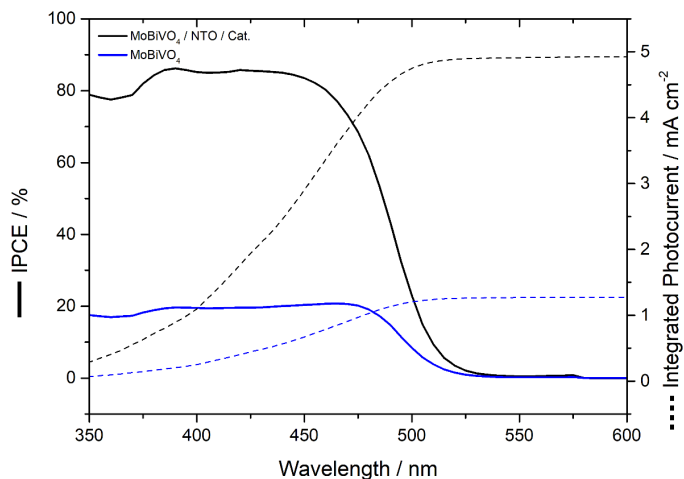


**Figure 5.6:** Incident photon-to-current efficiencies and integrated photocurrent (dashed) of a bare Mo:BiVO<sub>4</sub> and an NTO protected Mo:BiVO<sub>4</sub> device with additional co-catalyst at 1.23 V vs. RHE under a AM1.5G solar simulator.

IPCE measurements were performed with a home-built setup using a 150 W Xe short arc lamp (LOT Oriel) combined with a monochromator (Horiba microHR) and two Si-diodes (Hamamatsu) to calibrate the photon flux and compensate for light intensity fluctuations. The current was measured using a potentiostat (Metrohm Autolab) and a lock-in amplifier at 1 Hz at 1.23 V vs. RHE applied potential.

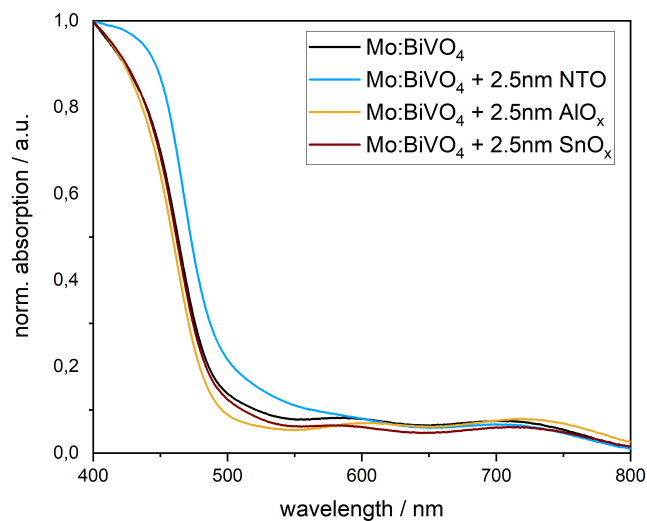


**Figure 5.7:** UV/VIS absorption spectra of bare Mo:BiVO<sub>4</sub> (black), with additional 2.5 nm NTO protective layer (blue), with additional 2.5 nm AlO<sub>x</sub> (orange) and with additional 2.5 nm SnO<sub>x</sub> protective layer (brown).

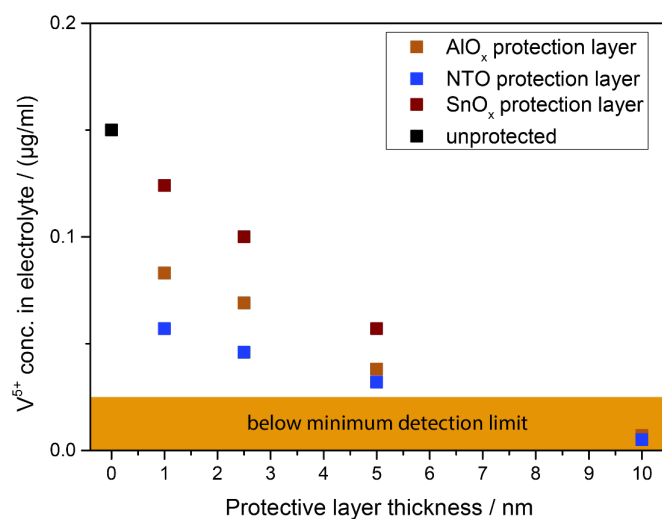


**Figure 5.8:** ICP-OES measurements of the electrolyte after 2 h photoelectrochemistry under standard conditions.

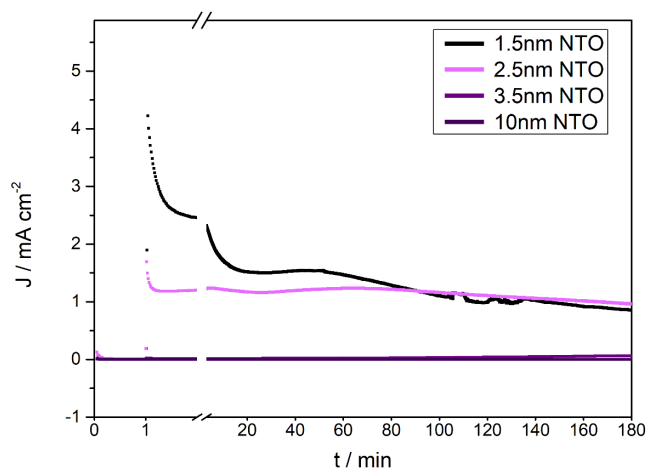


**Figure 5.9:** Chronoamperometric measurements at 1.23 V vs. RHE and pH 7 for 180 min of various Mo:BiVO<sub>4</sub> thin-films protected by 1.5 to 10 nm NTO layers, applied by ALD.

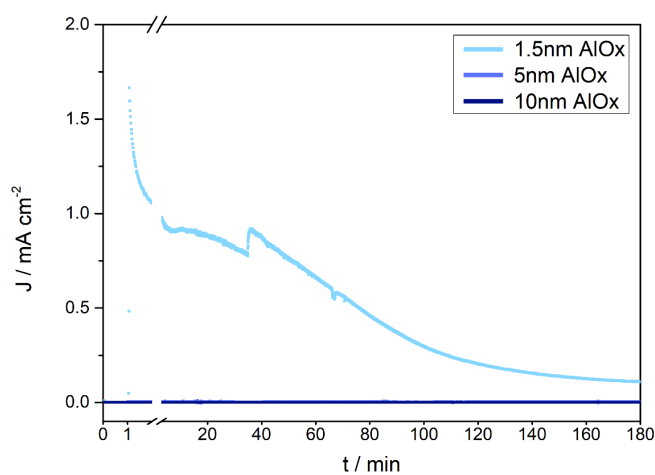


**Figure 5.10:** Chronoamperometric measurements at 1.23 V vs. RHE and pH 7 for 180 min of various Mo:BiVO<sub>4</sub> thin-films protected by 1.5 to 10 nm AlO<sub>x</sub> layers, applied by ALD.

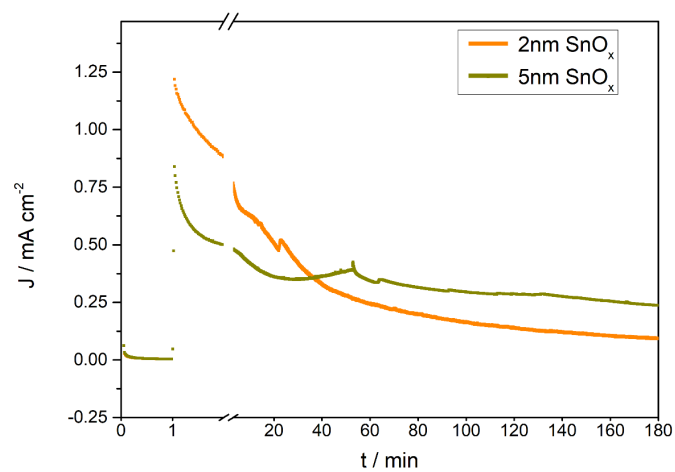


**Figure 5.11:** Chronoamperometric measurements at 1.23 V vs. RHE and pH 7 for 180 min of various Mo:BiVO<sub>4</sub> thin-films protected by 2 to 10 nm SnO<sub>x</sub> layers, applied by ALD.



**Figure 5.12:** Oxygen bubble formation on the electrode during photoelectrochemistry.

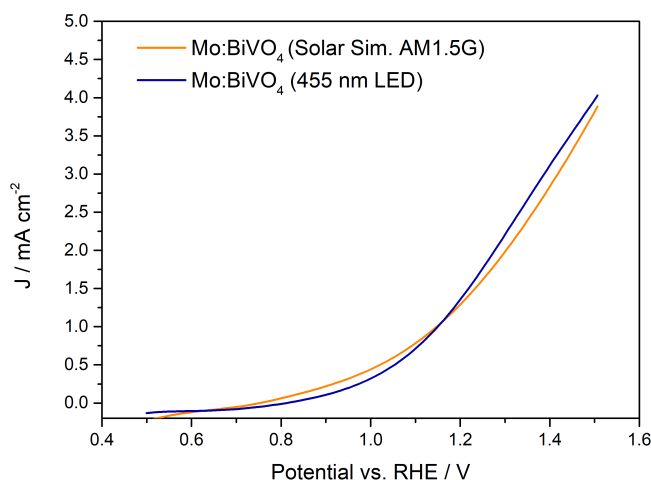


**Figure 5.13:** Linear sweep voltammetry of bare Mo:BiVO<sub>4</sub> exhibits a similar photocurrent response using a Xe lamp AM 1.5 solar simulator (Solar Light Co. Model 16S, class ABA) (orange) and a 455 nm LED, calibrated to 100 mW cm<sup>-2</sup> under consideration of the spectral mismatch of the LED to the sun's spectrum. Therefore, the spectral mismatch from the LED to the AM1.5G spectrum was determined using the spectrum of the LED and the spectral photocurrent response of a Hamamatsu Si-diode to calibrate the LED's intensity accordingly in the range of 0.5 – 1.5 V vs. RHE.

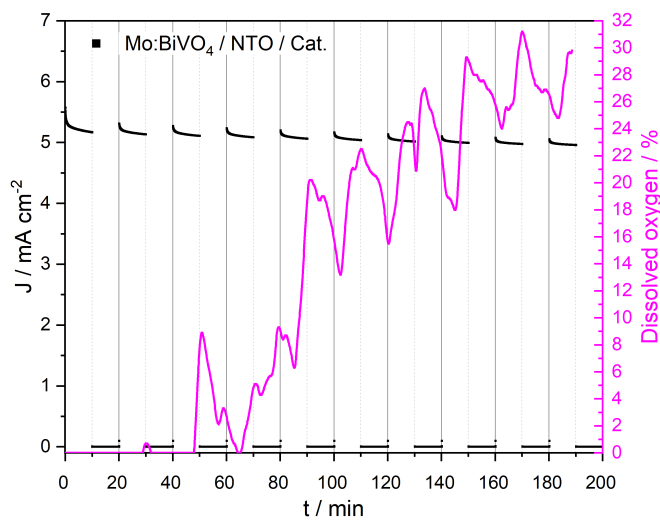


**Figure 5.14:** Detected dissolved oxygen during chronoamperometric measurements of a Mo:BiVO<sub>4</sub> / NTO / Cat. device at pH 7 and 1.23 V vs RHE and simulated AM1.5G illumination using an HANNA Instruments HI 2400 Dissolved Oxygen Meter. The electrolyte solution was stirred and flushed with nitrogen during the measurement to prevent oxygen saturation of the electrolyte.

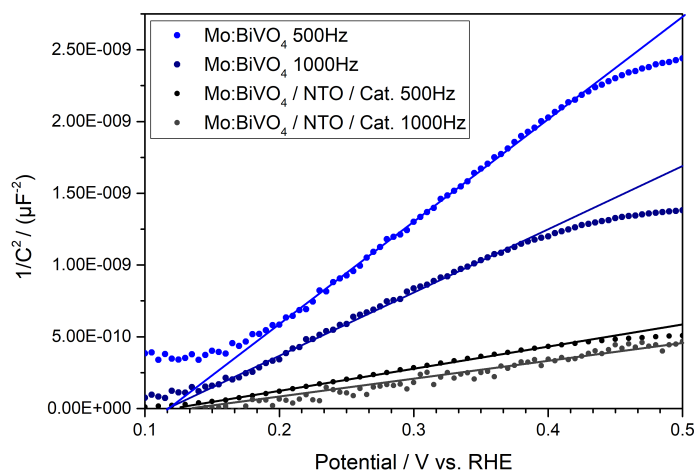


**Figure 5.15:** Mott-Schottky plots of bare Mo:BiVO<sub>4</sub> and Mo:BiVO<sub>4</sub>/ NTO/ Cat. at Nyquist frequencies of 500 Hz and 1000 Hz, respectively. The flatband potential of the bare Mo:BiVO<sub>4</sub> is determined as 0.12 V vs RHE while the flatband potential of the Mo:BiVO<sub>4</sub>/ NTO/ Cat. device was determined to 0.13 V vs. RHE.

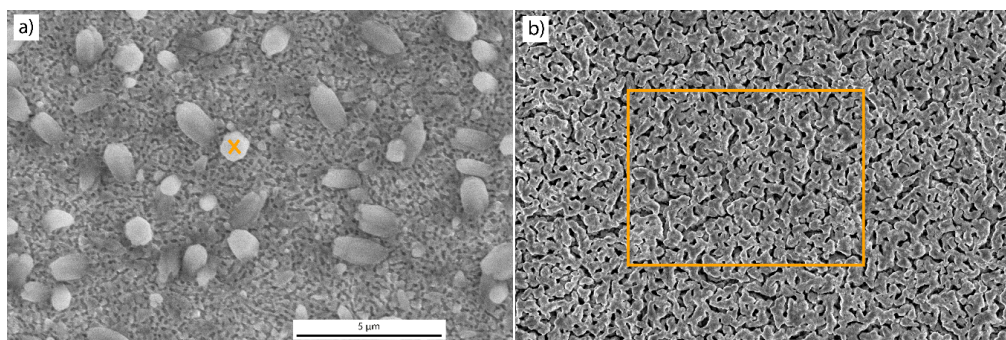


**Figure 5.16:** a) SEM images of an unprotected Mo:BiVO<sub>4</sub> film after 16 h reveals large crystallites grown from the Mo:BiVO<sub>4</sub> worm-like structure. EDX measurements (orange cross) reveal a elemental composition of 6.29 at% Bi to 93.71 at% O, indicating the presence of a bismuth oxide. Molybdenum and vanadium were not found at the marked position anymore. b) SEM image of an Mo:BiVO<sub>4</sub>/ NTO/ Cat. device after 16 h PEC revealing mostly intact worm-like structure of the Mo:BiVO<sub>4</sub>. The elemental composition at the orange rectangle was determined as 45.4 at% Bi, 46.2 at% V, 5.07 at% Mo and 3.33 at% Ti.

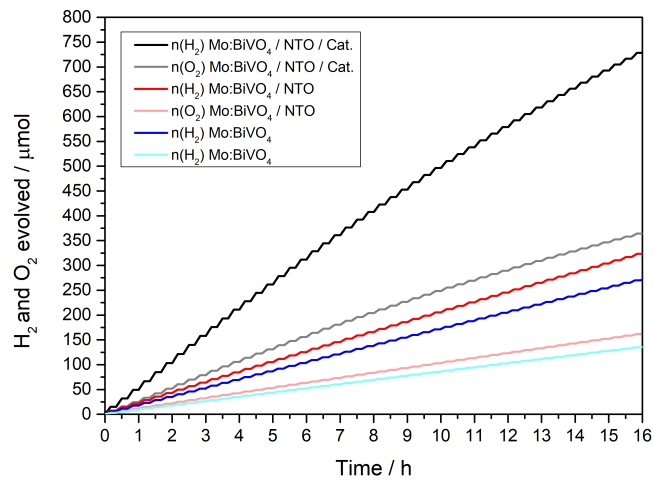


**Figure 5.17:** Calculated  $\text{H}_2$  and  $\text{O}_2$  evolution by  $\text{Mo:BiVO}_4/\text{NTO}/\text{Cat.}$  ( $\text{H}_2$ : black,  $\text{O}_2$ : gray),  $\text{Mo:BiVO}_4/\text{NTO}$  ( $\text{H}_2$ : red,  $\text{O}_2$ : light red) and  $\text{BiVO}_4$  ( $\text{H}_2$ : blue,  $\text{O}_2$ : light blue) at 1.23 V vs. RHE, pH 7 and simulated AM1.5G illumination assuming 100 % Faradaic efficiency from the chronoamperometric measurement shown in Fig. 5.5.

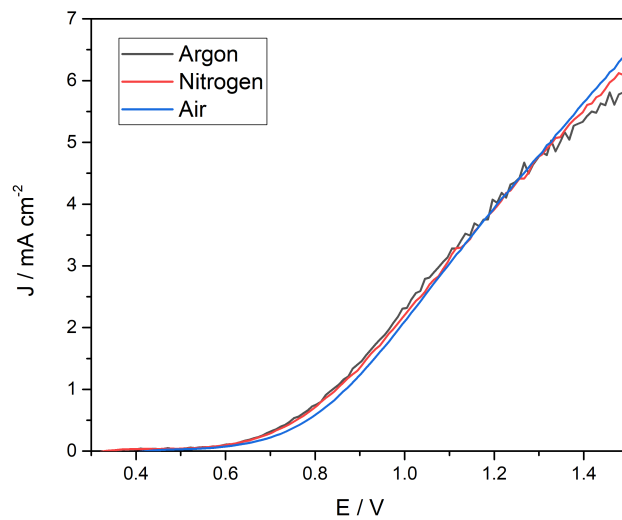
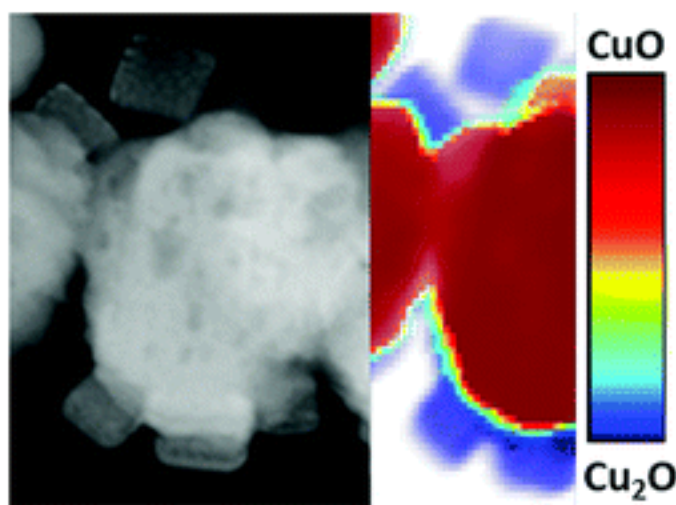


**Figure 5.18:** Linear sweep voltammetry of a  $\text{Mo:BiVO}_4/\text{NTO}/\text{Cat.}$  device in pH 7 buffer, saturated with air (blue), nitrogen (red) and argon (black) and illuminated by a AM1.5G solar simulator, exhibits no dependency of the photoelectrochemical current densities to the dissolved gases in the electrolyte.

## 6 How Photocorrosion Can Trick You: a Detailed Study on Low-bandgap Li doped CuO Photocathodes for Solar Hydrogen Production

This chapter is based on the following publication:

Jonathan Kampmann, Sophia Betzler, Hamidreza Hajiyani, Sebastian Häring, Michael Beetz, Tristan Harzer, Jürgen Kraus, Bettina V. Lotsch, Christina Scheu, Rossitza Pentcheva, Dina Fattakhova-Rohlfing\* and Thomas Bein\* *Nanoscale*, 2020, 12, 7766.



Sebastian Häring developed and optimized the deposition process for the ultra-thin protective coatings, contributed to the electrochemical analysis of the photoelectrodes and wrote the corresponding parts of the manuscript.

## Abstract

The efficiency of photoelectrochemical tandem cells is still limited by the availability of stable low band gap electrodes. In this work, we report a photocathode based on lithium doped copper(II) oxide, a black p-type semiconductor. Density functional theory calculations with a Hubbard U term show that low concentrations of Li ( $\text{Li}_{0.03}\text{Cu}_{0.97}\text{O}$ ) lead to an upward shift of the valence band maximum that crosses the Fermi level and results in a p-type semiconductor. Therefore, Li doping emerged as a suitable approach to manipulate the electronic structure of copper oxide based photocathodes. As this material class suffers from instability in water under operating conditions, the recorded photocurrents are repeatedly misinterpreted as hydrogen evolution evidence. We investigated the photocorrosion behavior of  $\text{Li}_x\text{Cu}_{1-x}\text{O}$  cathodes in detail and give the first mechanistic study of the fundamental physical process. The reduced copper oxide species were localized by electron energy loss spectroscopy mapping.  $\text{Cu}_2\text{O}$  grows as distinct crystallites on the surface of  $\text{Li}_x\text{Cu}_{1-x}\text{O}$  instead of forming a dense layer. Additionally, there is no obvious  $\text{Cu}_2\text{O}$  gradient inside the films, as  $\text{Cu}_2\text{O}$  seems to form on all  $\text{Li}_x\text{Cu}_{1-x}\text{O}$  nanocrystals exposed to water. The application of a thin  $\text{Ti}_{0.8}\text{Nb}_{0.2}\text{O}_x$  coating by atomic layer deposition and the deposition of a platinum co-catalyst increased the stability of  $\text{Li}_x\text{Cu}_{1-x}\text{O}$  against decomposition. These devices showed a stable hydrogen evolution for 15 minutes.

## 6.1 Introduction

Events like the Paris agreement in the year 2015 again demonstrate the desire of our modern society to reduce emissions caused by fossil fuels. Consequently, the focus on research for sustainable energy sources has been increasing in recent years. Compared to wind power, hydroelectric power and tidal power plants, sunlight is by far the most prominent energy source we can exploit to meet mankind's rising demands.<sup>[1]</sup> An additional challenge beside harvesting sunlight and converting it into electricity is large scale energy storage, which is essential for the replacement of fossil fuels. One approach to address this demanding task is the use of hydrogen gas for powering both fuel cells and fertilizer production, envisioning the establishment of a so called 'hydrogen economy'. Inspired by photosynthesis, photoelectrochemical (PEC) water splitting is a promising process to generate hydrogen and oxygen gas.<sup>[2-5]</sup> While there is lively discussion on the subject, potential advantages of a photoelectrochemical cell compared to the combination of an electrolyzer with a conventional solar cell can be the reduction of overpotentials as well as reduced fabrication cost and complexity of the final devices.<sup>[5,6]</sup> In contrast to photocatalysis, oxygen and hydrogen are produced in spatially separated compartments, hence avoiding subsequent separation, facilitating their storage and preventing the accumulation of an explosive gas mixture. Suitable semiconducting materials for

PEC cathodes are based on silicon,<sup>[6-9]</sup> metal oxides<sup>[3,5]</sup> or organic semiconductors.<sup>[10-12]</sup>

Many earth abundant metal oxides are known to exhibit reasonable stability as well as photoactivity in water splitting applications.<sup>[13–15]</sup> This led to the development of synthesis methods for novel binary<sup>[16–19]</sup> and ternary<sup>[20,21]</sup> metal oxides as well as doping of well-known metal oxides.<sup>[22–24]</sup> Besides the extensive work on materials with optical bandgaps in the range of 2.0–3.0 eV,<sup>[14,15,24–26]</sup> there is also need for low band gap photoabsorbers in order to build efficient PEC tandem cells. Such devices consist of an n-type photoanode connected to a p-type photocathode to harvest a substantial portion of the solar spectrum, reaching theoretical solar-to-hydrogen conversion efficiencies of up to 21.6 %.<sup>[5,25,27]</sup>

Copper oxide based photocathodes have aroused broad interest due to their low toxicity and the good availability of copper based compounds<sup>[22,28–34]</sup> The reported band gaps of 1.35–1.7 eV and 2.0–2.2 eV for CuO and Cu<sub>2</sub>O respectively, allow for significant light absorption in the visible range and provide enough energy for photoelectrochemical reactions.<sup>[35–39]</sup> The conduction band edges of the intrinsic p-type semiconductors CuO and Cu<sub>2</sub>O<sup>[36,37]</sup> fit both the reduction potentials of water,<sup>[14,38]</sup> and CO<sub>2</sub>,<sup>[40]</sup> which enables the reduction of these reagents by photo-generated electrons. The incorporation of Al or Pd into the structure of cupric oxide was shown to increase both the photo-corrosion stability and the performance of those devices significantly.<sup>[41,42]</sup> Besides this, doping CuO with Li has already been proven to be a suitable way to lower the optical band gap and increase the electrical conductivity<sup>[22,23,35,43]</sup> which is key to enhance its performance for photoelectrochemical water splitting applications. Therefore, the photoelectrochemical study solely covers results on Li doped CuO and does not compare it with undoped CuO. Several groups have reported the discovery of highly efficient photocathodes based on CuO.<sup>[22,33,44–47]</sup> However, it has been observed that photocurrents may be easily misinterpreted as evidence for hydrogen evolution which should be critically scrutinized.<sup>[44–46]</sup> On the other hand, also justified doubts exist already about the stability of this metal oxide under reductive potentials.<sup>[48,49]</sup> High cathodic dark currents and a significant decay in performance within the first minutes under operating conditions could point towards cathodic corrosion of this photoabsorber.<sup>[35,50,51]</sup> The reduction potential of CuO in aqueous electrolyte lies above the reduction potential of water.<sup>[29]</sup> This implies the possibility of a competitive reduction of water and the photoabsorber itself, leading to the formation of reduced copper species such as Cu<sub>2</sub>O and metallic copper under operating conditions, and consequently to a significant change of the photocathode morphology due to photocorrosion.<sup>[49,52,53]</sup> Other copper containing photocathode materials like Cu<sub>2</sub>O,<sup>[14,54]</sup> CuFeO<sub>2</sub><sup>[17]</sup> and CuBi<sub>2</sub>O<sub>4</sub><sup>[19]</sup> are also affected by photocorrosion, which further motivated us to investigate this phenomenon in detail. Recently, more detailed corrosion studies on CuO<sup>[55]</sup> and BiVO<sub>4</sub><sup>[56–58]</sup> concentrated on the mechanisms behind the loss in activity and addressed this by the use of protective layers and suitable cocatalysts. Here, we report on the first extensive photocorrosion study revealing detailed insights into the transformations taking place in copper(II) oxide thin film electrodes under operating conditions with special attention to the role of photo-induced electrons, which we propose to be applicable to various copper contain-

ing cathode materials used in photoelectrochemical measurements. We further describe a suitable approach to increase the stability of this p-type low bandgap semiconductor against decomposition and to decorate it with a Pt cocatalyst. With these results, we wish to contribute to the ongoing discussion about the stability of metal oxide photocathodes and point to ways towards the development of stable photoabsorbers for the generation of environmentally friendly hydrogen gas. Furthermore, we present a convenient method to manipulate the electronic structure of copper oxide which can be used to improve CO<sub>2</sub> reduction efficiencies.

## 6.2 Results and Discussion

Li<sub>x</sub>Cu<sub>1-x</sub>O photocathode layers were prepared by spin coating an ethanolic solution of Cu(NO<sub>3</sub>)<sub>2</sub> · 3H<sub>2</sub>O and LiNO<sub>3</sub> onto an FTO substrate. Calcination of these coatings at 400 °C resulted in homogeneous black films with a thickness of about 1 μm. The calcined films obtained from the precursor solution contain large amounts of non-reacted LiNO<sub>3</sub> and Li<sub>2</sub>CO<sub>3</sub> (Fig. 6.6) which can be removed by rinsing with water. X-ray diffraction (XRD) analysis (Fig. 6.1a) reveals that the films are structurally closely related to the CuO tenorite phase (space group: C2/c, a = 4.6803(8) Å; b = 3.4176(2) Å; c = 5.1278(8) Å; β = 99.442 (1)° (Fig. 6.7))<sup>[59,60]</sup> but exhibit slightly larger unit cell parameters (a = 4.6975(8) Å, b = 3.4346(6) Å, c = 5.1400(3) Å and β = 99.499(6) °). The small increase of the unit cell volume from 82.02(1) Å<sup>3</sup> for the pure CuO to 82.93(1) Å<sup>3</sup> for the CuO synthesized in the presence of Li salts indicates the incorporation of a small amount of Li<sup>+</sup> ions, with a somewhat bigger ionic radius of 0.90 Å (in CN = 6) compared to the ionic radius of Cu<sup>2+</sup> ions of 0.87 Å (in CN = 6), into the crystal lattice.<sup>[23]</sup> Inductively coupled plasma atomic absorption spectroscopy (ICP-AAS) analysis confirms the presence of 4 at% lithium in the sample, which is the maximum amount that can be incorporated in the tenorite crystal structure.<sup>[61]</sup>

Another evidence for the incorporation of Li in the structure is provided by solid state <sup>7</sup>Li nuclear magnetic resonance (NMR) analysis, which shows a multiplet (from spinning sidebands) centered at 1.3 ppm in the spectrum of a carefully washed Li<sub>x</sub>Cu<sub>1-x</sub>O powder (Fig. 6.1b). This signal is indicative for a non-metallic single phase, free of contaminations with diamagnetic compounds (i.e. Li<sub>2</sub>O, LiCO<sub>3</sub>, LiNO<sub>3</sub>). The electrical conductivity of Li-doped CuO was determined by Hall measurements (van der Pauw method) to be 6.0 × 10<sup>-3</sup> S cm<sup>-1</sup>, which is an increase by a factor of 2.5 compared to undoped CuO (2.4 × 10<sup>-3</sup> S cm<sup>-1</sup>). While films of undoped CuO are of dark brown color, films of Li<sub>x</sub>Cu<sub>1-x</sub>O are black. We attribute this observation to the formation of in-gap states, which can be caused by the introduction of point defects like cation doping or oxygen vacancies.<sup>[62]</sup> These optical properties were investigated by UV-Vis spectroscopy. Li<sub>x</sub>Cu<sub>1-x</sub>O films demonstrate favorable light harvesting efficiencies across a broad wavelength range between 350–800 nm, covering part of the near infra-red (IR) range, which exceeds that of our undoped CuO films (Fig. 6.1c). Absorbance data of Li<sub>x</sub>Cu<sub>1-x</sub>O films were used to calculate an indirect optical bandgap of 1.39 eV via Tauc

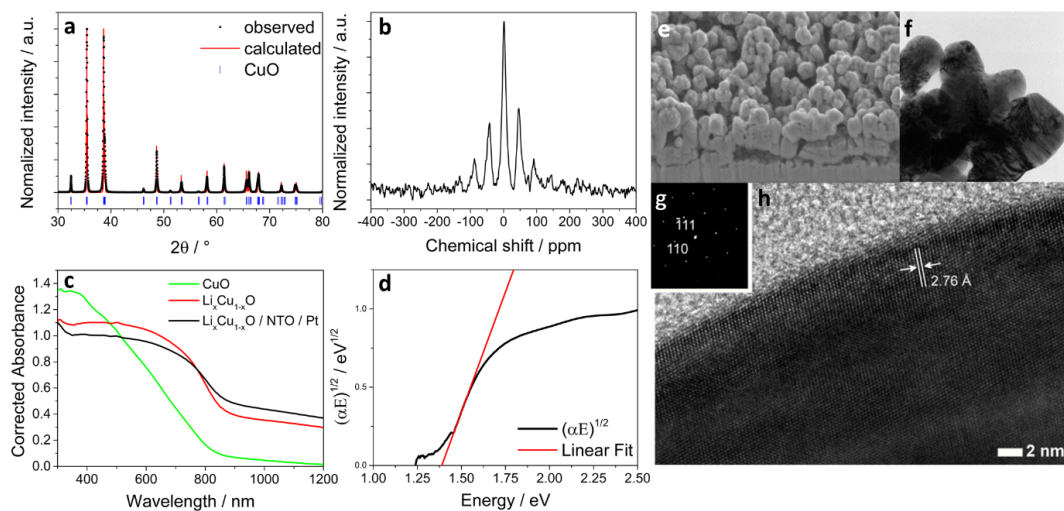


**Figure 6.1:** (a) Rietveld refinement of  $\text{Li}_x\text{Cu}_{1-x}\text{O}$  with observed data ( $\cdot$ ) and calculated pattern (red line), blue vertical bars mark the positions of the diffraction lines of CuO (tenorite). (b)  $^7\text{Li}$ -NMR spectra of  $\text{Li}_x\text{Cu}_{1-x}\text{O}$  showing a multiplet centered at 1.3 ppm. (c) UV-Vis absorption spectra of undoped CuO (green),  $\text{Li}_x\text{Cu}_{1-x}\text{O}$  (red) and protected  $\text{Li}_x\text{Cu}_{1-x}\text{O}/\text{NTO}/\text{Pt}$  films on FTO. (d) Tauc plot of a  $\text{Li}_x\text{Cu}_{1-x}\text{O}$  film on FTO showing an indirect bandgap of 1.39 eV. (e) SEM cross section image of  $\text{Li}_x\text{Cu}_{1-x}\text{O}$ . (f) TEM image of  $\text{Li}_x\text{Cu}_{1-x}\text{O}$  particles. (g and h) High-resolution TEM image of a highly crystalline  $\text{Li}_x\text{Cu}_{1-x}\text{O}$  nanoparticle and its corresponding electron diffraction pattern.

plot analysis<sup>[63]</sup> (Fig. 6.1d), which is nearly the theoretical optimum for bottom materials used for high-efficiency PEC tandem cells.<sup>[27]</sup> The morphology of our  $\text{Li}_x\text{Cu}_{1-x}\text{O}$  films was investigated by scanning electron microscopy (SEM, Fig. 6.1e). The films are nanostructured and composed of interconnected nanoparticles forming disordered porous layers covering the whole FTO substrate. Transmission electron microscopy (TEM) images of  $\text{Li}_x\text{Cu}_{1-x}\text{O}$  films reveal that they are composed of intergrown particles with a size of around 150-300 nm (Fig. 6.1f). High-resolution TEM (HR-TEM) images (Fig. 6.1h) and electron diffraction analysis (Fig. 6.1g) reveal that these particles are single crystalline. The  $d_{(110)}$ -spacing of monoclinic  $\text{Li}_x\text{Cu}_{1-x}\text{O}$  was determined to be 2.76 Å, being in good agreement with the XRD patterns.

To understand how the introduction of Li influences the electronic properties of CuO, we have performed density functional theory (DFT) calculations for Li-containing CuO including static electronic correlations within the GGA+U approach where the rotationally invariant formulation of Dudarev et al.<sup>[64]</sup> was employed (see appendix for further details). We have investigated the band gap as a function of the Hubbard  $U$  parameter and find that up to  $U = 8$  eV the indirect band gap of CuO increases monotonically with the band gap reaching 1.46 eV. Beyond  $U$  of 8 eV it changes to a direct band gap of 2.1 eV (SI Fig. 6.8a). The band gap of 1.46 eV obtained for  $U = 8$  eV is in good agreement with the band gap of 1.39 eV determined from the Tauc plot above and con-

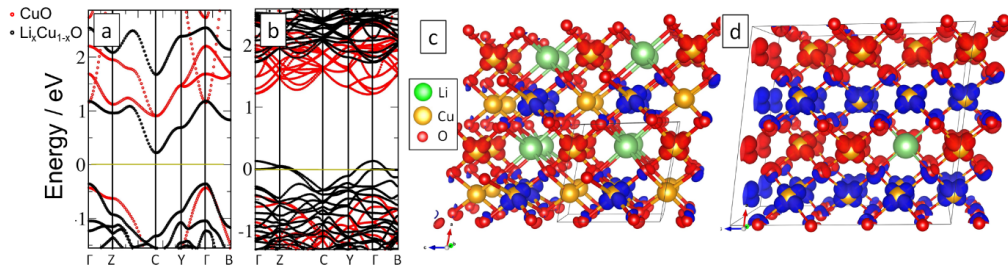


**Figure 6.2:** Electronic band structure of lithium doped CuO for two different Li concentrations of (a)  $\text{Li}_{0.25}\text{Cu}_{0.75}\text{O}$  and (b)  $\text{Li}_{0.032}\text{Cu}_{0.968}\text{O}$ . The different numbers of bands are related to different cell sizes. The yellow line marks the Fermi level. In contrast to the insulating behaviour for  $x_{\text{Li}} = 25\%$  (note the reduced band gap w.r.t. bulk CuO), the valence bands crossing the Fermi level for  $x_{\text{Li}} = 3.2\%$  indicate p-type conductivity. Spin density of lithium doped CuO in two different Li concentrations of (c)  $\text{Li}_{0.25}\text{Cu}_{0.75}\text{O}$  and (d)  $\text{Li}_{0.032}\text{Cu}_{0.968}\text{O}$  (isosurface of  $0.01 \text{ e } \text{\AA}^{-3}$ ). Majority and minority spin densities are shown by blue and red, respectively. Note the significant contribution of oxygen for the low Li doping concentration of  $3.2\%$ .

sistent with previous LDA+U studies with a somewhat lower value of  $U = 6.5 \text{ eV}$  by Heinemann et al.<sup>[37]</sup> The variation of lattice constants as a function of  $U$  is presented in Fig. 6.8b. The DFT predictions are in overall agreement with experimental lattice constants. The jump occurring between  $U = 8 \text{ eV}$  and  $U = 8.5 \text{ eV}$  is associated with the above-mentioned transition from indirect to direct band gap. To determine the preferential position of Li atoms in the CuO structure we have calculated the solution energy of Li at different lattice positions. For substitutional doping of Cu and O sites the calculated values are  $-4.20 \text{ eV}$  and  $1.04 \text{ eV}$ , respectively, while for the interstitial doping the solution energy was determined to be  $-0.025 \text{ eV}$ . Therefore, we can conclude that thermodynamically the preferred configuration corresponds to the substitutional doping of Cu sites with Li atoms. We have considered a high lithium content of  $x_{\text{Li}} = 25 \text{ at\%}$  and a low content of  $x_{\text{Li}} = 3.2 \text{ at\%}$ , which is close to the experimentally determined Li level of ca.  $4 \text{ at\%}$ . The solution energies of  $\text{Li}_{0.032}\text{Cu}_{0.968}\text{O}$  and  $\text{Li}_{0.25}\text{Cu}_{0.75}\text{O}$  are  $-4.2 \text{ eV}$  and  $-3.1 \text{ eV}$  respectively, indicating a reduction of tendency to incorporate with increasing Li concentration due to Li-Li repulsion. The band structure of  $\text{Li}_x\text{Cu}_{1-x}\text{O}$  (Fig. 6.2a and b) shows a very strong dependence on the amount of introduced Li. While for high concentration the band gap is strongly decreased to  $0.64 \text{ eV}$ , for low concentration the main effect is an upward shift of the valence band maximum that crosses the Fermi level and makes the system a p-type semiconductor. As shown in the spin density plots in Fig. 6.2c and d, the underlying mechanisms are distinct: for  $x_{\text{Li}} = 25 \text{ at\%}$  substitution of  $\text{Li}^+$  leads to a change in charge state of one copper to  $\text{Cu}^{3+}$ , while for  $x_{\text{Li}} = 3.2 \text{ at\%}$  the holes are delocalized at the oxygensites leading to a p-type semiconductor.

To sum up, lithium doping causes an increased optical absorption of CuO in the infrared range and significantly increases the p-type conductivity, therefore we expect facilitated charge separation. As our morphology is beneficial for the strongly surface-dependent water splitting reaction,<sup>[5]</sup> we determined the photoelectrochemical

performance of  $\text{Li}_x\text{Cu}_{1-x}\text{O}$  photocathodes by linear sweep voltammetry (LSV) in 0.1 M  $\text{Na}_2\text{SO}_4$  aqueous solution (pH 7) starting at 0.7 V vs. RHE and scanning down towards -0.1 V vs. RHE under chopped AM1.5 illumination. In the present case, the result of this procedure (Fig. 6.3a) is very misleading, as the  $\text{Li}_x\text{Cu}_{1-x}\text{O}$  film shows the typical behavior of a photocathode with instant photocurrent response upon illumination. This observation can easily be misinterpreted as a measure of hydrogen evolution efficiency, but indeed originates from both the reduction of water and the reduction of the transition metal oxide itself, which we elucidate in the present work. In addition, we performed cyclic voltammetry (CV) measurements in a potential range between 0.0 and 0.9 V vs. RHE (Fig. 6.3b). The material shows a negligible dark current, indicating electrochemical stability in the scanned potential range. Under AM1.5G illumination ( $100 \text{ mW cm}^{-2}$ ), a reductive current density can be observed below 0.5 V vs. RHE. However, significant oxidizing currents appear above 0.4 V vs. RHE in the back scan. To examine the electrochemical stability of our  $\text{Li}_x\text{Cu}_{1-x}\text{O}$  photocathodes, we applied different constant potentials from 0.0 to 0.6 V vs. RHE for 15 minutes each, in the dark as well as under illumination (Fig. 6.12). X-ray photoelectron spectroscopy (XPS) measurements of these films after electrochemical reaction were used to get further insights into the stability of the electrode material. From the binding energy of the Cu  $2p_{3/2}$ -peak (Fig. 6.3c and d), the oxidation state of the copper at the electrode surface could be assigned to Cu(II) (933.6 eV) or Cu(I) (932.4 eV).<sup>[65]</sup> As shown in Fig. 6.3c, copper(II) oxide remains stable without illumination down to 0.2 V vs. RHE. Below this potential a shift of the Cu  $2p_{3/2}$ -peak to lower binding energies is observed, indicative for the reduction of copper(II) oxide to copper(I) oxide. Under AM1.5G illumination, we observed copper(I) oxide formation already at 0.2 V vs. RHE, indicating photocorrosion by light induced electrons at this potential. Deconvolution of the Cu  $2p_{3/2}$ -peak as well as the corresponding Cu  $L_{3VV}$  Auger signals support this conclusion (Fig. 6.18).

In agreement with the XPS data<sup>[65,66]</sup> and the Pourbaix diagram of copper,<sup>[67]</sup> we attribute the reductive currents to a competitive reduction of both  $2 \text{ H}^+$  to  $\text{H}_2$  and  $\text{Cu}^{2+}$  to  $\text{Cu}^{1+}$ , while the oxidizing currents result from the oxidation of  $\text{Cu}^{1+}$  to  $\text{Cu}^{2+}$ .<sup>[35]</sup> Furthermore, we extended the potential range of several CV measurements stepwise on a new sample (Fig. 6.10). With scanning to lower potentials, more  $\text{Cu}^{2+}$  is photoreduced to  $\text{Cu}^{1+}$ , which gets reoxidized to  $\text{Cu}^{2+}$  at 0.75 V vs. RHE. This extremely sensitive method indicates a photocorrosion onset at approximately 0.45 V vs. RHE. Notably, photocorrosion starts right with the photoelectrochemical measurement (Fig. 6.25) and is fully noticeable after 15 minutes. Impedance plots illustrate the impairing effect of photocorrosion on the charge transport properties on the photocathode–electrolyte interface (Fig. 6.24). With proceeding  $\text{Cu}_2\text{O}$  formation on the surface, we observed an increase in charge transfer resistance on  $\text{Li}_x\text{Cu}_{1-x}\text{O}$  electrodes.<sup>[68]</sup> We attribute this phenomenon to the high conduction band energy level of  $\text{Cu}_2\text{O}$  compared to  $\text{CuO}$ , which hinders electron transfer from  $\text{Li}_x\text{Cu}_{1-x}\text{O}$  towards the electrolyte. Electron energy loss spectroscopy (EELS) allows one to directly monitor the oxidation states of elements on the nanometer scale using the near edge fine structure.

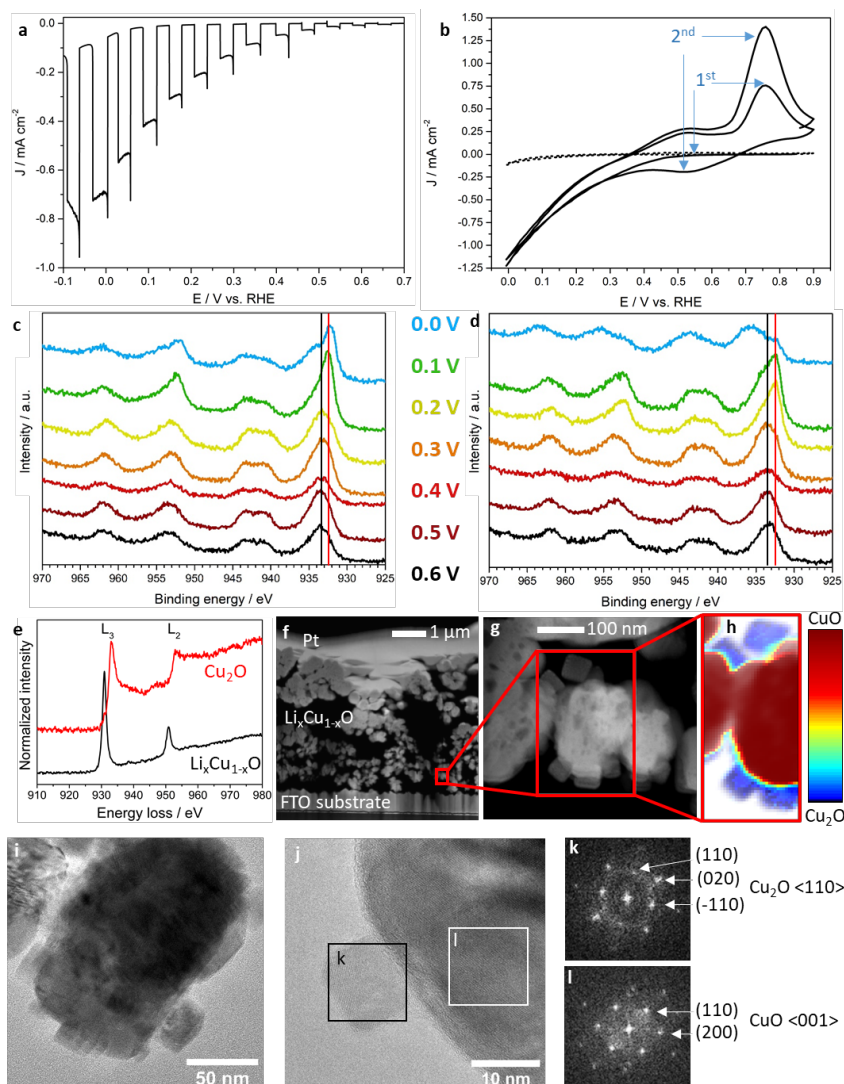


**Figure 6.3:** (a) Linear sweep voltammogram of a bare  $\text{Li}_x\text{Cu}_{1-x}\text{O}$  film under chopped AM1.5 illumination, showing no signs of photocorrosion. The assumption of a working photocathode based on this experiment is very misleading, as the reductive currents originate from both water reduction and photocorrosion. (b) Cyclic voltammetry characterization of an unprotected  $\text{Li}_x\text{Cu}_{1-x}\text{O}$  photocathode in 0.1 M  $\text{Na}_2\text{SO}_4$  at pH 7 in the dark (dashed line) and under AM1.5 illumination through the substrate (solid line). (c and d) Cu 2p XPS spectra measured of bare  $\text{Li}_x\text{Cu}_{1-x}\text{O}$  films held at the respective potentials vs. RHE for 15 minutes each in the dark (c) and under AM1.5G illumination (d) (bars: black:  $\text{Cu}^{2+}$ , red:  $\text{Cu}^0$  and  $\text{Cu}^{1+}$ ). At a potential of 0.2 V vs. RHE,  $\text{Li}_x\text{Cu}_{1-x}\text{O}$  is stable in the dark but corrodes to  $\text{Cu}_2\text{O}$  under illumination. (e) Cu-L<sub>2,3</sub> edges of CuO and  $\text{Cu}_2\text{O}$  distinguish between both copper oxidation states. The photocorrosion could be localized in a TEM cross section image (f and g) with corresponding EELS map (h), showing cubic  $\text{Cu}_2\text{O}$  crystals on the  $\text{Li}_x\text{Cu}_{1-x}\text{O}$  surface. (i) Overview image of one crystal scratched from a  $\text{Li}_x\text{Cu}_{1-x}\text{O}$  film after an electrochemistry experiment performed for 15 min at 0.2 V under illumination, showing a roundish crystal overgrown by square crystals. (j) Average background subtraction filtered (ABSF) high resolution TEM image showing one square crystal at the surface of a spherical one. The FFTs of the marked regions were indexed for  $\text{Cu}_2\text{O}$  (k) and CuO (l), respectively.

The Cu-L<sub>2,3</sub> edges of CuO and Cu<sub>2</sub>O are characterized by a pair of white lines which result from the excitation of 2p<sub>3/2</sub> (L<sub>3</sub>) and 2p<sub>1/2</sub> (L<sub>2</sub>) electrons to unoccupied 3d states (Figure 6.3e). The white lines of CuO are shifted to lower energy losses compared to Cu<sub>2</sub>O.<sup>[69,70]</sup> Thus, the energetic position of the two white lines was used in this study to identify the local distribution of the oxidation states in the thin films (Figure 6.11). EELS requires electron transparent samples (thickness below 100 nm),<sup>[67,70]</sup> which in this study was achieved by preparing thin lamellae with a focused ion beam microscope. The resulting lamella represents a cross-section through the thin film (Figure 6.3f and g). A platinum protection layer was used to protect the sample from the gallium ions used for sample cutting and thinning. Oxidation state maps illustrate the local distribution of Cu<sub>2</sub>O and CuO inside the thin film with the spatial resolution given by the pixel size of the map, which was commonly chosen between 2.5 and 5 nm using subpixel scanning to reduce beam damage. Both oxidation states are detected in the interfacial regions between the two phases. In the TEM images two different crystal morphologies are visible, large round crystals and smaller square crystals. The latter form preferably at the surface of the large crystals. EELS maps demonstrate that the two crystal morphologies correspond to the two oxidation states: the large crystals are pure CuO, while the smaller ones are Cu<sub>2</sub>O (Figure 6.3h). This is confirmed by high resolution TEM imaging of the two crystal morphologies (Figure 6.3i and j) with their corresponding fast Fourier transforms (FFTs) indexed for CuO and Cu<sub>2</sub>O (Figure 6.3k and l). Interestingly, Cu<sub>2</sub>O grows as distinct crystallites on the surface of CuO instead of forming a dense layer on its surface. Additionally, there is no obvious Cu<sub>2</sub>O gradient inside the films, as Cu<sub>2</sub>O seems to form on all CuO nanocrystals exposed to water. We see a similar photocorrosion behavior on undoped CuO. After a potentiostatic measurement for 15 minutes at 0.2 V vs. RHE, also the surface of CuO is covered with cubic crystallites. Both the post-photoelectrochemical XRD pattern of CuO as well as FFTs and electron diffraction pattern of the regions covered with cubic crystals indicate the formation of the cuprite phase (Cu<sub>2</sub>O) (Figure 6.17). Therefore, we expect the same corrosion mechanism like on Li<sub>x</sub>Cu<sub>1-x</sub>O photocathodes. To rule out artefacts introduced by the FIB sample preparation, FIB lamellae of reference samples that had not been used in photoelectrochemical experiments were investigated. The maps show a thin layer of reduced copper oxide at the surface of the CuO crystals (see Figure 6.13), but no Cu<sub>2</sub>O crystals. The reduction of the surface layer of CuO is most likely caused by a reaction of CuO with the Ga-ions used for the sample preparation.

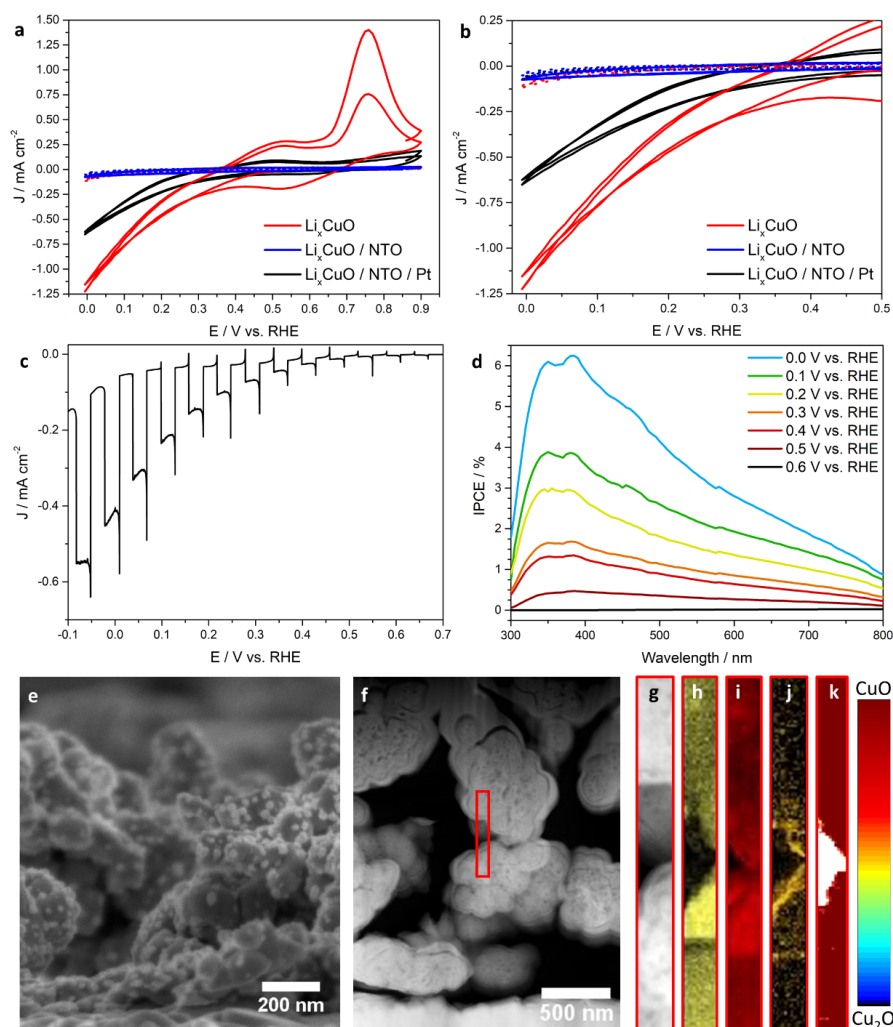


**Figure 6.4:** (a) Cyclic voltammety measurements of  $\text{Li}_x\text{Cu}_{1-x}\text{O}$  films protected with 2.5 nm thin  $\text{Ti}_{0.8}\text{Nb}_{0.2}\text{O}_x$  (NTO) layer (blue) and additionally functionalized with Pt nanoparticles (black) compared to a bare  $\text{Li}_x\text{Cu}_{1-x}\text{O}$  photocathode (red) in the dark (dashed) and under AM1.5 illumination (solid). (b) Magnification of (a) in the lower potential range. (c) Linear sweep voltammogram of a  $\text{Li}_x\text{Cu}_{1-x}\text{O}/\text{NTO}/\text{Pt}$  film under chopped AM 1.5 illumination. (d) Incident-photon-to-current-efficiency (IPCE) measurements at different potentials. (e) SEM image of a  $\text{Li}_x\text{Cu}_{1-x}\text{O}/\text{NTO}$  photocathode decorated with 20 nm sized Pt particles. (f) STEM image of a cross section of a  $\text{Li}_x\text{Cu}_{1-x}\text{O}/\text{NTO}/\text{Pt}$  device held for 15 min at 0.2 V vs. RHE under AM1.5 illumination. The marked area (red, g) was used for EDX mapping of Cu (h), O (i) and Ti (j). The corresponding EELS map (k) shows no sign of photocorrosion.

To stabilize our photoabsorber material, we coated our  $\text{Li}_x\text{Cu}_{1-x}\text{O}$  films with a protective layer by atomic layer deposition (ALD), as this is a proven approach to protect copper oxides against photocorrosion.<sup>[14,32,71]</sup> Among several tested coatings like  $\text{TiO}_2$ ,  $\text{Ti}_{0.8}\text{Nb}_{0.2}\text{O}_x$  (NTO),  $\text{SnO}_x$ ,  $\text{Al}:\text{ZnO}$  and  $\text{Al}_2\text{O}_3$ , NTO exhibited the best results on our

$\text{Li}_x\text{Cu}_{1-x}\text{O}$  morphology. After deposition, the applied  $\text{Ti}_{0.8}\text{Nb}_{0.2}\text{O}_x$  layers are amorphous (Figure 6.16),<sup>[72,73]</sup> covering the complete surface of the nanostructured morphology of the  $\text{Li}_x\text{Cu}_{1-x}\text{O}$  films without the formation of pinholes (Figure 6.20), which has already been demonstrated to successfully protect  $\text{Cu}_2\text{O}$ .<sup>[54]</sup> CV measurements of  $\text{Li}_x\text{Cu}_{1-x}\text{O}/\text{NTO}$  films in aqueous 0.1 M  $\text{Na}_2\text{SO}_4$  are free of oxidative current signals, indicating that the photoabsorber remains stable under illumination. In contrast to bare  $\text{Li}_x\text{Cu}_{1-x}\text{O}$ , NTO covered films showed no activity in terms of water reduction (Fig. 6.4a and b, blue) due to the lack of a suitable cocatalyst.<sup>[3]</sup> For this reason, we electrodeposited Pt nanoparticles on our  $\text{Li}_x\text{Cu}_{1-x}\text{O}/\text{NTO}$  from a 1 mM methanolic  $\text{H}_2\text{PtCl}_6$  solution (see Experimental details for further information), as this is a proven way to improve HER kinetics on ALD protected copper oxide based photocathodes.<sup>[14]</sup> 20 nm sized Pt particles are formed on the surface of the nanostructured  $\text{Li}_x\text{Cu}_{1-x}\text{O}/\text{NTO}$  films (Figure 6.4e). A protection layer of 2.5 nm NTO showed the highest activity compared slightly thinner or thicker NTO layers, still allowing sufficient charge transport to the Pt cocatalyst (Figure 6.19). We assume electron transport by tunneling through the protective layer due to its extremely small layer thickness. The described protection strategy causes no significant change in the light absorption properties of those devices compared to the pristine  $\text{Li}_x\text{Cu}_{1-x}\text{O}$  films (Fig. 6.1c). We see no signs of photocorrosion of  $\text{Li}_x\text{Cu}_{1-x}\text{O}/\text{NTO}/\text{Pt}$  devices held for 15 min at 0.2 V vs. RHE under AM1.5G illumination. This is verified by EELS oxidation state mapping (Figure 6.4f and k and Figure 6.21). Based on LSV measurements under chopped illumination, these devices show a distinct activity towards hydrogen evolution reaching up to  $350 \mu\text{A cm}^{-2}$  at 0.0 V vs. RHE with a photocurrent onset at around 0.50 V vs. RHE (Figure 6.4c). Furthermore, we quantified the incident-photon-to-current efficiency (IPCE) at different potentials from 0.6 to 0.0 V vs. RHE (Fig. 6.4d). The photocathode is active over the whole visible spectrum, reaching parts of the IR range, with an IPCE maximum at an excitation wavelength of 380 nm. The IPCE increases with lower potentials, reaching up to 6.25 % at 0.0 V vs. RHE.

In addition, we performed stability tests of bare  $\text{Li}_x\text{Cu}_{1-x}\text{O}$  and  $\text{Li}_x\text{Cu}_{1-x}\text{O}/\text{NTO}/\text{Pt}$  films under illumination and quantified the evolved hydrogen. At a constant potential of 0.3 V vs. RHE, both photoelectrodes show a current response under illumination which is directly correlated to hydrogen evolution. The photocurrent of bare  $\text{Li}_x\text{Cu}_{1-x}\text{O}$  decreases constantly and the hydrogen evolution stops after around 10 min of illumination due to photocorrosion of the material (Figure 6.23), which results in a faradaic efficiency of 61 % after 10 minutes (Figure 6.5a). In contrast, the  $\text{Li}_x\text{Cu}_{1-x}\text{O}/\text{NTO}/\text{Pt}$  device produces a stable photocurrent and evolves hydrogen with a faradaic efficiency of 96 % during the first 15 minutes after illumination (Figure 6.5b). Afterwards, both the hydrogen evolution and the current drop. We attribute the activity loss to the detachment of the Pt nanoparticles due to hydrogen bubble formation (see Figure 6.22), whereas the decrease of hydrogen concentration can be attributed to leakage from the photoelectrochemical cuvette-type cell used for hydrogen evolution experiments. We are currently working on the optimization of the cocatalyst deposition to increase both

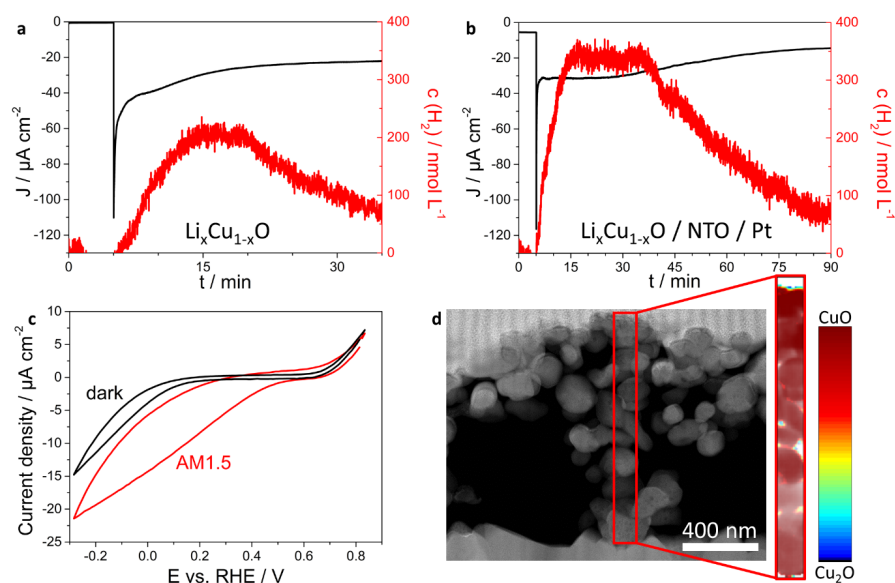


**Figure 6.5:** (a and b) Chronoamperometric data (black) at 0.3 V *vs.* RHE with corresponding H<sub>2</sub> evolution (red), which is directly correlated to illumination starting after 5 minutes. While unprotected Li<sub>x</sub>Cu<sub>1-x</sub>O films (a) start to degrade right after illumination, Li<sub>x</sub>Cu<sub>1-x</sub>O/NTO/Pt photocathodes (b) show stable hydrogen evolution during the first 30 minutes. (c and d) To probe the role of the water during the electrochemical reaction, a propylene carbonate electrolyte with an iodide triiodide redox couple was used as replacement. The CV measurement (c) as well as the TEM cross section with corresponding EELS map (d) of the film after a 15 minutes' stability test at 0.1 V *vs.* RHE show no sign of photocorrosion.

stability and activity of Li doped CuO photocathodes. Without direct contact to water, bare Li<sub>x</sub>Cu<sub>1-x</sub>O is stable in a comparable potential range, as shown in a photoelectrochemical measurement in 1 mM iodide/triiodide (I<sup>-</sup>/I<sub>3</sub><sup>-</sup>) propylene carbonate electrolyte (Fig. 6.5c). No oxidative currents are detectable, which would indicate a Cu<sup>1+</sup>/Cu<sup>2+</sup> reaction similar to the one shown in Figure 6.3b. Moreover, the Li<sub>x</sub>Cu<sub>1-x</sub>O film was held under illumination at 0.1 V *vs.* RHE for 15 minutes. The corresponding EELS map of this sample shows no sign of photocorrosion. From this observation, we conclude that Li<sub>x</sub>Cu<sub>1-x</sub>O could be used as stable photoabsorber as well as catalyst in a water-free electrolyte.

### 6.3 Conclusion

In this study, we have presented black Li-doped CuO thin films as cathodic light absorber for photoelectrochemical hydrogen evolution. The substitution of 4 at% of Cu<sup>2+</sup> with Li<sup>+</sup> ions has a substantial influence on the optical and electronic properties. The optical bandgap is reduced while both electrical conductivity and p-type character increase upon Li doping, which is beneficial for the application as photocathode material

in a PEC tandem cell. DFT+U calculations confirm that the system becomes a p-type semiconductor for low Li concentrations due to the pronounced delocalization of holes. While  $\text{Li}_x\text{Cu}_{1-x}\text{O}$  is stable in a non-aqueous electrolyte, it suffers from photocorrosion in contact with water. For the first time, the corrosion was studied in detail by cyclic voltammetry, X-ray photoelectron and electron energy loss spectroscopy. As a result, we present a detailed study on photocorrosion to provide a profound understanding of the underlying physical process which will be applicable to any copper based photocatalyst. Indeed, the performance of other reported photoelectrode systems should be critically revised. Under illumination and in direct contact with water, the reduced  $\text{Cu}_2\text{O}$  forms as distinct cubic crystals on the  $\text{Li}_x\text{Cu}_{1-x}\text{O}$  surface. We demonstrate that  $\text{Li}_x\text{Cu}_{1-x}\text{O}$  films can be stabilized to some degree against photocorrosion by using approaches common in photoelectrochemical research namely the application of a thin  $\text{Nb}:\text{TiO}_2$  protection layer in combination with a Pt cocatalyst. Still, our described approach cannot solve the fundamental problem of intrinsic instability of metal oxide-based photocathodes in aqueous electrolytes. We suggest that similar fundamental problems of photocorrosion stability will be witnessed also in other copper containing photoabsorbers, therefore the photoelectrochemical performance and possible light-triggered material transformation should be revisited with special care. We doubt that the intrinsic photocorrosion of copper oxide based photoelectrodes can be solved in any feasible way in aqueous electrolytes. However, the in situ growth of  $\text{Cu}_2\text{O}$  due to photoreduction could be used for other types of electrochemical processes. As an example, the use as specific catalyst for  $\text{CO}_2$  reduction in a water-free, methanolic electrolyte can be envisioned as both copper oxides were already described to be very active for this application.<sup>[74]</sup> By manipulating their electronic structure using various dopants like  $\text{Li}^+$ , we expect to enhance both the efficiency of copper oxides and also fine tune the formation efficiencies for hydrocarbons like methane and ethylene.

## 6.4 References

- [1] Basic research needs for solar energy utilization, Report, Office of Basic Energy Sciences, US Department of Energy, 2005.
- [2] L. Fornarini, A. J. Nozik, B. A. Parkinson, *J. Phys. Chem.* **1984**, *88*, 3238–3243.
- [3] A. Heller, *Science* **1984**, *223*, 1141–1148.
- [4] M. G. Walter, E. L. Warren, J. R. McKone, S. W. Boettcher, Q. Mi, E. A. Santori, N. S. Lewis, *Chem. Rev.* **2010**, *110*, 6446–6473.
- [5] R. van de Krol, Y. Liang, J. Schoonman, *J. of Mater. Chem.* **2008**, *18*, 2311.
- [6] O. Khaselev, A. Bansal, J. A. Turner, *Inter. J. Hydrogen Energy* **2001**, *26*, 127–132.
- [7] R. N. Dominey, N. S. Lewis, J. A. Bruce, D. C. Bookbinder, M. S. Wrighton, *J. Am. Chem. Soc.* **1982**, *104*, 467–482.

- [8] U. Sim, T.-Y. Yang, J. Moon, J. An, J. Hwang, J.-H. Seo, J. Lee, K. Y. Kim, J. Lee, S. Han, B. H. Hong, K. T. Nam, *Energy Environ. Sci.* **2013**, *6*, 3658–3664.
- [9] Y. Hou, B. L. Abrams, P. C. K. Vesborg, M. E. Björketun, K. Herbst, L. Bech, A. M. Setti, C. D. Damsgaard, T. Pedersen, O. Hansen, J. Rossmeisl, S. Dahl, J. K. Nørskov, I. Chorkendorff, *Nat. Mater.* **2011**, *10*, 434.
- [10] T. Sick, A. G. Hufnagel, J. Kampmann, I. Kondofersky, M. Calik, J. M. Rotter, A. Evans, M. Döblinger, S. Herbert, K. Peters, D. Böhm, P. Knochel, D. D. Medina, D. Fattakhova-Rohlfing, T. Bein, *J. Am. Chem. Soc.* **2018**, *140*, 2085–2092.
- [11] M. Haro, C. Solis, G. Molina, L. Otero, J. Bisquert, S. Gimenez, A. Guerrero, *J. Phys. Chem. C* **2015**, *119*, 6488–6494.
- [12] T. Bourgeteau, D. Tondelier, B. Geffroy, R. Brisse, S. Campidelli, R. Cornut, B. Jousseme, *J. Mater. Chem. A* **2016**, *4*, 4831–4839.
- [13] R. Sathre, C. D. Scown, W. R. Morrow, J. C. Stevens, I. D. Sharp, J. W. Ager, K. Walczak, F. A. Houle, J. B. Greenblatt, *Energy Environ. Sci.* **2014**, *7*, 3264–3278.
- [14] A. Paracchino, V. Laporte, K. Sivula, M. Grätzel, E. Thimsen, *Nat. Mater.* **2011**, *10*, 456–461.
- [15] K. Sivula, F. Le Formal, M. Grätzel, *ChemSusChem* **2011**, *4*, 432–449.
- [16] R. Patil, S. Kelkar, R. Naphade, S. Ogale, *J. Mater. Chem. A* **2014**, *2*, 3661–3668.
- [17] M. S. Prévot, N. Guijarro, K. Sivula, *ChemSusChem* **2015**, *8*, 1359–1367.
- [18] U. A. Joshi, A. M. Palasyuk, P. A. Maggard, *J. Phys. Chem. C* **2011**, *115*, 13534–13539.
- [19] S. P. Berglund, F. F. Abdi, P. Bogdanoff, A. Chemseddine, D. Friedrich, R. van de Krol, *Chem. Mater.* **2016**, *28*, 4231–4242.
- [20] I. Kondofersky, A. Müller, H. K. Dunn, A. Ivanova, G. Štefanić, M. Ehrensperger, C. Scheu, B. A. Parkinson, D. Fattakhova-Rohlfing, T. Bein, *J. Am. Chem. Soc.* **2016**, DOI 10.1021/jacs.5b08040.
- [21] K. Sliozberg, H. S. Stein, C. Khare, B. A. Parkinson, A. Ludwig, W. Schuhmann, *ACS Appl. Mater. Interfaces* **2015**, *7*, 4883–4889.
- [22] C.-Y. Chiang, Y. Shin, S. Ehrman, *Energy Procedia* **2014**, *61*, 1799–1802.
- [23] C.-Y. Chiang, Y. Shin, S. Ehrman, *J. Electrochem. Soc.* **2011**, *159*, B227–B231.
- [24] H. K. Dunn, J. M. Feckl, A. Müller, D. Fattakhova-Rohlfing, S. G. Morehead, J. Roos, L. M. Peter, C. Scheu, T. Bein, *Phys. Chem. Chem. Phys.* **2014**, *16*, 24610–20.
- [25] L. M. Peter, *J. Solid State Electrochem.* **2012**, *17*, 315–326.
- [26] A. L. Linsebigler, G. Lu, J. T. Yates, *Chem. Rev.* **1995**, *95*, 735–758.
- [27] M. S. Prévot, K. Sivula, *J. Phys. Chem. C* **2013**, *117*, 17879–17893.
- [28] Y. Yang, D. Xu, Q. Wu, P. Diao, *Sci. Rep.* **2016**, *6*, 35158.

- 
- [29] U. Shaislamov, H.-J. Lee, *J. Korean Phys. Soc.* **2016**, *69*, 1242–1246.
- [30] U. Shaislamov, K. Krishnamoorthy, S. J. Kim, A. Abidov, B. Allabergenov, S. Kim, S. Choi, R. Suresh, W. M. Ahmed, H.-J. Lee, *Int. J. Hydrogen Energy* **2016**, *41*, 2253–2262.
- [31] P. Basnet, Y. Zhao, *Catal. Sci. Technol.* **2016**, *6*, 2228–2238.
- [32] Y.-F. Lim, C. S. Chua, C. J. J. Lee, D. Chi, *Phys. Chem. Chem. Phys.* **2014**, *16*, 25928–25934.
- [33] C.-Y. Chiang, Y. Shin, K. Aroh, S. Ehrman, *Int. J. Hydrogen Energy* **2012**, *37*, 8232–8239.
- [34] D. Barreca, P. Fornasiero, A. Gasparotto, V. Gombac, C. Maccato, T. Montini, E. Tondello, *ChemSusChem* **2009**, *2*, 230–233.
- [35] F. P. Koffyberg, F. A. Benko, *J. Appl. Phys.* **1982**, *53*, 1173–1177.
- [36] B. K. Meyer, A. Polity, D. Reppin, M. Becker, P. Hering, P. J. Klar, T. Sander, C. Reindl, J. Benz, M. Eickhoff, C. Heiliger, M. Heinemann, J. Bläsing, A. Krost, S. Shokovets, C. Müller, C. Ronning, *Phys. Status Solidi B* **2012**, *249*, 1487–1509.
- [37] M. Heinemann, B. Eifert, C. Heiliger, *Phys. Rev. B: Condens. Matter Mater. Phys.* **2013**, *87*, 115111.
- [38] D. Chauhan, V. Satsangi, S. Dass, R. Shrivastav, *Bull. Materi. Sci.* **2006**, *29*, 709.
- [39] L. C. Olsen, R. C. Bohara, M. W. Urie, *Appl. Phys. Lett.* **1979**, *34*, 47–49.
- [40] X. Ba, L.-L. Yan, S. Huang, J. Yu, X.-J. Xia, Y. Yu, *J. Phys. Chem. C* **2014**, *118*, 24467–24478.
- [41] S. Masudy-Panah, Y.-J. K. Eugene, N. D. Khiavi, R. Katal, X. Gong, *J. Mater. Chem. A* **2018**, *6*, 11951–11965.
- [42] S. Masudy-Panah, R. Katal, N. D. Khiavi, E. Shekarian, J. Hu, X. Gong, *J. Mater. Chem. A* **2019**, *7*, 22332–22345.
- [43] P. Chand, A. Gaur, A. Kumar, U. Kumar Gaur, *Appl. Surf. Sci.* **2014**, *307*, 280–286.
- [44] S. Masudy-Panah, R. S. Moakhar, C. S. Chua, A. Kushwaha, T. I. Wong, G. K. Dalapati, *RSC Adv.* **2016**, *6*, 29383–29390.
- [45] Y. J. Jang, J.-W. Jang, S. H. Choi, J. Y. Kim, J. H. Kim, D. H. Youn, W. Y. Kim, S. Han, J. Sung Lee, *Nanoscale* **2015**, *7*, 7624–7631.
- [46] Z. Zhang, P. Wang, *J. Mater. Chem.* **2012**, *22*, 2456–2464.
- [47] C.-Y. Chiang, K. Aroh, N. Franson, V. R. Satsangi, S. Dass, S. Ehrman, *Int. J. Hydrogen Energy* **2011**, *36*, 15519–15526.
- [48] C.-M. Wang, C.-Y. Wang, *J. Nanophotonics* **2014**, *8*, 084095–084095.
- [49] X. Guo, P. Diao, D. Xu, S. Huang, Y. Yang, T. Jin, Q. Wu, M. Xiang, M. Zhang, *Int. J. Hydrogen Energy* **2014**, *39*, 7686–7696.
-

- [50] L. Chen, S. Shet, H. Tang, H. Wang, T. Deutsch, Y. Yan, J. Turner, M. Al-Jassim, *J. Mater. Chem.* **2010**, *20*, 6962–6967.
- [51] C.-Y. Chiang, M.-H. Chang, H.-S. Liu, C. Y. Tai, S. Ehrman, *Ind. Eng. Chem. Res.* **2012**, *51*, 5207–5215.
- [52] S. Emin, F. F. Abdi, M. Fanetti, W. Peng, W. Smith, K. Sivula, B. Dam, M. Valant, *J. Electroanal. Chem.* **2014**, *717–718*, 243–249.
- [53] H. Choi, M. Kang, *Int. J. Hydrogen Energy* **2007**, *32*, 3841–3848.
- [54] A. Paracchino, N. Mathews, T. Hisatomi, M. Stefik, S. D. Tilley, M. Gratzel, *Energy Environ. Sci.* **2012**, *5*, 8673–8681.
- [55] H. Xing, L. E, Z. Guo, D. Zhao, X. Li, Z. Liu, *Inorg. Chem. Front.* **2019**, *6*, 2488–2499.
- [56] S. Zhang, M. Rohloff, O. Kasian, A. M. Mingers, K. J. J. Mayrhofer, A. Fischer, C. Scheu, S. Cherevko, *J. Phys. Chem. C* **2019**, *123*, 23410–23418.
- [57] F. M. Toma, J. K. Cooper, V. Kunzelmann, M. T. McDowell, J. Yu, D. M. Larson, N. J. Borys, C. Abelyan, J. W. Beeman, K. M. Yu, J. Yang, L. Chen, M. R. Shaner, J. Spurgeon, F. A. Houle, K. A. Persson, I. D. Sharp, *Nat. Commun.* **2016**, *7*, 12012.
- [58] D. K. Lee, K.-S. Choi, *Nat. Energy* **2018**, *3*, 53–60.
- [59] G. tunell, E. Posnjak, C. J. Ksanda, *Z. Kristallogr. - Cryst. Mater.* **1935**, *90*, 120–142.
- [60] P. Niggli, *Z. Kristallogr. - Cryst. Mater* **1922**, *57*, 253–299.
- [61] P. Carretta, M. Corti, A. Rigamonti, *Phys. Rev. B: Condens. Matter Mater. Phys.* **1993**, *48*, 3433–3444.
- [62] C. Baeumer, C. Funck, A. Locatelli, T. O. Montes, F. Genuzio, T. Heisig, F. Hensling, N. Raab, C. M. Schneider, S. Menzel, R. Waser, R. Dittmann, *Nano Lett.* **2019**, *19*, 54–60.
- [63] D. Roy, G. F. Samu, M. K. Hossain, C. Janáky, K. Rajeshwar, *Catal. Today* **2018**, *300*, 136–144.
- [64] S. L. Dudarev, G. A. Botton, S. Y. Savrasov, C. J. Humphreys, A. P. Sutton, *Phys. Rev. B: Condens. Matter Mater. Phys.* **1998**, *57*, 1505–1509.
- [65] M. C. Biesinger, L. W. M. Lau, A. R. Gerson, R. S. C. Smart, *Appl. Surf. Sci.* **2010**, *257*, 887–898.
- [66] S. Poulston, P. M. Parlett, P. Stone, M. Bowker, *Surf. Interface Anal.* **1996**, *24*, 811–820.
- [67] B. Beverskog, I. Puigdomenech, *J. Electrochem. Soc.* **1997**, *144*, 3476–3483.
- [68] S. Masudy-Panah, R. Siavash Moakhar, C. S. Chua, H. R. Tan, T. I. Wong, D. Chi, G. K. Dalapati, *ACS Appl. Mater. Interfaces* **2016**, *8*, 1206–1213.
- [69] L. Laffont, M. Y. Wu, F. Chevallier, P. Poizot, M. Morcrette, J. M. Tarascon, *Micron* **2006**, *37*, 459–64.

- [70] R. D. Leapman, L. A. Grunes, P. L. Fejes, *Phys. Rev. B: Condens. Matter Mater. Phys.* **1982**, *26*, 614–635.
- [71] J. Azevedo, S. D. Tilley, M. Schreier, M. Stefik, C. Sousa, J. P. Araújo, A. Mendes, M. Grätzel, M. T. Mayer, *Nano Energy* **2016**, *24*, 10–16.
- [72] V. Pore, M. Ritala, M. Leskelä, T. Saukkonen, M. Järn, *Cryst. Growth Des.* **2009**, *9*, 2974–2978.
- [73] A. G. Hufnagel, S. Häringer, M. Beetz, B. Böller, D. Fattakhova-Rohlfing, T. Bein, *Nanoscale* **2019**, *11*, 14285.
- [74] S. Ohya, S. Kaneco, H. Katsumata, T. Suzuki, K. Ohta, *Catal. Today* **2009**, *148*, 329–334.

## 6.5 Appendix

### 6.5.1 Experimental Details

*Preparation of  $\text{Li}_x\text{Cu}_{1-x}\text{O}$  films:*  $\text{Li}_x\text{Cu}_{1-x}\text{O}$  thin film photocathodes were prepared by spin coating (1000 rpm, 30 s, 100  $\mu\text{L}$ ) a precursor solution containing 1 M  $\text{Cu}(\text{NO}_3)_2 \cdot 3\text{H}_2\text{O}$  and 1 M  $\text{LiNO}_3$  in ethanol. Undoped CuO films were prepared with the same method, but in absence of  $\text{LiNO}_3$ . Fluorine-doped tin oxide (FTO) coated glass (TEC 15 Glass, Dyesol) with a size of 1.5 cm  $\times$  2.0 cm was used as a substrate. The samples were subsequently calcined in air at 400  $^\circ\text{C}$  for 2 h (1.3  $^\circ\text{C}/\text{min}$ ) and slowly cooled down to room temperature.

*Atomic Layer Deposition of Niobium doped Titanium oxide films:* Atomic layer deposition of niobium doped titanium oxide thin films was carried out in a Picosun R-200 reactor at a temperature of 200  $^\circ\text{C}$  and a base pressure of 2 hPa. Nitrogen (Air Liquide, 99.999 %) was used as the purge and carrier gas. The carrier gas line flow during pulses was 40 sccm. Titanium isopropoxide (TIPO, Aldrich, 99.999 %) was supplied from a stainless steel vessel at 85  $^\circ\text{C}$ , niobium ethoxide (NEO, Strem, 99.9+ %) was evaporated from a glass vessel at 160  $^\circ\text{C}$ . Ultrapure water (MilliQ, 18.2 M $\Omega$  cm) was used as oxygen source and held in a stainless steel cylinder at room temperature. Each ALD cycle for  $\text{TiO}_2$  includes two TIPO pulses (1.6 s pulse, 4.5 s static exposure, 6 s purge) and one water pulse (2 s pulse, 4.5 s static exposure, 7.5 s purge). The resulting growth rate was 0.038 nm cycle $^{-1}$  with a non-uniformity of 4 % across a 20 cm wafer. The ALD cycle for niobium oxide consisted of four NEO pulses (1.6 s pulse, 6.5 s static exposure, 6 s purge) and one water pulse as in the  $\text{TiO}_2$  process. The resulting growth rate was 0.068 nm cycle $^{-1}$  with a non-uniformity of 4 % across a 20 cm wafer. Mixed oxide layers were grown by alternating 6  $\text{TiO}_2$  cycles with 1  $\text{NbO}_x$  cycle resulting in an amorphous  $\text{Ti}_{0.80}\text{Nb}_{0.20}\text{O}_x$  dense film.

*Pt Deposition:* For the deposition of Pt co-catalyst nanoparticles, an NTO-protected  $\text{Li}_x\text{Cu}_{1-x}\text{O}$  film, a platinum mesh counter electrode and a  $\text{Hg}/\text{Hg}_2\text{SO}_4/\text{K}_2\text{SO}_4$  (sat.) reference electrode were connected to a  $\mu$ -Autolab III potentiostat and immersed in a methanolic 1 mM  $\text{H}_2\text{PtCl}_6$  solution. Afterwards, a static potential of -0.557 V vs.  $\text{Hg}/\text{Hg}_2\text{SO}_4$  was applied for 10 minutes without illumination.

*Crystallographic Characterization:* Powder X-ray diffraction (XRD) patterns were acquired on a STOE powder diffractometer (Cu-K $\alpha$ ,  $\lambda = 1.5406 \text{ \AA}$ ) equipped with a position-sensitive Mythen-1K detector in transmission geometry. Lanthanum hexaboride (NIST LaB6 SRM 660b; space group: Pm3 m;  $a = 4.15689(8) \text{ \AA}$ ) was used as an internal standard for calibration of diffraction line positions. The XRD pattern of the sample and 5 % of lanthanum hexaboride were collected over a  $2\theta$  range of 10 to 81  $^\circ$  with a step size of 0.015  $^\circ$ .  $\text{Li}_x\text{Cu}_{1-x}\text{O}$  unit cell parameters were obtained using the results from the Rietveld refinements<sup>[1]</sup> of a powder diffraction pattern. The observed parameters are structurally closely related to those of tenorite (CuO, space group: C2/c;  $a = 4.6853(3) \text{ \AA}$ ;  $b = 3.4257(1) \text{ \AA}$ ;  $c = 5.1303(3) \text{ \AA}$ ;  $\beta = 99.549(4)^\circ$ ; JCPDS-ICDD PDF card No. 45-937). XRD patterns of the thin film electrodes were acquired on a Bruker D8

Discover with Ni-filtered Cu K $\alpha$  radiation and a LynxEye position-sensitive detector.

*Electron Microscopy:* Scanning electron microscopy (SEM) measurements were performed on an FEI Helios NanoLab G3 UC scanning electron microscope using a 1 - 30 kV field emission gun and an Oxford instruments energy dispersive X-ray (EDX) spectroscopy detector. A probe-corrected FEI Titan Themis transmission electron microscope (TEM) with a field emission gun (X-FEG) operated at 300 kV was applied to determine morphology, crystallography and elemental distribution. High-resolution TEM (HRTEM) and bright field (BF) images were received with a Ceta 16M camera while scanning TEM (STEM) measurements were performed with an annular dark field (ADF) detector. The thin film material was carefully scraped from the substrate with a razor blade and the powder was dispersed in ethanol. This liquid was deposited dropwise on a holey carbon grid to prepare the sample. In addition, focused ion beam (FIB)-machined lamellae of film cross-sections were prepared in a FEI Helios 600i Dual Beam workstation. To locally probe the oxidation state of Cu, electron energy loss spectroscopy (EELS) in a transmission electron microscope (TEM) was used. Ion beam assisted Pt deposition with dimensions of  $10 \times 2 \times 2 \mu\text{m}^3$  (length  $\times$  width  $\times$  height) was applied for sample surface protection during Ga<sup>+</sup> ion milling. 2  $\mu\text{m}$  thick TEM lamellae were cut out of the films, transferred to a Mo TEM grid and initially thinned down to a thickness of around 0.7  $\mu\text{m}$  using an acceleration voltage of 30 kV and beam currents of 430 pA and 230 pA. Final lamellae thinning was performed at 5 kV and 120 pA and subsequent polishing to minimize beam damage was carried out at 2 kV and 72 pA until a thickness of below 100 nm was reached. Electron energy loss spectroscopy (EELS) data were acquired in scanning transmission mode at 300 kV using a probe-corrected FEI Titan Themis equipped with a monochromator and an Gatan Enfinitum ER spectrometer. An energy resolution of 0.2 eV was realized during the experiment, using a dispersion of 0.1 channels/pixel and a spectrometer entrance aperture of 5 mm. Subpixel scanning was used to reduce the electron beam damage during the spectrum acquisition on the sample yielding pixel sizes between 2 and 5 nm.

*Solid State <sup>7</sup>Li NMR:* Solid-State MAS NMR: Experiments were performed at 11.74 T on a Bruker DSX 500 spectrometer equipped with a commercial 4 mm triple-resonance MAS probe at <sup>7</sup>Li frequencies of 194.399 MHz. All experiments were performed in ZrO<sub>2</sub> rotors at room temperature. The one-dimensional <sup>7</sup>Li NMR spectrum was acquired with a 90 ° pulse length of 2.0  $\mu\text{s}$ , a recycle delay of 64 s and at a sample spinning frequency of 8 kHz.

*Hall Measurements:* Hall measurements were performed using the van der Pauw technique in a four-point setup. For the characterization, pellets were pressed (80 kg/cm<sup>2</sup>) from powders (thickness 0.31 mm) and sintered at 400 °C for 24 h (2 °C/min) prior to the measurement.

*Optical Characterization:* UV-Vis spectra were obtained on a Perkin Elmer Lambda 1050 UV/Visible/NIR spectrophotometer with an integrating sphere. The absorbance of the films was calculated from both the transmittance and reflectance of the films correcting for the absorbance of the FTO substrate by applying an expression derived

by Klahr et al.<sup>[2]</sup> to the UV-Vis data.

*Photoelectrochemical Characterization:* Cyclovoltammetry (CV) and chrono-amperometry (CA) measurements were performed in a three electrode setup. A custom built closed one-compartment cell allowed a photoelectrochemical characterization in the absence of air. Therefore, argon or nitrogen purging of the aqueous 0.1 M Na<sub>2</sub>SO<sub>4</sub> or 1 mM iodide/triiodide (I<sup>-</sup>/I<sub>3</sub><sup>-</sup>) propylene carbonate electrolyte was started 30 minutes before the experiment and was continued during the measurement. The thin film photocathodes were masked with Teflon adhesive tape leaving free an area of 0.196 cm<sup>2</sup> for illumination. Argent conductive varnish was used to improve the electrical contact to the potentiostat. The photoelectrode, a Hg/Hg<sub>2</sub>SO<sub>4</sub>/K<sub>2</sub>SO<sub>4</sub> (sat.) or RHE reference electrode and a platinum mesh counter electrode were connected to a μ-Autolab III potentiostat. Measurements were either performed in the dark or under simulated sunlight illumination. For the latter, the thin film electrodes were illuminated through the substrate side by an AM1.5G solar simulator (Solar Light Model 16S) at 100 mW cm<sup>-2</sup>. CV measurements were performed either in the dark or under illumination by starting at 0.85 V vs. RHE, scanning at a sweep rate of 20 mV/s from positive to negative potentials down to 0.0 V vs. RHE and back to 0.9 V vs. RHE. In total, two cycles were performed for each measurement. Linear sweep voltammograms were performed at a scan rate of 2 mV/s, starting at 0.7 V vs. RHE and scanning down to -0.1 V vs. RHE. The light source was chopped manually. In the case of CA measurements, a steady potential was applied for a defined time and the resulting current was recorded in a time interval of 1 s. Electrochemical impedance spectroscopy was performed in nitrogen purged aqueous 0.1 M Na<sub>2</sub>SO<sub>4</sub> electrolyte at 0.3 V vs. RHE under AM1.5 substrate illumination with 10 mV amplitude over a frequency range between 1000000 and 100 Hz (logarithmic step size).

*Hydrogen Detection:* In order to verify that the observed photocurrent results from the reduction of water, a micro sensor (*Unisense A/S H<sub>2</sub>-NPLR*) with a hydrogen selective silicone membrane was combined with a three electrode PEC setup. The micro sensor was calibrated in a two-point measurement using the corresponding program (*Unisense A/S SensorTrace 1.4*). The data point for c = 0 mM was acquired in Nitrogen-purged electrolyte (aqueous 0.1 M Na<sub>2</sub>SO<sub>4</sub> solution at pH 7), while the second measuring point of c = 40.7 mM was recorded in the same electrolyte purged with forming gas (5 vol% H<sub>2</sub> in Ar, *AirLiquide ARCAL15*) for 20 minutes, taking in account the saturation concentration of pure H<sub>2</sub> gas in water of 813 μM atm<sup>-1</sup>.<sup>[3]</sup> To minimize the electrolyte volume and therefore maximize the detectable hydrogen concentration, a 2 mL poly(methyl methacrylate) (PMMA) cuvette was used as PEC cell. The working electrode was glued on a drilled-in hole (diameter ≈ 7 mm) and connected to the potentiostat together with a Platinum wire counter electrode and a Hg/Hg<sub>2</sub>SO<sub>4</sub>/K<sub>2</sub>SO<sub>4</sub> (sat.) reference electrode and filled with 1.7 mL electrolyte. The hydrogen micro sensor was placed in the cuvette, which was subsequently sealed using modelling clay. The hydrogen concentration was recorded with an interval time of 10 seconds. As the polarization of the micro sensor is very sensitive and critical for a correct measurement, magnetic stirring was not possible

in order to avoid any interfering signals.

*Computational Details:* Density-functional theory (DFT) calculations were performed using the VASP<sup>[4,5]</sup> code with projector-augmented wave (PAW) pseudopotentials.<sup>[6]</sup> The generalized-gradient approximation (GGA)<sup>[7]</sup> was used for the exchange-correlation functional, including an on-site Hubbard  $U$  term. The rotationally invariant approach of Dudarev et al.<sup>[8]</sup> was adopted for the GGA+ $U$  calculations. A Hubbard- $U$  value for Cu of 8.0 eV gives an indirect gap of 1.46 eV for CuO, in close agreement with the 1.39 eV determined from the Tauc plot. This is consistent with previous LDA+ $U$  results.<sup>[9]</sup> We note that previous experimental values range between 1.35-1.7 eV.<sup>[9-14]</sup> To model different doping concentrations two different cell sizes with 8 and 64 atoms were adopted, corresponding to the bulk CuO and a  $2 \times 2 \times 2$  supercell, respectively. A plane-wave cut-off of 500 eV and a Monkhorst-Pack k-point mesh of  $8 \times 8 \times 8$  and  $4 \times 4 \times 4$  were used for the two unit cells, respectively. The Li solution energy (SE) indicates the preferred lattice positions of Li incorporation in the CuO structure and is defined as follows:

$$SE_{Li} = E_{Li_xCu_{1-x}O} - E_{CuO} - NE_{Li} + ME_{O/Cu} \quad (6.1)$$

$E_{Li_xCu_{1-x}O}$  and  $E_{CuO}$  represent the total energy of the doped and undoped structure, respectively.  $E_{Li}$  and  $E_{O/Cu}$  is the energy of the elemental ground state of lithium, oxygen and copper.  $N$  is the number of lithium atoms substituted by  $M$  oxygen or copper. To calculate the solution energy a Cu or O was substituted by a Li atom and the structure fully relaxed.

## 6.5.2 Additional Figures

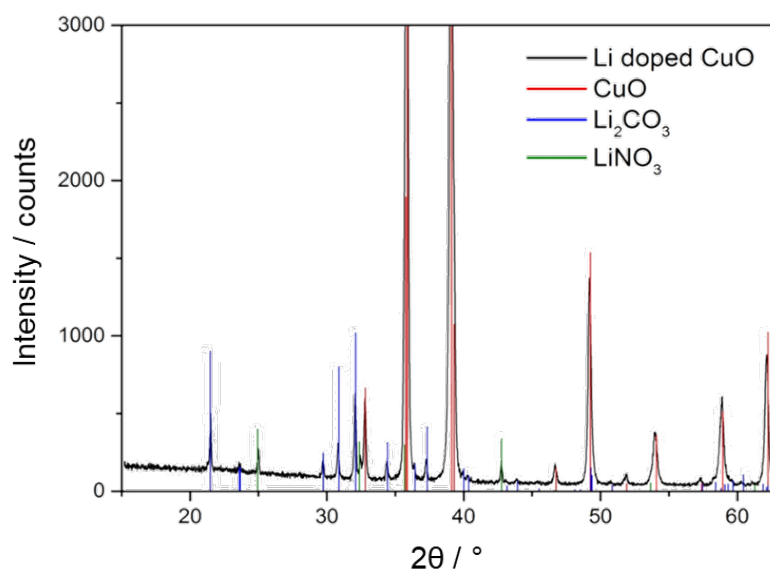


**Figure 6.6:** XRD pattern of the film obtained directly after calcination. The film is a mixture of Li doped CuO,  $\text{Li}_2\text{CO}_3$  and  $\text{LiNO}_3$ . To obtain the single Li doped CuO phase the film is immersed in water for 2 hours to remove  $\text{Li}_2\text{CO}_3$  and  $\text{LiNO}_3$ .

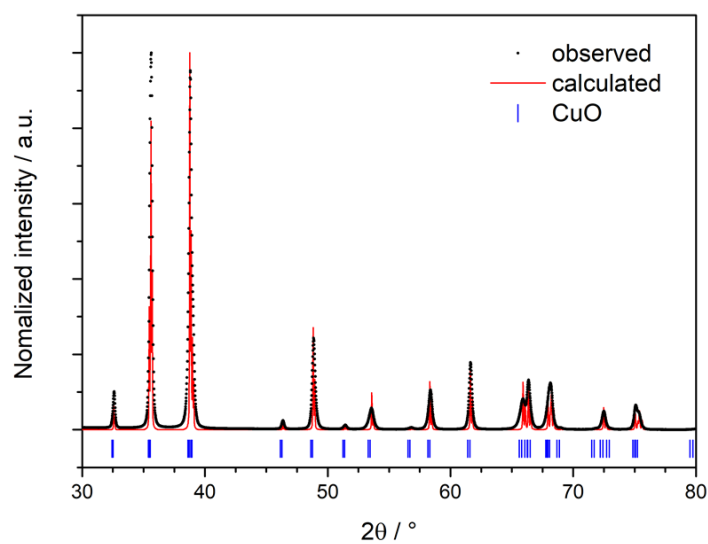


**Figure 6.7:** Rietveld refinement of undoped CuO with observed data (·) and calculated pattern (red line), blue vertical bars mark the positions of the diffraction lines of CuO (tenorite).

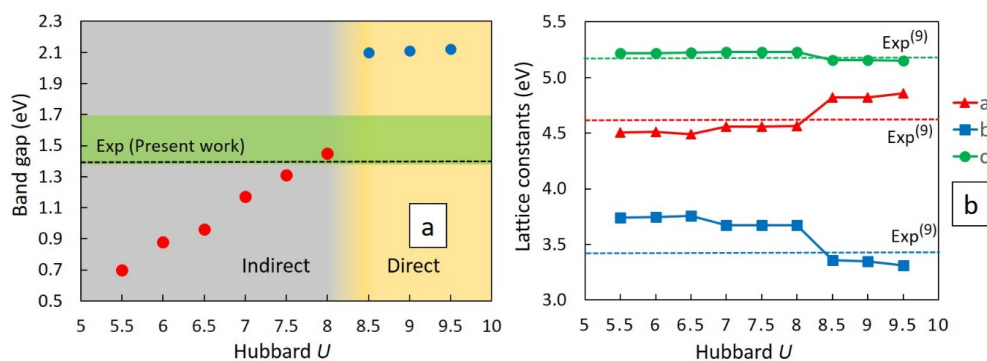


**Figure 6.8:** a) Band gap and b) lattice constants of CuO as a function of Hubbard  $U$ . Experimental band gaps range between 1.35-1.7 eV, highlighted in green.<sup>[10-13]</sup> The band gap of 1.39 eV determined from the Tauc plot in this work is marked by a dashed line in a). The experimental lattice parameters denoted by dashed lines in b) are from Åsbrink et al..<sup>[14]</sup>

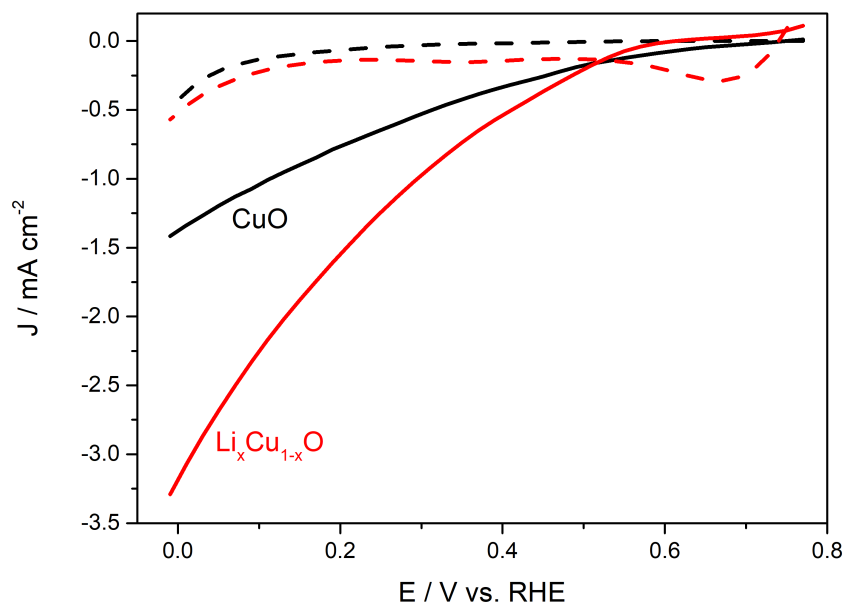


**Figure 6.9:** Linear sweep voltammetry measurements of bare copper oxide photocathodes in the dark (dashed lines) and under AM1.5 illumination (solid lines).  $\text{Li}_x\text{Cu}_{1-x}\text{O}$  films (red) exhibit significantly higher photocurrents compared to undoped CuO films.

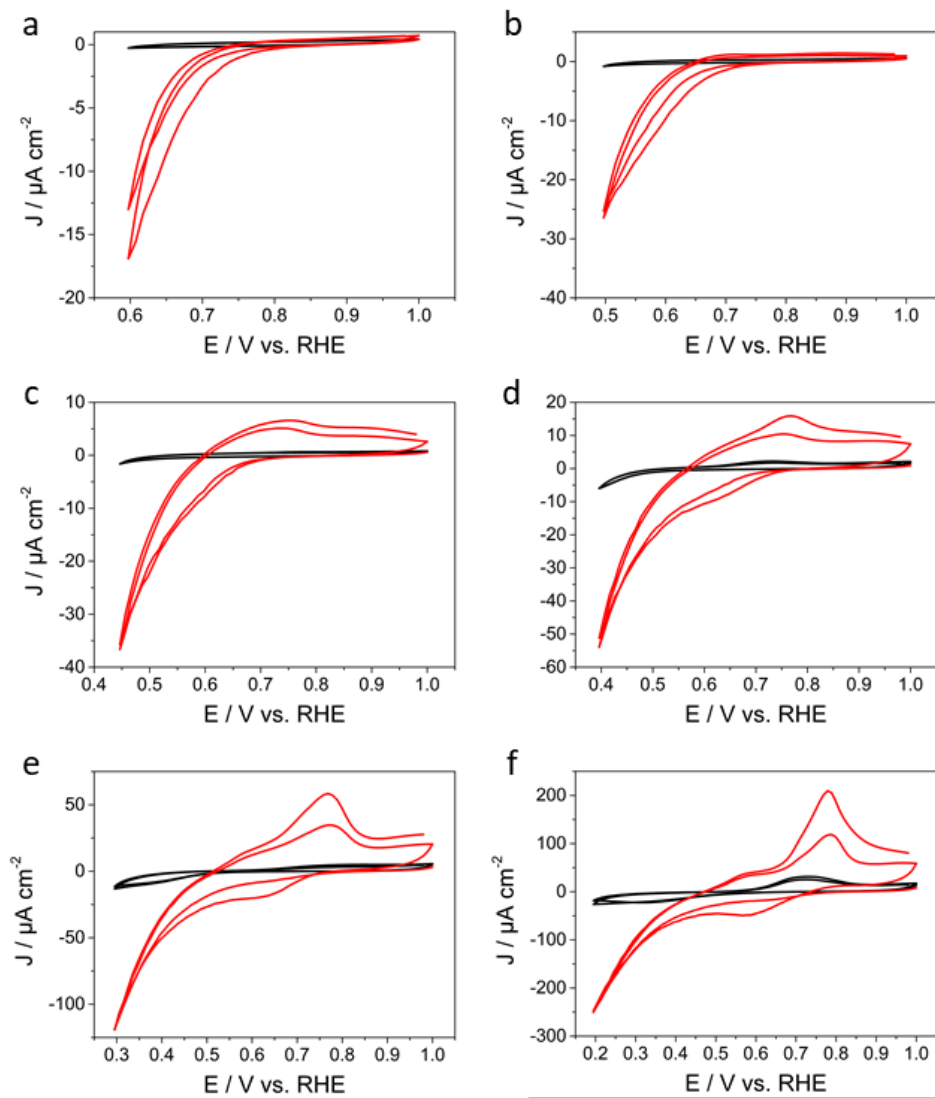


**Figure 6.10:** Cyclic voltammetry measurements of a bare  $\text{Li}_x\text{Cu}_{1-x}\text{O}$  electrode in successive order from a – f. The potential range was extended stepwise to lower potentials, and consequently the photocorrosion gets more and more pronounced.

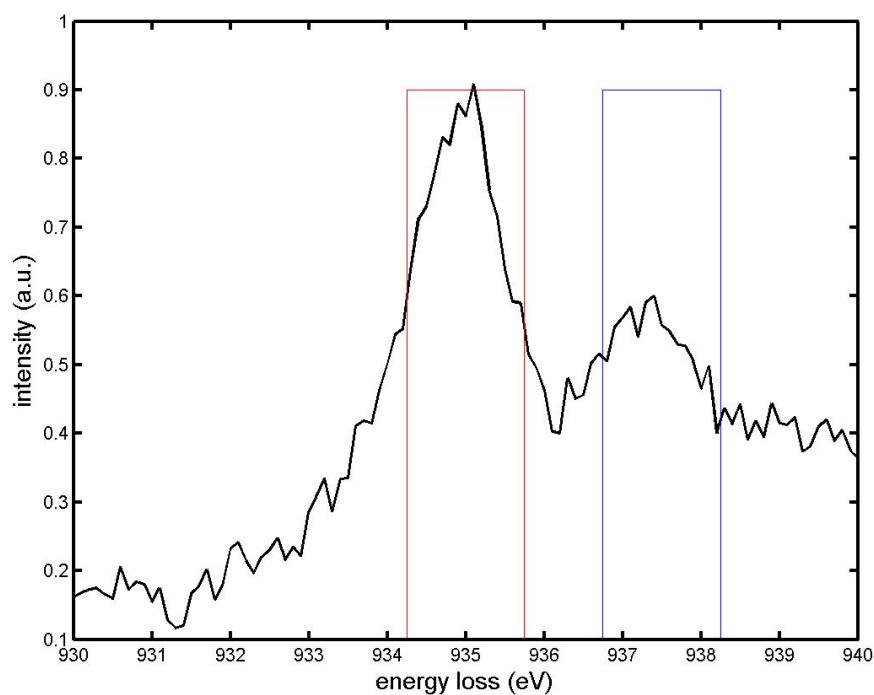


**Figure 6.11:** To generate the EELS map tracking the oxidation state of Copper, the spectra were first aligned. After subtraction of the background via a power-law fit the intensity ratio of the Cu-L<sub>3</sub> edge of CuO (red) and Cu<sub>2</sub>O (blue) were integrated in defined energy windows. The distribution of the two oxidation states is estimated by this intensity ratio.

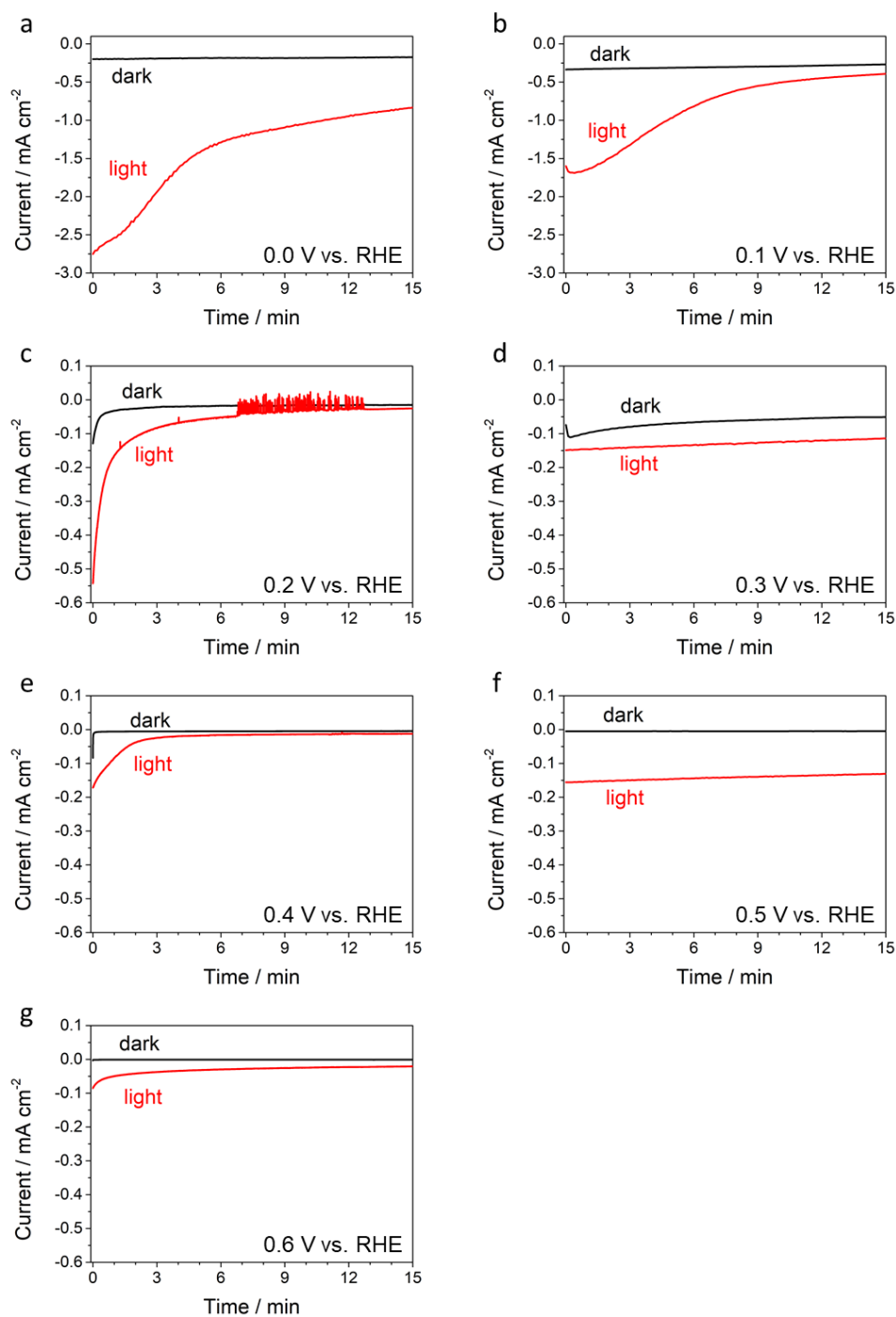


**Figure 6.12:** Chronoamperometric data of unprotected  $\text{Li}_x\text{Cu}_{1-x}\text{O}$  photocathodes at various potentials from 0.0 to 0.6 V vs. RHE in the dark (black) and under AM1.5 illumination (red). Afterwards, the respective samples were characterized by XPS (see Figure 6.3c, d). The spikes in (c) were caused by an increased flow of nitrogen purging.

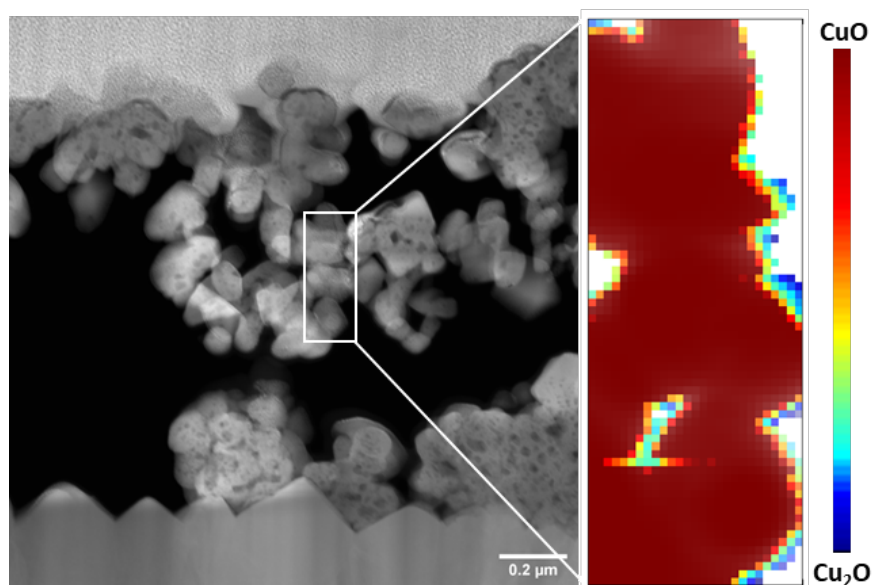


**Figure 6.13:** An as-synthesized sample, which was never used in an electrochemical measurement, was used to investigate the effect of the FIB sample preparation. While the sample preparation causes a slight reduction of some regions of the  $\text{Li}_x\text{Cu}_{1-x}\text{O}$  surface, no cubic  $\text{Cu}_2\text{O}$  crystals are formed by this procedure. Therefore, the FIB preparation method is supposed to have no effect on the photocorrosion study of  $\text{Li}_x\text{Cu}_{1-x}\text{O}$  photocathodes.

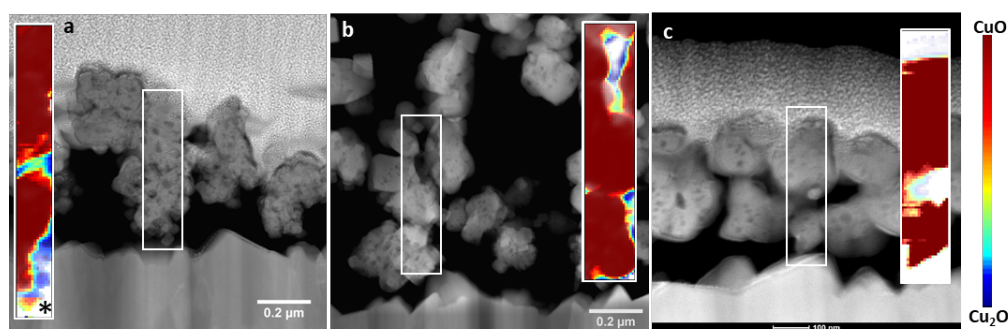


**Figure 6.14:**  $\text{CuO}/\text{Cu}_2\text{O}$  ratio maps based on EELS data of samples used for PEC water splitting at different potentials. (a) 0.1 V for 15 min, (b) 0.2 V for 15 min and (c) 0.3 V for 15 min. \*Artifact of the spectrum alignment, should be  $\text{Cu}_2\text{O}$ .

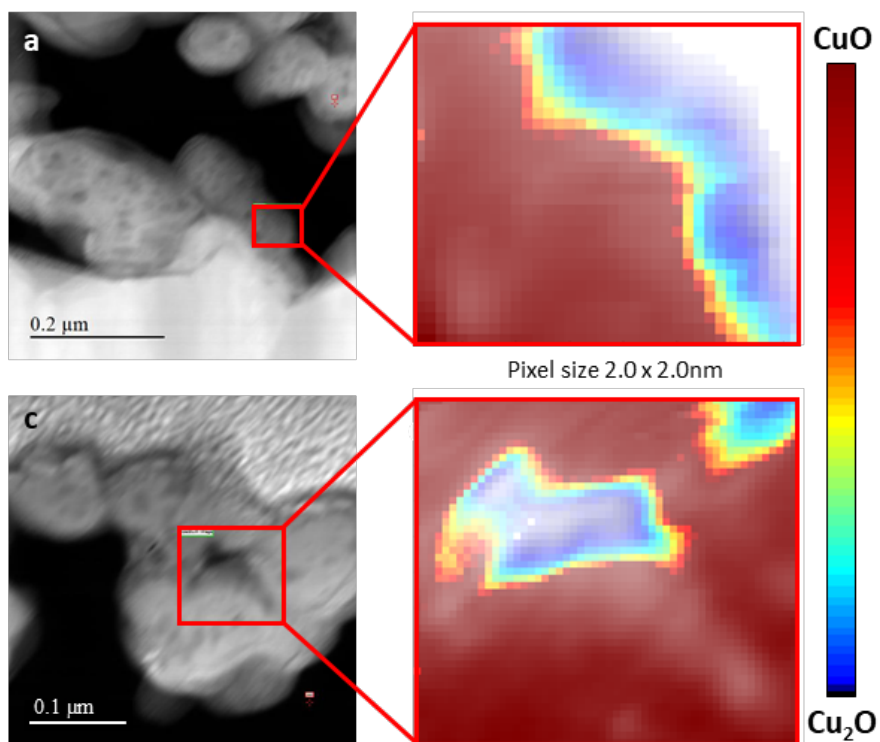


**Figure 6.15:** TEM cross section images of  $\text{Li}_x\text{Cu}_{1-x}\text{O}$  films after an electrochemistry experiment performed for 15 min at 0.3 V vs. RHE under illumination (a, c) with corresponding EELS maps (b, d, pixel size 4 nm<sup>2</sup>).

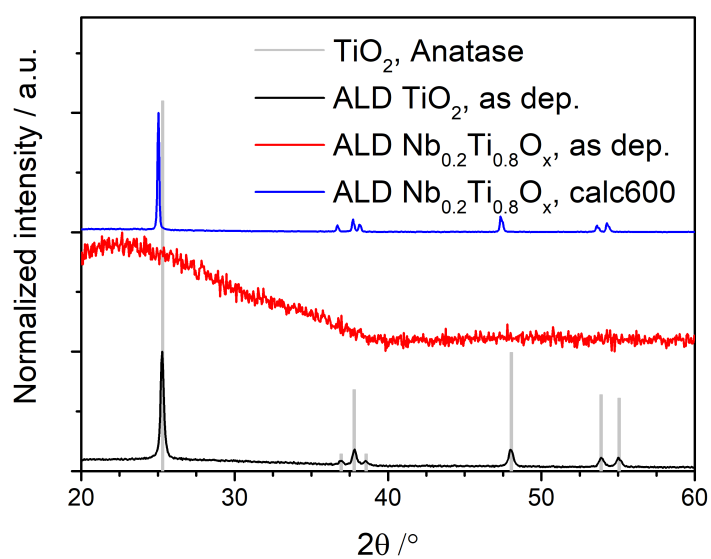


**Figure 6.16:** XRD pattern of  $\text{Ti}_{0.8}\text{Nb}_{0.2}\text{O}_x$  ALD films as deposited (black). These layers are amorphous, in contrast to pure  $\text{TiO}_2$  layers (black). After calcination in 5 %  $\text{H}_2/\text{N}_2$  atmosphere at 600 °C (blue), crystalline  $\text{Ti}_{0.8}\text{Nb}_{0.2}\text{O}_x$  ALD layers are obtained.

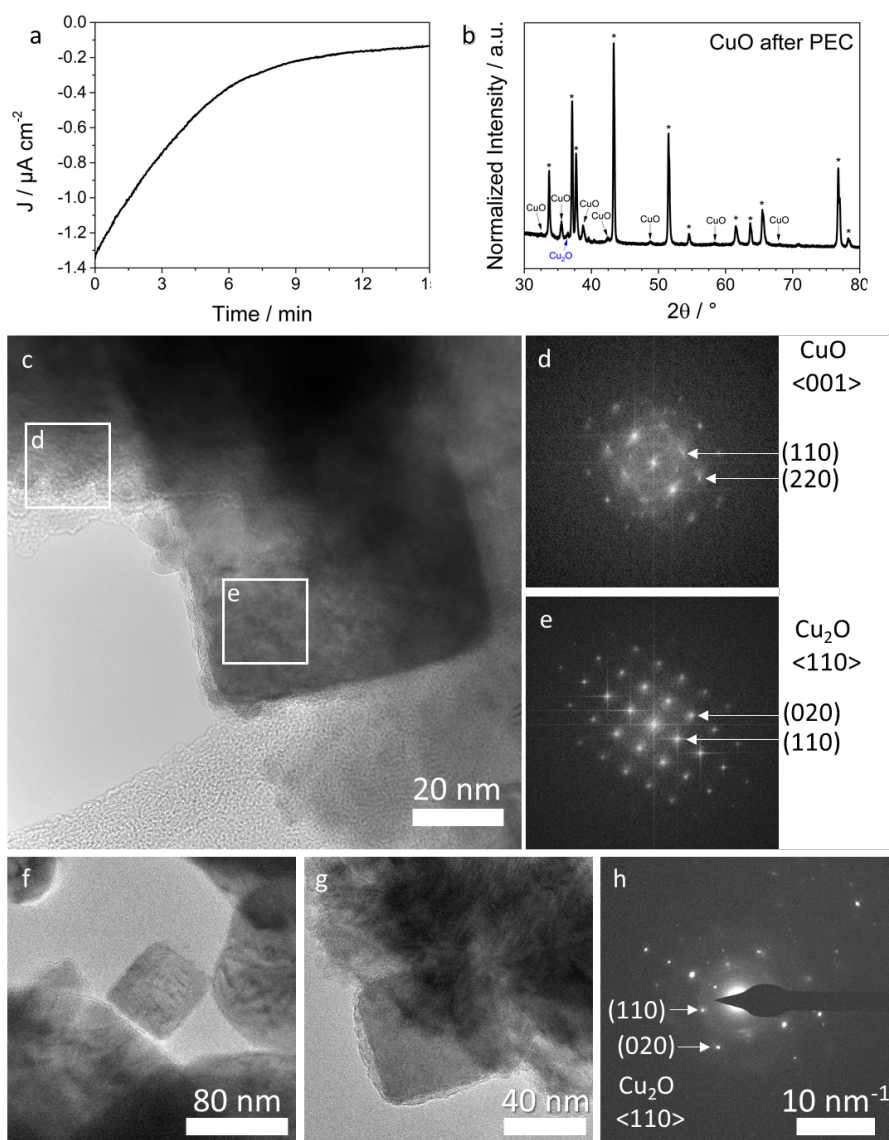


**Figure 6.17:** a) Potentiostatic measurement of a bare, undoped CuO electrode at 0.2 V vs. RHE under AM1.5 illumination. b) XRD pattern of the CuO film after the 15-minute stability test shown in (a), indicating the formation of Cu<sub>2</sub>O (blue). c) High resolution TEM image showing one square crystal grown on the surface of the CuO structure. The FFTs of the marked regions were indexed for CuO (d) and Cu<sub>2</sub>O (e). f, g) Further TEM images of Cu<sub>2</sub>O grown on different spots of the CuO surface. h) Electron diffraction pattern of the cubic crystal depicted in (g) with the reflections indexed for Cu<sub>2</sub>O.

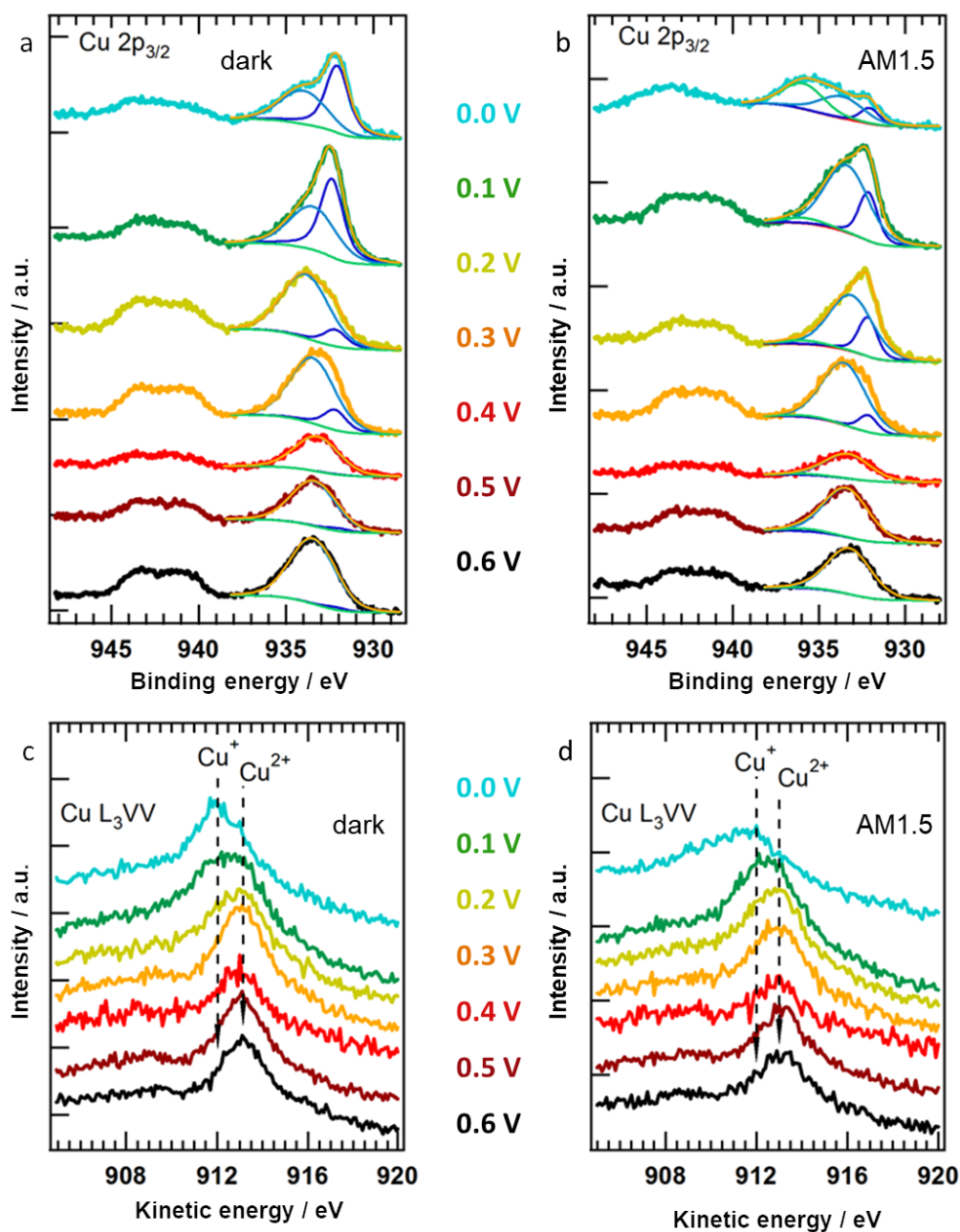


**Figure 6.18:** XPS characterization of  $\text{Li}_x\text{Cu}_{1-x}\text{O}$  photocathodes after electrochemical stability tests at the respective potentials vs. RHE for 15 minutes each in the dark (left side, a and c) and under AM1.5 illumination (right side, b and d). The upper two diagrams show the deconvolution of the  $\text{Cu } 2p_{3/2}$  peaks into a  $\text{Cu(I)}$ -component at 932.4 eV and a  $\text{Cu(II)}$ -component at ca. 933.6 eV. At the lowest potential (0.0 V vs. RHE) a third feature appears at higher binding energies, which might be caused by differential charging of the samples as a result of preceding corrosion. The corresponding  $\text{Cu L}_{3VV}$  Auger signals are displayed in the graphs (c) and (d) below with the positions of the  $\text{Cu(I)}$  and  $\text{Cu(II)}$  peaks indicated by the dashed lines.

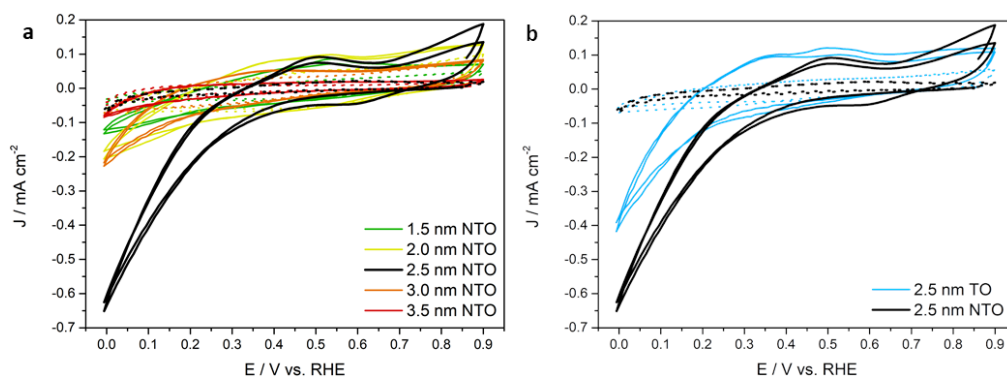


**Figure 6.19:** Cyclic voltammograms of  $\text{Li}_x\text{Cu}_{1-x}\text{O}$  photocathodes covered with Nb:TiO<sub>2</sub> (NTO) or TiO<sub>2</sub> (TO). A protection layer of 2.5 nm NTO showed the highest activity of all tested NTO layer thicknesses (a) and also an improvement compared to undoped TiO<sub>2</sub> (b).

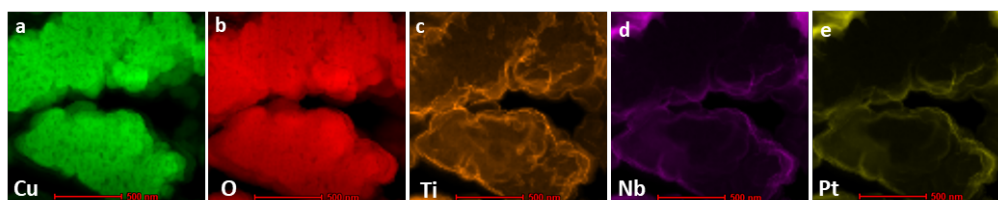


**Figure 6.20:** Energy dispersive X-ray (EDX) mappings of a  $\text{Li}_x\text{Cu}_{1-x}\text{O}/\text{NTO}/\text{Pt}$  TEM cross section. The  $\text{Li}_x\text{Cu}_{1-x}\text{O}$  structure (a, b) is homogeneously covered with Nb:TiO<sub>2</sub> (NTO, c, d) and Pt (e).

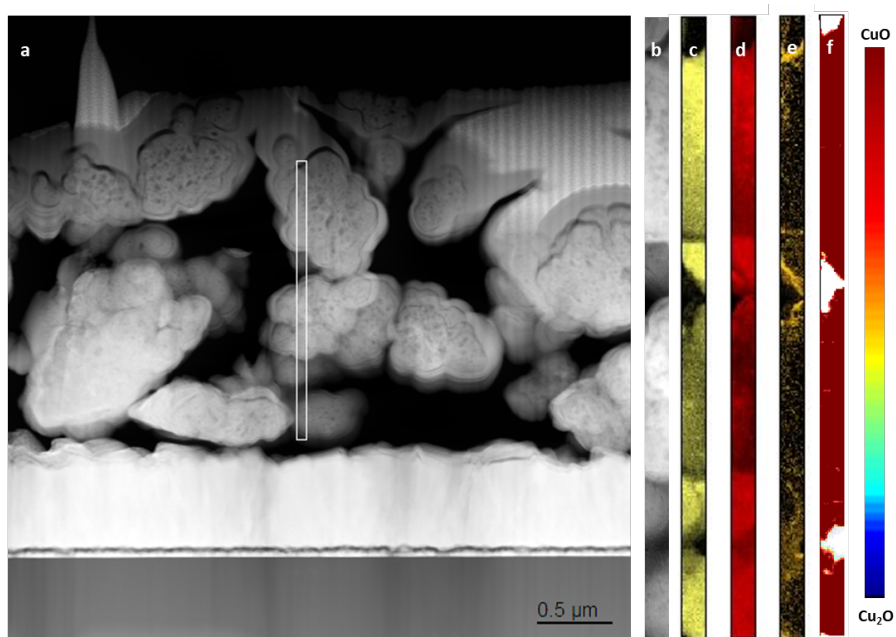


**Figure 6.21:** a) TEM cross section of a  $\text{Li}_x\text{Cu}_{1-x}\text{O}/\text{NTO}/\text{Pt}$  device held for 15 min at 0.2 V vs. RHE under AM1.5 illumination. The marked area (white, b) was used for EDX mapping of Cu (c), O (d) and Ti (e). The corresponding EELS map (f) shows no sign of photocorrosion.

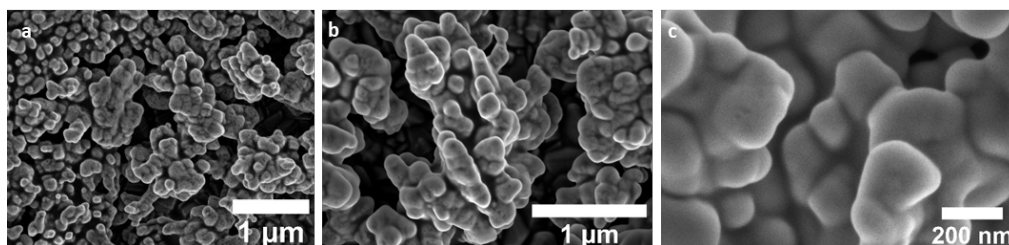


**Figure 6.22:** SEM top view images of a  $\text{Li}_x\text{Cu}_{1-x}\text{O}/\text{NTO}/\text{Pt}$  photocathode after 90 minutes at 0.3 V vs. RHE and AM1.5 substrate illumination. The 20 nm sized Pt particles are not adhering on the surface anymore, which is believed to cause the observed loss in activity.

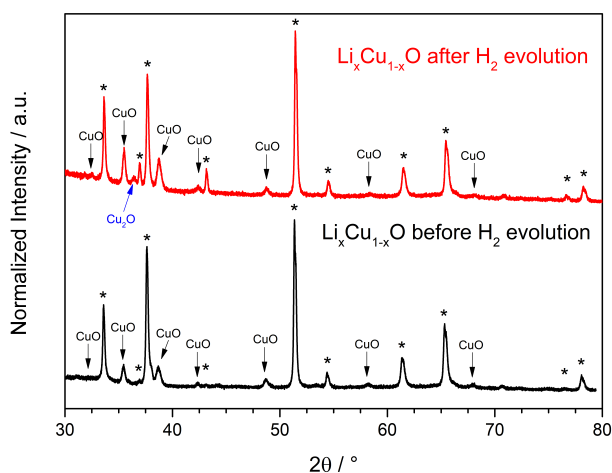


**Figure 6.23:** XRD patterns of unprotected Li<sub>x</sub>Cu<sub>1-x</sub>O films before (black) and after (red) the hydrogen evolution test at 0.3 V vs. RHE. After 30 minutes of illumination and progressing photocorrosion, the cuprite phase of Cu<sub>2</sub>O emerges (blue). Reflections of the FTO substrate are marked with (\*).

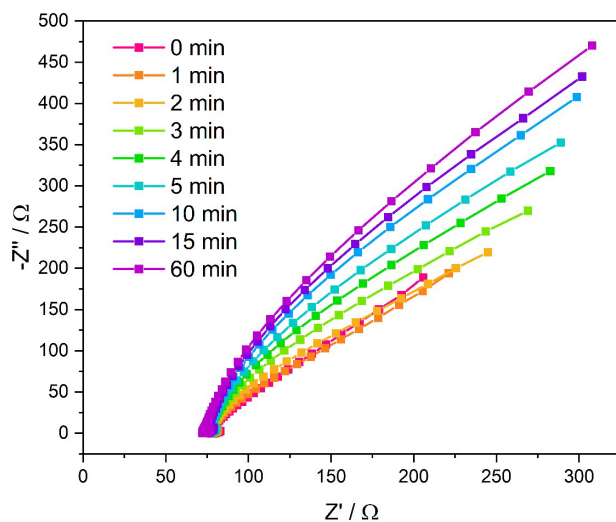


**Figure 6.24:** Nyquist plots of a single Li<sub>x</sub>Cu<sub>1-x</sub>O electrode. The photocathode was held at 0.3 V vs. RHE under AM1.5 illumination for a 60 minutes stability test, intermitted by impedance measurements at the same photoelectrochemical conditions. With advancing photocorrosion, the charge transport resistance on the photocathode - electrolyte interface increases.

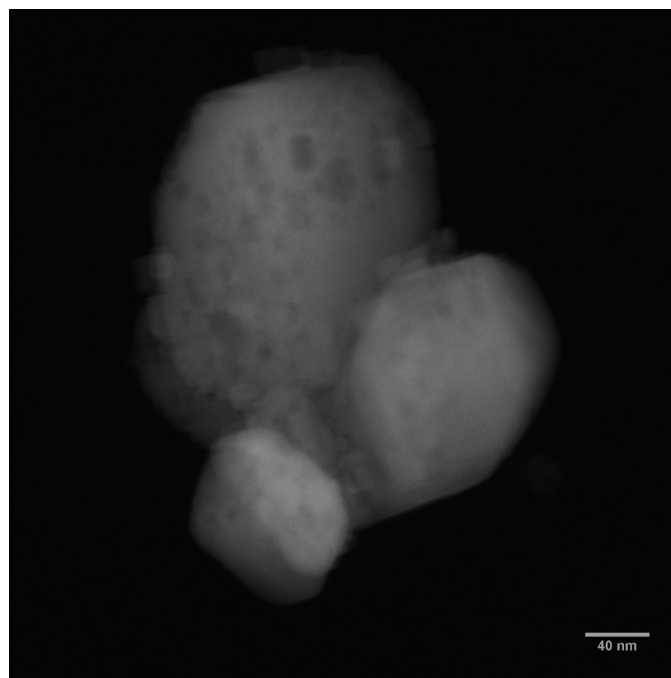


**Figure 6.25:** TEM image of unprotected  $\text{Li}_x\text{Cu}_{1-x}\text{O}$  after 60 s at 0.2 V vs. RHE under AM1.5 illumination. Cubic crystals on the surface indicate that photocorrosion starts directly with the photoelectrochemical stability test.

## References

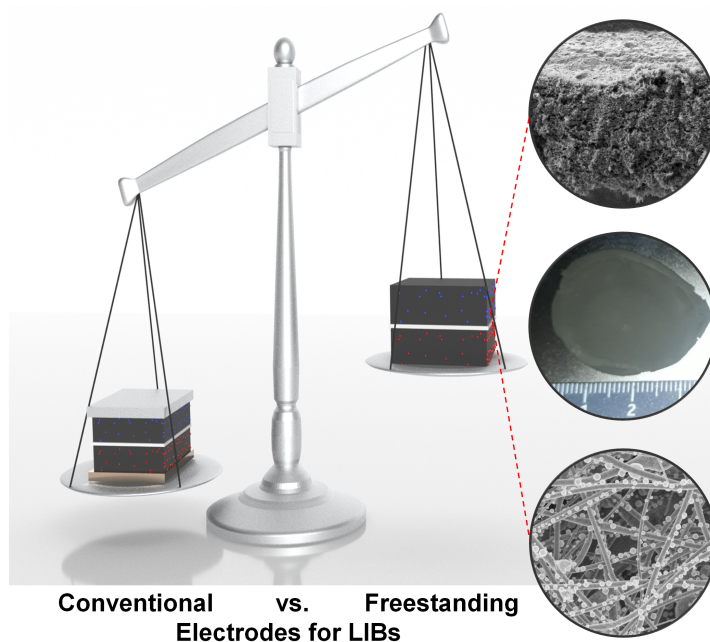
- [1] H. Rietveld, *J. Appl. Cryst.* **1969**, 2, 65–71.
- [2] B. M. Klahr, A. B. Martinson, T. W. Hamann, *Langmuir* **2011**, 27, 461–8.
- [3] D. A. Wiesenburg, N. L. Guinasso, *J. Chem. Eng. Data* **1979**, 24, 356–360.
- [4] G. Kresse, J. Hafner, *Phys. Rev. B: Condens Matter Mater.* **1994**, 49, 14251–14269.
- [5] G. Kresse, J. Furthmüller, *Comput. Mater. Sci.* **1996**, 6, 15–50.
- [6] P. E. Blöchl, *Phys. Rev. B* **1994**, 50, 17953–17979.
- [7] J. P. Perdew, K. Burke, M. Ernzerhof, *Phys. Rev. Lett.* **1996**, 77, 3865–3868.
- [8] S. L. Dudarev, G. A. Botton, S. Y. Savrasov, C. J. Humphreys, A. P. Sutton, *Phys. Rev. B: Condens. Matter Mater. Phys.* **1998**, 57, 1505–1509.
- [9] M. Heinemann, B. Eifert, C. Heiliger, *Phys. Rev. B: Condens. Matter Mater. Phys.* **2013**, 87, 115111.
- [10] B. K. Meyer, A. Polity, D. Reppin, M. Becker, P. Hering, P. J. Klar, T. Sander, C. Reindl, J. Benz, M. Eickhoff, C. Heiliger, M. Heinemann, J. Bläsing, A. Krost, S. Shokovets, C. Müller, C. Ronning, *Phys. Status Solidi B* **2012**, 249, 1487–1509.
- [11] J. Ghijsen, L. H. Tjeng, J. van Elp, H. Eskes, J. Westerink, G. A. Sawatzky, M. T. Czyzyk, *Phys. Rev. B: Condens. Matter Mater. Phys.* **1988**, 38, 11322–11330.

- 
- [12] F. P. Koffyberg, F. A. Benko, *J. Appl. Phys.* **1982**, *53*, 1173–1177.
- [13] F. Marabelli, G. B. Parravicini, F. Salghetti-Drioli, *Phys. Rev. B* **1995**, *52*, 1433–1436.
- [14] S. sbrink, L. J. Norrby, *Acta Cryst. B* **1970**, *26*, 8–15.

## 7 Overcoming the Challenges of Freestanding Tin Oxide-based Composite Anodes to Achieve High Capacity and Increased Cycling Stability

This chapter is based on the following publication:

Florian Zoller, Sebastian Häring, Daniel Böhm, Hannah Illner, Markus Döblinger, Zdeněk Sofer, Martin Finsterbusch, Thomas Bein, Dina Fattakhova-Rohlfing\*, *Advanced Functional Materials*, 2021, 2106373.



Sebastian Häring synthesized freestanding electrodes via electrospinning, performed and interpreted the morphological investigations, contributed to the electrochemical analysis of the electrodes and wrote the corresponding parts of the manuscript.

## Abstract

Freestanding electrodes are a promising way to increase the energy density of the batteries by decreasing the overall amount of electrochemical inactive materials. Freestanding antimony doped tin oxide (ATO)-based hybrid materials have not been reported so far, although this material has demonstrated excellent performance in conventionally designed electrodes. Two different strategies, namely electrospinning and freeze-casting, are explored for the fabrication of ATO-based hybrid materials. It is shown that the electrospinning of ATO/carbon based electrodes from polyvinyl pyrrolidone polymer (PVP) solutions was not successful, as the resulting electrode material suffers from rapid degradation. However, freestanding reduced graphene oxide (rGO) containing ATO/C/rGO nanocomposites prepared via a freeze-casting route demonstrate an impressive rate and cycling performance reaching 697 mAh g<sup>-1</sup> at a high current density of 4 A g<sup>-1</sup>, which is 40 times higher as compared to SnO<sub>2</sub>/rGO and also exceeds the freestanding SnO<sub>2</sub>-based composites reported so far. Antimony doping of the nanosized tin oxide phase and carbon coating are thereby shown to be essential factors for the appealing electrochemical performance. Finally, the freestanding ATO/C/rGO anodes are combined with freestanding LiFe<sub>0.2</sub>Mn<sub>0.8</sub>PO<sub>4</sub>/rGO cathodes to obtain a freestanding full cell operating without metal current collector foils showing nonetheless an excellent cycling stability.

## 7.1 Introduction

Batteries and in particular lithium-ion batteries (LIBs) became an indispensable part of daily life. The fast-paced development of new portable electronic devices, electromobility and large-scale energy storage demands LIBs with maximized capacities, advanced rate capability and a persistent cycling performance. In order to address those issues new electrode materials are explored, implying in case of the anode that the currently used graphite with its rather low theoretical capacity of 372 mAh g<sup>-1</sup> has to be replaced.<sup>[1-4]</sup>

SnO<sub>2</sub> attracted lots of attention as a promising alternative featuring a high theoretical capacity of 1494 mAh g<sup>-1</sup> and a low working potential.<sup>[1-3,5]</sup> Lithiation and delithiation of SnO<sub>2</sub> can be subdivided into two main steps. In a first step, SnO<sub>2</sub> undergoes a conversion reaction resulting in the formation of metallic Sn embedded into a Li<sub>2</sub>O matrix followed by alloying reactions between lithium and the previously formed Sn phase yielding Li<sub>x</sub>Sn (0 ≤ x ≤ 4.4).<sup>[2,3,5,6]</sup> However, the conversion reaction of macroscopic SnO<sub>2</sub> is irreversible, thus limiting the theoretical capacity to 782 mAh g<sup>-1</sup> representing the capacity of the alloying step only.<sup>[6]</sup> Moreover, the conversion reaction, as well as the subsequent alloying reactions are accompanied by huge volume variations of up to 358 % causing internal stress and a potential pulverization of the electrode. Nanosizing of SnO<sub>2</sub> is a well-known strategy to achieve reversibility of both conversion and alloying reactions and to accommodate the strong volume changes.<sup>[6,7]</sup> The performance of

SnO<sub>2</sub> based materials can be additionally enhanced by element doping, which increases the electrical conductivity up to several orders of magnitude.<sup>[3,8]</sup> A further increase of the overall electrical conductivity of the electrode can be achieved by embedding the (doped) SnO<sub>2</sub> nanoparticles into a carbonaceous support matrix that can be based on graphene oxide (rGO), carbon nanotubes (CNTs) or carbon nanofibers (CNFs). Another positive effect of the carbonaceous matrix is its ability to alleviate the volume changes of SnO<sub>2</sub> during lithiation and delithiation enhancing consequently the overall electrochemical performance.<sup>[1,9-11]</sup> These effects can be further improved by introducing a carbon coating layer.<sup>[12-16]</sup> Such a carbon coating layer additionally prevents the SnO<sub>2</sub> particles from a direct contact with the electrolyte, which leads to decreased number of side reactions, thus improving the cycling stability.<sup>[15]</sup> Moreover, carbon coating is also reported to separate individual SnO<sub>2</sub>/graphene sheets which can result in a higher accessibility of the active material reaching higher capacities.<sup>[12]</sup> Consequently, synergistic effects between nanosized doped SnO<sub>2</sub> particles, carbonaceous support materials and the carbon coating layer can be expected resulting in an improved overall electrochemical performance.

Besides improving the storage capacity of individual electrode materials, the optimization of the battery design and the minimization of the fraction of electrochemically inactive components is another means to increase the total energy density of the battery. Electrodes for LIBs are generally prepared in slurry casting approaches, in which a suspension containing the active material or its respective composite, a polymeric binder and conductive additives is coated onto a copper (anode) or aluminum (cathode) foil employed as current collector. Consequently, the electrodes consist of up to 50 wt% of electrochemically inactive materials, which decreases the overall energy density of the negative and positive electrode dramatically.<sup>[1]</sup> An attractive concept to reduce the amount of electrochemically inactive materials is the fabrication of so-called freestanding electrodes. Freestanding electrodes are based on conducting (mainly carbonaceous) materials that act simultaneously as current collector as well as conducting matrix incorporating and stabilizing the active material. Thus, freestanding electrodes have to face several challenges including a good electrical conductivity and sufficient mechanical stability to withstand the stress during the cell assembly and operation. Numerous SnO<sub>2</sub>-carbon hybrid materials have been reported, which are partially applicable as freestanding electrodes. The reported examples of freestanding electrodes include SnO<sub>2</sub> embedded into rGO,<sup>[1,10,11,17-21]</sup> CNTs,<sup>[9,22,23]</sup> CNFs,<sup>[24-27]</sup> carbon cloth,<sup>[5,28-30]</sup> carbon paper,<sup>[31]</sup> or carbon monoliths,<sup>[32]</sup> which have been prepared via electrospinning,<sup>[24]</sup> vacuum filtration,<sup>[1,11,19,22,33]</sup> a combination of in-situ hydrothermal synthesis and freeze-drying,<sup>[10,18]</sup> hydrothermal synthesis of SnO<sub>2</sub> on a preformed array,<sup>[28,29]</sup> or electrodeposition.<sup>[31]</sup> In contrast to the pure SnO<sub>2</sub>-based freestanding electrodes, their doped analogues are much less investigated, although published examples demonstrate the clear benefits of this approach for the electrode performance. Thus, Zhang et al. reported a Co doped SnO<sub>2</sub>/rGO/carbonized cotton composite that demonstrated a better conductivity and a superior electrochemical performance

as compared to the undoped equivalent.<sup>[30]</sup> In another publication, Zhang et al. described a Fe doped SnO<sub>2</sub>/rGO/carbonized cotton composite. The performance of this material was also superior to that of an undoped equivalent, but slightly inferior compared to the freestanding Co doped SnO<sub>2</sub> composite.<sup>[34]</sup> The Zn doped SnO<sub>2</sub>/rGO composite reported by Dou et al. is another example for combining doped SnO<sub>2</sub> and a current collector-free electrode architecture with a beneficial effect on the electrochemical performance.<sup>[35]</sup>

Sb doped SnO<sub>2</sub> (ATO) freestanding composites have not been reported so far, despite the fact that conventional Sb:SnO<sub>2</sub> composite coated onto Cu foil electrodes have demonstrated excellent rate and cycling stability superior to that of other SnO<sub>2</sub>-based materials.<sup>[2,36,37]</sup>

In this paper we have investigated different ways to prepare freestanding binder-free ATO/rGO electrodes. Two approaches were tested that are industrial applicable due to their scalability and are commonly used for freestanding electrode fabrication, namely freeze-casting and electrospinning. However, in our case the fabrication of ATO/carbon electrodes by electrospinning with polyvinyl pyrrolidone polymer (PVP) was not possible, as the pyrolysis step required to carbonize the fiber forming PVP employed in the spinning solution results in a reduction of ATO with a formation of poorly performing SbSn-alloy/carbon nanofiber (SbSn/CNF) composites. In contrast, freeze-casting enables the fabrication of freestanding ATO/C/rGO electrodes with a good rate performance and cycling stability due to a multi-step synthesis procedure compatible with the employed precursor solution resulting in a carbon coated rGO composite with a homogeneously dispersed nanosized ATO phase.

Finally, a freestanding full cell was produced, consisting of the freestanding ATO/C/rGO nanocomposite as an anode and a high voltage freestanding LiFe<sub>0.2</sub>Mn<sub>0.8</sub>PO<sub>4</sub>/C/rGO electrode as a cathode. The ATO/C/rGO – LFMP/C/rGO LIB cell reveals an excellent cycling stability at 1C reaching 116 mAh g<sup>-1</sup> (based on the weight of LFMP) in the 175th cycle showing practically no capacity fading.

## 7.2 Results and Discussion

Two different strategies were evaluated for the preparation of freestanding Sb doped SnO<sub>2</sub>/carbonaceous hybrid materials. In the first approach, Sb doped SnO<sub>2</sub>/graphene oxide (ATO/GO) nanocomposites (Figure 7.8, left) were prepared in a freeze-casting approach. In the first step, a basic (pH = 9) suspension containing tin (IV) chloride, antimony (III) chloride and GO was prepared. As follows from the previous reports, tin and antimony precursors hydrolyze with the formation of different tin hydroxides including for example [Sn(H<sub>2</sub>O)<sub>6-x</sub>(OH)<sub>x</sub>]<sup>(4-x)+</sup> species. The charged hydrolyzed species can interact with the hydroxyl, carboxyl and epoxy functional surface groups of GO which are detectable by FT-IR (Figure 7.9), resulting in a homogenous deposition of the amorphous ATO precursor on the surface of GO, which transforms to the crystalline ATO.<sup>[38,39]</sup> After repeated extensive washing and centrifugation, the ATO/GO compos-

ite was treated by ultrasonication forming a homogenous suspension. The suspension was subsequently freeze-cast and freeze-dried, resulting in dark yellowish/brownish ATO/GO monoliths (Figure 7.8, left) with a diameter of around 3.5 cm. After pyrolysis at 400 °C in nitrogen, black ATO/rGO nanocomposite monoliths (Figure 7.8 middle, Figure 7.10) are obtained. Further freestanding composite electrodes were prepared via a slightly modified route including the addition of different amounts of sucrose during the ultrasonication step to yield carbon coated ATO/rGO nanocomposites (labeled as ATO/C/rGO and ATO/C-2/rGO, with C-2 indicating the double amount of sucrose added in comparison to ATO/C/rGO). The additional carbon coating is thereby expected to improve the cycling stability and rate performance of SnO<sub>2</sub>-based composite materials.<sup>[9,14,15]</sup>

The successful formation of phase-pure crystalline ATO nanoparticles inside the hybrid composites is confirmed by the XRD (Figure 7.1a). The three diffraction peaks at 26.6, 33.9 and 51.8° 2 $\theta$  can be assigned to the (110), (101) and (211) reflections of tetragonal SnO<sub>2</sub> (ICDD card No. 00-41-1445). The average crystalline domain size of the ATO nanoparticles of the ATO/GO composite is estimated to be around 1.0 nm, based on the broadening of the (211) peak evaluated by using Scherrer's equation.<sup>[23]</sup> Even after pyrolysis, only a minor domain growth with an estimated average diameter of 2.0 nm is observed. Interestingly, the addition of sucrose during ultrasonication impedes the ATO particle growth upon subsequent pyrolysis resulting in average domain sizes of only 1.7 and 1.4 nm for the ATO/C/rGO and ATO/C-2/rGO composites (Figure 7.1a and 7.11a) according to the XRD peak broadening. In case of the undoped SnO<sub>2</sub>/rGO nanocomposites, an average particle size of 2.1 nm was observed. Thermogravimetric analysis (TGA) of the hybrid materials reveals that ATO nanoparticles have a share of around 75 wt% in the freestanding ATO/rGO composite (Figure 1b). Moreover, TGA identifies that GO has been successfully reduced to rGO during the pyrolysis step at the applied temperature of 400 °C, as only one major weight loss step between 400 and 500 °C was observed in the TGA, which is attributed to the combustion of rGO under air atmosphere.<sup>[39]</sup> In comparison, ATO/GO features an additional weight loss steps at 220 °C related to the loss of oxygen containing groups on the surface of GO.<sup>[40]</sup> The weight fraction of the ATO phase in the ATO/C/rGO and ATO/C-2/rGO composites is much lower, equaling 65 and 54 wt%, respectively, due to the additional carbon coating (Figure 7.1b and 7.11b).

The successful reduction of GO is also confirmed by the results obtained from FT-IR analysis (Figure 7.9). In case of GO and the respective ATO and SnO<sub>2</sub> containing composites, a large broad peak at around 3300 cm<sup>-1</sup> is visible which can be assigned to O-H stretching vibrations of adsorbed water molecules and structural -OH groups.<sup>[41]</sup> Moreover, the peaks at 1636, 1420, 1060 and 968 cm<sup>-1</sup> are attributed to bending vibration of -OH groups, and to the vibrations of carboxyl and epoxy functional groups, respectively.<sup>[42,43]</sup> ATO/sucrose/GO composites display additionally peaks between 1200 and 860 cm<sup>-1</sup> related to sucrose. These peaks vanish or at least drastically decrease in intensity after the pyrolysis step. Additionally, two new peaks are clearly

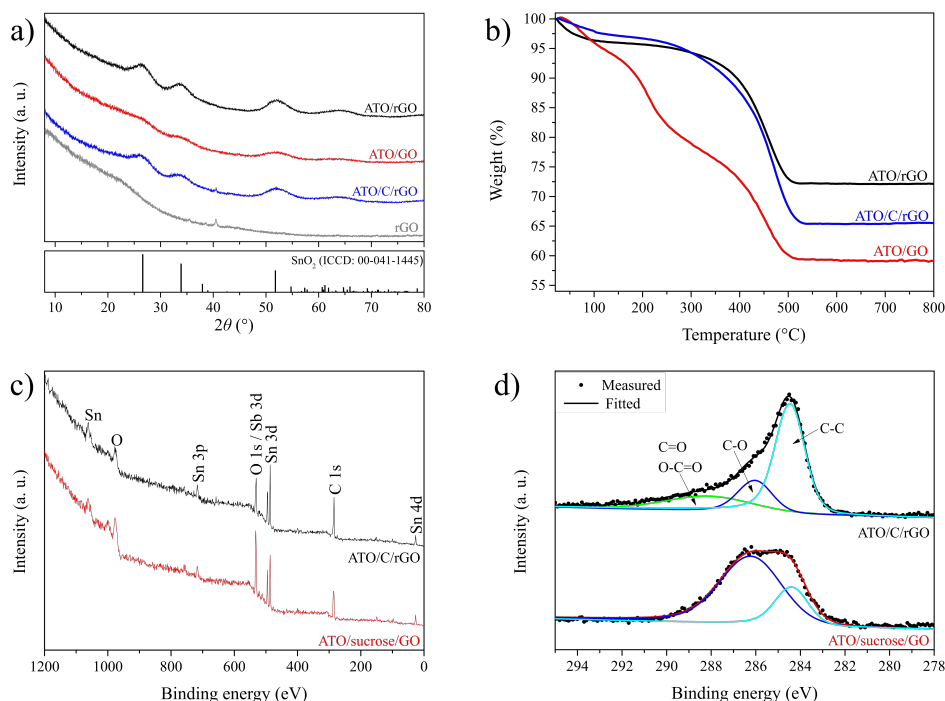


**Figure 7.1:** XRD patterns of ATO/rGO, ATO/GO, ATO/C/rGO and rGO. Bars in the box at the bottom mark the tetragonal SnO<sub>2</sub> (cassiterite) positions (ICDD card No. 00-41-1445) (a). TGA of ATO/GO, ATO/rGO and ATO/C/rGO (b). XPS survey spectra (c) and C1s region (d) of ATO/C/rGO and ATO/sucrose/GO.

visible at 1560 and 1220  $\text{cm}^{-1}$ . The former indicates a C=C stretching and skeletal vibration of the rebuild graphene structure.<sup>[39,41,44]</sup> The latter is assigned to residual epoxy groups on the surface of rGO and can be commonly found for rGO and rGO containing composite materials as reported in literature.<sup>[10,39,43,44]</sup>

ATO/sucrose/GO and ATO/C/rGO nanocomposite were also studied by X-ray photoelectron spectroscopy (XPS). The survey XPS spectra depicted in Figure 7.1c confirms the presence of C, O, Sn and Sb. Evaluation of the C 1s peak (Figure 7.1d) before (ATO/sucrose/GO) and after pyrolysis (ATO/C/rGO) reveals a severe decrease of the peak related to C-O containing groups which is a clear indication for the successful reduction of GO to rGO and the carbonization of sucrose, hence supporting the results of TGA and FT-IR analysis. The Sn 3d peak (Figure 7.13a) is composed of two peaks at 495.2 eV and 486.8 eV which can be assigned to Sn 3d<sub>3/2</sub> and Sn 3d<sub>5/2</sub>, respectively. Those binding energies are in the range typically associated with Sn<sup>4+</sup>, which additionally supports the presence of a SnO<sub>2</sub> phase.<sup>[13]</sup> Doping of tin oxide with antimony can be confirmed by XPS, as well. Antimony is mostly in the valence state Sb<sup>5+</sup> (Figure 7.13b) which indicates an enhanced electrical conductivity as Sb<sup>5+</sup> ions act as donor species; in contrast Sb<sup>3+</sup> ions are known as electron traps.<sup>[2,8]</sup>

Nitrogen sorption measurements were conducted to analyze the porosity of the free-

standing hybrid materials. As depicted in Figure 7.12, the composites display type IV isotherms with H<sub>2</sub>-type hysteresis loops, which is typical ascribed to mesoporous materials. Analysis of the pore size distribution based on DFT methods and a slit/cylindrical pore model (SnO<sub>2</sub>/rGO and ATO/rGO) or a slit pore model (ATO/C/rGO and ATO/C-2/rGO) reveals a maximum ranging between 20-50 nm, as shown in the insets of Figure 7.12 which further indicates a mesoporous structure of the hybrid materials. The total pore volume of the nanocomposites is dependent on the amount of the additionally added sucrose. The ATO/rGO showed a total pore volume of 0.156 cm<sup>3</sup> g<sup>-1</sup>, which decreased to 0.135 and 0.052 cm<sup>3</sup> g<sup>-1</sup> for ATO/C/rGO and ATO/C-2/rGO, respectively. A similar correlation is also obtained for the Brunauer-Emmett-Teller (BET) specific surface area. The nanocomposites without an additional carbon coating showed BET surface areas in the same range equaling to 179 and 163 m<sup>2</sup> g<sup>-1</sup> for SnO<sub>2</sub>/rGO and ATO/rGO, respectively. In case of the carbon-coated hybrid materials the BET surface area is significantly decreased to 60 m<sup>2</sup> g<sup>-1</sup> for ATO/C/rGO and to 21 m<sup>2</sup> g<sup>-1</sup> in case of ATO/C-2/rGO. Porosity and a large specific surface area are beneficial with regard to a high contact area between the active material and the electrolyte, enabling rapid charge transfer and hence an improved electrochemical performance.<sup>[29,39]</sup> However, large surface areas can be also disadvantageous, possibly leading to a large number of unwanted side reactions.<sup>[45]</sup> Therefore, we assume a medium surface area as exhibited by the ATO/C/rGO composite with moderate sucrose content to represent a suitable tradeoff.

The morphology of the freestanding nanocomposites was analyzed by scanning electron microscopy (SEM). The cross-sectional images of the three ATO/rGO based nanocomposites (Figure 7.2) reveal that the rGO sheets form an interconnected three-dimensional network homogeneously coated by the inorganic ATO phase. Such a spongy structure with its open channels can be very beneficial for infiltration with electrolyte throughout the composite electrode ensuring a maximized wetting and electrode electrolyte interface area shortening the Li<sup>+</sup> diffusion pathways. Moreover, the fluffy structure can also be advantageous for alleviating the volume changes of the ATO phase upon de-/lithiation.<sup>[39]</sup>

Interestingly, the addition of sucrose affects the overall morphology of the hybrid material. With increasing sucrose amount, the composite consists of more wrinkled and contracted ATO-coated rGO sheets in comparison to the rather flat rGO sheets in case of the ATO/rGO composite (Figure 7.2b, d, f). These observations also correlate with the decreasing BET surface area upon the sucrose addition. Moreover, the morphology of the ATO/rGO composites (with and without carbon coating) differs also from that of pure rGO obtained by the same freeze-casting procedure. Pure rGO monoliths feature a more crumpled-paper like structure (Figure 7.14e, f).

The homogenous distribution of ATO particles onto rGO sheets is visible in the SEM/EDX elemental maps (Figure 7.15), where Sn and Sb signals are co-localized with the C signals originating from rGO. Further evidence of a homogenous coverage of the rGO sheets by inorganic phase nanoparticles is given by a comparison of identi-

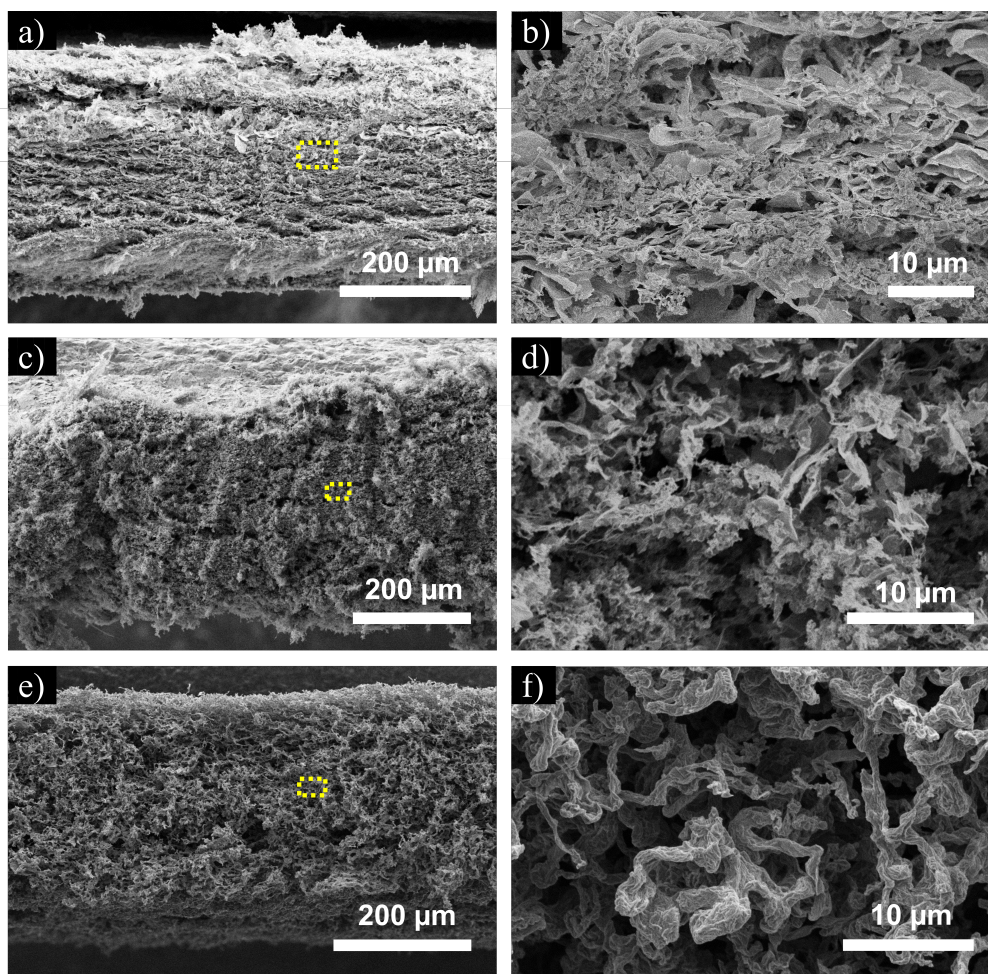


**Figure 7.2:** SEM images of cross sections (a, c, e) and magnification of the corresponding marked areas (b, d, f) of freestanding ATO/rGO (a, b), ATO/C/rGO (c, d) and ATO/C-2/rGO nanocomposites (e, f).

cal location SEM images acquired with a morphology contrast (secondary electron)-based versus an increased material contrast (back-scattered electrons)-based detector (Figure 7.16). Inorganic ATO nanoparticles thereby exhibit an increased intensity (in Figure 7.16b) compared to the underlying carbonaceous matrix due to an increased Z-contrast in the imaging mode. The Sb doping ratio inside the  $\text{SnO}_2$  particles is around 8 to 10 at% according to EDX data (Figure 7.15e).

Transmission electron microscopy (TEM) and high-resolution transmission electron microscopy (HRTEM) of the ATO/rGO, ATO/C/rGO and ATO/C-2/rGO nanocomposites (Figure 7.3a,b, d, e, 7.17 and 7.18) furthermore shows a homogenous distribution of the ATO nanoparticles on the rGO sheets. Sheets aligned perpendicular to the TEM grid are indicated by red arrows in Figure 7.3b. HRTEM of the nanoparticles in the ATO/rGO and ATO/C/rGO hybrid materials reveal their crystallinity (Figure 7.17),

with lattice spacing of approximately 0.34 nm corresponding to the (110) lattice plane of ATO. These results agree with the values obtained from the selected area electron diffraction (SAED) pattern. The patterns of all three composites show diffraction rings (Figure 7.3c, f and 7.18c), which can be assigned to the cassiterite structure of ATO (d-values: 3.4 Å(110), 2.7 Å(101) and 1.8 Å(211)) indicating the formation and random orientation of nanocrystalline ATO particles on the surface of rGO.<sup>[2,39,46]</sup> The additional ring at approximately 2.1 Å, which is detectable in all ATO/rGO based composites, can be attributed to rGO.<sup>[2,17,47]</sup> In case of the carbon coated ATO/rGO composites (ATO/C/rGO and ATO/C-2/rGO), the rings attributed to ATO are broader and less pronounced. The former is related to a smaller crystallite size with increasing carbon content, in agreement with the results obtained by XRD. The latter is related to an increasing background with increasing carbon content. Additionally, the size of ATO particles was evaluated from the TEM images depicted in Figure 7.3, 7.17 and 7.18. The resulting particle size distributions (Figure 7.19) show a similar trend in comparison to the average domain sizes calculated from XRD; the ATO particles decrease in size with increasing carbon content. The larger discrepancies between particle size (TEM) and average domain size (XRD) are observed for the carbon-coated materials probably due to the presence of carbon, which makes the determination of particle size in TEM less straightforward. In general, XRD analysis by using the Scherrer equation provides the average size of crystalline domain while TEM enables to determine the size of individual nanoparticles, but the information is less statistically representative. Particle and domain size analysis must not result in the same values. However, in total the particle sizes obtained by both methods are in a rather good agreement.

Different freestanding composites demonstrate similar electrical conductivity in the range from 2.3 to  $5.2 \times 10^1 \text{ S cm}^{-1}$  indicating a minor influence of the carbon coating on the overall conductivity. However, it cannot be excluded that the carbon coating increases the electrical conductivity locally around the ATO particles, thus improving the electrochemical performance.

In a second synthesis approach presented in this work, we have attempted to prepare ATO/carbon nanofiber (ATO/CNF) freestanding composite electrodes by electrospinning of an ethanolic spinning solution containing tin acetate, antimony acetate and polyvinyl pyrrolidone (PVP). The resulting flexible and mechanically stable mat has a size of approximately  $10 \times 25 \text{ cm}$  (Figure 7.21a) and consists of homogenous nanofibers with diameters of around 250 nm (Figure 7.21b) and a length of hundreds of micrometer and more. EDX analysis reveals a uniform distribution of Sn and Sb along the PVP nanofibers and an intended Sb amount of 10 at% in context to  $\text{Sb:SnO}_2$  (Figure 7.20). After stabilizing the composite mat in air, three very small broad bumps are observed at around  $26.6^\circ$ ,  $33.9^\circ$  and  $51.8^\circ$   $2\theta$  in the corresponding XRD pattern, which can be assigned to the (110), (101) and (211) reflections of  $\text{SnO}_2$  (ICCD card No. 00-041-1445), respectively, showing the formation of ATO.<sup>[2]</sup> In order to obtain a conductive framework, the composite has to be pyrolyzed to carbonize the PVP fibers. Different pyrolysis temperatures were tested ranging from 400 to 700 °C. Besides the diffraction

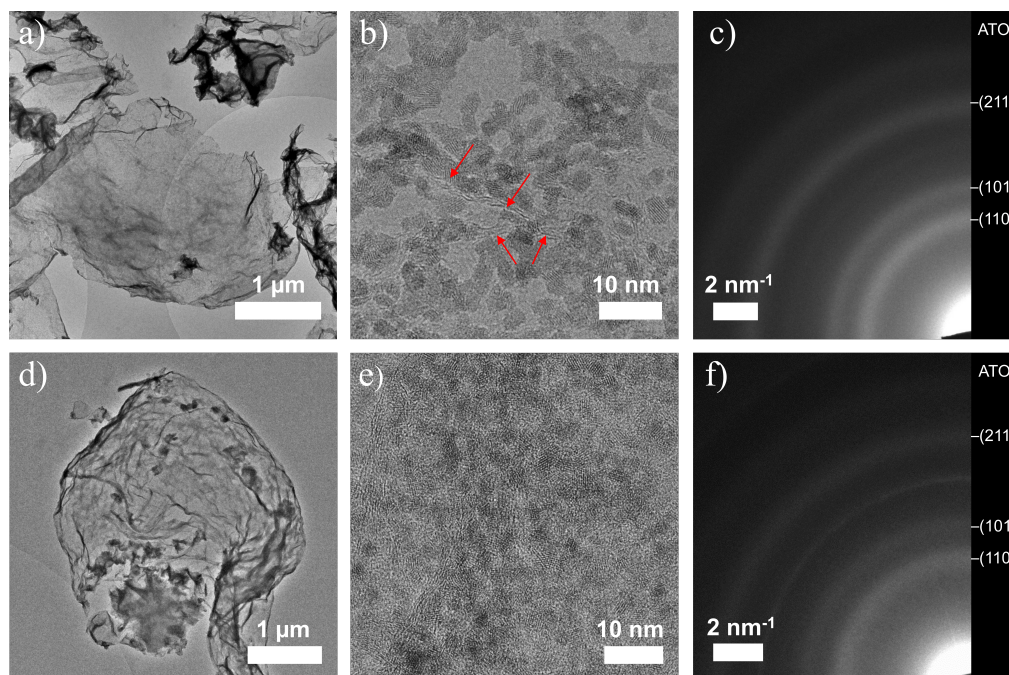


**Figure 7.3:** TEM images (a, b, d, e) and SAED patterns (c, f) of ATO/rGO (a-c) and ATO/C/rGO (d-f) nanocomposites. The red arrows in (b) mark rGO sheets aligned perpendicularly to the TEM grid. The rings in the SAED patterns (c, f) are assigned to the tetragonal structure of the ATO nanoparticles.

peaks assigned to  $\text{SnO}_2$ , additional reflections arise at a pyrolysis temperature of  $400\text{ }^\circ\text{C}$  that can be assigned to a SnSb-alloy (ICCD card No. 00-033-0118) and Sn (ICCD card No. 00-004-0673). With increasing temperature, the diffraction peaks of  $\text{SnO}_2$ , SnSb and Sn get sharper and gain in intensity, indicating an increase in crystallinity and growth of crystalline domain sizes. At a pyrolysis temperature of  $700\text{ }^\circ\text{C}$ , no diffraction peaks of the cassiterite phase (ATO) were detected, indicating a complete reduction to metallic Sn and SnSb (Figure 7.4a), most probably due to a reducing environment generated by the carbonization of PVP.<sup>[48]</sup> Chen et al. observed a similar effect with a reported reduction of a Mo: $\text{SnO}_2$ /polyacrylonitrile (PAN) composite to a Mo:Sn/CNF hybrid upon pyrolysis at  $700\text{ }^\circ\text{C}$ .<sup>[7]</sup>

Moreover, pyrolysis of the Sb: $\text{SnO}_2$ /PVP composites at different temperatures also resulted in different morphologies. After pyrolysis at  $400\text{ }^\circ\text{C}$ , the surface of the nanofibers appears to be rougher (Figure 7.4b) as compared to the non-pyrolyzed raw material (Figure 7.21b). At  $500\text{ }^\circ\text{C}$  additional small particles are visible at the surface of the nanofibers that increase drastically in size with increasing pyrolysis temperature (Figure 7.4b-e), which is furthermore in good agreement with increasingly sharp peaks visible in corresponding XRD patterns.

The SbSn/CNF composites pyrolyzed at  $400\text{--}700\text{ }^\circ\text{C}$  were analyzed by cyclic voltammetry (Figure 7.23 and 7.22a) and galvanostatic charge/discharge measurements (Fig-

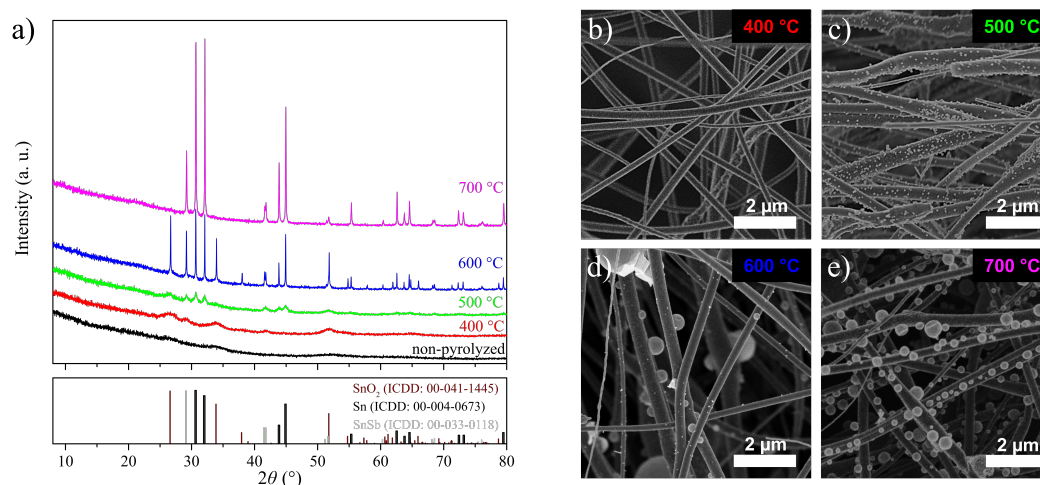


**Figure 7.4:** XRD patterns of electrospun non-pyrolyzed ATO/PVP and of the corresponding composites obtained after pyrolysis at 400, 500, 600 and 700 °C (a) and the respective SEM images (b-e).

ure 7.22b). As the composites were still maintained as paper-like mats after pyrolysis, they were used directly as freestanding electrode materials.

The results of electrochemical characterization of the SbSn/CNF composites, as discussed in the supporting information, suggest that they are not well suited for the application in LIBs. We assume that the poor performance of the composites pyrolyzed at 400 and 500 °C is due to the incomplete carbonization of PVP. The higher temperatures not only lead to a targeted carbonization of PVP but also to a non-desired reduction of ATO to Sn/Sb particles of up to several hundred nanometers in size as indicated in Figure 7.4. The particles are not embedded in the CNF fibers probably leading to an irreversible agglomeration and loss of active material upon cycling.

In contrast to the freestanding electrospun electrodes that feature low capacities and fast capacity fading, the ATO/rGO nanocomposites prepared by freeze-casting reveal a greatly improved and stable electrochemical behavior as shown in the following section. The nanocomposites were directly used as freestanding electrodes without the help of a copper foil current collector, polymeric binder or supplementary conductive additives.

In order to study the different reactions taking place during lithiation and delithiation, the freestanding ATO/rGO, ATO/C/rGO, ATO/C-2/rGO, SnO<sub>2</sub>/rGO, SnO<sub>2</sub>/C/rGO and rGO materials were analyzed using cyclic voltammetry in a potential range of 0.01 to 3.0 V vs. Li/Li<sup>+</sup> at a scan rate of 0.2 mV s<sup>-1</sup> (Figure 7.5a and 7.24).

During the first cycle a distinct cathodic peak at around 1.0 V vs. Li/Li<sup>+</sup> is observed for the ATO/C/rGO composite electrode (Figure 7.5a), which is also detectable as a voltage plateau in the respective galvanostatic discharge curves (Figure 7.5b). This feature is typical for SnO<sub>2</sub>-based compounds and corresponds to the conversion reaction of ATO nanoparticles to Sn and Sb as well as Li<sub>2</sub>O. During the first scans this process is accompanied by an irreversible formation of a solid electrolyte interface (SEI)

layer, which results in significant capacity losses during the first cycles.<sup>[2,49]</sup> Furthermore, a small shoulder at 0.5 V vs. Li/Li<sup>+</sup> and an intense peak at 0.04 V vs. Li/Li<sup>+</sup> can be observed during the first reduction scan, which correspond to the multistep alloying reactions between Sn/Sb and lithium ions with formation of Li<sub>4.4</sub>Sn and Li<sub>3</sub>Sb alloys.<sup>[2,42,50]</sup> The peaks at 0.6 and 1.3 V vs. Li/Li<sup>+</sup> observed during the reverse anodic scan correspond to the dealloying reaction and the conversion of Sn/Sb back to ATO.<sup>[42]</sup> Similar CV curves are also obtained for the SnO<sub>2</sub>/rGO, SnO<sub>2</sub>/C/rGO, ATO/rGO and ATO/C-2/rGO hybrid materials (Figure 7.24a-d).

Figure 7.5c and Figure 7.5d display the change in capacity of the ATO/rGO, ATO/C/rGO, ATO/C-2/rGO, SnO<sub>2</sub>/rGO and SnO<sub>2</sub>/C/rGO electrodes during multiple galvanostatic charge/discharge and at different rates, respectively. The charge and discharge capacities, as well as the discharging/charging current densities discussed in the following are based on the weight of the entire electrode, including the mass of ATO/SnO<sub>2</sub>, rGO and carbon coating.

The cycling measurements (Figure 7.5c) were conducted at a discharge and charge current of 1 A g<sup>-1</sup>. In the first cycle, the freestanding ATO/rGO composite reaches discharge and charge capacities of 1260 and 659 mAh g<sup>-1</sup>, respectively, corresponding to a Coulombic efficiency of 52 %. The low initial Coulombic efficiency is assigned to the formation of a SEI layer as discussed above. In the subsequent cycles stable Coulombic efficiencies approaching 100 % were obtained. The discharge and charge capacity values however slightly decrease resulting in capacities of 365 and 362 mAh g<sup>-1</sup> after 100 cycles, respectively. In case of the undoped SnO<sub>2</sub>/rGO composite, capacity fading is even more pronounced. After 100 cycles a reversible capacity of only 60 mAh g<sup>-1</sup> is retained demonstrating the benefits of antimony doping, which increases the reversibility of the conversion reaction and enhances the conductivity of SnO<sub>2</sub> particles.<sup>[2,3,37]</sup>

In case of the carbon-coated SnO<sub>2</sub>/C/rGO composite, a clear enhancement of the cycling stability can be detected when compared to SnO<sub>2</sub>/rGO. This is ascribed to the stabilization effect of the carbon coating layer. The advantage of using both carbon coating and antimony doping is demonstrated by the ATO/C/rGO composites. The ATO/C/rGO composites with a sucrose-derived carbon amount of 13 wt% demonstrated a drastically improved cycling stability as compared to the uncoated equivalent. In the first cycle, discharge and charge capacities of 1316 and 933 mAh g<sup>-1</sup> are reached, respectively, corresponding to a Coulombic efficiency of 71 %, which increases in the following cycles to almost 100 %. After 100 cycles a reversible capacity of 620 mAh g<sup>-1</sup> is retained, which is almost two times as high as in case of conventional graphite anodes. The improved stability as compared to ATO/rGO can be explained by the newly introduced carbon coating layer which is known to enhance the contact between ATO nanoparticles and rGO sheets upon cycling, thus enabling fast electron transfer, increasing the overall conductivity, stabilizing the large volume changes of the ATO particles during cycling and also preventing the Sn, Sb and SnSb nanoparticles from aggregation.<sup>[11,14,15,50,51]</sup> Moreover, comparison of the carbon-coated ATO/C/rGO and SnO<sub>2</sub>/C/rGO composites indicates that antimony doping can lead to higher reversible

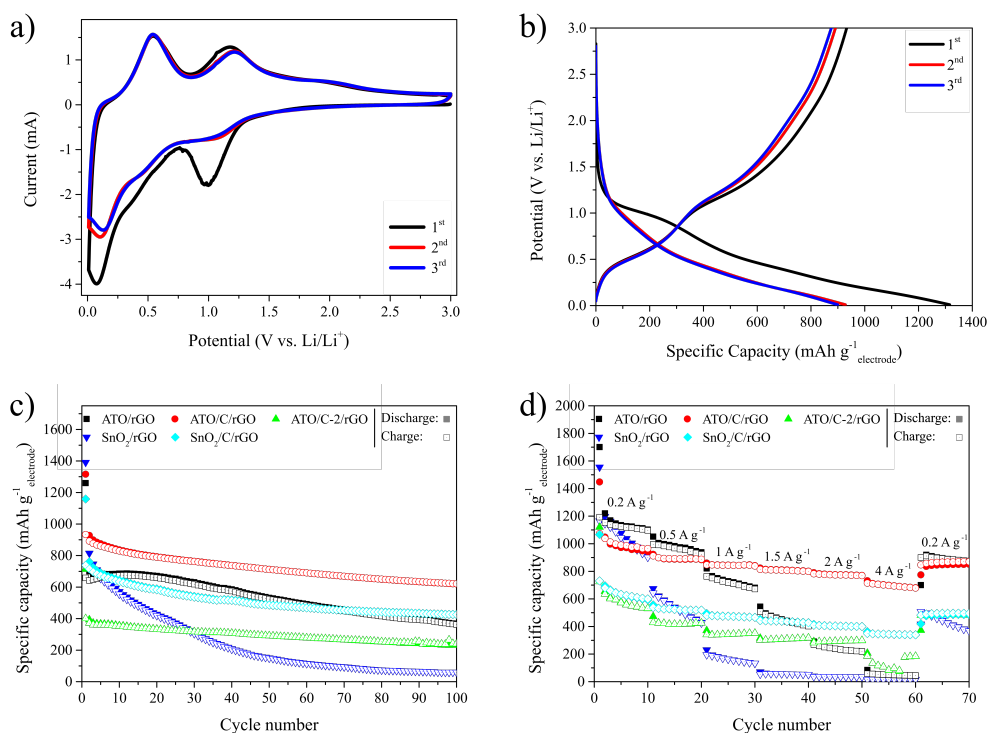


**Figure 7.5:** CV curves of freestanding ATO/C/rGO recorded in the potential range between 0.01 V and 3.0 V vs. Li/Li<sup>+</sup> at a scan rate of 0.2 mV s<sup>-1</sup> (a) and the corresponding charge/discharge curves at 1 A g<sup>-1</sup> (b). Cycling stability at 1 A g<sup>-1</sup> (c) and rate performance at current densities ranging from 0.2 to 4 A g<sup>-1</sup> (d) of freestanding ATO/rGO, ATO/C/rGO, ATO/C-2/rGO, SnO<sub>2</sub>/rGO and SnO<sub>2</sub>/C/rGO composites.

capacities which may be caused by a better conductivity inside the ATO nanoparticles and an improved reversibility of the electrochemical reactions.

ATO/C-2/rGO electrodes with an additionally increased amount of sucrose-derived carbon (28 wt%) show an even slightly better cycling stability, but significantly lower capacities as compared to the ATO/C/rGO electrodes. The charge capacities of ATO/C/rGO electrodes are 401, 360 and 242 mAh g<sup>-1</sup> in the 1st, 5th and 100th cycle, respectively. The lower capacity values of the ATO/C-2/rGO electrode are mainly attributed to the lower fraction of ATO in the electrode due to the increased amount of carbon. Moreover, the different morphologies of the ATO/rGO, ATO/C/rGO and ATO/C-2/rGO composites (Figure 7.2) can also have an impact on their respective electrochemical behavior. The crumpled structure with its slightly agglomerated rGO sheets and the lower surface area of ATO/C-2/rGO may limit the accessibility of the ATO particles, which could thereby explain a decreased capacity as compared to the bare ATO/rGO as well as to the optimized carbon coated ATO/C/rGO nanocomposite.

The cycling stability of the most promising freestanding ATO/C/rGO electrodes was additionally evaluated at a higher current density of 2 A g<sup>-1</sup>, with three preconditioning

cycles at  $0.2 \text{ A g}^{-1}$  in advance (Figure 7.25). The initial low current density cycles were conducted to assure the formation of a stable and homogenous SEI which can result in a favorable stable cycling behavior. After the preconditioning cycles, the composite reached reversible capacities of  $750 \text{ mAh g}^{-1}$ . After 1000 cycles at a high current density of  $2 \text{ A g}^{-1}$ , the freestanding ATO/C/rGO composite still maintained a reversible capacity of  $423 \text{ mAh g}^{-1}$  indicating a significant cycling stability even at high current densities.

The rate performance of the freestanding electrodes was evaluated at different charging and discharging current densities ranging between  $0.2$  and  $4 \text{ A g}^{-1}$  (Figure 7.5d). For low current densities, ATO/rGO and  $\text{SnO}_2/\text{rGO}$  demonstrate the highest specific capacities due to a larger fraction of active material as compared to the carbon coated ATO/C/rGO and ATO/C-2/rGO nanocomposites. With increasing current densities, however, the situation reverses, and the capacity of carbon-coated composites greatly outperforms that of the non-coated electrodes. The ATO/C/rGO composite reached  $991, 892, 844, 808, 774$  and  $697 \text{ mAh g}^{-1}$  (in the 5th cycle of each individual rate step) at  $0.2, 0.5, 1, 1.5, 2$  and  $4 \text{ A g}^{-1}$  respectively. When the current density was set back to  $0.2 \text{ A g}^{-1}$ , the freestanding ATO/C/rGO composite retained  $870 \text{ mAh g}^{-1}$ , corresponding to a capacity retention of  $81 \%$  compared to first cycle. The ATO/C-2/rGO demonstrated a similarly appealing rate performance, however accompanied by distinctly lower specific capacity values as compared to ATO/C/rGO which matches with the findings obtained in the cycling stability measurements. These results demonstrate both the advantage of introducing Sb as dopant and using an appropriate carbon coating layer to achieve an excellent rate performance even at a high current density of  $4 \text{ A g}^{-1}$ .

Compared with other freestanding (doped)  $\text{SnO}_2$  composites reported in the literature (see Table 7.2), a superior rate performance of the freestanding ATO/C/rGO electrode prepared by freeze-casting presented in this work can be observed. Among them, best performing freestanding  $\text{SnO}_2/\text{graphene}$  composite electrodes with  $\text{SnO}_2$  particle sizes of  $3\text{-}5 \text{ nm}$  prepared by Gao et al. exhibited a reversible capacity of  $1020$  and  $467 \text{ mAh g}^{-1}$  at  $0.2$  and  $4 \text{ A g}^{-1}$ , respectively.<sup>[10]</sup> Our best performing freestanding ATO/C/rGO nanocomposite with smaller active size nanoparticles of around  $1.7 \text{ nm}$  reached a similar specific capacity at the low current density and an almost  $50 \%$  higher value at  $4 \text{ A g}^{-1}$ . We attribute the better performance of our freestanding ATO/C/rGO nanocomposite especially to the synergistic effects between Sb doping, ultrasmall particle sizes and the utilization of a carbon coating layer.

Nyquist plots derived from electrochemical impedance spectroscopy (EIS) of  $\text{SnO}_2/\text{rGO}$ , ATO/rGO and ATO/C-2/rGO electrodes (Figure 7.26) show a semicircle in the high frequency region with a diameter corresponding to the charge transfer resistance at the electrode-electrolyte interphase. The slope in the lower frequency regime described by the Warburg impedance is thereby related to the  $\text{Li}^+$  diffusion through the electrode material.<sup>[39,42]</sup> Upon doping the charge transfer resistance decreases significantly, which is attributed to the increased conductivity inside the ATO nanoparticles.<sup>[8]</sup>

The charge transfer resistance (RCT) of carbon coated and uncoated ATO/rGO composites is very similar; the smallest resistance was however observed for the ATO/C/rGO nanocomposite indicating most favorable charge transfer kinetics. Additionally, lithium-ion diffusion coefficients ( $D_{Li^+}$ ) of the freestanding composites were calculated from EIS data using the following equations:<sup>[11,13,51]</sup>

$$Z' = R_S + R_{CT} + \sigma_W \omega^{-0.5} \quad (7.1)$$

$$D_{Li^+} = \frac{R^2 T^2}{2 A^2 n^4 F^4 C^2 \sigma_W^2} \quad (7.2)$$

where  $Z'$  is related to the real part of the impedance,  $R_S$  is the electrolyte resistance,  $R_{CT}$  represents the charge transfer resistance,  $\sigma_W$  is the Warburg impedance coefficient,  $\omega$  is the angular frequency,  $D_{Li^+}$  is the lithium-ion diffusion coefficient,  $R$  is the gas constant ( $8.314 \text{ J mol}^{-1} \text{ K}^{-1}$ ),  $T$  is the temperature (298 K),  $A$  is the surface area of the electrode (in this paper the geometrical surface area of  $2.54 \text{ cm}^2$  was used for simplicity),  $n$  is the number of electrons participating per formula unit,  $F$  is the Faraday constant ( $96485 \text{ C mol}^{-1}$ ) and  $C$  is the concentration of lithium ions in the electrode (1.15 M).

The Warburg impedance coefficient equals to the slope of the linear relationship between  $Z'$  and  $\omega^{-0.5}$  in the low frequency region depicted in Figure 7.26b. The resulting  $D_{Li^+}$  values are summarized in Table 7.1. It can be clearly seen that both doping and carbon coating are beneficial for obtaining high lithium-ion diffusion coefficients resulting in  $3.35 \times 10^{-10} \text{ cm}^2 \text{ s}^{-1}$  in case of the ATO/C/rGO. These results are also in good agreement with rate performance and cycling stability measurements.

In order to evaluate possible changes in morphology upon cycling, the Sb-doped freestanding composites ATO/rGO, ATO/C/rGO and ATO/C-2/rGO were analyzed after 100 cycles at  $1 \text{ A g}^{-1}$  (Figure 7.5c) by XRD, SEM and TEM measurements (Figure 7.6, 7.27 and 7.28). Prior to analysis the electrodes were washed with dimethylcarbonate to remove electrolyte residues. XRD analysis of the three composite reveals that the diffraction peaks associated with the  $\text{SnO}_2$  rutile structure disappear after cycling. However, in case of ATO/rGO small peaks at  $30.6^\circ$  and  $40.3^\circ$   $2\theta$  evolved which can be assigned to Sn (ICDD card No. 01-071-3772). Nevertheless, Sn and Sb are still present and highly distributed in all composites as proven by SEM/TEM-EDX measurements. Interestingly the morphology changed differently upon cycling for the coated and uncoated ATO based composites as evidenced by SEM analysis. In case of ATO/rGO larger agglomerates are visible on the surface of the rGO sheets, whereas for ATO/C/rGO a lot of small species can be detected and for ATO/C-2/rGO a more melt-like surface coverage (Figure 7.6 and Figure 7.27) can be observed. Therefore, it can be speculated that, in addition to increase in the local electronic conductivity, carbon coating confine the irreversible morphology changes accompanying the phase transformations in conversion/alloying-type electrodes, thus increasing the cycling stability of the ATO-based anodes.

Finally, the freestanding ATO/C/rGO composites were analyzed in a full cell con-

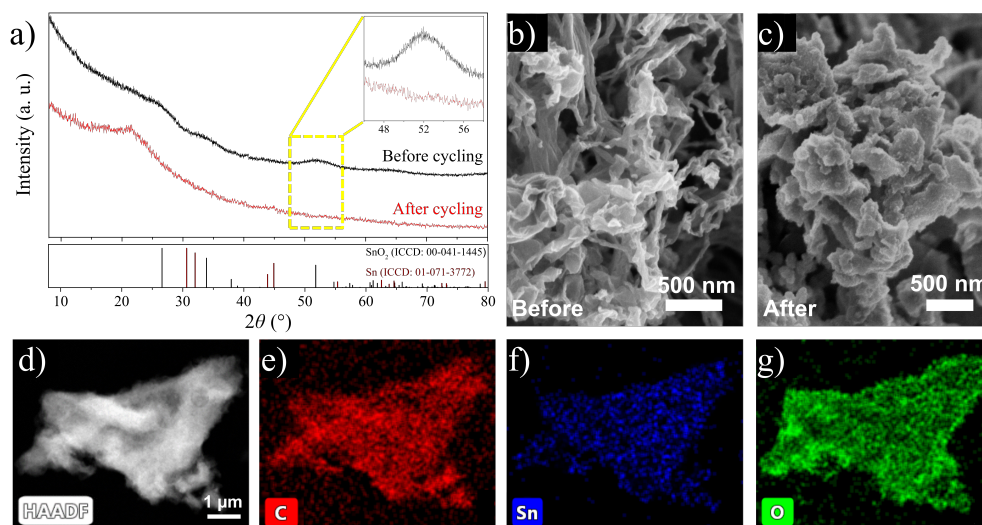


**Figure 7.6:** Ex situ analysis of ATO/C/rGO after 100 cycles at  $1 \text{ A g}^{-1}$  by XRD (a), SEM (c) in comparison to uncycled ATO/C/rGO (XRD (a) and SEM (b)). STEM image of ATO/C/rGO after cycling in HAADF mode (d) and the corresponding EDX mapping micrographs (e-g).

figuration using a high-voltage freestanding  $\text{LiFe}_{0.2}\text{Mn}_{0.8}\text{PO}_4/\text{C}/\text{rGO}$  composite as a cathode (Figure 7.7). Synthesis, characterization and half-cell performance of the freestanding LFMP/C/rGO nanocomposite can be found in our previous publication.<sup>[52]</sup> The rate performance and the cycling stability measurements of the full cells were conducted between 2.0 and 4.5 V vs.  $\text{Li}/\text{Li}^+$ . The observed capacity values are based on the mass of cathodic LFMP.

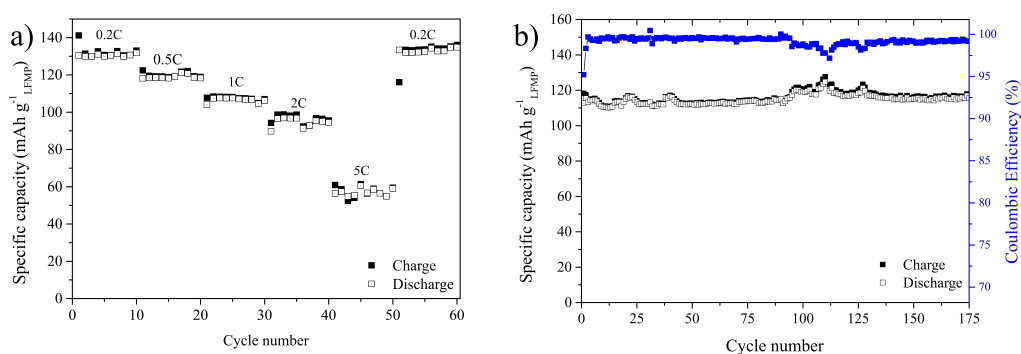


**Figure 7.7:** Rate performance (a), cycling stability (1C) and Coulombic efficiency (b) of a freestanding ATO/C/rGO – LFMP/C/rGO full cell. Performance data are based on the weight of the LFMP cathode.

The rate performance of the freestanding ATO/C/rGO–LFMP/C/rGO LIB cell was evaluated at different C-rates ranging from 0.2C to 5C ( $1\text{C} = 171 \text{ mA g}^{-1}_{\text{LFMP}}$ ). The full cell thereby reached 130, 118, 108, 98 and 61  $\text{mAh g}^{-1}_{\text{LFMP}}$  (in 5th cycle of each individ-

ual rate step) at 0.2, 0.5, 1, 2 and 5C, respectively (see also Figure 7.29). Furthermore, the cell fully retains its initial capacity when set back to 0.2C, indicating a high stability of the ATO/C/rGO and LFMP/C/rGO full cell configurations. Moreover, the rate performance measurement was also conducted in a 2-electrode configuration (Figure 7.30), instead of using a 3-electrode setup (Figure 7.7a).

Finally, the cycling stability of ATO/C/rGO–LFMP/C/rGO was analyzed at 1C. In the first cycle, charge and discharge capacities of 118 and 113 mAh g<sup>-1</sup><sub>LFMP</sub> were obtained, respectively, corresponding to a Coulombic efficiency of 95 %. In the subsequent cycles, highly stable Coulombic efficiencies of ≥99 % were reached. In the 175th cycle, the full cell delivered a discharge capacity of 116 mAh g<sup>-1</sup><sub>LFMP</sub> (Figure 7.7b), demonstrating the excellent cycling stability of the all-freestanding ATO/C/rGO–LFMP/C/rGO LIB cell.

### 7.3 Conclusion

Electrospinning and freeze-casting were tested as possible synthesis routes for the fabrication of freestanding antimony doped SnO<sub>2</sub> (ATO) based hybrid materials. ATO based freestanding composite electrodes have not been reported so far, although this material has demonstrated a very high and stable capacity in conventional electrode design with metal current collectors. Fabrication of ATO/CNFs electrodes by using electrospinning was not possible due to the high pyrolysis temperatures (above 600 °C) required for the carbonization of the PVP matrix, which is accompanied by a reduction of the oxide active material to metallic Sn and a SnSb alloy. The resulting electrodes showed therefore a low specific capacity and rapid capacity fading.

In contrast to electrospinning, freeze-casting enabled a successful fabrication of freestanding ATO electrodes. In a typical synthesis, a suspension containing hydrolyzed tin(IV) and antimony(III) chlorides and GO composites was freeze-cast and finally pyrolyzed resulting in freestanding ATO/rGO composites. Undoped SnO<sub>2</sub>/rGO and carbon coated ATO/C/rGO electrodes were prepared in a similar way in a slightly modified procedure. The ATO/C/rGO hybrid material demonstrated a superior rate performance reaching 697 mAh g<sup>-1</sup> at a high current density of 4 A g<sup>-1</sup> significantly outperforming the non-coated SnO<sub>2</sub>/rGO and ATO/rGO nanocomposites. Moreover, ATO/C/rGO demonstrated an appealing cycling stability retaining 423 mAh g<sup>-1</sup> after 1000 cycles at 2 A g<sup>-1</sup>. The distinctly improved electrochemical performance of the freestanding ATO/C/rGO composite is attributed to the synergistic effects of Sb doping, ultrasmall particle size, thin and homogenous carbon coating layer and good contact between the ATO nanoparticles and the rGO sheets, thus enhancing the electrical conductivity and stabilizing the ATO particles during the electrochemical reactions.

Finally, the freestanding ATO/C/rGO anodes were combined with freestanding Li-Fe<sub>0.2</sub>Mn<sub>0.8</sub>PO<sub>4</sub>/C/rGO composites employed as cathode to provide a freestanding full cell. The full cell exhibited an excellent cycling stability with practically no capacity decay during 175 cycles at 1C (1C = 171 mAh g<sup>-1</sup><sub>LFMP</sub>), reaching a capacity of

116 mAh g<sup>-1</sup><sub>LFMP</sub> based on the cathode mass. The full cell performance demonstrates the applicability of both ATO/C/rGO and LFMP/C/rGO freestanding electrodes also under more practical conditions. Based on the obtained results, application of free-standing ATO/C/rGO electrodes seem to be especially favorable for light-weight batteries applicable for example in small electric aerial vehicles at which the gravimetric specific capacity is more important than the volumetric energy density.

## 7.4 Experimental Section

*Materials:* All chemicals were used as-received unless otherwise noted: tin(IV) acetate (Sigma Aldrich), antimony(III) acetate (99.99 %, Sigma Aldrich), polyvinylpyrrolidone (PVP; Sigma Aldrich,  $M_w \approx 1,300,000$  by LS), tin (IV) chloride pentahydrate ( $\text{SnCl}_4 \cdot 5\text{H}_2\text{O}$ ; 99 %, Sigma Aldrich), L (+)-ascorbic acid ( $\text{C}_6\text{H}_8\text{O}_6$ , Riedel-de Haen), antimony (III) chloride ( $\text{SbCl}_3$ ; 99 %, abcr), hydrochloric acid solution (2 M, Bernd Kraft), ammonia solution (25 %, Acros), sucrose ( $\text{C}_{12}\text{H}_{22}\text{O}_{11}$ , Sigma-Aldrich), graphite microparticles (2–15  $\mu\text{m}$ , 99.9995 %, Alfa Aesar), PuriEL electrolyte (1.15 M  $\text{LiPF}_6$  in EC/EMC/DMC = 2:2:6 v/v + 1.0 %wt FEC, soulbrain MI), lithium metal (Rockwood). Sulphuric acid (98 %), phosphoric acid (85 %), potassium permanganate (99.5 %), hydrogen peroxide (30 %), barium nitrate (99.5 %) and N,N-dimethylformamide (DMF) were obtained from Penta, Czech Republic.

*Synthesis of graphene oxide suspension:* A graphene oxide suspension was synthesized according to our previous work<sup>[2,52]</sup> being a slightly modified synthesis route reported by Marcano et al.<sup>[53]</sup> 3.0 g graphite and 18.0 mg potassium permanganate were added to a cooled (below 0 °C) mixture of concentrated sulfuric acid (360 mL) and phosphoric acid (40 mL). Afterwards, the mixture was heated at 50 °C for 12 h under stirring, cooled to room temperature and finally poured on ice followed by the addition of a 30 % hydrogen peroxide (3.0 mL) solution. After the ice was molten, hydrogen peroxide (30 mL) and water (2500 mL) were subsequently added. The resulting graphene oxide was washed by repeated centrifugation and redispersion in deionized water until a negative reaction on sulfate ions with  $\text{Ba}(\text{NO}_3)_2$  was achieved. The graphene oxide slurry was ultrasonicated for 1 h to exfoliate the GO sheets. The concentration of GO in this suspension was measured to be 20.4 mg mL<sup>-1</sup> by gravimetric analysis.

*Fabrication of ATO/rGO freestanding nanocomposites by freeze-casting:* 263 mg tin(IV) chloride pentahydrate ( $\text{SnCl}_4 \cdot 5\text{H}_2\text{O}$ ; 0.75 mmol), 14 mg antimony(III) chloride ( $\text{SbCl}_3$ ; 0.061 mmol) and 30 mg ascorbic acid (1.7 mmol) were dissolved in 5 mL hydrochloric acid (HCl; 2 M). Afterwards 2 mL of the previously prepared GO suspension and 15 mL deionized water were added. The resulting suspension was stirred at room temperature for 20 min followed by the addition of ammonia solution until the pH reached 9 and another stirring period of 45 min. Afterwards, the suspension was washed by repeated centrifugation and redispersion in deionized water. Freestanding nanocomposites were obtained by dispersion of the brown composite material in 20 mL deionized water, subsequent ultrasonic treatment for 2 h and freeze-casting on

aluminum blocks, which were cooled in advance with liquid nitrogen. After removing the aluminum substrate, the frozen composite was finally freeze-dried. The resulting freestanding composites were pyrolyzed at 400 °C for 4 h in nitrogen atmosphere yielding ATO/rGO. ATO/C/rGO and ATO/C-2/rGO composites were prepared similarly except that 20 and 40 mg sucrose was added during ultrasonication, respectively.

*Fabrication of ATO/CNF freestanding nanocomposites by electrospinning:* In a typical procedure, 1.0 g tin(IV) acetate (2.8 mmol) and 0.1 g antimony(III) acetate (0.33 mmol) were dissolved in 4.5 mL ethanol for one day. A second polymer-containing solution was prepared by dissolving 0.3 g PVP in 4.5 mL ethanol. The slightly viscous electrospinning solution was obtained after dropwise addition of the acetate salt-containing solution to the polymer solution. After 1 h of vigorous stirring, the precursor solution was transferred into a syringe having a blunt stainless-steel needle, which was connected to a high voltage power supply. The spun fibers were collected on a rotating (300 rpm) stainless-steel drum collector placed at a distance of 8.5 cm to the needle tip. The electrospinning setup was operated at a voltage difference of 10.2 kV between the needle and the rotating drum collector and a precursor solution feeding rate of 10 mL h<sup>-1</sup> controlled by a syringe pump. After electrospinning the product was carefully removed from the drum collector, resulting in a mechanically stable fiber mat of approximately 8 × 20 cm in size that was dried at 80 °C for 1 h, stabilized at 250 °C for 2 h in air and finally pyrolyzed between 400 °C and 700 °C in nitrogen for 2 h.

*Battery assembly:* Electrochemical measurements were conducted on ECC-PAT-Core electrochemical test cells (EL-Cell). The analyzed freestanding composites were cut into size and used directly as working electrodes, without the addition of extra carbon black or PVDF. The freestanding ATO/rGO, ATO/C/rGO and SnO<sub>2</sub>/rGO electrodes prepared by freeze-casting had a composite mass loading of 1.6-2 mg cm<sup>-2</sup> and those prepared by electrospinning of 0.9-1.2 mg cm<sup>-2</sup>. The cells were assembled in an argon filled glove box (Labstar 1250/750, MBraun, Germany) with lithium metal foil as counter and reference electrode, glass fiber membrane (El-CELL ECC1-01-0011-A/L) as separator and a commercial electrolyte consisting of 1.15 M LiPF<sub>6</sub> in EC/EMC/DMC at a 2:2:6 vol ratio and 1.0 %wt FEC.

*Characterization methods:* Wide angle X-ray diffraction was conducted in transmission mode using a STOE STADI P diffractometer with Cu K $\alpha$ -radiation ( $\lambda = 1.54060$  ) and a Ge (111) single crystal monochromator equipped with a DECTRIS solid state strip detector MYTHEN 1K. Powder XRD patterns were measured in a  $2\theta$  range from 5° to 80° with a step size of 1° and a fixed counting time of 90 s per step.

FTIR measurements were performed on an BXII/1000 FTIR spectrometer (Perkin Elmer) equipped with an ATR unit (Smiths) in the range of 4000-550 cm<sup>-1</sup>.

TGA measurements were performed on a NETZSCH STA 440 C TG/DSC at a heating rate of 10 °C min<sup>-1</sup> in a stream of synthetic air of about 25 mL min<sup>-1</sup>.

XPS measurements were carried out using a VSW TA10 X-ray source providing Al K $\alpha$  radiation and a VSW HA100 hemispherical analyzer.

Nitrogen sorption measurements were carried out at 77 K using a QUANTACHROME

Nova Station C. Before the sorption experiments, the samples were degassed under vacuum for 12 h at 120 °C. The specific surface area was determined by the BET method in the range of  $p/p^0 = 0.05\text{--}0.2$ . Density functional theory (DFT)/Monte Carlo methods and a nonlocal density functional theory adsorption model with slit/cylindrical pores was used to calculate the pore size distribution.

SEM images were acquired with an FEI Helios NanoLab G3 UC scanning electron microscope having a field emission gun operated at 3–5 kV. EDX analysis was conducted at an operating voltage of 20 kV using an X MaxN Silicon Drift Detector with 80 mm<sup>2</sup> detector area (Oxford Instruments) and AZTec acquisition software (Oxford Instruments). The samples were suspended in ethanol and drop-coated on a silicon wafer, which was then glued onto a sample holder with silver lacquer. The freestanding composites were also measured on carbon tabs glued onto a sample holder. Cross-section samples were prepared by gluing the respective composites into a special cross-section holder.

S/TEM measurements were carried out on a FEI Titan Themis equipped with a field emission gun operated at 120 or 300 kV, a high-angle annular dark-field (HAADF) detector and a Super-X energy-dispersive X-ray spectrometer. The samples were dispersed in ethanol and drop-coated on a copper grid with a holey carbon film.

Four-point electrical conductivity measurements were carried out on an ECOPIA HMS 3000 system in Van der Pauw geometry.

Electrochemical measurements were carried out at 20 °C with ECC-PAT-Core (EL-Cell) battery test cells using an Autolab potentiostat/galvanostat (PGSTAT302N) with a FRA32M module or an Autolab Multipotentiostat M101 equipped with an 8AUT.M101 module operated with Nova 1.11 software. Cyclic voltammetry was conducted in a potential range of 3.0–0.01 V vs. Li/Li<sup>+</sup> at scan rates of 0.2 and 0.5 mV s<sup>-1</sup>. Galvanostatic charge/discharge measurements were carried out at different charging and discharging rates varying between 0.2 and 6 A g<sup>-1</sup> in a voltage window of 3.0–0.01 V. Electrochemical impedance spectroscopy (EIS) was performed on cells before the cycling test by applying a perturbation voltage of 10 mV in a frequency range of 100 kHz to 0.1 Hz.

## 7.5 References

- [1] S. Jiang, R. Huang, W. Zhu, X. Li, Y. Zhao, Z. Gao, L. Gao, J. Zhao, *Front. Chem.* **2019**, *7*, 878.
- [2] F. Zoller, K. Peters, P. M. Zehetmaier, P. Zeller, M. Döblinger, T. Bein, Z. Sofer, D. Fattakhova-Rohlfing, *Adv. Funct. Mater.* **2018**, *28*, 1706529.
- [3] F. Zoller, D. Böhm, T. Bein, D. Fattakhova-Rohlfing, *ChemSusChem* **2019**, *12*, 4140–4159.
- [4] Q. Xie, Y. Zhu, P. Zhao, Y. Zhang, S. Wu, *J. Mater. Sci.* **2018**, *53*, 9206–9216.
- [5] R. Jia, J. Yue, Q. Xia, J. Xu, X. Zhu, S. Sun, T. Zhai, H. Xia, *Energy Storage Mater.* **2018**, *13*, 303–311.

- 
- [6] B. Jiang, Y. He, B. Li, S. Zhao, S. Wang, Y.-B. He, Z. Lin, *Angew. Chem. Int. Ed.* **2017**, *56*, 1869–1872.
- [7] Y. Chen, D. Ge, J. Zhang, R. Chu, J. Zheng, C. Wu, Y. Zeng, Y. Zhang, H. Guo, *Nanoscale* **2018**, *10*, 17378–17387.
- [8] K. Peters, P. Zeller, G. Stefanic, V. Skoromets, H. Němec, P. Kužel, D. Fattakhova-Rohlfing, *Chem. Mater.* **2015**, *27*, 1090–1099.
- [9] B. Luo, T. Qiu, B. Wang, L. Hao, X. Li, A. Cao, L. Zhi, *Nanoscale* **2015**, *7*, 20380–20385.
- [10] L. Gao, G. Wu, J. Ma, T. Jiang, B. Chang, Y. Huang, S. Han, *ACS Appl. Mater. Interfaces* **2020**, *12*, 12982–12989.
- [11] X. Liu, J. Guo, T. Liu, J. Zhang, Z. Jia, C. Zhang, *Energy Storage Mater.* **2021**, *35*, 520–529.
- [12] C. Zhang, X. Peng, Z. Guo, C. Cai, Z. Chen, D. Wexler, S. Li, H. Liu, *Carbon* **2012**, *50*, 1897–1903.
- [13] Y. Dai, F. Li, Y.-X. Fu, D.-C. Mo, S.-S. Lyu, *RSC Advances* **2021**, *11*, 8521–8529.
- [14] H. Tao, S. Zhu, L. Xiong, X. Yang, L. Zhang, *ChemElectroChem* **2016**, *3*, 1063–1071.
- [15] Z. Shen, Y. Hu, Y. Chen, R. Chen, X. He, X. Zhang, H. Shao, Y. Zhang, *Electrochim. Acta* **2016**, *188*, 661–670.
- [16] C. Ma, W. Zhang, Y.-S. He, Q. Gong, H. Che, Z.-F. Ma, *Nanoscale* **2016**, *8*, 4121–4126.
- [17] J. Liang, H. Sun, Y. Xu, T. Liu, H. Wang, H. Liu, L. Guo, *Inorg. Chem. Front.* **2019**, *6*, 1367–1373.
- [18] J. Liang, H. Sun, Z. Zhao, Y. Wang, Z. Feng, J. Zhu, L. Guo, Y. Huang, X. Duan, *Science* **2019**, *19*, 728–736.
- [19] B. Wang, J. Ryu, S. Choi, G. Song, D. Hong, C. Hwang, X. Chen, B. Wang, W. Li, H.-K. Song, S. Park, R. S. Ruoff, *ACS Nano* **2018**, *12*, 1739–1746.
- [20] S. K. Park, H. K. Kim, K. C. Roh, K. B. Kim, H. S. Park, *CrystEngComm* **2016**, *18*, 6049–6054.
- [21] J. Liang, Y. Zhao, L. Guo, L. Li, *ACS Appl. Mater. Interfaces* **2012**, *4*, 5742–5748.
- [22] F. R. Bento, P. G. Corradini, L. H. Mascaro, *J. Solid State Electrochem.* **2019**, *23*, 1861–1870.
- [23] S. M. Jung, D. W. Kim, H. Y. Jung, *J. Mater. Chem. A* **2020**, *8*, 8244–8254.
- [24] S.-I. Oh, J.-C. Kim, D.-W. Kim, *Cellulose* **2019**, *26*, 2557–2571.
- [25] J. Ding, Z. Lu, M. Wu, C. Liu, Y. Yang, H. Ji, G. Yang, *Mater. Chem. Phys.* **2018**, *215*, 285–292.
- [26] J. Abe, K. Takahashi, K. Kawase, Y. Kobayashi, S. Shiratori, *ACS Appl. Nano Mater.* **2018**, *1*, 2982–2989.
-

- [27] L. Xia, S. Wang, G. Liu, L. Ding, D. Li, H. Wang, S. Qiao, *Small* **2016**, *12*, 853–859.
- [28] M. Liu, P. Xu, G. Wang, J. Yan, *J. Electron. Mater.* **2019**, *48*, 8206–8211.
- [29] X. Min, B. Sun, S. Chen, M. Fang, X. Wu, Y. Liu, A. Abdelkader, Z. Huang, T. Liu, K. Xi, R. Vasant Kumar, *Energy Storage Mater.* **2019**, *16*, 597–606.
- [30] X. Zhang, X. Huang, X. Zhang, L. Xia, B. Zhong, T. Zhang, G. Wen, *Electrochim. Acta* **2016**, *222*, 518–527.
- [31] C. Deng, Y. Liu, Z. Lu, C. Ma, T. Ge, W. Li, G. Yang, *Appl. Surf. Sci.* **2018**, *435*, 1307–1313.
- [32] Z. Wang, M. A. Fierke, A. Stein, *J. Electrochem. Soc.* **2008**, *155*, A658–A663.
- [33] H. Köse, Ş. Dombaycıoğlu, A. O. Aydın, *Int. J. Energy Res.* **2018**, *42*, 4710–4718.
- [34] X. Zhang, X. Huang, D. Liu, T. K. A. Hoang, X. Geng, P. Chen, X. Zhang, G. Wen, *Int. J. Hydrog. Energy* **2018**, *43*, 21428–21440.
- [35] P. Dou, Z. Cao, C. Wang, J. Zheng, X. Xu, *Chem. Eng. J.* **2017**, *320*, 405–415.
- [36] X. Zhao, J. Zhang, J. Zhang, C. Gong, X. Gu, Z. Ma, J. Zhou, L. Yu, Z. Zhang, *J. Power Sources* **2015**, *294*, 223–231.
- [37] Z. Xu, W. Yue, X. Yuan, X. Chen, *J. Alloys Compd.* **2019**, *795*, 168–176.
- [38] L. Li, S. He, M. Liu, C. Zhang, W. Chen, *Anal. Chem.* **2015**, *87*, 1638–1645.
- [39] D. Song, S. Wang, R. Liu, J. Jiang, Y. Jiang, S. Huang, W. Li, Z. Chen, B. Zhao, *Appl. Surf. Sci.* **2019**, *478*, 290–298.
- [40] E. A. Bondarenko, A. V. Mazanik, E. A. Streltsov, A. I. Kulak, O. V. Korolik, *Mater. Sci. Eng. B* **2015**, *202*, 61–67.
- [41] L. Liu, M. An, P. Yang, J. Zhang, *Sci. Rep.* **2015**, *5*, 9055.
- [42] L. Zhan, X. Zhou, J. Luo, X. Ning, *Ceram. Int.* **2019**, *45*, 6931–6936.
- [43] Y.-l. Dong, X.-f. Zhang, X.-l. Cheng, Y.-m. Xu, S. Gao, H. Zhao, L.-h. Huo, *RSC Adv.* **2014**, *4*, 57493–57500.
- [44] M.-S. Wang, Z.-Q. Wang, Z.-L. Yang, Y. Huang, J. Zheng, X. Li, *Electrochim. Acta* **2017**, *240*, 7–15.
- [45] N. Mahmood, Y. Hou, *Adv. Sci.* **2014**, *1*, 1400012.
- [46] M. Liu, S. Zhang, H. Dong, X. Chen, S. Gao, Y. Sun, W. Li, J. Xu, L. Chen, A. Yuan, W. Lu, *ACS Sustain. Chem. Eng.* **2019**, *7*, 4195–4203.
- [47] S. Cui, Z. Wen, E. C. Mattson, S. Mao, J. Chang, M. Weinert, C. J. Hirschmugl, M. Gajdardziska-Josifovska, J. Chen, *J. Mater. Chem. A* **2013**, *1*, 4462–4467.
- [48] J. Shin, B. Jeong, J. Kim, V. B. Nam, Y. Yoon, J. Jung, S. Hong, H. Lee, H. Eom, J. Yeo, J. Choi, D. Lee, S. H. Ko, *Adv. Mater.* **2020**, *32*, 1905527.
- [49] M. O. Guler, O. Cevher, T. Cetinkaya, U. Tocoglu, H. Akbulut, *Int. J. Energy Res.* **2014**, *38*, 487–498.

- [50] A. Birrozzi, J. Asenbauer, T. E. Ashton, A. R. Groves, D. Geiger, U. Kaiser, J. A. Darr, D. Bresser, *Batter. Supercaps* **2020**, *3*, 284–292.
- [51] L. Ao, C. Wu, X. Wang, Y. Xu, K. Jiang, L. Shang, Y. Li, J. Zhang, Z. Hu, J. Chu, *ACS Appl. Mater. Interfaces* **2020**, *12*, 20824–20837.
- [52] F. Zoller, D. Böhm, J. Luxa, M. Döblinger, Z. Sofer, D. Semenenko, T. Bein, D. Fattakhova-Rohlfing, *Mater. Today Energy* **2020**, *16*, 100416.
- [53] D. C. Marcano, D. V. Kosynkin, J. M. Berlin, A. Sinitskii, Z. Sun, A. Slesarev, L. B. Alemany, W. Lu, J. M. Tour, *ACS Nano* **2010**, *4*, 4806–4814.

## 7.6 Appendix



**Figure 7.8:** Images of the freestanding ATO/GO (brownish) and ATO/rGO (black) nanocomposites.

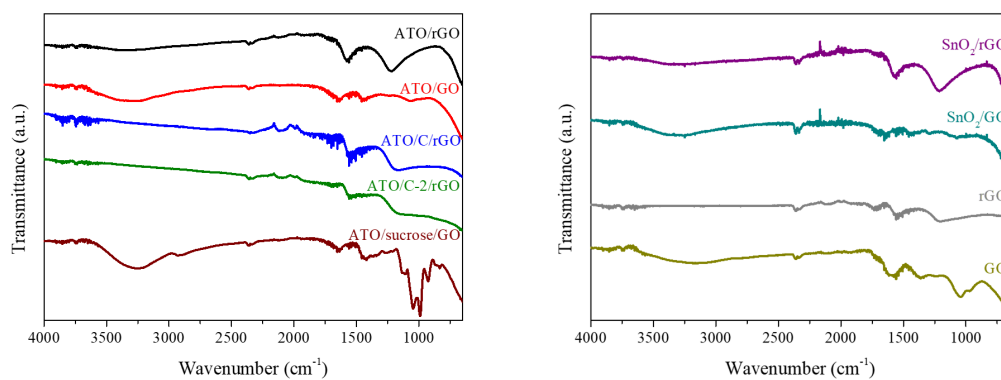


**Figure 7.9:** FT-IR spectra of ATO/GO, ATO/rGO, GO, rGO, SnO<sub>2</sub>/GO, SnO<sub>2</sub>/rGO, ATO/sucrose/GO and ATO/C/rGO freestanding composites.



**Figure 7.10:** Photograph of a freestanding ATO/C/rGO electrode showing its mechanical stability.

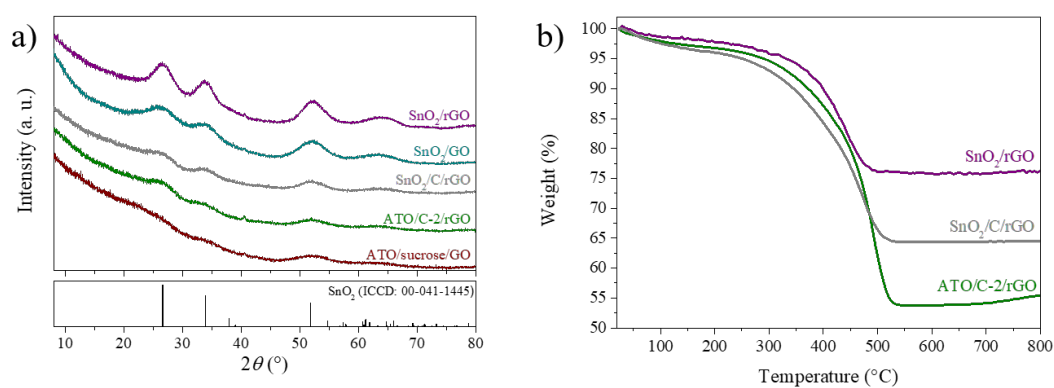


**Figure 7.11:** XRD patterns of SnO<sub>2</sub>/rGO, SnO<sub>2</sub>/GO, SnO<sub>2</sub>/C/rGO, ATO/C-2/rGO and ATO/sucrose/GO freestanding composites (a) and TGA curves of SnO<sub>2</sub>/rGO, SnO<sub>2</sub>/C/rGO, and ATO/C-2/rGO (b).

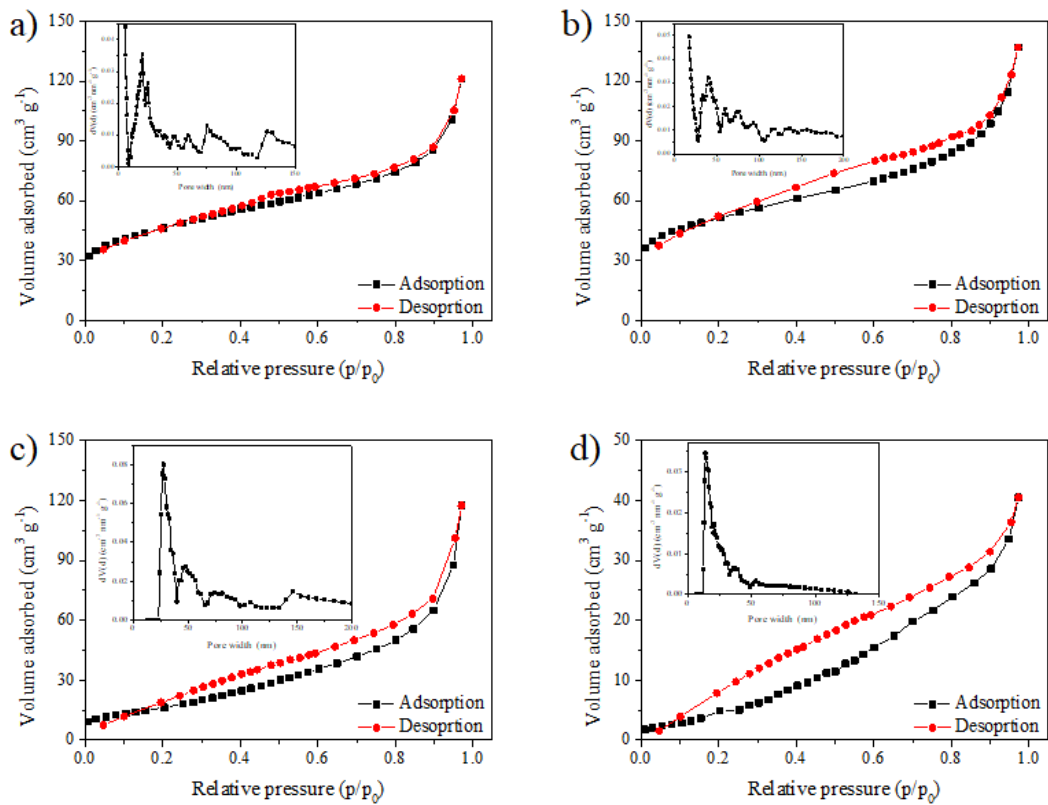


**Figure 7.12:** Nitrogen adsorption/desorption isotherms with pore size distribution curves (inset) of ATO/rGO (a), SnO<sub>2</sub>/rGO (b), ATO/C/rGO (c) and ATO/C-2/rGO nanocomposites (d).

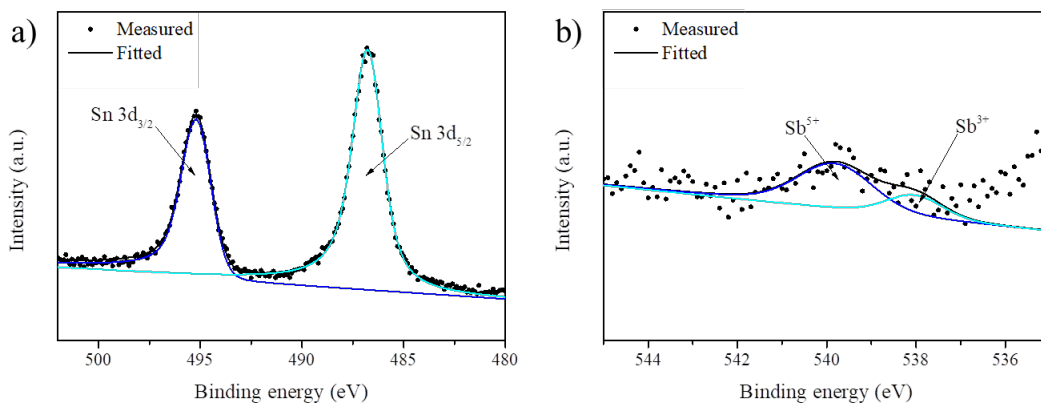


**Figure 7.13:** High-resolution XPS spectra of the Sn 3d (a) and Sb 3d (b) regions of ATO/C/rGO.

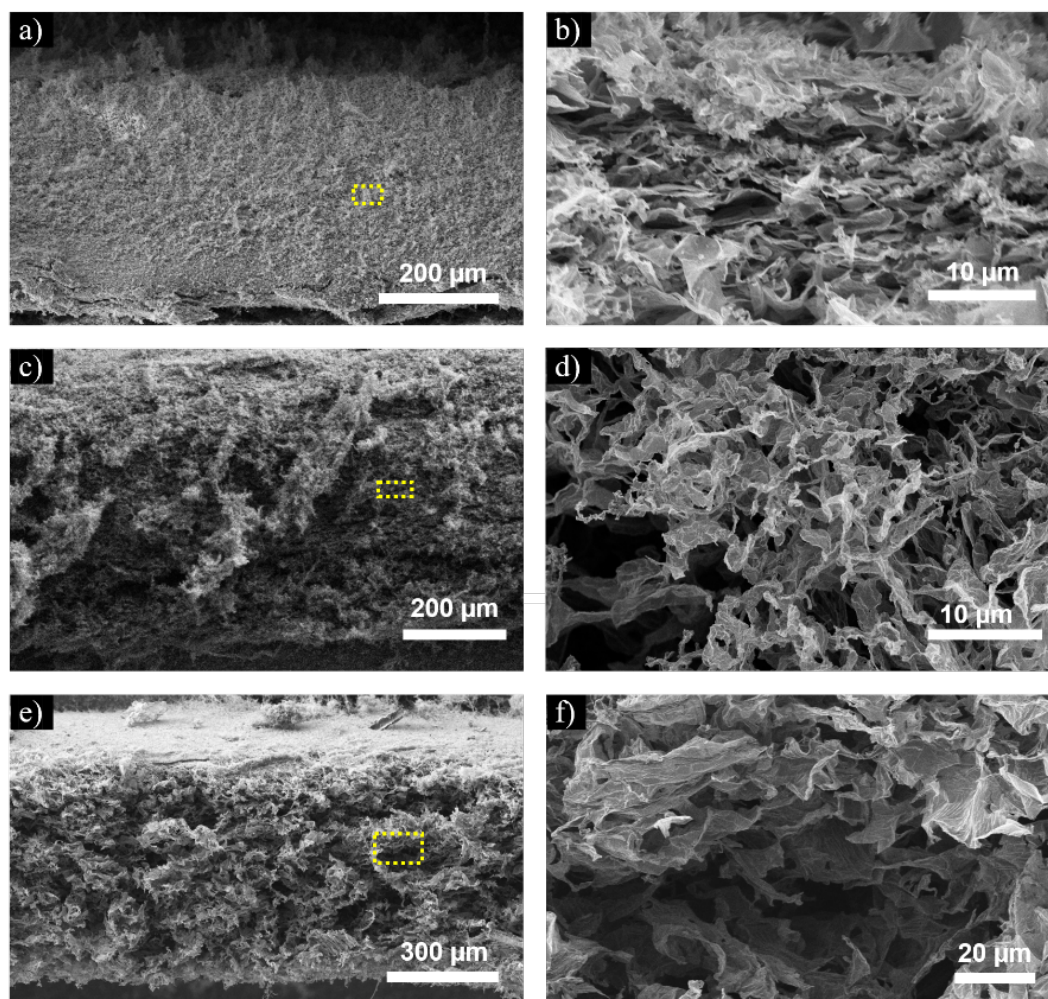


**Figure 7.14:** SEM images of cross sections (a, c, e) and magnification of the respective marked areas (b, d, f) of freestanding SnO<sub>2</sub>/rGO (a, b), SnO<sub>2</sub>/C/rGO (c, d) and rGO nanocomposites (e, f).

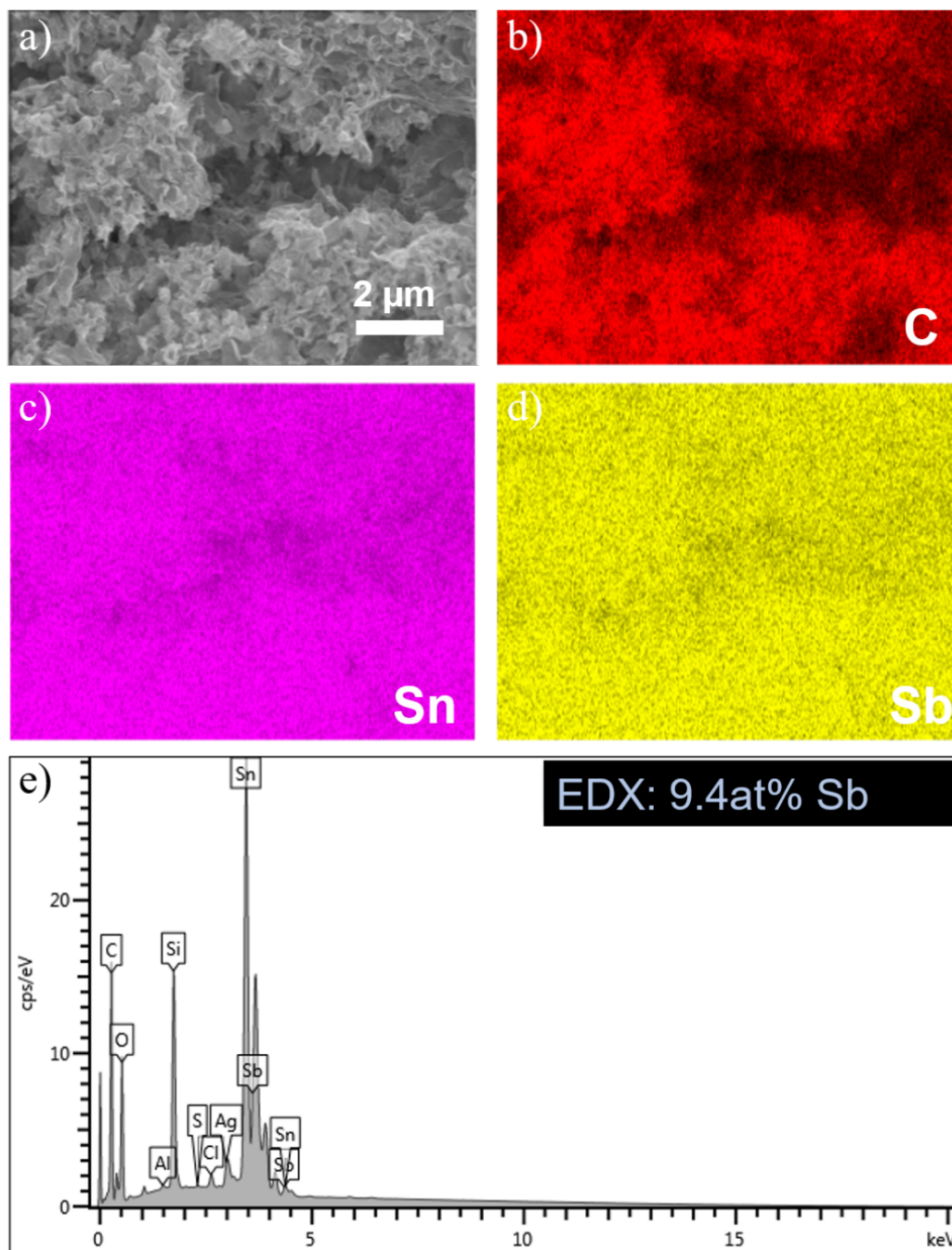


**Figure 7.15:** SEM micrograph of freestanding ATO/rGO (a) and corresponding EDX element mappings illustrating the homogenous distribution of Sn (c) and Sb (d) on rGO (b). The corresponding EDX spectrum (e) delivers a Sb doping ratio inside the SnO<sub>2</sub> particles of 9.4 at%.

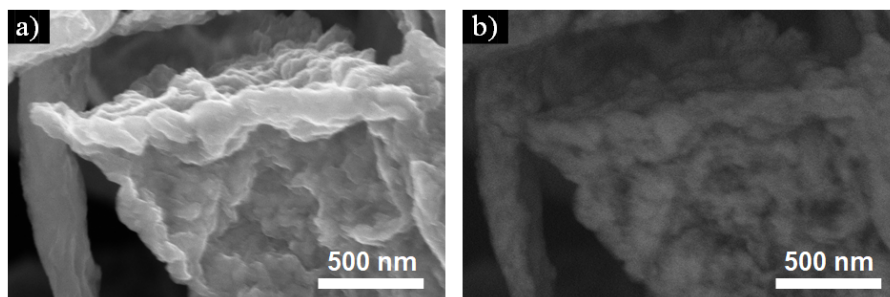


**Figure 7.16:** SEM images of freestanding ATO/C/rGO acquired with a through the lens detector (TLD) using secondary electrons (a) and a mirror detector (MD) using backscattered electrons (b).

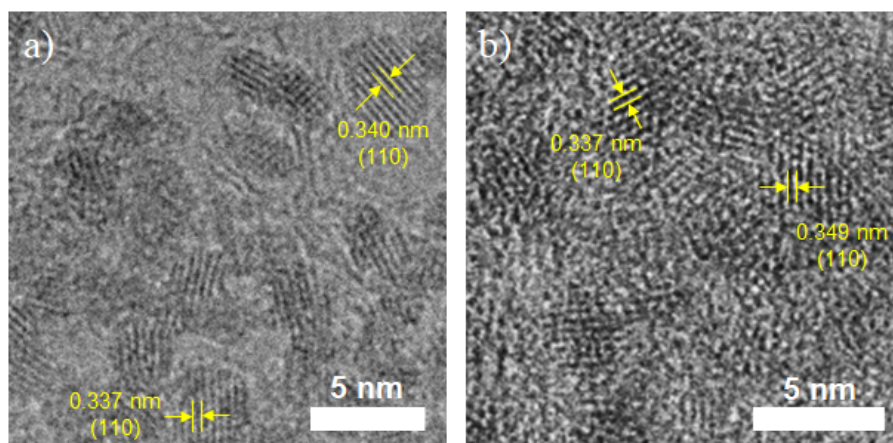


**Figure 7.17:** HRTEM images of ATO/rGO and ATO/C/rGO.

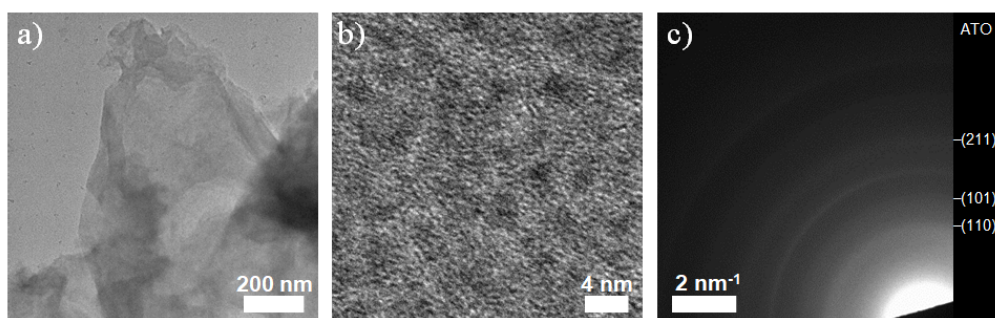


**Figure 7.18:** TEM images (a, b) and SAED pattern (c) of the ATO/C-2/rGO nanocomposite. The indexed rings in the SAED pattern (c) are assigned to the tetragonal structure of the ATO nanoparticles (cassiterite phase).

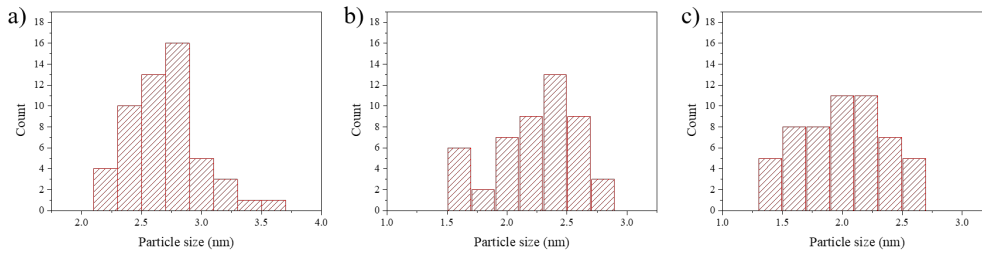


**Figure 7.19:** Particle size distribution of ATO particles in the composites ATO/rGO (a), ATO/C/rGO (b) and ATO/C-2/rGO (c). The particle size was evaluated from TEM images of the respective composites.

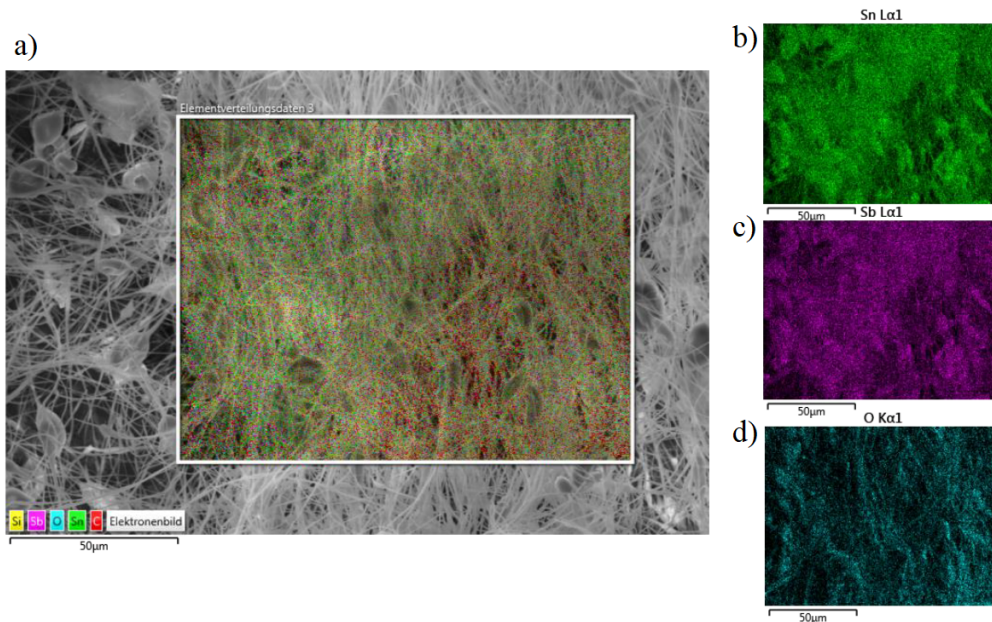


**Figure 7.20:** SEM image and EDX analysis of ATO/PVP fiber mat after stabilizing at 250 °C (a) and the corresponding EDX element mappings illustrating the homogenous distribution of Sn, Sb and O (b-d).

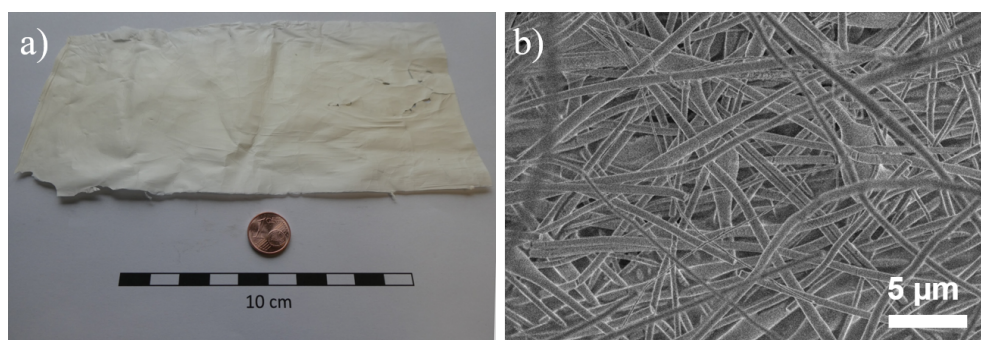


**Figure 7.21:** ATO/PVP fiber mat after stabilizing at 250 °C (a) and the corresponding SEM image (b).

### Electrochemical analysis of Sn based composites derived by electrospinning

Cyclic voltammetry measurements of the composites which were prepared by electrospinning were performed in a potential range between 0.01 and 3.0 V at a scan rate of  $0.5 \text{ mV s}^{-1}$ . Due to different composition of materials obtained at different pyrolysis temperatures, their cyclic voltammograms also differ strongly (Figure 7.23). The composite pyrolyzed at 400 °C demonstrated the worst electrochemical performance. In the first cycle, a broad reduction peak at 0.9 V can be observed, which disappears in the subsequent cycles. This peak is assigned to the formation of a solid electrolyte interphase (SEI) and the formation of amorphous  $\text{Li}_2\text{O}$  upon reduction of  $\text{SnO}_2$  to Sn.<sup>[1]</sup> The reduction current between 0.3 and 0 V can be associated with the alloying reactions forming  $\text{Li}_x\text{Sn}$  and the insertion of lithium into carbon. The corresponding  $\text{Li}_x\text{Sn}$  dealloying reactions occur at 0.6 V.<sup>[2]</sup> Interestingly, the reduction current increases during the subsequent cycles. The composite pyrolyzed at 500 °C showed similar voltammograms as the composite pyrolyzed at 400 °C, however with distinctly higher reduction and oxidation currents. Moreover, an additional small, rather broad anodic peak at 1.28 V could be observed, which corresponds to the re-oxidation of Sn to  $\text{SnO}_2$ .<sup>[3]</sup> The composites obtained after pyrolysis at 600 and 700 °C showed a greatly improved electrochemical performance as compared to the compounds obtained at lower temperatures. In the first cycle of CVs of these materials several small peaks between 0.7 and 0.4 V were visible, which were ascribed to the alloying reactions of Sn and SnSb phases formed by pyrolysis. The corresponding dealloying reactions visible as multiple peaks took place between 0.7 and 1.1 V. The individual peaks partially merged into broad peaks in the following cycles.<sup>[1-3]</sup> The rate performance of the composites pyrolyzed at 500-700 °C was analyzed at 0.2, 0.5, 1, 1.5, 2, 4 and 6  $\text{A g}^{-1}$  (Figure 7.22). Not including the 400 °C pyrolyzed sample, the composite obtained after pyrolysis at 500 °C demonstrated the worst electrochemical performance in this set with a low initial capacity and a rapid capacity fading at higher applied currents. The poor performance of this compound can be explained by an insufficient carbonization of the PVP fibers at 500 °C and, as a result, low overall conductivity. Moreover, ATO particles entrapped in the "PVP" fibers are possibly not completely accessible for lithiation

reactions. Interestingly, the specific capacity continuously increased during the first 20 cycles. Nevertheless, the observed specific capacities are still low reaching only  $200 \text{ mAh g}^{-1}$  at  $0.2 \text{ A g}^{-1}$ . In comparison, the composites pyrolyzed at  $600$  and  $700$  °C demonstrated initial capacities of  $691$  and  $602 \text{ mAh g}^{-1}$ , respectively. The higher initial capacity in case of the  $600$  °C composite is attributed to the presence of the  $\text{SnO}_2$  phase, which has a higher theoretical capacity ( $1400 \text{ mAh g}^{-1}$ )<sup>[4]</sup> as compared to metallic Sn ( $994 \text{ mAh g}^{-1}$ )<sup>[5]</sup> and Sb ( $660 \text{ mAh g}^{-1}$ ).<sup>[5]</sup> The capacity of the  $600$  °C composite however continuously decreased during the subsequent charge/discharge steps. In contrast to that, the initially lower capacity of the compound pyrolyzed at  $700$  °C increased during the charge/discharge steps at  $0.2 \text{ A g}^{-1}$ . In total, compounds pyrolyzed at  $600$  °C and  $700$  °C demonstrate similar charge/discharge performance during the prolonged cycling, showing rapid capacity fading at higher C-rates. When the charge/discharge current is set back to  $0.2 \text{ A g}^{-1}$  there is an ongoing capacity fading, resulting in a capacity of  $262 \text{ mAh g}^{-1}$  ( $600$  °C) and  $258 \text{ mAh g}^{-1}$  ( $700$  °C) in the 80th cycle equaling to a capacity retention of only 38 % and 43 % compared to the 10th cycle, respectively. Interestingly, in case of the composite pyrolyzed at  $500$  °C, the capacity is increased to  $266 \text{ mAh g}^{-1}$  in the 80th cycle indicating an activation of the composite upon cycling.

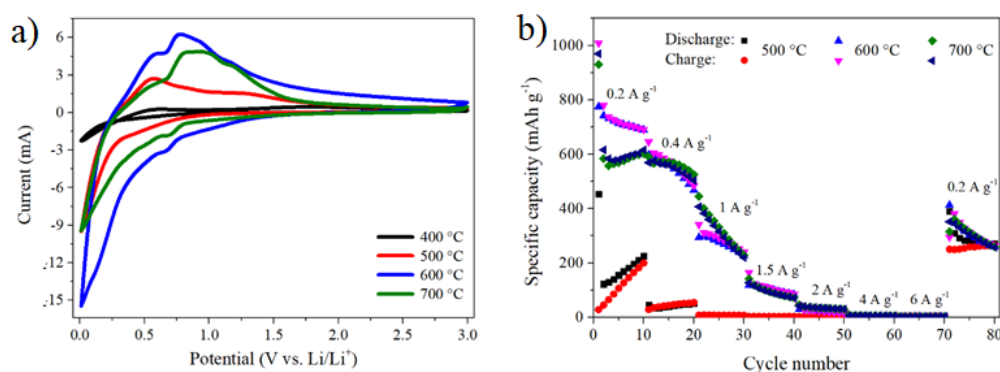


**Figure 7.22:** CV curves of electrospun Sn/Sb based composites pyrolyzed at 400, 500, 600 or 700 °C, recorded at a scan rate of  $0.2 \text{ mV s}^{-1}$  (5th cycle) (a) and their respective rate performance at charging/discharging rates varying between  $0.2$  and  $6 \text{ A g}^{-1}$  (b).

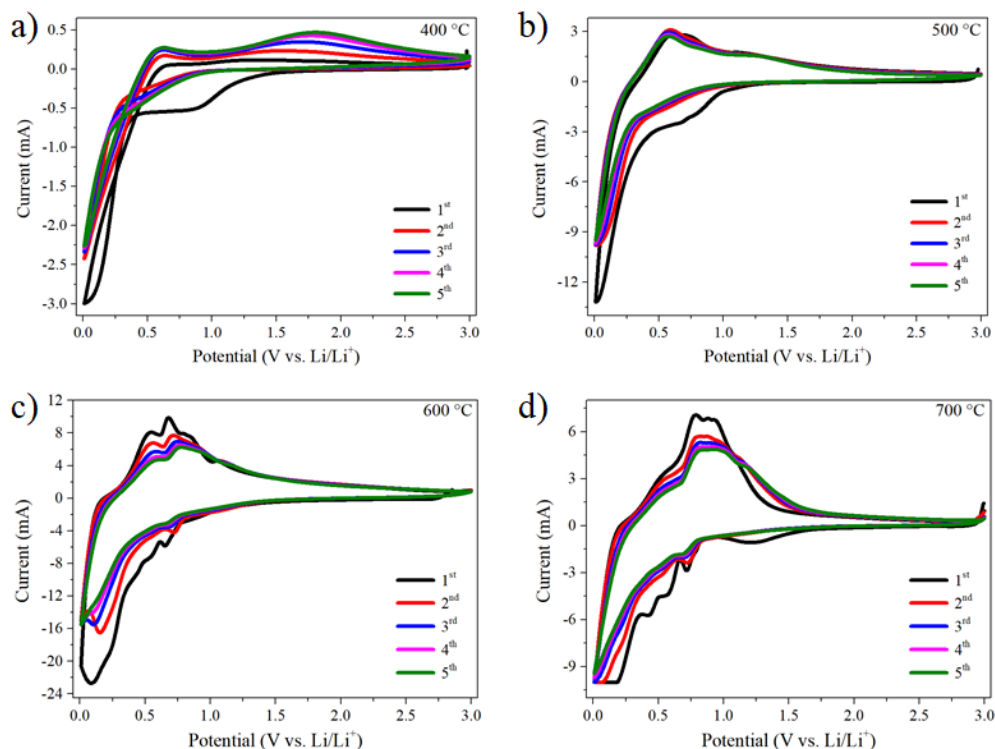


**Figure 7.23:** Cyclic voltammograms of electrospun Sn/Sb based composites obtained after pyrolysis at 400 °C (a), 500 °C (b), 600 °C (c) and 700 °C (d).

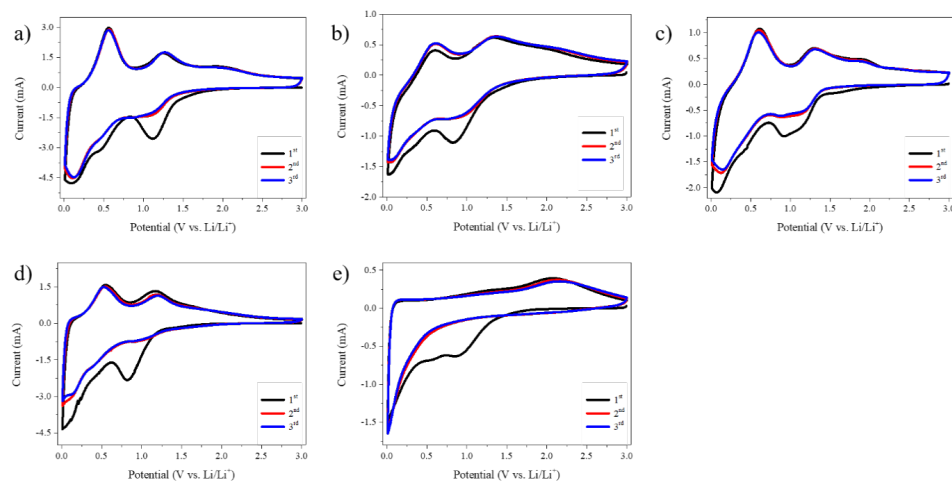


**Figure 7.24:** Cyclic voltammograms of freestanding ATO/rGO (a), ATO/C-2/rGO (b), SnO<sub>2</sub>/rGO (c), SnO<sub>2</sub>/C/rGO (d) and rGO (e), recorded each at a scan rate of 0.2 mV s<sup>-1</sup>.

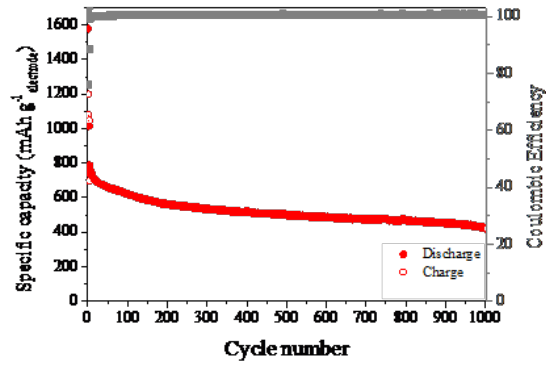


Figure 7.25: Cycling stability measurement of ATO/C/rGO at  $2 \text{ A g}^{-1}$ .

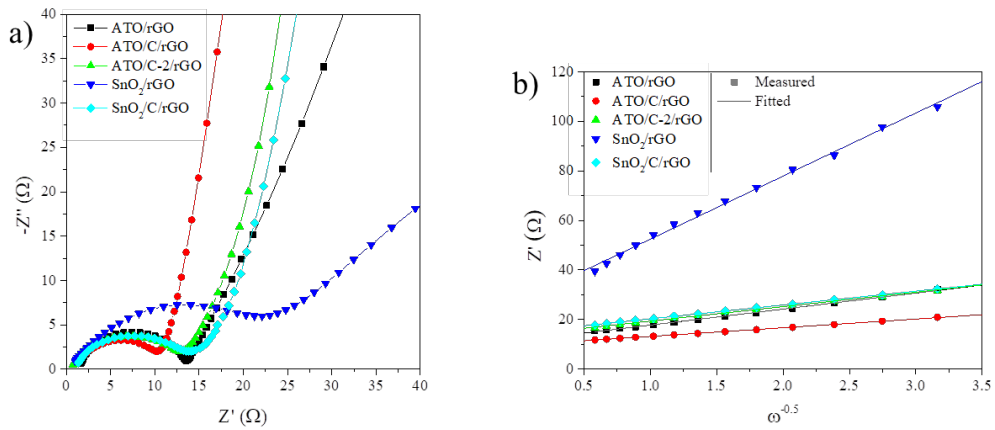
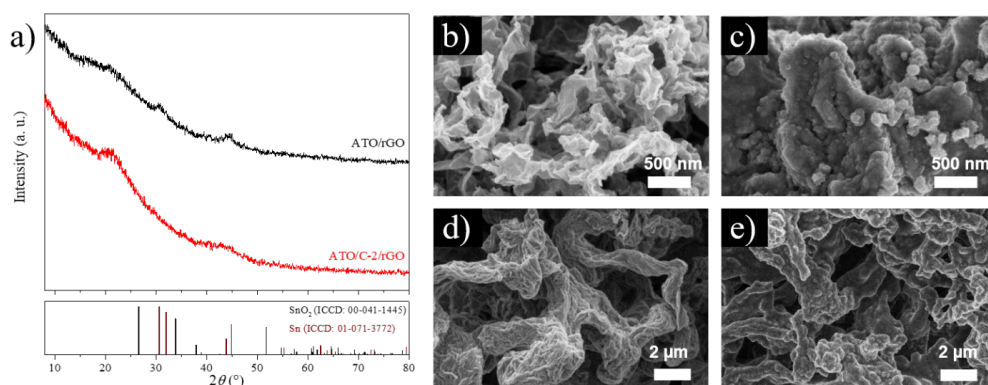


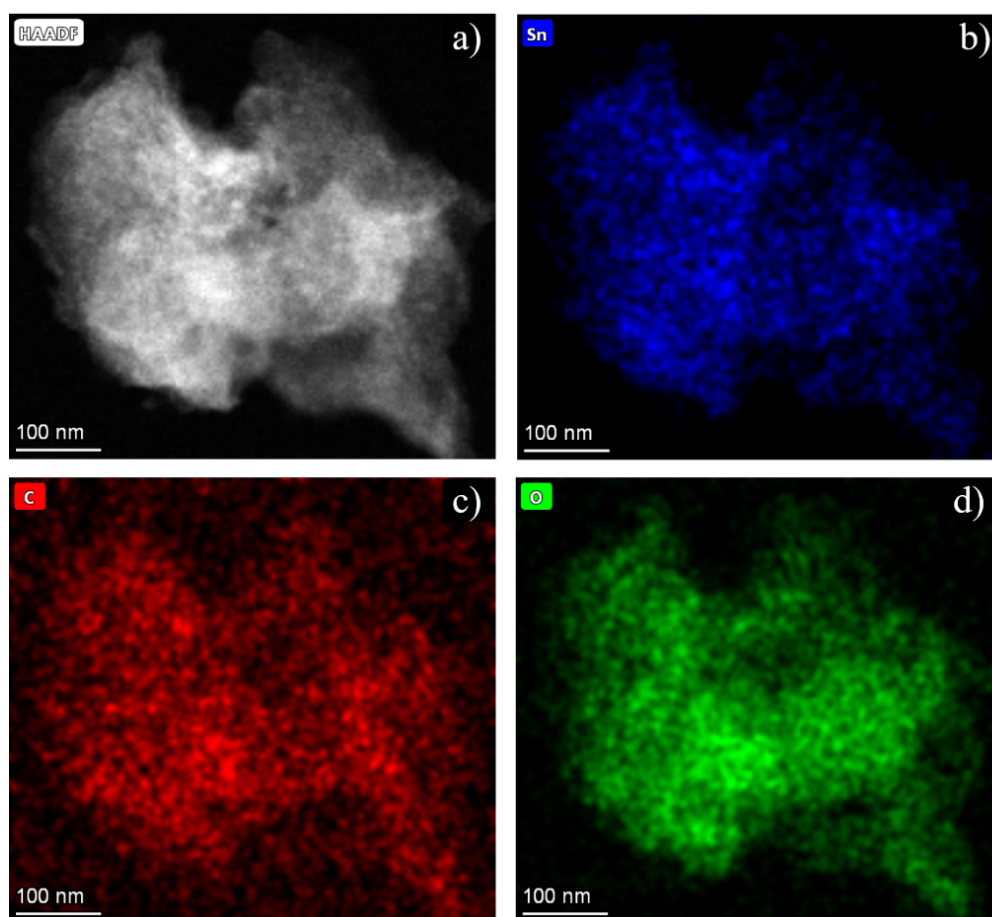
Figure 7.26: Nyquist plot of freestanding ATO/rGO, ATO/C/rGO, ATO/C-2/rGO,  $\text{SnO}_2/\text{rGO}$  and  $\text{SnO}_2/\text{C}/\text{rGO}$  nanocomposites before cycling (a) and the corresponding  $Z'$ - $\omega^{-0.5}$  plot in the low frequency range (b).

Table 7.1: Lithium-ion diffusion coefficients of freestanding tin oxide-based electrodes

Sample	Lithium diffusion coefficient $D_{\text{Li}^+}$ [ $\text{cm}^2 \text{ s}^{-1}$ ]
ATO/rGO	$9.88 \times 10^{-11}$
ATO/C/rGO	$3.35 \times 10^{-10}$
ATO/C-2/rGO	$1.22 \times 10^{-10}$
$\text{SnO}_2/\text{rGO}$	$6.37 \times 10^{-12}$
$\text{SnO}_2/\text{C}/\text{rGO}$	$1.32 \times 10^{-10}$



**Figure 7.27:** (a) XRD *ex-situ* analysis of ATO/rGO and ATO/C-2/rGO after 100 cycles at  $1 \text{ A g}^{-1}$ . SEM images of ATO/rGO (b, c) and ATO/C-2/rGO (d, e) before (b, d) and after cycling (c, e).



**Figure 7.28:** STEM image of ATO/rGO after cycling in HAADF mode (a) and the corresponding EDX mapping micrographs (c-d).

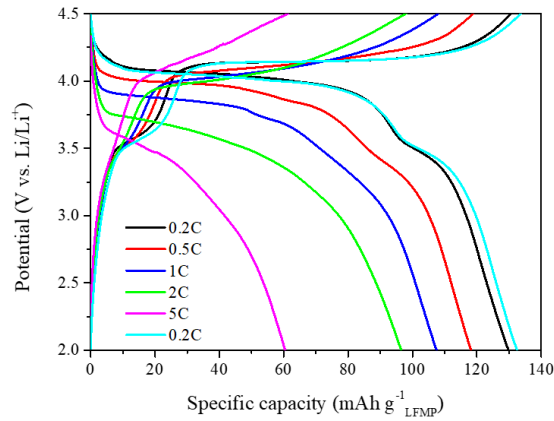


**Figure 7.29:** Charge and discharge curves of the freestanding ATO/C/rGO – LFMP/C/rGO full cell. The cell was measured in a 3-electrode configuration applying the freestanding LFMP/C/rGO electrode formally speaking as working and the ATO/C/rGO freestanding electrode as counter electrode.

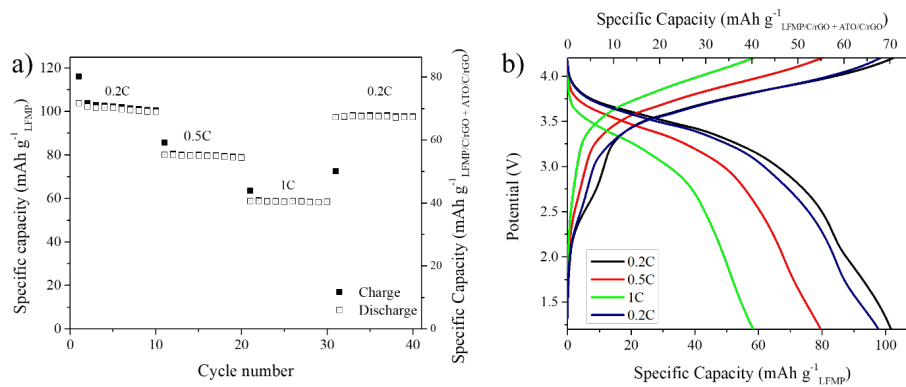


**Figure 7.30:** Rate performance of a freestanding ATO/C/rGO – LFMP/C/rGO full cell measured in a 2-electrode configuration (a) and the respective charge-discharge curves (b).

**Table 7.2:** Lithium-ion diffusion coefficients of freestanding tin oxide-based electrodes

Sample	Current density [A g <sup>-1</sup> ]	Specific capacity (cycle) [mAh g <sup>-1</sup> ]	Voltage window [V]	Mass loading	Lit.
Zn doped SnO <sub>2</sub> /rGO foam	0.1	725 (5)	0.01-2.5	2 mg cm <sup>-2</sup> (77 wt% SnO <sub>2</sub> )	[6]
	0.2	603 (15)			
	0.5	528 (25)			
	1	446 (35)			
	2	382 (45)			
	5	369 (55)			
Fe doped SnO <sub>2</sub> /graphene/cotton	0.1	516 (120)	0.001-3	2.3-2.8 mg cm <sup>-2</sup>	[7]
	0.05	582 (5)			
	0.1	506 (15)			
	0.2	418 (25)			
	0.4	289 (35)			
	0.8	162 (45)			
	0.1	485 (60)			

Co doped SnO <sub>2</sub> /graphene/cotton	0.05	638 (5)	0.001-3	n.a. (57 wt% SnO <sub>2</sub> )	[8]
	0.1	506 (15)			
	0.2	418 (25)			
	0.4	289 (35)			
	0.8	162 (45)			
SnO <sub>2</sub> QDs/graphene framework	0.1	485 (60)	0-3	2.5 mg cm <sup>-2</sup> (70 wt% SnO <sub>2</sub> )	[9]
	0.2	1020 (5)			
	0.4	≈ 870 (15)			
	0.8	≈ 820 (25)			
	1	≈ 770 (35)			
	2	≈ 650 (45)			
SnO <sub>2</sub> /N doped graphene aerogel	4	467 (55)	0.05-3	n.a. (49 wt% SnO <sub>2</sub> )	[10]
	0.2	988 (70)			
	0.1	1032 (2)			
	0.2	881 (7)			
	0.5	674 (12)			
	1	460 (17)			
SnO <sub>2</sub> /rGO	2	304 (22)	0.01-3	n.a. (70 wt% SnO <sub>2</sub> )	[11]
	0.1	998 (35)			
	0.1	1085 (3)			
	0.2	958 (9)			
	0.5	758 (15)			
ATO/C/rGO	1	480 (21)	0.01-3	1.6 mg cm <sup>-2</sup> (65 wt% Sb:SnO <sub>2</sub> )	This work
	0.1	1000 (30)			
	0.2	991 (5)			
	0.5	892 (15)			
	1	844 (25)			
	1.5	808 (35)			
	2	774 (45)			
4	697 (55)				
	0.2	870 (70)			

## References

- [1] D. C. Marcano, D. V. Kosynkin, J. M. Berlin, A. Sinitskii, Z. Sun, A. Slesarev, L. B. Alemany, W. Lu, J. M. Tour, *ACS Nano* **2010**, *4*, 4806–4814.
- [2] Y. Xu, T. Yuan, Z. Bian, J. Yang, S. Zheng, *J. Power Sources* **2020**, *453*, 227467.
- [3] C. Botas, D. Carriazo, G. Singh, T. Rojo, *J. Mater. Chem. A* **2015**, *3*, 13402–13410.
- [4] S. M. Jung, D. W. Kim, H. Y. Jung, *J. Mater. Chem. A* **2020**, *8*, 8244–8254.
- [5] R. Jia, J. Yue, Q. Xia, J. Xu, X. Zhu, S. Sun, T. Zhai, H. Xia, *Energy Storage Mater.* **2018**, *13*, 303–311.
- [6] P. Dou, Z. Cao, C. Wang, J. Zheng, X. Xu, *Chem. Eng. J.* **2017**, *320*, 405–415.
- [7] X. Zhang, X. Huang, D. Liu, T. K. A. Hoang, X. Geng, P. Chen, X. Zhang, G. Wen, *Int. J. Hydrog. Energy* **2018**, *43*, 21428–21440.
- [8] X. Zhang, X. Huang, X. Zhang, L. Xia, B. Zhong, T. Zhang, G. Wen, *Electrochim. Acta* **2016**, *222*, 518–527.
- [9] L. Gao, G. Wu, J. Ma, T. Jiang, B. Chang, Y. Huang, S. Han, *ACS Appl. Mater. Interfaces* **2020**, *12*, 12982–12989.
- [10] D. Song, S. Wang, R. Liu, J. Jiang, Y. Jiang, S. Huang, W. Li, Z. Chen, B. Zhao, *Appl. Surf. Sci.* **2019**, *478*, 290–298.
- [11] S. Jiang, R. Huang, W. Zhu, X. Li, Y. Zhao, Z. Gao, L. Gao, J. Zhao, *Front. Chem.* **2019**, *7*, 878.



# 8 Protection of Lithium Cobalt Oxide by Atomic Layer Deposition of Lithium Niobate for High-Voltage Cycling

This chapter is based on the following publication:

Sebastian Häring, Florian Zoller, Quirin Schmidt, Hannah Illner, Dina Fattakhova-Rohlfing and Thomas Bein\*, *manuscript in preparation*.

Sebastian Häring was in full charge of this project, performed all relevant material and electrode preparations, characterizations and electrochemical measurements, and wrote the complete manuscript.

## Abstract

Lithium cobalt oxide (LCO) is one of the most important cathode materials for lithium-ion batteries (LIBs). Owing to its high gravimetric energy density, LCO is expected to be used especially in portable devices in the future. By using higher cut-off potentials to increase the specific capacity further, LCO undergoes several phase transitions and thereby suffers from an insufficient long-term stability. Protective coatings applied to cathodes have been shown to overcome interface stability issues and to extend the cycle life of lithium-ion batteries. In this study we investigate the effect of amorphous lithium niobium oxide (LNO) layers with varying thickness on a 3D LCO cathode via SEM, TEM and electrochemical measurements. LCO cathodes with an optimized LNO coating thickness retained 75% of the starting capacity after 80 cycles at a cut-off potential of 4.3 V vs. Li/Li<sup>+</sup>, significantly outperforming unprotected LCO. Post-mortem analysis of long-term cycled electrodes show the beneficial effect of the LNO coating as surface degradation and structural breakup are inhibited.

## 8.1 Introduction

In the portable electronic domain, lithium-ion batteries (LIBs) have attracted a continuously increasing interest due to their high theoretical capacity and energy density.<sup>[1]</sup> Here, the focus is strongly on the volumetric energy density of LIBs rather than the gravimetric energy density due to the very finite space and the sophisticated requirements of portable devices, e.g., large screens, limited thickness and long desired standby times.<sup>[2]</sup>

Over the past 30 years, Lithium cobalt oxide, LiCoO<sub>2</sub> (LCO), has led to the unprecedented success of consumer electronics and is still the dominant cathode material due to its easy synthesis, highly compact density, high initial coulombic efficiency, excellent cycle stability, high-voltage plateau and stable charge/discharge voltage.<sup>[3-5]</sup> Used as a cathode, LCO exhibits a high theoretical specific capacity of 274 mAh g<sup>-1</sup> and a high volumetric energy density. LCO-based batteries have typically an upper voltage limit of 4.2 V vs. Li/Li<sup>+</sup> equaling a specific capacity of 137 mAh g<sup>-1</sup> and extraction of 0.5 Li per LCO. However, cycling to voltages greater than 4.2 V, causes a significant structural instability and severe capacity fading.<sup>[2,4-8]</sup>

During Li-ion extraction at voltages over 4.2 V vs. Li/Li<sup>+</sup>, LCO undergoes several phase transitions leading to surface degradation, structural damage, loss of oxygen, dissolution of Co and inhomogeneous reactions.<sup>[9,10]</sup> In order to overcome these critical problems, many different strategies have been reported aiming to promote long-term stability at high cut-off voltages, e. g. single<sup>[11-13]</sup> and mixed element doping,<sup>[14-16]</sup> morphology control,<sup>[17]</sup> post-thermal treatment<sup>[18-20]</sup> and corresponding modifications of electrolyte, separator and binder.<sup>[21-26]</sup>

Promising results have also been obtained by protecting the electrode surface using different solid lithium-ion conductive coatings, which can prevent a direct contact

between electrode and electrolyte and subsequently suppress side reactions, promote surface charge transfer, inhibit the dissolution of transition metal ions and prevent the structure from transformation and pulverization (see Scheme 8.1).<sup>[27-29]</sup> Among these surface coating methods, a great deal of attention has been paid to the atomic layer deposition (ALD) of various metal oxide coatings, including  $\text{Al}_2\text{O}_3$ ,  $\text{TiO}_2$  and  $\text{ZrO}_2$ .<sup>[30-33]</sup> ALD is based on a self-saturating gas-solid reaction, enabling conformal and uniform deposition at sub-nm thickness at elevated temperatures. These coatings significantly enhanced the cycling performance and rate capability of various cathode materials, but so far lack in ionic conductivity and thereby can result in hindered lithium-ion transport properties.<sup>[30-33]</sup>

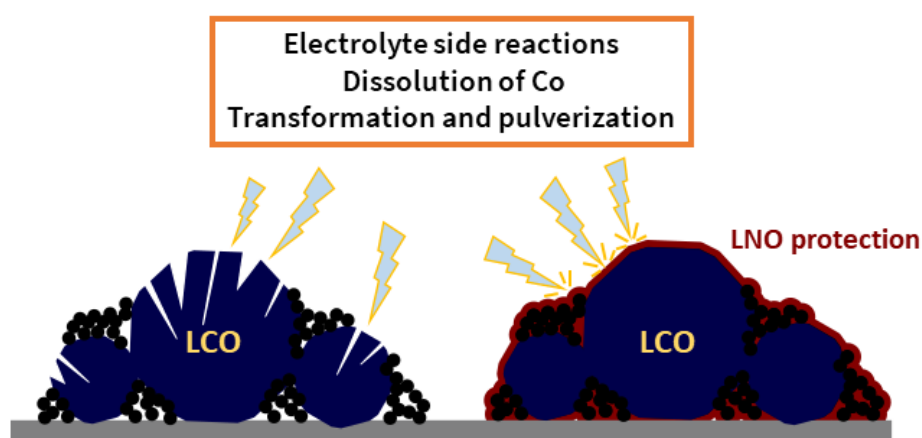


**Figure 8.1:** Schematic illustration of the protection effect of coatings against parasitic side reactions.

Lithium niobium oxide (LNO) has been proven to be a suitable candidate for the protection of different cathode materials because of its good chemical stability and high Li ion conductivity. Several different methods for coating LNO have been applied, including pulsed laser deposition,<sup>[27]</sup> sol-gel chemistry<sup>[34-36]</sup> and atomic layer deposition.<sup>[37,38]</sup> So far, only sol-gel based LNO has been used to coat LCO, demonstrating an improved performance. Controlling the uniformity and homogeneity of such protection layers is still challenging but very important for high cut-off cycling.

Herein, we have developed a ALD process to deposit lithium niobium oxide using a stop-flow protocol which enables the uniform coating of lithium cobalt oxide electrodes. After structural and morphological characterization of the protected electrodes, we have investigated the electrochemical performance and lithium diffusion characteristics dependent on the LNO film thickness. The superior stability of protected LCO has been demonstrated for more than 80 cycles at a high cut-off potential of 4.3 V vs.  $\text{Li}/\text{Li}^+$  with a charging current of  $200 \text{ mA g}^{-1}$ . Post-mortem analysis of cycled electrodes shows the beneficial effect of the LNO protective coating, keeping the cathode structure together and thereby retaining a higher specific capacity.

## 8.2 Results and Discussion

### 8.2.1 ALD of Lithium Niobate Coatings

Amorphous lithium niobate (LNO) layers were deposited at 200 °C resulting in a constant growth rate of 0.25 nm per cycle using a so-called stop-flow protocol, where the steady inert gas flow and vacuum process of the ALD was briefly interrupted, enabling diffusion of the precursor into high aspect ratio structures. To determine the appropriate ratio between  $\text{Li}_2\text{O}$  and  $\text{NbO}_x$  pulses, several different ratios of Li to Nb were prepared ranging from 1:1 up to 4:1. After heating the obtained films on silicon substrates in nitrogen atmosphere at a temperature of 550 °C, the resulting crystalline films were investigated *via* grazing incidence angle X-ray diffraction (see Figure 8.2). Only for a 3:1 ratio of Li to Nb pulses, phase-pure  $\text{LiNbO}_3$  was observed, whereas other ratios showed the presence of  $\text{Nb}_2\text{O}_5$  or did not crystallize at this elevated temperature. The XRD pattern for an 80 nm thick film of deposited  $\text{Li}_x\text{Nb}_y\text{O}_z$  is shown in Figure 8.2a before and after heating, showing phase-pure  $\text{LiNbO}_3$  for the heated sample without any side phases. The approximate crystallite size was calculated from the broadening of the (012) reflection using Scherrer's equation showing a mean size of 10 nm. The deposition of  $\text{LiNbO}_3$  reported by Østreng *et al.* was proposed to involve a so-called reservoir effect,<sup>[39]</sup> presumably caused by the lithium-containing material absorbing water during water pulses and the release of water during the metal pulses. However, no such reservoir effect was observed for the deposition recipes established here. We attribute this finding to the ALD reactor architecture, where the vacuum does not need to be interrupted between two different ALD processes because of an integrated antechamber.

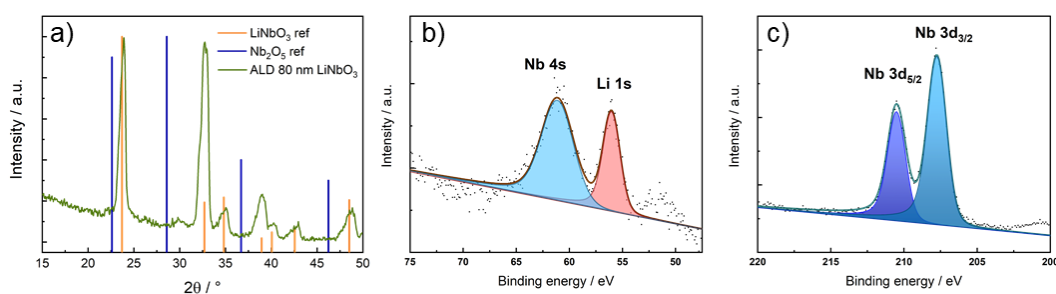


**Figure 8.2:** XRD pattern of 80 nm lithium niobate deposited on quartz and calcined at a temperature of 550 °C (a). Magnification of the Nb 4s, Li 1s (b) and Nb 3d<sub>3/2</sub>, Nb 3d<sub>5/2</sub> energy regions. The fit components in (b) and (c) are shown as colored areas.

We chose to use the oversaturated ratio of Li to Nb of 3:1 for the protection of LCO due to the crystallization to phase-pure  $\text{LiNbO}_3$  (while Wang *et al.* reported that ALD deposited lithium deficient  $\text{LiNbO}_3$  showed the highest conductivity).<sup>[37]</sup> The elemental composition of the as-deposited layers was studied using X-ray photoelectron spectroscopy (XPS). The survey XPS spectrum is provided in Figure 8.9, showing signals

for Li, Nb, O and small carbon impurities. These carbon impurities may result from the deposition procedure, typical environmental impurities in the instrument and the carbonization of LiOH surface layers into  $\text{Li}_2\text{CO}_3$  as already reported by Østreng *et al.*<sup>[39]</sup> The peak positions for Nb can be found at energy levels of 210.4 eV and 207.7 eV for the Nb  $3d_{5/2}$  and Nb  $3d_{3/2}$  states (see Figure 8.2b and c) confirming the presence of  $\text{Nb}^{5+}$  and showing positions typical for Nb surrounded by O.<sup>[40–42]</sup> Only one sharp and symmetric peak can be detected at 56.0 eV for Li 1s, revealing a single chemical state of  $\text{Li}^+$ . The peak at higher binding energy belongs to Nb 4s. By comparison of the Li and Nb peak areas, an approximate 2.75:1 ratio of Li to Nb can be verified, which is in good agreement with deposited pulse ratio.

### 8.2.2 Characterization of LNO-coated LCO

After adjustment of the LNO ALD process, four different cycle numbers were chosen to find the optimum thickness for protection of the lithium cobalt oxide cathodes. LCO based electrodes were prepared using a thin film applicator resulting in a loading of  $7.8 \text{ mg cm}^{-2}$ . A scanning electron microscopy (SEM) image of the unprotected LCO electrode shows that the LCO crystals are embedded in a three-dimensional carbon black matrix. Due to the high surface area of the electrodes (consuming more precursor) and in order to ensure a homogeneous coverage by LNO during the ALD process, only LCO coated foils with an approximate area of  $20 \text{ cm}^2$  were used for deposition. After deposition of different cycles numbers of LNO, no macroscopic changes are visible in the SEM overview pictures (Figure 8.3a-d). In the high magnification images a thin layer of LNO can be observed for LCO-25 and LCO-40, corresponding to a theoretical thickness of 6 nm and 10 nm, respectively. EDX measurements show an increased niobium content with increasing LNO cycle number as the amount of deposited niobium is increased. However, EDX measurements using SEM can only deliver semi-quantitative results as the LCO electrodes are varying slightly in overall film thickness, LCO distribution and morphology (Figures 8.10-8.14).

As shown in Figure 8.4, the XRD pattern of the freshly prepared LCO electrodes exhibits the expected diffraction peaks corresponding to rhombohedral  $\text{LiCoO}_2$  with the space group  $R\bar{3}m$  (PDF 01-070-2685). The marked reflections at  $38^\circ$  and  $44^\circ$   $2\theta$  correspond to the underlying Al foil current collector. The diffraction pattern of LCO-25 is similar to the XRD pattern of LCO-0, indicating no significant change in crystal structure of the LCO cathode or formation of alternate LCO phases during the LNO deposition at  $200^\circ\text{C}$ . The absence of further diffraction peaks or other features of LNO is due to its amorphous character and the ultra-low thickness of the deposited protective layer.

For detailed insight into the growth of LNO, lamellae of LCO-40 crystallites were prepared via the FIB technique in order to enable transmission electron microscopy imaging of the protective layer. An HAADF-STEM image of a complete LCO particle together with EDX elemental distribution maps of the marked area is shown in Figure 8.15. Nb can be found on the surface of the LCO particle showing a continuous

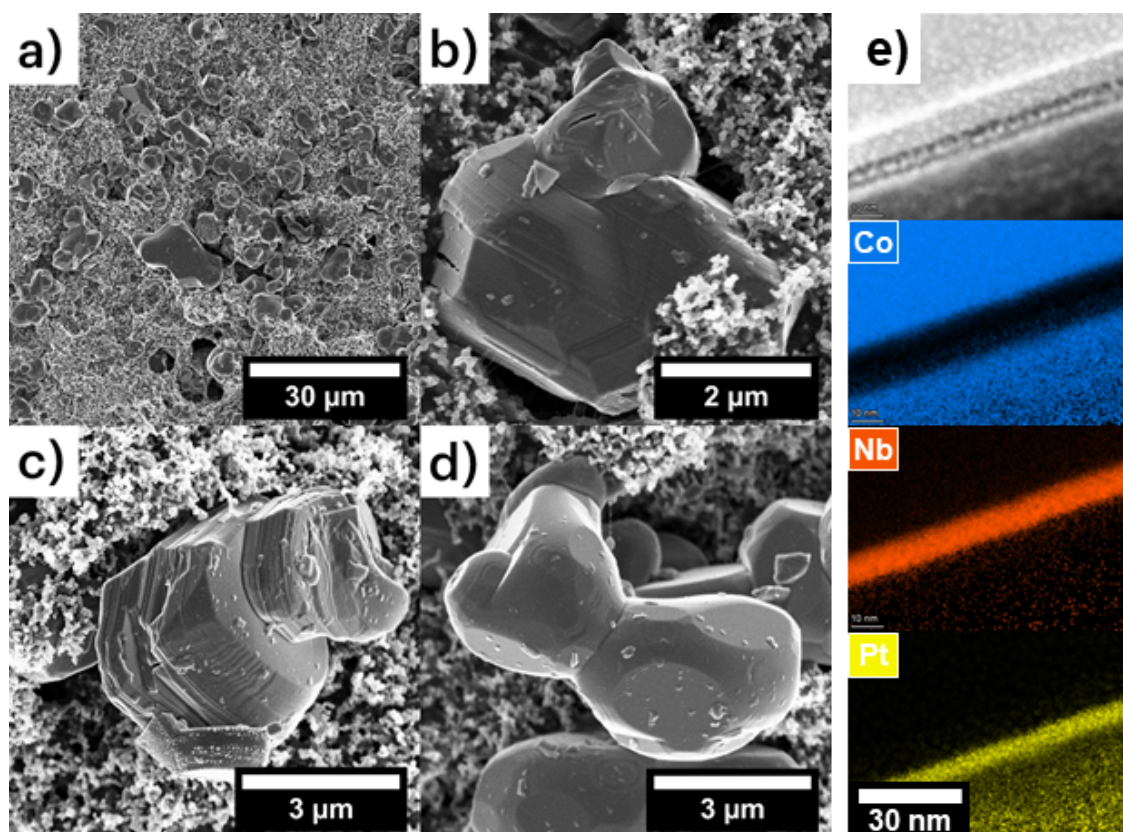


**Figure 8.3:** SEM images of LCO-0 electrodes in different magnifications (a) and b). High resolution images of LCO crystallites covered with 25 and 40 cycles of LNO, respectively (c) and d). HAADF-STEM image and the corresponding EDX distribution maps (e) of a single LCO crystallite with 40 cycles of LNO.

and homogeneous distribution. Note that due to the spherical form of the LCO crystallite, the surface edge is not perfectly perpendicular to the electron beam, thereby showing a broadened signal for the surface LNO layer. The LNO film thickness can be estimated from the on-edge tilted HAADF-STEM image and the corresponding EDX maps (see Figure 8.3e). The measured thickness of around 10 nm for the Nb signal fits very well with values from spectroscopic ellipsometry on Si substrates, implying a similar growth and resulting thickness on both oxidic surfaces.

### 8.2.3 Electrochemical Characterization

Figure 8.5a-e compares the CV profiles of LCO-0, LCO-5, LCO-15, LCO-25 and LCO-40 in the 1st, 2nd and 5th scans cycled between 3.0 and 4.3 V (vs. Li/Li<sup>+</sup>), obtained by scanning at a sweep rate of 0.2 mV s<sup>-1</sup>. For uncoated LCO-0 three pairs of current peaks corresponding to the oxidation and reduction reactions in LCO can be observed. The first pair of redox peaks at 4.08/3.84 V can be attributed to the oxidation of Co<sup>3+</sup> to Co<sup>4+</sup> for the first-order phase transformation (Li<sup>+</sup> extraction/insertion out of and

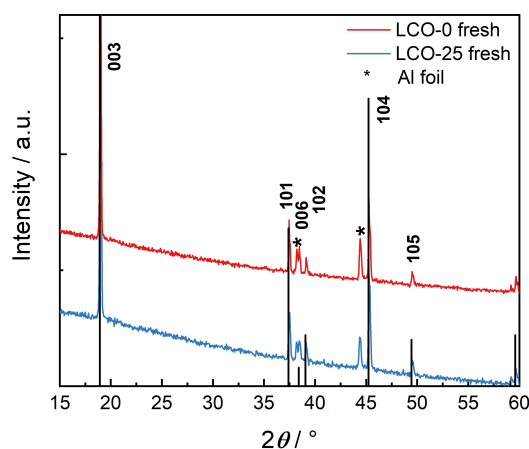


**Figure 8.4:** XRD pattern of freshly prepared LCO-0 (red) and LCO-25 (blue) electrodes. Marked reflections correspond to the underlying Al current collector foil.

into the  $\text{LiCoO}_2$  cathode) between H1 to H2 hexagonal phases.<sup>[43]</sup> The additional redox peaks at 4.15/4.00 V and at 4.22/4.14 V result from the order-disorder transformation between hexagonal and monoclinic phases.<sup>[44,45]</sup>

As shown by Li *et al.*, direct deposition of metal oxide coatings *via* ALD is beneficial compared to prior deposition on the powdered active material, as the contacting area between  $\text{LiCoO}_2$  and carbon black as the conductive agent is wrapped up by the protective layers.<sup>[32]</sup> Consequently, lithium diffusion and electron transport pathways are maintained and not blocked by the metal oxide coating.

For LNO-coated LCO electrodes with varying ALD cycle numbers, a shift in both oxidation and reduction peaks can be observed, resulting in a larger difference between cathodic and anodic peaks for thicker coatings obtained with larger cycle numbers (positions are summarized in Table 8.1). With increasing ALD cycle numbers, the cathodes exhibit a greater peak separation, leading to the conclusion that a high degree of electrochemical polarization occurs due to the low electrical conductivity of the thicker LNO coatings. However, LCO-5 still shows the typical redox features of unprotected LCO (with an increased peak separation), indicating that an optimized thickness of LNO is required to achieve an enhanced cyclic performance for the LCO cathodes.

In order to examine the influence of the LNO coating layer thickness on the lithium diffusion mechanism, CV measurements at different scan rates (0.1, 0.2, 0.5, 0.8, 1.0, 1.5 and  $2.0 \text{ mV s}^{-1}$ ) were carried out. A clear shift of the oxidation and reduction peaks to higher and lower potentials with increasing scan rate can be observed, resulting from increasing high electrochemical polarization. The apparent lithium-ion diffusion rates can be estimated by linear fitting of the peak current ( $i_p$ ) vs. the square root of the scan rate ( $v_{1/2}$ ) for the H1 to H2 phase transition in the voltammograms which are shown Figure 8.16a-e, respectively. According to the Randles-Sevcik equation (equation 8.1)

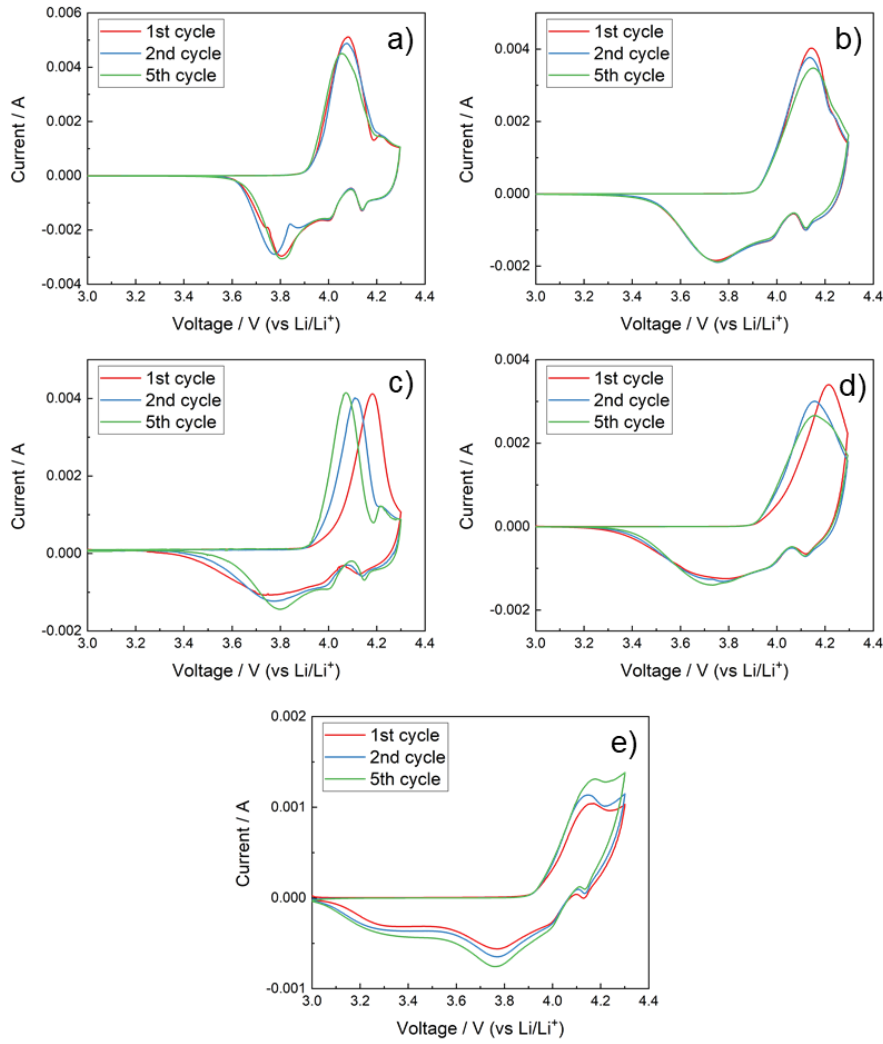


**Figure 8.5:** Cyclic voltammograms of (a) LCO-0, (b) LCO-5, (c) LCO-15, (d) LCO-25 and (e) LCO-40.

the peak current can be expressed by a function of the square root of the scan rate:

$$i_p = 2.69 \cdot 10^5 \cdot n^{3/2} \cdot A \cdot \nu^{1/2} \cdot D_{Li}^{1/2} \cdot C_{Li} \quad (8.1)$$

Where  $n$  is the number of electrons in the specific electrochemical reaction;  $A$  is the electrode area ( $\text{cm}^2$ );  $D_{Li}$  is the chemical diffusion coefficient and  $C_{Li}$  is the bulk concentration of the lithium ions in LCO ( $\text{mol cm}^{-3}$ ). With the knowledge of the common parameters assuming  $n = 1$  and  $C_{Li} = 0.013 \text{ mol cm}^{-3}$  for the anodic and cathodic peaks, the chemical diffusion coefficients of Li can be determined and are shown in Figure 8.6f and Table 8.2.<sup>[46]</sup> A clear drop from  $\approx 3 \times 10^{-9} \text{ cm}^2 \text{ s}^{-1}$  and a stabilization of the lithium diffusion coefficient (in the cathode) to  $\approx 2 \times 10^{-10} \text{ cm}^2 \text{ s}^{-1}$  can be observed, indicating

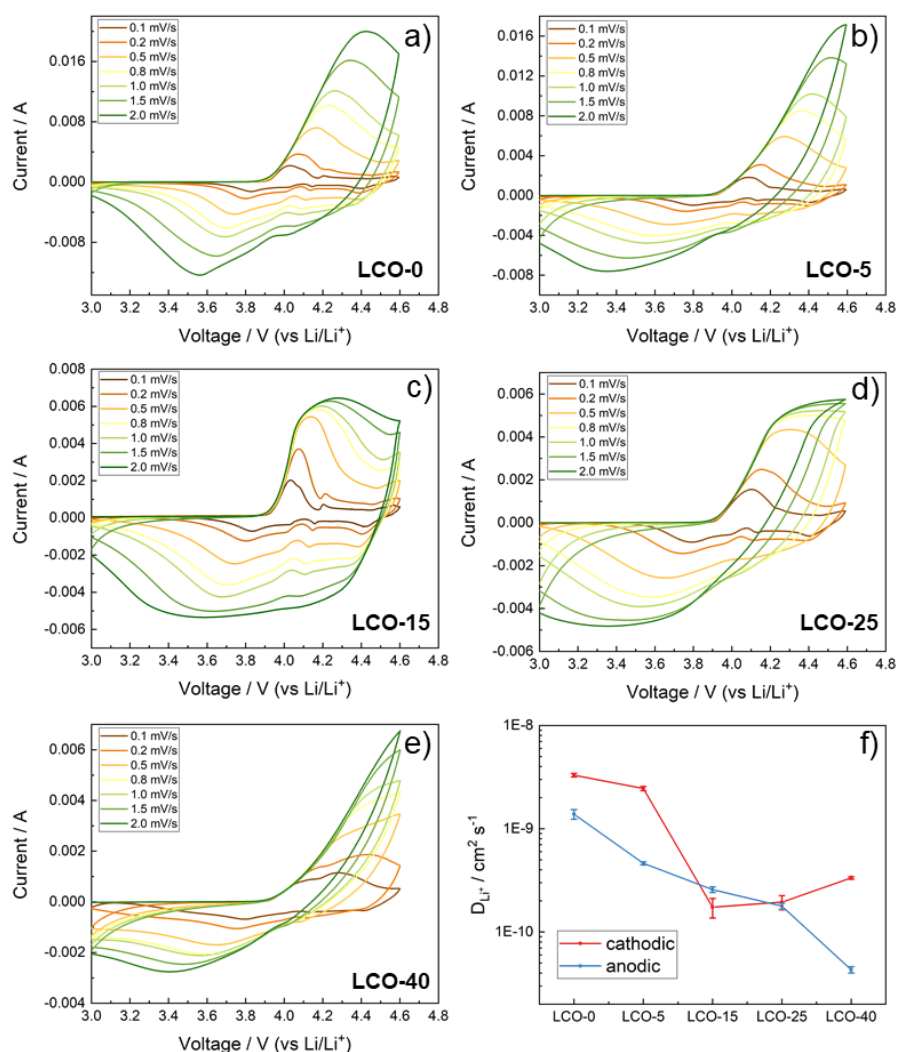


**Figure 8.6:** CVs of (a) LCO-0, (b) LCO-5, (c) LCO-15, (d) LCO-25 and (e) LCO-40 at different scan rates (0.1, 0.2, 0.5, 0.8, 1.0, 1.5 and 2.0 mV/s). Their corresponding plots of peak current vs. the square root of scan rates for the charge and discharge region can be found in Figure 8.16. (f) Plot of calculated lithium diffusion coefficients for cathodic (red) and anodic scan (blue) with the standard error of the linear fit.

the formation of a pinhole-free LNO film between 5 and 15 ALD cycles. The obtained diffusion coefficients are within the range of values reported in the literature, ranging from  $10^{-13}$  to  $10^{-7}$  cm<sup>2</sup> s<sup>-1</sup> depending on the techniques and evaluation methods used for their determination.<sup>[47–51]</sup>

In order to demonstrate the advantages of a protective layer for high-voltage cycling with the associated higher specific capacity, rate performance measurements of the LCO electrodes with different coating layer thicknesses were conducted. As shown in Figure 8.7a, the different samples were charged and discharged using current densities

between 100 and 1000 mA g<sup>-1</sup> in a voltage range from 3.0 to 4.3 V. For a better clarity of the graph, only the specific capacities extracted from discharging curves are shown, full rate performance plots can be found in Figure 8.16. Assuming an approximate extraction of  $x \approx 0.6$  for Li<sub>x</sub>CoO<sub>2</sub> at a cut-off potential of 4.3 V,<sup>[52]</sup> a minimal theoretical specific capacity of 164 mAh g<sup>-1</sup> can be expected, which at the charging current density of 100 mA g<sup>-1</sup> corresponds to a C-rate of 0.68C.

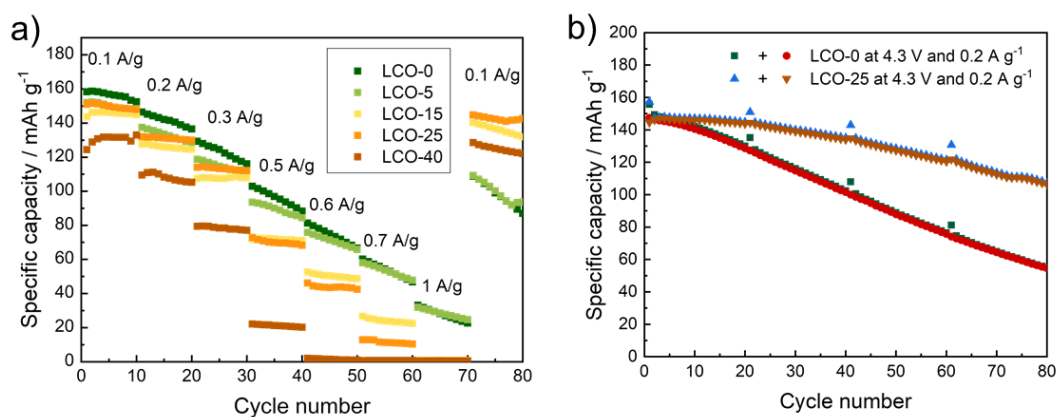


**Figure 8.7:** Rate capability of LCO-0, LCO-5, LCO-15, LCO-25 and LCO-40 at room temperature at different current densities (0.1, 0.2, 0.3, 0.5, 0.6, 0.7, and 1 A/g) (a). Cyclic stability at 0.2 A/g of LCO-0 and LCO-25 (b).

LCO-0 exhibits a specific capacity of 158 mAh g<sup>-1</sup> in the first discharge cycle at a charging current density of 100 mA g<sup>-1</sup>, which agrees well with the theoretically expected value. Over the whole rate performance measurement, a steady decrease at all different charging rates can be observed for the unprotected electrodes. This can be explained by the inferior structural stability and a poor cathode/electrolyte interface stability. After 80 cycles a capacity of only 86 mA g<sup>-1</sup> was retained. A behavior similar to unprotected LCO can be observed for the LCO-5 electrode, as the LNO layer is still not closed. LCO-40 shows a drastically reduced specific capacity compared to bare LCO, reaching only 130 mA g<sup>-1</sup>, but on the other hand for this cathode losses of only 6% are observed after 80 cycles as compared to the starting capacity. The rather low capacity values and the inferior insertion behavior at higher charging current densities can be attributed to the low lithium diffusion rate through the protective layer. A good trade-off between the two extreme cases can be found for LCO-15 and LCO-25, where a high and stable specific capacity at low charging current densities is observed. LCO-25 exhibits a capacity of 150 mA g<sup>-1</sup> in the first discharge cycle and of 142 mA g<sup>-1</sup> in cycle 80, corresponding to a high retention of 95%. However, at high charging current densities the performance decreases similar to that of LCO-40 due to the slower lithium diffusion in the amorphous LNO protection layer.

Because of the lower stress for the LCO-25 electrode compared to LCO-0 during rate performance tests at high charging rates, long-term measurements at a constant current density of 200 mA g<sup>-1</sup> and a cut-off potential of 4.3 V were conducted to verify

the superior stability of the LNO-protected LCO electrodes (see Figure 8.7b). In order to get some insight into the degradation process, impedance spectra were recorded every 20 cycles, which causes a short increase in capacity in the respective cycles. Both electrodes exhibit a starting specific capacity of  $147 \text{ mA g}^{-1}$  for the first discharge cycle. After 40 cycles LCO-0 already experienced a capacity decrease of 32% while LCO-25 shows a good stability with only 8% of capacity decline. After 80 cycles, only one-third of the initial performance is left for LCO-0. In comparison, LCO-25 still shows a good specific capacity of  $107 \text{ mA g}^{-1}$ , indicating a successful surface modification *via* an ultra-thin LNO layer as a facile and effective strategy to improve the cycling stability of  $\text{LiCoO}_2$  under a high cut-off voltage of 4.3 V.

Additionally, impedance spectra at 3.0 V vs.  $\text{Li}/\text{Li}^+$  were recorded during the long-term measurement every 20<sup>th</sup> cycle (see Figure 8.17). In the respective Nyquist plots of LCO-0 and LCO-25 a semicircle in the high frequency region with a diameter corresponding to the charge transfer resistance ( $R_{CT}$ ) at the electrode-electrolyte interphase is observed. The slope in the lower frequency region described by the Warburg impedance is thereby related to the  $\text{Li}^+$  diffusion through the electrode material.<sup>[49,53,54]</sup> The  $R_{CT}$  value stays nearly constant for LCO-0 whereas for LCO-25 a small increased semicircle diameter can be observed, indicating an increase of resistance between the protective LNO coating and the active material, possibly by small contact problems between the different layers due to the volume change of LCO during cycling. Additionally, lithium-ion diffusion coefficients ( $D_{Li}$ ) can be calculated from the impedance data using the following equations:<sup>[53]</sup>

$$Z' = R_S + R_{CT} + \sigma_W \omega^{-0.5} \quad (8.2)$$

$$D_{Li^+} = \frac{R^2 T^2}{2A^2 n^4 F^4 C_{Li}^2 \sigma_W^2} \quad (8.3)$$

Here,  $Z'$  is related to the real part of the impedance,  $R_S$  is the series resistance,  $R_{CT}$  represents the charge transfer resistance,  $\sigma_W$  is the Warburg impedance coefficient,  $\omega$  is the angular frequency,  $D_{Li}$  is the lithium-ion diffusion coefficient,  $R$  is the gas constant ( $8.314 \text{ J mol}^{-1} \text{ K}^{-1}$ ),  $T$  is the temperature (298 K),  $A$  is the surface area of the electrode,  $n$  is the number of electrons participating per formula unit,  $F$  is the Faraday constant ( $96485 \text{ C mol}^{-1}$ ) and  $C_{Li}$  is the concentration of lithium ions in the electrode. The Warburg impedance coefficient equals the slope of the linear relationship between  $Z'$  and  $\omega^{-0.5}$  in the low frequency region as depicted in Figure 8.17. The resulting  $D_{Li}$  values are summarized in Table 8.3. The diffusion coefficient for unprotected LCO stays approximately the same, whereas for the protected LCO-25 a moderate decrease within one order of magnitude can be observed. The loss of contact and the growth of a non-conducting layer on the active materials surface are probably again reasons for the observed effect.

So far, several different protection strategies have been reported in the context of using high-voltage cut-offs (4.3 – 4.6 V) to increase the specific capacity of LCO.<sup>[27,28,31,32,55]</sup> Among these so-called "zero-strain" cathodes coated with  $\text{ZrO}_2$ ,  $\text{Al}_2\text{O}_3$  and  $\text{TiO}_2$ , the

most promising results were obtained for  $\text{Al}_2\text{O}_3$  coatings, enhancing the cycling performance to  $140 \text{ mAh g}^{-1}$  after 100 cycles at a charging rate of  $140 \text{ mA g}^{-1}$ .<sup>[32]</sup> Nevertheless, due to a large electrochemical polarization caused by the coating layer, the supply of electrons becomes problematic and no increase in rate capability can be observed.<sup>[32]</sup> The  $\text{ZrO}_2$  based coating with a higher electrical conductivity shows a better rate capability but does not protect the LCO as well as the  $\text{Al}_2\text{O}_3$  coating. Further improvement could be shown by Xie et al. who used  $\text{LiAlO}_2$  as interfacial layer and could increase the specific capacity close to  $200 \text{ mAh g}^{-1}$  being stable over 50 cycles at a high cut-off potential of 4.6 V, however only at very low charging currents of  $50 \text{ mA g}^{-1}$ . The  $\text{LiAlO}_2$ -protected LCO electrodes were also able to outperform  $\text{Al}_2\text{O}_3$ -coated reference electrodes in direct comparison.<sup>[28]</sup> This shows the importance of a dense, stable and ion conductive coating on LCO.

### 8.2.4 Post-mortem analysis

LCO-0 and LCO-25 electrodes were collected after the long-term measurements for post-mortem investigation in order to evaluate the beneficial function of the protective LNO coating. The XRD patterns of the cycled electrodes are shown in Figure 8.8 and compared to the freshly prepared ones. For LCO-25 no change in crystal structure can be observed, whereas LCO-0 loses crystallinity and new reflections arise corresponding to  $\text{CoO}_2$ . These new reflections indicate the irreversible delithiation of LCO and a destruction of the crystal structure, explaining the much worse performance of LCO-0 after 80 cycles.

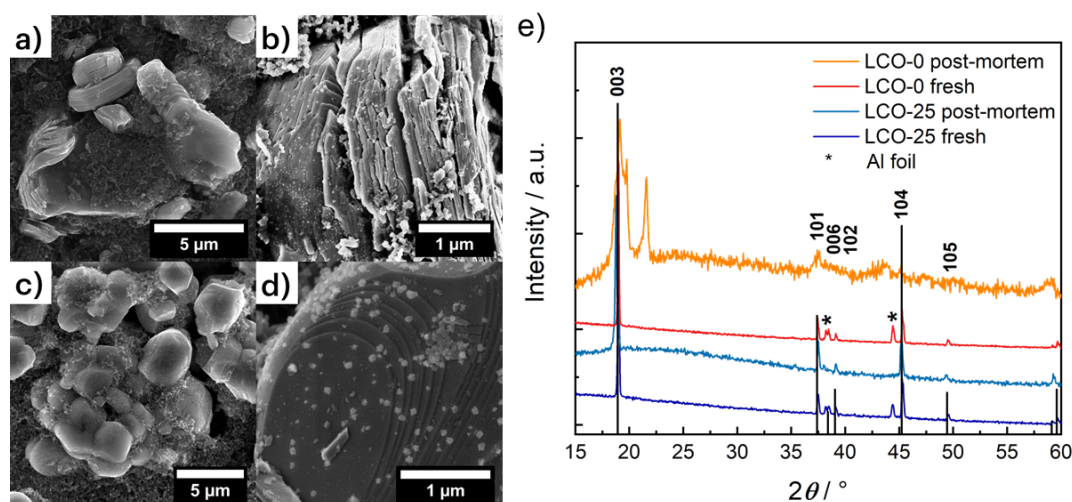


**Figure 8.8:** Post-mortem analysis of LCO-0 (a) and b) and LCO-25 (c) and d) disassembled electrodes after 80 cycles at 0.2 A/g by SEM (a-d). Comparison of XRD measurements of freshly prepared and post-mortem LCO-0 and LCO-25 electrodes (e).

The cycled electrodes were also analyzed microscopically (Figure 8.8a-d). For LCO-25 no significant changes in morphology could be observed; even at high resolution, the

crystal facets are intact and no cracks or particle detachment can be seen. LCO-0 shows a completely different picture, where the LCO particles are splintered and delaminated, even some loose particles can be observed. The SEM pictures of both electrodes clearly demonstrate the strong effect of the LNO protective coating on LCO for high cut-off cycling, where the original structure can be preserved and the destruction of the LCO particles and loss of active material can be prevented.

Taking all post-mortem data into account, the drop of capacity for LCO-0 can be explained by the destruction and delamination of LCO at higher cut-off potentials, and to a lesser extent by changes of charge and ion diffusion. On the other hand, LNO-protected LCO-25 retains its crystal structure and morphology, accompanied by a moderate decrease of interfacial conductivity and associated slightly reduced charging performance and capacity of the electrode.

### 8.3 Conclusions and Outlook

In this work, lithium niobate layers of different thickness were coated directly on LCO electrodes by means of atomic layer deposition. Depending on the thickness of the protective coating layers, a strongly improved electrode stability at high cut-off potentials and therefore an increase in specific capacity was observed. The results of electrochemical and structural characterization suggested a moderate lithium diffusion slow-down effect of the LNO layer for LCO leading to an increased cell impedance, while stabilizing the LCO structure and thereby retaining the high capacity over multiple cycles. This work offers a strategy for the stabilization of structurally sensitive cathodes in lithium-ion batteries at high cut-off potentials and thereby contributes to the development of batteries with enhanced energy storage capabilities.

### 8.4 Experimental Details

*LCO electrode preparation:* The working electrode was prepared by coating a homogeneous slurry consisting of lithium cobalt oxide (LCO, Alfa Aesar, 99.5 %), polyvinylidene fluoride (PVDF, Aldrich) and carbon black (TimCal) at a mass ratio of 8:1:1 in *N*-methyl-2-pyrrolidone (NMP, Aldrich) on Al foil. The slurry was stirred overnight and uniformly coated on an aluminum collector with a thin film applicator (wet film thickness: 150  $\mu\text{m}$ , corresponding to a loading of  $\approx 7.8 \text{ mg cm}^{-2}$ ). The electrodes were die-cut into round disks with a diameter of 18 mm ( $254.5 \text{ mm}^2$ ). After deposition of varying thicknesses of  $\text{LiNbO}_3$  by ALD, the electrodes were dried at 120  $^\circ\text{C}$  for 3 h in vacuum before use. The cells were assembled in an argon filled glove box using lithium metal as the counter and reference electrode in an EL-CELL ECC1-01-0011-A/L with a glass fiber membrane as separator. As electrolyte, a commercial mixture of 1.15 M  $\text{LiPF}_6$  in EC/EMC/DMC at a 2:2:6 volume-to-volume ratio and 1.0 %wt. fluoroethylene carbonate (FEC) was used.

*ALD of lithium niobate:* The deposition of  $\text{LiNbO}_3$  thin films was carried out in a Picosun R-200 reactor at 200 °C and a base pressure of approximately 6 hPa with  $\text{N}_2$  (Air Liquide, 99.999 %) as carrier and purging gas. Lithium-bis(trimethylsilyl)amide (LiHMDS, Aldrich, 97 %) was sublimed in a glass vessel at 80 °C and niobium ethoxide (NEO, Strem, 99.9+ %) was kept at 160 °C. Ultrapure water (MilliQ, 18.2 M $\Omega$  cm) was held in a stainless-steel cylinder at 18 °C.  $\text{LiNbO}_3$  was deposited by sequential pulsing of three subcycles of  $\text{Li}_2\text{O}$  and one subcycle of  $\text{NbO}_x$  resulting in a growth per supercycle of 0.25 nm cycle<sup>-1</sup>. The  $\text{Li}_2\text{O}$  ALD subcycle comprised three LiHMDS pulses (1.6 s pulse, 8 s purge) and one water pulse (4 s pulse, 4.5 s static exposure, 7.5 s purge) showing a growth per cycle of 0.061 nm, while the  $\text{NbO}_x$  subcycle consisted of four pulses NEO (1.6 s pulse, 6.5 s static exposure, 6 s purge) and one water pulse (1 s pulse, 4.5 s static exposure, 7.5 s purge) showing a growth per cycle of 0.068 nm. The thicknesses of the  $\text{LiNbO}_3$  protection layers on the LCO electrodes were controlled by varying the number of ALD supercycles (0, 5, 15, 25 and 40), and the corresponding electrodes are referred to as LCO-0, LCO-5, LCO-15, LCO-25 and LCO-40, respectively.

*Materials characterization:* Thickness and composition studies of the deposited LNO films were conducted on Si (100) substrates. Layer thicknesses were determined by spectroscopic ellipsometry (J. A. Woolam M-2000 VASE) and evaluated using the WVASE v 3.650 software package.

X-ray photoelectron spectroscopy (XPS) was conducted using a VSW Ta10 X-ray source providing  $K\alpha$  radiation by a non-monochromatized Mg anode system (Mg- $K\alpha$  = 1253.6 eV) and analyzed by a VSW HA 100 hemispherical electron analyzer. Fits of the photoelectron peaks are based on a convolution of a Doniach-Sunijic-function and a Gaussian function after subtraction of a linear background.

Ex-situ annealing of approx. 80 nm thick LNO films on Si substrates was performed in  $\text{N}_2$  at a temperature of 550 °C for 30 min.

X-ray diffraction (XRD) patterns were recorded on a Bruker D8 Discover diffractometer using  $\text{Cu-K}\alpha$  radiation ( $\lambda = 1.5418 \text{ \AA}$ ) in Bragg-Brentano geometry. For thin film characterization, a small grazing incidence angle of  $\theta = 0.7^\circ$  was used.

SEM imaging and FIB lamella preparation was carried out using a FEI Helios Nanolab G3 UC, equipped with a Schottky-type field-emitter, an Oxford EDX detector and Ga+-focused ion beam, operated between 1 and 30 kV. (S)TEM images and EDX maps were acquired on an FEI Titan Themis 80–300 microscope operated at 300 kV acceleration voltage, equipped with an X-FEG electron source, a monochromator, a Cs-corrector and an HAADF detector.

*Electrochemical measurements:* Battery testing cells were measured at room temperature using an Autolab potentiostat/galvanostat (PGSTAT302N) with an FRA32M module or a Autolab Multipotentiostat M101 with an 8AUT.M101 module operated with Nova 1.11 software. Cyclic voltammograms were recorded in a potential range of 3.0 to 4.3 V vs.  $\text{Li}/\text{Li}^+$  using a scan rate of 0.2 mV s<sup>-1</sup> and a step potential of 1.06 mV. Determination of the diffusion coefficients was done by cycling from 3.0 to 4.6 V with different scan rates ranging from 0.1 - 2.0 mV s<sup>-1</sup>. Charge-discharge characteristics

were galvanostatically tested between 3.0 and 4.3 V vs. Li/Li<sup>+</sup> using different current densities ranging from 0.1 to 1.0 mA g<sup>-1</sup>.

## 8.5 References

- [1] A. Manthiram, J. C. Knight, S.-T. Myung, S.-M. Oh, Y.-K. Sun, *Adv. Energy Mater.* **2016**, *6*, 1501010.
- [2] A. Kraysberg, Y. Ein-Eli, *Adv. Energy Mater.* **2012**, *2*, 922–939.
- [3] M. Xie, T. Hu, L. Yang, Y. Zhou, *RSC Adv.* **2016**, *6*, 63250–63255.
- [4] S. Kalluri, M. Yoon, M. Jo, S. Park, S. Myeong, J. Kim, S. X. Dou, Z. Guo, J. Cho, *Adv. Energy Mater.* **2017**, *7*, 1601507.
- [5] L. Wang, B. Chen, J. Ma, G. Cui, L. Chen, *Chem. Soc. Rev.* **2018**, *47*, 6505–6602.
- [6] D. D. MacNeil, J. R. Dahn, *J. Electrochem. Soc.* **2002**, *149*, A912.
- [7] J. W. Fergus, *J. Power Sources* **2010**, *195*, 939–954.
- [8] C. Li, H. P. Zhang, L. J. Fu, H. Liu, Y. P. Wu, E. Rahm, R. Holze, H. Q. Wu, *Electrochim. Acta* **2006**, *51*, 3872–3883.
- [9] J. B. Goodenough, Y. Kim, *Chem. Mater.* **2010**, *22*, 587–603.
- [10] R. V. Chebiam, A. M. Kannan, F. Prado, A. Manthiram, *Electrochem. Commun.* **2001**, *3*, 624–627.
- [11] R.-Z. Yin, Y.-S. Kim, S.-J. Shin, I. Jung, J.-S. Kim, S.-K. Jeong, *J. Electrochem. Soc.* **2012**, *159*, A253–A258.
- [12] R. Sathiyamoorthi, P. Shakkthivel, T. Vasudevan, *Mater. Lett.* **2007**, *61*, 3746–3750.
- [13] J.-M. Kim, S. Tsuruta, N. Kumagai, *Electrochem. Commun.* **2007**, *9*, 103–108.
- [14] Q. Liu, X. Su, D. Lei, Y. Qin, J. Wen, F. Guo, Y. A. Wu, Y. Rong, R. Kou, X. Xiao, F. Aguesse, J. Bareño, Y. Ren, W. Lu, Y. Li, *Nat. Energy* **2018**, *3*, 936–943.
- [15] C. Nithya, R. Thirunakaran, A. Sivashanmugam, S. Gopukumar, *ACS Appl. Mater. Interfaces* **2012**, *4*, 4040–4046.
- [16] L. M. Zhang, X. B. Wang, S. Tao, G. X. Wu, X. Z. Su, S. Q. Wei, H. F. Zhao, W. S. Chu, *Mater. Lett.* **2016**, *179*, 34–37.
- [17] P. M. Zehetmaier, A. Cornélis, F. Zoller, B. Böller, A. Wisnet, M. Döblinger, D. Böhm, T. Bein, D. Fattakhova-Rohlfing, *Chem. Mater.* **2019**, *31*, 8685–8694.
- [18] Z. Chen, J. R. Dahn, *Electrochem. Solid-State Lett.* **2004**, *7*, A11.
- [19] J. Zhang, Y. J. Xiang, Y. Yu, S. Xie, G. S. Jiang, C. H. Chen, *J. Power Sources* **2004**, *132*, 187–194.
- [20] J.-H. Shim, K.-S. Lee, A. Missyul, J. Lee, B. Linn, E. C. Lee, S. Lee, *Chem. Mater.* **2015**, *27*, 3273–3279.

- [21] J. Y. Lee, Y. M. Lee, B. Bhattacharya, Y.-C. Nho, J.-K. Park, *Electrochim. Acta* **2009**, *54*, 4312–4315.
- [22] Y. S. Jung, A. S. Cavanagh, L. Gedvilas, N. E. Widjonarko, I. D. Scott, S.-H. Lee, G.-H. Kim, S. M. George, A. C. Dillon, *Adv. Energy Mater.* **2012**, *2*, 1022–1027.
- [23] N. Yabuuchi, Y. Kinoshita, K. Misaki, T. Matsuyama, S. Komaba, *J. Electrochem. Soc.* **2015**, *162*, A538–A544.
- [24] G.-g. Park, Y.-k. Park, J.-k. Park, J.-w. Lee, *RSC Adv.* **2017**, *7*, 16244–16252.
- [25] W. J. Li, M. Hirayama, K. Suzuki, R. Kanno, *Solid State Ion.* **2016**, *285*, 136–142.
- [26] Y. Sun, K. Suzuki, K. Hara, S. Hori, T.-a. Yano, M. Hara, M. Hirayama, R. Kanno, *J. Power Sources* **2016**, *324*, 798–803.
- [27] M. Kato, T. Hayashi, G. Hasegawa, X. Lu, T. Miyazaki, Y. Matsuda, N. Kuwata, K. Kurihara, J. Kawamura, *Solid State Ion.* **2017**, *308*, 54–60.
- [28] J. Xie, J. Zhao, Y. Liu, H. Wang, C. Liu, T. Wu, P.-C. Hsu, D. Lin, Y. Jin, Y. Cui, *Nano Res.* **2017**, *10*, 3754–3764.
- [29] O. Lidor-Shalev, N. Leifer, M. Ejgenberg, H. Aviv, I. Perelshtein, G. Goobes, M. Noked, *Batter. Supercaps* **2021**, *4*, 1739.
- [30] Y. S. Jung, A. S. Cavanagh, A. C. Dillon, M. D. Groner, S. M. George, S.-H. Lee, *J. Electrochem. Soc.* **2010**, *157*, A75.
- [31] J.-T. Lee, F.-M. Wang, C.-S. Cheng, C.-C. Li, C.-H. Lin, *Electrochim. Acta* **2010**, *55*, 4002–4006.
- [32] X. Li, J. Liu, X. Meng, Y. Tang, M. N. Banis, J. Yang, Y. Hu, R. Li, M. Cai, X. Sun, *J. Power Sources* **2014**, *247*, 57–69.
- [33] D. Zuo, G. Tian, D. Chen, H. Shen, C. Lv, K. Shu, Y. Zhou, *Electrochim. Acta* **2015**, *178*, 447–457.
- [34] N. Ohta, K. Takada, I. Sakaguchi, L. Zhang, R. Ma, K. Fukuda, M. Osada, T. Sasaki, *Electrochem. Commun.* **2007**, *9*, 1486–1490.
- [35] H. Yu, S. Wang, Y. Hu, G. He, L. Q. Bao, I. P. Parkin, H. Jiang, *Green Energy Environ.* **2020**, *in press, corrected proof*, <https://doi.org/10.1016/j.gee.2020.09.011>.
- [36] A. Y. Kim, F. Strauss, T. Bartsch, J. H. Teo, J. Janek, T. Brezesinski, *Sci. Rep.* **2021**, *11*, 5367.
- [37] B. Wang, Y. Zhao, M. N. Banis, Q. Sun, K. R. Adair, R. Li, T.-K. Sham, X. Sun, *ACS Appl. Mater. Interfaces* **2018**, *10*, 1654–1661.
- [38] J. Liang, S. Hwang, S. Li, J. Luo, Y. Sun, Y. Zhao, Q. Sun, W. Li, M. Li, M. N. Banis, X. Li, R. Li, L. Zhang, S. Zhao, S. Lu, H. Huang, D. Su, X. Sun, *Nano Energy* **2020**, *78*, 105107.
- [39] E. Østreng, H. H. Sønsteby, T. Sajavaara, O. Nilsen, H. Fjellvåg, *J. Mater. Chem. C* **2013**, *1*, 4283–4290.

- 
- [40] N. Kaufherr, D. J. Eichorst, D. A. Payne, *J. Vac. Sci. Technol.* **1996**, *14*, 299–305.
- [41] N. Özer, M. D. Rubin, C. M. Lampert, *Sol. Energy Mater. Sol. Cells* **1996**, *40*, 285–296.
- [42] M. Aufray, S. Menuel, Y. Fort, J. Eschbach, D. Rouxel, B. Vincent, *J. Nanosci. Nanotechnol.* **2009**, *9*, 4780–4785.
- [43] Y. Gu, D. Chen, X. Jiao, F. Liu, *J. Mater. Chem.* **2007**, *17*, 1769–1776.
- [44] J. N. Reimers, J. R. Dahn, *J. Electrochem. Soc* **1992**, *139*, 2091–2097.
- [45] K. Dokko, S. Horikoshi, T. Itoh, M. Nishizawa, M. Mohamedi, I. Uchida, *J. Power Sources* **2000**, *90*, 109–115.
- [46] R. Pan, D. Rau, Y. Moryson, J. Sann, J. Janek, *ACS Appl. Energy Mater.* **2020**, *3*, 6065–6071.
- [47] L. Sebastian, J. Gopalakrishnan, *J. Mater. Chem.* **2003**, *13*, 433–441.
- [48] J.-P. Brog, A. Crochet, J. Seydoux, M. J. D. Clift, B. Baichette, S. Maharajan, H. Barosova, P. Brodard, M. Spodaryk, A. Züttel, B. Rothen-Rutishauser, N. H. Kwon, K. M. Fromm, *J. Nanobiotechnology* **2017**, *15*, 58.
- [49] K. Dokko, M. Mohamedi, Y. Fujita, T. Itoh, M. Nishizawa, M. Umeda, I. Uchida, *J. Electrochem. Soc* **2001**, *148*, A422.
- [50] Y. H. Rho, K. Kanamura, *J. Electrochem. Soc* **2004**, *151*, A1406.
- [51] N. H. Kwon, H. Yin, P. Brodard, C. Sugnaux, K. M. Fromm, *Electrochim. Acta* **2014**, *134*, 215–221.
- [52] G. G. Amatucci, J. M. Tarascon, L. C. Klein, *J. Electrochem. Soc* **1996**, *143*, 1114–1123.
- [53] H. Xia, L. Lu, G. Ceder, *J. Power Sources* **2006**, *159*, 1422–1427.
- [54] Y. Iriyama, M. Inaba, T. Abe, Z. Ogumi, *J. Power Sources* **2001**, *94*, 175–182.
- [55] J. Wang, *Int. J. Electrochem. Sci.* **2020**, 9282–9293.

## 8.6 Appendix

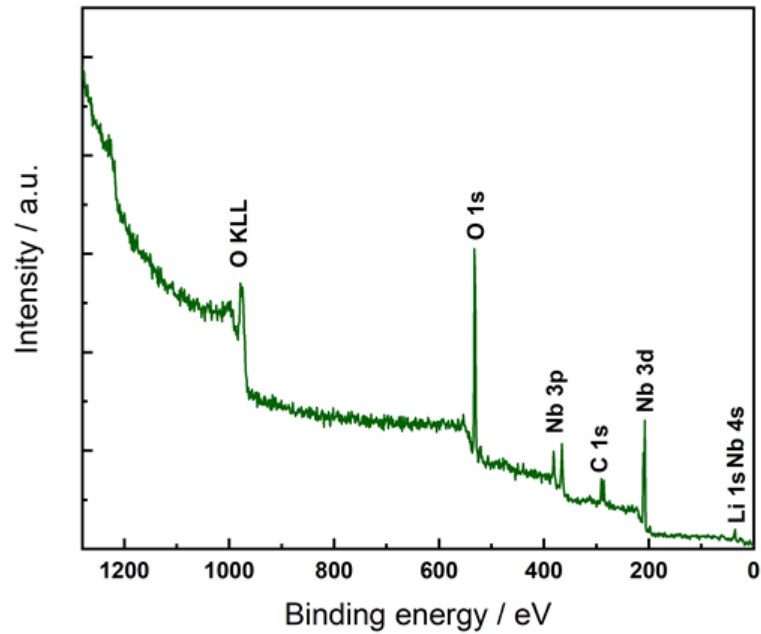


**Figure 8.9:** XPS survey spectra of 80 cycle as-deposited lithium niobate coated *via* ALD on a Si(100) substrate.

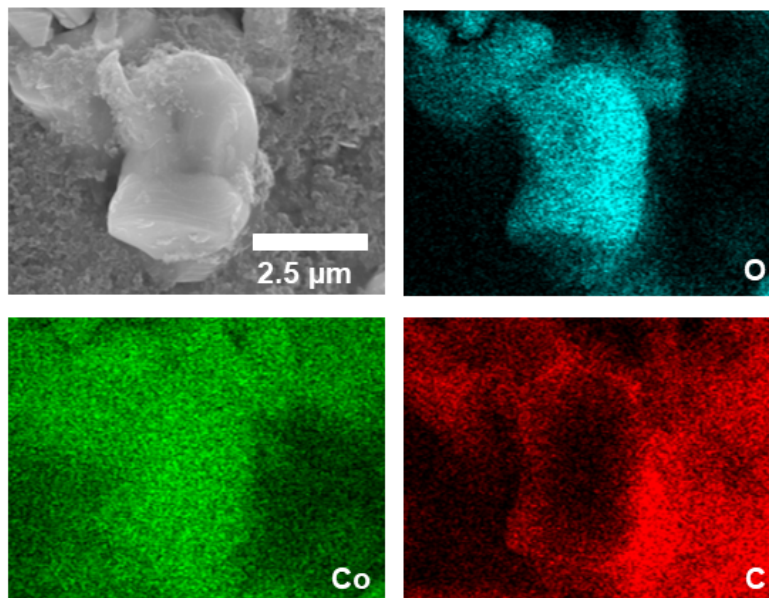


**Figure 8.10:** SEM micrograph of an LCO-0 electrode and corresponding EDX elemental maps (elements given in the figure panels).

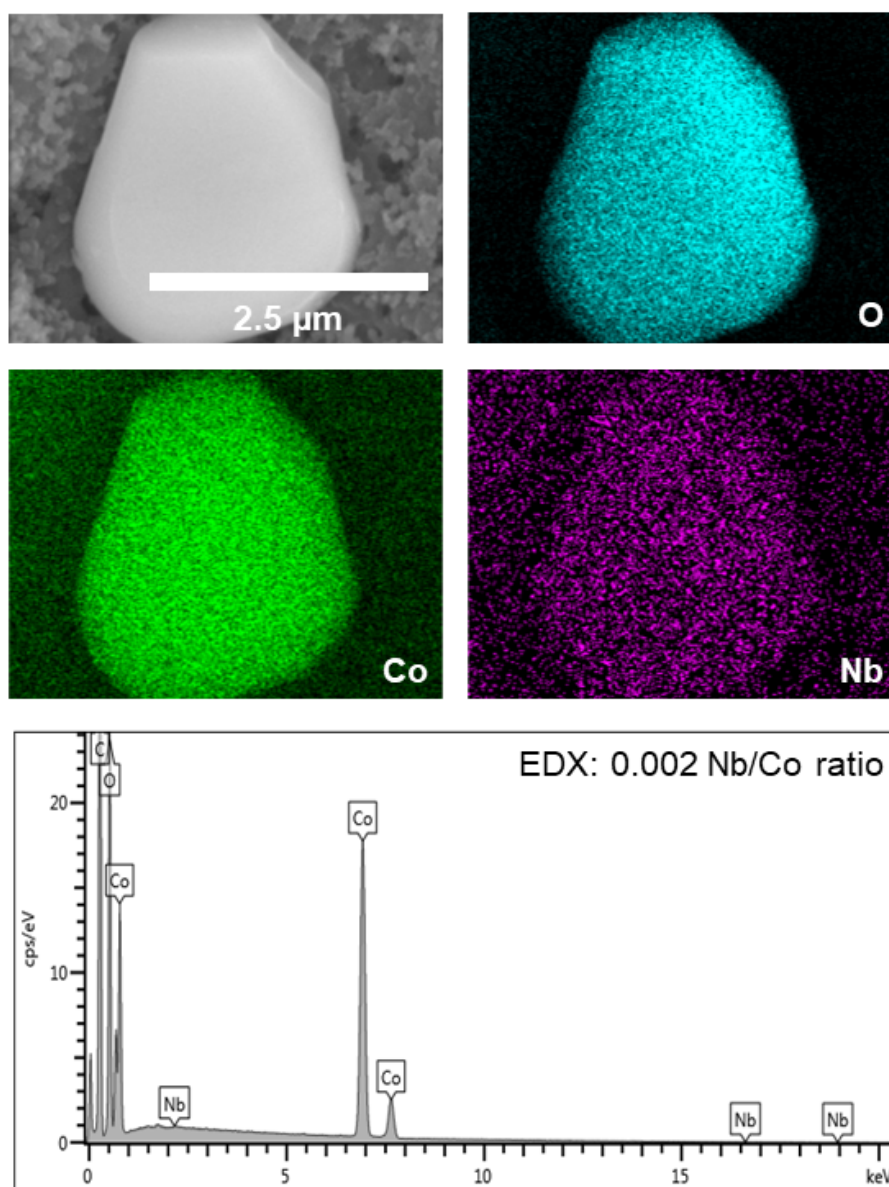


**Figure 8.11:** SEM micrograph of LCO-5 and corresponding EDX elemental maps illustrating the homogeneous distribution of Nb (purple) on the LCO particle (elements given in the figure panels). The corresponding EDX spectrum provides a Nb to Co ratio of 0.2 at%.

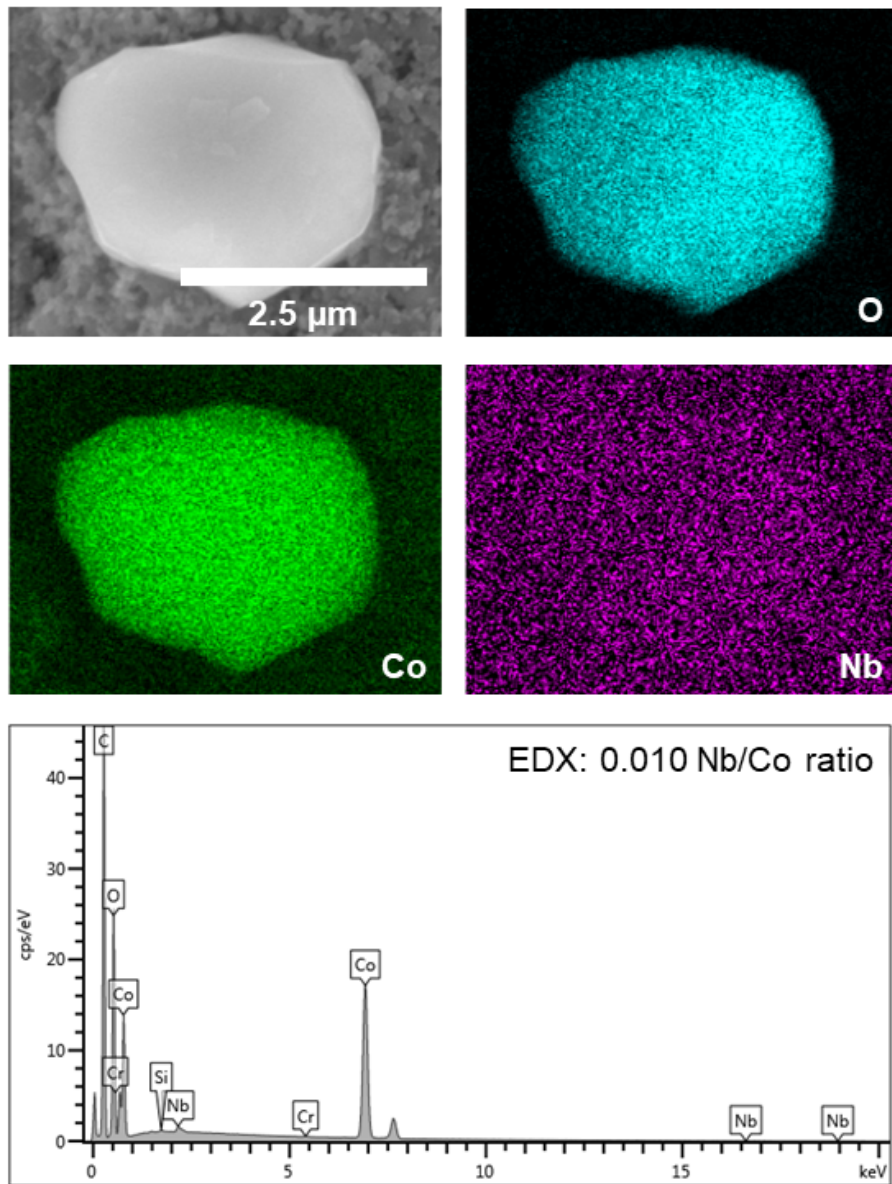


**Figure 8.12:** SEM micrograph of LCO-15 and corresponding EDX elemental maps illustrating the homogeneous distribution of Nb (purple) on the LCO particle (elements given in the figure panels). The corresponding EDX spectrum provides a Nb to Co ratio of 1.0 at%.

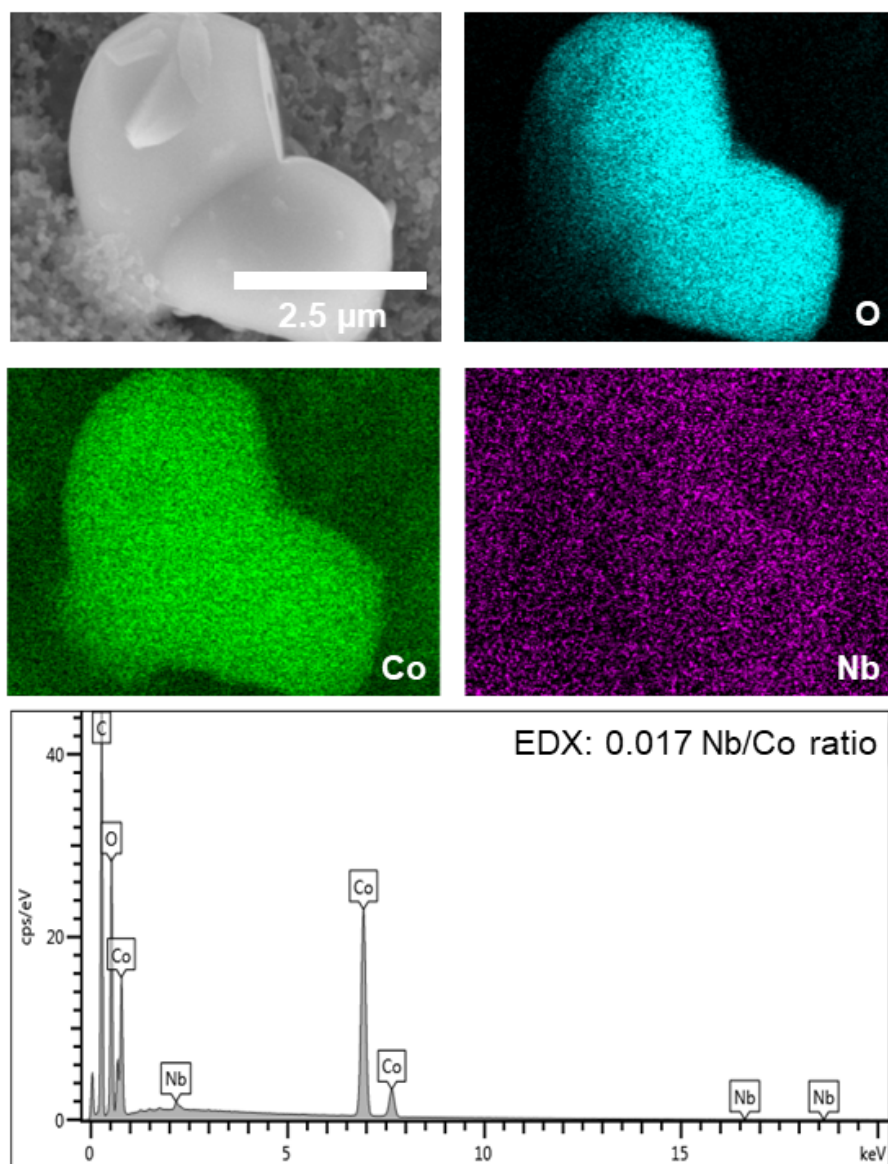


**Figure 8.13:** SEM micrograph of LCO-25 and corresponding EDX elemental maps illustrating the homogeneous distribution of Nb (purple) on the LCO particle (elements given in the figure panels). The corresponding EDX spectrum provides a Nb to Co ratio of 1.7 at%.

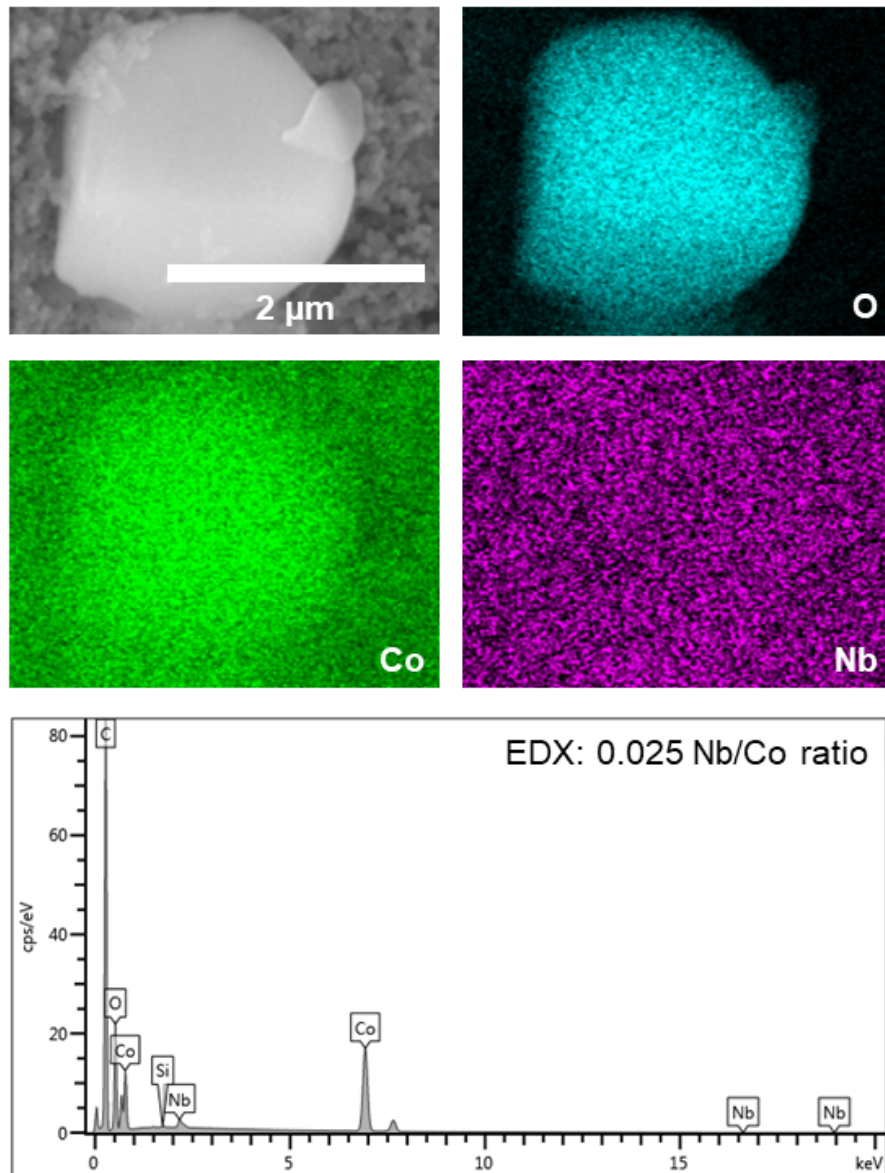


**Figure 8.14:** SEM micrograph of LCO-40 and corresponding EDX element maps illustrating the homogenous distribution of Nb (purple) on the LCO particle (elements given in the figure panels). The corresponding EDX spectrum provides a Nb to Co ratio of 2.5 at%

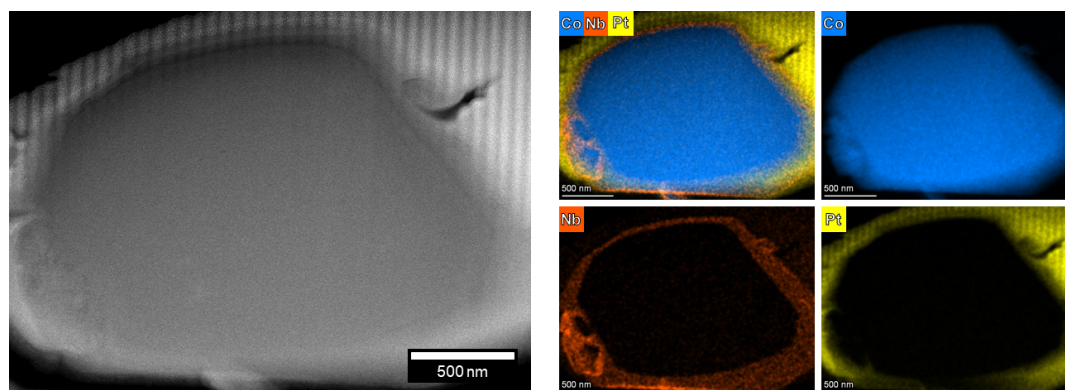


**Figure 8.15:** HAADF-STEM image and the corresponding EDX element distribution maps of Co (blue), Nb (red) and Pt (yellow) showing the cross-section of an LCO particle coated with 40 cycles of LNO without any further processing (elements given in the figure panels).

**Table 8.1:** Peak positions of 1st and 5th cycle from cyclic voltammograms of (a) LCO-0, (b) LCO-5, (c) LCO-15, (d) LCO-25 and (e) LCO-40 and their calculated distance.

	LCO-0	LCO-5	LCO-15	LCO-25	LCO-40
Cyc1 Ox.	4.081	4.142	4.183	4.215	4.168
Cyc1 Red.	3.807	3.744	3.751	3.785	3.767
$\Delta V$	0.274	0.398	0.432	0.43	0.401
Cyc5 Ox.	4.056	4.121	4.072	4.152	4.171
Cyc5 Red.	3.806	3.758	3.799	3.727	3.766
$\Delta V$	0.250	0.393	0.273	0.425	0.405

**Table 8.2:** Lithium diffusion coefficients calculated with Randles-Sevcik equation from CVs of (a) LCO-0, (b) LCO-5, (c) LCO-15, (d) LCO-25 and (e) LCO-40 at different scan rates (0.1, 0.2, 0.5, 0.8, 1.0, 1.5 and 2.0 mV/s).

	Lithium-ion diffusion coefficient $D_{Li} / \text{cm}^2 \text{s}^{-1}$	
	cathodic scan	anodic scan
LCO-0	$3.30 \times 10^{-9}$	$1.38 \times 10^{-9}$
LCO-5	$2.45 \times 10^{-9}$	$4.62 \times 10^{-10}$
LCO-15	$1.74 \times 10^{-10}$	$2.57 \times 10^{-10}$
LCO-25	$1.94 \times 10^{-10}$	$1.78 \times 10^{-10}$
LCO-40	$3.34 \times 10^{-10}$	$4.32 \times 10^{-11}$

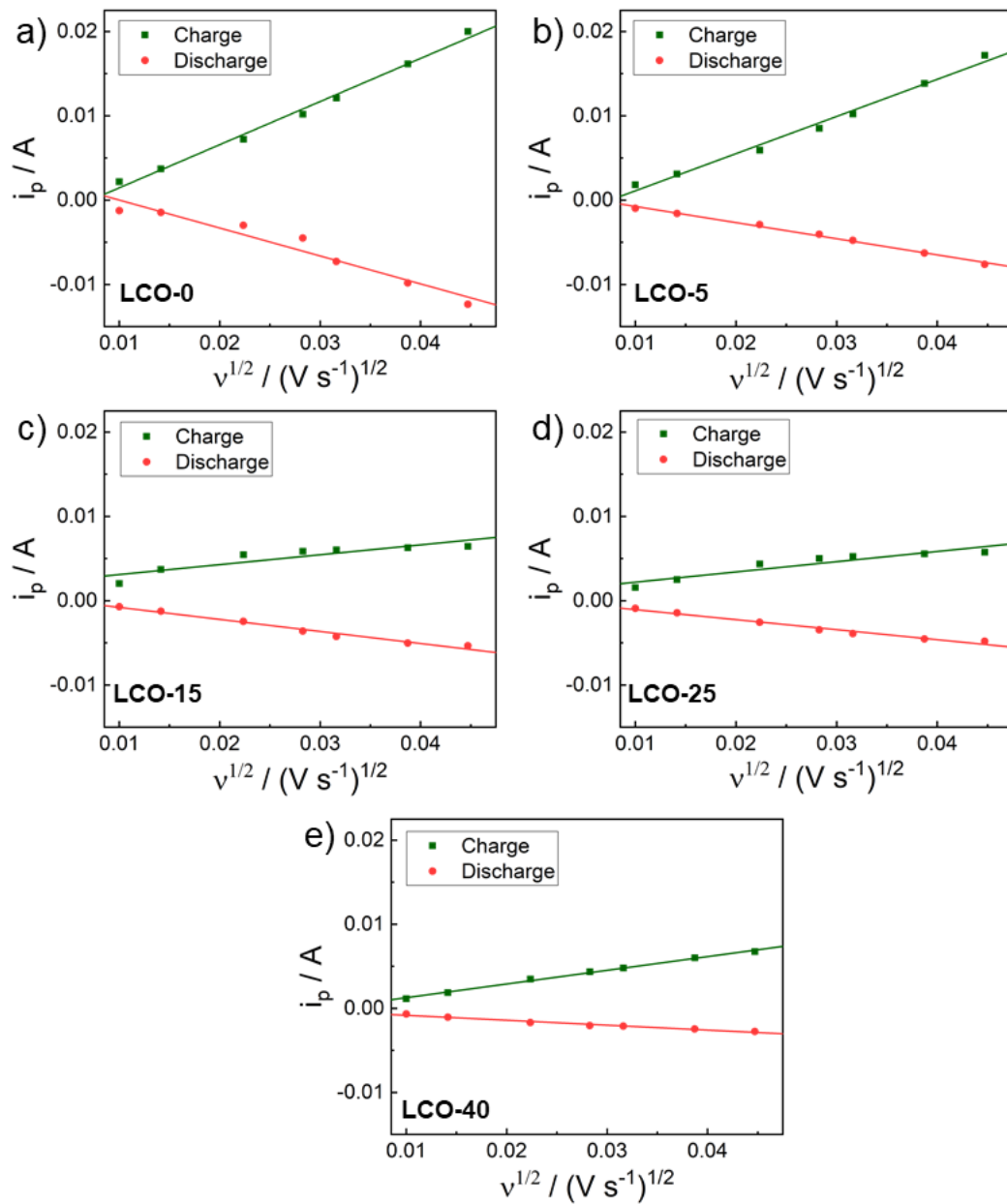
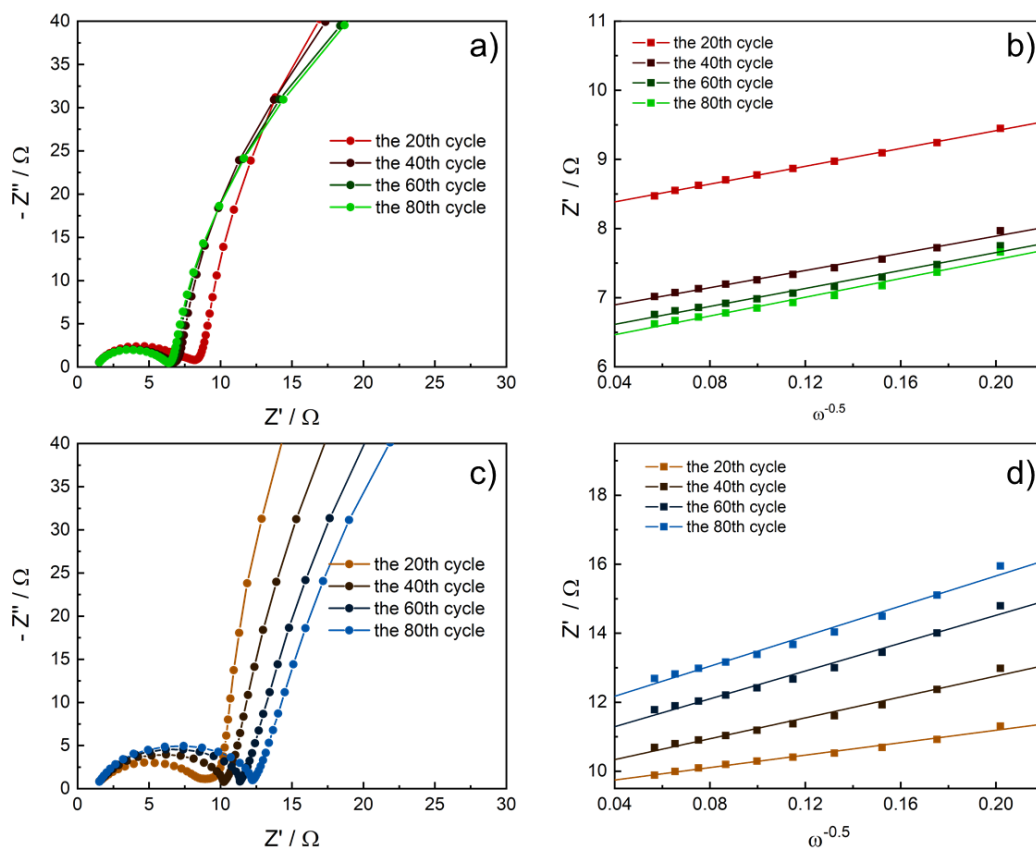


Figure 8.16: Figure 8.6 corresponding plots of peak current vs. the square root of scan rates for charge and discharge regions for (a) LCO-0, (b) LCO-5, (c) LCO-15, (d) LCO-25 and (e) LCO-40.



**Figure 8.17:** Nyquist plot of LCO-0 and LCO-25 after 20, 40, 60 and 80 cycle at  $0.2 \text{ A g}^{-1}$  charging rate and a cut-off potential of 4.3 V (a and c) and the corresponding  $Z' - \omega^{-0.5}$  plot in the low frequency range (b and d).

**Table 8.3:** Lithium diffusion coefficients of LCO-0 and LCO-25 after 20, 40, 60 and 80 cycle at  $0.2 \text{ A g}^{-1}$  charging rate and a cut-off potential of 4.3 V vs.  $\text{Li}/\text{Li}^+$ .

	Lithium-ion diffusion coefficient $D_{\text{Li}} / \text{cm}^2 \text{ s}^{-1}$			
	20 <sup>th</sup> cycle	40 <sup>th</sup> cycle	60 <sup>th</sup> cycle	80 <sup>th</sup> cycle
LCO-0	$7.23 \times 10^{-13}$	$9.48 \times 10^{-13}$	$9.38 \times 10^{-13}$	$8.99 \times 10^{-13}$
LCO-25	$4.06 \times 10^{-13}$	$1.79 \times 10^{-13}$	$1.02 \times 10^{-13}$	$8.70 \times 10^{-14}$



## 9 Enlarging the Imidazolate-based COF family for Lithium-Ion Conduction

This chapter is based on the following publication:

Sebastian Häringer<sup>‡</sup>, Stephan Reuter<sup>‡</sup>, Quirin Schmidt, Florian Zoller, Vivian Meier and Thomas Bein\*, *manuscript in preparation*.

---

<sup>‡</sup>These authors contributed equally.

Sebastian Häringer was in lead of this project, designed the concept of the used building blocks, conducted the material characterization and electrochemical measurements, and wrote the complete manuscript.

## Abstract

Covalent organic frameworks (COFs) offer the unique possibility to precisely design their covalently bound building blocks for various energy conversion applications and integrate them into stable, crystalline organic structures. Crystalline imidazolate-containing COFs were recently introduced as high performance lithium-conducting electrolytes. Herein, we expand the series of imidazolate-COFs by increasing their pore dimensions for improved accessibility as well as the density of lithium-ion binding sites within the framework. We obtained two novel, highly crystalline and porous COFs (**sCF3-TFPB** and **diCF3-TFPB**) with enlarged pore dimensions and increased imidazolate density and investigated their impact on lithium-ion conductivity.

## 9.1 Introduction

Covalent organic frameworks (COFs) are a relatively new class of crystalline, porous organic materials, where molecular building blocks (nodes or bridges) are linked by slightly reversible condensation reactions, thereby promoting a self-healing mechanism.<sup>[1-4]</sup> By controlling the properties of the building blocks, a large diversity of  $\pi$ -stacked "2D" COFs or 3D COFs can be realized.<sup>[5]</sup>

Dispersive  $\pi$ - $\pi$  interactions between the ordered 2D polymer sheets in 2D COFs result in ordered stacks with open channels along the c-axis. Implementation of specific functional groups into the respective building blocks allows for the integration of molecular moieties designed for the desired application of the resulting framework. As a result, diverse potential applications of the frameworks have been investigated, ranging from gas storage or separation<sup>[6,7]</sup> to optoelectronic applications,<sup>[8-11]</sup> insertion of guest molecules<sup>[12-15]</sup> as well as catalysis.<sup>[16,17]</sup>

In recent years, COFs have also been explored for energy storage systems in supercapacitors and metal ion batteries. Here, they are used as electrodes for ion/charge storage or as electrolytes for ion conduction by either using pre-designed building blocks or *via* post-synthetic modification of the organic frameworks.

Upon addition of commonly used additives in battery technology like conductive carbon or certain standard solvated Li salts (e.g.,  $\text{LiPF}_6$  in ethylene carbonate/dimethyl carbonate (EC/DMC),<sup>[18]</sup> lithium bis(trifluoromethanesulfonyl)imide ( $\text{LiTFSI}$ ),<sup>[19,20]</sup>  $\text{LiClO}_4$  in propylene carbonate (PC)<sup>[21]</sup>), COFs show competitive performance in comparison to already established inorganic and organic battery components. However, by the addition of the aforementioned additives, the systems become more complex and it is no longer trivial to attribute the observed performance solely to the COF under investigation.

Recently, Hu et al. introduced lithiated imidazolate COFs with high Li-ion conductivity of up to  $7.2 \times 10^{-3} \text{ S cm}^{-1}$ , low activation energy of down to 0.10 eV and a high transference number of 0.81, which is in the range of sulfur-based solid-state electrolytes.<sup>[22]</sup> By changing the substituent on the imidazole moiety to different electron withdrawing

groups (-H, -CH<sub>3</sub>, -CF<sub>3</sub>), they observed a weakening of the imidazole-lithium bond and thereby explain the enhancement in lithium-ion conductivity. The ionic conductivity of this COF system could be further increased upon the addition of propylene carbonate (PC), which is commonly used as a solvent for inorganic salts in Li-electrolytes.

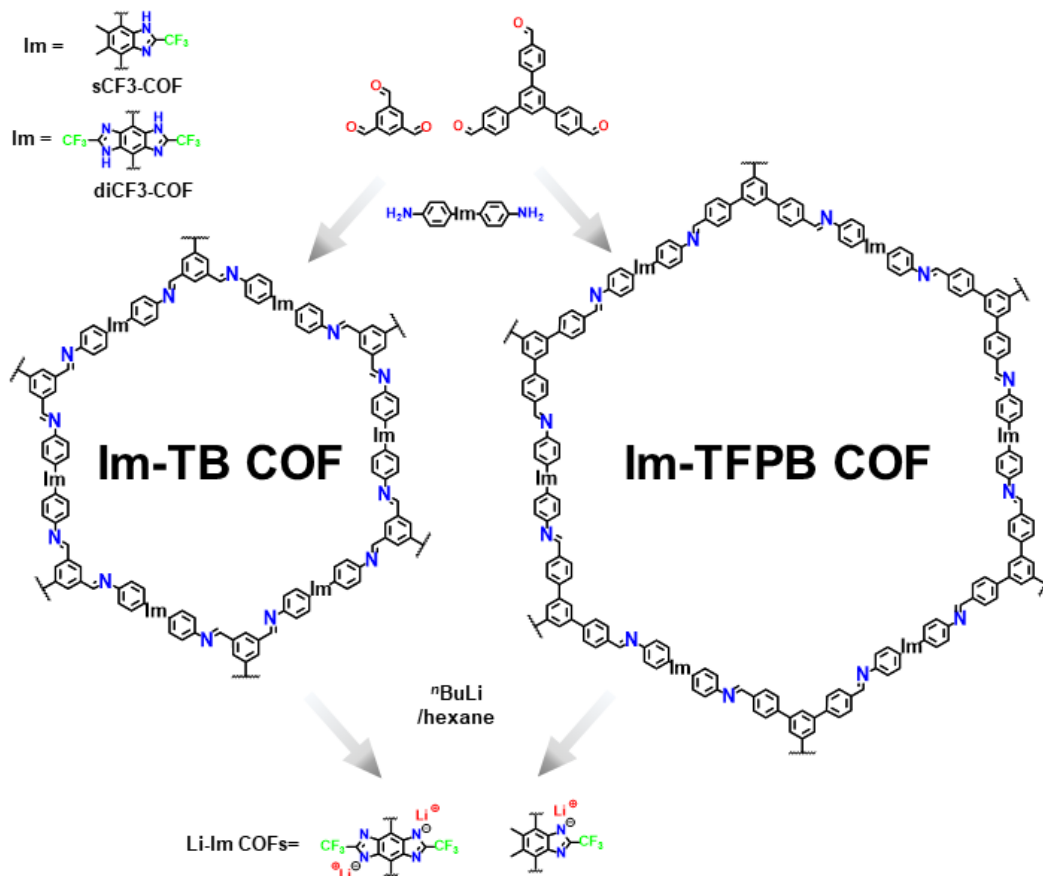


**Figure 9.1:** Schematic construction of novel imidazolate-COFs with varying size and density of Li-binding imidazolate moieties.

Here, we enlarge the family of imidazolate-based COFs by doubling the number of imidazole-groups (diCF<sub>3</sub>-) within the building blocks and increase the pore dimension by co-condensation with enlarged nodes (1,3,5-tris-(4-formyl-phenyl)-benzene (TFPB)). Utilizing supercritical CO<sub>2</sub> extraction of the newly designed COFs, residue-free and highly crystalline imidazole-COFs (**sCF<sub>3</sub>-TB**, **sCF<sub>3</sub>-TFPB** and **diCF<sub>3</sub>-TFPB**) were obtained and characterized.

## 9.2 Results and Discussion

In a previous study,<sup>[22]</sup> Hu et al. synthesized a variety of new imidazolate-based COFs via co-condensation of benzene-1,3,5-tricarbaldehyde (**TB**) and imidazole-substituted diamine building blocks containing a CF<sub>3</sub>-electron-withdrawing group (**sCF3**) on the imidazole moiety. In order to increase the number of imidazolate-based COFs for further investigation of the influence of pore size and thereby pore accessibility and the density of lithium-conducting moieties, we constructed a new building block with twice the number of imidazolate groups (**diCF3**) and increased the size of the linking node by one benzene group (**TFPB**). Due to the sterically demanding -CF<sub>3</sub> group on the imidazole ring, we investigated the impact of imidazole density only on the large-pore (and presumably more flexible) TFPB-COFs with enhanced pore accessibility. The COFs **sCF3-TB**, **sCF3-TFPB** and **diCF3-TFPB** were synthesized under solvothermal conditions within 6 mL reaction tubes catalyzed by aqueous acetic acid with different ratios of solvent described in detail in section C in the Supporting Information. After a 3 day reaction period at 120 °C, the obtained products were washed with tetrahydrofuran (THF) and further purified by CO<sub>2</sub>-extraction in order to fully remove solvent residues along with other remaining impurities. Lithiation of the respective COFs was conducted by dispersion of the material in hexane under argon atmosphere and treatment with *n*-BuLi in hexane solution at 0 °C for 16 h, leading to the lithiated products **Li-sCF3-TB**, **Li-sCF3-TFPB** and **Li-diCF3-TFPB**. The resulting powders were examined regarding their crystallinity, porosity and electrochemical properties.

Powder X-ray diffraction (XRD) analysis of the obtained powders revealed three highly crystalline COFs **sCF3-TB**, **sCF3-TFPB** and **diCF3-TFPB**, showing sharp and intense reflections in the low diffraction angle range with only minimal background (see Figure 9.2). Here, the first intense reflections correspond to the 100 plane, which can be directly attributed to the size of the unit cell for hexagonally shaped pore systems with P3 symmetry for **sCF3-TB** and **sCF3-TFPB** and P6 symmetry for **diCF3-TFPB**. Pawley refinement was used to confirm the unit cell parameters assuming an AA model layer arrangement (inset of Figure 9.2(a)-(c) and sections D and F in the SI). The experimental diffraction pattern was fully indexed and the observed reflections could be attributed. According to the obtained model, **sCF3-TB** has a smaller unit cell ( $a = b = 3.77$  nm,  $c = 0.42$  nm,  $\alpha = \beta = 90^\circ$ ,  $\gamma = 120^\circ$ ) compared to **sCF3-TFPB** ( $a = b = 5.21$  nm,  $c = 0.45$  nm,  $\alpha = \beta = 90^\circ$ ,  $\gamma = 120^\circ$ ) and **diCF3-TFPB** ( $a = b = 5.19$  nm,  $c = 0.45$  nm,  $\alpha = \beta = 90^\circ$ ,  $\gamma = 120^\circ$ ), as expected. The increased interlayer distance shown for **TFPB** linked compounds can be attributed to the more sterically demanding additional benzene group, which is tilted out of the plane (compare Figure S9.13-9.15).

Applying Bragg's equation (equation 9.2) the unit cell size and therefore the pore size can be estimated. For  $2\theta = 2.73^\circ$ ,  $1.98^\circ$  and  $1.85^\circ$  a unit cell size of 3.3 nm, 4.5 nm and 4.9 nm for **sCF3-TB**, **sCF3-TFPB** and **diCF3-TFPB** was calculated, respectively.

The nitrogen physisorption isotherms of the different COFs all exhibit a completely reversible Type IVb isotherm shape without hysteresis indicating a mesoporous structure (Fig. 9.2(d)-(f)).<sup>[23]</sup> All COFs show high BET surface areas values of 896 m<sup>2</sup> g<sup>-1</sup> for

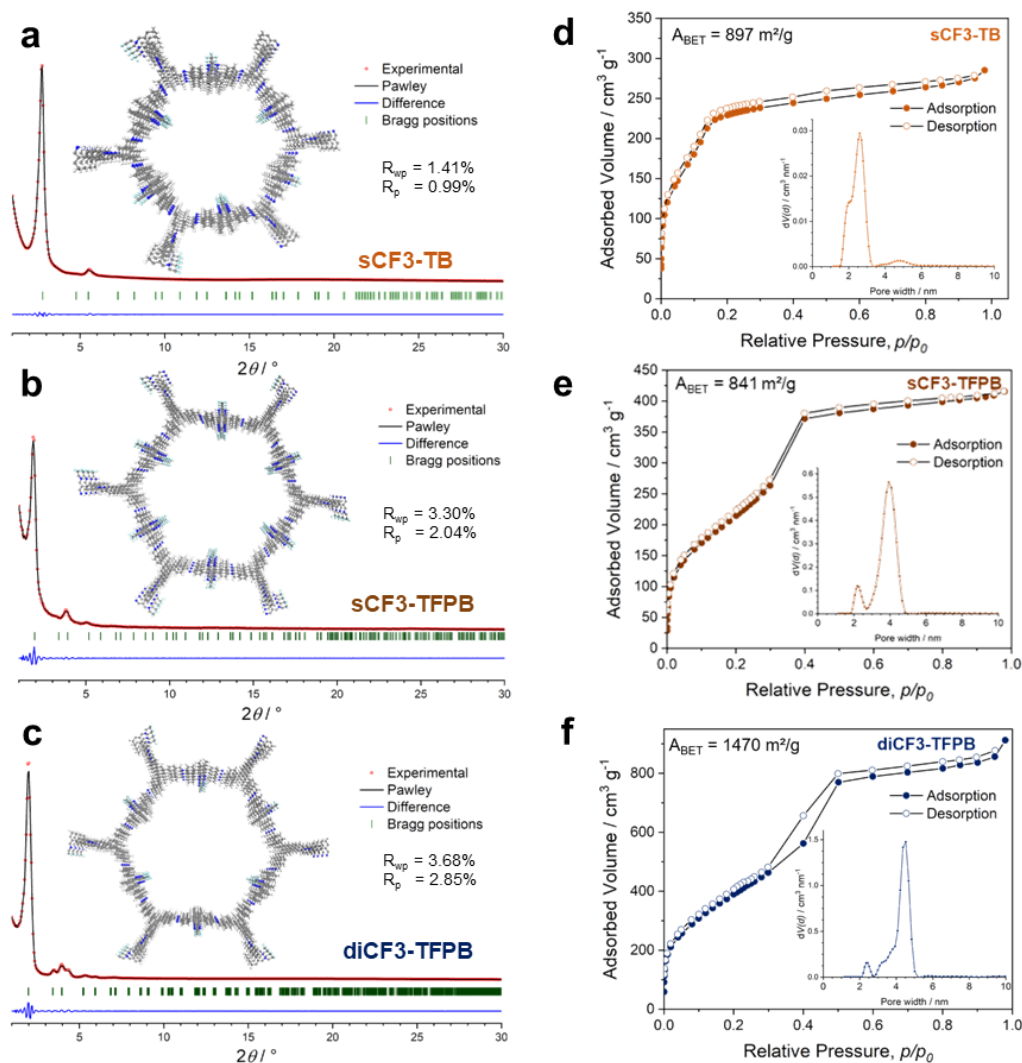


**Figure 9.2:** (a)-(c) PXRD patterns of sCF3-TB, sCF3-TFPB and diCF3-TFPB COFs with Pawley-refined simulations and the obtained theoretical structure. (d)-(f) Nitrogen physisorption isotherms, calculated BET-surface areas and pore size distributions of the respective COFs.

sCF3-TB,  $841 \text{ m}^2 \text{ g}^{-1}$  for sCF3-TFPB and  $1470 \text{ m}^2 \text{ g}^{-1}$  for diCF3-TFPB. Calculated pore size distributions based on a QSDFT carbon kernel for cylindrical pores show good agreement with the structurally modeled pore sizes (Fig. 9.2(a)-(c) and S9.10-9.12) for all different three COFs. DFT-calculated pore sizes were 2.6 nm (simulated 3.0 nm), 4.0 nm (simulated 4.0 nm) and 4.2 nm (simulated 4.2 nm) for sCF3-TB, sCF3-TFPB and diCF3-TFPB, respectively.

Scanning and transmission electron microscopy (SEM and TEM) images reveal the sheet-like nanocrystalline morphology of individual COF crystallites (Figure 9.3). The SEM images show a flake-like desert rose structure for the different COFs (Figure 9.3(a)-

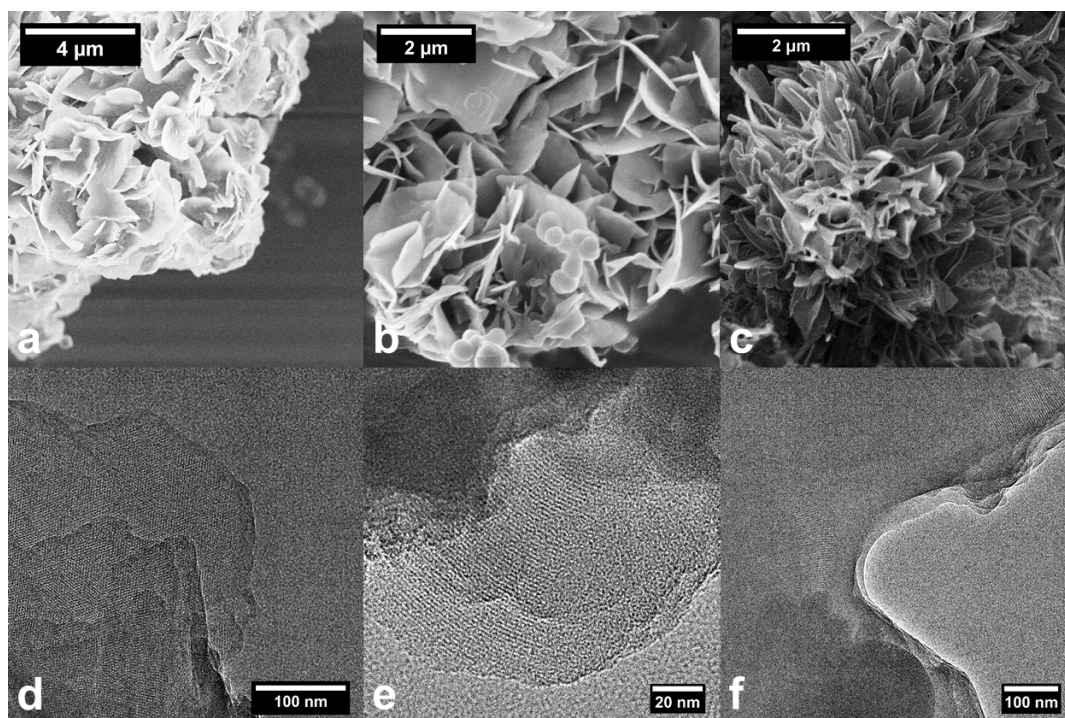


**Figure 9.3:** SEM (a)-(c) and TEM (d)-(f) micrographs of **sCF3-TB**, **sCF3-TFPB** and **diCF3-TFPB**, respectively.

(c). In the TEM images (Figure 9.3(d)-(f)), we observe crystallites that are either oriented with their crystallographic *c*-axis (i.e., along the pores) perpendicular (Figure 9.3(d)) or parallel to the viewing direction (Figure 9.3(e),(f)), showing the highly ordered hexagonal arrangement of the mesopores with spacings of around 2.6 nm for **sCF3-TB** and about 4.0 nm for **sCF3-TFPB** and **diCF3-TFPB**, which is in excellent agreement with the refined structure model and sorption data.

### Electrochemical Characterization

In order to investigate the influence of pore size and density of functional imidazole moieties, **sCF3-TB**, **sCF3-TFPB** and **diCF3-TFPB** were lithiated as previously described and thoroughly washed in order to remove excess lithium species from the COF. The Li elemental analysis showed the expected values for Li content based on the density of imidazole moieties in the COF and assuming a one-to-one stoichiometry between imidazole moieties and Li ions after lithiation. A comparison between theoretically expected and experimentally obtained values is given in the experimental section. Neither a change in color nor a degradation of structural integrity could be observed (characterized by PXRD (Figure S9.6)). The Li-COFs were vacuum-dried for 3 h at 120 °C prior to analysis to remove any residual moisture. The dried COF powders were then handled under argon atmosphere, pressed into dense pellets with a 13 mm stainless steel

die and electrochemically characterized between two stainless steel current collectors within a typical battery testing cell.

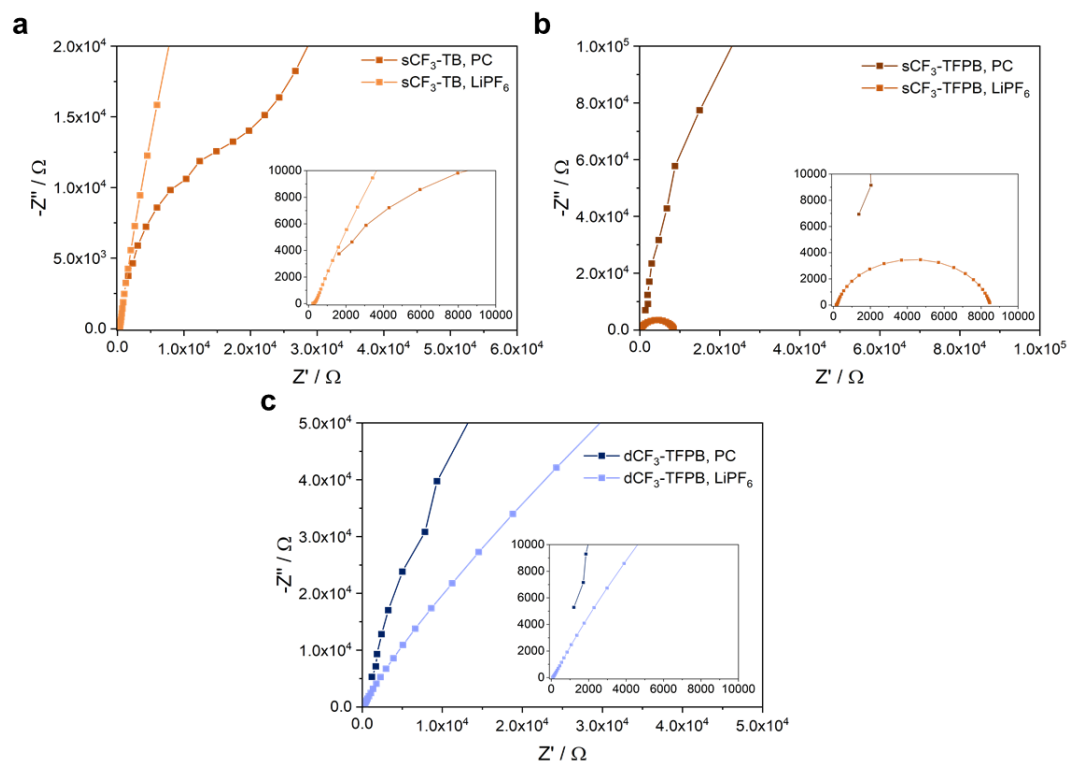


**Figure 9.4:** Nyquist plots of electrochemical impedance spectroscopy measurements of **sCF3-TB** (a), **sCF3-TFPB** (b) and **diCF3-TFPB** (c) after addition of propylene carbonate or commercial Li liquid electrolyte. Insets show a magnification of the beginning section.

According to Hu et al., we found all as-prepared Li-COF pellets to be modest Li-ion conductors (with a conductivity of  $8 \times 10^{-7} \text{ S cm}^{-1}$ ).<sup>[22]</sup> They claim that upon addition of small amounts of propylene carbonate the lithium-ion conductivity can be increased to values of up to  $7.2 \times 10^{-3} \text{ S cm}^{-1}$ . However, contrasting their findings, we were only able to boost the conductivity upon addition of PC to  $1 \times 10^{-5} \text{ S cm}^{-1}$ , presumably due to the improved contacts between the stainless steel current collector and the impregnated Li-COF pellet. The observed strong differences in lithium-ion conductivity may arise in small deviations between the prepared COFs. In general, propylene carbonate is commonly used as polar solvent for lithium salts in liquid Li-electrolytes, e.g. LiPF<sub>6</sub>. Impurities originating from the lithiation step of the imidazolate group may be necessary for the strong performance of **CF<sub>3</sub>-Li-ImCOF** prepared by Hu et al.<sup>[22]</sup>

In order to mimic the impact of possible impurities on Li-ion conduction in the COFs, we impregnated the Li-loaded COFs **Li-sCF3-TB**, **Li-sCF3-TFPB** and **Li-diCF3-TFPB** with the commonly used 1.15 M LiPF<sub>6</sub> in EC/EMC/DMC electrolyte. Using this method, we could obtain conductivity values in the range of  $7 \times 10^{-3} \text{ S cm}^{-1}$ , which

are now comparable to previously reported values and suggest that the reported values could indeed have resulted from Li-salt-loaded COFs (see Figure 9.4(a)-(c)).

Additionally, the morphological macro-structure of the COFs may influence conductivity as well. The domain size, shape and relative orientation of the crystallites can impact the transfer of the Li-ions between the conductive pore channels of individual crystallites. Hu et al. obtained a not clearly defined bulk, whereas in this work, a flake like structure for all products can be observed.<sup>[22]</sup> These findings can explain the differences in lithium-ion conductivity and should be further monitored in future studies in order to enlarge the understanding of ion conductivity in COFs.

### 9.3 Conclusions and Outlook

Herein, we extend the family of imidazolate-containing COFs for the potential use as solid-state electrolyte in LIBs. Two new, highly crystalline and porous COF structures with a flake like morphology and hexagonally shaped pores could be synthesized. The varying pore size and density of lithium-binding moieties did not lead to a significant change in lithium-ion conductivity, which is why the enlargement of a broader spectrum of different COF structure is necessary to further investigate the lithium-ion conduction mechanism in covalent organic frameworks.

### 9.4 Experimental Details

*Synthesis of sCF3-TB COF:* 4,7-di(4-aminophenyl)-5,6-dimethyl-2-(trifluoromethyl)-1H-benzimidazole (**sCF3**) (7.43 mg, 0.019 mmol, 1.00 equiv.), benzene-1,3,5-tricarbaldehyde (**TB**) (2.03 mg, 0.013 mmol, 0.67 equiv.) were combined and mixed with ethanol (125  $\mu$ L) and mesitylene (125  $\mu$ L) inside a 6 mL reaction tube under inert conditions. Subsequently, 3 M HOAc (50  $\mu$ L) were added. The sealed tube was heated at 120 °C for three days. After cooling to room temperature, the precipitate was collected by vacuum filtration, washed with tetrahydrofuran (THF) and further purified by supercritical CO<sub>2</sub>-extraction, yielding the **sCF3-TB** COF as yellow flakes (6.02 mg, 64 %). Anal. Calcd for (C<sub>28</sub>H<sub>19</sub>N<sub>4</sub>F<sub>3</sub>)<sub>n</sub>: C, 71.8; H, 4.1; N, 12.0. Found: C, 69.7; H, 4.0; N, 11.5.

*Synthesis of Li-sCF3-TB COF:* A 25 mL Schlenk flask was charged with **sCF3-TB** COF (130 mg) under inert conditions, which was well-dispersed in hexane (5.5 mL). The dispersion was cooled to 0 °C and a 2.5 M solution of *n*-butyllithium (in hexane, 0.35 mL) was added drop wise. The mixture was allowed to warm to room temperature whilst stirring overnight. The resulting solid was vacuum filtrated and dried under vacuum. **Li-CF3-TB** COF was obtained as a yellow powder (120 mg, 95 %). Anal. Calcd for (C<sub>28</sub>H<sub>18</sub>N<sub>4</sub>F<sub>3</sub>Li)<sub>n</sub>: C, 70.9; H, 3.8; N, 11.8; Li, 1.5. Found: C, 69.1; H, 4.4; N, 11.4; Li, 2.2.

**sCF3-TFPB**, **Li-sCF3-TFPB**, **diCF3-TFPB** and **Li-diCF3-TFPB** COFs were synthesized following the procedure similar to that described above for **sCF3-TB** and **Li-sCF3-TB**, using the same molar ratios and treatment conditions. Anal. Calcd for **sCF3-TFPB** (C<sub>40</sub>H<sub>31</sub>N<sub>4</sub>F<sub>3</sub>)<sub>n</sub>: C, 76.9; H, 5.0; N, 9.0. Found: C, 75.2; H, 4.9; N, 8.7. **Li-sCF3-TFPB**

(C<sub>40</sub>H<sub>30</sub>N<sub>4</sub>F<sub>3</sub>Li)<sub>n</sub>: C, 76.2; H, 4.8; N, 8.9; Li, 1.1. Found: C, 75.1; H, 4.5; N, 8.7; Li, 1.9.  
**diCF3-TFPB** (C<sub>20</sub>H<sub>13</sub>N<sub>3</sub>F<sub>3</sub>)<sub>n</sub>: C, 68.2; H, 3.7; N, 11.9. Found: C, 64.9; H, 4.1; N, 10.4.  
**Li-diCF3-TFPB** (C<sub>20</sub>H<sub>12</sub>N<sub>3</sub>F<sub>3</sub>Li)<sub>n</sub>: C, 67.0; H, 3.4; N, 11.7; Li, 1.9. Found: C, 63.1; H, 4.0; N, 10.4; Li, 3.2.

*Electrochemical characterization:* All electrochemical measurements were conducted on ECC-PAT-Core electrochemical test cells (EL-Cell) at 20 °C using an Autolab potentiostat/galvanostat (PGSTAT302N) with a FRA32M module operated with Nova 1.11 software.

Conductivity measurements were carried out by lightly compressing Li-COF pellets between stainless steel current collectors. COF pellets were prepared by pressing about 30 mg of sample powder in a 13 mm die for 1 h with an applied pressure of 1.5 GPa. Propylene carbonate loading was conducted according to Hu et al. with an amount of approx. 6  $\mu$ L.<sup>[22]</sup> The same amount of liquid electrolyte (1.15 M LiPF<sub>6</sub> in EC/EMC/DMC) was added to the dry COF pellets in a second experiment. Resistance of the pellet was determined as the extrapolated high frequency intercept with the real x-axis of the Nyquist plot. According to equation 9.1, the conductivity of the pellets was calculated depending on the pellet's thickness  $L$ , the cross-sectional area  $A$  and the measured resistance  $R$ .

$$\sigma = \frac{L}{R \times A} \quad (9.1)$$

A detailed description of building block and COF synthesis as well as additional information about applied analytical methods can be found in the provided Supporting Information.

## 9.5 References

- [1] L. Ascherl, T. Sick, J. T. Margraf, S. H. Lapidus, M. Calik, C. Hettstedt, K. Karaghiosoff, M. Döblinger, T. Clark, K. W. Chapman, F. Auras, T. Bein, *Nat. Chem.* **2016**, *8*, 310–316.
- [2] M. S. Lohse, T. Bein, *Adv. Funct. Mater.* **2018**, *28*, 1705553.
- [3] C. S. Diercks, O. M. Yaghi, *Science* **2017**, *355*, eaal1585.
- [4] J. W. Colson, W. R. Dichtel, *Nat. Chem.* **2013**, *5*, 453–465.
- [5] S. Ivanova, E. Köster, J. J. Holstein, N. Keller, G. H. Clever, T. Bein, F. Beuerle, *Angew. Chem. Int. Ed.* **2021**, *60*, 17455–17463.
- [6] S. B. Kalidindi, R. A. Fischer, *Phys. Status Solidi B* **2013**, *250*, 1119–1127.
- [7] Y. Zeng, R. Zou, Y. Zhao, *Adv. Mater.* **2016**, *28*, 2855–2873.
- [8] D. Bessinger, K. Muggli, M. Beetz, F. Auras, T. Bein, *J. Am. Chem. Soc.* **2021**, *143*, 7351–7357.

- [9] N. Keller, D. Bessinger, S. Reuter, M. Calik, L. Ascherl, F. C. Hanusch, F. Auras, T. Bein, *J. Am. Chem. Soc.* **2017**, *139*, 8194–8199.
- [10] L. Ascherl, E. W. Evans, J. Gorman, S. Orsborne, D. Bessinger, T. Bein, R. H. Friend, F. Auras, *J. Am. Chem. Soc.* **2019**, *141*, 15693–15699.
- [11] D. Bessinger, L. Ascherl, F. Auras, T. Bein, *J. Am. Chem. Soc.* **2017**, *139*, 12035–12042.
- [12] S. Rager, M. Dogru, V. Werner, A. Gavryushin, M. Götz, H. Engelke, D. D. Medina, P. Knochel, T. Bein, *CrystEngComm* **2017**, *19*, 4886–4891.
- [13] J. M. Rotter, R. Guntermann, M. Auth, A. Mähringer, A. Sperlich, V. Dyakonov, D. D. Medina, T. Bein, *Chem. Sci.* **2020**, *11*, 12843–12853.
- [14] B. Nath, W.-H. Li, J.-H. Huang, G. E. Wang, Z.-h. Fu, M.-S. Yao, G. Xu, *CrystEngComm* **2016**, *18*, 4259–4263.
- [15] L. Wang, B. Dong, R. Ge, F. Jiang, J. Xu, *ACS Appl. Mater. Interfaces* **2017**, *9*, 7108–7114.
- [16] T. Sick, A. G. Hufnagel, J. Kampmann, I. Kondofersky, M. Calik, J. M. Rotter, A. Evans, M. Döblinger, S. Herbert, K. Peters, D. Böhm, P. Knochel, D. D. Medina, D. Fattakhova-Rohlfing, T. Bein, *J. Am. Chem. Soc.* **2018**, *140*, 2085–2092.
- [17] J. M. Rotter, S. Weinberger, J. Kampmann, T. Sick, M. Shalom, T. Bein, D. D. Medina, *Chem. Mater.* **2019**, *31*, 10008–10016.
- [18] Y. Zhang, J. Duan, D. Ma, P. Li, S. Li, H. Li, J. Zhou, X. Ma, X. Feng, B. Wang, *Angew. Chem. Int. Ed.* **2017**, *56*, 16313–16317.
- [19] H. Chen, H. Tu, C. Hu, Y. Liu, D. Dong, Y. Sun, Y. Dai, S. Wang, H. Qian, Z. Lin, L. Chen, *J. Am. Chem. Soc.* **2018**, *140*, 896–899.
- [20] Z. Shan, M. Wu, Y. Du, B. Xu, B. He, X. Wu, G. Zhang, *Chem. Mater.* **2021**, *33*, 5058–5066.
- [21] D. A. Vazquez-Molina, G. S. Mohammad-Pour, C. Lee, M. W. Logan, X. Duan, J. K. Harper, F. J. Uribe-Romo, *J. Am. Chem. Soc.* **2016**, *138*, 9767–9770.
- [22] Y. Hu, N. Dunlap, S. Wan, S. Lu, S. Huang, I. Sellinger, M. Ortiz, Y. Jin, S.-h. Lee, W. Zhang, *J. Am. Chem. Soc.* **2019**, *141*, 7518–7525.
- [23] M. Thommes, K. Kaneko, A. V. Neimark, J. P. Olivier, F. Rodriguez-Reinoso, J. Rouquerol, K. S. Sing, *Pure Appl. Chem.* **2015**, *87*, 1051–1069.

## 9.6 Supporting Information

### A. Materials and Methods

**Nuclear magnetic resonance** (NMR) spectra were recorded on Bruker AV 400 and AV 400 TR spectrometers (400 MHz).

**Powder X-Ray diffraction** (PXRD) measurements were performed using a Bruker D8 Discover with Ni-filtered Cu K $_{\alpha}$  radiation and a LynxEye position-sensitive detector.

The initial **structure models of the COFs** were constructed using the Accelrys Materials Studio software package. Considering the symmetry of the building blocks, we applied the space group with highest possible symmetry. The structure models were optimized using the Forcite module with the Dreiding force-field. Unit cell parameters were determined using Pawley refinement of our PXRD data based on the proposed model.

The **nitrogen sorption** isotherms were recorded on a Quantachrome Autosorb 1 at 77 K in a pressure range from  $p/p_0 = 0.001$  to 0.98. Prior to the measurement of the sorption isotherm, the sample was heated for 24 h at 120 °C under turbomolecular pump vacuum. For the evaluation of the surface area, the BET model was applied between 0.05 and 0.2  $p/p_0$ . The calculation of the pore size distribution was done using the QSDFT equilibrium model with a carbon kernel for cylindrical pores on the adsorption branch.

**Scanning Electron Microscopy** (SEM) was carried out using a FEI Helios Nanolab G3 UC equipped with a Schottky-type field-emitter, an Oxford EDX detector and Ga+-focused ion beam, operated at 2 and 5 kV acceleration voltage.

**Transmission Electron Microscopy** (TEM) images were acquired on a FEI Titan Themis 80–300 microscope operated at 300 kV acceleration voltage, equipped with an X-FEG electron source, a monochromator, a C $_s$ -corrector and a HAADF detector.

## B. Building Block Syntheses

Unless stated otherwise, all reagents and solvents were purchased from commercial suppliers in high purity grades and were used without further purification. Typically, most reactions were performed in oven-dried glassware under argon atmosphere.

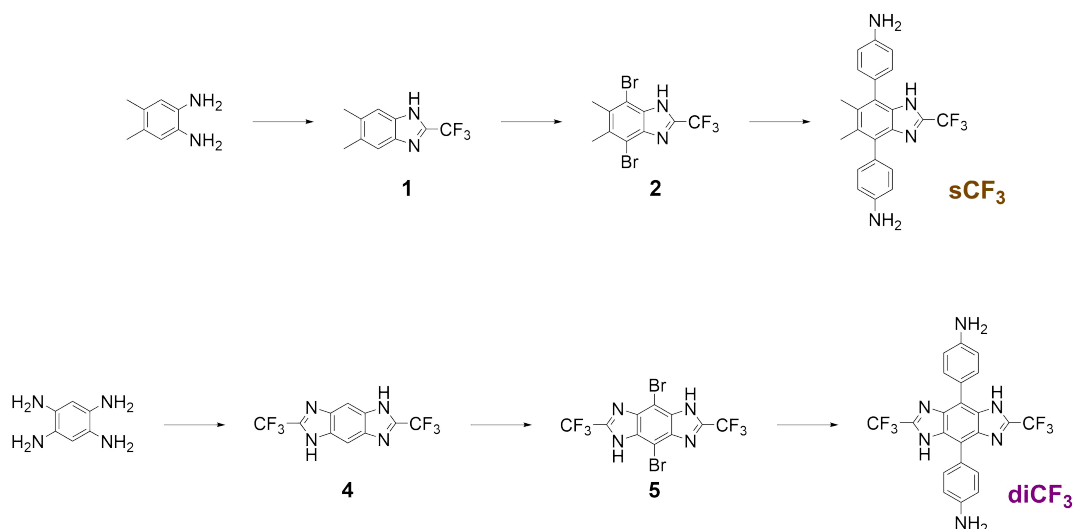
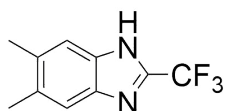


**Figure 9.5:** Schematic drawing for the synthesis of **sCF<sub>3</sub>** and **diCF<sub>3</sub>** building blocks.

### 5,6-dimethyl-2-(trifluoromethyl)-1H-benzimidazole (1)

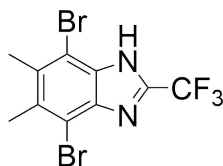


In a 100 mL round bottom flask, 4,5-dimethylbenzene-1,2-diamine (5.00 g, 37.3 mmol, 1.00 equiv.) was dissolved in trifluoroacetic acid (28 mL). The reaction was stirred at 70 °C for 16 h. After cooling to room temperature, surplus acid was removed by rotary evaporation and the residue was washed with water. Purification via column chromatography (silica gel, hexane : EtOAc, 1:1, v/v) yielding compound **1** (4.24 g, 19.8 mmol, 53 %) as a brown solid.

<sup>1</sup>H NMR (400 MHz, CDCl<sub>3</sub>): δ = 9.56 (s, 1H), 7.68 (s, 1H), 7.38 (s, 1H), 2.40 (s, 6H)

### 4,7-dibromo-5,6-dimethyl-2-(trifluoromethyl)-1H-benzimidazole (2)

Compound **1** (214 mg, 1 mmol, 1.00 equiv.) was placed into a 25 mL round bottom flask and dissolved in 48 % aqueous HBr solution (10 mL). Liquid bromine (0.15 mL, 3.00 mmol, 3.00 equiv.) was added in one portion and the reaction mixture was stirred

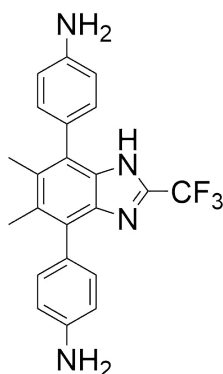


for 10 h under reflux. The mixture was allowed to cool to room temperature and afterwards poured on ice. A saturated solution of  $\text{Na}_2\text{SO}_3$  was added until pH 5. After vacuum filtration, washing with water and drying under high vacuum, compound **2** (313 mg, 0.84 mmol, 82 %) was obtained as a white solid.

$^1\text{H NMR}$  (400 MHz,  $\text{DMSO-d}_6$ ):  $\delta$  = 8.28 (s, 1H), 2.50 (s, 6H)

**MS (EI)**:  $m/z$  (%) = 372 (100), 353 (6), 291 (54), 271 (20), 191 (10), 117 (10), (calculated: 369.89)

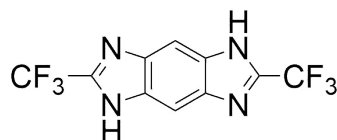
#### 4,7-di(4-aminophenyl)-5,6-dimethyl-2-(trifluoromethyl)-1H-benzimidazole (sCF3)



Under argon atmosphere, a 25 mL Schlenk flask was charged with compound **2** (38.0 mg, 0.640 mmol, 1.00 equiv.), 4-(4,4,5,5-tetramethyl-1,3,2-dioxaborolan-2-yl)aniline (309 mg, 1.41 mmol, 2.20 equiv.),  $\text{Pd}(\text{PPh}_3)_2\text{Cl}_2$  (45.0 mg, 0.064 mmol, 0.10 equiv.) and  $\text{K}_2\text{CO}_3$  (265 mg, 1.92 mmol, 3.00 equiv.). After adding water (0.80 mL) and dioxane (3.20 mL), the mixture was stirred for 20 h under reflux. After cooling to room temperature, the mixture was extracted with dichloromethane ( $3 \times 20$  mL), dried over  $\text{MgSO}_4$  and the organic solvents were removed through rotary evaporation. Purification via column chromatography (silica gel,  $\text{DCM} : \text{EtOAc}$ , 3:1, v/v  $\rightarrow$  EtOAc) yielded the linker **sCF3** (138 mg, 0.35 mmol, 55 %) as a pale yellow powder.

$^1\text{H NMR}$  (400 MHz,  $\text{CDCl}_3$ ):  $\delta$  = 7.27 (d,  $^3J$  = 7.8 Hz, 2H), 7.18 (d,  $^3J$  = 7.8 Hz, 2H), 6.84 (dd,  $^2J$  = 13.2 Hz,  $^3J$  = 7.7 Hz, 4H), 2.30 (d,  $^3J$  = 9.3 Hz, 6H)

**MS (EI)**:  $m/z$  (%) = 396 (100), 380 (6), 198 (4), (calculated: 396.16)

**2,6-bis(trifluoromethyl)-1,5-dihydrobenzo[1,2-d:4,5-d']diimidazole (4)**

Benzene-1,2,4,5-tetraamine tetrahydrochloride (600 mg, 2.11 mmol, 1.00 equiv.) was placed into a 25 mL round bottom flask and dissolved in trifluoroacetic acid (9.60 mL). The reaction mixture was stirred at 100 °C for 24 h. After cooling to room temperature the solution was poured into ice-cold water and neutralized with a saturated aqueous solution of K<sub>2</sub>CO<sub>3</sub>. After filtering and washing with cold water the resulting precipitate was dried under HV. Compound 4 (610 mg, 2.07 mmol, 98 %) was obtained as a white solid.

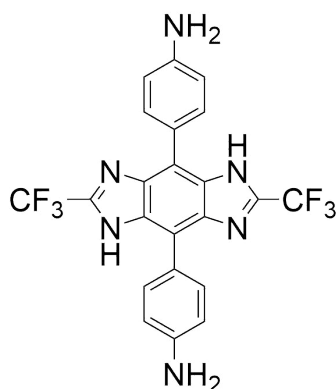
<sup>1</sup>H NMR (400 MHz, DMSO-d<sub>6</sub>): δ = 13.91 (s, 2H), 7.99 (s, 2H)

MS (EI): *m/z* (%) = 294 (100), 274 (35), 253 (54), 178 (10), (calculated: 294.03)

**4,8-dibromo-2,6-bis(trifluoromethyl)-1,5-dihydrobenzo[1,2-d:4,5-d']diimidazole (5)**

A 100 mL round bottom flask was charged with compound 4 (1251 mg, 4.25 mmol, 1.00 equiv.) and dissolved in 48 % aqueous HBr solution (42.5 mL). Liquid bromine (0.646 mL, 12.75 mmol, 3.00 equiv.) was added in one portion and the reaction mixture was stirred for 12 h under reflux. The mixture was cooled to room temperature and poured on ice. A saturated solution of Na<sub>2</sub>SO<sub>3</sub> was added for neutralization until pH 5. After vacuum filtration, washing with water and drying under high vacuum the desired product 5 (1127 mg, 2.49 mmol, 59 %) was received as a light brown solid. Due to low solubility of this compound in common deuterated solvents, a <sup>1</sup>H NMR spectrum could not be obtained.

MS (EI): *m/z* = 452 (100), 450 (47), 431(16), 411 (18), 304 (6), (calculated:449.86)



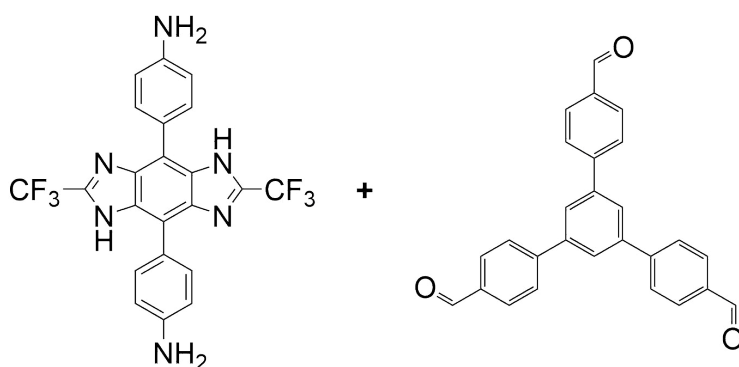
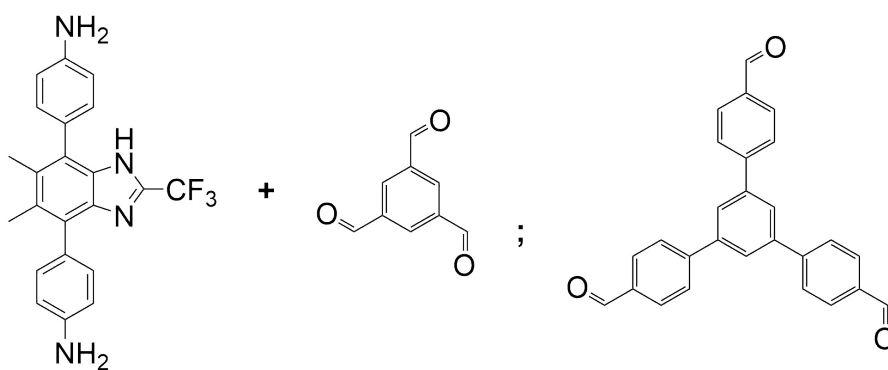
**4,4'-(2,6-bis(trifluoromethyl)-1,5-dihydrobenzo[1,2-d:4,5-d']diimidazole-4,8-diyl)dianiline (diCF3)**

Under inert conditions, a 25 mL round bottom flask was charged with compound **5** (1127 mg, 2.49 mmol, 1.00 equiv.), 4-(4,4,5,5-tetramethyl-1,3,2-dioxaborolan-2-yl)aniline (1200 mg, 5.48 mmol, 2.20 equiv.), Pd(PPh<sub>3</sub>)<sub>2</sub>Cl<sub>2</sub> (174.8 mg, 0.249 mmol, 0.10 equiv.) and K<sub>2</sub>CO<sub>3</sub> (1032 mg, 7.47 mmol, 3.00 equiv.). After adding water (3.06 mL) and dioxane (12.45 mL) the reaction mixture was stirred for 20 h under reflux. Solvents were removed by rotary evaporation. Purification via column chromatography (silica gel, DCM : EtOAc, 2:1 → EtOAc → Acetone) yielded **diCF3** (809 mg, 1.173 mmol, 47 %) as a red-brown powder.

**MS (EI):**  $m/z$  = 476 (100), 436 (5), 238 (3), (calculated: 476.12)

### C. Li-COF Syntheses

All COF syntheses were performed under argon atmosphere in PTFE-sealed glass reaction tubes (6 mL volume). Solvents and acetic acid were obtained in high purity grade from commercial suppliers and were, unless shipped under argon, degassed and saturated with argon prior to use.



### sCF3-TFPB COF

4,7-Di(4-aminophenyl)-5,6-dimethyl-2-(trifluoromethyl)-1H-benzimidazole (**sCF3**) (7.43 mg, 0.01875 mmol, 1.00 equiv.) and 1,3,5-Tris(p-formylphenyl)benzene (**TFPB**) (4.88 mg, 0.0125 mmol, 0.67 equiv.) were filled into a reaction tube, followed by the addition of mesitylene (187.5  $\mu\text{L}$ ), ethanol (62.5  $\mu\text{L}$ ), water (25  $\mu\text{L}$ ) and 6 M acetic acid (25  $\mu\text{L}$ ). The sealed tube was heated at 120  $^{\circ}\text{C}$  for three days. After cooling to room temperature, the product was collected by vacuum filtration, washed with tetrahydrofuran (THF) and further purified by supercritical  $\text{CO}_2$ -extraction, yielding the **sCF3-TFPB COF** as light yellow flakes (8.47 mg, 69 %).

### diCF3-TFPB COF

4,4'-(2,6-Bis(trifluoromethyl)-1,5-dihydrobenzo[1,2-d:4,5-d']diimidazole-4,8-diyl) dianiline (**diCF3**) (8.93 mg, 0.01875 mmol, 1.00 equiv.) and 1,3,5-tris(p-formylphenyl)benzene (**TFPB**) (4.88 mg, 0.0125 mmol, 0.67 equiv.) were filled into a reaction tube, followed by the addition of mesitylene (62.5  $\mu\text{L}$ ), ethanol (187.5  $\mu\text{L}$ ), water (25  $\mu\text{L}$ ) and 6 M acetic acid (25  $\mu\text{L}$ ). The sealed tube was heated at 120  $^{\circ}\text{C}$  for three days. After cooling to room temperature, the product was collected by vacuum filtration, washed with tetrahydrofuran (THF) and further purified by supercritical  $\text{CO}_2$ -extraction, yielding the **diCF3-TFPB COF** as light yellow flakes (8.47 mg, 69 %).

### COF-Lithiation

A 25 mL Schlenk flask was charged with **COF** (130 mg), which was well-dispersed in hexane (5.5 mL). The reaction mixture was cooled with an ice bath, while a 2.5 M solution of *n*-butyllithium in hexane (0.35 mL) was added slowly drop wise. The mixture was stirred at room temperature overnight. The resulting solid was vacuum filtrated and dried with vacuum. **Li-COF** was obtained as a yellow powder (120 mg, 95 %).

### D. X-Ray Diffraction Analysis

Determination of the unit cell size was additionally calculated with Bragg's equation, where  $n$  is the order of reflection,  $\lambda$  is the incident wavelength,  $d$  is the plane spacing and  $\theta$  the bragg angle between incident ray and the planes.<sup>[1]</sup>

$$n\lambda = 2d\sin(\theta) \quad (9.2)$$

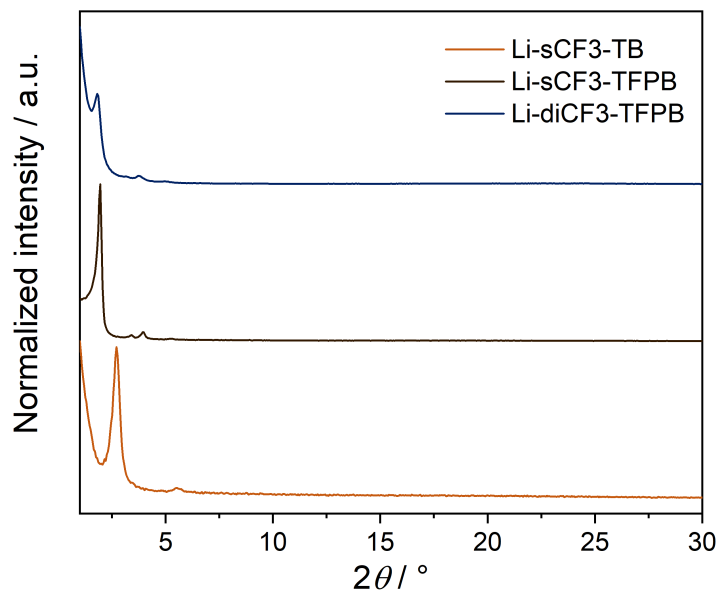


Figure 9.6: PXRD patterns of Li-sCF3-TB, Li-sCF3-TFPB and Li-diCF3-TFPB.

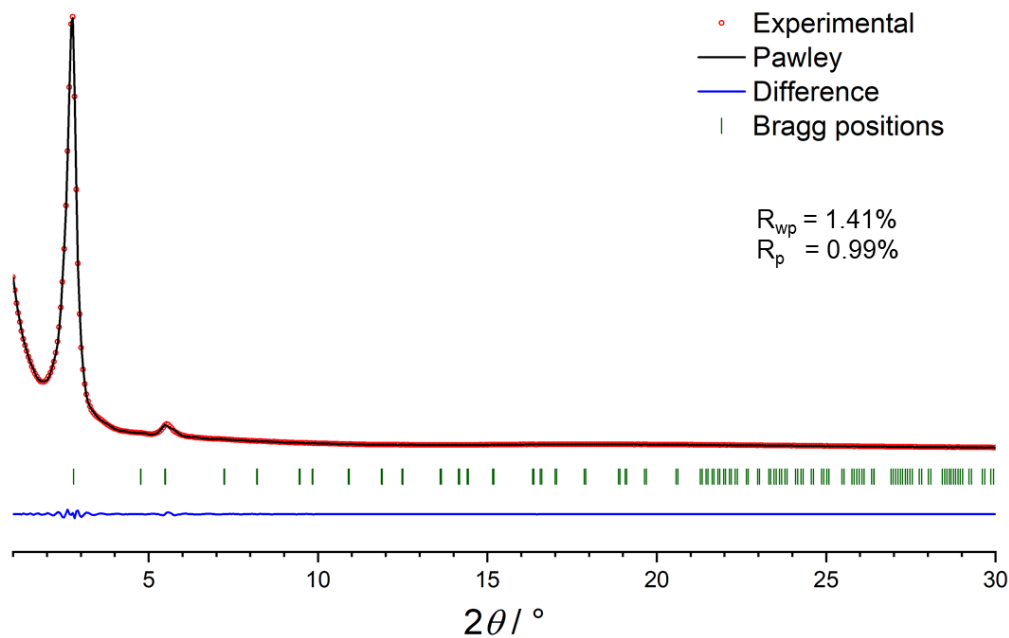
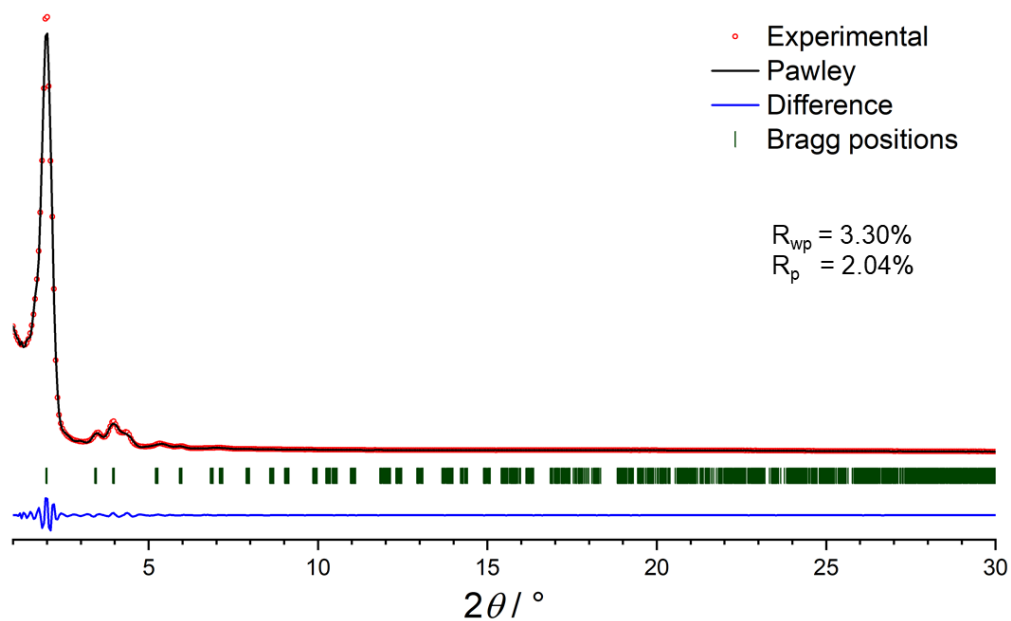
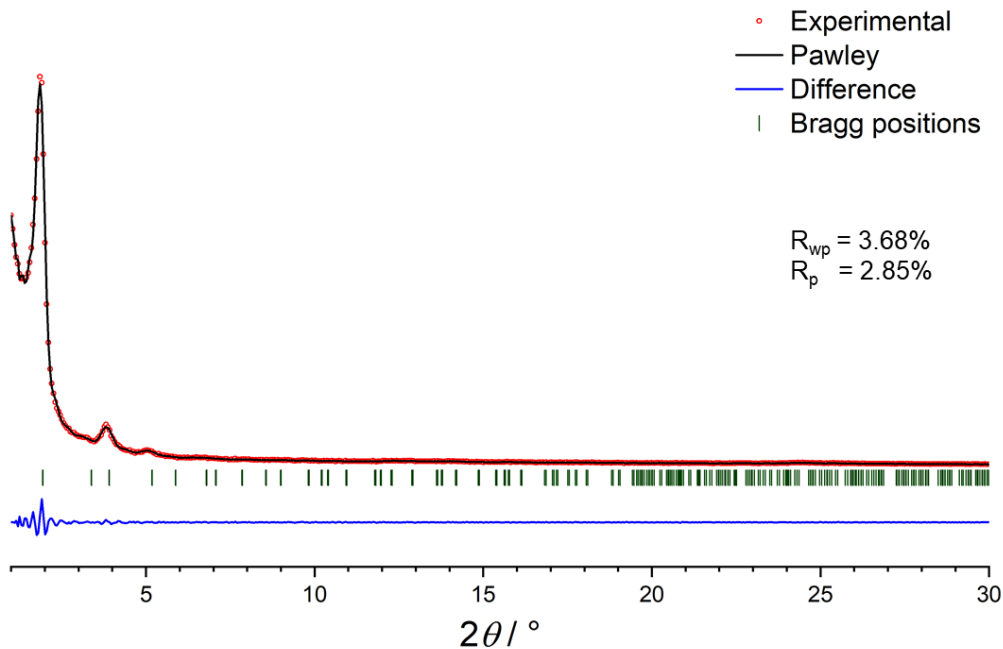


Figure 9.7: Pawley refinement of sCF3-TB COF. Experimental (red), Pawley refined simulation (black), difference (blue) and Bragg positions (olive) show good agreement of experimental and simulated PXRD patterns.



**Figure 9.8:** Pawley refinement of **sCF3-TFPB COF**. Experimental (red), Pawley refined simulation (black), difference (blue) and Bragg positions (olive) show good agreement of experimental and simulated PXRD patterns.



**Figure 9.9:** Pawley refinement of **diCF3-TFPB COF**. Experimental (red), Pawley refined simulation (black), difference (blue) and Bragg positions (olive) show good agreement of experimental and simulated PXRD patterns.

## E. Nitrogen Sorption

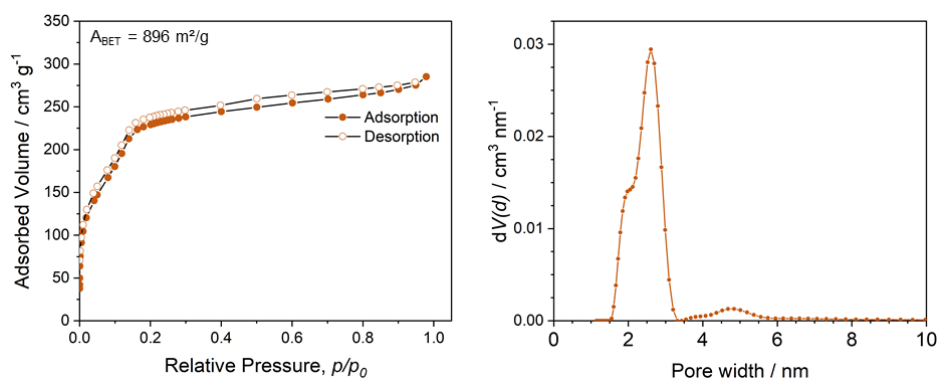


Figure 9.10: Nitrogen sorption isotherm of sCF3-TB recorded at 77 K (left). Fitting of isotherm with a QSDFT equilibrium model for cylindrical pores (right).

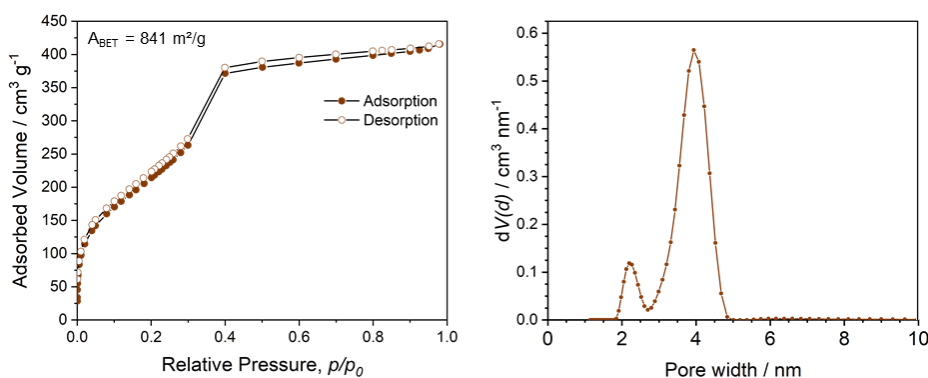


Figure 9.11: Nitrogen sorption isotherm of sCF3-TFPB recorded at 77 K (left). Fitting of isotherm with a QSDFT equilibrium model for cylindrical pores (right).

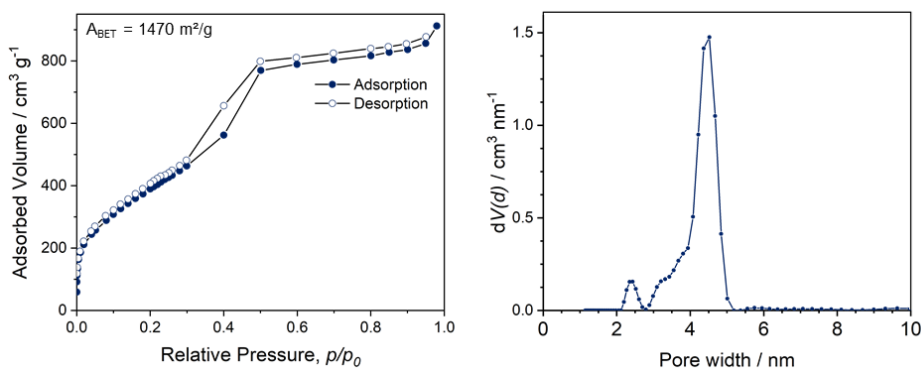
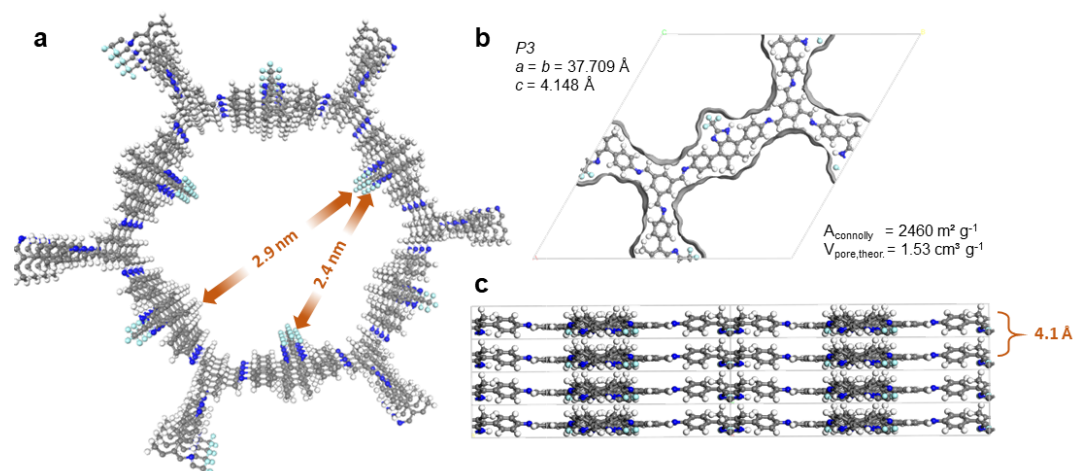


Figure 9.12: Nitrogen sorption isotherm of diCF3-TFPB recorded at 77 K (left). Fitting of isotherm with a QSDFT equilibrium model for cylindrical pores (right).

## F. COFs Structural Simulations



**Figure 9.13:** Illustration of the Pawley refined **sCF3-TB** structure viewed along the *c*-axis (a) showing the pore structure and distances between different moieties. Unit cell viewed perpendicular to the crystallographic *a-b* plane (b). The COF shows *P3* symmetry with AA-stacked layers with a distance of 4.1 Å (c).

**Table 9.1:** Fractional atomic coordinates of **sCF3-TB** unit cell.

sCF3-TB COF (space symmetry <i>P3</i> )				
a = b = 37.7093 Å, c = 4.1484 Å				
$\alpha = \beta = 90^\circ, \gamma = 120^\circ$				
No.	Name	x	y	z
1	C1	1.39355	0.84106	0.25736
2	C2	1.30161	0.67861	0.36862
3	C3	1.34363	0.70723	0.36918
4	C4	1.35725	0.75136	0.36995
5	H5	1.27976	0.68932	0.36803
6	C6	1.41202	0.82201	0.42389
7	C7	1.41129	0.88364	0.26356
8	C8	1.44728	0.90800	0.43918
9	C9	1.46590	0.88880	0.59995
10	C10	1.44862	0.84630	0.59006
11	C11	1.46689	0.95350	0.44257
12	C12	1.50771	0.97708	0.34583
13	C13	1.46841	1.01922	0.54706
14	H14	1.36614	0.82344	0.11561

9 Expansion of Li-conductive Imidazolate-COF family

---

No.	Name	x	y	z
15	H15	1.33451	0.76063	0.34070
16	H16	1.39666	0.89754	0.13348
17	H17	1.49405	0.90677	0.73132
18	H18	1.46353	0.83215	0.71599
19	N19	1.53406	0.96382	0.21891
20	C20	1.40234	0.95258	0.65437
21	H21	1.46553	1.07478	0.66832
22	H22	1.38794	0.91900	0.65160
23	N24	1.39542	0.77846	0.42008
24	C25	1.59920	1.14821	0.60505
25	C26	1.67591	1.30147	0.39814
26	C27	1.63373	1.28776	0.39857
27	C28	1.60307	1.24367	0.39776
28	H29	1.68647	1.27950	0.39717
29	C30	1.58691	1.17285	0.44386
30	C31	1.57395	1.10570	0.61035
31	C32	1.53599	1.08691	0.45079
32	C33	1.52436	1.11161	0.28027
33	C34	1.54933	1.15418	0.27811
34	C35	1.51029	1.04144	0.44677
35	C36	1.52814	1.01870	0.34526
36	C37	1.44657	0.97512	0.54331
37	H38	1.62829	1.16209	0.73036
38	H39	1.57108	1.23457	0.36989
39	H40	1.58411	1.08746	0.73908
40	H41	1.49582	1.09798	0.15011
41	H42	1.53960	1.17211	0.13984
42	N43	1.56813	1.03396	0.21495
43	C44	1.44647	1.04118	0.66559
44	H45	1.40030	0.96122	0.90614
45	H46	1.52943	0.93425	0.19822
46	H47	1.43586	1.03184	0.91663
47	H48	1.41972	1.03348	0.50908
48	N49	1.61399	1.21639	0.44352
49	C50	1.57032	1.00154	0.14374
50	C51	1.60701	1.00370	0.13452
51	F52	1.62665	1.03850	0.20228
52	F53	1.59500	0.96953	0.20460
53	F54	1.63388	1.00501	0.21851

---

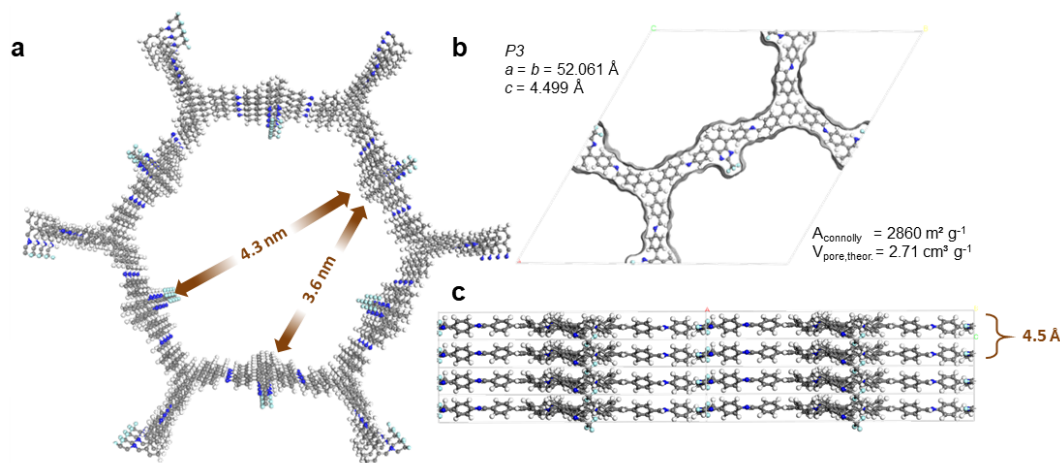


**Figure 9.14:** Illustration of the Pawley refined **sCF3-TFPB** structure viewed along the *c*-axis (a) showing the pore structure and distances between different moieties. Unit cell viewed perpendicular to the crystallographic *a*-*b* plane (b). The COF shows *P3* symmetry with AA-stacked layers with a distance of 4.5 Å (c).

**Table 9.2:** Fractional atomic coordinates of **sCF3-TFPB** unit cell.

<b>sCF3-TFPB</b> COF (space symmetry <i>P3</i> )				
$a = b = 52.0613 \text{ \AA}, c = 4.4993 \text{ \AA}$				
$\alpha = \beta = 90^\circ, \gamma = 120^\circ$				
No.	Name	x	y	z
1	C1	0.63423	0.31324	0.57695
2	C2	0.65315	0.30099	0.57638
3	C3	0.37168	0.64146	0.57291
4	C4	0.36538	0.61573	0.73757
5	C5	0.38431	0.60372	0.72801
6	C6	0.41071	0.61758	0.55943
7	C7	0.41761	0.64358	0.39992
8	C8	0.39819	0.65501	0.40314
9	C9	0.42999	0.60606	0.54824
10	N10	0.41929	0.57651	0.53138
11	H11	0.40361	0.67560	0.26734
12	C12	0.43478	0.56201	0.52920
13	C13	0.42408	0.53645	0.35103
14	C14	0.43965	0.52087	0.33294
15	C15	0.46572	0.52964	0.50168
16	C16	0.47579	0.55494	0.68647
17	C17	0.46083	0.57115	0.69742

9 Expansion of Li-conductive Imidazolate-COF family

---

No.	Name	x	y	z
18	C18	0.48159	0.51413	0.48713
19	C19	0.51294	0.52918	0.46415
20	C20	0.52935	0.51454	0.46819
21	N21	0.53201	0.55806	0.41430
22	C22	0.56031	0.56241	0.33573
23	N23	0.55798	0.53536	0.43305
24	C24	0.58791	0.59186	0.43127
25	F25	0.58659	0.61556	0.31456
26	F26	0.59074	0.59588	0.73070
27	H27	0.45501	0.62170	0.55335
28	H28	0.40262	0.52841	0.22079
29	H29	0.43133	0.50078	0.18043
30	H30	0.49639	0.56251	0.82995
31	H31	0.46972	0.59179	0.84276
32	C32	0.68411	0.32099	0.57695
33	C33	0.69637	0.35216	0.57638
34	H34	0.37838	0.58263	0.85708
35	H35	0.34447	0.60475	0.87982
36	C36	0.67636	0.36312	0.57695
37	C37	0.64520	0.34421	0.57638
38	C38	0.62568	0.35589	0.57291
39	C39	0.63197	0.38163	0.73757
40	C40	0.61305	0.39363	0.72801
41	C41	0.58664	0.37978	0.55943
42	C42	0.57975	0.35377	0.39992
43	C43	0.59917	0.34234	0.40314
44	C44	0.56737	0.39129	0.54824
45	N45	0.57807	0.42084	0.53138
46	H46	0.60930	0.29713	0.57791
47	H47	0.59375	0.32175	0.26734
48	H48	0.55828	0.34183	0.26687
49	C49	0.56257	0.43534	0.52920
50	C50	0.57327	0.46090	0.35103
51	C51	0.55771	0.47648	0.33294
52	C52	0.53163	0.46771	0.50168
53	C53	0.52156	0.44241	0.68647
54	C54	0.53653	0.42621	0.69742
55	C55	0.51576	0.48323	0.48713
56	C56	0.48441	0.46817	0.46415
57	C57	0.46801	0.48281	0.46819
58	C58	0.46534	0.43929	0.41430

---

---

No.	Name	x	y	z
59	H59	0.54235	0.37566	0.55335
60	H60	0.59474	0.46894	0.22079
61	H61	0.56603	0.49658	0.18043
62	H62	0.50096	0.43485	0.82995
63	H63	0.52764	0.40557	0.84276
64	H64	0.70022	0.31217	0.57791
65	C65	0.31324	0.67636	0.57695
66	C66	0.35216	0.65315	0.57638
67	H67	0.68519	0.38805	0.57791
68	H68	0.61898	0.41473	0.85708
69	H69	0.65289	0.39261	0.87982
70	H70	0.47440	0.42541	0.51702
71	H71	0.46245	0.43506	0.16467
72	H72	0.44298	0.43290	0.51890
73	C73	0.45540	1.48054	0.49693
74	H74	0.45075	1.45718	0.54977
75	H75	0.43361	1.48074	0.49076
76	H76	0.47042	1.49651	0.67568
77	H77	0.52451	0.57452	0.43724
78	F78	0.60858	0.59225	0.34153
79	H79	0.64432	0.27605	0.57549
80	H80	0.72130	0.36827	0.57549
81	H81	0.43908	0.65552	0.26687
82	H82	0.29802	0.68623	0.57791

---

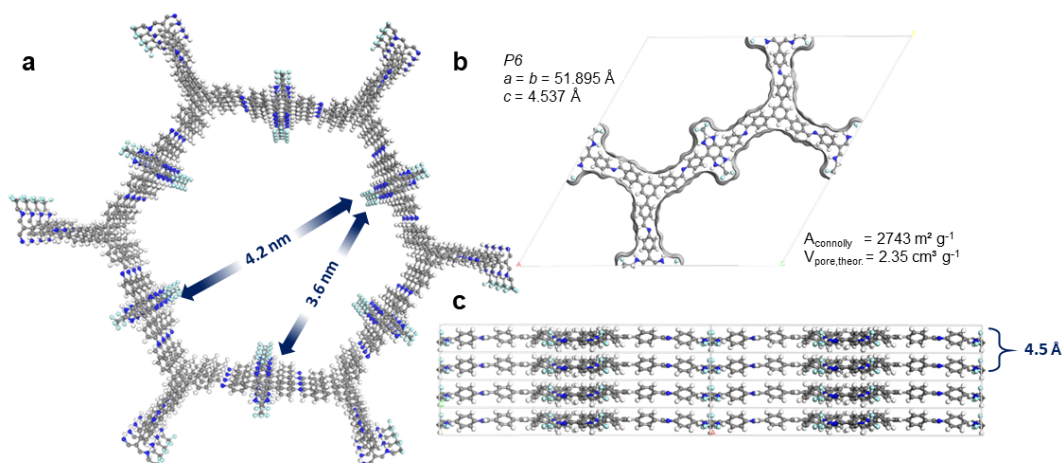


**Figure 9.15:** Illustration of the Pawley refined diCF3-TFPB structure viewed along the  $c$ -axis (a) showing the pore structure and distances between different moieties. Unit cell viewed perpendicular to the crystallographic  $a$ - $b$  plane (b). The COF shows a  $P6$  symmetry with AA-stacked layers with a distance of 4.5 Å(c).

**Table 9.3:** Fractional atomic coordinates of diCF3-TFPB unit cell.

diCF3-TFPB COF (space symmetry $P6$ )				
$a = b = 51.8950 \text{ \AA}$ , $c = 4.5365 \text{ \AA}$				
$\alpha = \beta = 90^\circ$ , $\gamma = 120^\circ$				
No.	Name	x	y	z
1	C1	0.63627	0.31425	0.57222
2	C2	0.65524	0.30195	0.57166
3	C3	0.37287	0.64352	0.56822
4	C4	0.36655	0.61770	0.73152
5	C5	0.38554	0.60566	0.72205
6	C6	0.41203	0.61955	0.55484
7	C7	0.41895	0.64564	0.39665
8	C8	0.39946	0.65711	0.39984
9	C9	0.43137	0.60801	0.54375
10	N10	0.42063	0.57836	0.52703
11	H11	0.38680	0.70040	0.57218
12	H12	0.40495	0.67551	0.27403
13	H13	0.43802	0.65630	0.27373
14	H14	0.41371	0.79370	0.84143
15	H15	0.39323	0.74125	0.86189
16	C16	0.43618	0.56381	0.52487
17	C17	0.42544	0.53817	0.34816

---

No.	Name	x	y	z
18	C18	0.44105	0.52254	0.33021
19	C19	0.46722	0.53134	0.49757
20	C20	0.47732	0.55672	0.68085
21	C21	0.46230	0.57297	0.69170
22	C22	0.48314	0.51577	0.48314
23	C23	0.51458	0.53088	0.46034
24	C24	0.53104	0.51619	0.46435
25	N25	0.53372	0.55985	0.41091
26	C26	0.56211	0.56421	0.33298
27	N27	0.55976	0.53707	0.42950
28	C28	0.58980	0.59376	0.42773
29	F29	0.58847	0.61753	0.31199
30	F30	0.59263	0.59778	0.72471
31	F31	0.61524	0.59481	0.32609
32	H32	0.45386	0.62239	0.53671
33	H33	0.40643	0.53100	0.22665
34	H34	0.43317	0.50487	0.18899
35	H35	0.49577	0.56366	0.81052
36	H36	0.47034	0.59127	0.82511
37	H37	0.52831	0.57523	0.40392
38	H38	0.56222	0.56328	0.09317
39	H39	0.57635	0.53346	0.44025

---

## References

- [1] W. L. Bragg, W. H. Bragg, *Proc. Math. Phys* **1913**, 89, 248–277.



## 10 Conclusions and Outlook

In this thesis, innovative ways of interface engineering for energy conversion and energy storage applications are presented. Especially the interface between two different phases plays a crucial role in the context of efficient charge carrier transfer. A wide variety of materials were investigated regarding their electrochemical performance and stability under working conditions. The change of surface area by nanostructuring and the modification of the surface by ultrathin corrosion-stable films led to a strong increase in device life-time and overall-efficiency.

For the deposition of these thin and conformal films, atomic layer deposition was utilized due to its unique properties, enabling the homogeneous coating of nanostructured high-aspect-ratio surfaces. The film thickness can be tuned depending on the desired application by variation of the ALD cycles. For example in Chapter 3, a conductive and corrosion-stable NTO layer with a thickness of around 60 nm was applied on an inexpensive carbon soot template followed by ALD of a sub-nanometer thin IrO<sub>2</sub> catalyst layer for the acidic oxygen evolution reaction. This concept allows the optimal utilization of the rare noble metal due to the high dispersion on a corrosion-stable high surface-area support material and shows a promising way for the reduction of catalyst loading.

Potential IrO<sub>2</sub> catalyst substitutes made from carbon-based materials were reviewed in Chapter 4, showing good values for the alkaline-based oxygen evolution reaction. However, in acidic environments only poor stability could be observed for most materials, leaving IrO<sub>2</sub> as one of the most desired catalysts for proton exchange membrane electrolysis.

In the context of photoelectrochemical water-splitting, stability and efficiency of photoelectrodes are still serious issues. Based on detailed studies on the corrosion mechanisms of the electrodes, we could design a protection concept, again using ALD, described in Chapters 5 and 6. The application of a corrosion-stable and dense, but still charge carrier permeable film and the subsequent coating with a catalyst yielded efficiencies near the theoretical maximum and increased the stability under working conditions. However, for commercial applications of PEC water-splitting, there are still some steps to go. Although extended, the stability is still significantly too low. At least a factor of 1000 would be necessary for this approach to be really relevant for industry. Additionally, the efficiency of hydrogen production is still too low; photovoltaic cells coupled to an electrolyzer are significantly better and more attractive due to the possible modular design.

A similar protection concept was also applied for a cathode battery material, described in Chapter 8. The atomic layer deposited film keeps the active material together

during intercalation and extraction of lithium and thereby prevents cation leaching and contact losses caused by pulverisation of the compound.

ALD has proven to be a perfect tool for the protection and functionalization of different materials. It has been shown that both thickness and composition play an important role and have to be optimized for every targeted material. So far, many different precursors for various target compounds are available for ALD. However, the low amount of deposited material make the accurate analysis of the resulting films challenging. Especially, for not completely irreversible gas-solid reactions or very slow reaction kinetics, impurities can't be excluded and create a significant challenge for the synthesis of totally new materials. Highly desirable insight into the growth characteristics and mechanisms can be obtained by the implementation of already existing *in-situ* techniques.

The last section of this thesis was dedicated to the emerging material class of covalent organic frameworks. Here, we enlarged the family of imidazolate-containing covalent organic frameworks for the use as lithium-ion electrolytes by elongation and functional group doubling in the linking building blocks. The concept appears to be promising to be able to change the optical and physical properties by exchanging functional building blocks. So far, COFs play virtually no role in commercial applications in practice. The macrostructure in particular plays a major role in energy conversion applications, where grain boundaries and domain sizes lead to additional resistances that can obstruct the charge carrier "highways" through the pore structure. Therefore it would be attractive to obtain pure single crystallites with micrometer size to study the underlying conduction mechanism inside the pores and build pure COF devices without any necessary additives. The absence of rare or environmentally problematic elements makes COFs an extremely interesting material class for sustainable energy conversion applications, but some key issues such as processability or suitable (opto)electronic properties still need to be resolved in order to move these materials closer to applications.

In conclusion, this thesis evaluates the ability to functionalize the surface of already existing, highly active energy conversion materials by ALD and to protect them against parasitic corrosion reactions to achieve an increased device life-time. New design concepts of parts or whole devices for the oxygen evolution reaction, PEC water-splitting and electrochemical energy storage are presented. All in all, the presented work highlights the importance of better utilization of existing materials, the development of innovative preparation ways and the search for new materials for a better and sustainable future.

# Publications and Conference Contributions

## Publications

- 1) *2D/3D Hybrid Cs<sub>2</sub>AgBiBr<sub>6</sub> Double Perovskite Solar Cells: Improved Energy Level Alignment for Higher Contact-Selectivity and Large Open Circuit Voltage*  
Sirtl M. T., Hooijer, R., Armer, M. M., Ebadi, F. G., Mohammadi, M., Maheu, C., Weis, A., Gorkom van, B. T., Häringer, S., Jansen, R. A. J., Mayer, T., Dyakonov, V., Tress, W. and Bein, T.  
*Adv. Energy Mater.* **2022**, *12*, 2103215.
- 2) *Ultra-Thin Protective Coatings for Sustained Photoelectrochemical Water Oxidation with Mo:BiVO<sub>4</sub>*  
Beetz, M., Häringer, S., Elsässer, P., Kampmann, J., Sauerland, L., Wolf, F., Günther, M., Fischer, A. and Bein, T.  
*Adv. Funct. Mater.* **2021**, *31*, 2011210.
- 3) *Overcoming the Challenges of Freestanding Tin Oxide-Based Composite Anodes to Achieve High Capacity and Increased Cycling Stability*  
Zoller, F., Häringer, S., Böhm, D., Illner, H., Döblinger, M., Sofer, Z., Finsterbusch, M., Bein, T. and Fattakhova-Rohlfing, D.  
*Adv. Funct. Mater.* **2021**, *31*, 2106373.
- 4) *Carbonaceous Oxygen Evolution Reaction Catalysts: From Defect and Doping-Induced Activity over Hybrid Compounds to Ordered Framework Structures*  
Zoller, F., Häringer, S., Böhm, D., Luxa, J., Sofer, Z. and Fattakhova-Rohlfing, D.  
*Small* **2021**, 2007484.
- 5) *Nanocellulose-Mediated Transition of Lithium-Rich Pseudo-Quaternary Metal Oxide Nanoparticles into Lithium Nickel Cobalt Manganese Oxide (NCM) Nanostructures*  
Zehetmaier, P. M., Zoller, F., Beetz, M., Plaß, M. A., Häringer, S., Böller, B., Döblinger, M., Bein, T. and Fattakhova-Rohlfing, D.  
*ChemNanoMat* **2020**, *6*, 618.
- 6) *How photocorrosion can trick you: a detailed study on low-bandgap Li doped CuO photocathodes for solar hydrogen production*  
Kampmann, J., Betzler, S., Hajiyani, H., Häringer, S., Beetz, M., Harzer, T., Kraus, J., Lotsch, B. V., Scheu, C., Pentcheva, R., Fattakhova-Rohlfing, D. and Bein, T.  
*Nanoscale* **2020**, *12*, 7766-7775.

- 7) *Carbon-templated conductive oxide supports for oxygen evolution catalysis*  
Hufnagel, A. G., Häring, S., Beetz, M., Böller, B., Fattakhova-Rohlfing, D. and Bein, T.  
*Nanoscale* **2019**, *11*, 14285-14293.
- 8) *Electron-Blocking and Oxygen Evolution Catalyst Layers by Plasma-Enhanced Atomic Layer Deposition of Nickel Oxide*  
Hufnagel, A. G., Henß, A.-K., Hoffmann, R., Zeman, O. E. O., Häring, S., Fattakhova-Rohlfing, D. and Bein, T.  
*Adv. Mater. Interfaces* **2018**, *5*, 1701531.
- 9) *Protection of Lithium Cobalt Oxide by Atomic Layer Deposition of LiNbO<sub>3</sub> for high-voltage cycling*  
Häring, S., Zoller, F., Schmidt, Q., Illner, H., Döblinger, M., Fattakhova-Rohlfing, D. and Bein, T.  
**2023**, in preparation.
- 10) *Expansion of the Li-conductive Imidazolate-COF family and the challenges in electrochemical property determination*  
Häring, S., Reuter, S., Schmidt, Q., Zoller, F., Meier, V. and Bein, T.  
**2023**, in preparation.

## Presentations

### Oral Presentations

- 1) *Katalysatorsynthese/-charakterisierung – Upscaling of macroporous TiO<sub>2</sub> microparticle support*  
Häring, S., Böhm, D., Beetz, M., Fattakhova-Rohlfing, D., and Bein, T.  
BMBF Kopernikus project Power-2-X – FC-A1 Cluster Meeting at Bayerisches Zentrum für Angewandte Energieforschung e. V. (ZAE Bayern), **2019**, Garching, Germany.
- 2) *Katalysatorsynthese/-charakterisierung – Upscaling the synthesis of oxide supported IrO<sub>x</sub> OER catalyst*  
Häring, S., Böhm, D., Beetz, M., Fattakhova-Rohlfing, D., and Bein, T.  
BMBF Kopernikus project Power-2-X – FC-A1 Cluster Meeting at Technical University (TU) Munich, **2019**, Garching, Germany.
- 3) *Katalysatorsynthese/-charakterisierung – Electrospinning of Transparent Conductive Oxides as OER catalyst support*  
Häring, S., Böhm, D., Beetz, M., Fattakhova-Rohlfing, D., and Bein, T.  
BMBF Kopernikus project Power-2-X – FC-A1 Cluster Meeting, **2020**, online.

- 
- 4) *Improved Stability of Photoelectrodes by Ultra-thin Protection Layers for Photoelectrochemical Water-Splitting*  
Häringer, S., Beetz, M. and Bein, T.  
Soltech LMU Keylab workshop, 2020, online.

### Poster Presentations

- 1) *Carbon templated Nb:TiO<sub>2</sub> nanostructures as oxygen evolution catalyst supports for PEM electrolyzers*  
Häringer, S., Böhm, D., Beetz, M., Hufnagel, A. G., Fattakhova-Rohlfing, D., and Bein, T.  
Nanosystems Initiative Munich (NIM) summer-school, 2017, Beilngries, Germany.
- 2) *Carbon templated conductive oxides as oxygen evolution catalyst supports for PEM electrolyzers*  
Häringer, S., Hufnagel, A. G., Beetz, M., Fattakhova-Rohlfing, D., and Bein, T.  
E-MRS Fall Meeting, 2018, Warsaw, Poland.
- 3) *Development of nanosized OER catalysts and high surface area conductive oxide supports*  
Hufnagel, A. G., Böhm, D., Beetz, M., Häringer, S., Fattakhova-Rohlfing, D., and Bein, T.  
BMBF "Power-2-X Tag" Meeting, 2018, Frankfurt am Main, Germany.
- 4) *Development of nanosized OER catalysts and high surface area conductive oxide supports*  
Häringer, S., Böhm, D., Beetz, M., Hufnagel, A. G., Fattakhova-Rohlfing, D., and Bein, T.  
BMBF "Power-2-X Tag" Meeting, 2019, Frankfurt am Main, Germany.
- 5) *Development of nanosized OER catalysts and high surface area conductive oxide supports*  
Häringer, S., Kost, M., Böhm, D., Beetz, M., Fattakhova-Rohlfing, D., and Bein T.  
BMBF "Power-2-X Tag" Meeting, 2020, Frankfurt am Main, Germany.
- 6) *Development of electrospun doped titanium oxide supports for OER catalysis*  
M. Kost, Häringer, S. and Bein T.  
BMBF "Power-2-X Tag" Meeting, 2021, online.